Quantifying uplift and denudation of a thermally heterogeneous crust; a detailed multi-thermochronometeric study of central west Britain

Katarzyna Łuszczak
B.Sc. (Hons.)

Submitted in fulfilment of the requirements for the
Degree of Doctor of Philosophy (Ph.D.)

School of Geographical and Earth Sciences
College of Science and Engineering
University of Glasgow

June, 2016

Abstract

Topography is often thought as exclusively linked to mountain ranges formed by plates collision. It is now, however, known that apart from compression, uplift and denudation of rocks may be triggered by rifting, like it happens at elevated passive margins, and away from plate boundaries by both intra-plate stress causing reactivation of older structures, and by epeirogenic movements driven by mantle dynamics and initiating long-wavelength uplift. In the Cenozoic, central west Britain and other parts of the North Atlantic margins experienced multiple episodes of rock uplift and denudation that have been variable both at spatial and temporal scales. The origin of topography in central west Britain is enigmatic, and because of its location, it may be related to any of the processes mentioned above.

In this study, three low temperature thermochronometers, the apatite fission track (AFT) and apatite and zircon (U-Th-Sm)/He (AHe and ZHe, respectively) methods were used to establish the rock cooling history from 200°C to 30°C. The samples were collected from the intrusive rocks in the high elevation, high relief regions of the Lake District (NW England), southern Scotland and northern Wales. AFT ages from the region are youngest (55–70 Ma) in the Lake District and increase northwards into southern Scotland and southwards in north Wales (>200 Ma). AHe and ZHe ages show no systematic pattern; the former range from 50 to 80 Ma and the latter tend to record the post-emplacement cooling of the intrusions (200–400 Ma).

The complex, multi-thermochronometric inverse modelling suggests a ubiquitous, rapid Late Cretaceous/early Palaeogene cooling event that is particularly marked in Lake District and Criffell. The timing and rate of cooling in southern Scotland and in northern Wales is poorly resolved as the amount of cooling was less than 60°C. The Lake District plutons were at >110°C prior to the early Palaeogene; cooling due to a combined effect of high heat flow, from the heat producing granite batholith, and the blanketing effect of the overlying low conductivity Late Mesozoic limestones and mudstones. Modelling of the heat transfer suggests that this combination produced an elevated geothermal gradient within the sedimentary rocks (50–70°C/km) that was about two times higher

than at the present day. Inverse modelling of the AFT and AHe data taking the crustal structure into consideration suggests that denudation was the highest, 2.0–2.5 km, in the coastal areas of the Lake District and southern Scotland, gradually decreasing to less than 1 km in the northern Southern Uplands and northern Wales.

Both the rift-related uplift and the intra-plate compression poorly correlate with the timing, location and spatial distribution of the early Palaeogene denudation. The pattern of early Palaeogene denudation correlates with the thickness of magmatic underplating, if the changes of mean topography, Late Cretaceous water depth and eroded rock density are taken into consideration. However, the uplift due to underplating alone cannot fully justify the total early Palaeogene denudation. The amount that is not explained by underplating is, however, roughly spatially constant across the study area and can be referred to the transient thermal uplift induced by the mantle plume arrival. No other mechanisms are required to explain the observed pattern of denudation. The onset of denudation across the region is not uniform. Denudation started at 70–75 Ma in the central part of the Lake District whereas the coastal areas the rapid erosion appears to have initiated later (65–60 Ma). This is ∼10 Ma earlier than the first volcanic manifestation of the proto-Iceland plume and favours the hypothesis of the short period of plume incubation below the lithosphere before the volcanism.

In most of the localities, the rocks had cooled to temperatures lower than 30°C by the end of the Palaeogene, suggesting that the total Neogene denudation was, at a maximum, several hundreds of metres. Rapid cooling in the last 3 million years is resolved in some places in southern Scotland, where it could be explained by glacial erosion and post-glacial isostatic uplift.

Contents

List of Tables

List of Figures

Acknowledgements

First of all, I would like to thank my supervisors, Dr. Cristina Persano and Prof. Fin Stuart. Their scientific support and guidance, assistance in the labs and friendship were unprecedented. Cristina is specially thanked for fission track training, checking apatite grains, her exceptional patience, our regular, exhaustive brainstorming, help with living-in-Scotland issues and an arm to cry on. Special thanks to Fin go for training and assistance when working on the Helium line in SUERC, field assistance and collecting some samples, thought-provoking questions and for his incredible sense of humour. Finally, both are thanked for their understanding and patience during a long, on-going process of polishing my Polish English.

Special thanks are to Prof. Jean Braun (Joseph Fourier University, Grenoble) for his hospitality during my time in Grenoble, training in numerical modelling, access to a computer cluster, all updates made for me to Pecube, and all later Skype chats resolving many problems. I would also like to thank Prof. Kerry Gallagher (University of Rennes) for providing the Exhume code and for tones of e-mails exchanged about the QTQt modelling and help with software crashes. Prof. Roderick Brown (GES, University of Glasgow) and Dr. Romain Beucher (University of Bergen) are thanked for providing the Helfrag code and help with running models. Rod is additionally thanked for enthusiastic discussion about Helfrag results and a short introduction to using GMT. Special thanks are also for Mark (current Dr. Wildman) for being my 'older brother' in the labs and for our unforgettable *'good Durango chats'*.

I would also like to thank all members of staff in GES at the University of Glasgow and at SUERC. Special thanks in GES are for: Robert McDonald for help with mineral separation and preparation of fission track mounts, as well as for sorting out all non-scientific problems; Gary Tait for his patience and help with my 'computer adventures', Peter Chung for help with taking SEM images, Les Hill for printing conference posters; and in SUERC for: Dr. Luigia Di Nicola for assistance in the Helium and U-Th labs, running ICP-MS analyses and all discussions about the data quality, and Dr. Valerie Olive for assistance with running the ICP-MS.

I thank my fellow officemates for a friendly atmosphere and accepting my strange, non-chatty nature, with special thanks to Caroline Miller for all funny cats movies

that helped to relax during stressing period of writing. Massive thanks are for Callum Graham and Domokos Gyore for being my 'slaves' during field works and being able to break for me everything, including a hammer. Also, I thank Domokos Gyore, Angel Rodes, Luigia Di Nicola and Ana Carracedo for making travelling to SUERC much easier and enjoyable.

I would like to thank my amazing Polish friends for the friendship that can live on despite these 1000 km. Special thanks are for Michalina Knyś for every day chats, trying to keep my Polish up-to-date, our extraordinary travels that let to forgot about the PhD stresses, as well as for support in the worst moments and trying to help even if I know that your favourite 'geological' epoch is the '*New Look*'.

Not only completion of this thesis, but being in the place and being the person I am now would not be possible without my family, and especially without my wonderful parents. I am grateful for your love, every day support and motivation that is even more appreciated, as I know how difficult it is for you to have your only child living far away in a different country. To them this thesis is dedicated. *Mamo i Tato, dziękuję.*

At the end, I would like to make a step back in the past and give my sincere thanks to Dr. Michał Śmigielski, without whom getting this PhD opportunity would not be possible. Thanks for all the help with the application process, but especially for lying to me that I probably do not have any chances; otherwise, I would be too scared and certainly would not apply to this PhD project. Moving back a bit further, I have to mention my extraordinary Geography teacher, Mr Andrzej Adamiak, who sadly passed away in the autumn last year, and who not only convey his passion to Earth Science on me, but also help to do the first step to believe that an normal girl from a little town in eastern Europe can achieve success.

The funding for this PhD project was provided by the College of Science and Engineering Scholarship. The Sir Alwyn Williams Scholarship provided the funds for a one month long visit in Grenoble. The School of Geographical and Earth Sciences is thanked for the conference support. Helfrag results were obtained using the EPSRC funded ARCHIE-WeSt High Performance Computer; EPSRC grant no. EP/K000586/1.

Declaration

I declare that, except where explicit reference is made to the contribution of others, that this dissertation is the result of my own work and has not been submitted for any other degree at the University of Glasgow or any other institution.

Katarzyna Łuszczak

List of symbols and abbreviations

Abbreviations

ADFD	Age Dispersion Fragment Distribution
AFT	Apatite Fission Track
AHe	Apatite (U-Th-Sm)/He
AN	Anglesey
CH-B	Cheshire Basin
EISB	East Irish Sea Basin
FI	Faroe Islands
FSB	Faroe-Shetland Basin
FTLD	Fission Track Length Ddistribution
GSR	Greenland–Scotland Ridge
IOM	Isle of Man
ISB	Irish Sea Basin
KDE	Kernel Density Estimator
LLSVP	Large Low Shear Velocity Province
LTT	Low Temperature Thermochronology
MB	Møre Basin
MTL	Mean Track Length
NNSB	Northern North Sea Basin
NU-B	Northumberland Basin
PAZ	Partial Annealing Zone
PRZ	Partial Retention Zone
RB	Rockall Basin
RMSD	Root Mean Square Deviation
SI	Shetland Islands
SV-B	Solway Basin
VB	Vøring Basin
VR	Vitrinite Reflectance
ZHe	Zircon (U-Th)/He

Symbols

a	dimension to the diffusion domain
A	the heat production
A_{LD}	heat production of the Lake District batholith
A_0	background heat production of the crust
A_{Scot}	heat production of granite bodies in Scotland
c	geometry factor for the external-detector method (Chapter 2)
	or heat capacity (Chapter 5)
D	amount of denudation
D_0	diffusivity
D_T	total denudation
D_X	amount of denudation caused by underplating
D-Par	length of fission track etch pit
E	exhumation rate
Ea	activation energy
eU	effective Uranium
F_T	α-recoil correction factor
ϕ	the thermal-neutron fluence
H	rate of the radiogenic heat production per unit mass
h_i	present-day surface elevation
h_0	initial surface elevation
I	isotope abundance ratio (Chapter 2) or isostatic rebound (Chapter 6)
k	thermal conductivity
κ	thermal diffusivity
L	length
L_i	length of a crystal fragment
L_0	initial length of a crystal
λ	decay constant
λ_D	total decay constant for ^{238}U
λ_f	spontaneous-fission decay constant for ^{238}U
MTL m	mean track length measured
MTL p	mean track lengths projected
μ	misfit
N_D	number of tracks on the dosimeter
N_i	number of induced tracks
N_s	number of spontaneous tracks
ND/NP	ratio of the daughter product to the parent
p	number of model parameters
P	probability that the grains pass χ^2 test

Pe	Pécelet number
R	radius
R^*	effective spherical radius
ρ	density
ρ_D	tracks density in the dosimeter
ρ_m	density of asthenosphere/mantle
ρ_i	induced track density in the sample
ρ_s	spontaneous track density in the sample (Chapter 2 and 3) or density of eroded rocks (Chapter 6)
ρ_x	density of magmatic underplating
ρ_w	density of water
S	surface
σ	standard deviation or thermal-neutron fission cross-section for ^{235}U (in equation 2.3)
t	time or fission track age (in equation 2.3)
T	temperature or average present-day topography (in Chapter 6)
T_C	closure temperature
THK	thickness of the sedimentary layer
t_{std}	age of the standard sample
τ	cooling rate
τ_c	timescale for conduction
τ_a	timescale for advection
U_r	rock uplift
U_T	tectonic uplift
V	volume
v_x, v_y, v_z	components of rock velocity
W	water depth
W1	width of a crystal
W2	thickness of a crystal
X	thickness of magmatic underplating
x, y, z	spatial coordinates of the rock particle
ζ	calibration factor for external detector method

Chapter 1

Introduction

1.1 Project rationale

It is common to associate areas of high elevation and relief with convergent plate margins. There are, however, many mountain regions on the Earth which are far away from the converging plate boundaries. These include elevated passive margins, for example South West Africa (Gallagher & Brown 1999) and South East Australia (Lister et al. 1991), and elevated plate interiors such as Yellowstone area in North America (Wegmann et al. 2007) and the Southern African Plateau (Lithgow-Bertelloni & Silver 1998). Topography may be created not only by compression, but also by rifting (Lister et al. 1991, Huismans & Beaumont 2008), intra-plate stress (Lundin et al. 2013, Cloetingh et al. 2013) and epeirogenic movements reflecting the mantle dynamics, for instance mantle plumes (Braun 2010, Braun et al. 2013).

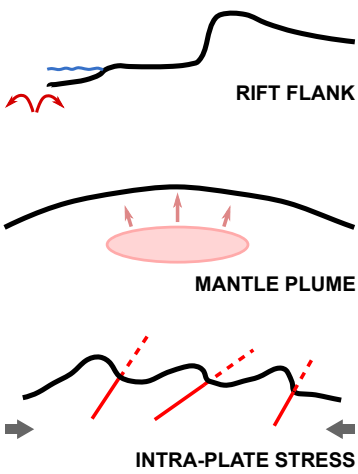

Figure 1.1: Simple sketch illustrating the first order topography caused by rifting, a mantle plume and intra-plate compressional stress.

Each of these plate-scale tectonic processes results in a characteristic spatial pattern of topographic development (Fig. 1.1) that allows the underlying cause of uplift to be identified. Rifting causes the flexural uplift of rift flanks, as a result of isostatic rebound due to lithospheric stretching and erosion (Beaumont et al. 1982, Braun & Beaumont 1989). The maximum elevation is expected to occur in a narrow zone parallel to the rift axis and is predicted to decrease inland into the continental interior. Perhaps the clearest contemporary example is the Red Sea margin, where the uplifted flank is only about 50 km wide, but reaches elevation up to 2.5 km (e.g. Balestrieri et al. 2005).

It is widely proposed that mantle plumes create a transient, dynamic topography via dynamic support by the hot, upwelling mantle and the thermal expansion of the lithosphere (Hager et al. 1985, Braun 2010). Permanent uplift is generated when a layer of low density magma is emplaced beneath the crust (McKenzie 1984, Cox 1993, Maclennan & Lovell 2002). The pattern of the plume-related topography is predicted to be low-amplitude, long-wavelength and/or resembling the shape of the underplating pod (Tiley et al. 2004, Braun 2010). A present-day example of dynamic topography is the area surrounding the Snake River watershed, which forms a parabolic-shape, >150 km wide mountain belt with elevations of 3,000–3,500 m reflecting the passage of the Yellowstone hot spot (Wegmann et al. 2007).

Plate collision induces stresses that are transmitted far from the plate boundaries, causing long-wavelength folding and often reactivation of pre-existing tectonic structures (e.g. Cloetingh et al. 1999, 2013). The expected pattern of topography is related to the presence of compressional or extensional structures generated in previous continent collisions. The present topography of the Rhine Graben, for instance, is considered to be the result of extensional reactivation of the Late Palaeozoic structure during the Alpine orogeny that formed a low elevation area bounded by several hundreds of metres high massifs and distinct fault scarps (Cloetingh et al. 2006a).

These examples demonstrate that the landscape away from orogenic belts is directly linked to deep Earth processes. The ability to precisely resolve ancient patterns of denudation can provide insight on the large scale processes that were responsible for the development of present-day topography. Low temperature thermochronometers, such as the apatite fission track and apatite and zircon (U-Th-Sm)/He methods are sensitive to processes affecting the thermal structure of the shallow crust (<5km) (Gallagher et al. 1998, Ehlers & Farley 2003, Braun et al. 2006). Cooling ages determined by both techniques provide a quantifications of the amount and rates of rock cooling, which can be transformed into the amount of denudation, assuming that the geothermal gradient within the crust is known. In thermochronometric studies it is common practice to assume a spatially and temporally constant geothermal gradient, despite the fact that measurements in the field demonstrate that they are highly variable even at short distances, both spatially and with depth (Blackwell & Steele 1989, Eppelbaum et al. 2014). Geothermal gradients are also predicted to vary in time as they directly depend on the thermal conductivity of the rocks, on the thickness of the crust, i.e. the distance from the hot mantle, and on the rates of denudation, as fast erosion advects hot rocks toward the surface (Braun et al. 2006). The understanding of the impact of such crustal thermal heterogeneities on the thermochronometric data is, therefore, crucial for accurate quantification of denudation amounts that can be later used in deciphering the uplift causes.

The mountainous landscape of the English Lake District has been celebrated in the literature for centuries (e.g. William Wordsworth, Arthur Ransome, Beatrix Potter). It contains England's highest peak, Scafell Pike (978 m ASL). The Lake District is surrounded by high elevation landscapes in the Scottish Southern Uplands and northern Wales. These regions are also characterized by an absence of sedimentary rocks that are younger than the Lower Palaeozoic. Without the information available from sediment stratigraphy determining the regional geological history is challenging. Where only the basement rocks are exposed, the denudational history of the area can be best quantified via the application of the low temperature thermochronology techniques. This, in turn, requires that the thermal properties of the eroding crust are taken into consideration.

The aim of this study is to better constrain the post-Palaeozoic history of central west Britain and, in particular, its Cenozoic evolution, unravelling the possible mechanisms beyond uplift and denudation. The aims have been reached by applying three low temperature thermochronometers, followed by 1-D and 3-D thermal modelling to accurately translate the amounts of cooling into denudation history. The main objectives of this study are to:

- Precisely quantify the timing, duration and rate of the early Palaeogene cooling in central west Britain;
- Resolve the regional denudational pattern by quantifying the impact of local crustal heterogeneities, including the role of radiogenic heat production and thermal conductivity of the rocks, on the upper crustal geothermal gradient;
- Use the timing and spatial pattern of denudation to assess the possible tectonic mechanisms responsible for the uplift and denudation;
- Add some additional constraints on the Mesozoic evolution of the region and revise the Neogene cooling episode, in the regions areas it has been previously suggested.

1.2 Regional background

The North Atlantic region experienced a major reorganization in the Cenozoic. Rifting on the UK margin started in the Permian and lasted for ∼240 Ma until the final break-up and opening of the North Atlantic Ocean at 53–55 Ma (Lundin & Doré 2005). In general, the post-rift evolution of the North Atlantic resembles the 'stretching and cooling' model of McKenzie (1978) that predicts the rate of subsidence of the margin decreases exponentially, after break-up. There are, however, several places where either 'anomalous subsidence' or significant uplift are observed (Fig. 1.2; Ceramicola et al. 2005, Praeg et al. 2005, Anell et al. 2009). The present-day high elevation of the North Atlantic margins is considered to be an effect of Cenozoic exhumation episodes, which

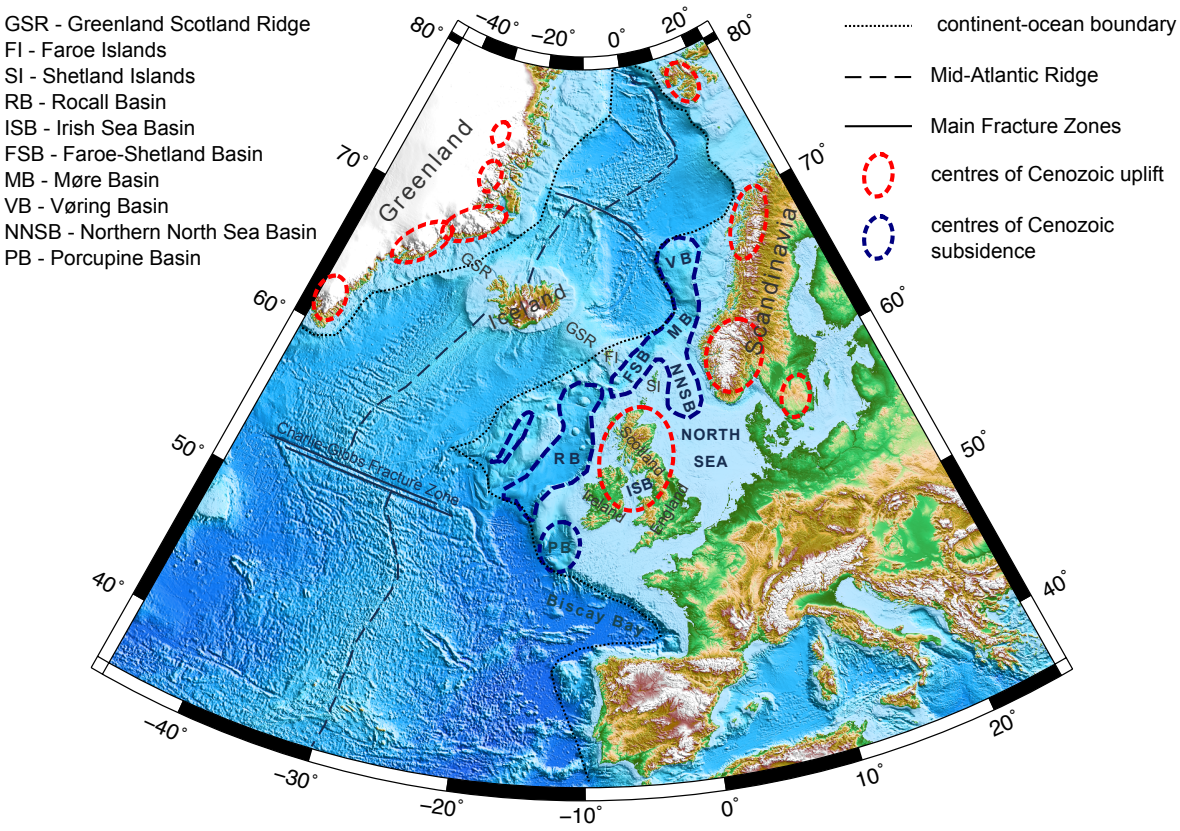

Figure 1.2: Map of the North Atlantic region with main areas of Cenozoic uplift and subsidence; the background map is based on the ETOPO1 Global relief model data and produced using Generic Mapping Tools; the location of Cenozoic uplift and subsidence after Praeg et al. (2005).

were locally and temporally variable in scale and have been reviewed in several summary papers (e.g. Doré et al. 1999, 2002, Japsen & Chalmers 2000, Anell et al. 2009; see, however, Swift et al. 2008 for a different interpretation).

The Cenozoic uplift and denudational history of the North Atlantic region has direct implications for the development of the oil and gas resources in the North Sea, Irish Sea and the Faroe-Shetland Basins (Hardman et al. 1993, Doré & Jensen 1996, Doré & Lundin 1996, Green et al. 1997, Davies et al. 2004, Scotchman et al. 2006, Japsen et al. 2010, Fletcher et al. 2013, Tassone et al. 2014). During the early Cenozoic the North Atlantic region was affected by widespread basaltic magmatism in response to the arrival of the proto-Iceland plume (Stuart et al. 2000, Kent & Fitton 2000, Saunders et al. 2007, Ganerød et al. 2010). Despite numerous studies of seismic reconstructions, mass balance and sediment supply estimates and apatite fission track and vitrinite reflectance analyses there is active debate regarding the mechanisms responsible for the regional uplift (Green et al. 1997, Doré et al. 2002, Nielsen et al. 2007, Persano et al. 2007, Swift et al. 2008, Shaw Champion et al. 2008, Hartley et al. 2011, Lundin et al. 2013). High elevation passive margins were uplifted during the rifting episode (e.g. Braun & Beaumont 1989, Lister et al. 1991). A rift-flank topography is present, for instance, in Scandinavia and in parts of eastern Greenland, where the elevation

of the present mountains is considered to be a direct result of Mesozoic rifting and early Cenozoic break-up (Rohrman et al. 1995, Swift et al. 2008). Mantle plumes are known to cause dynamic and thermal transient uplift along with a permanent component due to magmatic underplating; the earliest (∼62–58 Ma) magmatism in the North Atlantic has been related to the impingement of the proto-Icelandic plume just prior to the onset of spreading (∼55–53 Ma) (White & McKenzie 1989, Lundin & Doré 2005, Saunders et al. 2007). A dome-shaped mantle plume-driven uplift has been proposed in many parts of the region, but its amplitude, wavelength, and, in some cases, presence, are still debated (Cope 1994, Nadin et al. 1997, White & Lovell 1997, Jones et al. 2002). Some studies suggest that the Cenozoic uplift of the North Atlantic margin was episodic and not directly linked to rifting or to the arrival of the proto-Iceland plume. For instance, elevated erosional surfaces in Greenland are interpreted as peneplains and have been proposed to represent evidence of Cenozoic multiple phases of uplift and erosion to the base level (Japsen et al. 2010, 2012). A phase of Neogene uplift has been identified at several parts of the North Atlantic region, and has been explained by the intra-plate compressional stress transmitted from the Alpine foreland (Cloetingh et al. 1990, 2006b). However, the Late Cenozoic was also a time of important climate changes, including the onset of glaciation across the northern hemisphere. The Neogene uplift may, therefore, lack a tectonic component and be explained by isostatic rebound in response to glacial melting and erosion (Molnar & England 1990).

This project focuses on central west Britain, where the high topography and high relief cannot be simply explained as a product of rift flank uplift, as the region was ∼1000 km away from the rift axis. The existing thermochronometric data indicate that both the Irish Sea and the English Lake District were subjected to exceptionally high exhumation in the early Cenozoic (Green 1986, Lewis et al. 1992). This is predicated solely on the apatite fission track analyses and on the assumption of constant, equal to present-day value of geothermal gradient, and is not supported by the stratigraphic reconstuctions (Holliday 1993). The availability of new thermochronometers, like apatite (U-Th-Sm)/He (Wolf et al. 1996, Farley 2000) and new numerical modelling techniques (Gallagher 2012, Braun et al. 2012, Beucher et al. 2013) provide the potential to resolve the timing and spatial pattern of denudation more precisely and, based on that, indicate the processes affecting the region in the Cenozoic.

1.3 Study area

Central west Britain comprises three elevated regions surrounding the East Irish Sea Basin (EISB): the Lake District (NW England), southern Scotland and northern Wales (Fig. 1.3). The earliest major tectonic event preserved in the region is the Early Palaeozoic Caledonian orogeny, which resulted from the amalgamation of the Laurentia (Scotland) and Avalonia (England and Wales) sub-continents (Ziegler 1988, Woodcock &

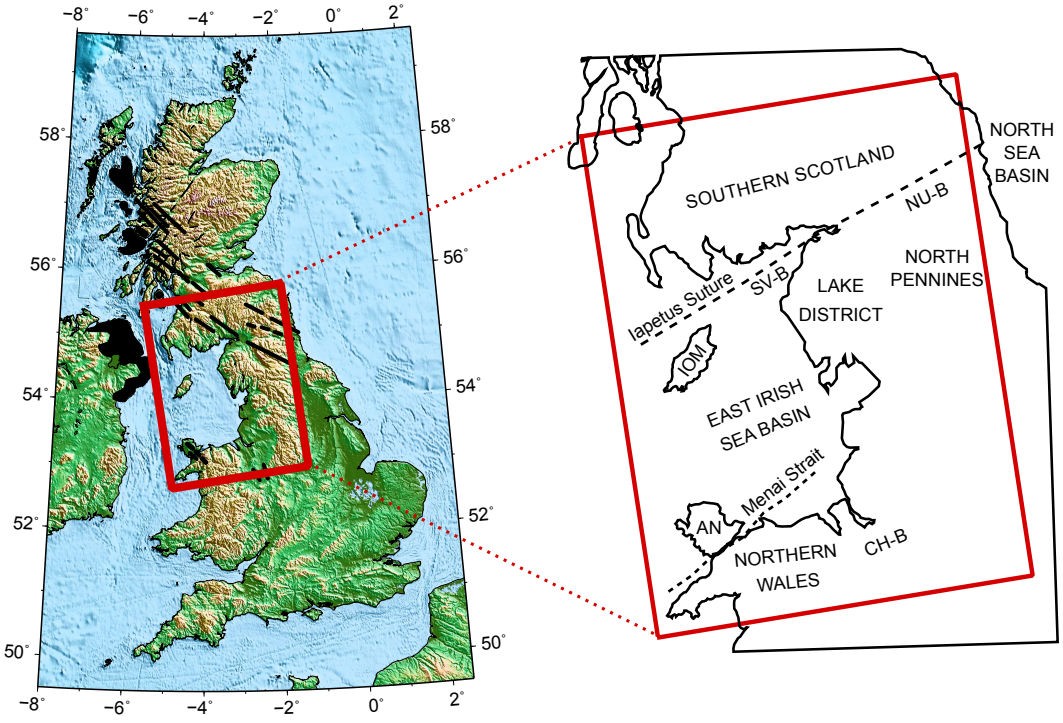

Figure 1.3: Left: Topographical map of Britain with the location of the study area marked as a red rectangular; the map is based on the ETOPO1 Global relief model data and produced using Generic Mapping Tools. Black features represent the location of early Palaeogene magmatic centres and more important dike swarms. Right: Detailed view of the study area; IOM—Isle of Man, AN—Anglesey, CH-B—Cheshire Basin, SV-B—Solway Basin, NU-B—Northumberland Basin.

Strachan 2000). The suture between the continents, marking the closure of the Iapetus Ocean, is located roughly along the border between Scotland and England (Soper et al. 1992). The post-Caledonian history of the region can be inferred from the sedimentary successions in the adjacent basins, which record a Carboniferous extensional phase with sedimentation of up to 7 km in the Midland Valley and Northumberland-Solway Basins (Fraser & Gawthorpe 1990). This was followed by a compressional episode during the Variscan orogeny (∼310–280 Ma), which resulted in the regional exhumation and removal of large amounts of Carboniferous rocks. During a second phase of extension in the Permo-Triassic, several deep basins were formed, these include the East Irish Sea, Solway, and North Sea Basins (Ziegler 1992, Coward 1995). The extension probably continued in the Jurassic (Ziegler 1992, Woodcock & Strachan 2000). The Late Mesozoic and Cenozoic history of the region is difficult to assess as the youngest sedimentary rocks in the region are represented by a small outlier of Lias limestones in the EISB (Warrington 1997).

The lack of sediments younger than Early Jurassic is a result of the substantial Cenozoic uplift and denudation (e.g. Anell et al. 2009). A purely tectonic mechanism, driven for instance by stress transmission from the Alpine foreland, is at odds with the fact that the existing faults were not reactivated in the Cenozoic (Needham & Morgan 1997, Akhurst et al. 1998). There are, however, exceptions, such as the sinistral movements

along the Menai Strait line between the Welsh mainland and Anglesey (Bevins et al. 1996). The possibility that uplift and denudation were caused by intra-plate stresses cannot be, therefore, completely ruled out, also because the faults could have been indeed reactivated, but Cenozoic movement is not yet detected. The existing thermochronological data from the British Isles indicates that the main phase of Cenozoic cooling took place in the early Palaeogene, ∼60 Ma (e.g. Green 1986, Green et al. 1997). During this time NW Scotland records voluminous magmatic activity. Minor dykes and sills were emplaced as far south as northern Wales (Fig. 1.3). The EISB and the surrounding areas are underlain by a layer of the high velocity material that has been interpreted as a plume related, low density magmatic underplating. The underplating is a maximum thickness beneath the EISB and Isle of Man and gradually decreases onshore (Al-Kindi et al. 2003, Tomlinson et al. 2006). The denudation pattern that would result from the given thickness of underplating has been modelled by Tiley et al. (2004). According to this model onshore denudation should not be greater than few hundreds of metres, which is inconsistent with other reconstructions based on stratigraphical and thermochronometric data (e.g. Green 1986, Holliday 1993).

Another hindrance for assessing the causes of the early Palaeogene event comes from the spatial distribution of cooling and, therefore, denudation. The highest, pre-uplift palaeotemperatures of >110°C were reached in the small, ∼60 km wide area of the Lake District (Green 1986, 1989, 2002, Lewis et al. 1992, Green et al. 1997, 2012, Thomson et al. 1999, Persano et al. 2007). The 3–4 km Cenozoic denudation derived from using an average geothermal gradient of 25–30°C/km (Green 1986, Lewis et al. 1992), is at odds with the stratigraphical reconstructions and would be higher than the Cenozoic denudation in the nearby basins (Holliday 1993). There are, however, some thermochronological indications that the early Palaeogene geothermal gradient was elevated, which would reduce the amount of denudation (Green et al. 1997, Green 2002). The causes for a higher than normal geothermal gradient have not been, however, convincingly justified, and so the spatial distribution of the Cenozoic denudation in central west Britain remains poorly understood. To date little attention has been given to the fact that the study area is formed by structurally defined, distinctive blocks composed of different types of rocks and presenting a highly spatially variable present-day surface heat flow, from <40 mW/m^2 in the Cheshire Basin to >100 mW/m^2 in the Skiddaw area in the Lake District (Busby et al. 2011). These heterogeneities of the crustal thermal properties may have an influence on the thermochronometrically resolved palaeotemperatures and, therefore, affect the reconstructed amounts of denudation. In the next section, the thesis outline is given, highlighting the contribution that this study brings to the knowledge of the Cenozoic evolution of central west Britain and, more in general, to the importance of using a multi-thermochronometric approach and a rigorous interpretation of the thermal structure of the upper crust to unravel the denudational history of an area.

1.4 Thesis outline

In this thesis I present the first multiple low temperature thermochronology data set from southern Scotland, northern England and northern Wales. New apatite fission track data are integrated with apatite and zircon (U-Th-Sm)/He ages to establish the regional rock cooling history. To precisely constrain the early Palaeogene cooling history, and to better define the possible Neogene cooling event, more than 20 single grain apatite (U-Th-Sm)/He ages have been determined on four key samples and modelled using both standard software and the newly codified Helfrag code (Beucher et al. 2013). Because the upper crust in central west Britain is highly heterogeneous, the calculation of the amounts of denudation requires a careful analysis of the thermal properties of the crust at each site. This new reconstruction of the regional denudation history allows the most probable causes of the early Palaeogene uplift and the Cenozoic evolution of the region to be established.

The thesis outline is presented below.

Chapter 2 presents a brief introduction to the thermochronology methods used in this study;

Chapter 3 outlines the geological constraints, as well as the existing thermochronometric data from the Lake District, southern Scotland and northern Wales separately, and then the new apatite fission track, and apatite and zircon (U-Th-Sm)/He data are presented for each of the three regions; a regional summary is provided at the end of the chapter; the data quality is critically assessed and the factors that have affected the thermochronometric ages are presented and discussed;

Chapter 4 shows the results from the inverse modelling of the data presented in Chapter 3. It is divided into two sections: the first reports time-temperature (t-T) paths derived from modelling using QTQt (Gallagher 2012); the second reports the t-T paths derived from modelling the four multi-grain samples using Helfrag (Beucher et al. 2013); the quality of the obtained models and some modelling aspects are reviewed; the Helfrag modelling section ends with a critical assessment of the technique and its applicability to different samples and tectonic settings;

Chapter 5 focuses on the influence of the local thermal properties of the upper-crust, and deep thermal anomalies (e.g. magmatic underplating), on the geothermal gradient in the uppermost 3-5 km) crust and its influence on thermochronometric ages; the results of a 1-D model of the crustal heat production and thermal conductivity of the rocks in central west Britain are presented followed by the results from the 3-D forward and inverse modelling using Pecube (Braun 2003);

CHAPTER 6 presents a geological interpretation of the thermal histories; in the first part, the new constraints on the pre-Cenozoic history are briefly reviewed; the second part is the complex analysis of the new constraints of the early Palaeogene cooling; the timing, amount and spatial distribution of cooling are transferred into uplift and denudation and the possible causes of exhumation are reviewed; the third part reports the constraints on the Neogene section of the thermal history and quantify the Neogene uplift and denudation, briefly discussing its possible causes; in the end, the most probable post-Caledonian history of the region is presented;

CHAPTER 7 presents the wider implications of this study, and suggests further work that could help in resolving the issues that remain unresolved.

Chapter 2

Low temperature thermochronology

2.1 Introduction

Geochronological methods are based on a process of radioactive decay of unstable nuclides in a range of rock-forming minerals. The most common types of radioactive decay, exploited by geochronology, are: i) α-decay producing atoms of ^{4}He, ii) β-decay producing an electron or positron, iii) spontaneous nuclear fission. All of the common decay processes proceed at the same rate, irrespective of the host mineral, temperature or pressure. Thus the ratio of the parent to daughter isotopes is a measure of the time since both elements have been retained in the mineral. It is commonly assumed that the parent isotope is trapped within the mineral and its concentration only changes because of radioactive decay, whereas in many cases the daughter isotope is retained in a mineral only below certain critical temperatures (Fig. 2.1). These thermochronometers provide a way of determining the time when a rock cooled through a particular temperature range. Rapid cooling after crystallization means that most high temperature geochronometers record the crystallization age when applied to igneous rock. In the case of most metamorphic rocks and detrital minerals in sedimentary rocks, the measured mineral age often reflects its post-crystallization thermal history. Each mineral thermochronometer is characterized by a temperature above which the daughter product is entirely lost by diffusion (open system), and below which it accumulates within the crystal (closed system). In low temperature thermochronometers, the temperature range where partial diffusive loss of daughter occurs is called the Partial Retention Zone (PRZ). When rock cooling through the PRZ is rapid the closure temperature

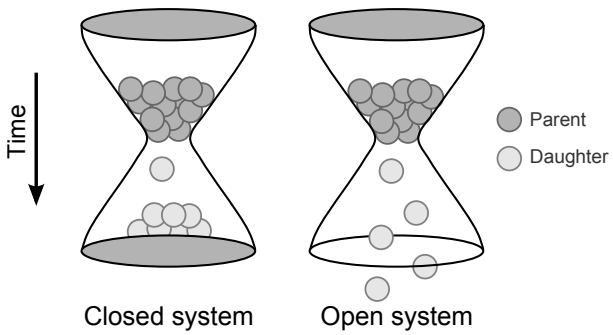

Figure 2.1: Open and closed system behaviours illustrated as hour glasses. In closed system, all daughter product is kept inside the system. In the open system, the daughter product leaks entirely from the system simultaneously with its production; after Braun et al. (2006), modified.

concept holds (Dodson 1973) and the apparent age can be used to reflect the time of rock cooling. When rock cooling through the PRZ is slow, a significant proportion of the daughter isotope can be lost and the apparent age records the integrated rock cooling history. The ratio of the daughter product to the parent (N_D/N_P) depends on time, cooling rate, diffusion parameters and production rate. The duration of cooling events is usually much shorter than the half-life of the commonly used radiometric decay schemes, for closure system behaviour N_D/N_P can be approximated by a linear relationship, depending only on the time and production rate. Extrapolation of this relationship to zero indicates the closure time, which can be then converted into corresponding temperature (Dodson 1973). In this approach the closure temperature (T_C) is:

$$T_C = \frac{E_a}{R \ln(A\tau D_0/a^2)} \tag{2.1}$$

where:
E_a is the activation energy
R is the gas constant
A is numerical constant depending on geometry
τ is time taken for the diffusivity to decrease by a factor of e^{-1}, which may be referred to the cooling rate ($\partial T/\partial t$, by $\tau = \frac{R}{E_a - \partial T/\partial t}$)
D_0 is diffusivity at infinite temperature
a is dimension to the diffusion domain

This implies that the closure temperature and therefore the apparent age of the rock depends not only on the mineral thermochronometer, but also on the cooling rate and the size of the domain for diffusion of the daughter isotope.

The commonly-used thermochronometers are shown in Fig. 2.2. High temperature thermochronometers (e.g. U-Pb titanite and zircon) have closure temperatures in excess of 400°C and are typically used to determine the crystallization age of rocks or the time of high grade metamorphic events. Thermochronometers with closure temperatures of 200–400°C are used to date lower grade metamorphic events, or the exhumation of rocks from the middle crust (5–13 km), or the cooling history of intrusive igneous bodies. Low temperature thermochronometers are characterized by closure temperatures of less than 150°C, which makes them sensitive to rock cooling in the upper crust (<5 km, for a normal geothermal gradient of 30°C/km).

In this study I use three low temperature thermochronology (LTT) methods to provide an insight into the exhumation history of central west Britain: apatite and zircon (U-Th)/He and apatite fission track. The following sections provide brief descriptions of the techniques, the main issues affecting data quality and examples of common applications.

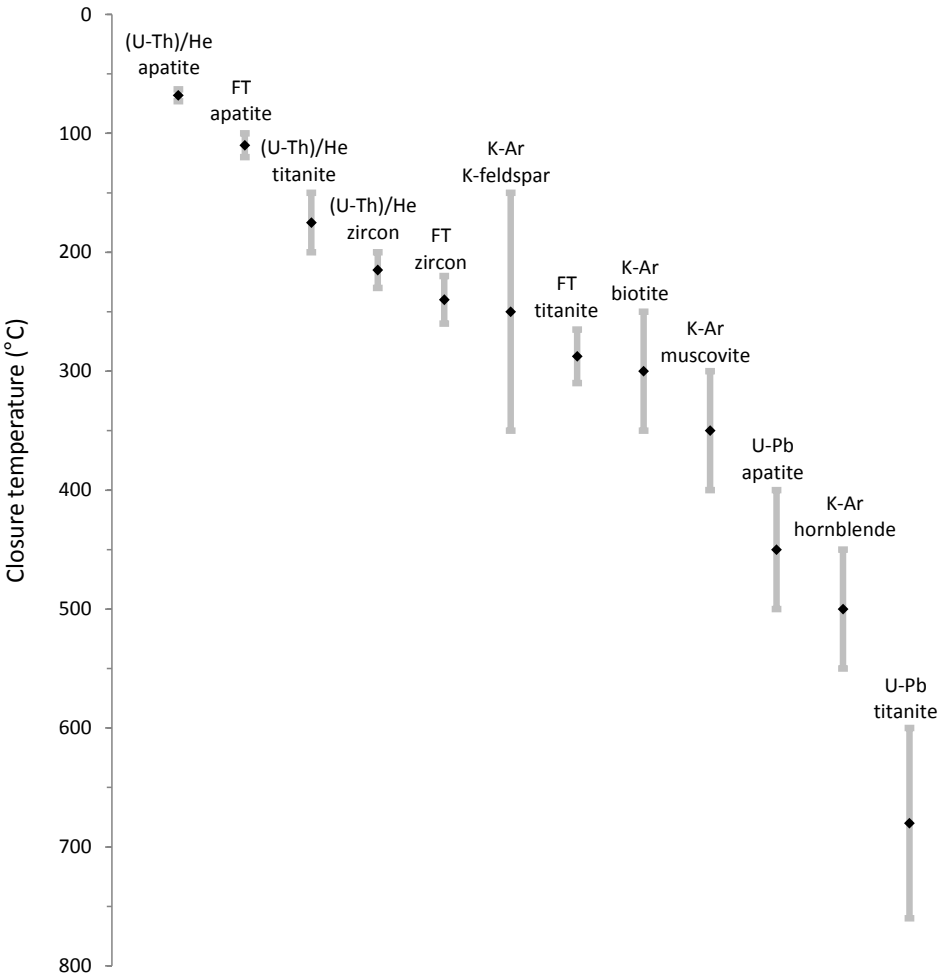

Figure 2.2: Average closure temperatures for different thermochronometers. Data after: apatite fission track - Gleadow & Duddy (1981), titanite fission track - Coyle & Wagner (1998), zircon fission track - Brandon et al. (1998), apatite (U-Th)/He - Farley (2000), titanite (U-Th)/He - Reiners & Farley (1999), zircon (U-Th)/He - Reiners et al. (2002), K-Ar K-feldspar - Lovera et al. (1989), K-Ar biotite - Harrison et al. (1985), K-Ar muscovite - Hames & Bowring (1994), K-Ar hornblende - Harrison (1981), U-Pb apatite - Chamberlain & Bowring (2000), U-Pb titanite - Cherniak (1993)

2.2 Apatite fission track thermochronology

2.2.1 Introduction

Latent fission tracks were observed for the first time using a transmission electron microscope in muscovite in the late 1950s (Silk & Barnes 1959). The first comprehensive summary of the study of fission tracks, including their application to geology, was presented in the book "Nuclear tracks in solids" by Fleischer et al. (1975). Since then there have been several detailed methodological studies aimed at improving the understanding of the process of formation and annealing of fission tracks in different minerals, including apatite, zircon and titanite (Wagner & den Haute 1992, Gallagher et al. 1998, Tagami & O'Sullivan 2005).

2.2.2 Fission track formation

Spontaneous nuclear fission is a process that occurs when a heavy, unstable actinide nucleus splits into two highly positively charged particles. This is accompanied by the release of approximately 200 MeV of energy, which mostly comprises kinetic energy of the moving fission fragments. According to the "ion explosion spike" model (Fleischer et al. 1975), the fragments travel with a high velocity through the host material and interact with atoms within the crystal lattice by electron stripping and ionization (Fig. 2.3 a). Positively ionized atoms repel each other due to Coulomb repulsion, and create interstitial vacancies, while the stressed region relaxes elastically (Fig. 2.3 b). Due to interaction with the atomic lattice, fission fragments gradually lose their kinetic energy and stop. If fission occurs within a dielectric solid, the displaced atoms cannot easily return to their initial positions, and the process results in a damage trail within the crystal lattice that is called a fission track (Fig. 2.3 c). In terrestrial minerals, such as apatite and zircon, fission tracks are produced almost entirely by the spontaneous fission of ^{238}U; the long fission half-lives of other heavy nuclides such as ^{235}U and ^{232}Th (Table 2.1) means that the number of tracks produced by the fission of these nuclides is too small to be significant (Wagner & den Haute 1992). The width of latent tracks depend on the host material, but for the commonly analysed minerals, it is usually in the range 4–10 nm (Tagami & O'Sullivan 2005). Latent fission track can be observed only by transmission electron microscopy. Even then, a track density in the case of commonly dated minerals is usually too low to be scanned conveniently. Thus fission track analysis requires the tracks to be enlarged. This is usually performed using chemical etching and enables tracks to be observed under an ordinary optical microscope (Fleischer et al. 1975).

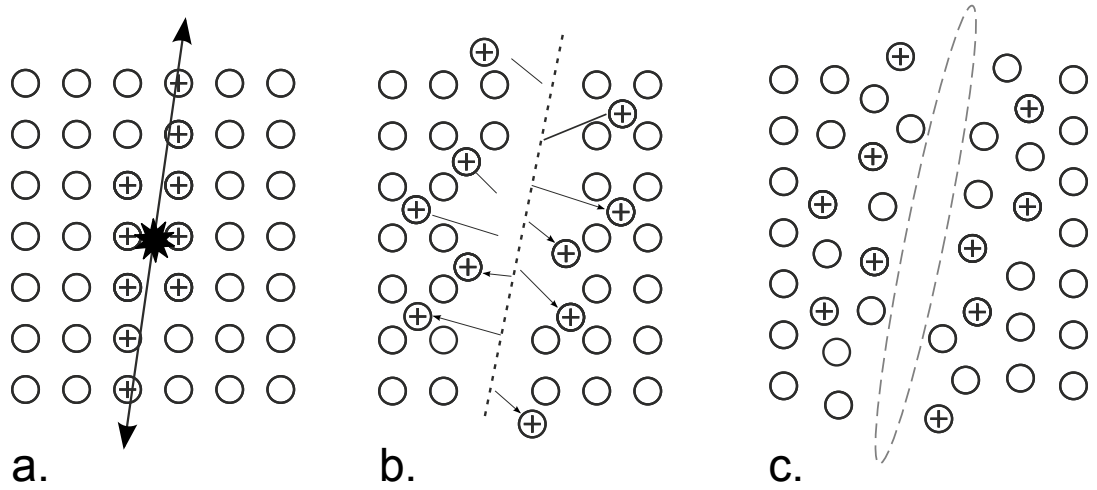

Figure 2.3: The process of track formation: a. spontaneous fission of a heavy nuclide produces two positively charged fragments, which rapidly move through the crystal lattice and cause ionization of atoms, b. positively-ionized atoms become displaced due to Coulomb repulsion, c. if the host material is dielectric the damage trail is preserved in the crystal lattice; after Fleischer et al. (1975), modified.

Table 2.1: Spontaneous fission half-lives ($t_{1/2}$) of three most abundant radioactive nuclides, after Holden & Hoffman (2000).

Nuclide	$t_{1/2}$ (years)
^{232}Th	$(1.2 \pm 0.4) \times 10^{21}$
^{235}U	$(1.0 \pm 0.3) \times 10^{19}$
^{238}U	$(8.2 \pm 0.1) \times 10^{15}$

2.2.3 Annealing of fission tracks in apatite

Fission tracks are not stable features and are subjected to a temperature dependent process of annealing whereby displaced atoms tend to return to their initial position. During the annealing process tracks are shortened and may be entirely annealed if the temperature and time are high and long enough (Fleischer et al. 1975).

The rate of annealing depends on the host mineral. Long-term annealing of fission tracks in apatite, $Ca_5(PO_4)_3(OH, F, Cl)$, from deep borehole samples occurs at temperatures between ∼60 and ∼120°C (Gleadow & Duddy 1981, Naeser 1981, Green et al. 1989). This temperature range is called the Partial Annealing Zone (PAZ) and is an equivalent to the PRZ for radiometric mineral thermochronometer schemes Laboratory annealing experiments have been performed under different conditions, including heating lasting from 20 minutes to 500 days, and temperatures ranging from 95 to 400°C (Laslett et al. 1987, Green et al. 1986, 1989). The extrapolations of these results to geological time scale are, in general, consistent with the borehole data, suggesting that the PAZ lies between 60 and 120°C, for a time scale of 1–100 Myrs (Laslett et al. 1987). Fission track lengths in minerals which have cooled rapidly and then remain in near surface temperature are, however, 1.0–1.5 μm shorter than lengths of induced tracks, suggesting that slow annealing may occur also in low, near surface temperatures (Green 1988, Donelick et al. 1990, Spiegel et al. 2007).

The fission track annealing rate also depends on the chemical composition of the mineral. For instance, it is slower in Cl-rich than in OH and F-rich apatites (Green et al. 1986, Carlson et al. 1999, Barbarand et al. 2003). Determining mineral chemistry is usually performed by a direct measurement of Cl content using a microprobe, or by measuring the length (diameter) of tracks etch pits parallel to the crystallographic c-axis, the so called D-Par (Donelick et al. 1999). The kinetics of fission track annealing is not isotropic. Tracks perpendicular to the crystal c-axis in many minerals anneal faster than c-axis parallel tracks (Green et al. 1986, Donelick 1991, Donelick et al. 1999). Recent models of annealing kinetics are a subject of continuous improvement and new algorithms are formulated to take the crystallographic orientation and grain chemistry into consideration (Ketcham et al. 1999, 2007b).

2.2.4 Fission track age and track length distribution

The apparent fission track age provides the time when a crystal cooled below the fission track annealing temperature and started to accumulate fission tracks in the lattice. The number of fission tracks intersecting a polished grain surface may be then converted into an age if the rate of track production and the concentration of the parent isotope are known. The fission track age equation (see Table 2.2 for the list of all symbols) is:

$$t = \frac{1}{\lambda_D} \ln\left(\frac{\lambda_D}{\lambda_f} \frac{N_s}{^{238}\mathrm{U}} + 1\right) \tag{2.2}$$

Although, the number of spontaneous tracks can be determined by counting tracks intersecting a polished surface of a grain, determining the number of ^{238}U atoms is more complicated. Two methods are commonly used. The conventional technique applies the external detector method (Hurford & Green 1982). In the last few years, it is, however, gradually losing its popularity in favour of the laser ablation-inductively coupled plasma-mass spectrometry (LA-ICP-MS) that is based on the direct measurement of the ^{238}U content in the sample (Hasebe et al. 2004). In the external detector method, mounted and polished grains are covered by low-U mica sheets and irradiated together by a neutron flux to induce fission tracks within the mica (for detailed description see Appendix A). ^{238}U contents are estimated based on the number of tracks induced in the mica. The formula to calculate the fission track age may be then substituted by:

$$t = \frac{1}{\lambda_D} \ln\left(1 + \frac{\lambda_D \phi \sigma c I \rho_s}{\lambda_f \rho_i}\right) \tag{2.3}$$

Because the spontaneous fission decay constant of ^{238}U (λ_f) is know only with high uncertainties and thermal-neutron fluence (ϕ) cannot be determined precisely, calibrated

Table 2.2: The list symbols used in the equations.

t	the age of the sample
λ_D	the total decay constant for ^{238}U
λ_f	the spontaneous-fission decay constant for ^{238}U
N_s	the number of spontaneous-fission tracks present in the sample
^{238}U	the number of ^{238}U atoms in the sample
ϕ	the thermal-neutron fluence (in cm^2/s)
σ	the thermal-neutron fission cross-section for ^{235}U (580.2×10^{-24} cm^2)
c	geometry factor for the external-detector method
I	the isotope abundance ratio (I = ^{235}U/^{238}U = 7.253×10^{-3})
ρ_s	the spontaneous track density
ρ_i	the induced track density in the sample
ρ_d	the track density in the dosimeter
t_{std}	the age of the standard samples

standard samples of known age are irradiated with unknown age samples and a ζ-factor is determined (Hurford & Green 1983):

$$\zeta = \frac{\phi\sigma I}{\lambda_f \rho_d} = \frac{e^{\lambda_D t_{std}} - 1}{\lambda_D (\rho_s/\rho_i)_{std} c \rho_d} \tag{2.4}$$

Then, the new fission track age (2.5) may be easily solved.

$$t = \frac{1}{\lambda_D} \ln(1 + \frac{\lambda_D \zeta \rho_s c \rho_d}{\rho_i}) \tag{2.5}$$

In this study, the calibration of the ζ-factor for IRMM standard dosimeters was obtained by counting tracks on 27 standard samples including Durango, Fish Canyon Tuff and Mt. Dromedary apatites (Fig. 2.4). The average ζ-value is 313.7 ± 8.3 (eight recounted samples were excluded from calculation of the average).

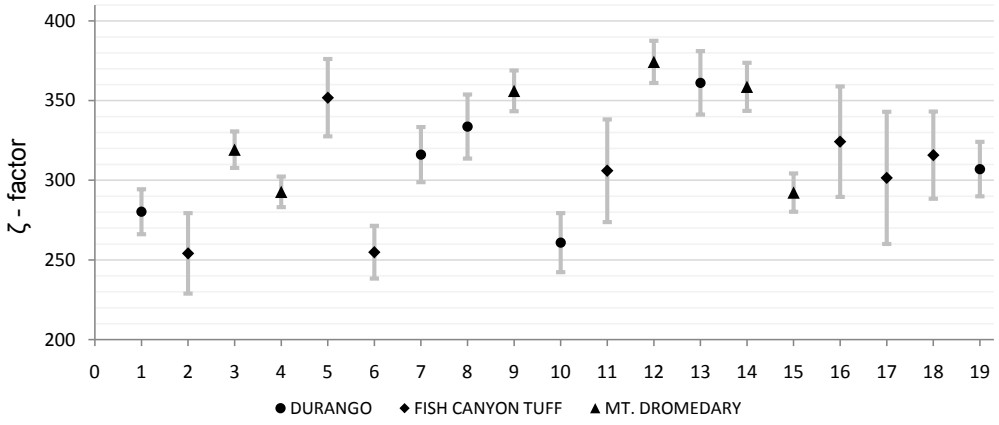

Figure 2.4: The values of the ζ-factor for the IRMM standard dosimeter based on Durango, Fish Canyon Tuff and Mt. Dromedary apatites obtained during four months long training.

A fission track age is a combination of a series of ages calculated on single grains. Usually a fission track age is calculated using a minimum of 20 grains, in the case of igneous rocks, and a minimum of 30 grains, in the case of sedimentary rocks. There are three different ways of presenting the sample age:

i) mean age, which is the arithmetic mean of the single-grain ages,

ii) pooled age, which is a result of summing spontaneous and induced track from all grains; in this case the assumption is that all grains belong to the same population,

iii) central age with the age dispersion, which is a mean of $log(\rho_s/\rho_i)$ and standard error of single-grain ages, approximated by a Normal distribution (Galbraith & Laslett 1993). This is now the preferred method as it can deal with samples containing more than one grain population.

The probability that long fission tracks intersect the surface is higher than for short (i.e. annealed) tracks. Consequently fewer tracks will be counted on the grain surface of slowly-cooled samples which will tend to lower fission track ages. Understanding of this phenomenon is strongly connected with understanding of Dodson's idea of the closure temperature: slower cooling and longer exposition to high temperatures lower the closure temperature and decrease the age (Dodson 1973). Deciphering the underlying thermal history of a rock requires the age to be complemented by information about a fission track length distribution (FTLD).

Because fission tracks are formed continuously, each track records a different portion of the thermal history of the rock from which the apatite crystals were separated. The FTLD are sensitive tool in distinguishing thermal histories (e.g. Gallagher et al. 1998). Depending on a relation of depth of rock in the crust to the location of the PAZ, fission tracks will be annealed with varying degrees. After exhumation event rocks coming from different elevations will record different AFT ages and different FTLD (Fig. 2.5). Rapid cooling throughout the PAZ produces a narrow, unimodal distribution of long fission tracks. Slow cooling generates a wide distribution of tracks of different lengths, the form depends on the number and extent of cooling episodes. For standard analysis of fission track length distribution, measurements of at least 100 fission track lengths per sample are required to be statistical meaningful (Galbraith 2005). Measurements are performed only on grains lying parallel to the c-axis, and only horizontal, confined tracks can be measured. The number of such tracks is limited, because an etchant may reach them only through other tracks intersecting the polished grain surface (TINT – track-in-track) or through cleavage (TINCLE – track-in-cleavage). It is recommended to measure only TINTs, as TINCLEs may be subjected to natural etching, and their length may bias the resulting thermal history (Jonckheere & Wagner 2000).

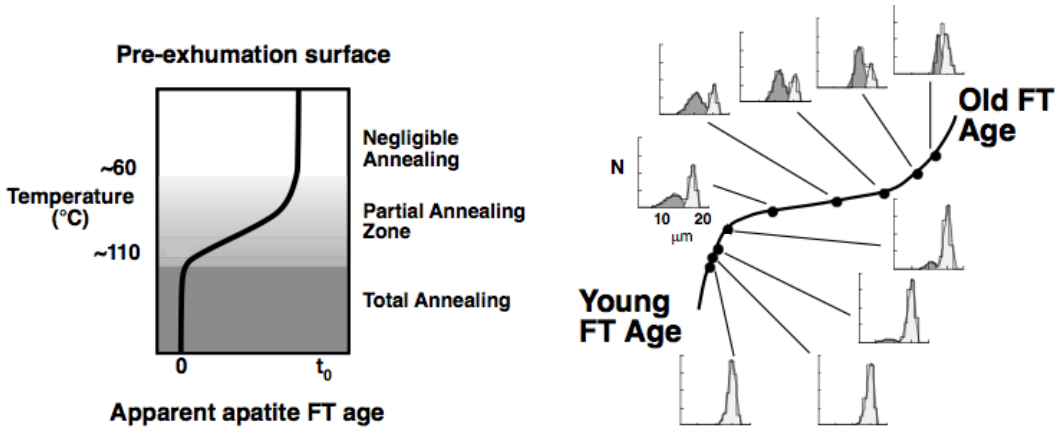

Figure 2.5: Partial annealing zone (PAZ) of apatite fission track system; modified from Gallagher et al. (1998). Left: AFT age as a function of temperature change with depth before an exhumation event; t_0—initial AFT age. Right: The expected trend of AFT ages and track length distributions along the vertical profile after exhumation. Notice two components of the track length distribution; dark shading part represents tracks formed before the last cooling event and light shading part represents long tracks formed during the last cooling event.

Some discrepancies have been found between measurements of the same samples performed by different analysts, with great implication for the validity of modelling AFT data (Barbarand et al. 2003, Ketcham et al. 2009). Ketcham et al. (2009) demonstrated that even small differences in track length distribution have an effect on the accuracy of thermal modelling, especially on the lowest temperatures range; track shortening, observed in temperatures <60°C (Spiegel et al. 2007), is in the order of few tenths of a micron, similar to noted deviations. The source of these discrepancies may lie in microscope calibration, but most importantly in different sampling of track populations by different analysts. Tracks parallel to the c-axis are thinner than perpendicular tracks and may be more difficult to observe. Similarly, short tracks may not be as easily observed and counted as long tracks. The first annealing models (e.g. Laslett et al. 1987) solved equations describing time and temperature dependent shortening of tracks for Durango fluoroapatite kinetics and constant value of an initial track length. The higher reproducibility of track length distribution and thermal histories is reached if track lengths are c-axis projected and multi-kinetic annealing is applied (Ketcham et al. 1999, 2007b). The projection in regard to the crystallographic c-axis deals with annealing anisotropy and standardizes measurement for the effect of sampling different track populations. The use of the multi-kinetic model, usually by applying the D-Par value for each grain, enables calculation of chemistry-dependent initial track length and annealing kinetics.

The average D-Par value measured on Durango apatite during this study is 1.82 ± 0.13 μm (n=60) and is statistically the same as the value of 1.83 ± 0.13 μm reported by Donelick et al. (1999). All track lengths are projected according to the Ketcham et al. (2007b) model and initial track length is calculated individually for each track using the measured D-Par values. Fig. 2.6 presents histograms of FTLD of measured and projected track populations analyzed during this study on Durango apatite crystals subjected to different degree of annealing; FTLD of projected tracks are in high consistency with expected thermal histories.

2.2.5 Application of apatite fission track thermochronometer and its limitations

The apatite fission track (AFT) thermochronometer is sensitive to the temperature range of ∼60–120°C (Gleadow & Duddy 1981, Naeser 1981, Green et al. 1989), which in most of the geological settings corresponds to 2–4 km deep in the continental crust. The AFT thermochronometer has developed into a useful tool for deciphering the exhumation history of rocks at shallow crustal levels. Over the last decades it has been applied successfully in many geological problems and settings. Despite the relative

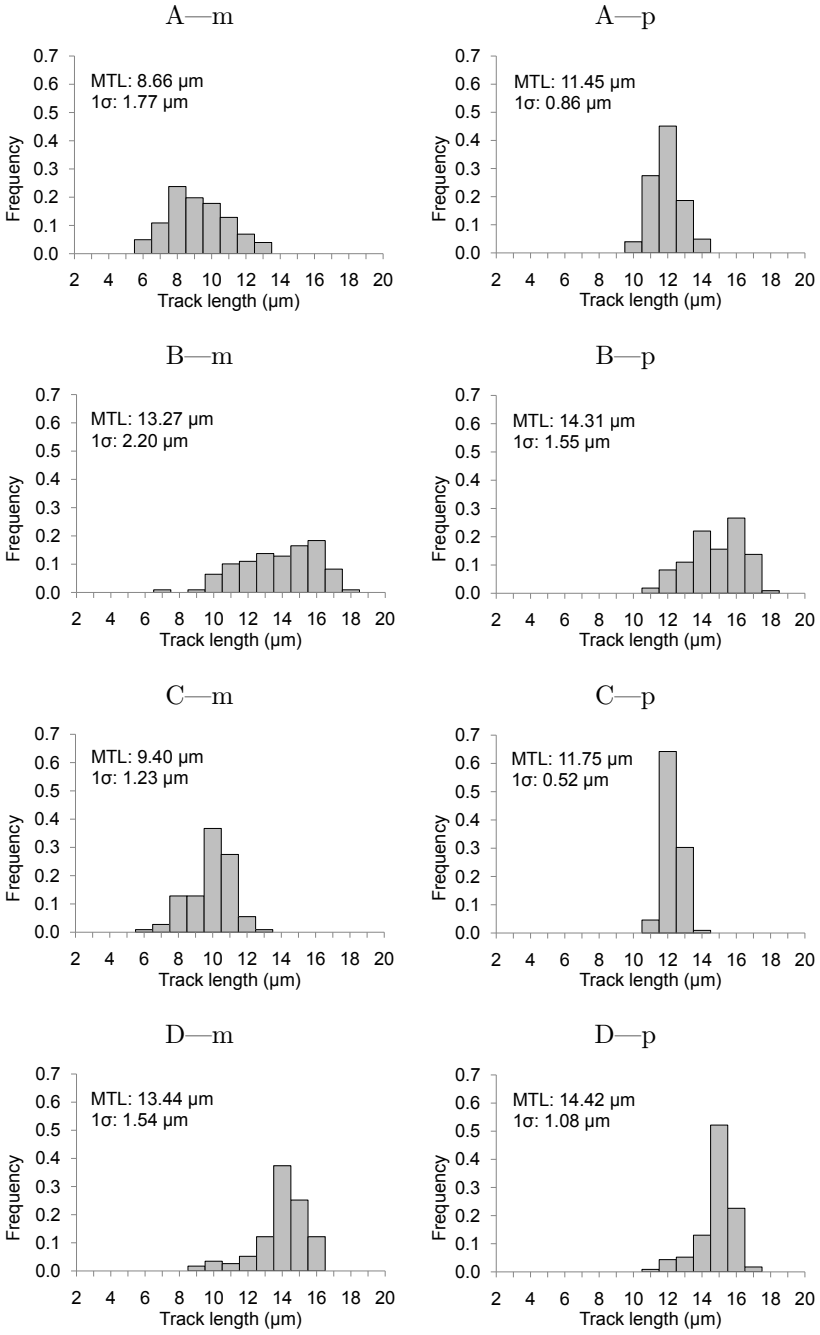

Figure 2.6: Histograms of fission track length distribution measured on four Durango crystals subjected to different degree of annealing; MTL—mean track length, m—measured tracks, p—c-axis projected tracks (using c-axis projection model by (Ketcham et al. 2007b). The histograms of measured track lengths are wider because of the effect of annealing anisotropy, which cause additional variation of track lengths; tracks perpendicular to the c-axis are shorter than parallel tracks. Due to the c-axis projection track lengths do not show differentiation from the anisotropy and the histograms become narrower.

softness of apatite and its low resistance to chemical weathering, fission track analysis on detrital apatites have been successfully performed (e.g. Corrigan & Crowley 1992, van der Beek et al. 2006, Glotzbach et al. 2011). The AFT thermochronometer is successfully applied in deciphering thermal history of sedimentary basins (e.g. Bray et al. 1992, Green et al. 1995, Osadetz et al. 2002). Its sensitivity overlaps with the range of temperatures corresponding to the generation of hydrocarbons, and contrary to other

tools used in thermal modelling of sedimentary basins, such as vitrinite reflectance and sediment compaction studies, it provides constraints not only on palaeotemperatures, but also on the timing of thermal events. AFT thermochronometry is extensively applied in deciphering exhumational history of orogenic belts and fault movements in compressional settings (e.g. Foster et al. 1994, Fitzgerald et al. 1995, Nadin & Martin 2012). Data from high mountain ranges confirm strong correlation of AFT ages with elevation, as well as the presence of characteristic concave sections in age-elevation plots, corresponding to exhumed PAZs (Fitzgerald et al. 1995). The AFT thermochronometer is also successfully used to quantify rift flank uplift and denudation in passive margin settings (Brown et al. 1994, Gallagher et al. 1994, Jelinek et al. 2014).

The strength of AFT thermochronometry lies in the fact that information retrieved from the AFT analysis (age + FTLD) are more meaningful than single ages of many other thermochronometers. The spread in the AFT single-grain ages and FTLD allows for the reconstruction of time-temperature paths over the temperature range of the AFT system sensitivity. The analysis is, however, time consuming and strongly dependent on availability of apatite crystals in the rock. Apatite is not resistant to chemical weathering and alteration; these issues may strongly hamper the availability of suitable grains. Crystal quality also affects the accuracy of measurements; fractures and microcleavage are common in apatites, and may significantly hinder track counting. The presence of discrepancies between track length measurements done by different analysts is still not fully understood. The information derived from FTLD analysis may also be biased by over- or under-etching of tracks, which may be present in cases of some grains having atypical chemical composition, even if the standard etching protocol is used.

2.3 (U-Th-Sm)/He thermochronology

2.3.1 Introduction

Although dating of minerals using an accumulation of ^{4}He from U and Th series decay has been proposed in the early twentieth century (Rutherford 1905), the method was quickly abandoned because most of the ages were too young due to diffusive loss of ^{4}He. Resurgence of interest in the technique was initiated by Zeitler et al. (1987), who proposed that, if ^{4}He diffusion can be well quantified, it may be become a useful tool for deciphering rock cooling through low temperatures. Following this idea, a multitude of diffusion experiments on different minerals, including apatite, zircon and titanite, were developed and new powerful thermochronometer was established (Farley 2000, 2002, Reiners et al. 2002, 2004).

2.3.2 (U-Th-Sm)/He system

Almost all the ^{4}He in nature is produced by series decay of ^{238}U, ^{235}U, ^{232}Th and ^{147}Sm. The ingrowth equation of α-particles (^{4}He nuclei) is:

$$^{4}\mathrm{He} = 8\ ^{238}\mathrm{U}\ e^{\lambda_{238}t} + 7\ ^{235}\mathrm{U}\ e^{\lambda_{235}t} + 6\ ^{232}\mathrm{Th}\ e^{\lambda_{232}t} + {}^{147}\mathrm{Sm}\ e^{\lambda_{147}t} \tag{2.6}$$

where
^{4}He, ^{238}U, ^{235}U, ^{232}Th and ^{147}Sm are in numbers of atoms
λ_{238}, λ_{235}, λ_{232}, λ_{147} are the decay constants (Table 2.3)

^{147}Sm produces only one α-particle during one decay process (Equation 2.6), and its decay constant is two orders of magnitude lower than decay constants of U isotopes (Table 2.3), the contribution of ^{4}He from ^{147}Sm decay is usually much lower than the contribution from ^{238}U, ^{235}U, ^{232}Th in most minerals used for He thermochronology. For instance, in the commonly used laboratory standard Durango apatite, the amount of ^{4}He produced by ^{147}Sm is 100 times lower than ^{4}He produced by the actinides (Persano 2003, McDowell et al. 2005). In Durango apatite aliquots analysed during this study, the ^{147}Sm produced ^{4}He was 0.17–0.48% of the total ^{4}He produced. Such small contribution is usually within the analytical precision of the measurements and, in practice, the equation 2.6 is simplified to the contribution from U and Th only. However, in case of samples enriched in Sm, the contribution of ^{4}He from ^{147}Sm may be as high as 70% (unpubl. ARHDL Report, Reiners & Nicolescu 2006). In samples analysed during this study, up to 25% of ^{4}He has been derived from ^{147}Sm, however, in most of the samples, ^{147}Sm contribution was clearly below 10% (Fig. 2.7).

The age equation (2.6) holds only if all the ^{4}He present in the crystal derives from the radioactive decay of the parent isotopes. Excess ^{4}He may, however, be present due to fluid inclusions and/or inclusions of U- and Th-rich minerals within the crystal lattice (Farley 2002) or by implantation from neighbouring U-rich minerals (Gautheron et al. 2012). For these reasons, crystals are hand-picked and scrutinized under the microscope to avoid analysis of inclusion bearing crystals, and thereby reduce the age dispersion.

Table 2.3: Decay constants and half-lives of ^{4}He, ^{238}U, ^{235}U, ^{232}Th and ^{147}Sm, after Dickin (2005).

parent isotope	decay constant (yr^{-1})	half-life
^{238}U	1.55×10^{-10}	4 468.0 Myr
^{235}U	9.85×10^{-10}	703.8 Myr
^{232}Th	4.95×10^{-11}	14.0 Byr
^{147}Sm	6.54×10^{-12}	106.0 Byr

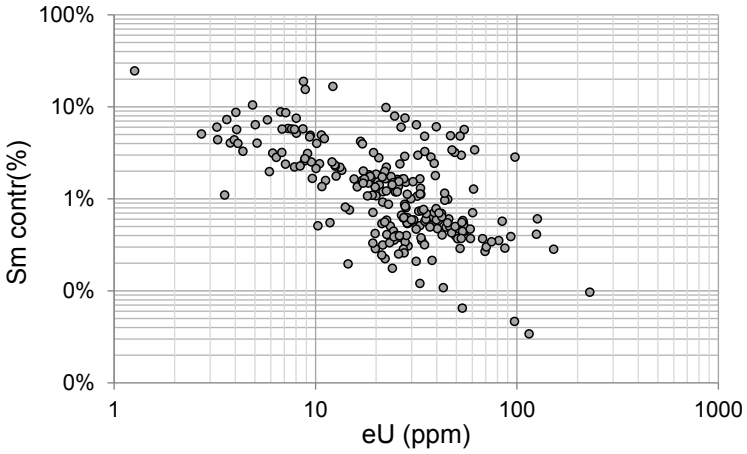

Figure 2.7: Contribution of ^{147}Sm to total ^{4}He production versus [eU] (ppm) in samples analysed during this study.

The age equation (2.6) assumes also that, at temperatures cooler than the PRZ, no ^{4}He is lost. The process of radioactive decay, however, is accompanied by a release of energy, which is transmitted in the form of kinetic energy to the α-particles. Each α-particle travels about 20 μm from the place where the decay reaction has occurred, and if the parent nuclide is located close to the edge of the crystal, ^{4}He may be ejected from the host mineral (Farley et al. 1996); this process is called "α-ejection" (Fig. 2.8). The stopping distance depends on the host mineral as well as the parent nuclide. The values of the stopping distance of ^{238}U, ^{235}U, ^{232}Th and ^{147}Sm, for apatite, zircon and titanite are given in Table 2.4. Because the diameter of routinely analysed crystals ranges from 60–150 μm, α-ejection may cause significant difference in ages.

A simple age correction for the effect of the α-ejection has been proposed by Farley et al. (1996). The correction requires computing the F_T factor, which depends on the crystal size and geometry, as well as on the distribution of parent nuclides. The "corrected" age is then obtained by dividing a measured age by the F_T factor:

$$\text{Corrected Age} = \frac{\text{Measured Age}}{F_T} \tag{2.7}$$

Table 2.4: Mean α-stopping distance of ^{238}U, ^{235}U, ^{232}Th and ^{147}Sm for different minerals, after Ketcham et al. (2011).

Mineral	Mean stopping distance (μm)			
	^{238}U	^{235}U	^{232}Th	^{147}Sm
Apatite	18.81	21.8	22.25	5.93
Zircon	15.55	18.05	18.43	4.76
Titanite	17.46	20.25	20.68	5.47

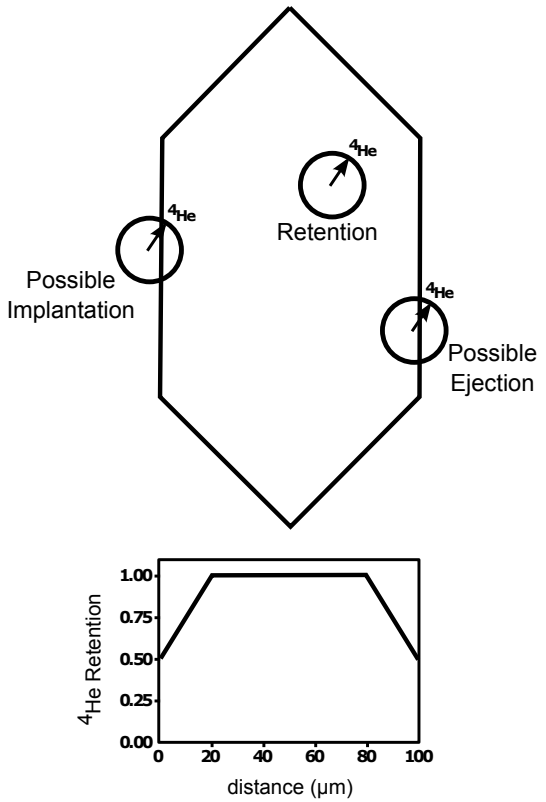

Figure 2.8: Schematic illustration of α-ejection and implantation, depending on the position of the parent nuclide within the crystal. The bottom panel presents the fraction of ^{4}He preserved in the crystal as a function of the distance from the edges of the crystal; after Farley (2002).

Farley (2002) presented the calculation of F_T factor only for simple crystal geometries and homogeneous distribution of parent nuclides within the grain. Often, especially in case of zircon, the distribution of U and Th is not homogeneous within the crystal (Dobson et al. 2008) and application of the F_T correction is complicated. Further studies by Meesters & Dunai (2002a,b) proposed a new way of calculating F_T factor for more realistic geometries and U and Th zoned crystals. However, even if zonation can be quantified and applied precisely, the further complication lies in the fact, that for rocks which have spent prolonged time in the partial retention zone, the ^{4}He distribution profile in the crystal is rounded enough to make the α-ejection effect less significant. Corrected ages calculated by simple application of the F_T factor will tend to be older than the true age by about 3–8% (Gautheron et al. 2012). Moreover, the crystals used for (U-Th-Sm)/He determination are often fragments of broken crystals. The α-ejection occurs only within the outermost 20 μm of the grain, and therefore the effect is not present along the broken faces. To deal with this issue, in some laboratories, the measured length of crystal fragment is multiplied by a factor of 1.5, in order to account for breakage and to derive the F_T factor which would characterize unbroken, original length crystal (Farley 2002). The most recent correction (Gautheron & Tassan-Got 2010), based on the Monte Carlo simulation, allows considering more realistic geometries characterized by a hexagonal prism with pyramidal terminations, which is

very common for apatite crystals, and broken faces. Modelling of ^{4}He diffusion requires, however, an uncorrected age to be an input value and it is performed often using the effective spherical radius of the crystal (R*) as a diffusion domain; R* is a radius of the sphere having the same surface to volume ratio (S/V) like the analysed crystal. Calculation of R* usually does not include the effect of broken faces, and tends to underestimate the real R* by 20–50% (Brown et al. 2013) and therefore also biases the size of the diffusion domain.

2.3.2.1 Apatite (U-Th-Sm)/He thermochronology

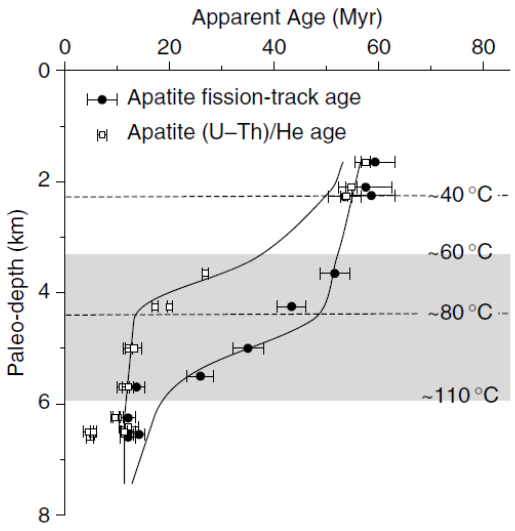

Figure 2.9: Partial retention zone (PAZ) of the AHe system (dashed lines) and partial annealing zone of the AFT system (grey shaded area) versus palaeodepth based on data of Stockli et al. (2000) from the White Mountains, California (rapid exhumation at ∼12 Ma); after Braun et al. (2006).

Apatite (U-Th-Sm)/He (hereafter AHe) thermochronometry has recently become one of the most used thermochronometeric techniques because of its unique sensitivity to the shallowest crustal processes. The first laboratory step-heating experiments of ^{4}He diffusion in Durango apatite by Zeitler et al. (1987) indicated that the closure temperature of AHe system is 105 ± 30°C. These results have been confirmed by a study of Lippolt et al. (1994), who compared AHe ages with AFT ages from rocks from different localities, and estimated the same range of temperatures. Wolf et al. (1996) narrowed down this range to 75 ± 7°C and suggested that the closure temperature depends on a cooling rate, but not on grain size, and can be applied to a variety of different crystal sizes. More detailed studies on Durango apatite by Farley (2000) indicated that the crystal itself is the diffusion domain and thus ^{4}He diffusivity and closure temperature depend on grain size. All experiments confirmed a strongly linear Arrhenius behavior of ^{4}He diffusion at temperatures less than 265°C, so in the range relevant to temperatures at which ^{4}He diffusion occurs over the geological time scale. Diffusion of ^{4}He in apatite seems to have only a weak anisotropy (Farley 2000) and this enables all crystal geometries to be used in diffusion modelling, including a sphere (Meesters & Dunai 2002a). Farley (2000) proposed that the activation energy (E_a) and diffusivity (D_0) for ^{4}He diffusion in Durango apatite are 33 ± 0.5 kcal/mol and 1.5 ± 0.6 cm^2 respectively, which implies a closure temperature of 68°C for a grain of 90 μm and a cooling rate of 10°C/Myr. A PRZ for the AHe system between ∼40 and 80°C (Farley 2002) has also been confirmed by deep borehole studies (Warnock et al. 1997, House et al. 1999). This temperature range partially overlaps with the PAZ of the apatite fission track system (Fig. 2.9).

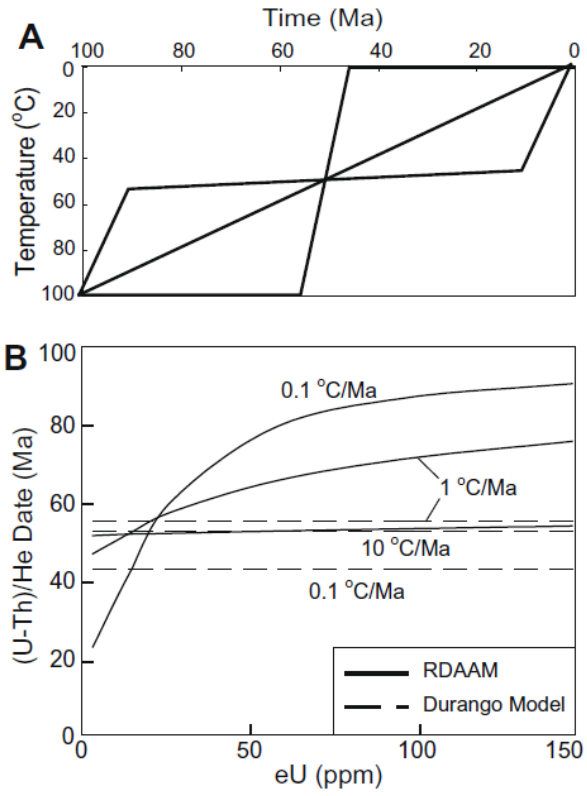

Figure 2.10: Influence of radiation damage on apatite (U-Th-Sm)/He ages for different thermal histories; after Flowers et al. (2009). A: Three thermal histories of rocks that have spent different time spans within the PRZ; B: Predicted relationship between [eU] and AHe age for given thermal histories assuming standard Durango kinetics and RDAAM—radiation damage model of Flowers et al. (2009).

The AHe method has been widely used in different geological settings, often in combination with AFT thermochronometer (e.g. Persano 2003, Balestrieri et al. 2005). According to the closure temperatures of both systems, and AHe age should not exceed the AFT age for the same rock. However, reported AHe ages, especially those from old cratonic rocks, are very often distinctly older than the corresponding AFT ages (e.g. Hendriks & Redfield 2005). This phenomenon has been related to the effect of radiation damage associated with the decay of U and Th (Green et al. 2006, Shuster et al. 2006). The α-recoil and fission tracks act as a trap for ^{4}He, inhibiting its diffusion out of crystal (Fig. 2.11). Trapped ^{4}He requires higher E_a to move out from the trap than E_a of diffusion within an undamaged apatite crystal. This effect increases with the amount of radiation damage and results in higher values of the closure temperature that for the AHe system may exceed 100°C (Flowers et al. 2009, Gautheron et al. 2009, Shuster & Farley 2009). Two radiation damage models, which incorporate both processes in predicting ^{4}He diffusion kinetics, have been proposed (Flowers et al. 2009, Gautheron et al. 2009). Both models use the effective U concentration: [eU] = [U] + 0.24 [Th] as a proxy for radiation damage, but the assumed relationship between the amount of defects and the trapped ^{4}He is either linear (Gautheron et al. 2009), or cubic form (Flowers et al. 2009). The models will be discussed in more detail in Chapter 4, Section 4.3. Nonetheless, in both models, the diffusion kinetics correlates with the eU concentration and differs from those presented by Farley (2000) for Durango apatite and are expected to produce positive correlation between [eU] and age (Fig. 2.10; Flowers et al. 2009, Gautheron et al. 2009). Therefore, if the correct kinetics are not used the thermal history modelling may be significantly biased, especially in the case of slowly cooled, old and/or U-rich apatites. An added complication lies in the fact that the annealing of radiation damage may depend on grain chemistry, in a manner similar to fission track annealing.

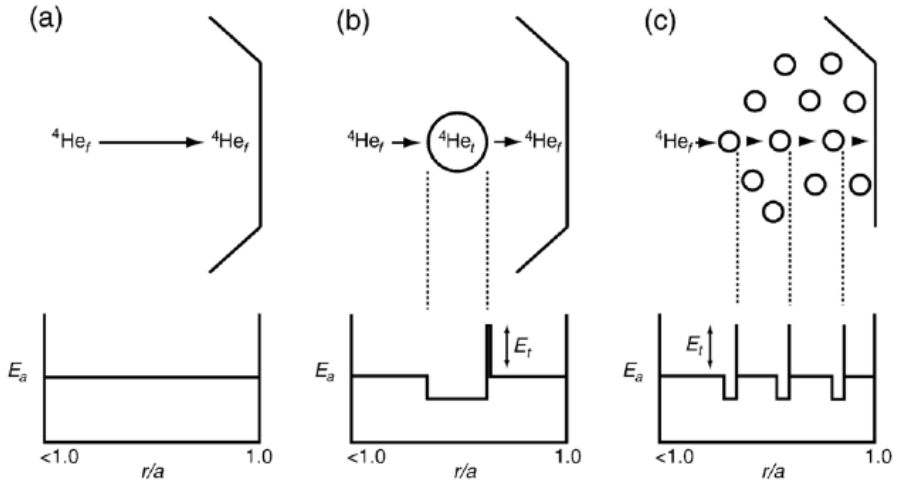

Figure 2.11: Schematic diagram illustrating an impact of radiation damage on ^{4}He diffusion in a mineral; after Shuster et al. (2006). Top panel shows a passage of a ^{4}He particle throughout a crystal. Bottom panel presents the activation energy (E_a) for ^{4}He diffusion plotted versus radial position (r/a =1—grain surface). (a) Diffusion within the undamaged crystal: free ^{4}He particle (^4He_f) has a constant E_a; (b) Diffusion within the crystal with radiation damage: trapped ^{4}He particle (^4He_t) requires E_a to increase by a factor E_t to move out from a trap into undamaged zone; (c) Diffusion within the highly damaged crystal: ^{4}He particle has to pass through several traps, the closure temperature increases.

Compared to zircon and monazite, the U concentration in apatite is relatively low; U-rich, small inclusions within the apatite crystal may produce enough ^{4}He to affect the AHe age. Standard determination of U and Th concentrations in apatite samples does not allow for the total dissolution of zircon and monazite; the age is calculated including this excess ^{4}He and therefore will be spuriously old. Additional ^{4}He may also come from ^{4}He-rich fluid inclusions. However, such inclusions have to be abundant or larger than few microns, to contribute significant amounts of ^{4}He (Vermeesch 2008). Careful scanning and picking inclusion free grains is highly recommended. It requires apatite grains to be transparent, which, especially for detrital grains, it is not often the case. Prismatic crystals are also required if the α-ejection correction has to be applied. The age may also be biased by U and/or Th zonation and implantation of ^{4}He from

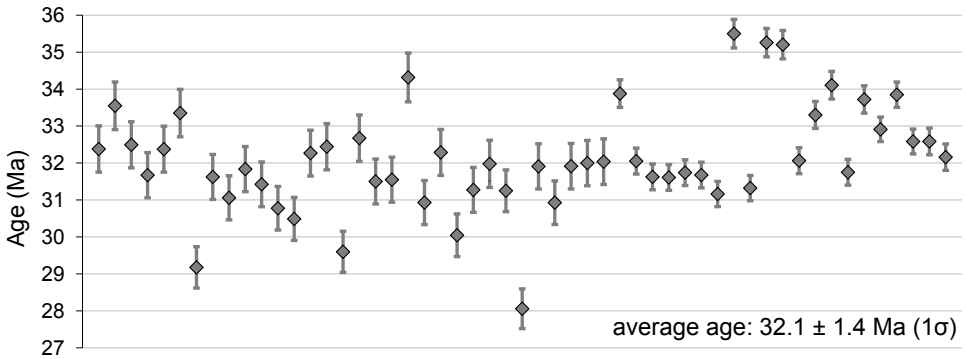

Figure 2.12: (U-Th-Sm)/He ages and analytical uncertainties of Durango apatite aliquots analysed during this study.

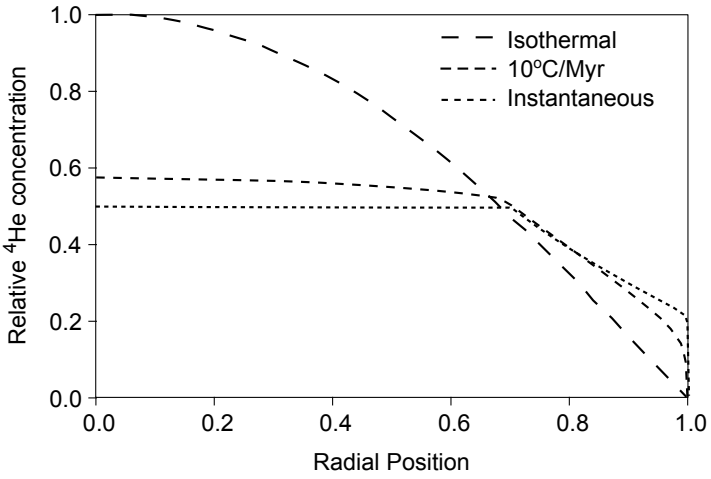

Figure 2.13: Radial concentration of ^{4}He within a crystal for three different thermal histories: isothermal, 10°C/Myr and instantaneous cooling. Isothermal cooling shows significant rounding of ^{4}He profile, whereas in case of rapid cooling the ^{4}He concentration is close to uniform, with break in slope in the outermost 20 μm due to α-ejection effect; after Farley (2002).

neighbouring crystals (Gautheron et al. 2012), and these factors cannot be easily accounted for.

The accuracy of measurements is monitored by analyses of Durango apatite aliquots along with the samples (31.44 ± 0.18 Ma (2σ); McDowell et al. 2005). The average (U-Th)/He age of Durango apatite aliquots (n=53) analysed during this study is 32.1 ± 1.4 (1σ) (Fig. 2.12).

Interpretation of the AHe ages is usually not straightforward. The apparent age of the grain reflects its time-temperature path within the PRZ. Different thermal histories may result in identical ages, and one single-grain age is not informative. The key to constraining the time-temperature path experienced by the rock lies in establishing the spatial distribution of ^{4}He within the crystal. Different thermal histories result in a different shape of the ^{4}He concentration profile (Fig. 2.13); rapid cooling does not produce rounding of the ^{4}He concentration profile, only the effect of the α-ejection is seen, whereas if the rock has spent prolonged time in the PRZ, the profile will be significantly rounded as radiogenic production and diffusive loss were occurring simultaneously (Farley 2002). Extracting the ^{4}He concentration profiles is the base of the ^{4}He/^{3}He technique (Shuster & Farley 2004). This method can be performed only on a whole, good quality crystal, during step-heating measurements, preceded by proton irradiation of the sample in order to produce uniformly distributed ^{3}He as a reference isotope. The ratio of ^{4}He/^{3}He is then measured and the derived ^{4}He concentration profile may be converted into possible thermal histories. However, due to relatively high cost, high analytical and crystal quality requirements ^{4}He/^{3}He thermochronometry is not yet commonly used.

Dispersion of single ages calculated for single-grain aliquots from the same rock is mostly an effect of grain size and radiation damage (Reiners & Farley 2001, Farley 2002, Flowers et al. 2009, Gautheron et al. 2009). Even though initially dispersion was considered as a problem, now that the causes of dispersion and the mechanisms controlling them are better understood, it is regarded as a new source of information (e.g. Flowers & Kelley 2011). Because grain size and radiation damage influence the closure temperature, particular grains may act as slightly different thermochronometers. Larger spreads in ages, bigger difference of the closure temperature, and thereby information from a wider temperature span may be extracted. Additional age dispersion may be derived from the fact that most of the grains used for AHe analysis are fragments of broken crystals (Brown et al. 2013, Beucher et al. 2013). Due to dependence of the shape of the axial concentration profile of ^{4}He in apatite on its thermal history, crystal fragments, depending on where they have been broken, may be "depleted" or "enriched" in ^{4}He when compared to whole crystals. This processes will be discussed extensively in Chapter 4, Section 4.3. Nonetheless, dispersion arising from analysis of large numbers (>20) of crystal fragments seems to provide a good measure of a diffusion profile, similar to the results derivable from ^{4}He/^{3}He analyses. The advantage over ^{4}He/^{3}He lies, however, in its low relative cost and simplicity.

2.3.2.2 Zircon (U-Th)/He thermochronology

The hardness and resistance to chemical weathering, as well as its relative abundance in many igneous and metamorphic rocks, leaves zircon as a commonly used mineral in geo- and thermochronology. Based on step-heating measurements of ^{4}He and data from vertical transects, the closure temperature of the zircon (U-Th)/He system (hereafter ZHe) has been estimated to be 170–200°C, for typical plutonic cooling rates and crystal size (Reiners et al. 2002, 2004). This makes the thermochronometer applicable to studies of cooling through the mid-crust.

As with apatite, radiation damage has been found to affect the ^{4}He diffusivity in zircon (Nasdala et al. 2001, 2004, Reiners 2005). Nasdala et al. (2004) reported that the real amount of radiation damage, equivalent to an α-dose, the parameter describing the amount of α-recoil events based on eU concentration, may be highly overestimated if the annealing of damage is not considered. The radiation damage model developed by Guenthner et al. (2013) deals with production and annealing of damage in the crystal lattice and suggests that, depending on the effective α-dose, ^{4}He diffusivity may either decrease, for small doses of 1.2 $\times 10^{16} \alpha$/g, or increase dramatically, for doses higher than 1.4 $\times 10^{18} \alpha$/g. Such behaviour was explained as an effect of initial lowering of the diffusivity by trapping ^{4}He within the damage structures, and further fast increase of diffusivity due to interconnection of the damage structures, and probable shrinking of the effective diffusion domain size. This process may result in either positive or negative correlations between [eU] and ZHe age (Fig. 2.14; Guenthner et al. 2013).

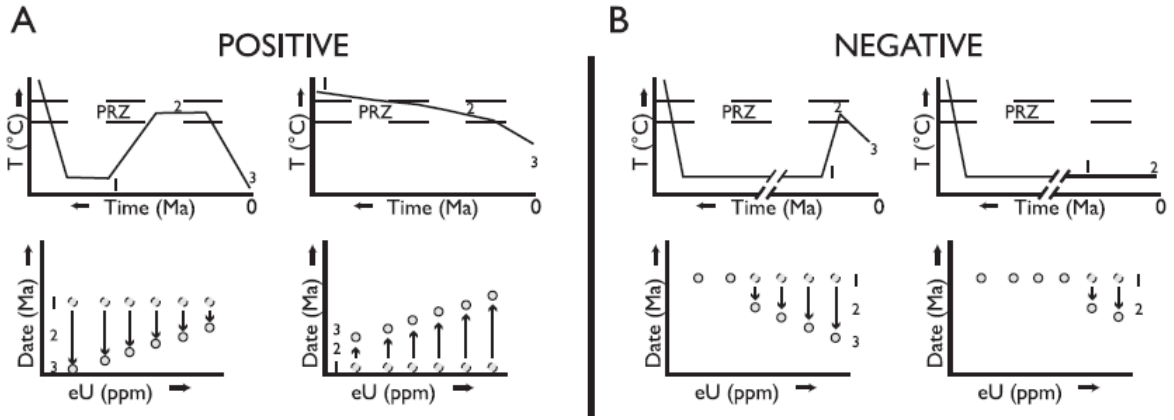

Figure 2.14: Exemplary thermal histories that produces positive (A) and negative (B) correlations between [eU] and ZHe age, after Guenthner et al. (2013). Positive correlations can be produced if diffusion occurs simultaneously with damage in-growth, e.g. when a rock cools slowly through the PRZ or experiences a thermal pulse. Negative correlation may be observed in cases of high accumulation of radiation damage, e.g. when an old rock spends a long time at low temperatures or when after that experiences a short reheating episode.

Excess ^{4}He from inclusions is not important in the case of zircons, because the U concentration is usually higher than in other common accessory minerals. U-Th zonation is common in zircon and causes poor reproducibility of ages (Dobson et al. 2008), and has a significant influence on the α-ejection effect (Hourigan et al. 2005). Ideally, the zonation pattern should be determined for each dated grain and included in further corrections. However, the conventional dating procedure, where the amount of parent isotopes is measured on a whole grain, does not allow for such determinations. Data free from the α-ejection and zonation effects may be acquired using a laser ablation method (Boyce et al. 2006). In this method, the concentration of ^{4}He is determined by measurement of ^{4}He amount released by laser ablation of a small pit within the polished crystal and further measurement of the pit volume. Subsequently the existing pit is widened and deepened for determination of parent isotope concentration. The use of this technique is limited to grains which are large and/or have high concentration of ^{4}He; this requirement excludes most apatites, but makes it successfully applicable for zircons (Tripathy-Lang et al. 2013).

The accuracy of measurements is monitored by analyses of aliquots of Fish Canyon Tuff zircons with the samples. The reproducibility of Fish Canyon Tuff aliquots in laboratories making the analyses routinely is lower that for standards used in AHe thermochronology, probably due to U-Th zonation and exceeds 10%, 28.3 $\pm$ 3.1 Ma (Dobson et al. 2008). The average (U-Th)/He age of aliquots of Fish Canyon Tuff zircons analysed during this study is 30.49 $\pm$ 3.03 (1σ).

2.3.3 Application of (U-Th-Sm)/He thermochronometers and their limitations

Isotherms in the shallow crust mimic the shape of the topography, especially those closest to the surface. That effect makes the AHe thermochronometer sensitive to past surface processes and changes of topography (e.g. House et al. 2001, Persano et al. 2002, Ehlers & Farley 2003). The sensitivity to low temperatures allows the AHe thermochronometer to be successfully used in investigation of faults movements; exhumation causes characteristic upward sweeping of isotherms and depending on fault regime, a different pattern of AHe ages in footwall and hanging walls may be observed and applied in interpretation of fault movements and exhumation (e.g. Ehlers et al. 2001, Ehlers & Farley 2003, Clark et al. 2010).

The AHe thermochronometer is, however, rarely used independently, as the ages alone usually do not provide comprehensive information on the rock thermal history. Easy to interpret AHe ages are almost entirely restricted to instantaneous cooling, such as volcanism or sub-surface intrusion cooling. Most often, AHe is combined with the AFT thermochronometer, which has overlapping sensitivity. This set of thermochronometers has been used in many different geological settings including mountain ranges (e.g. Van Der Beek et al. 2009, Vernon et al. 2009) and passive margins (e.g. Persano 2003, Balestrieri et al. 2005, Wildman 2015).

Similarly, the ZHe thermochronometer is usually combined with other methods. For example, combining ZHe ages with U-Pb ages can be used for provenance of detrital zircons (e.g. Rahl et al. 2003). Combining it with other methods, e.g. ^{40}Ar–^{39}Ar, AHe and apatite and zircon fission track analysis, has been applied in complex studies of exhumation in orogenic settings (e.g. Kirby et al. 2002, Reiners et al. 2003). ZHe ages can also be used for investigation of the cooling rates of intrusions (e.g. Dobson et al. 2010).

As already mentioned, the analysis of mineral thermochronometers strongly depends on availability of crystals of the mineral in the rock. Whereas zircon is usually well preserved in most clastic sedimentary rocks and quite abundant in igneous rocks, apatite is not resistant to chemical weathering and alteration. High quality apatite crystals are essential for AHe analysis, thus restricting the lithologies that can be sampled. Moreover, radiation damage, grain chemistry and analysis of broken crystals, are not yet fully understood.

2.4 Modelling of thermochronometric data

A qualitative interpretation of the thermochronometric ages and fission track length distribution can be achieved directly, but quantitative constraints on the thermal his-

tories of rocks can only be acquired through the use of numerical algorithms that describe the complex mechanisms of fission track annealing and ^{4}He diffusion. Because equations describing the annealing and diffusion are only a simplification of complex processes and the accuracy of the measurements is limited, the model will never be a real reflection of the modelled thermal event, but only its approximation. However, as George E.P. Box said: *"All models are wrong, but some are useful"* and testing various scenarios may give us better understanding of modelled processes and thermal histories.

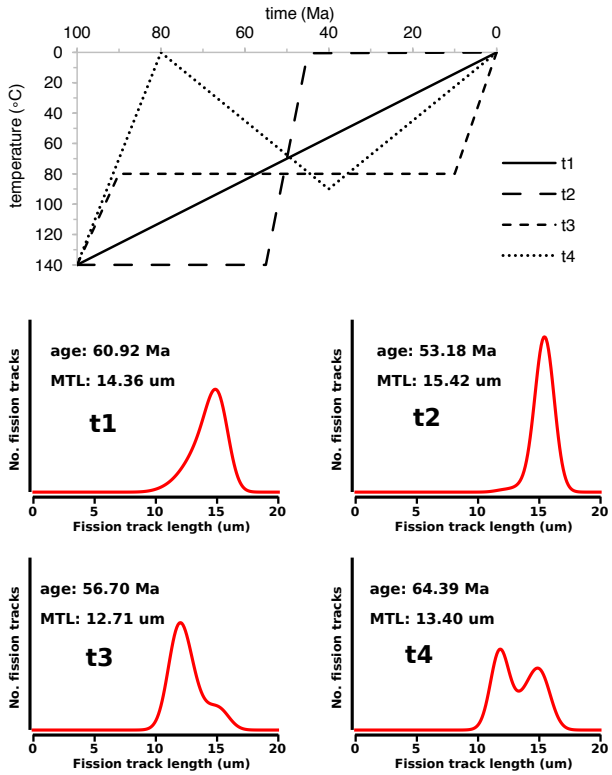

Figure 2.15: Apatite fission track ages, mean track lengths and fission track length distributions predicted for four thermal histories. Forward models computed using the QTQt software. Mean track length is given for track length projected using model of (Ketcham et al. 2007b).

Software based on the algorithms describing fission track annealing and ^{4}He diffusion is used to predict the data consistent with a set of time-temperature histories. These are called forward models. Forward models are a useful tool to understand a possible variation of thermochronometric ages or fission track length distributions for different thermal histories. Fig. 2.15 shows fission track ages and fission track length distributions predicted for four thermal histories characterized by different time spans that a rock particle spent the PAZ. In case of rapid cooling ($t2$) the age is the youngest, the MTL is the longest and the distribution of fission track lengths is narrow. As the time that the rock spend within the PAZ increases, the age increases and MTL decreases, whereas the shape of track length distribution is more complex, e.g. showing two peaks for the thermal history with a reheating episode ($t4$).

Similar simulations have been run for AHe and ZHe ages and the results are presented in Fig. 2.16 and Fig. 2.17, respectively. Ages of grains having different size and different [eU] have been predicted for four thermal histories. In case of AHe ages, the effect of grain size (Fig. 2.16 b) induces an age dispersion even for a rock that experienced rapid cooling (10°C/Myr—$t2$), but it is more pronounced for rocks that have spent long time within the PRZ ($t3$ and $t4$). The presence of radiation damage has negligible effect on

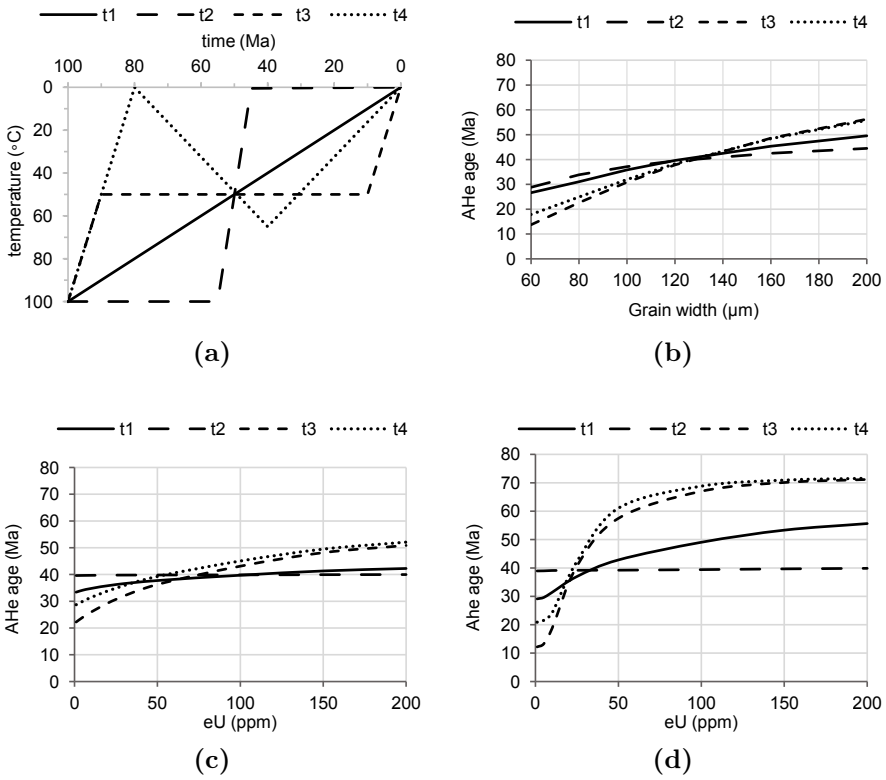

Figure 2.16: Apatite (U-Th-Sm)/He ages predicted for four thermal histories, different grain size and [eU]; (a) thermal histories; (b) AHe ages versus grain witdh (assuming constant diffusion parameters of Farley (2000)); (c) AHe ages versus [eU] assuming radiation damage of Gautheron et al. (2009) (for constant grain width of 120 μm); (d) AHe ages versus [eU] assuming radiation damage of Flowers et al. (2009) (for constant grain width of 120 μm). Forward models computed using the QTQt software.

the AHe ages for rapidly cooled rocks independently on the radiation damage model used (Fig. 2.16 C and D—$t2$). In case of rocks that resided in PRZ for a long time, the AHe ages may be significantly dispersed, e.g. for [eU] variation from 1 to 200 ppm and history $t3$ the ages vary from 13 to 71 Ma for the radiation damage model of Flowers et al. (2009) and from 22 to 51 Ma for the radiation damage model of Gautheron et al. (2009). The grain size variation in zircon causes similar, positive correlations with ZHe ages for all thermal histories (Fig. 2.17-b). The presence of radiation damage induces complex relationships (Fig. 2.17-b); rapid cooling results in almost no differentiation of the ages ($t2$), whereas for complex histories, e.g. samples that were reheated or subjected to some diffusive loss of He in lower temperatures ($t3$ and $t4$), the ZHe ages show either positive or negative correlation with [eU], for low [eU] and high [eU] crystals, respectively.

The presented forward models illustrate that track length distributions and dispersion patterns of AHe and ZHe ages may be powerful in resolving thermal histories of rocks. Forward modelling approach is, however, inefficient as it requires a large number of models to be run in order to find a thermal history that well fits the data. The

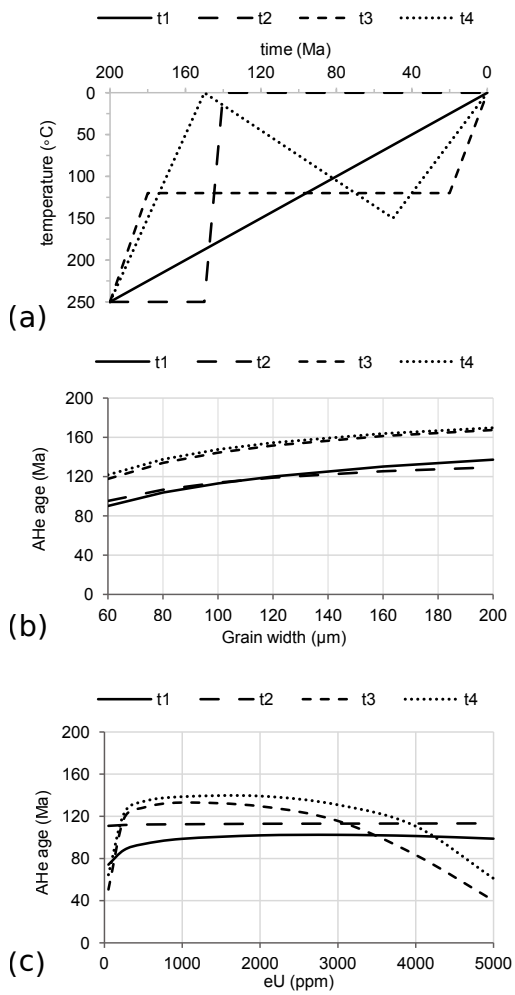

Figure 2.17: Zircon (U-Th-Sm)/He ages predicted for four thermal histories, different grain size and [eU]; (a) thermal histories; (b) ZHe ages versus grain witdh (assuming constant diffusion parameters); (c) ZHe ages versus [eU] assuming radiation damage of Guenthner et al. (2013) (for constant grain width of 100 μm). Forward models computed using the QTQt software.

inverse approach enables computing time-temperature paths consistent with the input data. Several inverse modelling codes have been proposed for fission track data (e.g. Gallagher 1995, Ketcham et al. 2000). More recently, new software has been developed to model the fission track and (U-Th)/He data together, with the possibility of adding other constraints, such as vitrinite reflectance, ^{40}Ar-^{39}Ar ages or ^{4}He/^{3}He diffusion profiles. The algorithms describing the annealing and diffusion processes, upon which the software is built, are also continuously improved.

Recently, numerical modelling of thermochronological data is dominated by two programmes: HeFTy (Ketcham 2005) and QTQt (Gallagher 2012). A robust comparison of the algorithms, upon which they are based, is presented by Vermeesch & Tian (2014). The advantage of both models lies in a user-friendly interface and a possibility of implementation of data from multiple thermochronometers to be modelled together; they differ in terms of their statistical approach.

HeFTy (Ketcham 2005) is based on a frequentist algorithm, which explores the model space using random sampling of points. It evaluates the likelihood, by calculating a chi-square goodness-to-fit test of each point. In the inverse modelling mode, computed time-temperature paths, are coloured in red or green, which refer to "good", p>0.5, and "acceptable", p>0.05, fit to the data. The main disadvantage of HeFTy is that for complex, large and/or high-resolution data sets HeFTy cannot find any probable time-temperature path.

QTQt (Gallagher 2012) uses Bayesian statistics, which requires the knowledge of the prior probability, which in case of thermochronological modelling, comprises the knowledge of the track annealing kinetics and the He diffusion. Prior determines the size of the

time-temperature space, inside which the model parameters are sampled. The model space is explored along a random walk (Markov Chain) and the likelihood and posterior probability are calculated, where the former is a fit of the observed data to the model in a particular point, and the latter reflects the ratio of the likelihood of recent and previous sampling points. The number of time-temperature points is not given, allowing the code to determine the complexity of the thermal history based on the given prior constraints and data. Usually, the higher the number of time-temperature points, the higher the likelihood of the model, but lower its posterior probability; it is an effect of a preference of the Bayesian approach to simpler thermal histories (Gallagher 2012). Additionally, the data and/or kinetics and diffusion parameters can be re-sampled by the software based on the input value and given uncertainties. This mode deals more efficiently with the noise on the data, which is a result of the measurement errors and complexity of geological processes, and is usually poorly known.

QTQt ranks all the models according to their posterior probability and plots only the most likely ones, whereas in HeFTy the final plot refers to the actual value of the model's likelihood. Thus, unlike HeFTy, increasing the amount of data enhances the QTQt modelling. The risk when using QTQt is that thermal histories will always be obtained even if the data and/or thermal model are geologically and theoretically impossible (Vermeesch & Tian 2014). Whatever model is used, it is the responsibility of the user to judge the quality of the results, which has to be done by carefully monitoring the discrepancies between the values predicted by the model and the real data, as well as geological knowledge. Data sets presented in this study include results from two or three thermochronometers per sample. For such complex data sets application of QTQt modelling is essential.

Both QTQt and HeFTy model He diffusion assuming spherical geometry for a diffusion domain. It has been shown that such approach, called a spherical approximation, is valid for whole crystals and requires calculation of the radius of the sphere that has the same surface to volume radio as the prismatic crystal (Meesters & Dunai 2002a). Because the analysed grains are often broken, using the spherical approximation approach may lead to inaccuracies; in case of fragments, without knowing an initial length of the crystal, the size of diffusion domain will be underestimated (Fig. 2.18-A; Brown et al. 2013, Beucher et al. 2013). Additionally fragmentation causes a characteristic pattern of dispersion that can be used to better constrain thermal histories; according to forward models, the ages of grains with one termination and one broken face are expected to decrease with decreasing length of the grain (Fig. 2.18-B; Brown et al. 2013).

The Helfrag code (Beucher et al. 2013) and the most recent versions of the QTQt software are able to model grains as fragments. When fragmentation is included, the diffusion of He has to be modelled in both the axial and radial direction and the shape

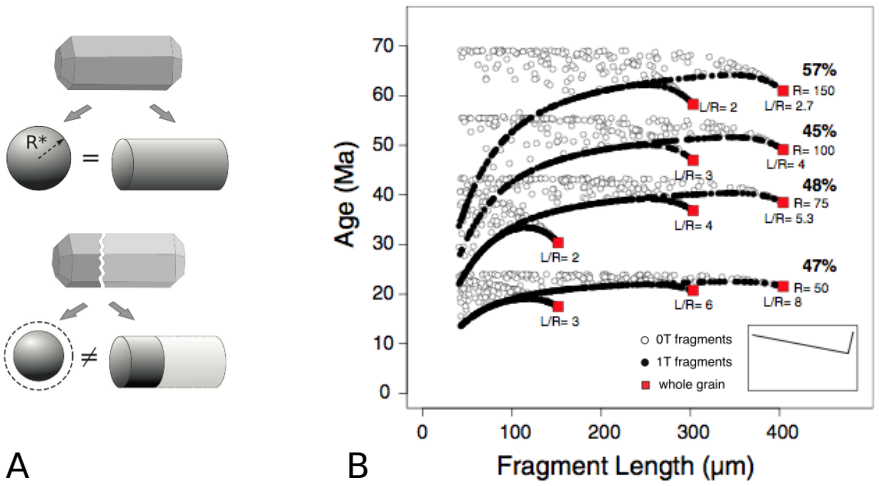

Figure 2.18: (A) Approximation of a hexagonal crystal to a sphere and cylinder for a whole crystal and a crystal fragment; after Beucher et al. (2013), and (B) predicted dispersion of AHe ages for different fragment types, fragment lengths and grain sizes (R = 50, 75, 100, 150 μm); after Brown et al. (2013). R* is a radius of the sphere that has the same surface to volume radio as the hexagonal crystal. 1T—grains with one natural termination, 0T—grains with no termination, both natural terminations broken. Box in the bottom right corner shows a schematic thermal history for which the age dispersion was predicted.

of the diffusion domain is approximated to a finite cylinder, rather than a sphere. The He profile is then predicted for different thermal histories by assuming that in the rock the crystals were unbroken and have been cut into fragments with the measured length during the mineral separation process. This assumption implies that modelling 1T crystals is straightforward, as the He concentration and, therefore the age, depends on only three parameters: the radius, the fragment length and the original length of the crystals. For 0T grains, instead, a fourth parameter is required, which is the position of the fragment within the original crystal, and the current version of the software does not provide the option of modelling 0T grains.

The initial length (L_0) of the crystal is unknown and can be treated as a parameter to be estimated during the inversion. This increases the computing time significantly and, as Beucher et al. (2013) have shown in an empirical experiment, may be substituted by a constant value of the initial length that is large enough. This simplification is due to the fact that for fragments longer than their radius, diffusion occurs only radially and it is insensitive to the axial length. A L_0 longer than the true value will therefore have no effect on short grains, or may slightly overestimate the modelled age in the case of longer fragments. This over-estimation is, however, unlikely to exceed 10%. It is suggested that good approximation of the L_0 may be obtained from a maximum fragment length plus two times the maximum radius of a given fragment set (Beucher et al. 2013).

Once plausible time-temperature paths are derived from the model, they need to be converted into exhumation histories, taking past changes in the thermal field within the crust into consideration. The thermal field of the upper crust may be a result of

multiple processes: magmatism, fluid flow, changes in heat flow, different heat conduction of rocks and vertical advection of the heat due to exhumation (Ehlers 2005, Braun et al. 2006). Complex modelling of these effects can be performed in the Pecube software (Braun 2003, Braun et al. 2012). Pecube is a user-friendly Fortran code, designed to predict low temperature thermochronological ages from an input tectonic scenario and changes of the topography (Fig. 2.19). It solves the heat transport equation in three dimensions, including the effects of heat production, diffusion and advection. In its initial version (Braun 2003), the algorithm worked in the forward mode and predicted AHe, AFT and Ar-Ar mica ages of rocks that will end up on the surface at the end of the scenario, assuming spatially and temporally uniform thermal properties of the modelled crust and spatially uniform uplift velocity. Further development broadened both the range of analysed thermochronometric systems including detrital datasets and the possibility of predicting sub-surface age patterns (boreholes and tunnels), and the variety of possible tectonomorphic scenarios such as the ability to include uplift kinematics due to fault movements (Braun et al. 2012). In this study a newly developed version of the code that provides the possibility to set variable heat production and thermal diffusivity parameters has been tested and used. Recent versions of Pecube are integrated with the Neighbourhood Algorithm of Sambridge (1999a,b), which allows Pecube to be used in the inversion mode. In this mode, the range of parameters is being searched to find values, usually rates and timing of exhumation, that have the lowest misfit with the input thermochronometric data. Pecube deals with topography changes and rock uplift separately; the exhumation is calculated after Molnar & England (1990), as a difference between the regional rock uplift and changes in elevation of the surface.

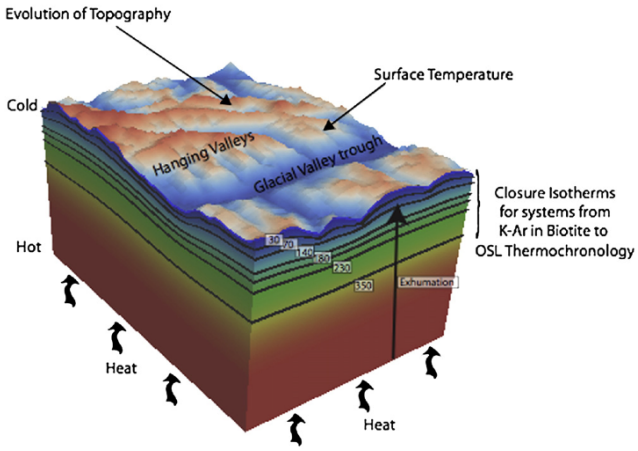

Figure 2.19: Exemplary illustration of a PECUBE model; after Braun et al. (2012). Black lines are the isotherms corresponding to different thermochronometers. Surface and bottom of the block have fixed temperatures and the crustal block is subjected to uplift assuming time-varying topography. The cooling path recorded by an exhumed rock particle is used to predict thermochronometric ages.

The methods described in this chapter have been used to analyse apatite and zircons from central west Britain in order to unravel Cenozoic geological history of the region. The results of the analyses will be presented in Chapter 3. The results of inverse modelling of the data using QTQt and Helfrag software are shown in Chapter 4, whereas the modelling of heat transfer using Pecube in Chapter 5.

Chapter 3

Low temperature thermochronology in central Britain

3.1 Introduction

During the early Cenozoic, the arrival of the Iceland plume was followed by the last stage of continental rifting and separation of the British Isles and Scandinavia from Greenland, with the consequent formation of the North Atlantic Ocean. This led to widespread surface uplift and erosion of the continental margins (Anell et al. 2009). The British Isles experienced significant uplift and denudation at that time. Evidence for both are recorded by unconformities in the most proximal sedimentary basins, such as the Celtic Sea Trough, Bristol Channel basin, the near complete lack of Cenozoic sediments in the Irish Sea basin (Ziegler 1988), and the increase in volumes and rates of sedimentation in the distal basins (e.g. Porcupine and Faroe-Shetland Basins) and in the North Sea (Anderton 1993, White & Lovell 1997). The East Irish Sea Basin (EISB) appears to have experienced the highest Cenozoic denudation in the UK; vitrinite reflectance and apatite fission track data indicate burial by ∼3 km of sediments in the Late Cretaceous with subsequent removal of ∼2 km during the early Palaeogene (Lewis et al. 1992, Green et al. 1997, Holford et al. 2005a).

The time and rate of denudation of basement rocks can usually be constrained by detailed thermochronological studies. Apatite fission track thermochronology has been used to constrain the Early Cenozoic cooling history of the basins and the surrounding, onshore regions (e.g. Green 1986, Lewis et al. 1992, Green 2002). Late Cretaceous temperatures similar to those constrained in the EISB have been reconstructed onshore, in the Lake District (Green 1986, 2002); however, the derived 3–4 km (Green 1986, Lewis et al. 1992) of denudation is at odds with of an estimation of removed overburden based on the regional geology (Holliday 1993). The amount and rates of Palaeogene denudation of southern Scotland and northern Wales, adjacent to the Lake District, are practically unknown. This study combines AFT and (U-Th-Sm)/He analyses of apatite and zircon, to constrain, for the first time, the amount and rate of cooling of

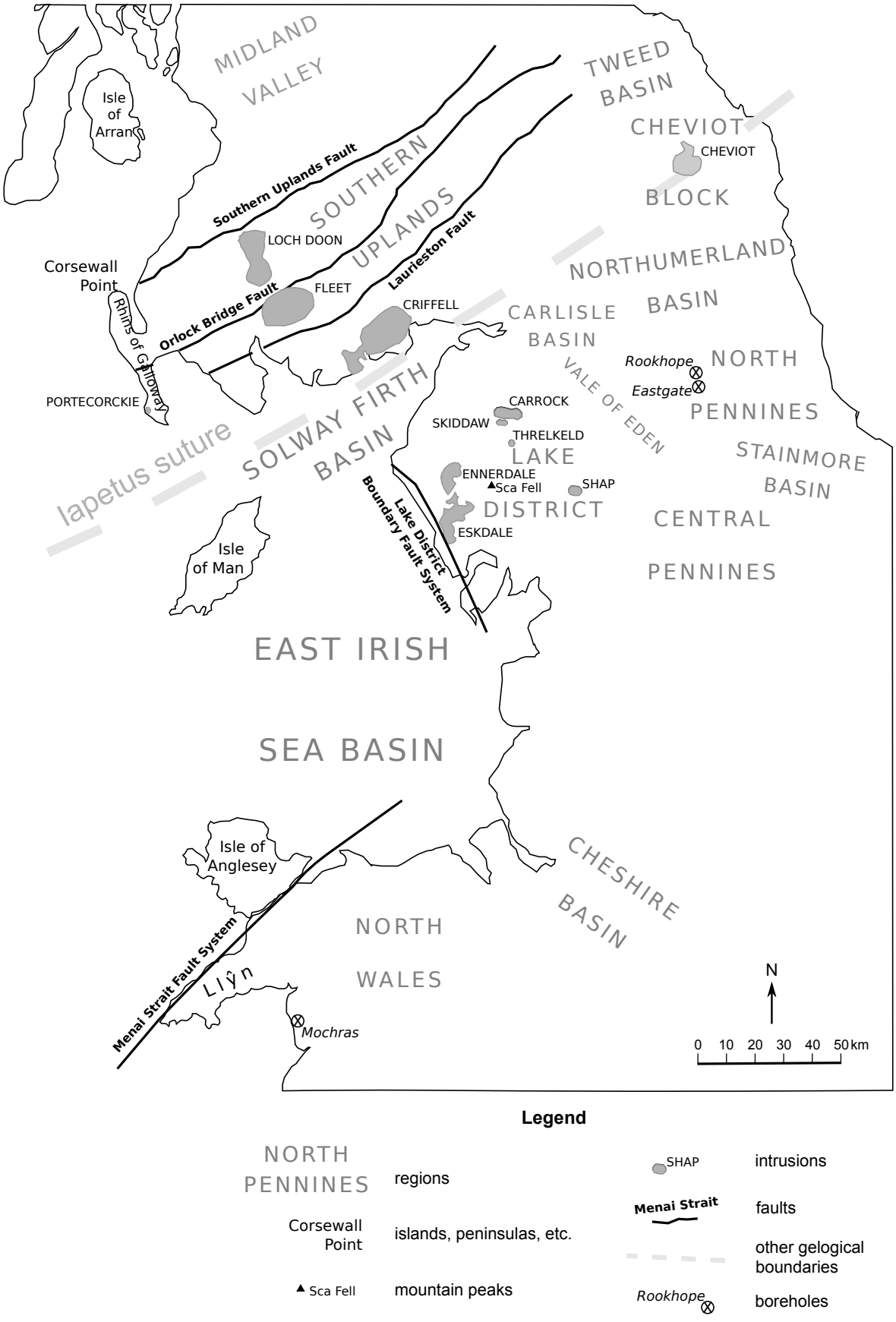

Figure 3.1: The study area with locations of all places mentioned in the text.

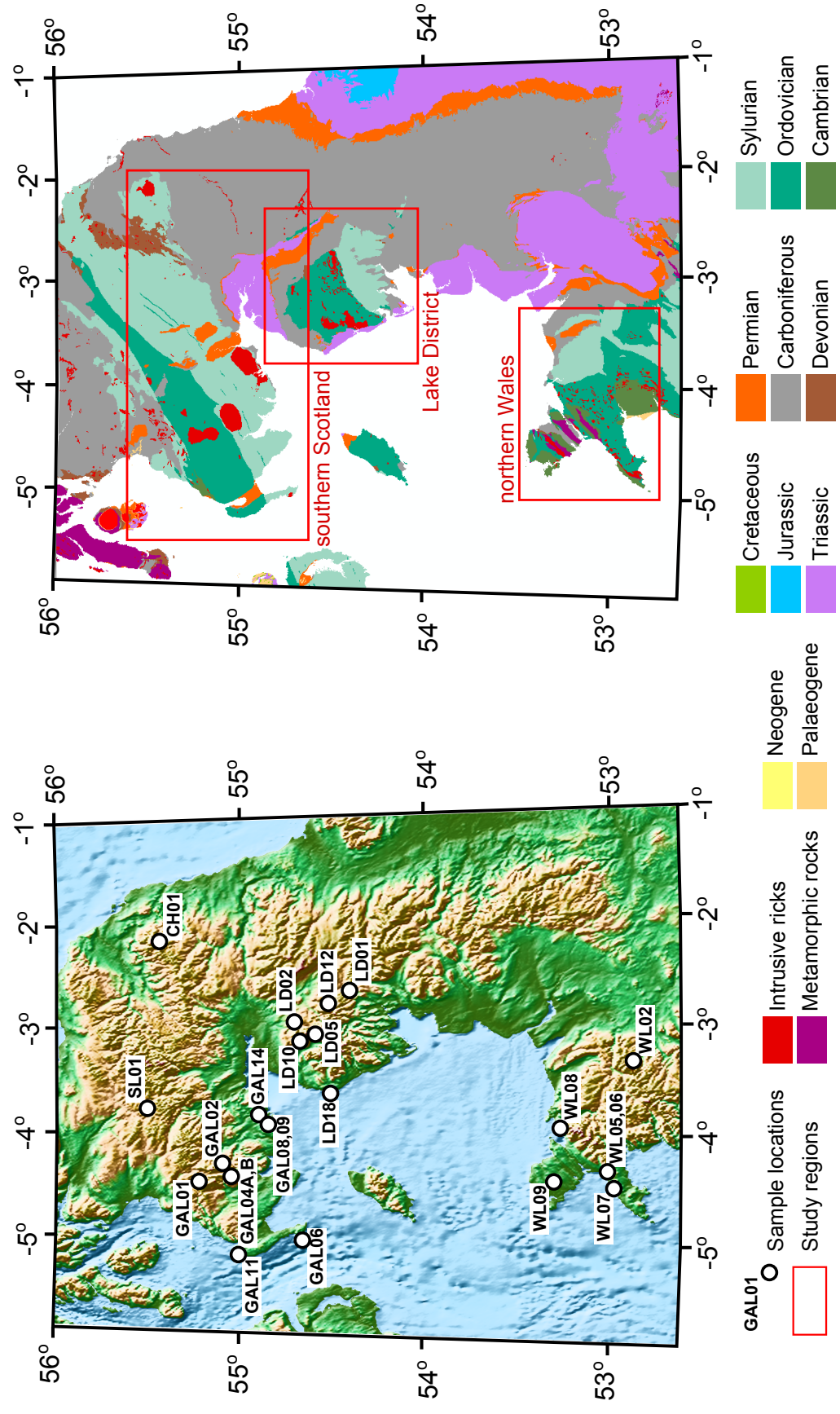

Figure 3.2: Left: Topographical map of the study area with locations of all samples analysed during this study; the map is based on the ETOPO1 Global relief model data and produced using Generic Mapping Tools. Right: Geological map of the study area with positions of three sampling regions; the map based on the Digital Geological Map of Great Britain 1:650 000 (DiGMapGB-625), British Geological Survey materials © NERC [2016].

Table 3.1: Sample locations and apatite fission track (AFT), apatite (U-Th-Sm)/He (AHe) and zircon (U-Th)/He (ZHe) ages for all samples analysed during this study. AFT ages are given as central ages and 1σ, AHe and ZHe data are given as an age range and number of analysed aliquots.

Sample name	Grid reference	Elevation (m)	Pluton/locality	AFT age (Ma)	AHe ages (Ma)	No. aliquots	ZHe ages (Ma)	No. aliquots
Lake District								
LD01	NY 55500 08400	380	Shap	75.0 ± 3.1	19.7–49.9	10	202.6–393.2	4
LD02	NY 35005 33359	445	Carrock	64.5 ± 6.2	24.3–56.5	14	-	-
LD03	NY 35125 33476	345	Carrock	-	-	-	290.6–416.0	4
LD05	NY 32874 24395	192	Threlkeld	74.9 ± 7.6	-	-	-	-
LD10	NY 29679 27869	347	Skiddaw	55.4 ± 3.6	-	-	78.3–128.3	3
LD12	NY 49456 15212	258	Haweswater	35.9 ± 8.5	41.0–48.8	5	-	-
LD18	NX 96725 17881	10	Whitehaven	48.5 ± 3.1	38.4–66.5	6	-	-
southern Scotland								
GAL01	NX 47635 94078	224	Loch Doon	199.5 ± 8.9	32.5–92.2	25	-	-
GAL02	NX 64563 74160	50	Fleet	78.1 ± 4.4	31.5–105.7	24	-	-
GAL04A	NX 58574 73491	110	Fleet	83.7 ± 3.8	51.5–109.0	5	-	-
GAL04B	NX 58574 73491	110	Fleet	79.3 ± 4.5	61.3–93.9	5	-	-
GAL06	NX 08932 35394	50	Portencorkie	159.5 ± 7.3	36.5–76.8	8	-	-
GAL08	NX 83910 60950	56	Criffell	52.1 ± 2.5	49.8–81.4	4	-	-
GAL09	NX 84373 60303	60	Criffell	55.0 ± 2.4	41.4–64.1	5	-	-
GAL11	NX 98074 72683	1	Corsewall Point	197.9 ± 10.1	24.8–62.8	25	-	-
GAL14	NX 83910 60950	65	Criffell	63.4 ± 2.8	37.1–59.8	19	147.5–296.3	5
SL01	NS 91901 23753	310	Crawfordjohn	215.0± 14.3	36.0–64.7	5	-	-
CH01	NT 94308 21496	260	Cheviot	290.5 ± 13.2	40.1–69.8	4	-	-
northern Wales								
WL02	SJ 19114 34708	168	Ffestiniog	172.1 ± 28.6	51.5–77.2	3	-	-
WL05	SH 36559 45979	219	Llŷn	187.0 ± 13.7	54.3–75.6	7	-	-
WL06	SH 36559 45980	220	Llŷn	195.5 ± 20.1	40.3–64.1	5	-	-
WL07	SH 31833 42093	26	Llŷn	188.4 ± 14.2	32.3–44.1	5	-	-
WL08	SH 71565 75663	200	Penmaenmawr	150.2 ± 11.2	29.5–45.4	5	-	-
WL09	SH 39503 79488	60	Coedana	50.6 ± 4.8	21.2–51.8	2	-	-

onshore central Britain from 200°C to 40°C, in order to provide insights on its causes. The study area includes three Caledonian basement terranes surrounding the EISB: the Lake District in northern England, the Southern Uplands and the Cheviot block in southern Scotland, and northern Wales (Fig. 3.1 and 3.2). Grid references, elevation and thermochronometric ages for all analysed samples are given in Table 3.1.

Rocks were collected with the aim of investigating the relationship between the pattern of cooling and pre-existing geological structures and/or lithologies. The sampling strategy was also driven by the need to acquire good quality, clear, prismatic apatite crystals for the (U-Th-Sm)/He determinations. Typically samples have been restricted to intrusive rocks. Some granites did not yield good quality apatite grains either because of hydrothermal fluid alteration or the chemical composition of the granitic bodies. Rocks were collected to cover the maximum possible elevation range; the highest peaks, however, are not made by intrusive rocks and the maximum difference between outcrop samples is ∼500 m (Fig. 3.2, Table 3.1).

In the next three sections, the detailed sampling strategy and the low temperature thermochronometric data will be presented: Lake District (3.2), southern Scotland(3.3) and northern Wales (3.4). Section 6.5 provides an overview of the geographical distribution of the data across the whole region of onshore central Britain.

3.2 The Lake District

3.2.1 Geological setting

The Lake District comprises an elevated block of basement rocks bounded by Carboniferous and Permo-Triassic basins. In the north and north-east, it borders with the Solway Firth Basin and the Vale of Eden. In the south-east it is separated from the Askrigg block by the Dent Fault, and on the west from the East Irish Sea Basin by the Lake District Boundary Fault Zone.

The oldest rocks in the Lake District are the Lower Ordovician turbidite layers of the Skiddaw Group and mid-Ordovician volcano-clastics (e.g. Borrowdale and Eycott Volcanics). They are intruded by Early Devonian granitic plutons (Table 3.2). The biggest granite outcrops are the Eskdale and Ennerdale granites on the western flank of the Lake District. An extensive area of low gravity Bouger anomalies underneath the Lake District suggest the presence, at depth, of a large granitic batholith (Bott 1974). The Lake District granites are characterized by high heat production, with maximum values of 5.2 $\mu W/m^3$ measured in the Shap granite (Webb et al. 1987). Present day heat flow in the region is clearly elevated and exceeds 90 mW/m^2 near the Skiddaw granite (Lee et al. 1987, Busby et al. 2011). Ore mineralization in the Lake District includes

lead, zinc, iron and copper. The main phases of mineral veins formation occurred in the Early Devonian and Early Carboniferous and their distribution correlates with the presence of underlying granite batholiths, that probably provided the heat for the hot fluid circulation (Moseley 1978, Stanley & Vaughan 1982). The Lake District block formed a structural high during the Carboniferous and Permo-Mesozoic extensional phases (Woodcock & Strachan 2000); post-Caledonian sediments are scarce, condensed and are exposed only on the block margins. That the block was elevated during at least part of the Mesozoic is documented by the presence of Borrowdale Volcanics in the EISB and by the fact that the Permo-Triassic strata within the basin get thinner towards the block (Chadwick et al. 1994, Akhurst 1997). The dome-like shape of the Lake District has been considered to result from the early Palaeogene regional uplift (Bott 1974, Moseley 1978, Green 1986).

Table 3.2: The age of emplacement of some of the more important intrusions in the Lake District.

Intrusion	Age (Ma)	Method	References
Shap	∼393	K-Ar (biotite)	Brown et al. (1964)
	390 ± 6	U–Pb (zircon)	Pidgeon & Aftalion (1978)
Carrock	416 ± 20	Rb–Sr	Rundle (1979)
Skiddaw	∼399	K-Ar (biotite)	Brown et al. (1964)
	399 ± 9	K–Ar (biotite)	Shepherd et al. (1976)
Threlkeld	439 ± 9	Rb-Sr	Rundle (1981)
Eskdale	429 ± 4	Rb–Sr	Rundle (1979)
Ennerdale	420 ± 4	Rb–Sr	Rundle (1979)

3.2.2 Existing thermochronological constraints

AFT ages vary from 44.9 to 235 Ma with the youngest ages, 45–65 Ma, found for Stockdale rhyolite and in the Carrock–Skiddaw area (Green 1986, Lewis et al. 1992). The thermal modelling of the ages and the track length distributions indicate rapid exhumation in the early Palaeogene, at ∼60 Ma, from more than 100°C. Such temperatures corresponds to ∼3–4 km of burial, if the modern geothermal gradient (∼30°C/km) is assumed. The AFT study from the Scafell Pike region suggests that the early Palaeogene geothermal gradient was two times higher than the present-day value and that, therefore, the total Cenozoic denudation in the Lake District was 1 to 2 km (Green 2002). Although, there is a relatively large AFT data set available for the Lake District, the maximum late Cretaceous temperatures are not well constrained, as in many localities they exceeded 110°C and were outside the sensitivity of the AFT system. Timing and rate of cooling, which are crucial for deciphering processes governing Cenozoic evolution of the region, are also not constrained precisely.

3.2.3 Sampling strategy

In order to obtain good quality apatites suitable for AHe analysis, the samples were collected mostly from intrusive rocks. Because the yield of apatites was low, three additional samples, two from the Borrowdale Volcanics and one from the Whitehaven Sandstone Formation, were collected. About 2.5 kg of rock was collected and processed using standard separation procedures for apatites and zircons (see Appendix A.1). Of the sixteen rocks, only seven yielded enough apatite crystals for thermochronological analyses. The locations of the analysed samples are shown in Fig. 3.2 and given in Table 3.1. Samples showing a Palaeogene AFT age have also been analysed for ZHe in order to add constraints on temperatures at which these rocks were in the end of the Cretaceous. The detailed information of the samples are available in the Appendix B.

3.2.4 Apatite fission track analysis

Fission track age and track length distributions have been determined on six samples, following the procedure given in Appendix A.2. The central age, MTL and average D-Par values are reported in Table 3.3; single-grain data are presented in Appendix B.

3.2.4.1 Fission track age

Apatite fission track ages from the Lake District vary from 35.9 ± 8.5 Ma to 75.0 ± 3.1 Ma and are significantly younger than the emplacement age of the plutons, ∼400 ± 20 Ma (Table 3.2). All samples passed the χ^2 test, although the apatite crystals are usually of low quality and the age determinations could only be done in fewer than the normal 20 grains. The youngest age, which comes from the Haweswater gabbro (LD12) on the east flank of the block is, for example, calculated based on only seven single-grain ages, and, therefore, has to be taken with caution. Similarly, one of the oldest ages, ∼75 Ma, in the Threlkeld microgranite (LD05) in the central Lake District is based on 11 single-grain ages and has relatively large error associated with the central

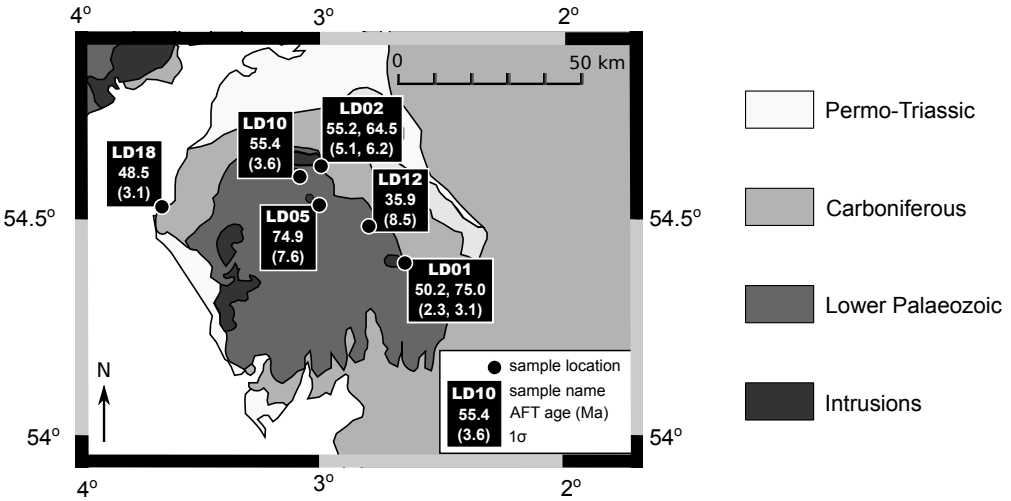

Figure 3.3: Map of apatite fission track ages in the Lake District.

age (Table 3.3). Of the nine slides analysed, two (LD05 and LD12) were over-etched, hampering an accurate determination of D-par and track length values, that would be artificially too long. Samples LD01 and LD02, from Shap granite and Carrock gabbro respectively, have possibly been slightly under-etched (slides 1) and new AFT mounts from the remaining apatite grains were prepared and counted (slides 2). In case of LD01, the change in the age is 25 Ma, far outside the 2σ error (6.2 Ma). LD02 becomes 9.3 Ma older, which is outside the 1σ, but within 2σ error (12.4 Ma).

D-Par values have not been measured on LD05 and LD12, due to clear over-etching. Measured D-Par values vary from 1.60 $\pm$ 0.1 μm to 3.78 $\pm$ 0.42 μm. There is no significant difference between two slides of LD01, but in the case of LD02, the difference is 0.77 μm, outside the 2σ variation (0.22 μm).

3.2.4.2 Track length distribution

Track lengths were measured on three samples. To account for anisotropy, every track has been c-axis projected, using the angle of the track with the c-axis of the crystal and the D-Par value of the grain in which the track was measured (Ketcham et al. 2007a,b). The MTL vary from 13.14 $\pm$ 1.78 μm to 14.55 $\pm$ 1.49 μm for measured track lengths and 14.35 $\pm$ 1.29 μm to 15.38 $\pm$ 0.99 μm for c-axis projected tracks. Only in the case of LD01, >100 horizontal, confined tracks have been measured. LD02 is characterized by low U concentration and only 16 tracks were measured in the mount used to calculate the age (slide 3); an additional slide was prepared for track length determination (slide 2). Because track lengths were measured only on three samples, a discussion about the correlation between AFT age and MTL is not possible.

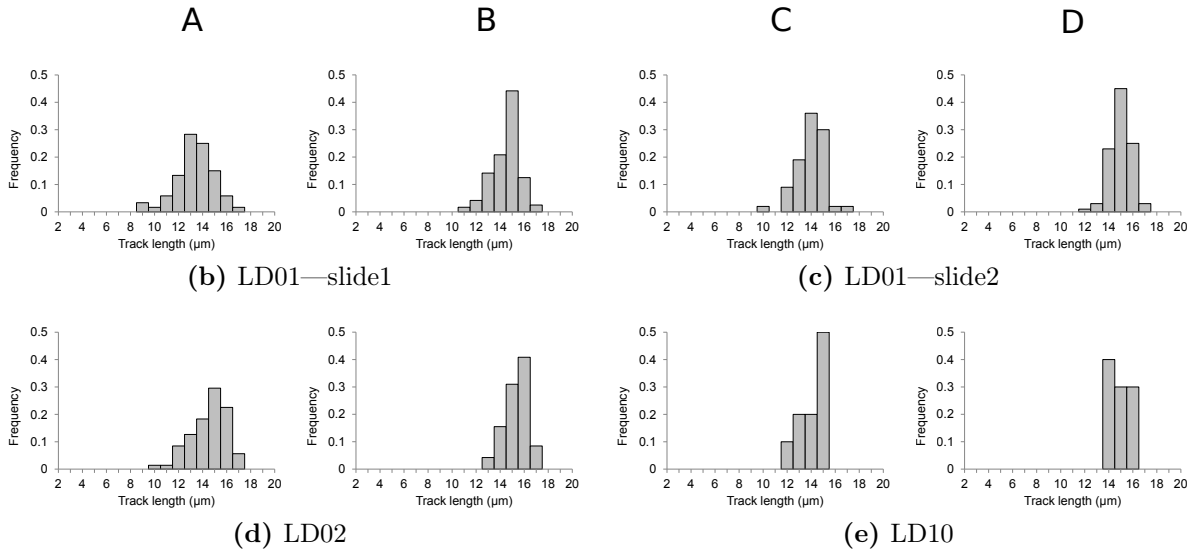

(b) LD01—slide1 **(c)** LD01—slide2

(d) LD02 **(e)** LD10

Figure 3.4: Histograms of track length distribution of samples from the Lake District. Columns A and C—measured track lengths, columns B and D—projected track lengths. Track length projection after Ketcham et al. (2007a).

Table 3.3: Apatite fission track data from the samples in the Lake District. Symbols: ρ_D—tracks density on the dosimeter, ρ_s—spontaneous track density, ρ_i—induced track density, P—probability that the grains pass χ^2 test, MTL m—mean track length measured, MTL p—mean track lengths projected, N_D—number of tracks on the dosimeter, N_s—number of spontaneous tracks, N_i—number of induced tracks

Sample name No. grains [lengths]	ρ_D (cm^2) N_D	ρ_s (cm^2) N_s	ρ_i (cm^2) N_i	χ^2	P (%)	age (Ma)	$\pm1\sigma$	MTL m (μm)	$\pm1\sigma$	MTL p (μm)	$\pm1\sigma$	DPar (μm)	$\pm1\sigma$
|Shap|													
LD01_slide1 20 [120]	1.72E+06 11903	4.1E-07 868	2.21E-06 4645	10.6	93.8	50.2	2.3	13.35	1.55	14.48	1.16	1.60	0.10
LD01_slide2 22 [110]	1.27E+06 8874	6.33E-07 1608	1.67E-06 4247	16.5	73.9	75.0	3.1	13.14	1.78	14.35	1.29	1.82	0.08
|Carrock|													
LD02_slide1 26 [4]	1.73E+06 11903	5.24E-08 156	2.58E-07 764	15.6	92.7	55.2	5.1	13.59	0.68	14.66	0.28	1.63	0.11
LD02_slide2 0 [76]	- -	- -	- -	-	-	-	-	14.55	1.49	15.39	0.99	2.99	0.52
LD02_slide3 20 [16]	1.23E+06 8874	7.06E-08 157	2.1E-07 467	9.2	96.9	64.5	6.2	13.79	1.36	14.90	0.97	2.40	0.11
|Threlkeld|													
LD05 11 [0]	8.87E+05 6478	4.52E-07 164	8.17E-07 303	3.1	98.0	74.9	7.6	-	-		-	-	-
|Skiddaw|													
LD10 17 [0]	8.83E+05 6478	4.47E-07 435	1.11E-06 1083	14.6	48.3	55.4	3.6	14.16	1.14	14.87	0.83	2.20	0.13
|Hawerwater|													
LD12 7 [0]	8.87E+05 6478	1.09E-07 23	3.83E-07 89	4.2	65.2	35.9	8.5	-	-		-	-	-
|Whitehaven fm.|													
LD18 16 [0]	8.71E+05 6478	5.77E-07 459	1.61E-06 1285	18.5	23.9	48.5	3.1	-	-	-	-	3.78	0.42

The histograms of track length distribution are shown on Fig. 3.4. In all cases, the c-axis projected tracks are characterised by a narrower distribution than the measured ones. All histograms are negatively skewed with many long tracks. Only 10 tracks were measured in LD10, but even in this case, the same trend can be observed.

3.2.4.3 Summary

The AFT ages from the Lake District are much younger than the intrusion emplacement age and range from 50 to 60 Ma. The track length distributions are characterized by long tracks and negatively skewed histograms. The MTLs are ∼14 μm.

3.2.5 Apatite and zircon (U-Th-Sm)/He analyses

Apatite (U-Th-Sm)/He (AHe) analyses have been carried out on single-grain aliquots from the four samples that provided acceptable quality apatite crystals. Zircon (U-Th)/He (ZHe) analyses have been performed on three samples. The analytical procedure for both AHe and ZHe is described in Appendix A.3.

Aliquots with clear analytical problems were discarded from the calculation of the central ages, modelling and interpretation and are not presented here. Data from all analysed aliquots and comments on discarded grains are, however, given in data logs for each sample in Appendix B. Central ages, used for graphical presentation purposes, were calculated after Vermeesch (2008). The α-recoil correction was performed using 'Alpha F_T-ejection factor' software (Gautheron & Tassan-Got 2010, Ketcham et al. 2011).

3.2.5.1 Apatite (U-Th-Sm)/He data

AHe data of aliquots used for modelling and interpretation are presented in Table 3.4 and uncorrected central AHe ages are shown on a map in Fig. 3.5. The number of aliquots analysed per sample vary from 5 to 14 and the majority of aliquots included only one grain. Because of analytical difficulties due to both low [eU] (<10 ppm) and small grain size, additional one multi-grain aliquot (M1) has been analysed

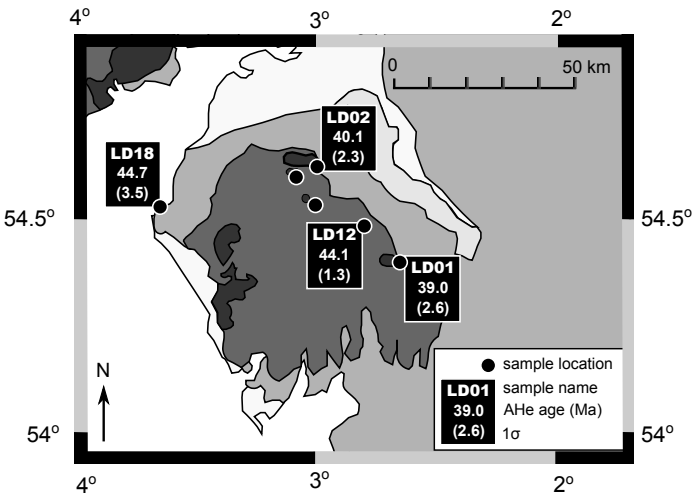

Figure 3.5: Map of apatite (U-Th-Sm)/He ages in the Lake District. For the legend to geological map see Fig. 3.3.

Table 3.4: Single grain apatite (U-Th-Sm)/He data from samples from the Lake District. Symbols: L—length, W1—width, W2—thickness, R*—equivalent radius, T—terminations, eU—effective Uranium, age—uncorrected age, age$_c$—age corrected for α-recoil, † analytical error; ‡ analytical error + 10% of the age (based on the reproducibility of Durango aliquots). Central ages and central age uncertainties calculated using Radial Plotter software (Vermeesch 2009).

Sample	No.	L (μm)	W1 (μm)	W2 (μm)	R* (μm)	T	He (μcc/g)	U (ppm)	Th (ppm)	Sm (ppm)	Th/U	eU (ppm)	age (Ma)	error†	error‡	F_T	age_c (Ma)	error‡	central age ± 1σ (Ma)
LD01 (Shap)	1	173	122	99	60	0	217.8	29.1	39.4	198.4	1.4	38.3	46.5	1.1	5.8	0.81	57.1	6.9	39.0 ± 2.6
	2	130	128	99	57	1	68.3	20.9	32.4	127.4	1.6	28.5	19.7	0.5	2.5	0.79	25.0	3.0	
	3	167	121	86	56	1	116.0	21.8	37.9	148.2	1.7	30.7	30.9	0.7	3.8	0.78	39.9	4.7	
	4	100	120	87	49	0	118.6	25.9	33.1	96.5	1.3	33.7	28.9	0.7	3.6	0.80	36.1	4.3	
	5	191	118	110	62	1	159.0	25.7	32.7	102.5	1.3	33.4	39.1	0.9	4.9	0.80	49.2	5.9	
	6	83	178	126	58	1	154.3	17.5	73.6	89.8	4.2	34.8	36.4	1.0	4.6	0.80	45.3	5.5	
	7	230	75	64	43	2	190.9	16.2	69.7	195.6	4.3	32.5	47.9	1.4	6.2	0.66	72.1	8.6	
	8	115	184	132	68	1	180.1	15.1	70.1	120.9	4.6	31.6	46.6	1.2	5.9	0.82	56.6	6.8	
	9	158	122	70	52	1	271.5	21.5	97.8	179.1	4.6	44.5	49.9	1.3	6.3	0.75	66.9	8.0	
	10	235	94	81	52	2	214.0	18.8	154.9	202.4	8.3	55.2	31.7	0.8	4.0	0.72	44.4	5.2	
LD02 (Carrock)	1	225	91	72	49	0	12.7	3.0	4.4	198.0	1.5	4.1	24.3	1.6	4.1	0.75	32.4	4.9	40.1 ± 2.3
	2	297	135	116	72	0	15.2	2.3	3.8	168.4	1.6	3.2	36.3	1.1	4.8	0.83	43.5	5.5	
	3	199	149	153	76	0	19.4	3.0	5.0	142.9	1.7	4.2	36.7	1.1	4.7	0.86	42.9	5.3	
	4	139	148	136	68	1	27.7	4.4	8.3	167.2	1.9	6.4	34.8	1.1	4.5	0.82	42.4	5.3	
	5	185	122	100	61	0	14.1	1.3	5.9	117.9	4.4	2.7	40.6	1.7	5.8	0.81	50.4	6.8	
	6	350	260	156	111	1	32.3	3.0	8.8	175.1	2.9	5.1	49.7	0.9	5.9	0.88	56.4	6.6	
	7	155	70	61	38	1	26.5	3.1	12.0	96.8	3.9	5.9	36.2	7.4	11.0	0.66	55.2	12.9	
	8	160	184	131	76	0	19.7	1.7	6.8	122.1	4.1	3.3	47.3	1.3	6.0	0.86	54.8	6.8	
	9	208	143	111	70	1	29.1	2.4	10.6	134.6	4.4	4.9	47.6	2.1	6.9	0.81	58.6	8.0	
	10	274	112	130	65	0	22.9	1.9	7.2	231.2	3.7	3.6	48.1	2.2	7.1	0.81	59.6	8.2	
	11	140	124	97	57	0	37.0	4.6	17.8	190.2	3.8	8.8	33.6	1.6	5.0	0.81	41.7	5.8	
	12	82	131	112	50	0	18.0	1.9	9.3	189.9	4.8	4.1	34.0	0.8	4.2	0.82	41.4	4.9	
	13	135	83	66	42	1	19.3	0.6	8.6	127.2	13.9	2.6	56.5	1.7	7.4	0.68	83.6	10.1	
	14	271	236	112	89	0	22.3	2.0	7.8	230.2	3.9	3.8	44.7	0.7	5.2	0.87	51.6	5.9	
LD12 (Haweswater)	1	126	84	65	39.4	2	47.7	4.9	12.7	145.1	2.6	7.9	48.8	2.4	7.3	0.64	76.1	10.0	44.1 ± 1.3
	2	113	88	69	41.6	0	37.9	4.3	11.7	140.6	2.7	7.1	42.9	2.3	6.6	0.74	58.4	8.1	
	3	147	82	49	37.4	1	45.4	6.0	12.4	202.3	2.1	8.9	41.0	2.1	6.2	0.66	62.3	8.3	
	4	113	94	65	38.5	2	44.8	5.4	12.8	158.5	2.4	8.4	43.0	5.9	10.2	0.63	67.8	12.7	
	M1	100	67	58	33.8	-	52.9	5.8	15.8	272.0	2.7	9.5	44.1	2.0	6.4	0.63	70.5	9.1	

Table 3.4: (continued)

Sample	No	L (μm)	W1 (μm)	W2 (μm)	R* (μm)	T	He (mcc/g)	U (ppm)	Th (ppm)	Sm (ppm)	Th/U	eU (ppm)	age (Ma)	error†	error‡	F_T	age_c (Ma)	error‡	central age $\pm$ 1σ (Ma)
LD18 (Whitehaven)	1	230	72	68	42	0	53.5	7.4	7.2	238.0	1.0	9.1	46.8	1.8	6.5	0.71	66.1	8.4	44.7 $\pm$ 3.5
	2	220	44	40	27	2	267.1	27.4	110.0	241.5	4.0	53.3	41.0	1.2	5.3	0.49	84.0	9.6	
	3	89	85	83	40	0	368.3	18.1	115.3	203.0	6.4	45.2	66.5	1.7	8.4	0.74	90.4	10.8	
	4	170	107	95	55	1	255.5	16.2	18.9	480.6	1.2	20.6	41.4	1.1	5.3	0.77	53.7	6.5	
	5	124	105	100	51	1	252.9	40.2	54.0	159.9	1.3	52.9	39.2	0.9	4.9	0.76	51.4	6.1	
	6	175	83	69	44	1	454.3	39.9	243.7	36.8	6.1	97.2	38.4	0.7	4.5	0.70	55.2	6.2	

for the sample LD12. Single- and multi-grain aliquots yielded AHe ages that are statistically indistinguishable.

The central ages vary from 39.0 ± 2.6 Ma in Shap granite to 44.7 ± 3.5 Ma in a sandstone from the western flank of the block. The uncorrected single-grain ages in the region vary from 19.7 ± 2.5 Ma to 66.5 ± 8.4 Ma and corrected ages vary from 25.0 ± 3.0 Ma to 90.4 ± 10.8 Ma. Many corrected AHe ages are older than the corresponding AFT age, however, the α-recoil correction may introduce inaccuracy. The central ages, calculated based on uncorrected ages, are younger than the AFT age for samples LD01, LD02 and LD18. The AHe central age is, however, older than the AFT age in sample LD12, but this is probably due to a likely under-estimation of the AFT age, as explained in the previous section. When, however, the associated uncertainties are taken into consideration, the central age and all single aliquot ages are younger or indistinguishable from the AFT age. The uncorrected single-grain ages of other samples are rarely older than the corresponding AFT age; only one AHe single-grain age (LD18—3), is older than the AFT age even when the uncertainties on both age determinations are considered. This old grain comes from a clastic sedimentary rock, and consequently that apatite may have an unusual chemical composition, which could influence the closure temperature of He (Gautheron et al. 2013).

The ages have been plotted versus [eU] and grain thickness on Fig. 3.6 and 3.7. In both cases, there are no clear trends; the lack of a relationship between ages and [eU] may be due to the values of [eU] themselves. Two samples, LD02 and LD12, have low

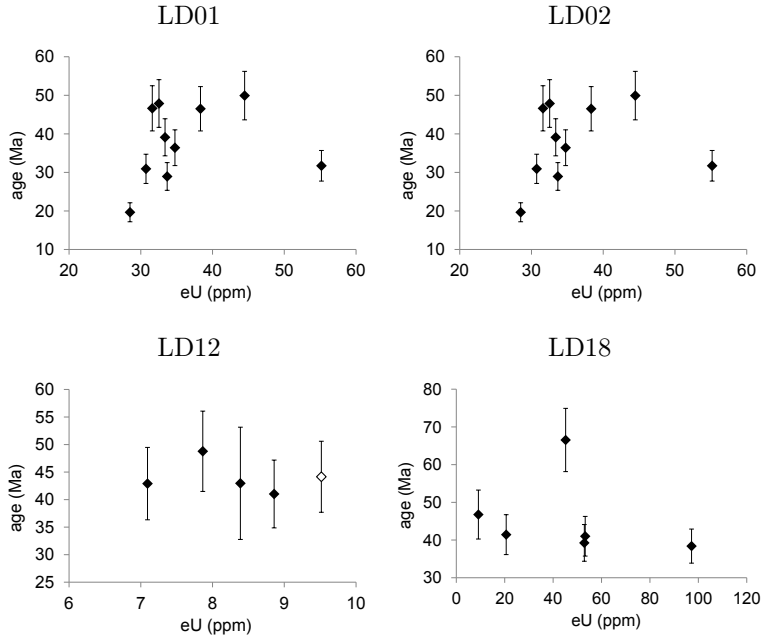

Figure 3.6: Apatite (U-Th-Sm)/He age (Ma) versus eU concentration (ppm) in samples from the Lake District; black—single-grain aliquots, white—multi-grain aliquots. The error bars show analytical error + 10% of the age (based on the reproducibility of Durango aliquots).

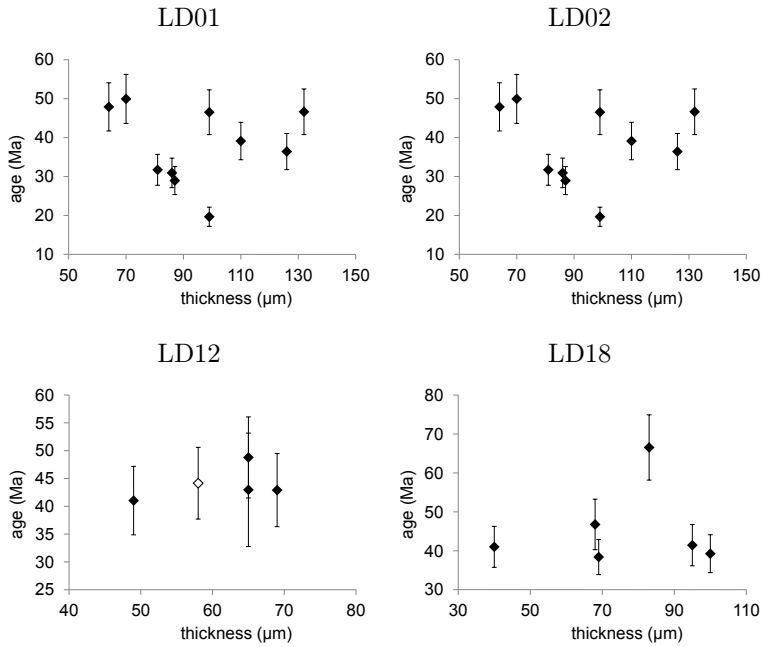

Figure 3.7: Apatite (U-Th-Sm)/He age (Ma) versus grain thickness (μm) in samples from the Lake District; black—single-grain aliquots, white—multi-grain aliquots. The error bars show analytical error + 10% of the age (based on the reproducibility of Durango aliquots).

[eU] of 2.7–8.8 ppm and 7.1–9.5 ppm, respectively. In LD01, [eU] is higher and more variable, however, the range of 28.5–55.2 ppm is still relatively small when compared with the range in samples from other regions. Low variation of [eU] may make observing the trend difficult, especially when the spread of ages is relatively low. The oldest aliquot of the LD02, with an uncorrected age of 56.5 Ma, is characterized by significantly different Th/U ratio, 13.9, than other aliquots, ∼1.5–4.4. Although, this abnormal value may be inaccurate, there are no apparent analytical reasons to discard this measurement, and therefore the age has been included in the modelling.

All AHe single-grain ages from the region have been plotted on a radial plot (Fig. 3.8a) and on a KDE plot (Fig. 3.8b). Even though, the total number of ages from the region is not high, and the sample size is not constant, the ages form a clear group, with 86% of the ages lying within a range 30–60 Ma and central age of 40.2 ± 1.6 Ma. The KDE, as well as the histogram, are negatively skewed with a short tail of young ages. The number of the ages is, however, relatively small, and the skewness may be just an artefact of sample size.

3.2.5.2 Zircon (U-Th)/He data

Zircon (U-Th)/He analyses have been performed on three samples, which provide the best quality, prismatic crystals. The data are presented in Table 3.5. The uncorrected single-grain ages vary from 78.3 ± 12.1 to 416.0 ± 50.0 Ma and corrected ages from 102.6 ± 14.6 to 562.9 ± 64.7 Ma, respectively. The youngest ages are from the Skiddaw granite (sample LD10), giving a sample central age of 101 ± 11 Ma. This is significantly

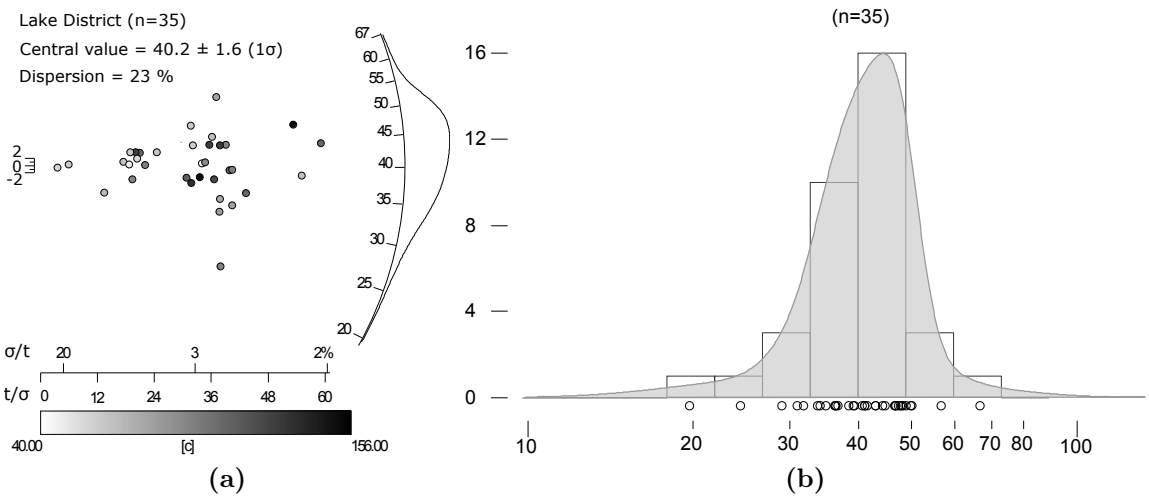

Figure 3.8: Distribution of all single-grain AHe ages from samples from the Lake District: (a) a radial plot of the single-grain ages, bottom panel and circles fill is grain thickness in μm (the smallest dimension, perpendicular to the c-axis), and (b) a Kernel Density Estimator (KDE) calculated using adaptive bandwidth (Vermeesch 2012) and plotted on a histogram of single-grain ages. Both graphs have been produced using Radial Plotter software (Vermeesch 2009).

younger than the intrusion emplacement age (see Table 3.2). The majority of corrected ages from other two samples (Carrock—LD03 and Shap—LD01) are around 400 Ma and reflect the post-emplacement cooling of the plutons. One corrected age from Carrock microgranite is older than the intrusion age. The uncorrected age is, however, acceptable, so the overestimation is probably due to the correction rather than, an inaccurate measurement and may be caused by crystal zonation (Dobson et al. 2008).

Two samples, LD01 and LD10, show strong positive correlation with grain size, R^2 of 0.917 and 0.825, respectively (Fig. 3.9). Sample LD01 also shows very strong negative correlation with [eU] ($R^2 = 0.986$) (Fig. 3.10). The number of single-grain ages is relatively low, however, at least in case of sample LD01, both trends seem to be real, as the spacing between the points is relatively large and R^2 is >0.9. Negative correlation

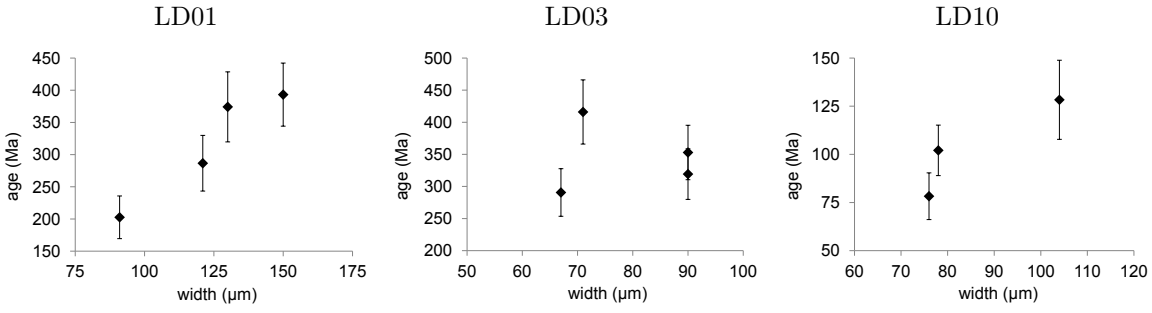

Figure 3.9: Zircon (U-Th)/He age (Ma) versus grain width (μm) in samples from the Lake District. The error bars show analytical error + 10% of the age (based on the reproducibility of Fish Canyon Tuff aliquots).

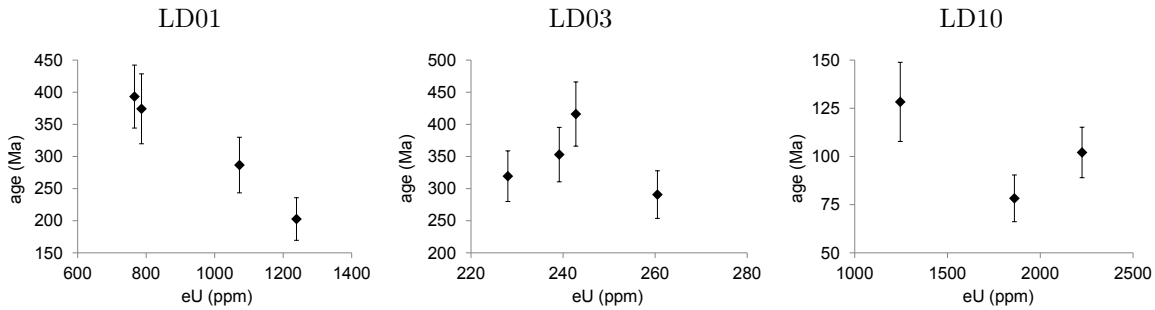

Figure 3.10: Zircon (U-Th)/He age (Ma) versus eU concentration (ppm) in samples from the Lake District. The error bars show analytical error + 10% of the age (based on the reproducibility of Fish Canyon Tuff aliquots).

Table 3.5: Zircon (U-Th)/He data from samples from the Lake District. Symbols: L—length, W1—width, R*—equivalent radius, eU—effective Uranium, age—uncorrected age, age$_c$—age corrected for α-recoil, † analytical error; ‡ analytical error + 10% of the age (based on the reproducibility of Fish Canyon Tuff aliquots). Central ages and central age uncertainties calculated using Radial Plotter software (Vermeesch 2009).

Sample name	No	L (μm)	W1 (μm)	R* (μm)	He (μcc/g)	U (ppm)	Th (ppm)	Th/U	eU (ppm)
LD01	1	605	150	101	37568.3	586.0	765.3	1.31	765.9
	2	527	130	88	36671.1	629.8	666.0	1.06	786.4
	3	295	121	75	38054.0	908.6	696.7	0.77	1072.3
	4	406	91	62	30858.2	1046.5	818.3	0.78	1238.8
LD03	1	226	90	56	9029.8	175.0	225.4	1.29	228.0
	2	180	71	44	12619.1	182.5	256.4	1.40	242.8
	3	205	90	55	10498.2	185.4	228.8	1.23	239.2
	4	160	67	41	9373.2	210.7	211.9	1.01	260.5
LD10	1	420	104	70	19524.7	1120.5	531.6	0.47	1245.4
	2	187	76	47	17707.6	1801.2	252.6	0.14	1860.5
	5	265	78	52	27685.3	2001.1	953.2	0.48	2225.1

Table 3.5: (continued)

	No	age (Ma)	error†	error‡	F_T	age$_c$ (Ma)	error‡	central age (Ma) $\pm 1\sigma$
LD01	1	393.2	9.7	49.0	0.87	445.8	54.3	308 ± 40
	3	374.2	17.0	54.4	0.85	432.6	60.3	
	4	286.6	14.6	43.3	0.83	339.6	48.6	
	5	202.6	12.9	33.1	0.80	248.9	37.8	
LD03	1	319.3	7.5	39.4	0.78	403.1	47.8	343 ± 23
	2	416.0	8.4	50.0	0.72	562.9	64.7	
	3	352.9	7.1	42.4	0.77	448.4	52.0	
	4	290.6	8.0	37.1	0.71	401.4	48.1	
LD10	1	128.3	7.7	20.5	0.82	153.7	23.0	101 ± 11
	2	78.3	4.3	12.1	0.75	102.6	14.6	
	5	102.1	2.9	13.1	0.76	131.2	16.0	

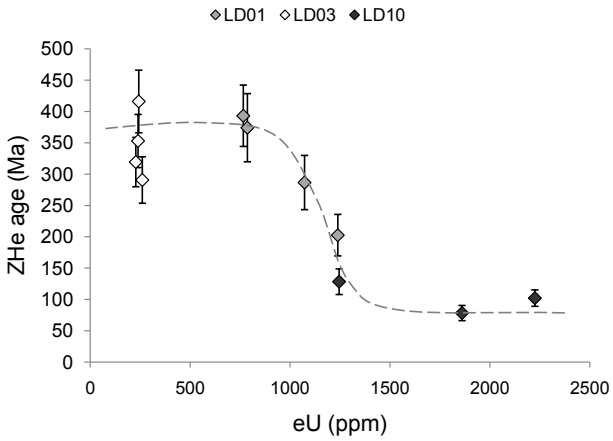

Figure 3.11: Zircon (U-Th)/He age versus eU concentration (ppm) in all single-grain aliquots from the Lake District.

between the ZHe age and [eU] is common in zircons and may be explained by radiation damage (Guenthner et al. 2013). When the age of the aliquots from all three samples are plotted together, the negative correlation between ZHe age and [eU] can be even better resolved (Fig. 3.11); the samples with [eU] <1000 ppm have ages ranging 300–400 Ma, which, when corrected, give the intrusion emplacement age; the samples with [eU] >1200 ppm yield ages of ∼100 Ma; between these two groups, there is an age decrease. Even though the ages are not from the same sample, they come from localities not more than 30 km away from each other and, very likely, experienced the same thermal history; thus, the trend may be accepted with a high confidence.

3.3 Southern Scotland

3.3.1 Geological setting

Southern Scotland lies on the north side of the Iapetus suture zone and is comprised of an accretionary prism formed during the Caledonian orogeny (Stone & Merriman 2004). In post-Caledonian times, the Cheviot and the Southern Uplands blocks were separated in the east by the Carboniferous Tweed Basin. To the north, the Southern Uplands block is separated from the Midland Valley by the NE–SW trending Southern Upland Fault. Similarly oriented faults cut the block and divide it in a series of lithostratigraphic units. Rocks of the Southern Uplands consist of Ordovician-Silurian turbidite-facies strata and several Early Devonian intrusions. The plutons, which are exposed in the Southern Uplands were emplaced at 410–390 Ma (Table 3.6), in the last phase of the Caledonian orogeny. They form part of the post-collisional Caledonian granites suite, the so called "Newer Granites" (Read 1961, Brown et al. 1981). Younger, post-Caledonian rocks comprise minor early Palaeogene dykes, and sills and dykes, which are remnants of Variscian magmatism. There are several small outliers of Permian breccias, conglomerates and sandstones (Brookfield 1980). The Cheviot block is characterized by a "Newer Granite" pluton, which intruded Silurian sedimentary rocks and Lower Devonian lavas (Mitchell 1972, Robson 1977).

Intrusion	Age (Ma)	Method	References
Loch Doon	408 ± 2	Rb-Sr (whole rock isochron)	Halliday et al. (1979)
Fleet	390 ± 6	K-Ar (biotite)	Brown et al. (1968)
	392 ± 2	Rb-Sr (whole rock isochron)	Halliday et al. (1979)
Criffell	397 ± 8	K-Ar (biotite)	Brown et al. (1968)
	391 ± 8	K-Ar (hornblende)	Brown et al. (1968)
	397 ± 2	Rb-Sr (whole rock isochron)	Halliday et al. (1979)
Cheviot	∼380	K-Ar (biotite)	Mitchell (1972)

Table 3.6: The emplacement age of the important intrusions in southern Scotland.

The post-Caledonian evolution of southern Scotland is poorly constrained due to the lack of Mesozoic and Cenozoic strata. Post-Caledonian sediments are partially preserved within the surrounding basins: there are Upper Devonian-Carboniferous sequences in the Tweed Basin between and NE of the Southern Uplands and Cheviot block; in the Midland Valley, north of the Southern Uplands and in the Northumberland-Solway Basin to the south. The Cheviot and Southern Uplands blocks were structural highs since, at least, the beginning of the Carboniferous, shedding sediments to the surrounding basins (Fraser & Gawthorpe 1990, Chadwick et al. 1993). Post-Carboniferous sediments are scarce, and are preserved only in the Solway Basin.

3.3.2 Existing thermochronological constraints

Hurford (1977) published fission track analyses on apatites, zircons and sphenes from the Criffell and Fleet plutons. Zircon and sphene ages vary from 360 to 410 Ma and were interpreted as emplacement ages, whereas apatite ages vary from 58.0 to 94.3 Ma. The data lack information about track length distribution and were obtained when the fission track techniques was still in its infancy and the population method was used that causes that the ages may be less accurate than if obtained using the external detector or LA-ICP-MS. Green (1986) presented AFT data for the Cheviot granite with ages ranging from 264 to 279 Ma and mean track length from 11.79 to 12.68 μm; he interpreted the data as indicating that surface rocks were at 80–90°C prior to experiencing rapid cooling at ∼60 Ma. Early Palaeogene palaeotemperatures of some sites in the Southern Uplands are provided by Green et al. (1997) and suggest that coastal localities near the Criffell pluton, Dumfriesshire, were at temperatures higher than 110°C, whereas coastal areas in SW Scotland were at less than 70°C. However, the raw data, on which this interpretation has been made are not published. In summary, these studies indicate that Early Cenozoic palaeotemperatures in the coastal areas in southern Scotland decrease westward, but the data are too sparse to provide a solid indication of the distribution of cooling and denudation.

3.3.3 Sampling strategy

The aim of the sampling strategy was to unravel the spatial distribution of the early Palaeogene cooling within the region, with the intent of monitoring changes in cooling histories north of the Lake District, close to large fault zones. Most of the samples in southern Scotland were collected from intrusive rocks: twelve samples are from Caledonian plutons, two from Variscian dykes and one from a granite boulder from a Silurian conglomerate. Eleven samples gave enough good quality apatite crystals for both AFT and AHe determinations. Rocks that yielded a Palaeogene AFT age were also analysed for ZHe. The locations of the analysed samples are shown in Fig. 3.2 and given in Table 3.1. The detailed information of the samples are available in the Appendix B.

3.3.4 Apatite fission track analysis

A fission track age and track length distribution have been determined on eleven samples, following the procedure given in Appendix A.2. The central age, MTL and average D-Par value are reported, for each sample, in Table 3.7, and single-grain data and radial plots are presented in the data logs in Appendix B.

3.3.4.1 Fission track age

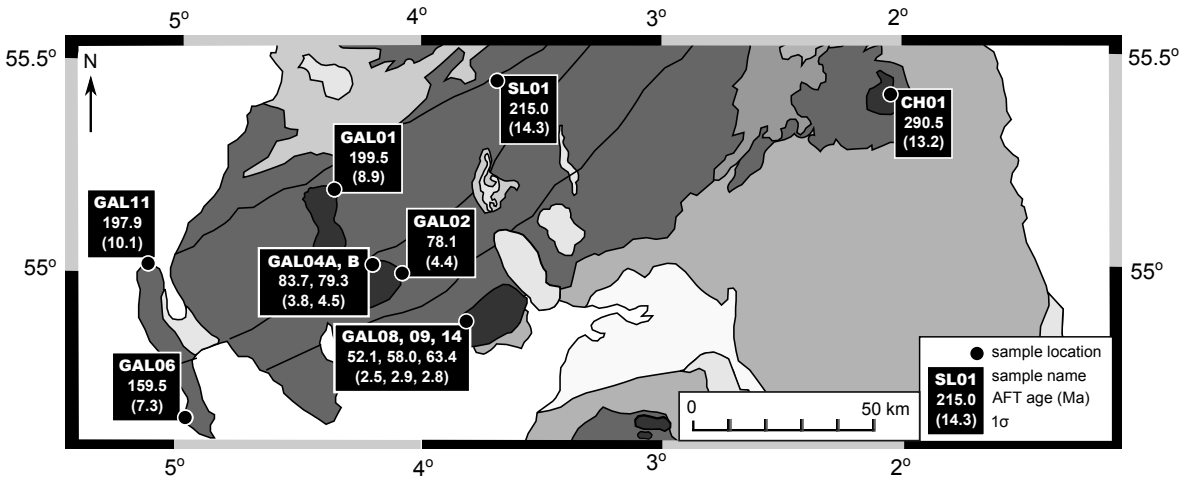

Figure 3.12: Map of apatite fission track ages of samples from southern Scotland. The values in brackets are 1σ errors on the ages. In case of samples that were under-etched and have been counted twice, only the age from the correctly etched slide is shown on the map. All the ages are also reported in Table 3.7. For the legend to geological map see Fig. 3.3.

Apatite fission track ages in southern Scotland are highly variable, ranging from 52.1 ± 6.4 Ma to 290.5 ± 13.2 Ma. The youngest ages are ∼60 Ma and are from the Criffell pluton, on the south coast of the Southern Uplands. Ages tend to increase northward, e.g. the Fleet granite pluton is ∼80 Ma, westward, to 160 Ma at Portencorkie granite, and eastwards, where ages of 290.5 Ma are measured within the Cheviot block (Fig. 3.12). All AFT ages are, however, significantly younger than the emplacement age of the plutons (Table 3.6).

Apatite mounts that were under-etched yielded very young ages of 44.8 and 55.0 Ma (GAL08 and GAL09 slides 1; Table 3.7); this inaccuracy is probably due to the fact that not all the tracks intersecting the polished surface of the apatite grains were visible. For this reason, two new mounts were prepared (slide 2; Table 3.7). Apatites on the first slides have D-Par values that are significantly ($>2\sigma$) shorter than those on the later slides, demonstrating that the first mounts were under-etched. Ages determined on the new slides are 52.1 and 58.0 Ma, respectively. The age of the sample GAL09 is underestimated by 3.0 Ma which is close to the 1σ error on the age. The underestimation of the age by 7.3 Ma in case of the sample GAL08 is, however, large and lies above the variation within 2σ. Based on that evidence, the data derived from under-etched slides were discarded and will not be used for the modelling.

The number of clear, prismatic apatite grains was high in most of the rocks allowing for 18–24 single-grain aliquots per sample to be analysed. Dispersion in most of the cases was <8%, with six samples showing no dispersion. Four samples (GAL01, GAL04B, GAL11 and CH01) are characterized by $P(\chi^2) < 5\%$, which suggests that the single-grain ages form two populations. However, no evidence for two populations of ages is found on the radial plots (see Appendix B). Samples GAL04B, GAL11 and, in particular, CH01 have the $P(\chi^2) < 1\%$, but are also characterised by an age dispersion of 12–14%, which, although not extreme in absolute terms, is the highest of the entire datase. The failure of the χ^2 test is attributed to the dispersion rather than to the presence of two populations. Additionally, in sample GAL04B all ages are similar, with four, clear outliers (see Appendix B). If they are removed there is no dispersion within 2σ and the $P(\chi^2)$ is 86.32%. This change the samples central age from 79.3 ± 4.5 Ma to 76.5 ± 4.0 Ma. There is no analytical reason to discard those four single-grain ages and they will be used for the modelling. In case of sample GAL01, the $P(\chi^2)$ value of 4.55% is just below the threshold used to indicate an inhomogeneous age population and dispersion of single-grain ages is 8.5%. The analysis of the radial plot suggests the presence of two populations of ages, with peaks at around 178 ± 12 Ma (9 grains) and

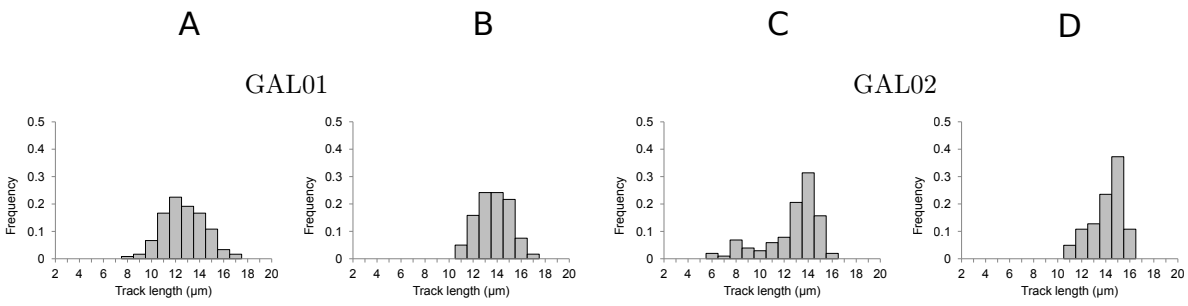

Figure 3.13: Histograms of track length distributions in samples from southern Scotland. Columns A and C—measured track lengths, columns B and D—projected track lengths. Track length projection after Ketcham et al. (2007a).

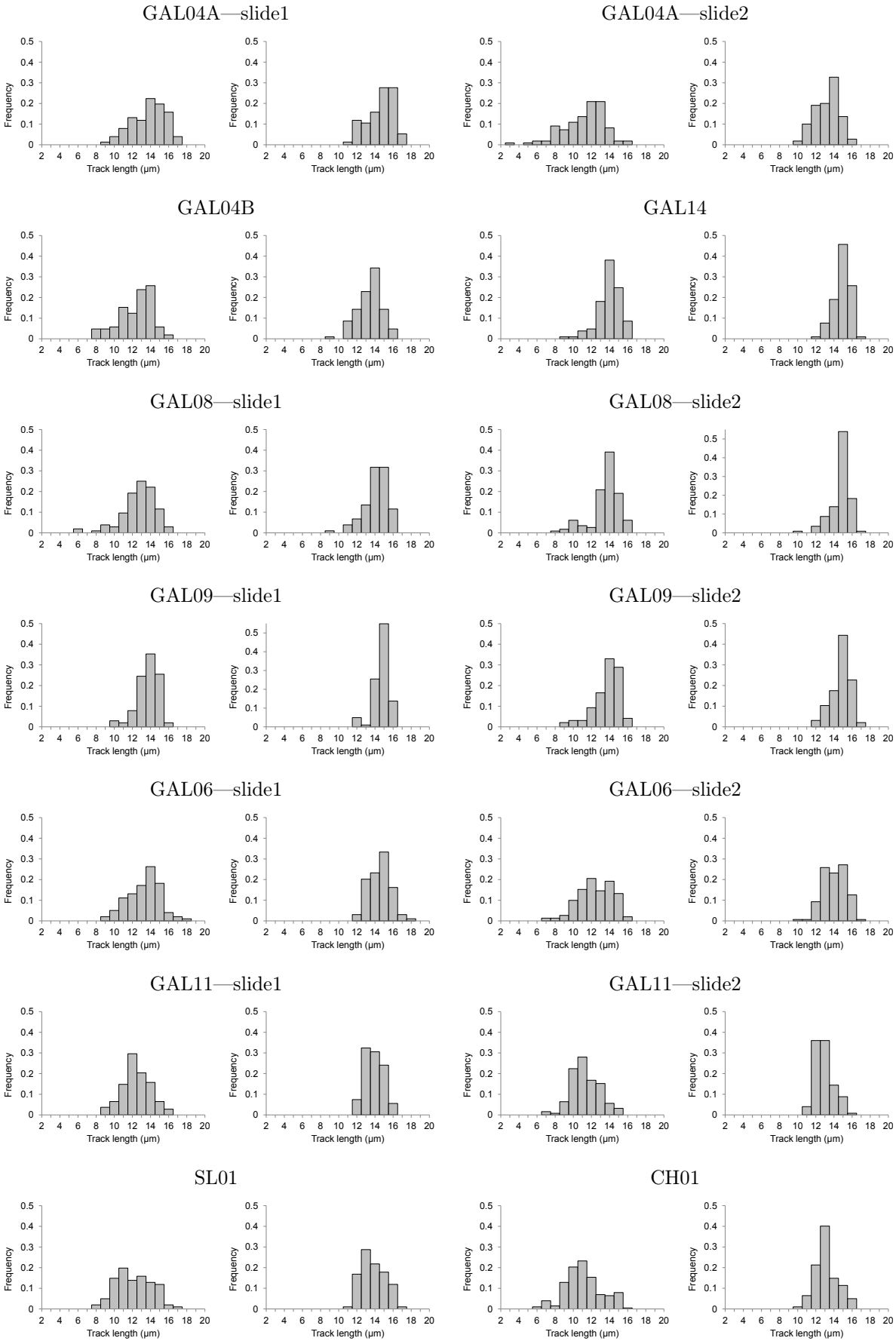

Figure 3.13: (continued)

± 13 Ma (11 grains) (see Appendix B). However, sample GAL01 is derived from an intrusive rock where only compositional variations among the apatite crystals would explain the presence of two populations (O'Sullivan & Parrish 1995). There is no correlation between AFT single-grain ages and D-par values. The fact that the peaks are not well defined and that the mount is slightly over-etched suggest that age dispersion is the cause of a low $P(\chi^2)$, rather than the presence of two populations.

D-Par values were determined for every counted grain (5–10 per grain). The average sample D-Par varies from 1.43 to 4.64 μm, however, the highest values, >3 μm, are from the samples which were ascertained to be over-etched. The majority of samples have a D-Par value from a range 1.5–2.5 μm, which is close or slightly above the value measured for Durango apatite, 1.82 ± 0.13 (n=60).

3.3.4.2 Track length distribution

Confined, horizontal tracks were measured in all samples. The number of measured track lengths varies from 76 to 202, but in most cases it slightly exceeds 100 lengths per slide (Table 3.7). To account for anisotropy due to the track orientation and the apatite composition, every track has been c-axis projected, using the angle of the track with the c-axis of the crystal and the D-Par value to take the chemical composition of the grain in which the track has been measured into consideration, according to the projection model of Ketcham et al. (2007a,b). The c-axis projection, always caused a narrowing of the track length distribution and slightly increased the MTL value, as expected by the projection model (Fig. 3.13). The values of MTL vary from 11.08 to 13.89 μm for measured track lengths and from 12.83 to 14.78 μm for projected track lengths, respectively. The standard deviation of the MTL vary from 1.17 to 2.31 μm for measured tracks and from 0.87 to 1.48 μm for projected tracks, respectively.

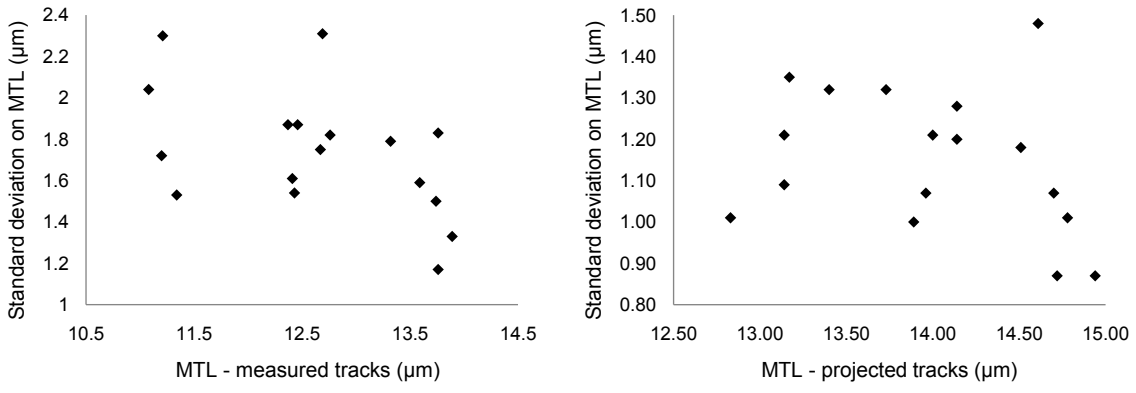

Figure 3.14: Mean track length versus standard deviation for (a) measured track lengths and (b) projected track lengths in the samples from southern Scotland. Track length projection after Ketcham et al. (2007a).

Table 3.7: Apatite fission track data from the samples in southern Scotland. Symbols: ρ_D—tracks density on the dosimeter, ρ_s—spontaneous track density, ρ_i—induced track density, P—probability that the grains pass χ^2 test, MTL m—mean track length measured, MTL p—mean track lengths projected, N_D—number of tracks on the dosimeter, N_s—number of spontaneous tracks, N_i—number of induced tracks

Sample name No. grains [lengths]	ρ_D (cm^2) N_D	ρ_s (cm^2) N_s	ρ_i (cm^2) N_i	χ^2	P (%)	age (Ma)	$\pm 1\sigma$	MTL m	$\pm 1\sigma$ (μm)	MTL p	$\pm 1\sigma$ (μm)	DPar	$\pm 1\sigma$ (μm)
|Loch Doon|													
GAL01 20 [120]	9.44E+05 6478	2.48E-06 3217	1.83E-06 2353	30.5	4.6	199.5	8.9	12.67	1.75	13.73	1.32	2.94	0.14
|Fleet|													
GAL02 19 [102]	1.24E+06 8874	5.79E-07 620	1.38E-06 1537	19.0	39.1	78.1	4.4	12.69	2.31	14.14	1.28	1.57	0.11
GAL04A_slide1 18 [76]	9.36E+05 6478	1.44E-06 1346	2.45E-06 2346	9.3	93.2	83.7	3.8	13.76	1.83	14.61	1.48	1.47	0.18
GAL04A_slide2 0 [110]	- -	- -	- -	-	-	-	-	11.21	2.30	13.17	1.35	1.43	0.10
GAL04B 20 [105]	9.31E+05 6478	1.13E-06 1302	2.11E-06 2315	36.5	0.9	79.3	4.5	12.37	1.87	13.4	1.32	2.24	0.12
|Portencorkie|													
GAL06_slide1 20 [99]	9.27E+05 6478	1.22E-06 1959	1.11E-06 1760	23.9	19.9	159.5	7.3	13.32	1.79	14.51	1.18	4.64	0.72
GAL06_slide2 0 [151]	- -	- -	- -	-	-	-	-	12.46	1.87	14	1.21	2.28	0.09

Table 3.7: (continued)

Sample name No. grains [lengths]	ρ_D (cm^2) N_D	ρ_s (cm^2) N_s	ρ_i (cm^2) N_i	χ^2	P (%)	age (Ma)	$\pm 1\sigma$	MTL m	$\pm 1\sigma$ (μm)	MTL p	$\pm 1\sigma$ (μm)	DPar	$\pm 1\sigma$ (μm)
|Criffell|													
GAL08_slide1 20 [104]	1.63E+06 11903	3.95E-07 826	2.23E-06 4699	14.0	78.6	44.8	2.1	12.76	1.82	14.14	1.20	1.53	0.07
GAL08_slide2 20 [115]	1.22E+06 8874	4.58E-07 988	1.66E-06 3615	22.8	24.8	52.1	2.5	13.59	1.59	14.7	1.07	1.92	0.08
GAL09_slide1 18 [102]	1.73E+06 11903	5.56E-07 1035	2.74E-06 5086	6.9	98.5	55.0	2.4	13.76	1.17	14.72	0.87	1.54	0.08
GAL09_slide2 21 [97]	1.21E+06 8874	6.43E-07 993	2.12E-06 3226	25.8	17.2	58.0	2.9	13.74	1.50	14.78	1.01	2.26	0.21
GAL14 24 [105]	1.22E+06 8874	6.07E-07 1148	1.84E-06 3450	16.5	83.2	63.4	2.8	13.89	1.33	14.94	0.87	2.07	0.12
|Corsewall Point|													
GAL11_slide1 20 [108]	9.23E+05 6478	1.43E-06 3167	1.04E-06 2272	46.0	0.1	197.9	10.1	12.43	1.54	13.89	1.00	3.46	0.90
GAL11_slide2 0 [125]	- -	- -	- -	-	-	-	-	11.34	1.53	12.83	1.01	1.77	0.09
|Crawfordjohn|													
SL01 24 [101]	1.25E+06 8874	4.65E-07 582	4.1E-07 522	8.4	99.8	215.0	14.3	11.20	1.72	13.14	1.09	1.82	0.08
|Cheviot|													
CH01 20 [202]	1.20E+06 8874	4.32E-06 5289	2.8E-06 3339	53.6	0.0	290.5	13.2	11.08	2.04	13.14	1.21	2.04	0.16

There is no clear correlation between MTLs and their standard deviation (Fig. 3.14); the lack of correlation may be partially explained by different D-Par values. The longest MTL values are found where the AFT ages are the youngest, in the south, along the Solway Firth coast; moving northward and westward, as the ages increase, the MTLs decrease (Fig. 3.15).

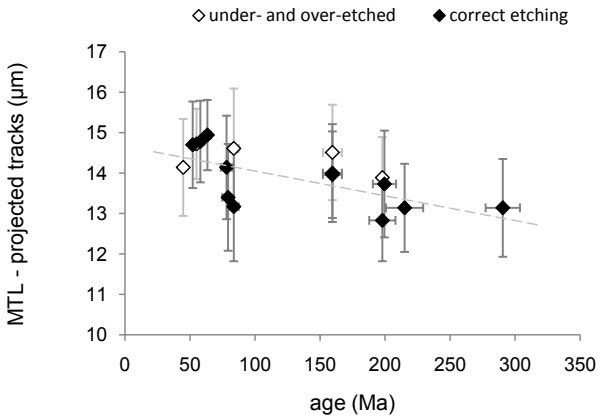

Figure 3.15: The AFT age versus the MTL in the samples from southern Scotland. The error bars represent the one standard deviation. The dashed line is a linear trend line, best fitting to the correctly etched samples ($R^2 = 0.45$).

The projected track length distributions may be divided into three groups: 1) narrow histograms with long track lengths, characterized by small negative skewness due to a 'tail' of shorter tracks (samples: GAL08, GAL09, GAL14); 2) moderately-wide histograms of long tracks with a peak of long tracks and a small positive skewness or uniform distribution (samples: GAL01, GAL02, GAL04A, GAL04B, GAL06-slide1, GAL06-slide2); and 3) moderately-wide histograms with a peak at medium tracks, characterised by positive skewness (samples: SL01, GAL11 and CH01). The measured track length distributions can also be divided in the same three groups, but the variability within each group is higher than in the case of the projected tracks. Both histograms, for measured and projected tracks, of the slide 2 of GAL06 and slide 1 of GAL04A are slightly bimodal, however, the peaks are not well separated.

3.3.4.3 Summary

The youngest AFT ages in southern Scotland are found on the Solway Firth coast and they increase northward and westward. As the AFT ages increase, MTL decreases. The AFT data from southern Scotland can be divided in three groups:

- GROUP 1: the Criffell pluton, yielding ages <60 Ma and characterized by long tracks and narrow, negatively skewed track length distributions (samples: GAL08, GAL09, GAL14);
- GROUP 2: inland Southern Uplands and from the Rhins of Galloway (Fig. 3.1) yielding ages from ∼80–200 Ma and characterized by wide track length distributions (samples: GAL01, GAL02, GAL04A, GAl04B, GAL06, GAL11);
- GROUP 3: the Cheviot block and northern flank of the Southern Uplands, yielding ages >200 Ma and characterized by shorter track lengths and positively skewed histograms(samples SL01, CH01).

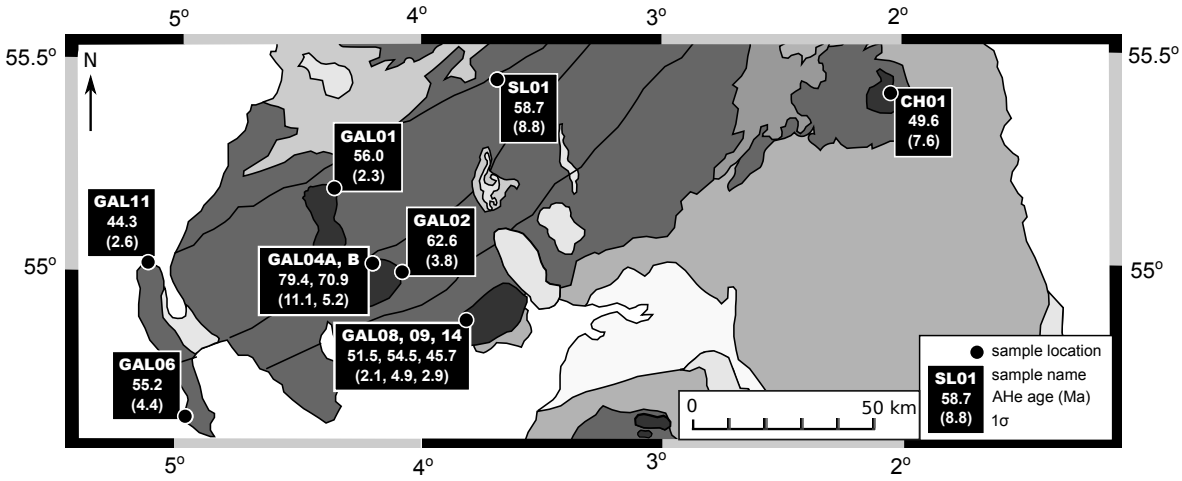

Figure 3.16: The central AHe ages of the samples in southern Scotland. The uncorrected central age was calculated after Vermeesch (2008). For the legend to geological map see Fig. 3.3.

3.3.5 Apatite and zircon (U-Th-Sm)/He analyses

Apatite (U-Th-Sm)/He (AHe) analyses have been carried out on single-grain aliquots from all eleven samples. Zircon (U-Th)/He (ZHe) analyses have been performed only on a sample from the Criffell granite, which yielded very similar AHe and AFT ages and therefore a higher temperature thermochronometer is required to constrain the maximum early Palaeogene cooling. The analytical procedure for AHe and ZHe analyses is given in Appendix A.3.

Aliquots demonstrating analytical inaccuracies were discarded from calculation of central ages, modelling and interpretation and are not presented here. Data from all analysed aliquots and comments on discarded grains are, however, given in data logs for each sample in Appendix B. Central ages, used for graphical presentation purposes, were calculated after Vermeesch (2008). The α-recoil correction was performed using the 'Alpha F_T-ejection factor' software (Gautheron & Tassan-Got 2010, Ketcham et al. 2011).

3.3.5.1 Apatite (U-Th-Sm)/He data

Single aliquot data used for modelling are presented in Table 3.8 and Fig. 3.16 shows the location of the uncorrected central AHe ages. Number of aliquots analysed per sample vary from 4 to 25, including four samples with >20 single-grain ages. The central ages vary from 43.9 ± 2.4 Ma in Corsewall Point to 77.0 ± 8.9 Ma in the Fleet pluton and they do not show any spatial trend. The uncorrected and α-recoil corrected AHe ages vary from 24.8 to 109.0, and from 31.3 to 168.8 Ma, respectively.

For each sample, dispersion of single-grain ages vary from 3 to 28% and, in general, low dispersion (<20%) is found on the south coast of the Southern Uplands (Criffell pluton) and increases northwards. Therefore, the AHe age dispersion increases along with

increasing AFT ages. Dispersion of AHe ages may be referred to three main factors: crystal size, [eU], due to radiation damage, and the use of broken crystals (this issue will be examined in detail in Chapter 4). Theoretically, the AHe age should increase with increasing crystal size and [eU] (see Chapter 2 Section 3.2.1). Fig. 3.17 and 3.18 present the single-grain ages plotted versus grain thickness (the smallest dimension) and [eU]. A clear positive correlation between the age and grain thickness is found only in samples GAL14 and SL01. Weak positive correlations may be seen in few other samples, but there is also one showing a negative correlation (CH01). The correlation between AHe ages and [eU] is poor and slight negative correlations exist; for example, GAL14. Correlations between AHe ages and grain size and/or [eU] are difficult to identify in most natural samples, as they both affect the ages; correlations can be seen only if one of the two variables is roughly constant. The small range of [eU] of sample GAL14 may be the reason why there is a strong relationship between the single-grain AHe ages and the thickness of the grains.

Uncorrected ages that are older than the corresponding AFT age cannot be, however, easily explained. The old ages do not correlate with either large crystal size or high [eU]. Eleven grains have a He age that is <15% older than the AFT ages. This is outside the analytical uncertainties of the measurements (usually ∼2%), but close to the ∼10% dispersion of the Durango standard ages (see Chapter 2, Figure 2.12). Given that the analytical error is not an accurate representation of the uncertainties associated with the AHe ages produced, the ages are reported with an uncertainty which is the sum of the analytical error plus the 10% uncertainty on the Durango ages. If this new, more 'realistic' uncertainty is taken into account, then only 3 from 129 single-grain AHe ages are older than AFT ages (rows marked in italics in Table 3.8). Given that, in this case, there would only be three problematic grains, i.e. 2.3% of the entire dataset, it is possible, that the few old ages may reflect zonation, He implantation or small inclusions.

Most of the single-grain AHe ages are younger than the corresponding AFT age. However, many corrected and some uncorrected AHe single-grain ages from Criffell and Fleet plutons are older than the same sample AFT age. As discussed earlier in Section 2.3.2.1., even if the applied correction scheme deals with hexagonal geometry and broken crystals, the accuracy of the recoil correction is hampered by issues such as parent zonation, He implantation from neighbouring crystals (Gautheron et al. 2012), diffusion of He from the crystal rim at elevated temperatures (Brown et al. 2013), which are not recognisable when picking the grains. For all these reasons, the recoil correction may be over-estimated, producing spuriously old AHe ages.

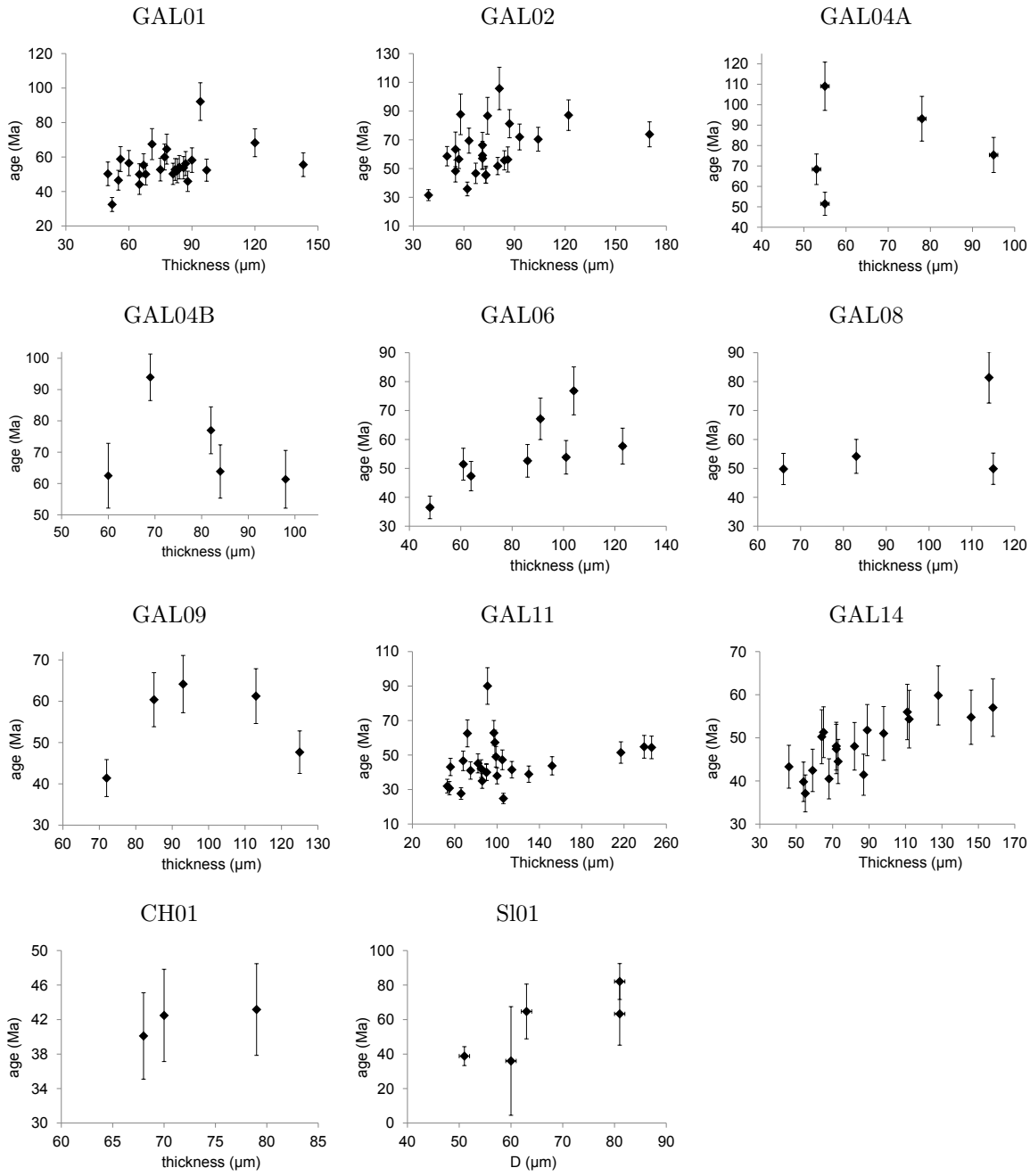

Figure 3.17: Apatite (U-Th-Sm)/He age (Ma) versus grain thickness (μm) in samples from southern Scotland. The error bars show analytical error + 10% of the age (based on the reproducibility of Durango aliquots).

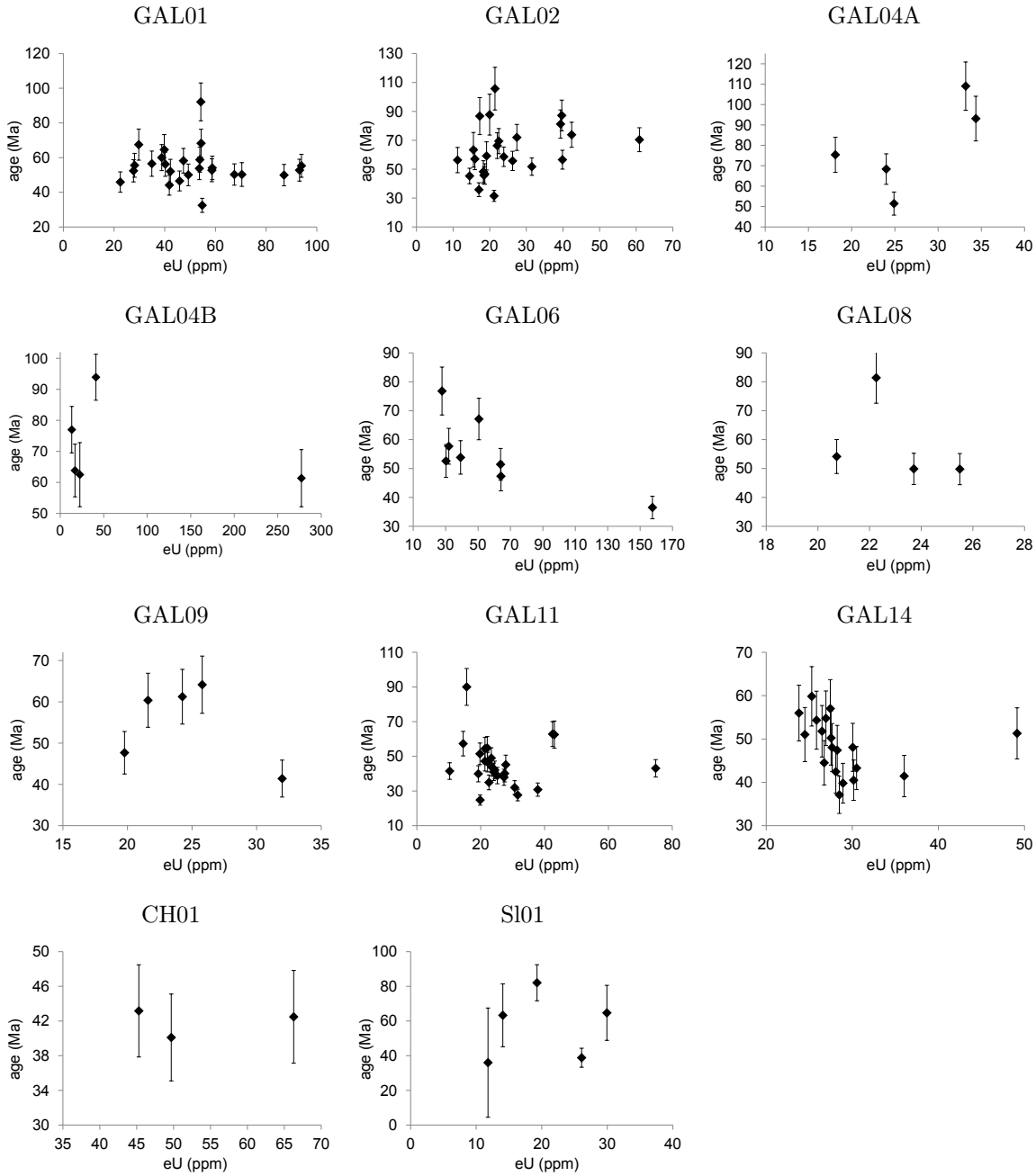

Figure 3.18: Apatite (U-Th-Sm)/He age (Ma) versus eU concentration (ppm) in samples from southern Scotland. The error bars show analytical error + 10% of the age (based on the reproducibility of Durango aliquots).

Table 3.8: Single grain apatite (U-Th-Sm)/He data from samples from southern Scotland. Symbols: L—length, W1—width, W2—thickness, R*—equivalent radius, T—terminations, eU—effective Uranium, age—uncorrected age, age$_c$—age corrected for α-recoil, † analytical error; ‡ analytical error + 10% of the age (based on the reproducibility of Durango aliquots). Central ages and central age uncertainties calculated using Radial Plotter software (Vermeesch 2009).

Sample	No.	L (μm)	W1 (μm)	W2 (μm)	R* (μm)	T	He (μcc/g)	U (ppm)	Th (ppm)	Sm (ppm)	Th/U	eU (ppm)	age (Ma)	error†	error‡	F_T	age_c (Ma)	error‡	central age ± 1σ (Ma)
|Crawfordjohn|																			
SL01	1	155	80	63	41	0	237.5	10.4	83.1	145.0	8.0	29.9	64.7	9.4	15.8	0.70	92.5	18.6	58.7 ± 8.8
	2	167	113	81	54	0	194.4	5.7	57.9	112.6	10.2	19.3	82.1	2.2	10.4	0.77	106.2	12.9	
	3	218	60	51	35	1	123.8	6.7	82.5	84.8	12.3	26.1	38.8	1.6	5.4	0.61	63.5	7.9	
	4	162	100	81	50	0	109.4	5.3	37.2	93.8	7.0	14.1	63.3	11.8	18.1	0.76	83.3	20.1	
	5	156	70	60	38	0	52.0	4.6	30.5	53.2	6.6	11.8	36.0	27.9	31.5	0.67	56.6	33.3	
|Loch Doon|																			
GAL01	1	128	89	83	45	1	269.3	22.1	85.6	240.0	3.9	42.2	52.0	1.8	7.0	0.72	72.5	9.0	56 ± 2.3
	2	110	89	78	41	1	315.2	17.3	95.8	193.0	5.5	39.8	64.6	2.2	8.7	0.65	98.8	12.1	
	3	135	60	60	34	2	241.6	15.3	83.6	162.9	5.5	34.9	56.5	1.7	7.3	0.58	98.3	11.5	
	4	195	63	55	36	2	261.4	20.6	107.6	227.4	5.2	45.9	46.5	1.1	5.8	0.61	76.8	8.8	
	5	110	88	77	41	1	285.5	21.3	74.6	225.7	3.5	38.8	60.0	1.5	7.5	0.66	91.3	10.7	
	6	194	98	84	52	2	387.6	44.7	59.8	177.2	1.3	58.7	54.1	1.4	6.8	0.73	73.7	8.7	
	7	110	93	71	43	0	246.9	17.3	52.8	244.9	3.0	29.7	67.5	2.2	9.0	0.75	90.6	11.3	
	8	197	109	94	57	1	612.4	41.7	53.5	242.3	1.3	54.2	92.2	1.7	10.9	0.78	118.8	13.6	
	9	200	61	52	35	1	217.1	38.6	68.7	221.7	1.8	54.8	32.5	0.8	4.1	0.63	52.0	6.0	
	10	85	95	81	41	0	413.5	49.8	75.1	202.8	1.5	67.5	50.3	1.1	6.2	0.77	65.6	7.7	
	11	114	76	65	39	2	190.5	22.6	54.2	173.0	2.4	41.8	44.1	1.4	5.8	0.64	69.1	8.3	
	12	134	105	88	51	0	127.0	13.9	36.3	225.0	2.6	22.5	45.9	1.3	5.9	0.78	58.7	7.2	
	13	109	86	82	43	1	599.7	71.6	92.0	295.2	1.3	93.2	52.8	1.0	6.3	0.72	73.6	8.4	
	14	109	70	65	36	1	529.4	70.1	72.3	206.2	1.0	87.1	49.9	1.2	6.2	0.67	75.0	8.7	
	15	140	78	67	42	2	547.3	62.4	80.1	232.7	1.3	93.9	55.3	1.1	6.6	0.67	83.0	9.4	
	16	212	65	56	37	0	387.2	39.1	62.6	255.3	1.6	53.8	58.8	1.4	7.2	0.67	88.4	10.2	
	17	95	58	50	30	0	431.5	48.4	93.7	172.1	1.9	70.4	50.3	1.8	6.9	0.63	80.4	9.9	
	18	134	100	86	49	1	352.1	44.5	38.8	193.7	0.9	53.7	53.8	1.1	6.5	0.75	71.6	8.3	
	19	138	135	120	62	1	386.4	36.5	41.7	188.9	1.1	54.3	68.3	1.3	8.1	0.81	84.4	9.7	
	20	104	104	90	47	1	336.6	37.2	43.1	164.7	1.2	47.4	58.2	1.3	7.1	0.75	77.6	9.1	
	21	114	105	75	46	1	377.0	43.7	63.2	224.1	1.4	58.6	52.7	1.3	6.6	0.74	71.4	8.5	
	22	80	85	68	37	0	301.4	34.7	62.1	201.4	1.8	49.3	50.1	1.2	6.2	0.73	68.4	8.1	
	23	90	114	97	48	0	178.0	16.9	45.8	197.9	2.7	27.7	52.4	1.2	6.4	0.80	65.6	7.7	
	24	108	159	143	64	0	191.4	20.1	34.1	184.1	1.7	28.1	55.6	1.3	6.9	0.86	64.6	7.8	
	25	150	125	87	56	1	244.1	25.9	40.7	200.3	1.6	40.2	56.2	1.4	7.0	0.78	72.0	8.6	

Table 3.8: (continued)

Sample	No.	L (μm)	W1 (μm)	W2 (μm)	R* (μm)	T	He (μcc/g)	U (ppm)	Th (ppm)	Sm (ppm)	Th/U	eU (ppm)	age (Ma)	error†	error‡	F_T	age_c (Ma)	error‡	central age ± 1σ (Ma)
|Fleet|																			
GAL02	1	121	138	122	60	1	425.1	19.2	87.1	254.6	4.5	39.7	87.2	1.9	10.6	0.80	109.5	12.9	62.6 ± 3.8
	2	158	77	63	41	0	194.2	13.0	40.1	412.2	3.1	22.5	69.4	1.8	8.8	0.70	98.7	11.7	
	3	133	101	71	47	1	112.9	10.5	23.1	269.6	2.2	15.9	57.0	1.7	7.4	0.73	77.8	9.5	
	4	100	104	73	44	1	104.2	13.4	21.2	278.2	1.6	18.4	45.7	1.5	6.1	0.73	62.7	7.8	
	5	136	87	62	42	1	75.3	12.4	19.8	222.5	1.6	17.1	35.8	1.3	4.9	0.70	51.2	6.5	
	6	142	90	71	45	1	181.5	13.0	38.3	362.6	2.9	22.0	66.3	2.3	8.9	0.71	92.8	11.6	
	7	160	181	170	80	1	383.7	17.0	107.7	221.3	6.3	42.4	73.8	1.3	8.7	0.84	87.6	10.1	
	8	292	97	84	55	0	182.1	18.3	33.7	522.5	1.8	26.2	55.7	1.1	6.7	0.77	72.4	8.3	
	9	109	121	93	52	0	244.0	21.0	27.0	373.7	1.3	27.4	72.0	1.8	9.0	0.81	89.1	10.7	
	10	228	121	104	64	1	528.2	43.7	72.9	638.8	1.7	60.9	70.4	1.2	8.3	0.80	88.3	10.1	
	11	111	107	86	48	1	78.0	7.2	17.0	146.5	2.4	11.2	56.3	3.1	8.8	0.75	75.4	10.7	
	12	*82*	*118*	*81*	*45*	*0*	*281.3*	*14.3*	*30.6*	*305.8*	*2.1*	*21.4*	*105.7*	*4.2*	*14.8*	*0.79*	*133.7*	*17.6*	
	13	172	64	55	36	0	108.8	10.5	33.1	223.4	3.2	18.3	48.3	2.8	7.6	0.65	74.1	10.2	
	14	99	107	74	45	0	186.3	9.3	33.8	287.4	3.6	17.3	86.7	4.1	12.8	0.77	113.2	15.5	
	15	120	82	67	41	1	107.8	10.1	36.5	270.9	3.6	18.7	46.7	2.5	7.1	0.69	68.0	9.3	
	16	159	108	87	53	0	396.0	31.4	33.7	581.3	1.1	39.3	81.2	1.7	9.8	0.79	102.7	11.9	
	17	105	76	55	36	1	122.0	8.3	30.7	211.1	3.7	15.5	63.4	5.7	12.1	0.65	98.0	15.5	
	18	131	68	58	36	1	215.9	14.1	24.9	176.8	1.8	20.0	87.7	5.4	14.2	0.65	135.0	18.9	
	19	82	88	71	38	1	139.2	13.9	22.4	171.9	1.6	19.1	59.2	3.8	9.8	0.70	85.0	12.3	
	20	274	58	50	35	1	174.5	11.0	54.6	502.0	5.0	23.8	58.6	0.9	6.7	0.60	97.7	10.7	
	21	106	48	39	26	1	81.9	8.5	53.7	150.7	6.3	21.2	31.5	0.8	3.9	0.50	63.1	7.1	
	22	76	89	73	38	0	81.8	8.8	24.2	286.0	2.7	14.5	45.3	0.9	5.4	0.74	61.0	7.0	
	23	138	89	57	41	1	278.8	31.2	36.9	585.9	1.2	39.8	56.6	0.9	6.5	0.70	81.4	9.0	
	24	115	96	80	45	0	202.0	25.4	25.9	527.3	1.0	31.5	51.7	0.8	6.0	0.77	67.3	7.6	
GAL04A	1	118	100	95	49	1	167.9	17.1	4.4	159.5	0.3	18.1	75.4	2.9	10.4	0.76	99.5	12.8	79.4 ± 11.1
	2	110	64	55	33	1	157.5	20.7	17.8	243.0	0.9	24.9	51.5	2.0	7.1	0.63	81.2	10.1	
	3	*180*	*72*	*55*	*38*	*2*	*447.5*	*26.1*	*30.2*	*356.0*	*1.2*	*33.2*	*109.0*	*2.5*	*13.4*	*0.65*	*168.8*	*19.4*	
	4	118	73	53	35	1	202.4	19.5	19.2	280.5	1.0	24.0	68.4	2.2	9.1	0.66	104.4	12.7	
	5	141	110	78	50	1	392.8	33.3	4.7	214.7	0.1	34.4	93.1	3.8	13.1	0.76	122.1	16.0	
GAL04B	1	92	92	82	42	1	2067.2	260.7	70.3	217.3	0.3	277.2	61.3	2.1	8.2	0.73	84.0	10.5	70.9 ± 5.2
	2	95	129	98	51	1	133.3	16.1	3.7	187.7	0.2	17.0	63.8	3.1	9.5	0.78	81.6	11.2	
	3	96	110	81	46	0	172.1	21.1	6.3	107.7	0.3	22.5	62.5	2.7	8.9	0.79	78.9	10.6	
	4	139	65	52	34	0	472.7	28.6	52.7	235.1	1.8	41.0	93.9	2.3	11.7	0.66	143.4	16.7	
	5	166	143	121	67	1	126.7	10.3	12.6	241.9	1.2	13.2	77.0	2.0	9.7	0.82	94.1	11.4	

Table 3.8: (continued)

Sample	No.	L (μm)	W1 (μm)	W2 (μm)	R* (μm)	T	He (μcc/g)	U (ppm)	Th (ppm)	Sm (ppm)	Th/U	eU (ppm)	age (Ma)	error†	error‡	F_T	age_c (Ma)	error‡	central age ± 1σ (Ma)
|Portencorkie|																			
GAL06	1	194	120	104	63	2	262.1	16.5	47.9	198.5	2.9	27.8	76.8	1.4	9.1	0.77	100.0	11.4	55.2 ± 4.4
	2	169	103	101	55	1	258.8	22.4	71.6	239.0	3.2	39.2	53.8	1.0	6.4	0.77	70.4	8.1	
	3	148	92	86	48	1	194.7	16.0	60.6	153.1	3.8	30.2	52.6	1.2	6.5	0.73	71.9	8.4	
	4	106	96	91	47	2	415.1	25.4	106.7	195.8	4.2	50.5	67.1	1.5	8.2	0.69	97.2	11.2	
	5	185	158	123	74	1	226.0	22.1	41.8	216.9	1.9	31.9	57.7	1.4	7.2	0.83	69.5	8.4	
	6	84	62	48	30	2	701.2	118.0	168.7	529.1	1.4	157.6	36.5	1.1	4.7	0.56	65.8	7.6	
	7	131	75	64	40	2	369.9	45.8	78.0	150.8	1.7	64.1	47.3	1.4	6.1	0.65	72.4	8.6	
	8	104	71	61	37	2	400.9	45.2	79.7	191.7	1.8	63.9	51.4	1.7	6.8	0.62	82.8	10.0	
|Corsewall Point|																			
GAL11	1	232	108	106	60	0	59.9	11.9	33.8	46.4	2.8	19.8	24.8	0.5	3.0	0.80	31.1	3.6	44.3 ± 2.6
	2	276	136	114	72	1	52.1	6.1	17.8	42.8	2.9	10.3	41.5	0.6	4.8	0.81	51.0	5.7	
	3	130	135	97	58	0	326.3	25.3	73.3	140.4	2.9	42.5	62.8	0.9	7.2	0.82	76.8	8.6	
	4	106	75	56	36	1	392.9	50.1	105.3	208.2	2.1	74.8	43.1	0.7	5.0	0.66	65.8	7.3	
	5	145	117	90	55	0	93.7	11.1	34.7	51.9	3.1	19.3	39.9	0.7	4.6	0.80	50.2	5.7	
	6	168	194	152	82	0	125.7	13.8	41.4	97.1	3.0	23.5	43.7	0.9	5.3	0.88	49.9	5.9	
	7	192	83	72	45	2	328.0	31.9	47.6	37.9	1.5	43.1	62.5	1.6	7.8	0.70	89.9	10.6	
	8	171	110	85	54	0	125.4	14.4	42.5	88.8	2.9	24.4	42.1	0.9	5.1	0.78	53.7	6.3	
	9	93	112	90	47	1	134.5	14.8	54.1	79.9	3.7	27.5	40.1	0.9	4.9	0.75	53.8	6.2	
	10	204	106	91	56	1	172.8	5.7	42.2	97.1	7.4	15.6	90.0	1.6	10.6	0.76	118.9	13.5	
	11	215	101	82	54	1	153.4	16.7	47.5	77.2	2.8	27.8	45.2	1.0	5.5	0.75	60.1	7.0	
	12	102	86	75	41	1	120.3	14.3	41.5	34.5	2.9	24.1	41.1	1.0	5.1	0.70	58.6	6.8	
	13	80	73	55	33	1	142.0	22.6	65.0	66.1	2.9	37.9	30.8	0.8	3.8	0.63	48.7	5.6	
	14	124	124	99	55	1	139.4	13.3	42.7	63.3	3.2	23.3	49.0	1.1	6.0	0.78	63.1	7.4	
	15	215	292	246	119	1	142.1	12.3	38.7	93.9	3.3	21.4	54.4	1.1	6.6	0.90	60.7	7.2	
	16	135	270	217	93	1	124.2	11.4	35.4	67.8	3.1	19.8	51.4	1.1	6.2	0.88	58.7	6.9	
	17	233	302	239	123	1	147.8	12.4	40.9	100.8	3.3	22.1	54.8	1.1	6.6	0.90	60.9	7.2	
	18	160	140	130	67	1	119.6	15.1	43.0	82.4	2.8	25.2	38.9	0.8	4.7	0.81	47.9	5.6	
	19	180	105	68	49	1	126.0	12.3	41.8	40.3	3.4	22.2	46.6	1.0	5.7	0.73	63.6	7.4	
	20	144	132	100	59	1	126.1	16.1	47.4	63.3	2.9	27.3	37.9	0.9	4.6	0.79	48.1	5.7	
	21	94	140	105	54	1	122.8	11.8	40.4	42.6	3.4	21.3	47.2	1.0	5.7	0.78	60.5	7.0	
	22	109	108	66	44	0	106.4	17.2	61.1	53.9	3.5	31.6	27.7	0.6	3.4	0.75	36.7	4.3	
	23	112	125	98	53	0	101.3	9.2	22.4	23.2	2.4	14.5	57.3	1.3	7.1	0.81	70.6	8.4	
	24	143	112	86	53	1	96.4	13.6	38.2	75.5	2.8	22.6	35.0	0.8	4.3	0.76	46.1	5.4	
	25	92	80	53	35	1	119.0	18.6	51.2	0.0	2.8	30.6	32.0	0.8	4.0	0.65	49.3	5.7	

Table 3.8: (continued)

Sample	No.	L (μm)	W1 (μm)	W2 (μm)	R* (μm)	T	He (μcc/g)	U (ppm)	Th (ppm)	Sm (ppm)	Th/U	eU (ppm)	age (Ma)	error†	error‡	F_T	age_c (Ma)	error‡	central age ± 1σ (Ma)
|Criffell|																			
GAL08	1	183	93	66	46	0	156.9	16.1	39.8	342.4	2.5	25.5	49.8	1.0	6.0	0.74	67.4	7.7	51.5 ± 2.1
	2	*220*	*141*	*114*	*70*	*0*	*224.4*	*14.7*	*32.3*	*304.1*	*2.2*	*22.3*	*81.4*	*1.5*	*9.6*	*0.84*	*97.5*	*11.2*	
	3	95	100	83	44	0	138.4	15.1	24.0	241.1	1.6	20.7	54.2	1.3	6.7	0.77	70.0	8.3	
	4	175	126	115	63	0	146.3	17.2	27.9	342.0	1.6	23.7	49.9	0.9	5.9	0.83	60.5	7.0	
GAL09	1	95	116	85	47	1	160.3	17.5	17.3	211.6	1.0	21.6	60.4	1.4	7.4	0.76	79.9	9.4	54.5 ± 4.9
	2	135	145	125	64	1	116.1	14.1	24.1	218.6	1.7	19.8	47.7	0.9	5.7	0.81	58.6	6.8	
	3	100	77	72	38	1	162.4	24.3	32.8	280.0	1.4	32.0	41.4	1.0	5.1	0.69	60.4	7.0	
	4	130	107	93	51	1	204.0	18.0	33.0	288.2	1.8	25.8	64.1	1.3	7.7	0.76	84.4	9.7	
	5	210	122	113	64	0	183.3	18.5	24.6	298.7	1.3	24.3	61.2	1.1	7.3	0.82	74.6	8.6	
GAL14	1	272	184	158	92	1	191.6	16.4	47.0	140.4	2.9	27.4	57.0	1.0	6.7	0.86	66.5	7.6	45.7 ± 2.9
	2	154	117	98	57	1	152.6	14.4	43.1	77.2	3.0	24.5	51.0	1.1	6.2	0.78	65.8	7.7	
	3	262	75	64	43	2	168.7	16.1	48.8	58.0	3.0	27.5	50.2	1.2	6.3	0.67	74.8	8.7	
	4	91	152	112	55	1	171.1	17.8	34.2	52.9	1.9	25.8	54.3	1.3	6.7	0.80	68.3	8.1	
	5	311	84	72	49	1	163.5	17.1	47.5	92.2	2.8	28.2	47.4	1.0	5.7	0.72	65.9	7.6	
	6	300	63	46	35	1	162.3	15.9	62.2	258.2	3.9	30.5	43.3	0.6	5.0	0.61	70.9	7.7	
	7	151	68	54	36	1	147.1	16.4	53.1	1214.0	3.2	28.9	39.8	0.6	4.6	0.64	62.4	6.8	
	8	130	96	82	47	1	162.5	15.8	50.5	128.5	3.2	27.7	48.0	0.7	5.5	0.73	65.6	7.3	
	9	77	93	72	39	1	178.4	16.7	57.0	370.7	3.4	30.1	48.1	0.7	5.5	0.70	69.2	7.7	
	10	110	164	111	61	1	163.1	13.8	42.4	115.5	3.1	23.8	56.0	0.8	6.4	0.81	69.6	7.8	
	11	224	171	128	80	1	184.2	14.8	44.6	0.9	3.0	25.3	59.8	0.9	6.9	0.84	71.4	8.0	
	12	100	177	146	65	1	179.9	18.1	37.6	65.5	2.1	26.9	54.8	0.8	6.3	0.83	66.4	7.5	
	13	180	138	89	61	1	167.2	15.7	46.0	55.9	2.9	26.5	51.8	0.8	5.9	0.79	65.6	7.3	
	14	75	90	59	36	1	146.1	15.5	53.4	182.8	3.4	28.1	42.5	0.7	4.9	0.67	63.6	7.1	
	15	170	74	65	41	1	308.0	28.7	87.0	187.2	3.0	49.1	51.3	0.8	5.9	0.68	75.8	8.3	
	16	125	70	55	36	2	129.5	14.5	59.5	168.6	4.1	28.5	37.1	0.6	4.3	0.61	60.9	6.7	
	17	71	104	87	41	0	181.8	22.2	58.8	58.0	2.6	36.0	41.4	0.6	4.8	0.78	53.1	5.9	
	18	110	102	73	45	1	145.4	15.3	48.8	111.8	3.2	26.7	44.5	0.7	5.1	0.72	61.5	6.8	
	19	192	95	68	48	1	148.6	17.0	56.0	29.5	3.3	30.2	40.5	0.6	4.7	0.72	56.1	6.2	
|Cheviot|																			
CH01	1	117	94	58	41	2	315.6	15.7	89.4	341.8	5.7	36.7	69.8	1.4	8.4	0.65	107.3	12.1	49.6 ± 7.6
	2	164	80	68	44	2	244.1	38.5	47.5	392.8	1.2	49.7	40.1	1.0	5.0	0.68	59.0	6.9	
	3	100	92	70	42	1	344.2	50.0	69.2	382.8	1.4	66.3	42.5	1.1	5.3	0.71	59.6	7.0	
	4	85	78	79	37	1	240.3	29.6	66.7	428.7	2.3	45.3	43.2	1.0	5.3	0.68	63.2	7.3	

All uncorrected single-grain ages from the region have been plotted on a radial plot, similar to that used in the fission track analysis (Fig. 3.19a), and on a Kernel Density Estimator (KDE) (Fig. 3.19b), which has been shown as a better alternative to the probability density plot (Vermeesch 2012). Around 75% of ages in the region are in the range 40–70 Ma, with the regional central age of 53.4 ± 1.3 Ma and 27% of dispersion. The ages seems to belong to one population with a clear peak at 50–55 Ma. The number of single-grain ages vary between the samples, but the four samples having 20–25 single-grain ages are from different parts of the regions, making spatial distribution of the ages quasi-uniform. Therefore, the peak on the Fig. 3.19b seems to be a true estimate of the regional pattern of cooling, rather than an artefact due to a sample bias. Thus, the whole region seems have been affected by the same thermal event, although, to a different degree; the latter, combined with the effects of varied grain size, [eU] and fragmentation, could explain the relatively large age spread.

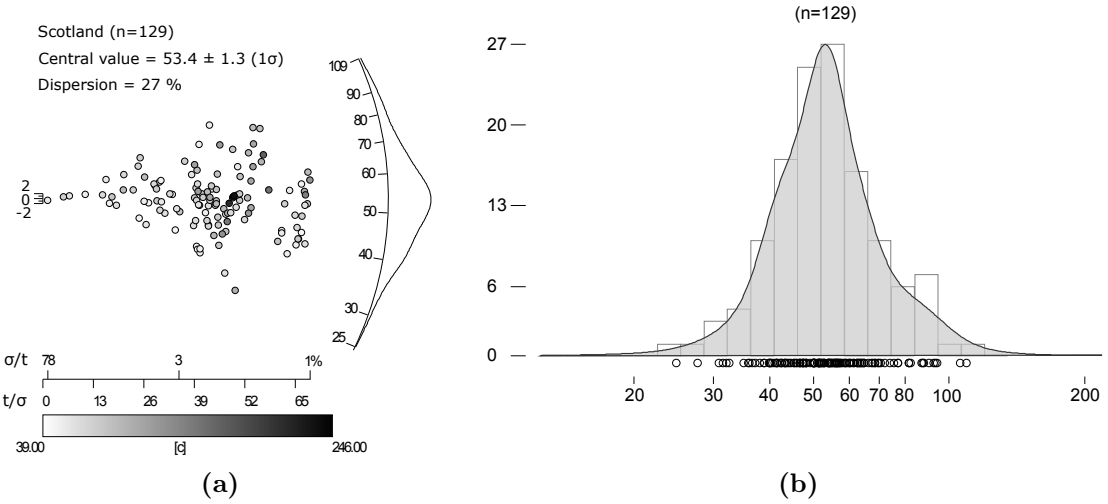

(a) **(b)**

Figure 3.19: Distribution of all single-grain AHe ages from samples from southern Scotland: (a) a radial plot of the single-grain ages, bottom panel and circles fill is grain thickness in μm (the smallest dimension, perpendicular to the c-axis), and (b) a Kernel Density Estimator (KDE) calculated using adaptive bandwidth (Vermeesch 2012) and plotted on a histogram of single-grain ages. Both graphs have been produced using Radial Plotter software (Vermeesch 2009).

3.3.5.2 Zircon (U-Th)/He data

ZHe analyses were carried out on one sample (GAL14), which yielded good quality crystals and has similar, young AHe and AFT ages. The data from five single-grain aliquots are presented in Table 3.9.

The ZHe ages vary from 147.5 to 296.3 Ma and from 186.5 to 367.7 Ma, uncorrected and α-recoil corrected respectively. The oldest three ages may be related to the emplacement age of the intrusion, 397 ± 2 Ma (Halliday et al. 1979). The ages show relatively

Table 3.9: Zircon (U-Th)/He data from Criffell pluton in southern Scotland. Symbols: L—length, W1—width, R*—equivalent radius, eU—effective Uranium, age—uncorrected age, age$_c$—age corrected for α-recoil, † analytical error; ‡ analytical error + 10% of the age (based on the reproducibility of Fish Canyon Tuff aliquots). Central ages and central age uncertainties calculated using Radial Plotter software (Vermeesch 2009).

Sample name	No.	L (μm)	W1 (μm)	R$*$ (μm)	He (μcc/g)	U (ppm)	Th (ppm)	Th/U	eU (ppm)
GAL14	1	238	88	55.8	29213.7	1270.7	1478.8	1.2	1618.2
	2	216	100	60.0	28832.6	959.8	454.3	0.5	1066.6
	3	168	62	39.3	25386.9	808.7	562.5	0.7	940.9
	4	180	73	45.3	23683.7	614.4	442.4	0.7	718.3
	5	202	102	59.6	29626.2	703.0	440.8	0.6	806.6

Table 3.9: (continued)

	No.	age (Ma)	error†	error‡	F_T	age$_c$ (Ma)	error‡	central age (Ma) $\pm$ 1σ
GAL14 (continued)	1	147.5	7.9	22.7	0.79	186.5	26.6	224 $\pm$ 24
	2	219.5	11.8	33.7	0.81	271.7	38.9	
	3	219.1	11.9	33.8	0.71	306.9	42.6	
	4	266.7	14.1	40.8	0.75	356.1	49.7	
	5	296.3	15.5	45.2	0.81	367.7	52.3	

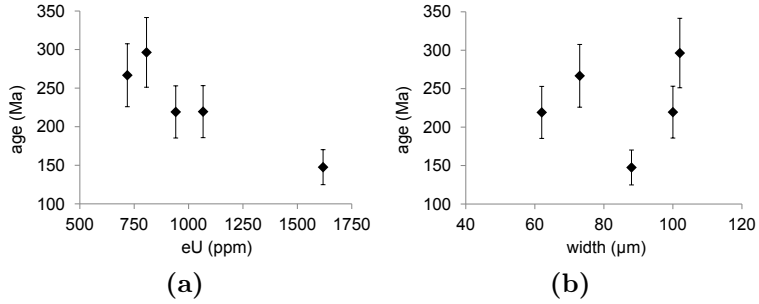

(a) **(b)**

Figure 3.20: Zircon (U-Th)/He age versus (a) eU concentration in ppm and (b) crystal width in μm in Criffell pluton in the Southern Uplands. The error bars show analytical error + 10% of the age (based on the reproducibility of Fish Canyon Tuff aliquots).

strong (R^2=0.86) negative correlation with [eU] (Fig. 3.20a) and no correlation with crystal width (Fig. 3.20b). The presence of negative correlation between the ZHe ages and [eU] is a common feature in zircons and can be explained by the presence of radiation damage (Nasdala et al. 2004, Guenthner et al. 2013). The negative correlation between the ages may occur if the rock was subjected to a reheating episode; highly damaged crystals have lower closure temperature and may be partially reset during reheating, resulting in a younger age (Guenthner et al. 2013). The correlation may be exploited by numerical modelling to constrain the duration and maximum temperature of the reheating event.

3.4 Northern Wales

3.4.1 Geological settings

Northern Wales comprises a part of Eastern Avalonia, a Palaeozoic palaeocontinent, that was a marginal crustal block of Gondwana during the Precambrian (Woodcock & Strachan 2000). It borders the Cheshire Basin on the east, the East Irish Sea Basin on the north, the Central Irish Sea Basin on the north-west and the Cardigan Bay on the west (Fig. 3.1). The Eastern Avalonia basement comprises two crustal blocks: the Avalon and Monian-Rosslare, separated by the Menai Strait Line (Woodcock & Strachan 2000). The blocks were amalgamated by the end of the Cadomian orogeny (Precambrian).

The oldest rocks in the region are Monian Precambrian blueschists and metasediments that are intruded by late Precambrian/earliest Cambrian Coedana Granite (on Anglesey) and the Sran complex (on Llŷn peninsula) (Woodcock & Strachan 2000). Lower Palaeozoic sedimentary and volcanic rocks formed in a Caledonian back-arc basin are intruded by a group of Ordovician, small intrusive bodies at Llŷn (Woodcock & Strachan 2000, Croudace 1982). After the Caledonian orogeny, the region is considered to have formed an emerged stable block (Ziegler 1988, Woodcock & Strachan 2000). The surrounding basins contain Carboniferous and Permo-Triassic sediments; the Central Irish Sea and the Cardigan Basins also include Cenozoic sediments. Several Palaeogene dykes are exposed onshore. An aeromagnetic survey revealed that the dyke swarm was displaced by sinistral movement along pre-existing faults in the vicinity to the Menai Strait Line (Bevins et al. 1996).

3.4.2 Existing thermochronological constraints

Thermochronometric data from northern Wales are scarce. Green et al. (1997) and Holford et al. (2005a) used AFT data to conclude that rocks now at the surface were at temperatures of 90–100°C in the early Palaeogene, but they do not provide raw data. Holford et al. (2005b) analysed rock samples from the onshore Mochras borehole, western coast of northern Wales. The borehole penetrates Miocene–Oligocene rocks lying uncomfortably on the Lower Jurassic sediments, structurally belonging to the Cardigan Bay Basin. The rocks have been processed for AFT, vitrinite reflectance and compaction studies and the results were interpreted as indicative of two exhumation episodes: ∼2.5 km of rocks removed in the Early Cretaceous and ∼ 1.5 km removed in the Neogene. Holford et al. (2005b) found no evidence at Mochras for an early Palaeogene exhumation event and argued that the event has a regional significance.

3.4.3 Sampling strategy

The main aim of the study in northern Wales was to provide thermochronometric data in this area and to investigate the cooling pattern of rock either side of the Menai Strait Line (Fig. 3.1). In order to obtain good quality, clear, prismatic apatite crystals, only intrusive rocks were sampled. About 2.5 kg of rock was collected from each site and processed using standard separation procedures for apatites (see Appendix A.1). Most separates contain clear, prismatic, good quality apatite grain and the samples have been processed for both AFT and AHe analyses. However, measurement of track length distributions was hampered by low U concentration in most of the samples. This meant also that multi-grain aliquots had to be analysed for AHe ages determinations. The locations of the analysed samples are shown in Fig. 3.2 and given in Table 3.1. The detailed information of the samples are available in the Appendix B.

3.4.4 Apatite fission track analysis

Fission track age and track length distribution were determined on six samples, following the procedure given in Appendix A.2. The central age, MTL and average D-Par value are reported for each sample in Table 3.10, and single-grain data are presented in Appendix B.

3.4.4.1 Fission track age

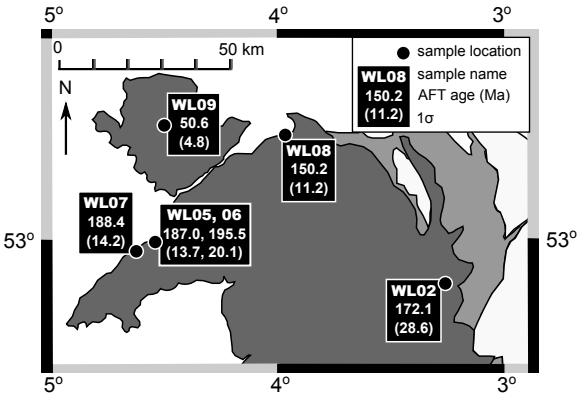

Figure 3.21: Map of apatite fission track ages of the samples from northern Wales. For the legend to geological map see Fig. 3.3.

AFT central ages vary from 50.6 ± 4.8 Ma to 195.5 ± 20.1 Ma (Fig. 3.21) and all are significantly younger than the emplacement age of the intrusions. The youngest age is documented on Anglesey (sample WL09). Ages on the mainland are significantly older, always >150 Ma. The Anglesey sample was of very low quality and the central age is calculated based on only 15 single grains. In contrast, 19–21 single grains have been counted for each sample from the mainland. Only WL06 failed the χ^2 text, with a P(χ^2) value of 2.93. The low P(χ^2) value may be an effect of high dispersion (27%), rather than the presence of two populations, which are not visible in the radial plot nor in the D-Par values. D-Par values were determined on all correctly etched samples. The average sample D-Par values vary from 1.61 to 2.26 μm and are similar to Durango apatite, 1.82 ± 0.13 μm.

Table 3.10: Apatite fission track data from the samples from northern Wales. Symbols: ρ_D—tracks density on the dosimeter, ρ_s—spontaneous track density, ρ_i—induced track density, P—probability that the grains pass χ^2 test, MTL m—mean track length measured, MTL p—mean track lengths projected, N_D—number of tracks on the dosimeter, N_s—number of spontaneous tracks, N_i—number of induced tracks

Sample name No. grains [lengths]	ρ_D (cm^2) N_D	ρ_s (cm^2) N_s	ρ_i (cm^2) N_i	χ^2	P (%)	age (Ma)	$\pm1\sigma$	MTL m (μm)	$\pm1\sigma$	MTL p (μm)	$\pm1\sigma$	DPar (μm)	$\pm1\sigma$
WL02 19 [0]	9.11E+05 6478	1.16E-07 83	9.43E-08 68	4.4	100.0	172.1	28.6	-	-	-	-	-	-
WL05 21 [0]	1.26E+06 8874	5.62E-07 431	5.82E-07 449	11.1	94.4	187.0	13.7	-	-	-	-	1.61	0.11
WL06 20 [0]	9.03E+05 6478	5.22E-07 422	3.75E-07 295	32.3	2.9	195.5	20.1	-	-	-	-	1.86	0.09
WL07 19 [100]	8.99E+05 6478	3.38E-07 488	2.44E-07 360	4.4	100.0	188.4	14.2	12.89	1.74	13.82	1.41	1.94	0.15
WL08 20 [100]	8.95E+05 6478	4.22E-07 447	3.87E-07 413	13.4	81.9	150.2	11.2	12.82	1.81	13.81	1.36	2.26	0.07
WL09 15 [0]	8.91E+05 6478	2.77E-07 174	7.43E-07 479	17.0	25.7	50.6	4.8	-	-	-	-	-	-

3.4.4.2 Track length distribution

The samples from the mainland are characterized by low U-concentration (usually <10 ppm). This made the determination of a statistically significant number of track lengths possible in only two samples (WL07 and WL08), which yielded large amounts of good quality crystals. On each slide, 100 horizontal, confined track were measured. To account for anisotropy, every track has been c-axis projected, using the angle of the track with the c-axis of the crystal and the D-Par value of that grain to take the apatite composition into consideration, according to the projection model of Ketcham et al. (2007a,b). The MTL and standard deviation of both samples are very similar: 12.89 ± 1.74 μm and 12.82 ± 1.81 μm, respectively. Track length projection increases the MTL and decreases the standard deviation to about 13.8 ± 1.4 μm in both samples. Histograms of track length distribution are shown on Fig 3.22. Both samples show two small peaks. The histograms of projected track lengths are narrower, as it is expected by the model prediction, and, in the case of WL07, the bimodality of the measured track lengths disappears, as it has happened for the samples in southern Scotland. The histogram of the projected track lengths for WL08 still shows small two peaks. The peaks differ by ∼1 μm and they are not well defined, but bimodality is likely to occur. The AFT age is relatively old and, more importantly, geological constraints from the region suggest that more than one cooling event might have affected the area and the rocks have experienced a reheating period. Two peaks may, therefore, reflect the complex thermal history of the sample (Gallagher et al. 1998).

3.4.4.3 Summary

The single AFT age of the Isle of Anglesey (∼50 Ma) is significantly younger than the mainland (150–200 Ma) but if it is to be used to assess potential fault reactivation along the Menai Strait Line, it needs to be repeated on a better quality apatite crystals, and AFT age has to be implemented by fission track length measurements and more AHe age determiantions.

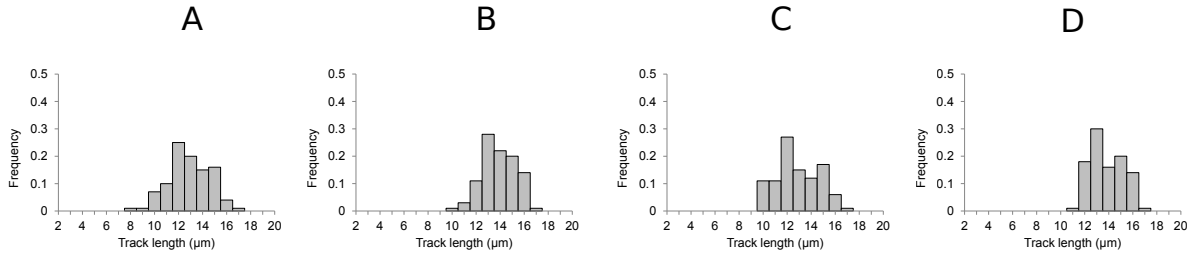

(b) WL07 **(c)** WL08

Figure 3.22: Histograms of the track length distribution of the samples from northern Wales. Columns A and C—measured track lengths, columns B and D—projected track lengths. Track length projection after Ketcham et al. (2007a).

3.4.5 Apatite (U-Th-Sm)/He analyses

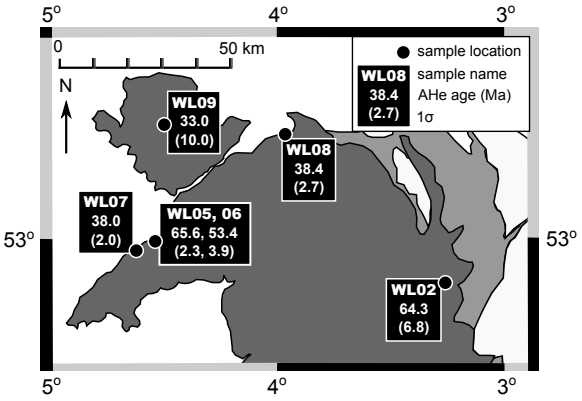

Figure 3.23: Map of apatite (U-Th-Sm)/He ages of the samples from northern Wales. For the legend to geological map see Fig. 3.3.

Apatite (U-Th-Sm)/He analyses have been carried out both on single-grain and multi-grain aliquots from all six samples. The analytical procedure of AHe analyses is described in Appendix A.3. Application of multi-grain analyses was motivated by the relatively high analytical error on either He or U-Th measurements due to small crystal size and low U-Th concentration. Four to six aliquots were analysed. Multi-grain samples aimed to incorporate grains of similar radius.

Aliquots demonstrating analytical inaccuracies were discarded from modelling and interpretation and are not presented here. Data from all analysed aliquots and comments on discarded grains are given in data logs for each sample in Appendix B. In case of multi-grain aliquots, marked by 'M' in Table 3.11, crystal dimensions given in the table are the mean values of all the grains in the packet. The α-recoil correction was performed using 'Alpha F_T-ejection factor' software (Gautheron & Tassan-Got 2010, Ketcham et al. 2011).

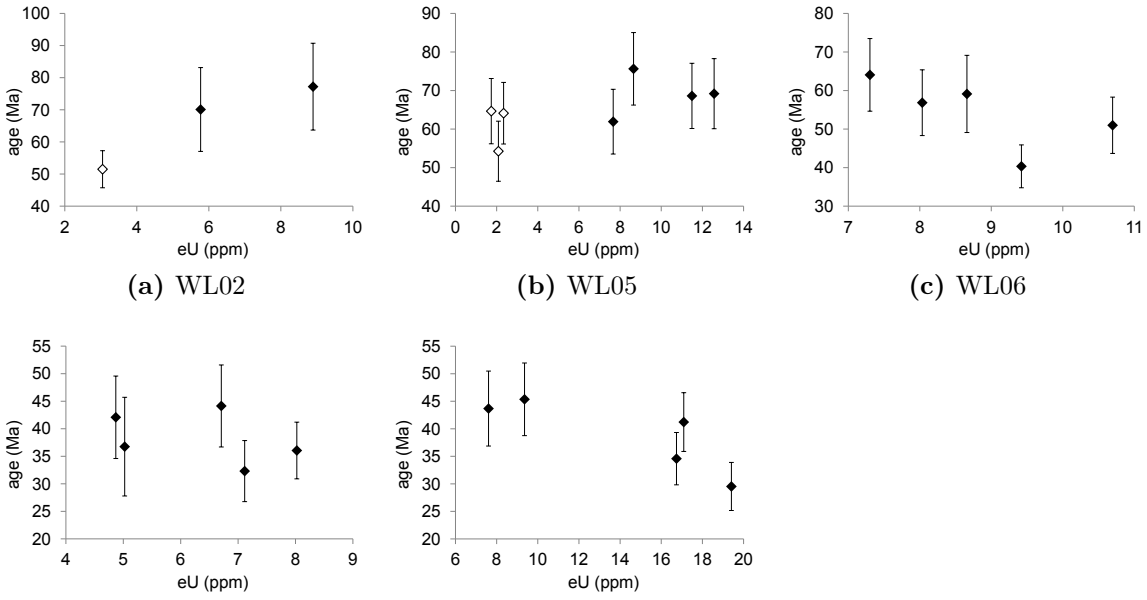

(a) WL02 **(b)** WL05 **(c)** WL06

(d) WL07 **(e)** WL08

Figure 3.24: Apatite (U-Th-Sm)/He age (Ma) versus eU concentration(ppm) in samples from northern Wales; black—single-grain aliquots, white—multi-grain aliquots. The error bars show analytical error + 10% of the age (based on the reproducibility of Durango aliquots).

Single aliquot data are shown in the Table 3.11. The uncorrected AHe ages of single aliquots vary from 21.2 ± 2.5 Ma to 77.2 ± 13.5 Ma and corrected ages from 27.8 ± 3.2 Ma to 135.9 ± 19.4 Ma. The central ages range from 33.0 ± 10 Ma to 65.6 ± 2.3 Ma. The youngest central age, 33 ± 10 Ma, is from Anglesey (WL09) and shows high dispersion, 45%, because it is based on only two aliquots, which are significantly different. The mean grain size of the aliquot M1 is bigger than aliquot M2 and has higher [eU]. It is suspiciously much younger than any other AHe age in the region and, although no analytical inaccuracies were evident for this sample, it is likely that the age has been underestimated and should not be used for calculation of the central age and for the data modelling. In other samples, dispersion of single-grain ages is lower than 20% and there is no clear difference between the ages of single- and multi-grain aliquots. All corrected AHe ages are younger than the corresponding AFT age.

The AHe ages have been plotted versus [eU] and grain thickness (the smallest dimension) in Fig. 3.24 and 3.25, respectively. Correlation with [eU] is either positive—samples WL02 and WL05, or negative—sample WL06 and there is a weak correlation in WL08. WL05 and WL08 show also a positive correlation between the age and grain thickness.

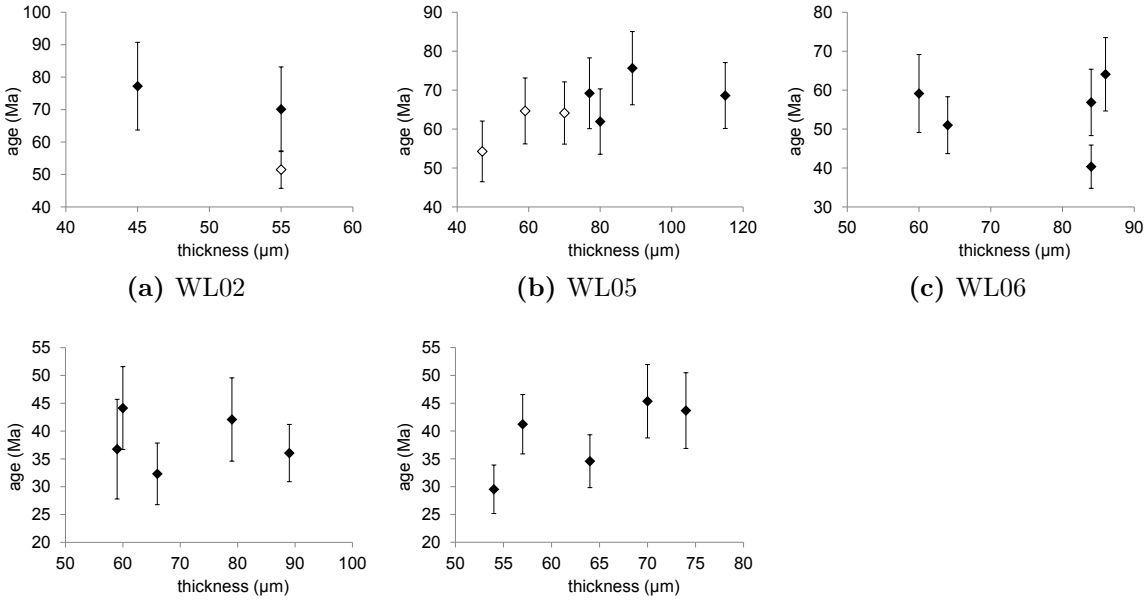

(a) WL02 **(b)** WL05 **(c)** WL06

(d) WL07 **(e)** WL08

Figure 3.25: Apatite (U-Th-Sm)/He age (Ma) versus grain thickness (the smallest dimension) in samples from northern Wales; black—single-grain aliquots, white—multi-grain aliquots. The error bars show analytical error + 10% of the age (based on the reproducibility of Durango aliquots).

Table 3.11: Single grain apatite (U-Th-Sm)/He data from samples from northern Wales. Symbols: L—length, W1—width, W2—thickness, R*—equivalent radius, T—terminations, eU—effective Uranium, age—uncorrected age, age_c—age corrected for α-recoil, † analytical error; ‡ analytical error + 10% of the age (based on the reproducibility of Durango aliquots). Central ages and central age uncertainties calculated using Radial Plotter software (Vermeesch 2009).

Sample	No.	L (μm)	W1 (μm)	W2 (μm)	R* (μm)	T	He (μcc/g)	U (ppm)	Th (ppm)	Sm (ppm)	Th/U	eU (ppm)	age (Ma)	error†	error‡	F_T	age_c (Ma)	error‡	central age ± 1σ (Ma)
WL02	1	135	53	45	29	0	99.1	2.9	25.6	1325.3	8.9	8.9	77.2	5.8	13.5	0.57	135.9	19.4	64.3 ± 6.8
	2	130	64	55	34	0	53.2	1.1	19.7	366.3	17.2	5.8	70.1	6.0	13.0	0.63	111.1	17.1	
	M1	*118*	*64*	*55*	*34*	-	*23.0*	*1.0*	*8.5*	*497.1*	*8.1*	*3.0*	*51.5*	*0.6*	*5.8*	*0.65*	*79.6*	*8.6*	
WL05	1	120	115	115	55	1	100.0	6.1	22.8	389.9	3.7	11.5	68.6	1.6	8.5	0.78	88.5	10.5	65.6 ± 2.3
	2	169	89	89	49	1	84.6	4.1	19.4	425.0	4.7	8.7	75.6	1.8	9.4	0.73	103.6	12.2	
	3	138	93	80	47	1	61.3	3.7	16.7	378.9	4.5	7.7	61.9	2.2	8.4	0.72	85.5	10.8	
	4	125	77	77	42	1	111.0	5.7	29.2	483.8	5.1	12.6	69.2	2.2	9.1	0.69	100.9	12.3	
	M1	*103*	*81*	*70*	*40*	-	*95.9*	*6.1*	*23.9*	*484.8*	*3.9*	*11.7*	*64.1*	*1.6*	*8.0*	*0.71*	*90.6*	*10.6*	
	M2	*106*	*55*	*47*	*30*	-	*72.4*	*5.2*	*22.1*	*429.0*	*4.2*	*10.4*	*54.3*	*2.4*	*7.8*	*0.58*	*94.0*	*11.8*	
	M3	*153*	*69*	*59*	*38*	-	*71.9*	*5.1*	*15.4*	*355.6*	*3.0*	*8.7*	*64.7*	*2.0*	*8.5*	*0.67*	*96.4*	*11.6*	
WL06	1	154	75	64	40	1	69.7	8.6	8.8	450.6	1.0	10.7	51.0	2.2	7.3	0.69	74.2	9.6	53.4 ± 3.9
	2	92	96	60	37	1	66.0	7.4	5.4	428.6	0.7	8.7	59.1	4.1	10.0	0.69	85.2	12.6	
	3	112	107	86	48	1	60.4	5.8	6.3	365.9	1.1	7.3	64.1	3.0	9.4	0.75	85.1	11.5	
	4	161	85	84	46	1	48.5	7.6	8.0	394.4	1.1	9.4	40.3	1.5	5.6	0.73	55.3	7.1	
	5	127	90	84	44	1	58.5	6.4	6.9	355.0	1.1	8.0	56.8	2.8	8.5	0.73	77.9	10.6	
WL07	1	110	106	60	42	0	39.4	5.1	6.7	525.7	1.3	6.7	44.1	3.0	7.4	0.75	59.0	8.9	38.0 ± 2.0
	2	170	96	89	51	0	37.9	6.0	8.4	529.3	1.4	8.0	36.0	1.5	5.1	0.77	46.6	6.2	
	3	125	69	59	36	1	23.9	4.1	3.8	278.0	0.9	5.0	36.8	5.3	9.0	0.66	55.8	10.9	
	4	123	90	79	45	0	27.8	3.9	4.3	462.0	1.1	4.9	42.1	3.3	7.5	0.76	55.5	8.8	
	5	145	81	66	41	1	30.5	5.6	6.5	544.7	1.2	7.1	32.3	2.3	5.5	0.70	46.2	6.9	
WL08	1	214	95	64	48	0	73.3	13.3	14.6	597.5	1.1	16.7	34.6	1.3	4.8	0.75	46.4	5.9	38.4 ± 2.7
	2	120	104	74	46	0	42.8	5.9	7.4	376.0	1.3	7.6	43.7	2.4	6.8	0.77	56.6	8.1	
	3	148	73	54	37	1	71.8	15.4	17.2	516.8	1.1	19.4	29.5	1.4	4.4	0.66	44.6	5.9	
	4	149	82	70	43	0	54.1	7.1	9.6	374.6	1.4	9.4	45.4	2.1	6.6	0.73	62.0	8.3	
	5	191	83	57	42	0	89.1	11.9	21.9	571.6	1.8	17.1	41.2	1.2	5.3	0.71	58.2	7.0	
WL09	*M1*	*137*	*99*	*85*	*49*	-	*78.4*	*26.3*	*17.5*	*70.0*	*0.7*	*30.4*	*21.2*	*0.4*	*2.5*	*0.76*	*27.8*	*3.2*	*33.0 ± 10*
	M2	*110*	*78*	*67*	*38*	-	*106.9*	*12.2*	*19.9*	*78.7*	*1.6*	*16.9*	*51.8*	*1.2*	*6.4*	*0.70*	*73.8*	*8.6*	

All single-grain AHe ages from the region have been plotted on a radial plot (Fig. 3.26a) and on the Kernel Density Estimator (KDE) (Fig. 3.26b). Analysis of the radial plot may suggest a presence of two populations of ages, having peaks around 38 and 68 Ma. The histogram displayed on the background of the KDE shows the same pattern with two peaks. However, the aliquot having the highest precision lies exactly in the middle of the two peaks and there are few other aliquots yielding ages of about 50 Ma. The clear presence of the two populations is also not supported by the KDE. Because the number of aliquots is low, it is likely, that the two peaks are an effect of different size or chemical composition of the aliquots, rather than the result of two different thermal events.

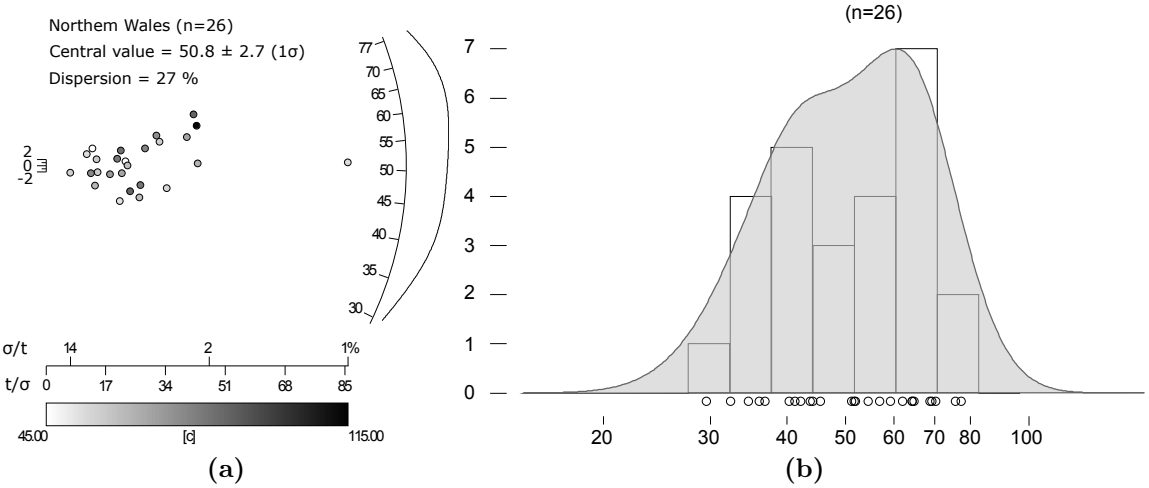

Figure 3.26: Distribution of all single-grain AHe ages from samples from northern Wales: (a) a radial plot of the single-grain ages, bottom panel and circles fill is grain thickness in μm (the smallest dimension, perpendicular to the c-axis), and (b) a Kernel Density Estimator (KDE) calculated using adaptive bandwidth (Vermeesch 2012) and plotted on a histogram of single-grain ages. Both graphs have been produced using Radial Plotter software (Vermeesch 2009). WL09-M1 is removed from the plot—see text for the explanation.

3.5 Regional summary

The study area encompasses a small region in central Britain, about 300 km long and 200 km wide. The AFT ages are highly variable, with the youngest ages of ∼50–70 Ma in the Lake District, within the Criffell pluton on the south coast of the Southern Uplands and on the Isle of Anglesey (Fig. 3.27). The ages increase rapidly northwards in southern Scotland and southwards in northern Wales, exceeding 200 Ma in the northernmost flank of the Southern Uplands and in the Cheviot

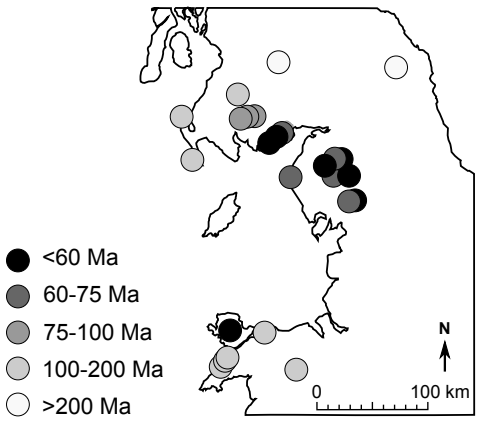

Figure 3.27: Simplified map of the AFT ages in central west Britain.

block. All ages are substantially younger than the emplacement age of the intrusions, which in most of the cases, occurred in the Ordovician to Lower Devonian at 480–400 Ma (Brown et al. 1968, Halliday et al. 1979, Rundle 1979, Croudace 1982).

Most of the ZHe ages correspond to the time of intrusion emplacement. Only one sample from the Skiddaw granite in the central Lake District has an uncorrected central age of 101 ± 11 Ma, which is ∼300 Ma younger than the granite emplacement.

The AHe ages in the region are not as variable as the AFT ages. They are substantially younger than the intrusion emplacement age and only few single aliquots in southern Scotland are older than corresponding AFT age. No clear spatial pattern is observed, although, most of the ages older than 100 Ma are in northern Wales. The majority of ages lie within the range of 30–70 Ma; these values are present everywhere and they constitute 91% of the total AHe ages in the Lake District, where there are no older grains, 85% in southern Scotland, with 14% of the total ages older then 70 Ma, and 71% in northern Wales (27% of ages are older than 70 Ma, but they are mostly associated with multi-grain aliquots). The number of aliquots analyses per sample is variable, from 2 to 25, and vary between the regions, with 60% of all single-grain ages coming from southern Scotland. Because of the uneven distribution of the data, a regional central age and an analysis of a density plot would be meaningless.

Valuable information is obtained from quasi-north-south oriented section of AFT and AHe ages (Fig. 3.28). In the south coast of Scottish Southern Uplands and in the Lake

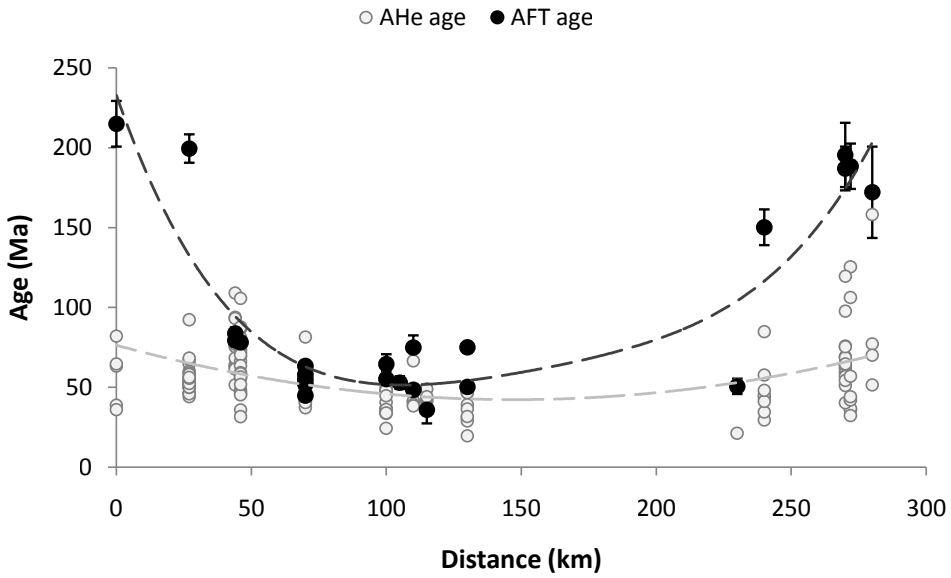

Figure 3.28: Apatite fission track central ages and single aliquot apatite (U-Th-Sm)/He ages of all the samples plotted versus the distance from the north along a quasi-north–south oriented profile. Three samples (GAL06, GAL11 and CH01) have not been included because they are located substantially far away from the profile line. Locations of other samples were interpolated on the profile line. Dashed lines are polynomial trend lines of the central ages: dark grey—AFT, light grey—AHe.

District, the AFT and AHe ages are similar, 50–70 Ma. The AFT ages form a characteristic U-shaped pattern, whereas the AHe ages are either constant, or show a weak and broad U-shape. In general, dispersion of AHe ages increase with increasing AFT age, and there are only a few single aliquots with older AHe ages than the corresponding AFT age. A thorough investigation of the significance of this U-shape pattern is hindered by the fact that the samples are not evenly distributed; for instance, there is a large gap south of the Lake District where intrusive rock are rare. The young sample from the Isle of Anglesey (WL09) has a crucial influence on the shape of the plot; if its AFT age is accurate, then the graph will have a broad base with steep shoulders; if, however, the AFT age is an artefact of low sample quality, then the graph will be south-skewed rather than being a more defined real U-shape.

ZHe age were performed only on the samples which yield younger than ∼60 Ma AFT ages. ZHe ages from outcrop samples usually correspond to the intrusion age; when they are younger, due to the radiation damage. Highly damaged crystals, usually with [eU]>1000 ppm have lower closure temperature and may be partially reset during a reheating event, resulting in a younger age (Guenthner et al. 2013).

The data presented in this chapter have been modelled to derive time-temperature paths of the rocks and the results of the modelling are shown in Chapter 4. To retrieve as much information as possible from the dispersion of single-grain ages, samples with more than 20 single-grain ages have been additionally modelled as fragments of broken crystals using the newly codified Helfrag software (Beucher et al. 2013). The results are also presented in Chapter 4.

Chapter 4

Quantifying thermal histories

4.1 Introduction

The combination of apatite fission track ages and track length distributions, and AHe and ZHe ages provides the opportunity to retrieve the history of the rocks over the whole temperature range consistent with the sensitivity of these thermochronometric systems. Combining the integrated thermochronometric data with strong geological constraints allows precise and accurate exhumation-burial histories to be resolved. The number of data and the complexity of the algorithms that describe the annealing of fission tracks and the diffusion of He requires the use of software that can perform inverse modelling to extract the best thermal histories that fit the data. A brief introduction of the inverse modelling technique and of the two commonly used software packages has been given in section 2.4. In general, rapid cooling events from high temperatures are much easier to resolve than slow cooling through the PAZ and PRZ. In such samples, valuable information may be obtained from AHe analysis of different grain size (Reiners & Farley 2001), variation in the degree of radiation damage (Flowers & Kelley 2011) or fragmentation (Brown et al. 2013). The accuracy and precision of models depends on the data quality; therefore thermal histories have to be carefully assessed based on how well they fit the data and the regional geological history.

This chapter is divided into two parts that presents the results of the inverse modelling of the fission track and (U-Th-Sm)/He data (section 4.2) using the QTQt software (Gallagher 2012) and the dispersion of multiple AHe ages (section 4.3) using the Helfrag code (Beucher et al. 2013). All the data were presented in Chapter 3.

4.2 Inverse modelling of thermochronometric data

4.2.1 Introduction

Inverse modelling was performed on samples for which the apatite fission track age has been implemented by track length distribution and/or (U-Th-Sm)/He. All fission

track data have been modelled using the multi-kinetic annealing model of Ketcham et al. (2007b) using c-axis projected lengths and compositionally dependent initial track length, calculated based on an input D-Par value for each grain. The models including (U-Th)/He ages have been run both with and without incorporation of the effect of radiation damage. The latest radiation damage algorithms (Flowers et al. 2009, Gautheron et al. 2009) were used for the AHe data and the model of (Guenthner et al. 2013) for the ZHe data. The uncertainty on (U-Th-Sm)/He age was set to the 'total' error, i.e. the analytical uncertainty plus one standard deviation of the mean age of standards, Durango for apatite and Fish Canyon Tuff for zircon, which were analysed at the same time as the unknowns. During modelling, the age was resampled from a distribution of a given observed age and uncertainty. This procedure deals with the fact that the data may be more noisy than it is suggested by the input values, because the fission track annealing and He diffusion kinetics are not fully understood and the observed age is not well known as it contains an unknown measurement error (Gallagher 2012). The resampling scheme has also been applied to the fission track data, using the D-par values as the observed kinetic parameters.

The general prior time-temperature box was set at temperature of 75 ± 75°C for AFT and AFT + AHe data and to 120 ± 120°C if ZHe ages were included; the range set for time was based on the oldest observed age (the oldest age ± the oldest age) or to the emplacement age if the latter was the oldest. Most of the samples come from intrusive rocks, for which the only available thermal constraint is the age of emplacement. The ages of the plutons are given in Tables 3.6 and 3.2 (Chapter 3). All the granitic intrusions in southern Scotland and Lake District belong to the 'Newer Granites' suite and yield biotite K-Ar ages (T_C = 300°C; Harrison et al. 1985) ranging from 390 to 440 Ma ±20 Ma (Brown et al. 1964, 1968, Halliday et al. 1979, Rundle 1979). The initial time-temperature constraints applied for the models has been set to 300 ± 100°C at 400 ± 20 Ma. The Crawfordjohn essexite from the northern most part of the Southern Uplands is a Variscan dyke, emplaced in the Late Carboniferous–Early Permian (Stephenson 2003); the initial constraints box was set to 300 ± 20 Ma and 300 ± 100°C. In case of sedimentary samples, the stratigraphic age was used as an additional constraint. For the granite boulder from the Ordovician conglomerate at Corsewall Point two constraints have been used: the emplacement age of the granite, 474 ± 15 Ma and 300 ± 100°C and the depositional age 458 ± 2 Ma and 20 ± 20°C based on the ages determined by Bluck et al. (2006). For the Whitehaven sandstone from the western coast of the Lake District, the only available constraint is the Upper Carboniferous (Bolsovian) depositional age (Akhurst 1997) and the initial constrain box was set in the model to 310 ± 15 Ma and 20 ± 20°C. The timing of the intrusion and cooling of granites in northern Wales is not well constrained. The Ll$\hat{y}$n, intrusions are early Caledonian (Ordovician) (Croudace 1982), the initial constraints of 460 ± 20 Ma and 300 ± 100°C has been used.

Four types of models have been produced for most samples: i) AFT and AHe data with the radiation damage model of Gautheron et al. (2009), ii) AFT and AHe data with the radiation damage model of Flowers et al. (2009), iii) AFT and AHe data with diffusion kinetics of Durango apatite (Farley 2000), and iv) AFT data only. Hereafter, the models will be called: G-rad-dam, F-rad-dam, no-rad-dam and AFT-only. When ZHe data were included, the radiation damage model of Guenthner et al. (2013) was used in the G-rad-dam and F-rad-dam models. For each sample, two outputs are presented; the maximum likelihood model (the model that best fits to the data) and the expected model (a weighted mean model where the weighted value is the posterior probability) (Gallagher, 2015, QTQt v 5.3.0 User Guide).

4.2.2 The Lake District

The thermal histories of the Lake District samples are generally similar to each other and all show a rapid cooling event in the latest Cretaceous/early Palaeogene. Samples from Carrock and Shap plutons have a complete thermochronology data sets. In these cases constraints on the pre-Cenozoic cooling history are also available. Without the ZHe ages the pre-Cenozoic history of the rocks cannot be predicted because, at the time of the rapid cooling event the rocks now at the surface were at temperature higher than the AFT PAZ. Some samples from the region are accompanied by only a few track length measurements; the models predictions are therefore not well constrained and should be taken as tentative. All models are shown on Fig. 4.1.

Thermal histories of the Carrock pluton (LD02) vary depending on whether the models include ZHe radiation damage. If the radiation damage model for ZHe (Guenthner et al. 2013) is not used, the ages are significantly underestimated and the maximum Late Cretaceous temperature exceeds 180°C. Two models that include radiation damage for both AHe and ZHe data give similar t-T paths. According to these models, the rock cooled to less than 120°C shortly after pluton emplacement and was then reheated prior to the final cooling in the latest Cretaceous/Palaeogene. The rapid cooling from temperatures of 125°C, or even 140°C in the case of the maximum likelihood models, started ∼65–75 Ma at a rate of 3–4°C/Myr. The data predictions are generally good, there is only one unpredicted AHe age and ZHe age. The AFT-only model produces similar results, although the t-T path constraints are weaker and no valuable information is provided on the pre-Cenozoic history.

The Shap granite (sample LD01) experienced a similar thermal history to Carrock; however, there are some differences in the timing and rate of cooling. When the radiation damage model for the ZHe data is included, the t-T paths show a post-emplacement cooling to 40–140°C that ended at ∼250–300 Ma. Since then the rocks have been probably reheated until ∼90 Ma when the maximum temperature of 125°C was reached. This time marks the onset of a rapid cooling episode, ∼10 Ma earlier than at Carrock. The

maximum likelihood models suggest, however, that the cooling started slightly later, and from slightly lower temperatures, 111°C in case of G-rad-dam and 116°C in case of F-rad-dam. The cooling rate estimated from the expected models was 1.8°C/Myr and 2.4°C/Myr for G- and F-rad-dam, respectively, and decreased after ∼50 Ma. The maximum likelihood models suggest even faster rates, up to 7.6°C/Myr for F-rad-dam, and shorter period of accelerated cooling. Both models show a generally good fit with the data, although, the dispersion pattern of AHe and ZHe ages is not well resolved. When the ZHe radiation damage algorithm is not used, the model cannot predict the ZHe ages, an issue that has been already observed in Carrock. The results from the AFT-only model are similar to those obtained from both rad-dam models; the late Cretaceous/Palaeocene rapid cooling event is even more rapid and no constraints can be given for the time before 80 Ma.

Figure 4.1: (On the next page.) Thermal histories of the samples from the Lake District and model predictions extracted from inverse modelling using QTQt software (Gallagher 2012). Thermal history graphs: thick red line is the maximum likelihood model; thick blue line is the expected model and dashed blue lines are the 95% credible intervals; thin red line defining a box shows the general range of prior; the light yellow shadow marks the Cenozoic era, 66–0 Ma. Although most of the models start from temperatures of 300±100°C (see text for more details), to make the plots easier to read, the temperature space shown on the graphs is 0–150°C for AFT and AFT + AHe data or 0–200°C for AFT + AHe + ZHe data. Model predictions graphs: top graph presents predictions for projected FTLD (fission track length distribution); the histogram shows the observed data, the red and grey lines are the predicted FTLD and the 95% credible intervals, respectively; the numbers in the top left corner are the observed (O) and predicted (P) AFT age, MTL and D-Par. Bottom graph shows the predicted versus observed AHe ages with the error bars; dashed line is a 1:1 line; in case of samples which have more than two AFT input files, the bottom graph shows predictions for AFT data of the 2nd slide and the predictions for AHe data are superimposed on the thermal history plot; in case of samples having ZHe ages, the predictions are superimposed on the thermal history graph. Three or four models are shown for each sample: G-rad-dam—radiation damage model of (Gautheron et al. 2009), F-rad-dam—radiation damage model of (Flowers et al. 2009), no-rad-dam—no radiation damage model, standard Durango kinetics, AFT only—model without (U-Th)/He data. If ZHe are modelled, the radiation damage model of (Guenthner et al. 2013) has been used in G-rad-dam and F-rad-dam and standard kinetics in no-rad-dam.

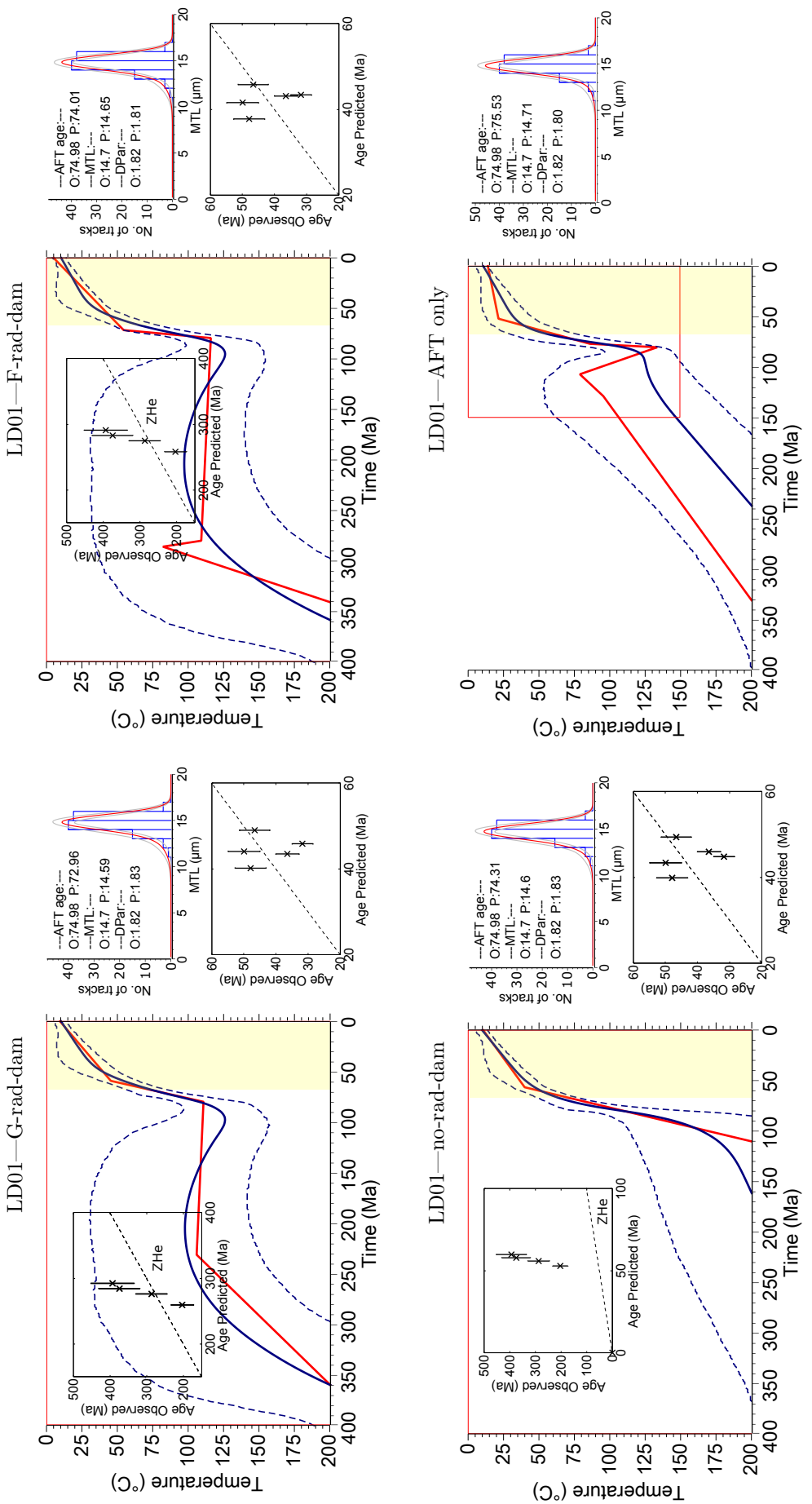

Figure 4.1: (Caption on the previous page.)

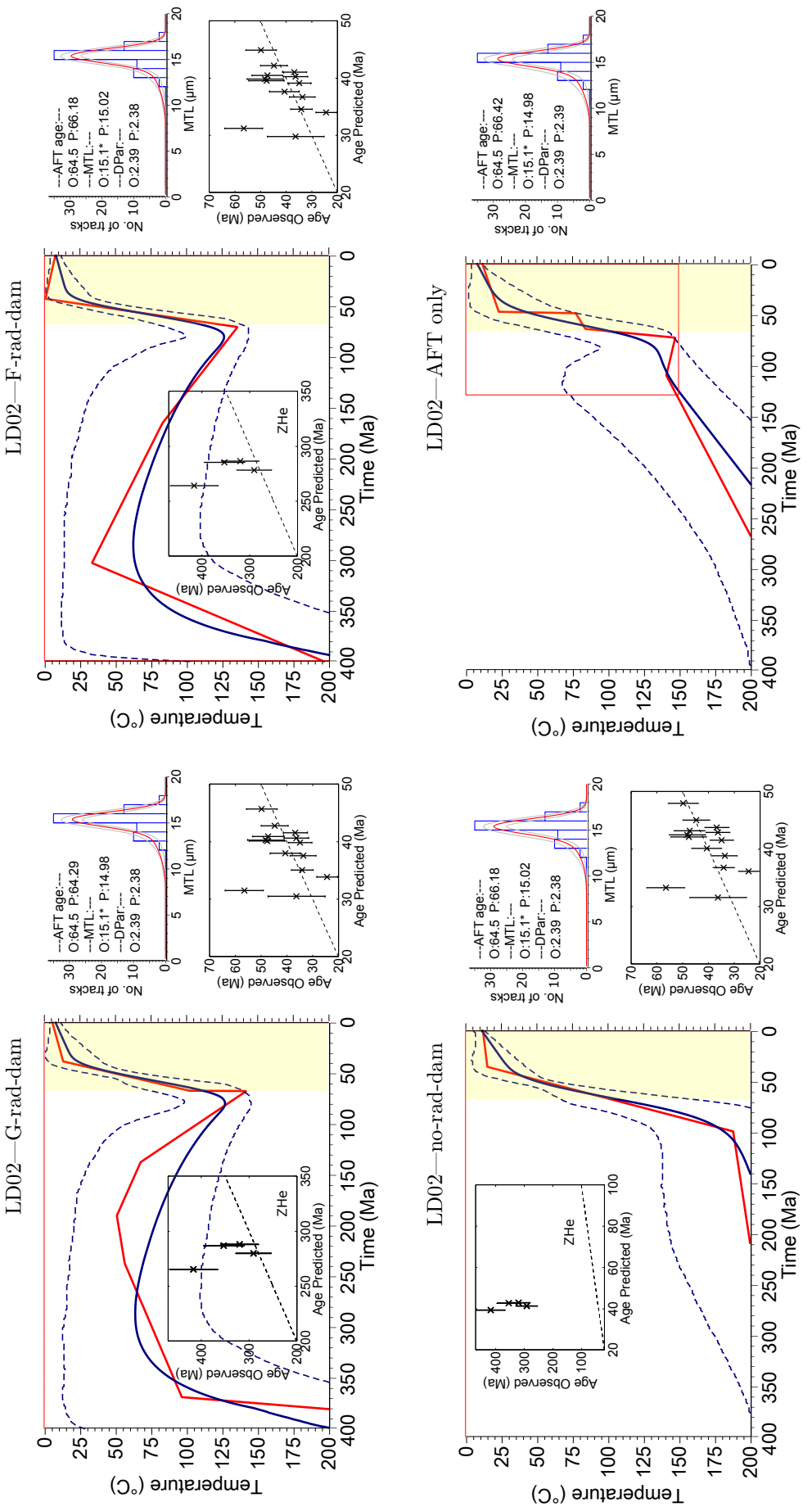

Figure 4.1: (continued)

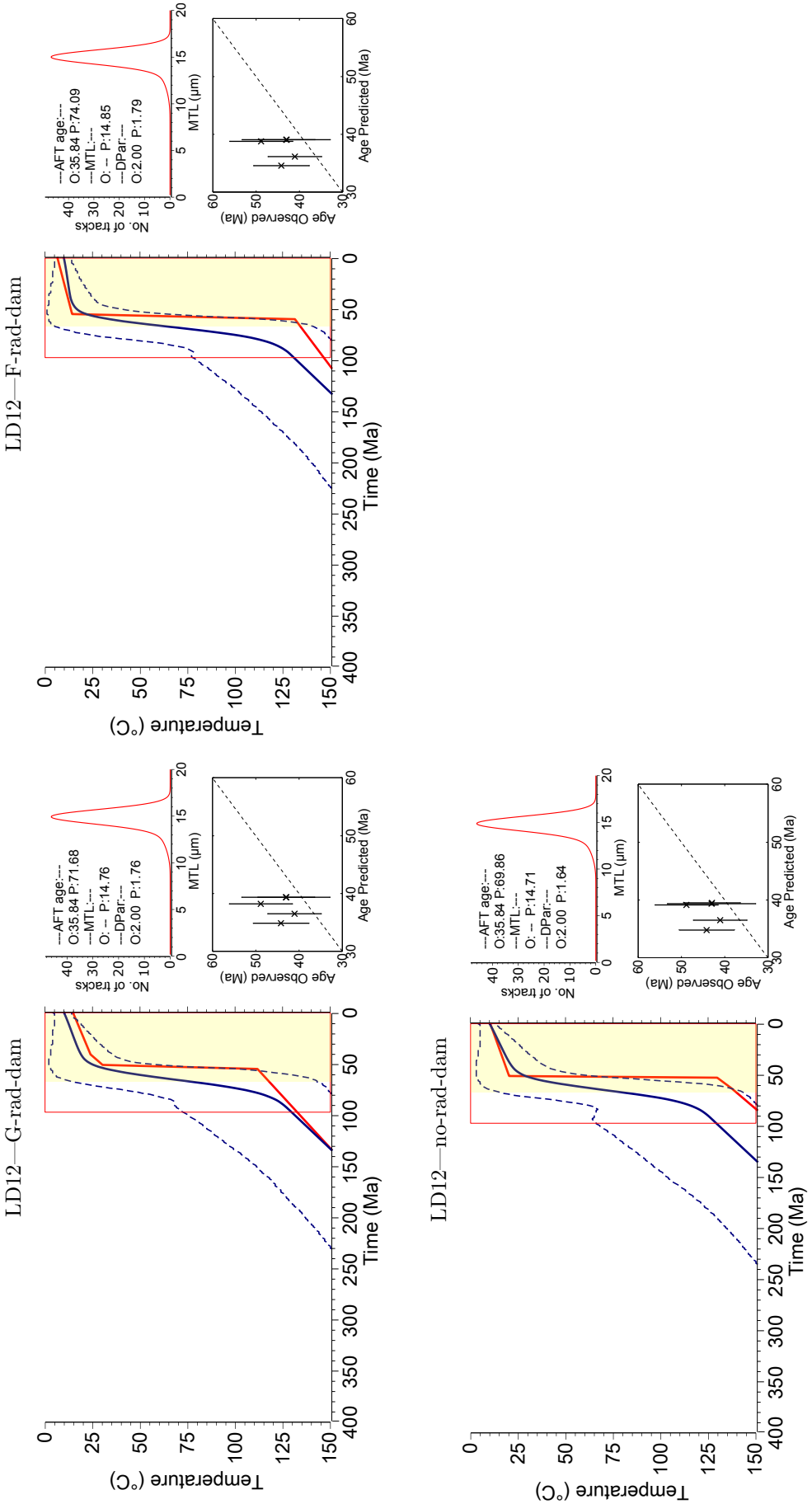

Figure 4.1: (continued)

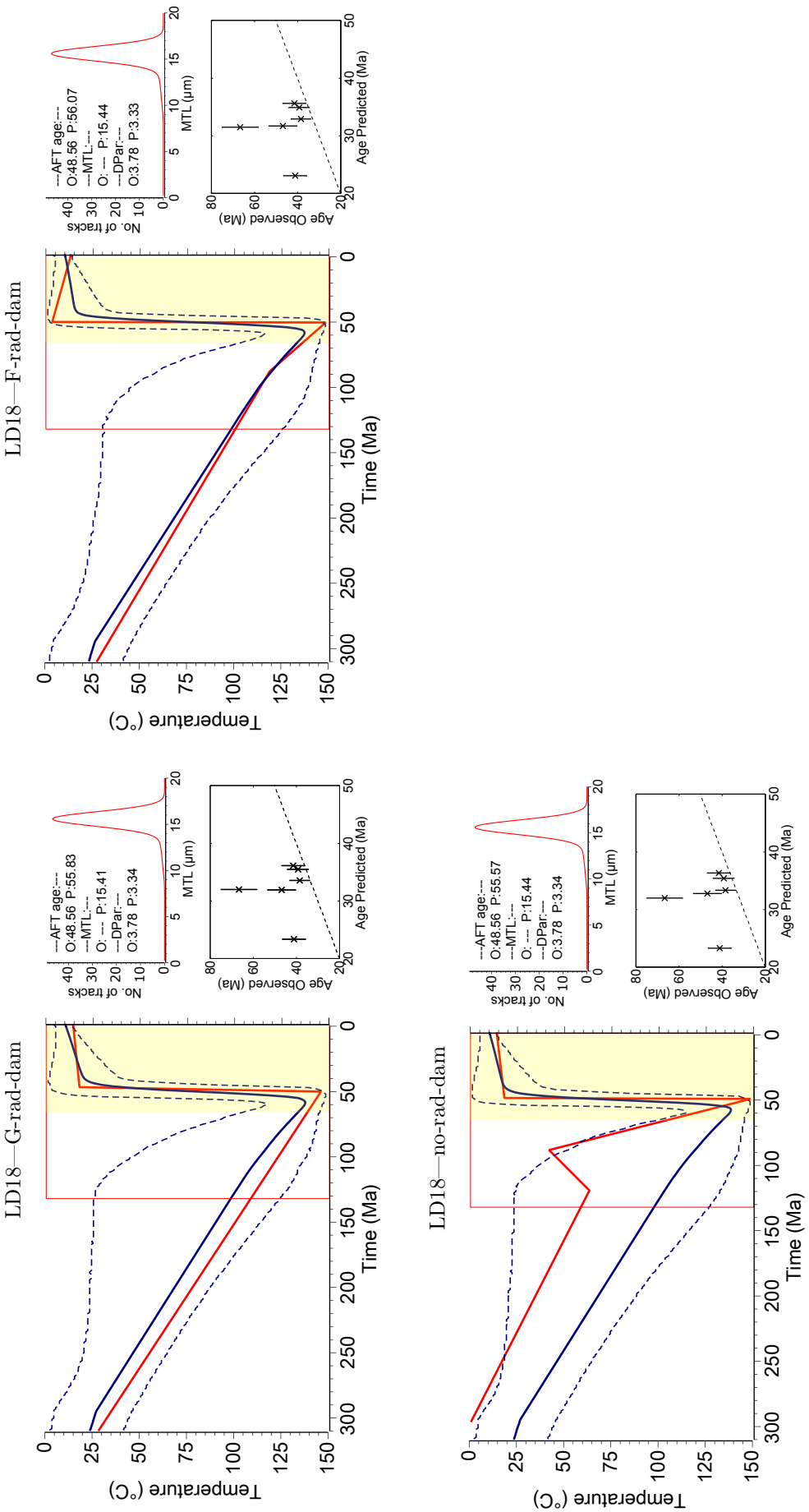

Figure 4.1: (continued)

The modelling results for the Haweswater gabbro (sample LD12) and the sandstone from the western coast of the Lake District block (sample LD18) are, in general, consistent with the thermal histories of the Carrock and Shap plutons. The additional geological constraints provided by the age of deposition of the sandstone produces thermal histories similar to those implied by the ZHe ages in Carrock and Shap, corroborating the possibility that the entire area was exhumed soon after pluton emplacement and then reheated in the Mesozoic. Timing of the early Palaeogene cooling event and the maximum pre-cooling temperatures are not well constrained, especially in LD12; however, for both samples, the most probable onset of cooling is 60–70 Ma. The observed AFT age is not predicted for LD12. However, as it was discussed in Chapter 3, data from this sample are of low quality and have a large analytical uncertainty. In that case, the resampled age predicted by the model is consistent with the AFT ages observed elsewhere in the region, and so the thermal history seems to be plausible.

4.2.3 Southern Scotland

The rocks from the region display a range of thermal histories that imply variation in the magnitude of Cenozoic cooling. For instance, the samples from the Criffell granite pluton show a distinctive thermal history, characterized by a rapid cooling event from in excess of 110°C in the latest Cretaceous/early Palaeogene. The majority of the region has experienced less Cenozoic cooling and their thermal histories are locally dependent. Several groups of thermal histories are identified and are discussed in this section. All models from the samples from southern Scotland along with the data predictions are presented in Fig. 4.2.

The three samples from the Criffell pluton yield similar cooling histories. Of the three samples from the Criffell pluton, GAL14 has the strongest constraints on the thermal history, as it yielded 19 AHe and 5 ZHe ages. The AFT and AHe data are well predicted by all four model types. The ZHe ages are well predicted by incorporating radiation damage, though they are significantly underestimated if not incorporated. The pluton was cooled after the emplacement and was subsequently buried since at least 150 Ma reaching 140 ± 15°C in the Late Cretaceous. The reheating is required to produce the ZHe age range, as well as the apparent negative correlation between the ages and [eU]. The cooling started at ∼70–80 Ma and was rapid, with rates of ∼5–10°C/Myr. A similar conclusion is reached if only the AFT data are used; albeit the Late Cretaceous/early Palaeogene cooling is modelled to be less rapid (2–5°C/Myr). The modelled thermal histories of GAL08 and GAL09, which do not have ZHe data, are similar to the AFT-only model of GAL14. The models, however, underestimate the AHe ages by 10–20 Ma, but predict the AFT data, both the age and track length distribution well. The cooling rate in both samples is 2–5°C/Myr for the AHe + AFT models and ∼1–3°C/Myr for AFT-only. The cooling started from maximum temperatures of 125 ± 15°C at 60–75 Ma. There are no constraints on the pre-75 Ma history as the AFT

thermochronometer is insensitive to temperatures higher than ∼120°C and so the possible reheating in the last 100 Ma resolved by the models has to be taken with caution. Such scenario is, however, supported by the GAL14 models that use the ZHe radiation damage diffusion kinetics. In general, it can be concluded that the Criffell pluton and surrounding region cooled to lower than 150°C shortly after pluton emplacement and then reheated to up to 140°C prior to the rapid cooling event at ∼75–60 Ma.

The three samples from the Fleet granite pluton produce different thermal histories. The AHe ages from GAL04A and GAL04B are younger than predicted by the models. The 'expected' thermal histories for GAL04B show a simple, monotonic cooling since at least 150 Ma, however, the maximum likelihood models suggest a period of accelerated cooling at ∼50–60 Ma. The thermal history of GAL04A is complex, with at least three cooling episodes: the initial one with unclear onset, that lasted until ∼130 Ma, the 2nd one between 80–50 Ma from the maximum temperature of ∼80°C and the recent cooling event that took place in the last 10 Ma from up to 50°C. The AFT-only and AFT + AHe (24 ages determinations) models of GAL02 differ. The AFT-only model suggests a monotonic cooling history, with perhaps small reheating event at 100–70 Ma. Incorporating the AHe ages requires a rapid cooling event from ∼80°C at 90–70 Ma, with rates of about 2°C/Myr. All models that use AHe slightly overestimate the AFT age and underestimate the AHe ages; the software struggles to predict AHe ages older than 70 Ma. The local variability in thermal histories and inability to reproduce the data suggests that there is an inaccuracy in the inverse models. It may be due to the fact that the AHe ages from all three samples are similar or slightly older than AFT ages of the same sample, and so the models are not able to reproduce the AHe ages. This applies to almost all the ages from this pluton and, therefore, may suggest that explaining the excess of He by inclusions or implantation is inconceivable. The crystals were analysed at different times and so it cannot be a result of an analytical problem. The application of the radiation damage models does not help. The most probable explanation of the old ages is strong U zonation, which was observed during the AFT analysis in the prints of apatite crystals on mica. Another possibility is unusual grain chemistry. These factors cannot be accounted for in the modelling and the models that include AHe data have to be treated with caution. At this stage, only the models based on the AFT data will be discussed.

The Portencorkie intrusion from the Rhins of Galloway (sample GAL06) seems to have had a simple thermal history. All models give similar t-T paths: monotonic cooling from ∼80°C in the last 100 Ma, preceded by a possible, small re-heating episode, up to 30°C, between ∼125–100 Ma. Maximum likelihood models do not show discrepancies from the expected models and the data are quite well predicted. Two AHe ages cannot be fitted, especially when the radiation algorithm of Flowers et al. (2009) is used. An early Cenozoic cooling pulse cannot be resolved, as the temperature at the beginning at the

Palaeogene was ∼60°C, outside the sensitivity range of the AFT thermochronometer.

The Loch Doon pluton (sample GAL01) seems to have a similar thermal history to the Portencorkie intrusion. There is no difference between the AFT-only and AFT + AHe models, but the former is less well constrained. The models suggest that the rock entered the PAZ at ∼250 Ma and after about 100 Ma within the PAZ, has been cooled monotonously. The timing of the onset of the monotonic cooling varies between the models, from 120 to 150 Ma, from a maximum temperature of 80–90°C. The cooling is preceded by a possible Jurassic reheating episode, which started at ∼200 Ma and could have a magnitude of up to 50°C. Some differences may be found between the maximum likelihood and the expected t-T paths both in case of AFT-only and F-rad-dam models. Both suggest a rapid cooling episode from temperatures of 50–60°C in the last 15–20 Ma. Additionally, the F-rad-dam model suggests the presence of a rapid, almost instantaneous, cooling episode at ∼75–85 Ma from ∼90°C. The maximum likelihood models may be, however, overcomplicated (Gallagher 2012) and even though the presence of small cooling events is possible, their magnitude and rate is more likely to be smaller than predicted. The models fit the data well. Small discrepancies from the observed FTLD are, however, produced by both rad-dam models. The predicted AHe age dispersion is also slightly higher than the true dispersion observed in the data set. One age is a clear outlier, but it does not influence the thermal history.

GAL11 from the Corsewall Point yields similar AFT age to the sample from Loch Doon; however, the proposed thermal histories are much more complex. After deposition, at 458 ± 2 Ma (Bluck et al. 2006), the rock was reheated to ∼120°C at ∼260–280 Ma. After a cooling episode between 260 and 200 Ma, the rock remained within the PAZ or at even lower temperatures and has been re-heated again prior to another cooling event. The timing, rate and magnitude of the most recent cooling event varies between models. The models including AHe ages support the onset of the cooling event at the beginning of the Cenozoic. The AFT-only models, instead, suggest a monotonic cooling in the last 40 Ma, from 60–65°C. Additionally, the t-T path of F-rad-dam model varies from those of G-rad-dam and no-rad-dam models. The former shows a cooling episode from ∼90°C starting at ∼80 Ma at a rate of ∼2°C/Myr; the final cooling from >60°C takes place in the last 10 Ma at a rate of ∼7°C/Myr, or faster for the maximum likelihood model. In the case of the G-rad-dam model and no-rad-dam model, the expected thermal histories show a slow monotonic cooling in the last 60–70 Ma from ∼70°C. The shape of the 95% credible intervals and the maximum likelihood models support, however, the cooling event with a rate of ∼1.5°C/Myr between 60–40 Ma and a possible final rapid cooling in the last few Ma, from up to 40–50°C. The models, even though different than the AFT model, predict the AFT data well. Some discrepancies are seen for the prediction of the AHe ages, but the overall dispersion pattern, apart from one clear outlier, is relatively well resolved.

All the models predict an overall similar thermal history for the Crawfordjohn dyke (sample SL01). The rock has been cooled quickly to below 100°C after emplacement at 300 ± 20 Ma and could have been even brought to the surface at ∼270–280 Ma. The thermal history shows a reheating until ∼130–140 Ma when the rock reached the maximum temperature of 90–100°C. All expected models show a long period of monotonic cooling; however, the maximum likelihood model of G-rad-dam and the shape of the 95% credible intervals suggest the presence of two episodes of accelerated cooling between 140–100 Ma and in last 20 Ma. Model predictions are generally good, however, the dispersion pattern of the AHe ages is not fully resolved.

The thermal histories of the Cheviot pluton (CH01) are, generally, similar irrespective of the model used, and predict the AFT and AHe ages well. It seems likely that the rock cooled to ∼20°C shortly after emplacement, was slightly reheated and cooled around 350 Ma and then remained within the PAZ temperatures or lower for at least 250 Ma. The final cooling episode was preceded by reheating to 90–100°C. The cooling started at 70–100 Ma and was monotonous; however, the shape of the 95% credible intervals and the maximum likelihood t-T path of models that include AHe data suggest

Figure 4.2: (On the next page.) Thermal histories of the samples from southern Scotland and model predictions extracted from inverse modelling using QTQt software (Gallagher 2012). Thermal history graphs: thick red line is the maximum likelihood model; thick blue line is the expected model and dashed blue lines are the 95% credible intervals; thin red line defining a box shows the general range of prior; the light yellow shadow marks the Cenozoic era, 66–0 Ma. Although most of the models start from temperatures of 300±100°C (see text for more details), to make the plots easier to read, the temperature space shown on the graphs is 0–150°C for AFT and AFT + AHe data or 0–200°C for AFT + AHe + ZHe data. Model predictions graphs: top graph presents predictions for projected FTLD (fission track length distribution); the histogram shows the observed data, the red and grey lines are the predicted FTLD and the 95% credible intervals, respectively; the numbers in the top left corner are the observed (O) and predicted (P) AFT age, MTL and D-Par. Bottom graph shows the predicted versus observed AHe ages with the error bars; dashed line is a 1:1 line; in case of samples which have more than two AFT input files, the bottom graph shows predictions for AFT data of the 2nd slide and the predictions for AHe data are superimposed on the thermal history plot; in case of samples having ZHe ages, the predictions are superimposed on the thermal history graph. Three or four models are shown for each sample: G-rad-dam—radiation damage model of (Gautheron et al. 2009), F-rad-dam—radiation damage model of (Flowers et al. 2009), no-rad-dam—no radiation damage model, standard Durango kinetics, AFT only—model without (U-Th)/He data. If ZHe are modelled, the radiation damage model of (Guenthner et al. 2013) has been used in G-rad-dam and F-rad-dam and standard kinetics in no-rad-dam.

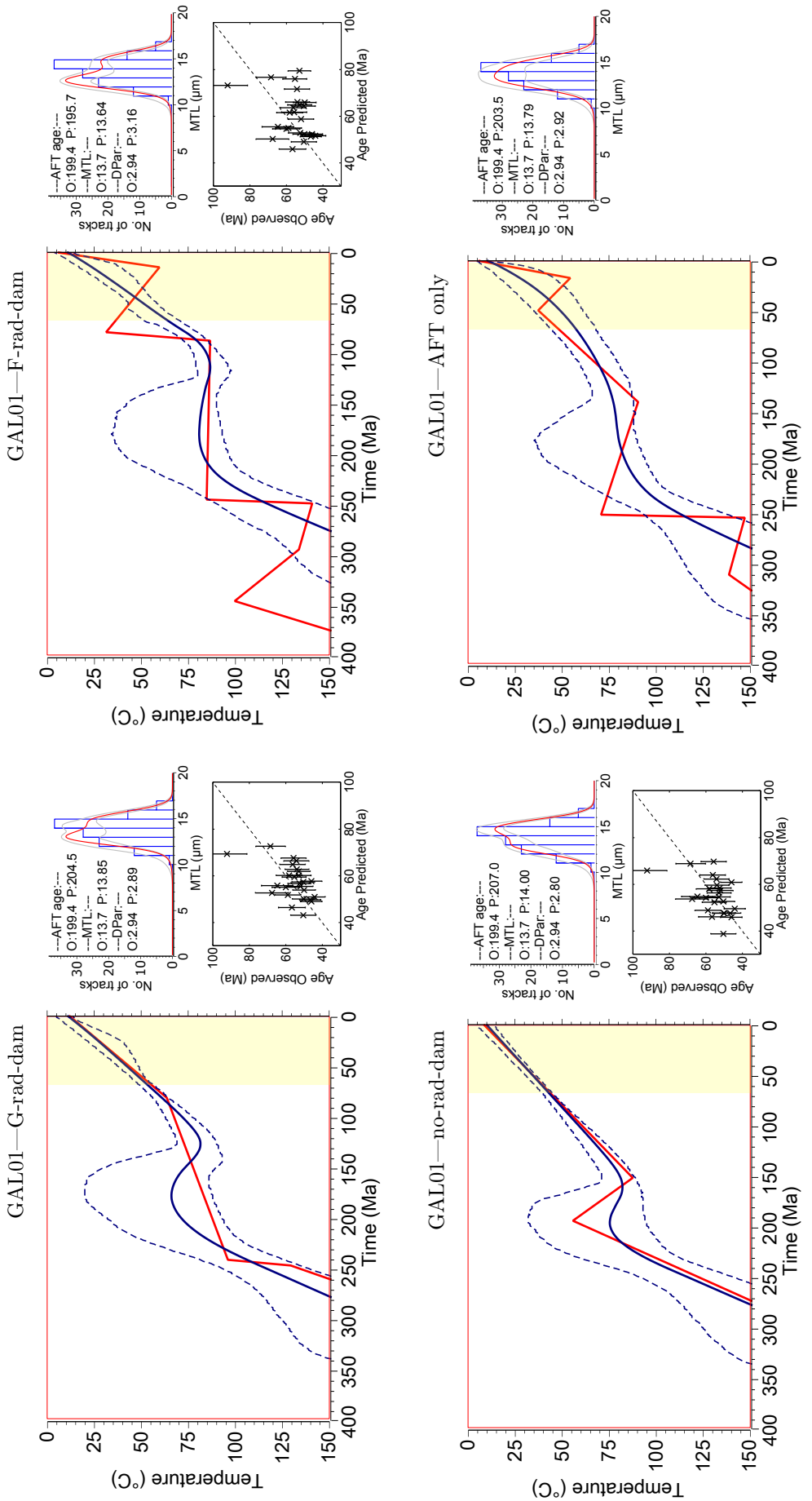

Figure 4.2: (Caption on the previous page.)

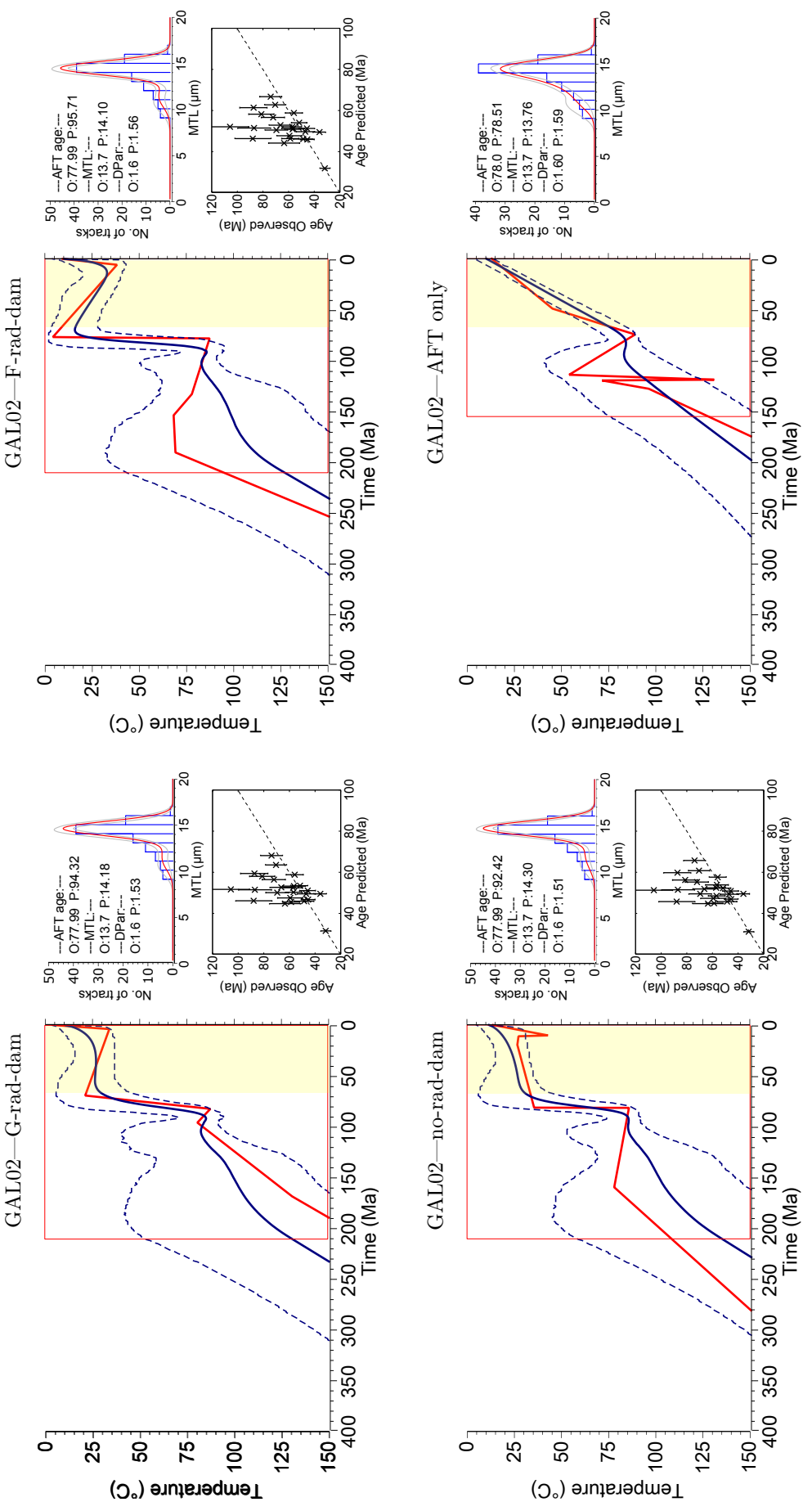

Figure 4.2: (continued)

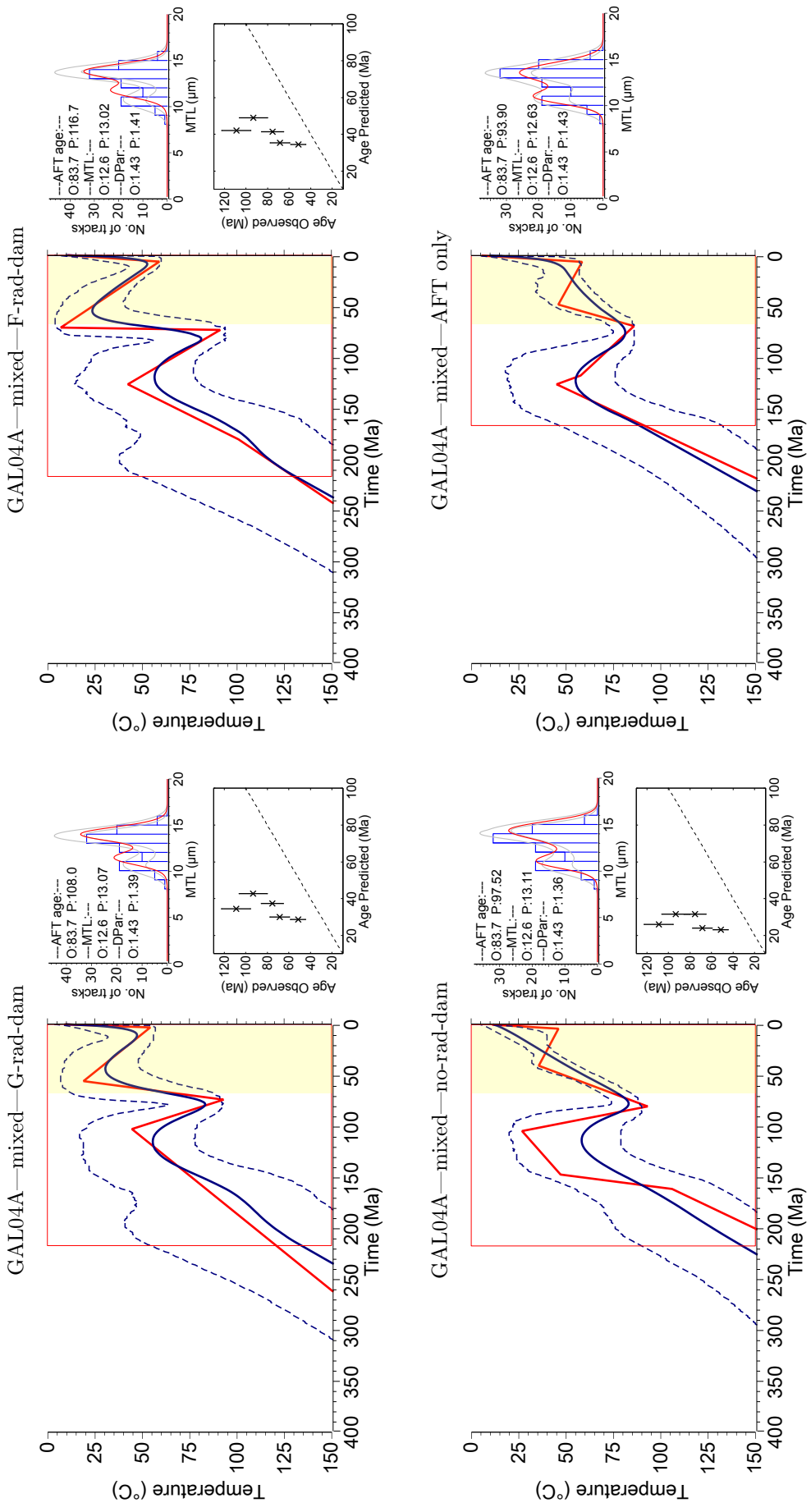

Figure 4.2: (continued)

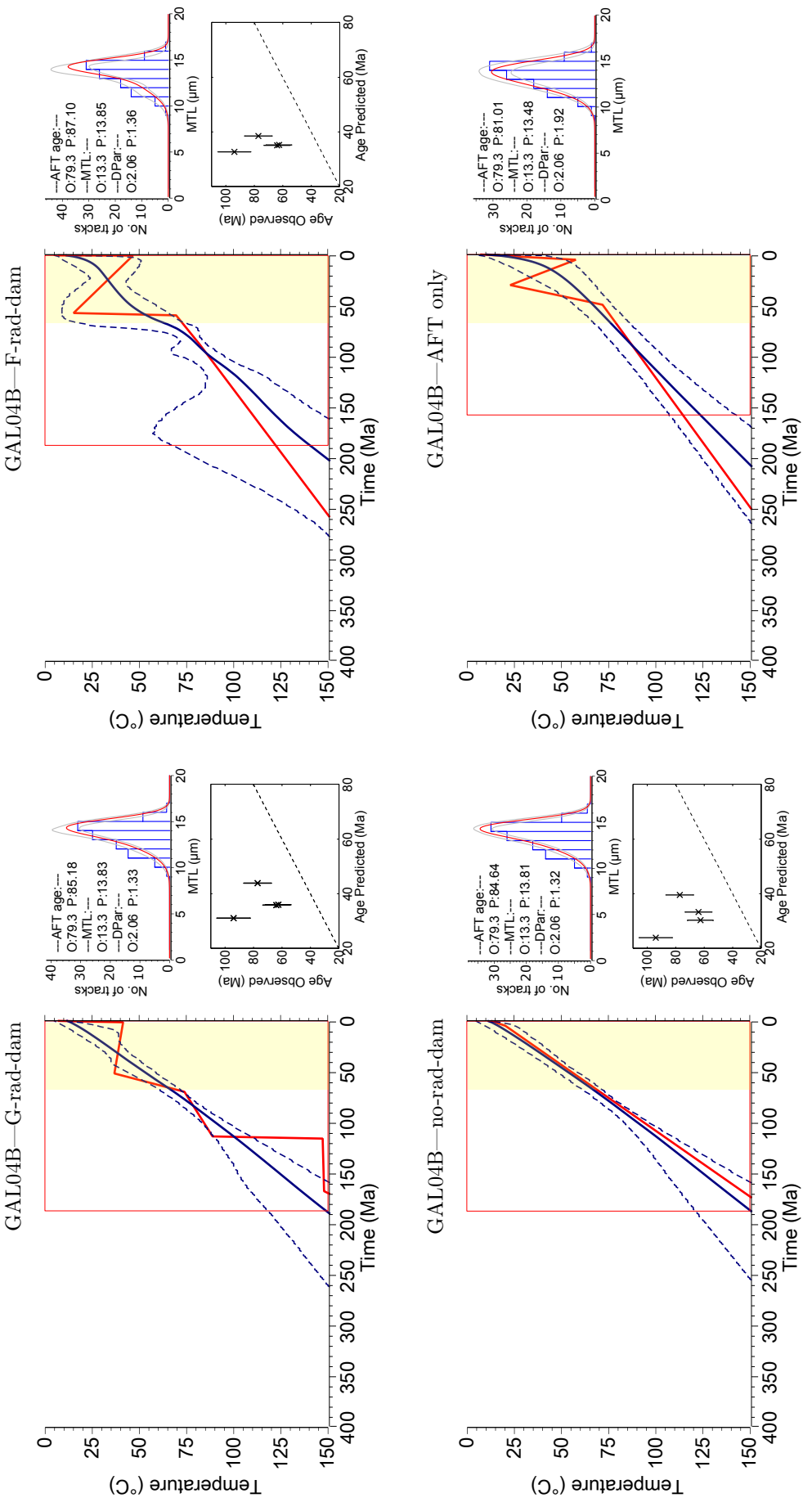

Figure 4.2: (continued)

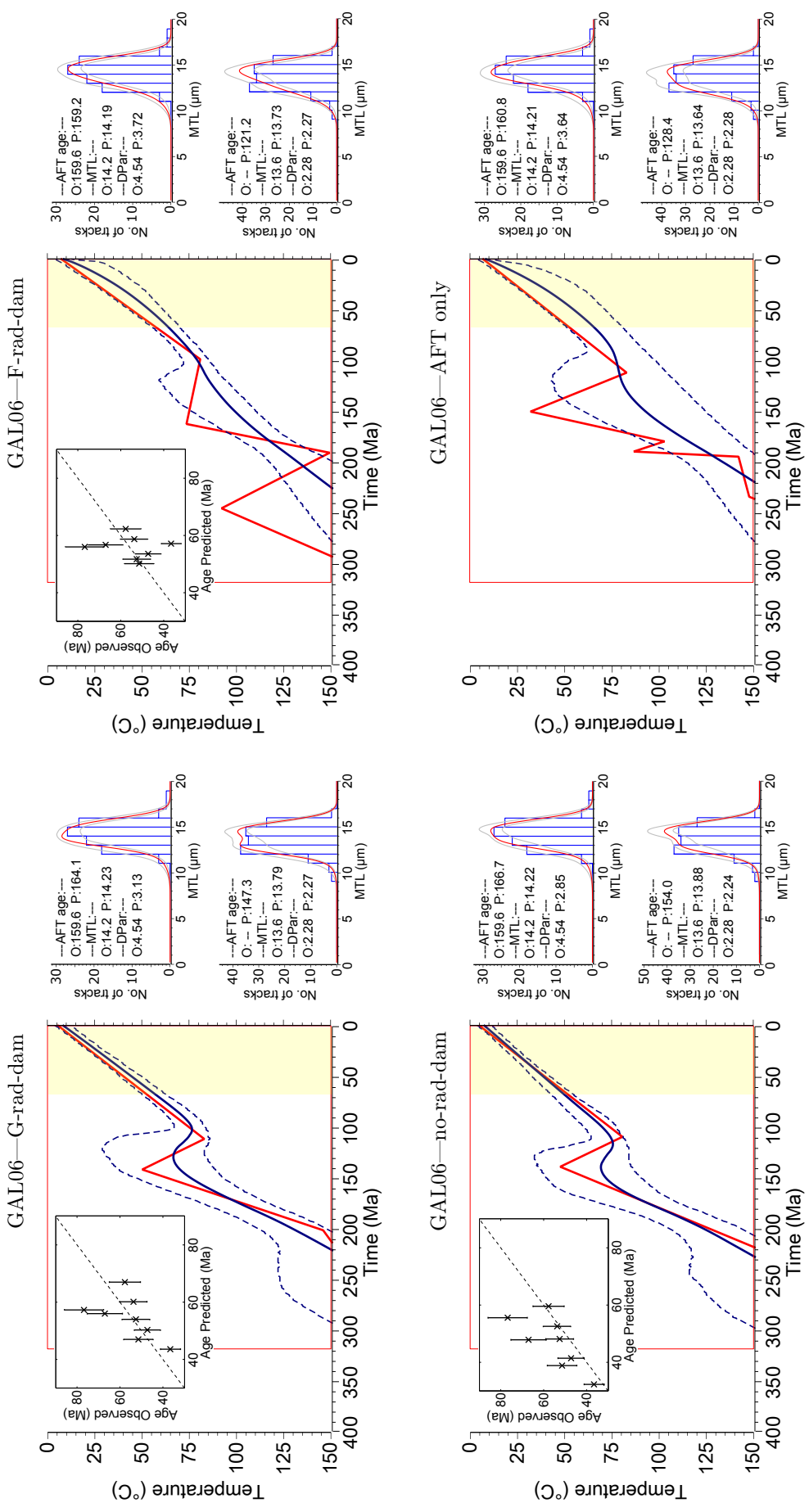

Figure 4.2: (continued)

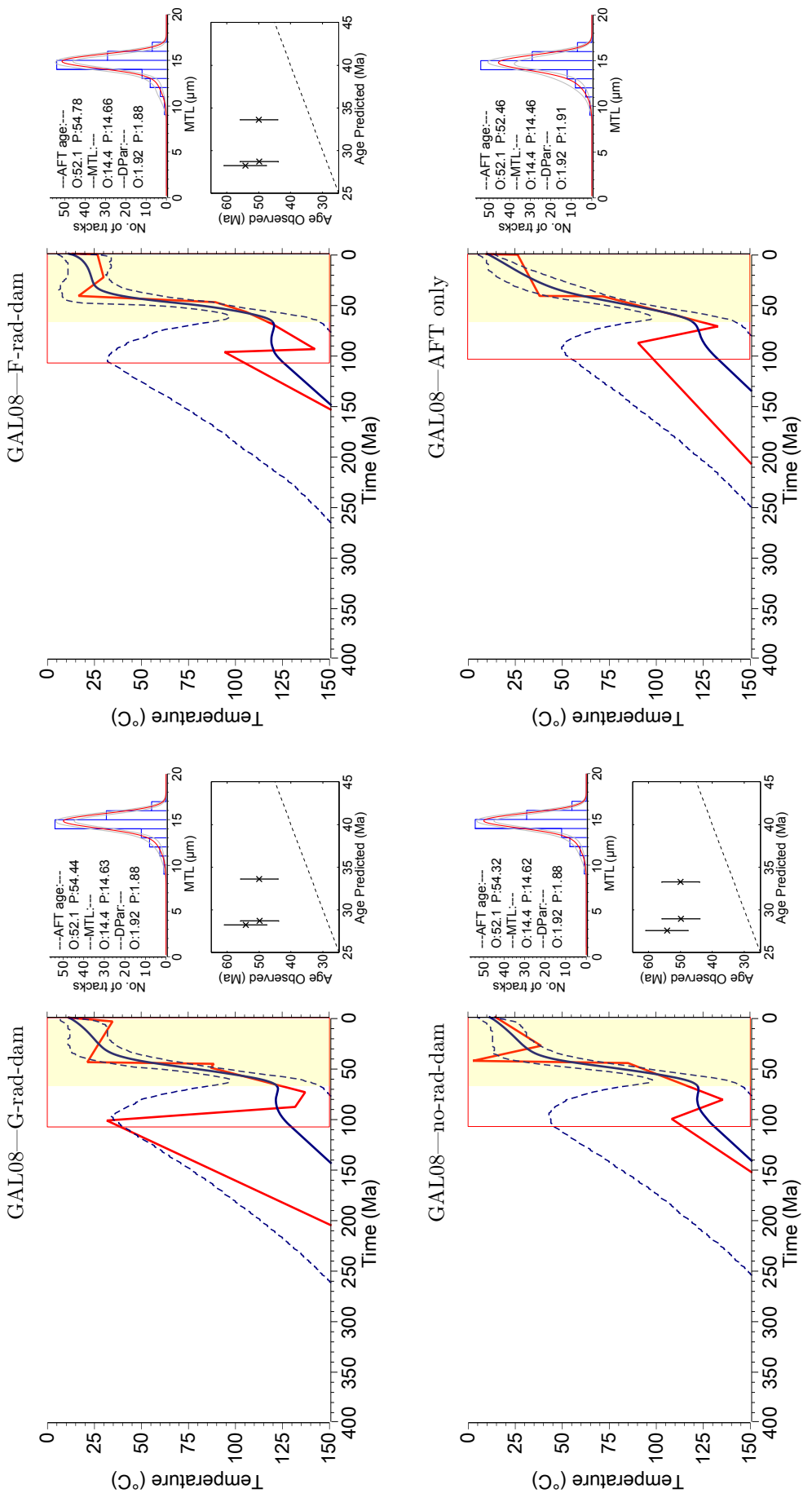

Figure 4.2: (continued)

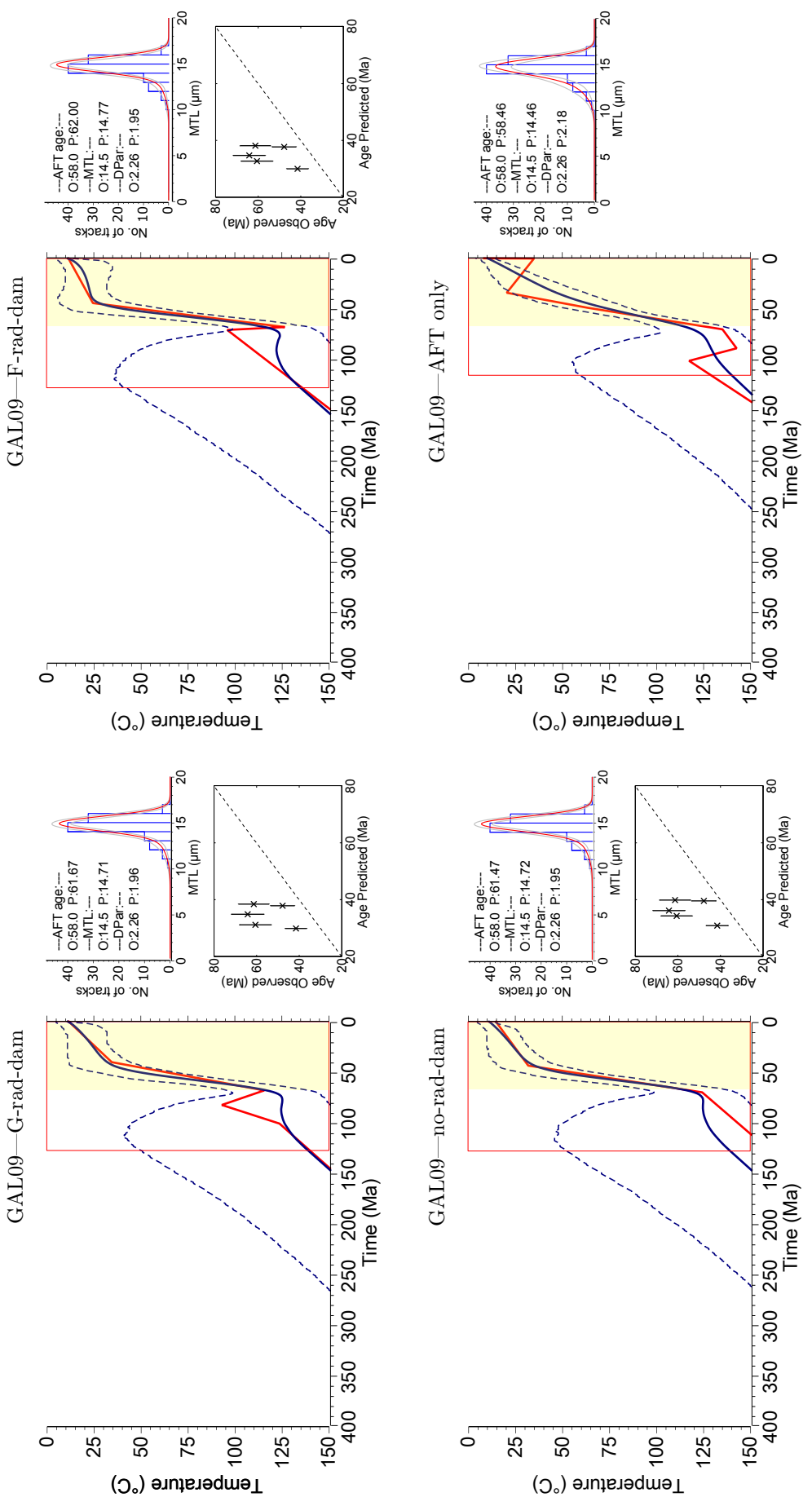

Figure 4.2: (continued)

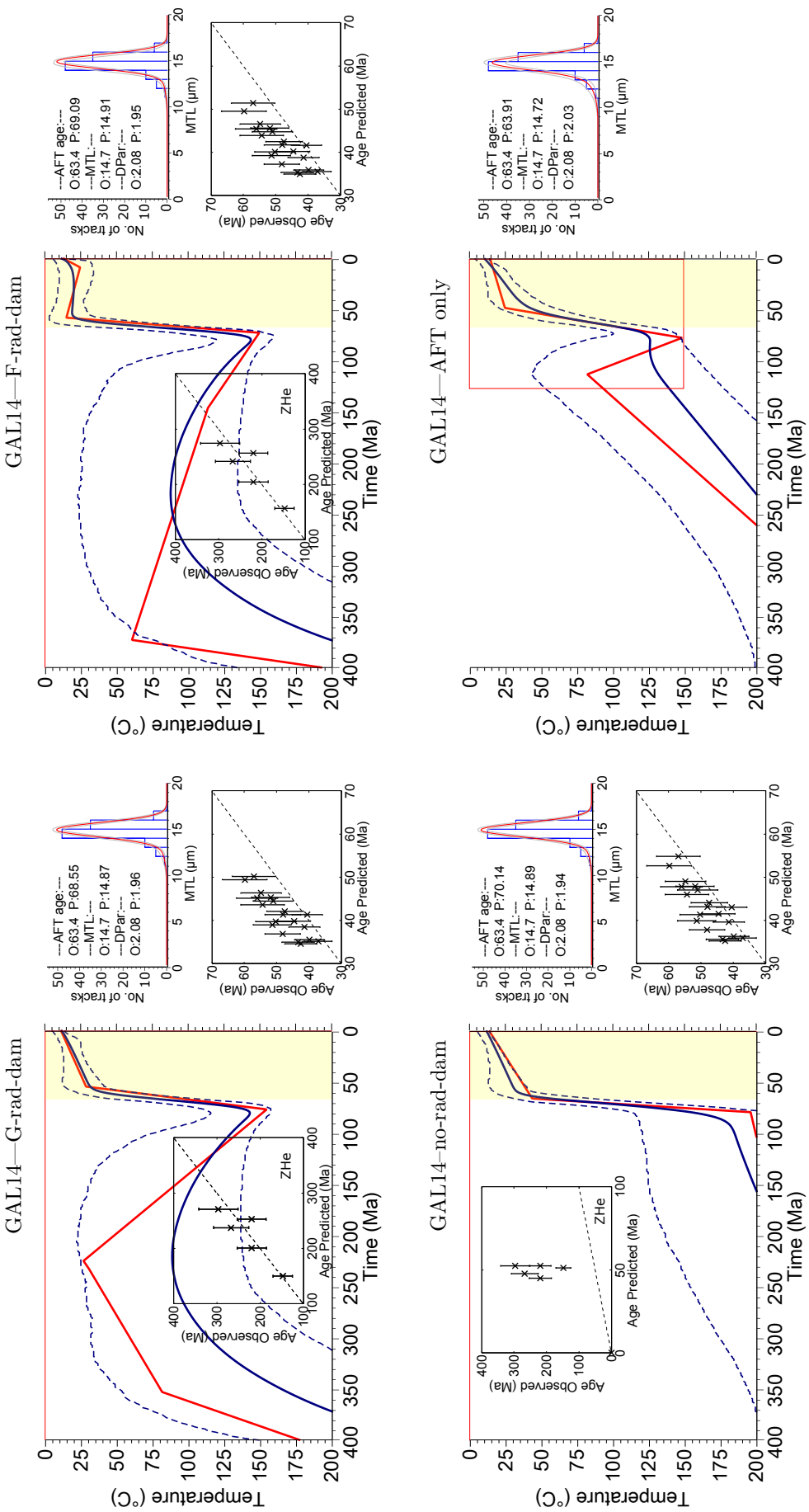

Figure 4.2: (continued)

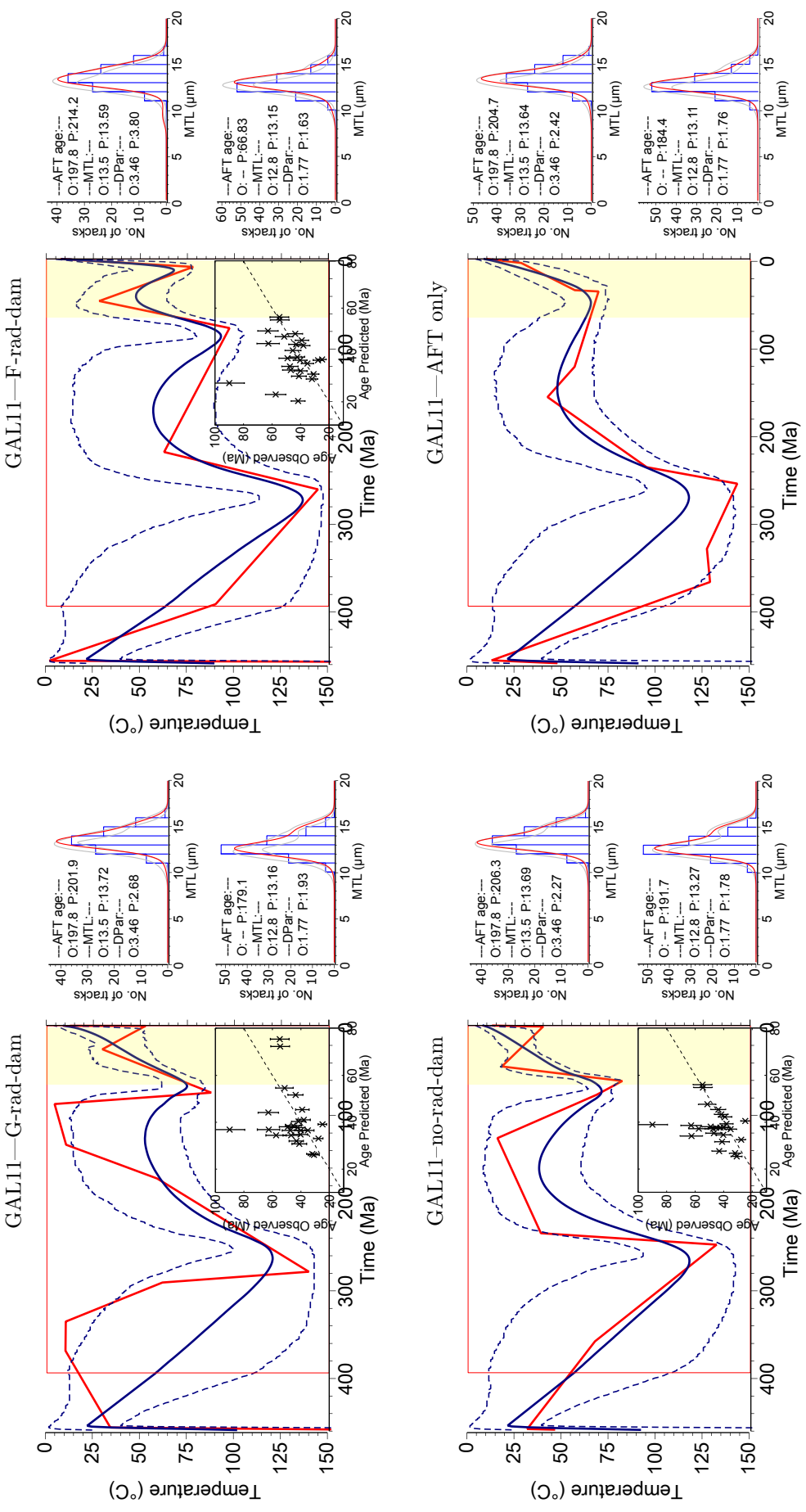

Figure 4.2: (continued)

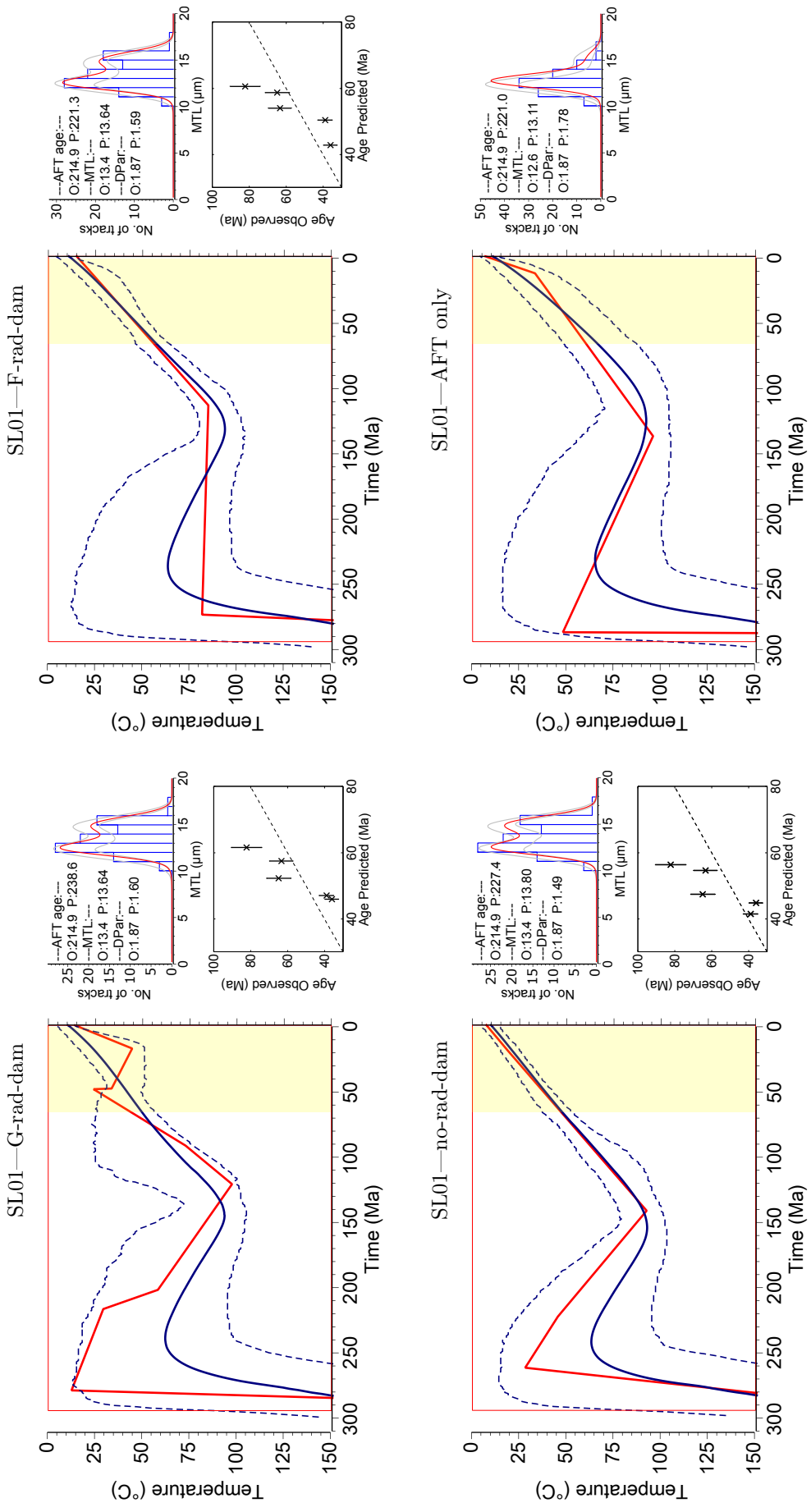

Figure 4.2: (continued)

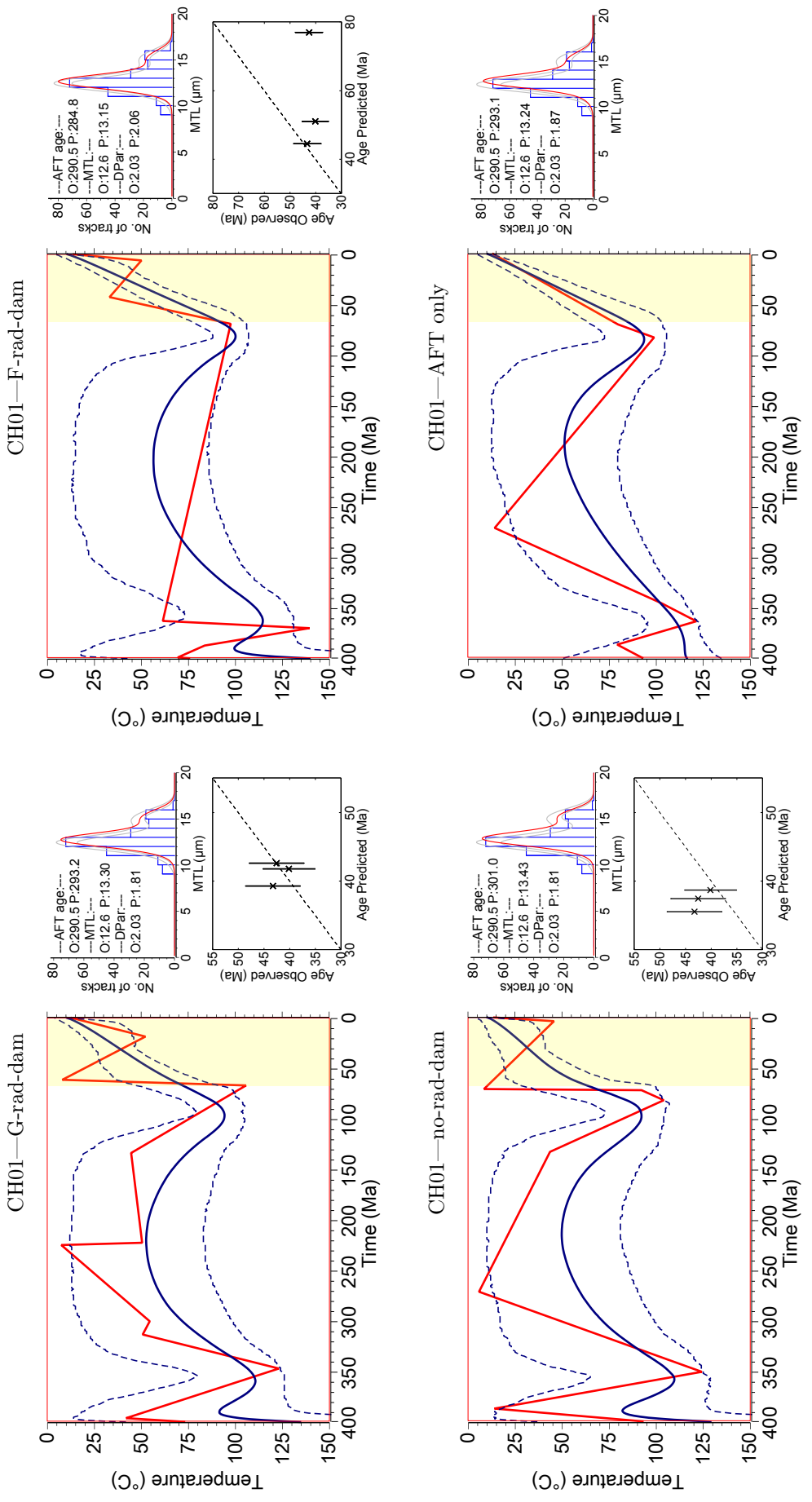

Figure 4.2: (continued)

the presence of a rapid cooling event at 60–70 Ma. According to the maximum likelihood models, the cooling was almost instantaneous. Such fast cooling episodes are unlikely and it is probably an effect of the low AHe age dispersion. To check if this lack of dispersion is statistically significant, more single-grain ages would be necessary. All the models predict the AFT and AHe ages very well.

Summary—Resolving the rate and timing of cooling precisely in most of the samples from southern Scotland is difficult, because the maximum temperature at the beginning of the Cenozoic was 50–60°C. Although a clear rapid signature at ∼70 Ma is resolved only at Criffell, the acceleration of cooling rate or the presence of small rapid cooling pulse on the max-like models at 60–80 Ma is observed in most of the localities.

4.2.4 Northern Wales

Only two samples from northern Wales, WL07 and WL08, have enough fission track length measurements to provide robust constraints for data modelling. Modelling has also been attempted on samples WL05 and WL06 for which an AFT age and at least five AHe single-grain ages were determined. Without the track length distribution, however, the models results are tentative. All models are shown on the Fig. 4.3.

Figure 4.3: (On the next page.) Thermal histories of the samples from northern Wales and model predictions extracted from inverse modelling using QTQt software (Gallagher 2012). Thermal history graphs: thick red line is the maximum likelihood model; thick blue line is the expected model and dashed blue lines are the 95% credible intervals; thin red line defining a box shows the general range of prior; the light yellow shadow marks the Cenozoic era, 66–0 Ma. Although most of the models start from temperatures of 300±100°C (see text for more details), to make the plots easier to read, the temperature space shown on the graphs is 0–150°C for AFT and AFT + AHe data or 0–200°C for AFT + AHe + ZHe data. Model predictions graphs: top graph presents predictions for projected FTLD (fission track length distribution); the histogram shows the observed data, the red and grey lines are the predicted FTLD and the 95% credible intervals, respectively; the numbers in the top left corner are the observed (O) and predicted (P) AFT age, MTL and D-Par. Bottom graph shows the predicted versus observed AHe ages with the error bars; dashed line is a 1:1 line; in case of samples which have more than two AFT input files, the bottom graph shows predictions for AFT data of the 2nd slide and the predictions for AHe data are superimposed on the thermal history plot; in case of samples having ZHe ages, the predictions are superimposed on the thermal history graph. Three or four models are shown for each sample: G-rad-dam—radiation damage model of (Gautheron et al. 2009), F-rad-dam—radiation damage model of (Flowers et al. 2009), no-rad-dam—no radiation damage model, standard Durango kinetics, AFT only—model without (U-Th)/He data.

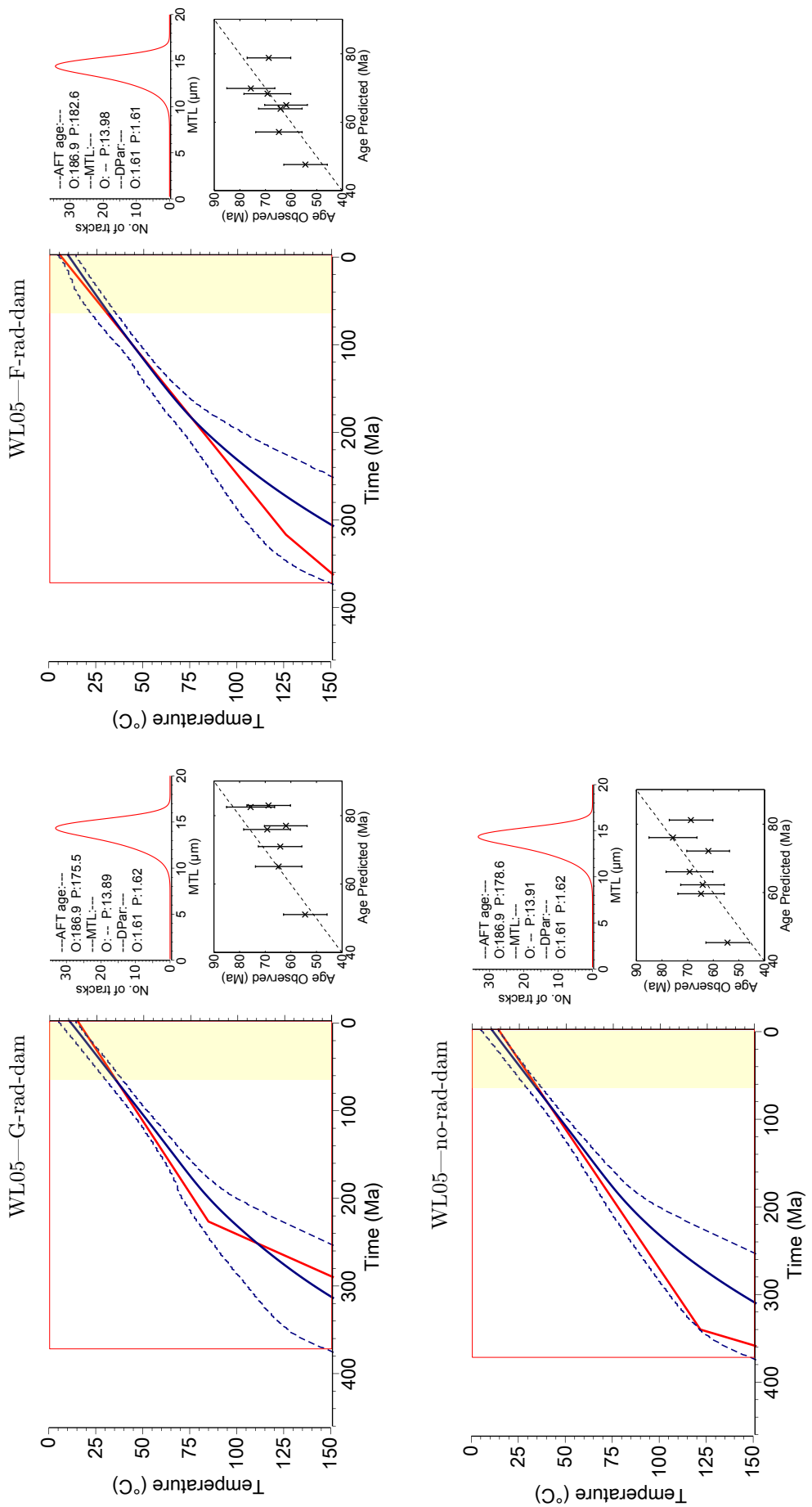

Figure 4.3: (Caption on the previous page.)

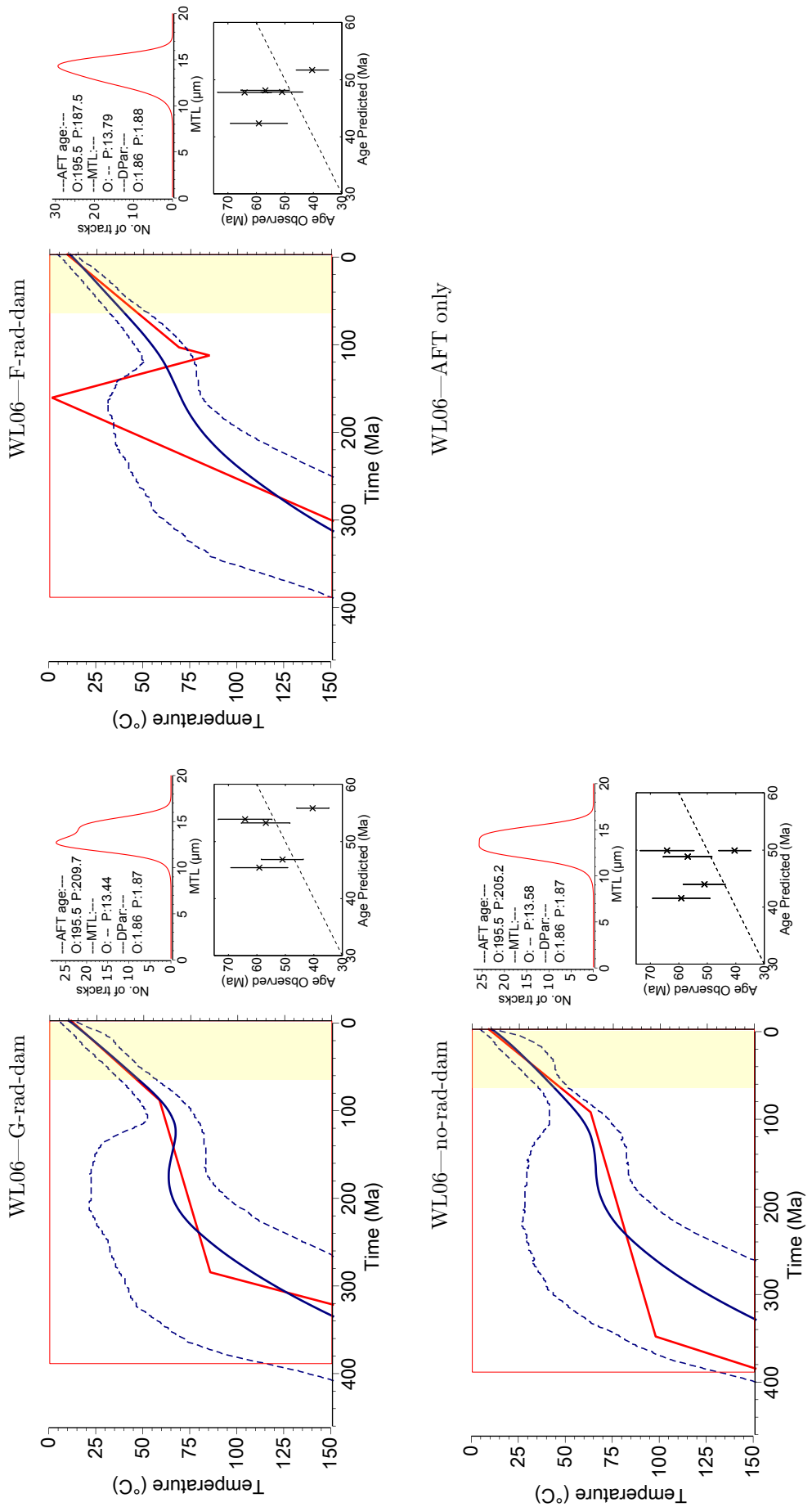

Figure 4.3: (continued)

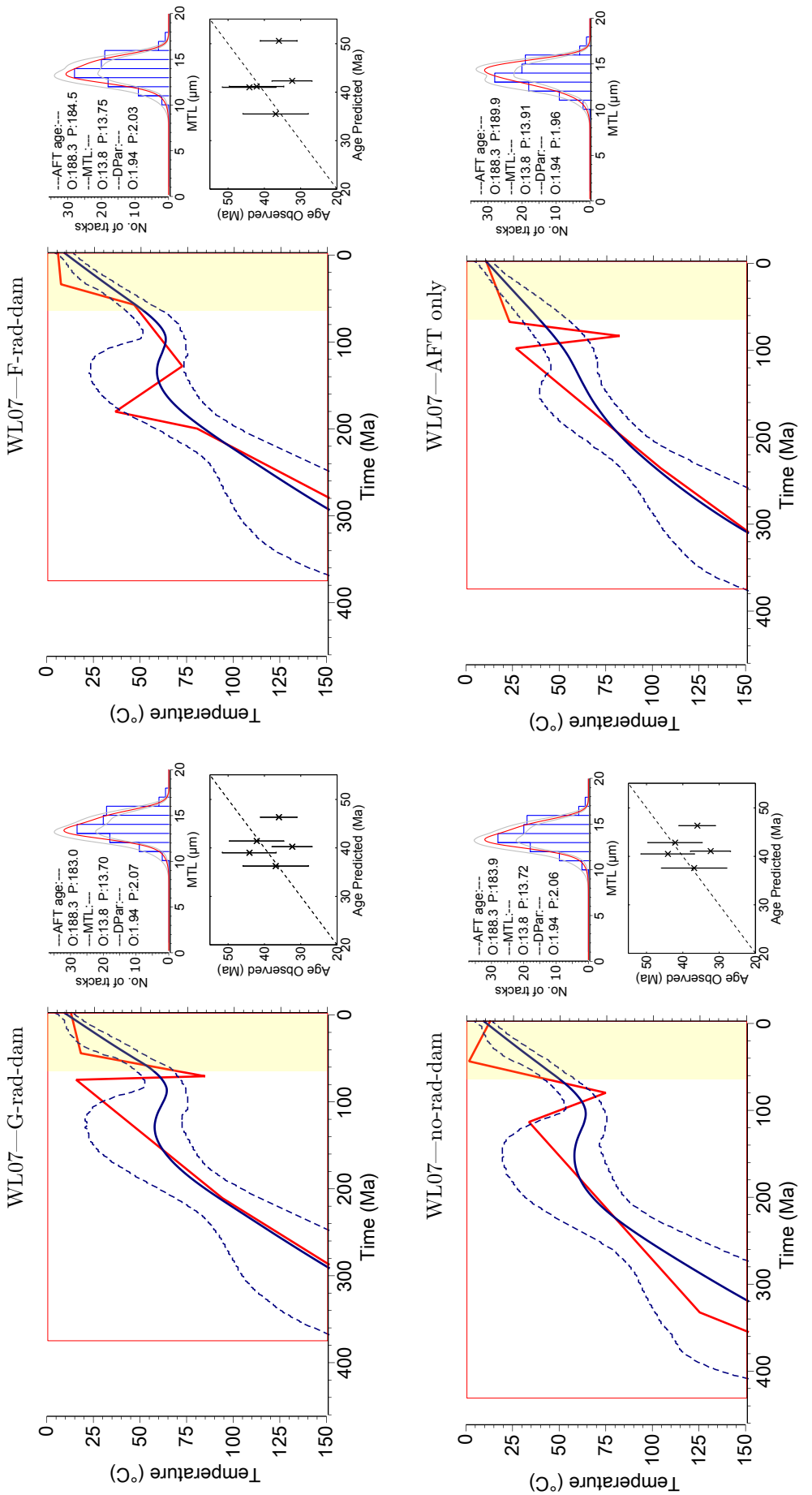

Figure 4.3: (continued)

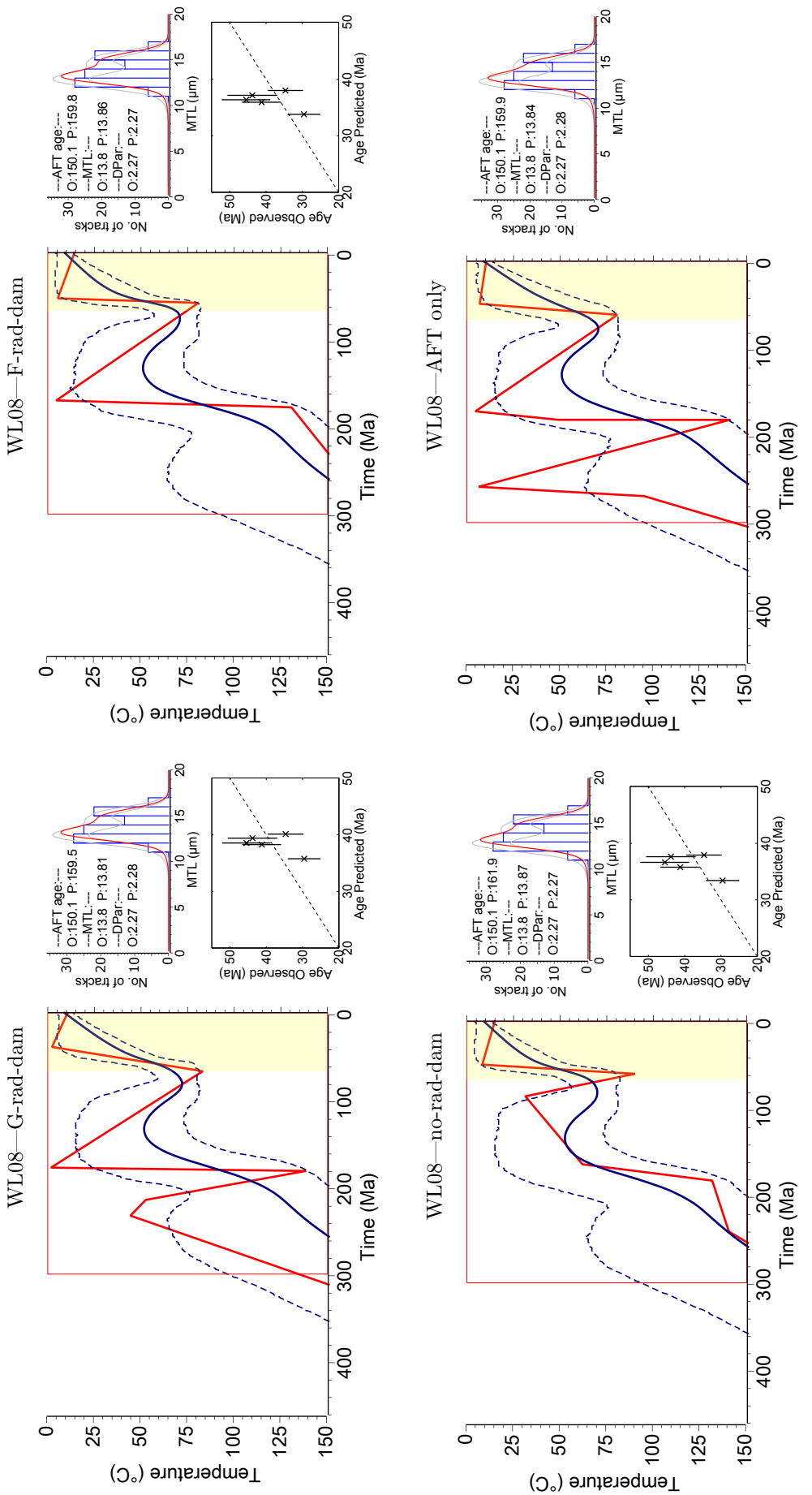

Figure 4.3: (continued)

The models of WL05 and WL06 show simple thermal histories with a slow, monotonic cooling from maximum temperatures of 100°C at ∼250 Ma. No difference is observed between the rad-dam and no-rad-dam models. A similar thermal history is shown by WL07, with a possible acceleration of cooling in the last 100 Ma. The maximum likelihood t-T paths suggest, however, a rapid cooling event from 80–90°C at ∼80 Ma or from 50°C at ∼60 Ma. More complex thermal histories are shown by WL08. The rock entered the PAZ at ∼200 Ma and was subsequently cooled; even though this part of the thermal history in not well resolved, the rock could have reached temperatures as low as 20°C. A reheating event preceded the final cooling event from ∼70–80°C in the last 60–70 Myr. The expected models predict monotonous cooling; however, the maximum likelihood t-T paths and the shape of the 95% credible intervals support the presence of an early Palaeogene rapid cooling event with rates of up to 14°C/Myr for the F-rad-dam model. Generally, the models fit the data well.

4.2.5 Discussion of some modelling aspects

4.2.5.1 Over- and under-etched fission track mounts

Some AFT mounts were under- or over-etched. Under-etched slides are not used in the modelling, as both AFT age and track length distribution may be inaccurate. Such samples were mounted again and then re-counted and re-measured, and only the data from the new slides were used to extract thermal histories. The AFT ages of over-etched mounts should still be accurate and so only new fission track length analyses have been performed. In many cases, over-etching has been difficult to assess; in some samples, even if the difference between the D-Par sizes from different mounts was significant, sometimes the shape of the D-Pars did not show a clear over-etching pattern with pointed, diamond shape edges. In these cases, the track length measurements from both slides were used for the modelling and during the resampling process, the software was allowed to assess the noise of the measurements, including that associated with etching inaccuracies. The model, however, was not able to predict the AFT data of GAL04A; in this case, in the next step, the track lengths and D-Par measurements were taken only from the 'properly'-etched mount and mixed with the track counts from the over-etched slide. The obtained thermal history for the mixed model was quite different than the one for both slides modelled together and the data were better resolved. The results from the mixed-slide experiment show that the latter is the best procedure to obtain the best fit prediction. The same procedure has been applied to GAL06 and GAL11; however, in these cases there is not significant difference between the predictions showed by mixing the data or modelling together the data from the two slides. For these samples, the models from the two slides modelled together are taken further and discussed.

4.2.5.2 Influence of the (U-Th)/He data

By adding the (U-Th)/He data, the models seems to be better constrained and more precise, even in the case of the rapidly cooled samples (e.g. GAL14, LD01 LD02). In such samples, the influence of ZHe ages was also important, as it allows the maximum pre-Cenozoic cooling temperatures to be resolved and adds constraints on the earlier thermal history. In the case of slowly cooled samples, the AFT-only models sometimes do not resolve an acceleration of cooling, especially if that initiate at temperatures less than 80°C, and the AHe ages were required to accurately determine the timing of the cooling event (e.g. GAL11).

The influence of AHe ages increases with the number of single-grain ages. Incorporating AHe age determinations into thermal models need to be done with caution, since they are strongly influenced by complex processes that cannot be included in the modelling (e.g. U zonation in apatites from the Fleet granite) and the presence of 'inaccurate' ages can bias the cooling history. The best example in this study is GAL02 which experienced slow monotonic cooling for the AFT-only model, and the presence of a rapid cooling event between 90–70 Ma if the AHe ages are included. The predictions of the model that includes AHe data are, however, poor; the AFT age is overestimated by ∼15 Ma and many AHe ages are under-predicted. The (U-Th)/He data from both zircons and apatites are a powerful tool and significantly improve the thermal history determinations.

4.2.5.3 Influence of radiation damage

The AHe rad-dam models (Flowers et al. 2009, Gautheron et al. 2009) do not seem to influence the modelled thermal histories in the case of rapidly cooled samples. This is consistent with the theory behind the annealing models upon which the radiation damage algorithms are based; damage is totally annealed at high temperatures and therefore have no effect on He diffusivity. Incorporating radiation damage in slowly cooled samples usually changes the timing and magnitude of the thermal events slightly, but it does not affect the overall shapes of the thermal histories. The results from the G-rad-dam and no-rad-dam models are typically similar; different results are obtained when the F-rad-dam model is used (e.g. samples WL07, GAL01, GAL11, CH01). The differences are both in the thermal history itself as well as in how well the models predict the single-grain AHe ages. These conclusions confirm that the two models are not equivalent and more work needs to be done on determining their accuracy.

The use of the radiation damage model for ZHe age interpretation is essential; models fail to satisfy both AFT and ZHe ages if the standard, constant diffusion parameters are used. The ZHe radiation damage model improves ZHe age predications, but often also allows the observed age dispersion pattern and the negative correlation between

ZHe ages and [eU] to be resolved.

4.2.5.4 Multi-sample modelling

More than one sample was collected from the Criffell and Fleet plutons in the Southern Uplands and on the Llŷn Peninsula in northern Wales. The thermal history of Criffell is well constrained due to the high quality of AFT, AHe and ZHe data. The thermal histories of some samples from Fleet and Llŷn are poorly resolved due to relatively low number of data.

In the case of Fleet, for instance, the inverse modelling is not able to reproduce the AHe ages; the resulting thermal history are not well resolved, as they are based on the AFT data only. However, the three samples are closely spaced and the three AFT data sets can be combined and modelled together. This approach could add stronger constraints on the modelled t-T paths and deal better with the noise of the data. The multi-sample model is shown in Fig. 4.4. The thermal history is similar to those of the single samples, but better constrained. The model predictions are generally good; however, none of the AFT data sets is fully predicted, in each case there are some deviations from the observed FTLD. Track length distributions can be imprecise; they can change with the analysts and they are dependent on small inaccuracies in etching or measurement protocol. The multi-sample approach forces the model to find thermal histories that fit all the datasets and it may be the best suited technique to deal with data noise. The multi-sample thermal histories suggest that the rock cooled after emplacement and then was reheated to up to ∼90°C at about 110–80 Ma, when the final cooling episode begun. The model also suggests that cooling accelerated in the last 5–10 Ma. The maximum likelihood model, as well as the shape of the 95% credible intervals, includes a reheating event also between 170–130 Ma.

The AFT ages of the two samples from Llŷn peninsula that are not accompanied by a track length distributions have been combined with the sample that has a full AFT dataset (WL07) and the five single-grain AHe ages. The multi-sample model is based on three AFT ages, one track length distribution and 17 AHe ages. The obtained modelled t-T paths (Fig. 4.4) are similar to the thermal histories derived from the single-sample models, but they are better constrained and supported by good predictions. The new thermal histories are almost identical for all types of He diffusion kinetics (only F-rad-dam is shown in Fig. 4.4) and suggests the presence of a cooling episode between 260–160 Ma, a small reheating episode between 160–100 Ma, followed by a final cooling from 60–70°C in the last 100 Ma.

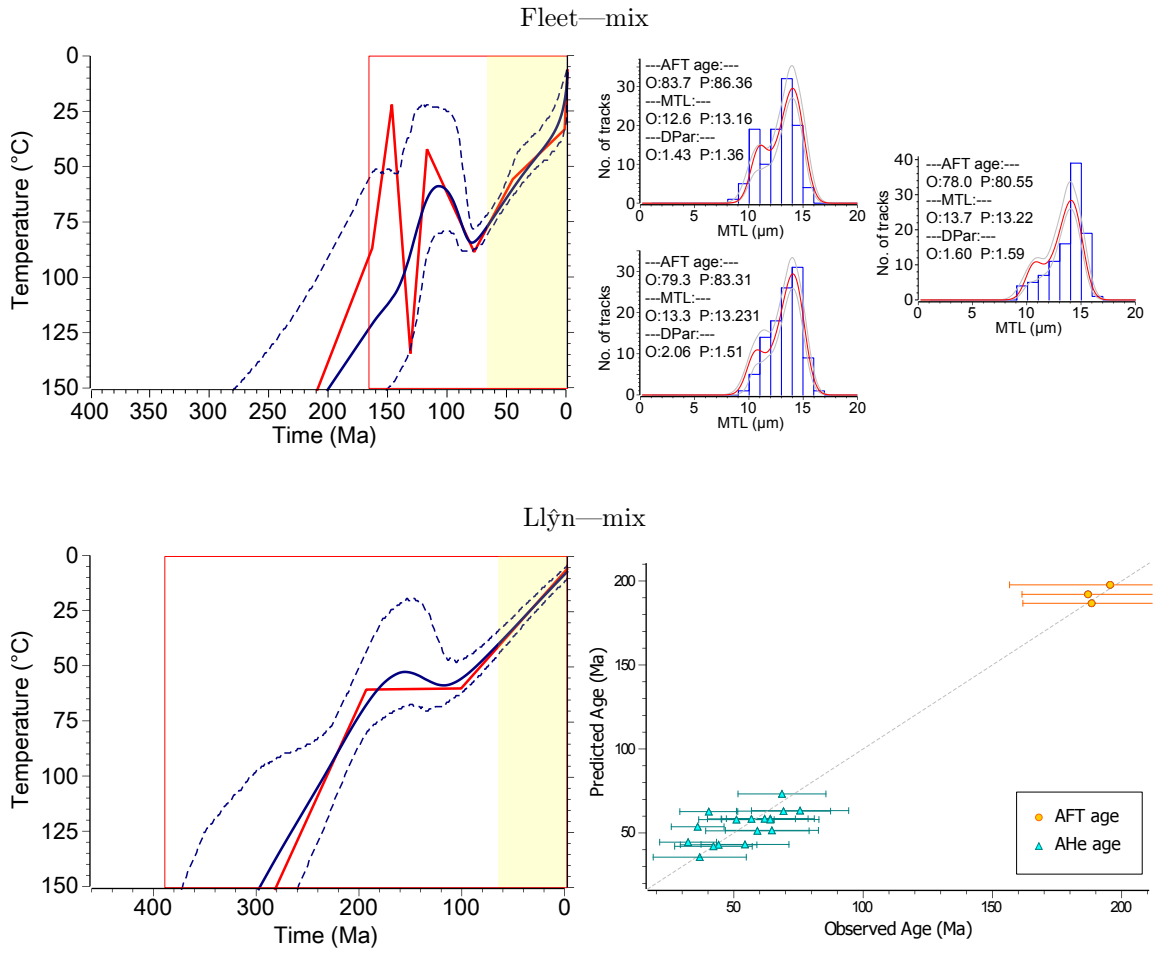

Figure 4.4: Multiple samples models and models predictions of the Fleet pluton in the Southern Uplands and the Llŷn peninsula in northern Wales extracted from inverse modelling using QTQt software (Gallagher 2012). Thermal history graphs: thick red line is a maximum likelihood model; thick blue line is an expected model and dashed blue lines are 95% credible intervals; thin red line rectangular shows the general range for prior; the light yellow shadow marks the Cenozoic era, 66–0 Ma; although the models have been started from temperature of 300±100°C (see text for more details), to improve readability of the plots, the temperature space shown on the graphs is set to 0–150°C. Model predictions graphs: a histogram shows observed projected FTLD, red and grey line are predicted FTLD and 95% credible intervals, respectively; numbers in the top left corner gives observed and predicted AFT age, MTL and D-Par; in case of Llŷn model a graph of observed versus predicted ages is presented for both AHe and AFT data.

4.2.5.5 Adding more thermal constraints

Thermal constraints on the geological history of onshore central Britain are sparse. In the case of sedimentary rocks (GAL11 and LD18), samples yielding >200 Ma AFT age (SL01, CH01) and with ZHe data (LD01, LD02, GAL14), the models suggest that the rocks experienced low temperatures (<70°C) after pluton emplacement and started being reheated at some point before 150 Ma. That is consisted with the regional geological history; the Permo-Triassic was a time of dynamic clastic sedimentation in the surrounding basins and the sampled areas are regarded as having been the uplifted blocks supplying the sediments (Akhurst 1997, Woodcock & Strachan 2000). Some of

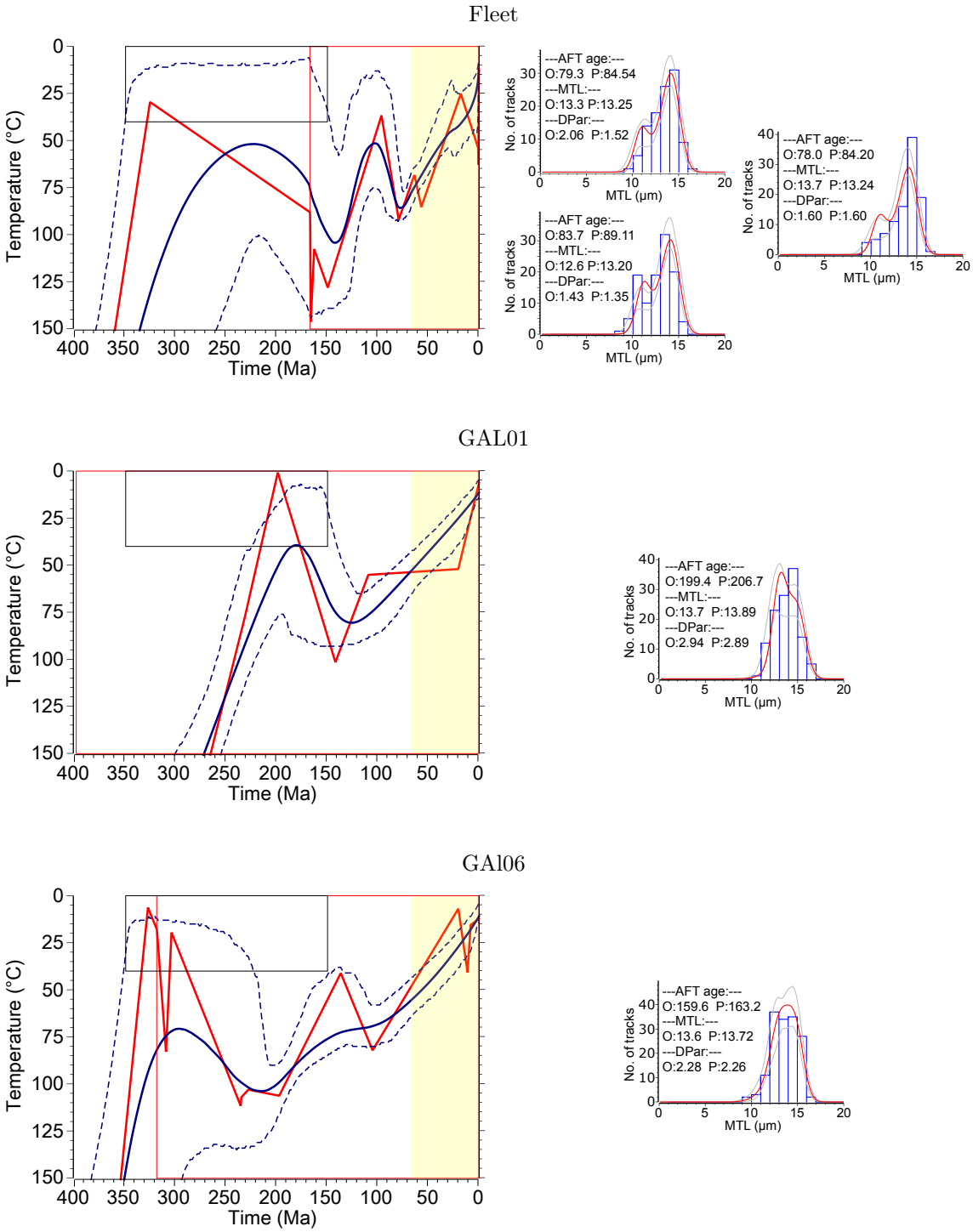

Figure 4.5: Thermal histories forced to be cooled to 20±20°C at 250±100 Ma (thin black line box)and models predictions of the Fleet (mix: GAL02, GAL04A ad GAL04B), Portencorkie (GAL06) and Loch Doon (GAL01) plutons in the Southern Uplands and extracted from inverse modelling using QTQt software (Gallagher 2012). Thermal history graphs: thick red line is a maximum likelihood model; thick blue line is an expected model and dashed blue lines are 95% credible intervals; thin red line rectangular shows the general range for prior; the light yellow shadow marks the Cenozoic era, 66–0 Ma; although the models have been started from temperature of 300±100°C (see text for more details), to improve readability of the plots, the temperature space shown on the graphs is set to 0–150°C. Model predictions graphs: a histogram shows observed projected FTLD, red and grey line are predicted FTLD and 95% credible intervals, respectively; numbers in the top left corner gives observed and predicted AFT age, MTL and D-Par.

the thermal models (e.g. GAL01, GAL06) are inconsistent with these conclusions as they predict that in the Permo-Triassic the rocks were at the temperatures higher than in the PAZ. To further investigate this discrepancy an experimental modelling with a forced sub-surface exposure constraint has been carried out on samples from Fleet (the multi-samples model), Loch Doon (GAL01) and Portencorkie (GAL06) (AFT data only). The thermal histories were forced to pass through the box 20 ± 20°C at 250 ± 100 Ma; this time interval encompasses the Permo-Triassic as well as the latest Carboniferous and the earliest Jurassic and therefore allows the model to explore other possibilities. The results are shown on Fig. 4.5.

Adding the geological constraint seems to improve the thermal history of Fleet. The post-140 Ma part of the t-T path remains unchanged. At earlier times the rock is forced to being cooled until ∼240 Ma and then is reheated to reach ∼100–120°C at ∼140 Ma. This thermal history is in agreement with the regional geological history. Adding the same constraint does not change the shape of the thermal history of the Loch Doon pluton; the reheating episode at 200–130 Ma is only more pronounced and begins from surface/subsurface conditions. The model suggests that after emplacement the region cooled slowly and remained at high temperatures until 250 Ma. The parametrization of the model and the prediction of the FTLD are, however, relatively low and other post-emplacement cooling episodes cannot be excluded. In the case of the sample of the Portencorkie granite, the use of the additional constraint produces either post-emplacement cooling followed by reheating or, as with the samples from Loch Doon, only reinforces the already resolved reheating episode at 160–110 Ma and keeps the rock at high temperatures prior to 250 Ma. The former model is shown in Fig. 4.5 as it has better parametrization. The post-200 Ma part of the t-T path is very similar to previous models, but it is preceded by a reheating event between 300–200 Ma.

4.2.6 Regional summary

The Late Cretaceous palaeotemperatures derived from the modelled thermal histories define a regional pattern (Fig. 4.6). The Lake District and the Criffell pluton form a 'hot-spot' with temperatures in excess of 120°C. Palaeotemperatures decrease northwards, into S Scotland, and southwards, in England. In the Southern Uplands, excluding the Criffell area, rocks were not at high temperatures in the Late Cretaceous. In general, a decrease of palaeotemperatures is observed inland, reaching less than ∼60°C at the Crawfordjohn dyke in the northernmost part of the Southern Uplands block. Relatively high temperatures of about 90°C, are noted in the Cheviot pluton. Although these temperatures are not well constrained and contrast with those found in the Southern Uplands. The Cheviot pluton formed a separate structural block at least since the Late Devonian and, as such, could have had a different thermal history than the surrounding areas. In northern Wales, the Late Cretaceous palaeotemperatures

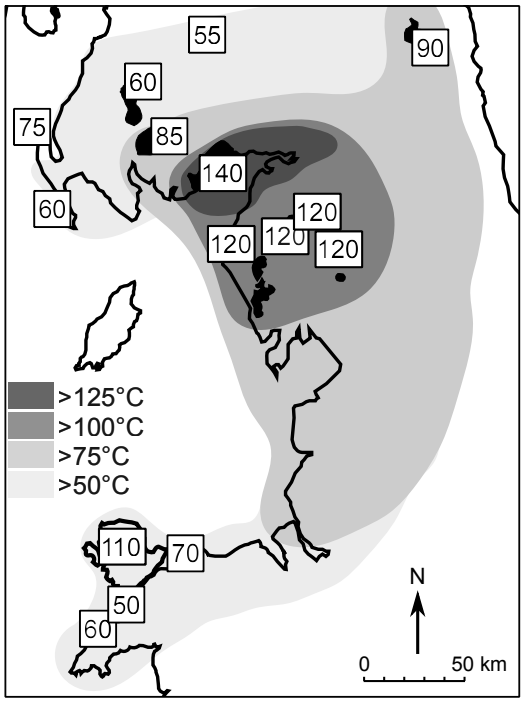

Figure 4.6: The Late Cretaceous palaeotemperatures derived from modelled thermal histories. Number in the box is a representative temperature for a given site, usually the average from the models including (U-Th-Sm)/He data.

are generally lower than 70°C, with the highest noted on the EISB coast. The sample from Anglesey has an AFT age of 50.6 ± 4.8 Ma and, therefore, it likely experienced temperatures of more than 110°C in the early Palaeogene. If so, there is a sharp contrast between Anglesey and northern Wales mainland. The observed pattern of palaeotemperatures is generally consistent with the published data (Green 1986, Lewis et al. 1992, Green et al. 1997); however, this new data set, expands further northwards in southern Scotland and southward into northern Wales and it improves the precision of the palaeotemperature determinations in the Lake District and Criffell using the ZHe ages. The published works of Green (1986) and Lewis et al. (1992) were based on the AFT data only and could only constrain palaeotemperatures up to 120°C.

Fig. 4.7 presents the thermal histories of all the localities that have been modelled. When more than one sample was analysed for one locality, the best predicted history is shown; for example the thermal history shown for the Criffell pluton is derived from the rad-dam models of GAL14, whereas Fleet and Llŷn are described by the multi-sample models. There is support for a regional cooling event, that started in the Late Cretaceous/early Palaeogene (60–75 Ma). In general, inland of the Lake District and southern Scotland cooling started ∼10–15 Ma earlier than at the coastal areas. The Late Cretaceous-early Palaeogene rapid cooling event is well resolved in the Lake District and in the Criffell pluton. The same episode may be present in other places in southern Scotland, especially in the Cheviot block and in the west coast of the Southern Uplands at Corsewall Point, as well as in northern Wales, on the EISB coast. In some of the localities in the Southern Uplands, the cooling started earlier, at 100–120 Ma, and the Late Cretaceous-early Palaeogene rapid cooling is not found nor can be discounted, as the palaeotemperatures may be just too low for it to be resolved.

Almost all the thermal histories show a reheating prior to the Late Cretaceous-early Palaeogene cooling. Although the data cannot precisely resolve this episode, the Lake District, Criffell and Cheviot may have experienced reheating since the Triassic or even the Permian. The thermal history from the Fleet pluton is complex. The pluton was

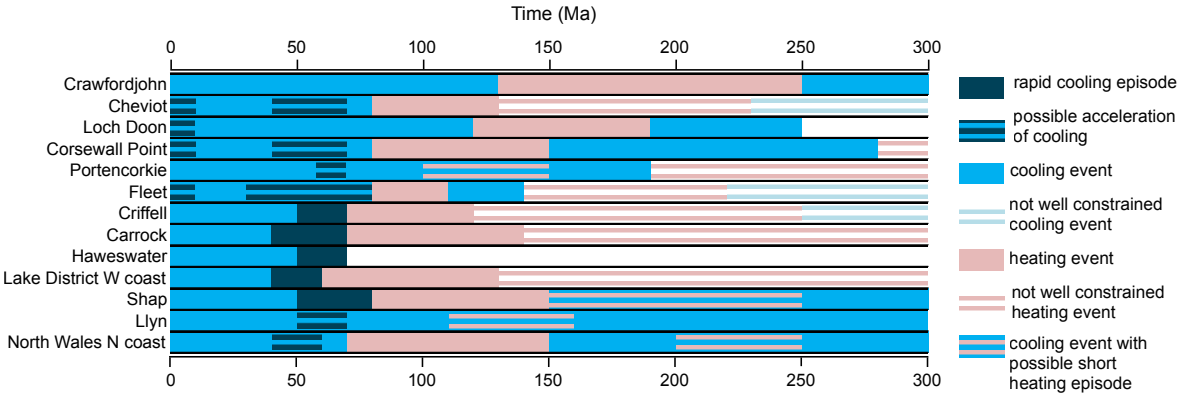

Figure 4.7: Compilation of cooling and reheating events in the localities that have thermal histories extracted from the inverse modelling. The localities are ordered along the quasi-north-south profile. If more than one sample have been analysed for a give site, the most representative history have been chosen (see text for further details).

reheated in the Triassic-Jurassic and that was followed by a short cooling episode at the Jurassic-Cretaceous boundary and the subsequent reheating in the Late Cretaceous. In the Lake District and Criffell, the Late Jurassic-Early Cretaceous cooling episode cannot be either corroborated or excluded by the thermal histories, as the thermochronometric-derived constraints on the pre-Cenozoic history are weak.

In the Southern Uplands the reheating episode is spatially diachrononous; starting earlier in the east and north. For example, the Crawfordjohn essexite dyke seems to have been reheated in the Triassic and Jurassic and cooled since then, whereas in the area around Loch Doon the reheating episode started in the Jurassic, but had ceased already in the Early Cretaceous. The rocks at the western coast, at Portencorkie and Corsewall Point, were cooled in the Jurassic, possibly, at least at Corsewall Point, even in the Permo-Triassic and they were reheated in the Cretaceous. The Permian-Jurassic cooling episode has been resolved also in northern Wales, where it could have been interrupted by a short reheating phase in the Triassic.

Results of the experimental modelling of samples from Criffell, Fleet, Loch Doon and Corsewall Point using the Helfrag code are presented in the next section in order to investigate the impact of fragmentation on the ages, as well as to examine whether the presence of a Late Cretaceous reheating event followed by early Palaeogene cooling can be resolved in these locations using the dispersion of the AHe ages.

4.3 Modelling the age dispersion

4.3.1 Introduction

Interest in the apatite (U-Th)/He dating method in the last decade or so has brought the need to better understand the processes governing He diffusion in apatite. Significant effort has been put into resolving why AHe ages are sometimes older than the

same-sample AFT ages and of high single-grain age dispersion (e.g. Fitzgerald et al. 2006, Flowers & Kelley 2011). These studies have resulted in the formulation of two radiation damage models (Flowers et al. 2009, Gautheron et al. 2009) and have led to the conclusion that single-grain age dispersion, if interpreted correctly in terms of grain size variation and/or [eU], may add further constraints to the derived thermal histories (Flowers & Kelley 2011). Recently, another factor, grain fragmentation, has been added to those that contribute to age spread (Brown et al. 2013). The combined effect of fragmentation, crystal size and [eU] may produce an age spread of >100%, but, if interpreted correctly, it can be used in the inverse modelling of the data to better constrain the thermal histories in the low temperature span, where the AFT data alone do not provide strong constraints.

In this section, the most common causes of dispersion will be discussed in more detail. Results from modelling dispersion, including fragmentation, will be presented and the usefulness of such modelling will be discussed. As age dispersion often does not follow a normal distribution, rather than defining it as the standard deviation of the mean, dispersion is here defined as the difference between the maximum and minimum age divided by the mean age and presented as a percentage (Brown et al. 2013).

4.3.2 Causes of dispersion

4.3.2.1 Grain size

The influence of grain size on the AHe ages was pointed out in the early studies (e.g. Farley 2000, Reiners & Farley 2001, Farley 2002). Larger grains have a higher closure temperature and, therefore, when their AHe age is compared to those of smaller grains from the same sample, they appear older. The influence of the grain size on the age is usually negligible if the rock has been cooled rapidly. In the case of slowly cooled rocks and/or rocks that have experienced at least one reheating event, the correlation between grain size and age may be resolvable and used to quantify the rock thermal history between 30 and 70°C (Reiners & Farley 2001). For instance, for grains with effective radius ranging 50–100 μm, the age dispersion caused solely via the grain size effect may reach 50–100%, depending on the thermal history (Brown et al. 2013).

4.3.2.2 Radiation damage

It has been shown that radiation damage in the apatite crystal lattice affects He diffusivity (Shuster et al. 2006, Flowers et al. 2009, Gautheron et al. 2009). The α-recoil and fission tracks act as traps for He, inhibiting its diffusion out of crystals, and thus increasing the closure temperature of the AHe system. This phenomenon has been observed in many datasets that include slowly cooled rocks and is demonstrated by a positive correlation of the age with either [He] or [eU] (e.g. Green et al. 2006, Shuster et al. 2006, Flowers et al. 2009, Gautheron et al. 2009, Flowers & Kelley 2011). Simi-

larly to a varying grain size, dispersion arising from the radiation damage is dependent on the thermal history and is more pronounced if the rock resided in the PRZ for a long time.

In the first experiments, Shuster et al. (2006) used [He] as a proxy for radiation damage. Further experiments on He diffusion in samples with alpha induced radiation damage demonstrated that, as in the case of fission tracks, damage due to α-recoil anneals with increasing temperature and, therefore, the He diffusion parameters are temperature dependent (Shuster & Farley 2009). Two radiation damage models that incorporate both accumulation and annealing of radiation damage have been developed to predict a change of He diffusion kinetics through time (Flowers et al. 2009, Gautheron et al. 2009). Both models use [eU] as a proxy for radiation damage; however, in the model of Gautheron et al. (2009), there is a linear relationship between He retention and number of crystallographic defects, whereas Flowers et al. (2009) used empirically derived cubic form algorithm, which predicts a non-linear rapid increase of He retentivity in highly damaged crystals, and lower retentivity than standard kinetics for very low [eU]. Another difference between the two models lies in the numerical method used to calculate He diffusion. Nonetheless in both models, the diffusion kinetics correlates with the [eU] and differs from those presented by Farley (2000) for Durango apatite (Flowers et al. 2009, Gautheron et al. 2009). Irrespective of which of the two approaches is used, radiation damage should be included in thermal histories prediction, especially in the case of slowly cooled samples, to avoid significant inaccuracies in the interpretation of the data. For instance, the presence of radiation damage can explain AHe ages older than the corresponding AFT ages, in case of old and/or U-rich apatites with a complex thermal history (Flowers et al. 2009, Flowers & Kelley 2011).

The amount of age dispersion arising from the presence of the radiation damage may be significant and exceed 200% for some thermal histories, if the difference in [eU] between the grains is large(Brown et al. 2013). In such cases, the age dispersion may be successfully used to better constrain thermal histories (Flowers et al. 2009, Gautheron et al. 2009).

4.3.2.3 Fragmentation

Apatite crystals often break during rock crushing and fragments rather than whole crystals can be picked. Uncertainties regarding the original size of the apatites affect the calculation of the α-recoil correction and of the grain equivalent radius (R^*), a parameter used for modelling thermal histories. Even though the most recently proposed α-recoil correction (Gautheron & Tassan-Got 2010) uses the real grain geometry, such as the number of terminations present and of broken faces, the current modelling approaches are still based on the spherical approximation to He diffusion. The spherical approximation has been shown to accurately reflect the isotropic diffusion process

in apatite and allows for the efficient and relatively fast inversion, however, it was designed for modelling the whole crystals (Meesters & Dunai 2002a). The R^* is defined as a radius of the sphere having the same surface to volume radio as the prismatic apatite crystal and it is calculated directly from the given grain dimensions. This assumption works well only if the analysed grains were not broken during mineral separation; in the case of a grain fragment, the R^* and diffusion domain will be underestimated, resulting in an inaccurate 'young' He age. This may cause an underestimation of the effective diffusion domain size ranging from 20 to 50% (Brown et al. 2013).

Fragmentation produces inaccuracies especially in rocks that spent a long time in the PRZ, where the He profile in apatite grains became 'rounded', due to both processes of α-ejection and He diffusion (Fig. 4.8) (Brown et al. 2013). As different thermal histories produce different He profiles, fragmentation may be exploited to constrain precisely the low temperature thermal history of the rock, similarly to $^4He/^3He$ technique (Shuster & Farley 2004). Depending of the position of the fracture, the amount of He measured in a fragment may be either proportionally higher or lower than in a whole crystal. Generally, in the case of fragments with one natural termination (1T grains), the shorter the fragment length, the younger the age. With fragments with both natural terminations missing (0T grains) the age will be older (Fig. 4.8). According to the theoretical model, fragmentation alone may easily generate 50% age dispersion in samples which spent prolonged time in the PRZ (Brown et al. 2013). Extracting thermal histories from the grain fragments may be even more valuable than from the whole grains. The newly proposed approach of the modelling grain fragments (Beucher et al. 2013) uses the finite cylinder approximation instead of the R^* and solves the He diffusion both in radial and axial direction.

4.3.2.4 Other causes of dispersion

A dispersion pattern arising from grain size, radiation damage and fragmentation is directly caused by the thermal history of the rock. There is, however, a batch of dispersion causes, which produce a dispersion pattern insensitive to the thermal history; these include: U and/or Th zonation, mineral and fluid inclusions and He implantation. Another source of dispersion may also come from the chemical composition of individual grains, which would change the annealing rate of the radiation damage (Gautheron et al. 2013).

When modelling AHe age data it is often assumed that the U and Th are uniformly distributed in the crystal lattice; however, etched fission track mounts and the recently developed [eU] mapping produced using LA-ICP-MS (Farley et al. 2011, Flowers & Kelley 2011, Ault & Flowers 2012) show that apatite crystals are often zoned. The spatially variable concentration of the parent isotopes influences the He profile within the crystal and has several consequences. When compared to the amount of He lost

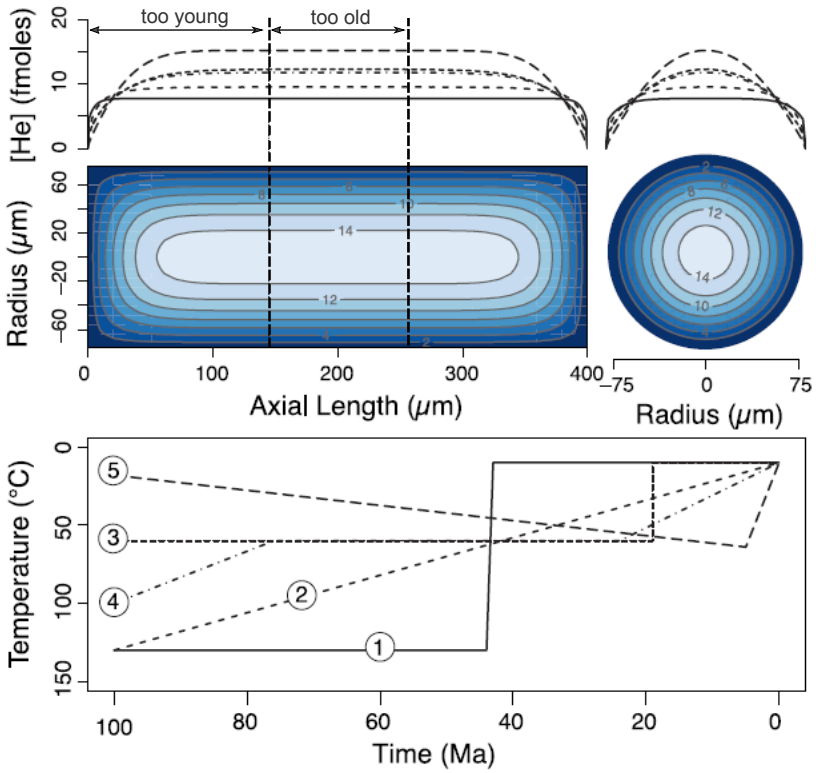

Figure 4.8: The theoretical He profile in an apatite crystal for five thermal histories after Brown et al. (2013). On the axial He profile graph, the dashed lines shows the positions of two exemplary fractures, that will produce either 'too young' or 'too old' AHe age of the corresponding fragments.

via α-ejection from an unzoned crystal, more He will be ejected from an apatite with U- and Th-rich rim and less in case the of a crystal with an enriched core, resulting in an older and younger age respectively (Fitzgerald et al. 2006, Farley et al. 2011). Additionally, zonation may create a [He] gradient, which will affect He diffusion, especially in slowly cooled samples. Radiation damage and parent zonation interfere with each other, creating complex effects on the AHe ages; for instance, a grain with an enriched rim should lose more He than its homogeneous equivalent; however, the radiation damage trapping effect will lower the diffusivity and the processes may cancel each other's effect (Farley et al. 2011, Ault & Flowers 2012). In extreme cases the effect of the U-Th zonation on the age may produce 30–40% age dispersion; however, for the most common types of zonation, it should not exceed 10–15% (Brown et al. 2013).

The presence of U-Th rich mineral phases or He-rich fluid inclusions in the crystal lattice may be a source of external He that result in old ages (Farley 2002, Fitzgerald et al. 2006). Apatite crystals are, however, carefully hand-picked and screened prior to the analysis and grains having even small inclusions and imperfections are excluded. Vermeesch et al. (2007) showed that only if inclusions comprise 10% or more of the apatite crystal and are at least one thousand times richer in U-Th than apatite they will cause significant change to the age. A careful picking, therefore, should reduce the dispersion arising from the presence of inclusions to a few percent.

Excesses of He may also come from outside the crystal. If in the host rock, the apatite is next to an U and/or Th rich phase, e.g. zircon, He may be ejected from the crystals from which it originated and be implanted into the apatite (Spiegel et al. 2009, Gautheron et al. 2012). This effect may result in up to 50% of excess He, and in extreme cases even up to 250–300% (Gautheron et al. 2012) and make the age significantly older. It is, of course, impossible to define at the stage of picking, which minerals were next the apatite crystals in the rock. Apatites are, however, rarely close to U- and/or Th-rich mineral phases and implantation-derived single-grain AHe ages would be much older than the others and therefore easy to spot and discard.

4.3.3 Sampling strategy

Apatite fission track data from rocks in the Southern Uplands exhibit a distinctive pattern: the AFT age increase northwards along with shortening of the MTL and broadening the FTLD (Fig. 4.9). Even though dispersed, all Southern Uplands samples are characterized by a similar range of AHe ages with a peak around 50 Ma. The analysed rocks are from nearby outcrops and there is no evidence that the tectonic discontinuities in between could have been active during post-Palaeozoic history of the area; for these reason, it is plausible to assume that all the rocks experienced the same thermal histories, although they were possibly subjected to different palaeotemperatures.

Apatites from Criffell, Fleet and Loch Doon plutons and from Corsewall Point are abundant and of good quality: many grains are clear with a prismatic shape and variable grain sizes. Crystal fragments were picked aiming to maximise dispersion: short

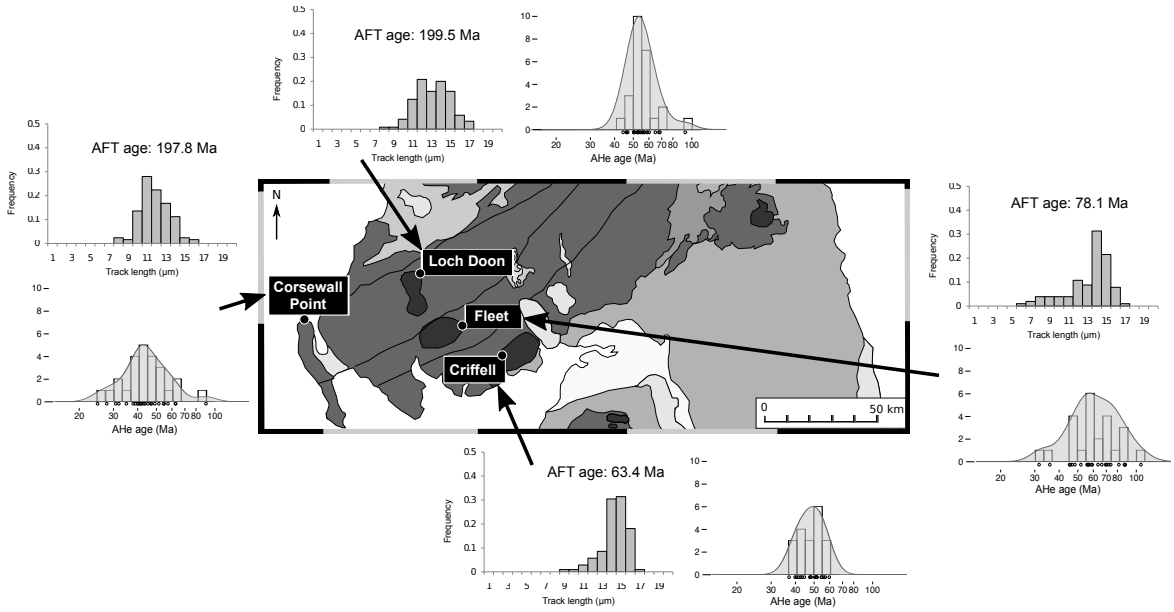

Figure 4.9: Apatite fission track data, apatite (U-Th)/He data (AHe) and locations of samples used for Helfrag modelling. The histograms shows the track length distributions and the graph on the right are PDF plots of AHe ages.

and long grains of different width were picked, along with different number of terminations that have been carefully noted. Preliminary analysis of five grains per sample revealed that the intra-sample range of [eU] was broad, 10–80 ppm, which is the range expected to produce the highest differentiation of ages according to the RDAAM model of Flowers et al. (2009).

The AFT ages range from 63.4 to 199.5 Ma (Fig. 4.9). The results from the QTQt modelling strongly support a rapid cooling event at ∼60 Ma at the Criffell pluton (Fig. 4.2). The thermal histories of GAL02 from the Fleet pluton were not well resolved by the QTQt model, but they suggest a rapid cooling episode at ∼90 Ma rather than at ∼70–60 Ma (Fig. 4.2). The thermal histories do not reproduce the measured AHe ages, which are dispersed and often older than the AFT age. Two samples from Loch Doon and Corsewall Point yielded similar AFT ages of ∼200 Ma. The thermal histories derived for the Loch Doon pluton show that the rock cooled slowly and spent 10's Myr in the PRZ, whereas at Corsewall Point a rapid cooling episode at ∼60 Ma has been resolved. The thermal models are inconclusive regarding the nature of the early Cenozoic cooling event, which could be either regional, present, but not resolved at Loch Doon, or local, only affecting the coastal areas. The limitations of the QTQt models in this case, are to be referred to the fact that grains are modelled using a spherical approximation, excluding the effects of fragmentation. To investigate the full dispersion pattern of the single-grain AHe ages, the grains have to be modelled as fragments and the finite cylinder geometry has to be used for solving the He diffusion equations. The results of the modelling using the Helfrag code will be presented below, after the observed age dispersion is analysed in detail.

4.3.4 Observed age dispersion

The single-grain AHe ages range and dispersion are presented for each sample in Table 4.1. The age dispersion is least at Criffell (47%) where the rocks have experienced rapid cooling from high temperatures. Nonetheless, it is higher than it should be in the case of a rock cooled instantaneously. Age dispersion from the Fleet and Loch Doon granites are comparable (118% and 108%, respectively; Table 4.1), despite the fact that a cooling signature at Fleet is expected to be larger and/or more rapid than at Loch Doon. It could be argued whether the dispersion at Fleet is too high, or the one at Loch Doon is too low. The AHe ages from Loch Doon show less dispersion than those at Corsewall Point, although both samples have similar AFT age and rocks at Loch Doon have probably spent the longer time in the PRZ. The unexpected low age dispersion at Loch Doon is also reflected in the PDF plots that show a narrow distribution of AHe ages with only one old grain that significantly increases the total dispersion value; the age distribution plots are much broader at Corsewall Point and Fleet (Fig. 4.9).

Dispersion at Corsewall Point seems to be correlated to the largest range of grain radii

Location	No.fragments 0T-1T-2T	Li (μm)	R (μm)	[eU] (ppm)	age (Ma)	dispersion
Loch Doon	8-12-5	80–212	27–76	22.5–93.9	32.5–92.2	108%
Fleet	9-15-0	76–292	22–88	11.2–60.9	31.5–105.7	118%
Corsewall Point	7-17-1	80–276	32–135	10.3–74.8	24.8–90.0	143%
Criffell	2-16-1	71–311	27–86	23.8–49.1	37.1–59.8	47%

Table 4.1: The number of particular fragment types (0T, 1T and 2T) and the ranges of fragment length (Li) and radius (R), [eU] and age for four samples analysed during this experiment. The last column shows the total age dispersion calculated, following Brown et al. (2013), as: MaxAge - MinAge / MeanAge.

and the highest number of 1T grains, which, according to the fragmentation model, should be the type of grains producing the largest age spread (Table 4.1; Brown et al. 2013). The largest range of [eU] is displayed by the apatite crystals at Loch Doon, whereas, of the four samples presented here, the radius is the least variable and the number of 1T grains is the lowest. It is possible that the relatively low age dispersion observed at Loch Doon is the results of variable [eU] and a long residence time in the PRZ, with the other factors having a less significant effect. The [eU] variation observed in the other samples is large, encompassing the range that, according to the model of Flowers et al. (2009), produces the highest differentiation in ages. According to this model, once the [eU] is greater than ∼80 ppm, the aliquots reach a plateau age and the He retentivity becomes practically insensitive to radiation damage.

It is common practice to search for positive correlations of ages with the grain size and [eU]. Plots of single-grain age versus grain thickness and [eU] for all samples analysed during this study were presented in Chapter 3. The plots for the Criffell, Fleet, Corsewall Point and Loch Doon samples are given in Fig. 4.10. Additionally, a plot of grain thickness versus [eU] is also shown, to explore the relationship between these two factors in all the datasets; it is important to verify that the two factors are independent variables, as there are no obvious processes that would produce a relationship between grain thickness and [eU]. If a relationship was going to be noticed, it had to be explained as an artefact of the picking process that would have to be highlighted. A strong positive correlation is only observed between age and grain thickness in Criffell (Fig. 4.10d). The correlation is more evident in this sample because the [eU] range is relatively low. If two outliers are removed, there is also strong, negative correlation between the AHe ages and [eU] at Criffell. The [eU] range is small and it is possible that the correlation is an artefact caused by the predominant role of grain size. The other samples do not show any clear correlation. The AHe ages at the Fleet granite may show a general positive trend with grain size, but no correlation with [eU]. The Loch Doon samples also show a weak correlation with grain size, as do the Corsewall Point apatites, although, in this case, two trends can be seen. Correlation with [eU] at Corsewall Point would be negative, if any, and there is no correlation with [eU] in

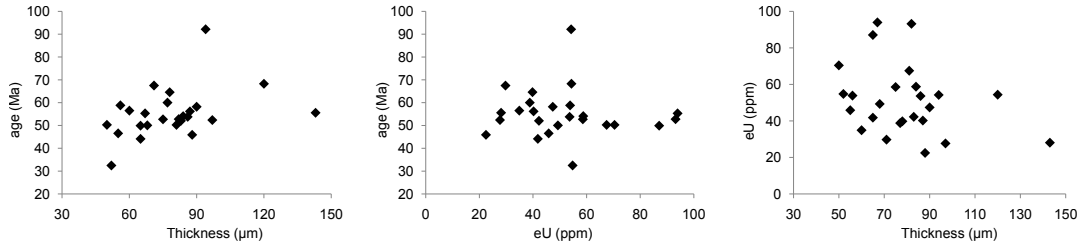

(a) Loch Doon

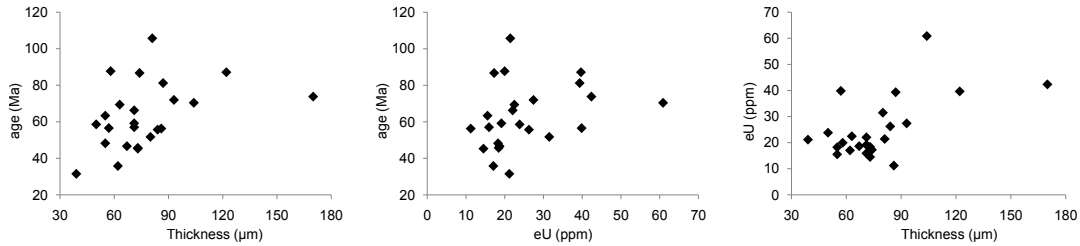

(b) Fleet

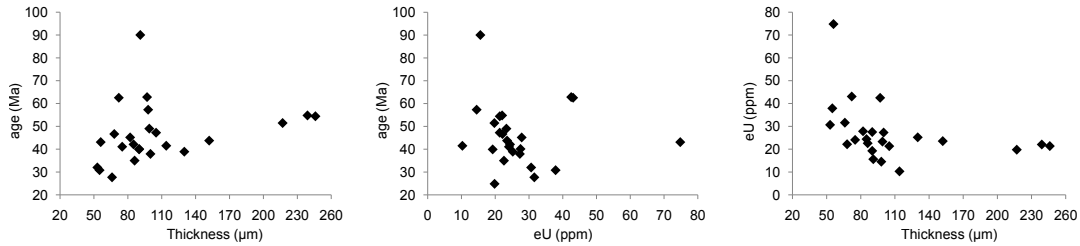

(c) Corsewall Point

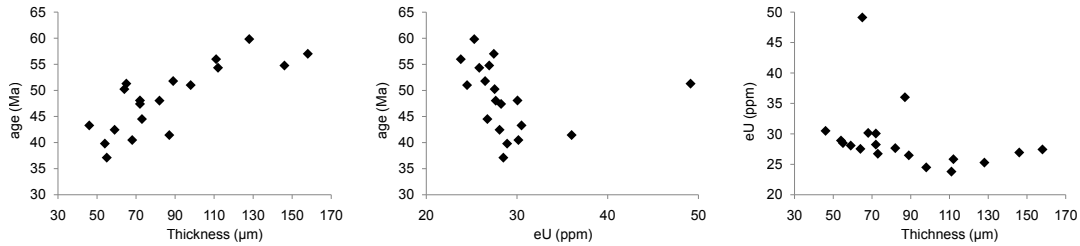

(d) Criffell

Figure 4.10: Single-grain AHe ages of samples GAL01, GAL02, GAL11 and GAL14 age plotted versus grain thickness (the smallest dimension) and eU concentration, the first and the second column, respectively. The last column shows plots of the grain thickness versus eU concentration.

the Loch Doon samples. The Fleet and Corsewall Point data show some relationship between the grain thickness and [eU]. Generally the larger the grain from Fleet, the higher the value of [eU]; the two factors combine to enhance dispersion. The opposite is true at Corsewall Point where small grains have the highest [eU], although, some of the crystals do not show any correlation. These grains, which have similar [eU], show a positive correlation between age and grain thickness that is demonstrated by a best fit line in Fig. 4.10c.

Fragmentation can be investigated by using the Age Dispersion Fragment Distribution (ADFD) plots (Brown et al. 2013), which show, for each fragment type, the correla-

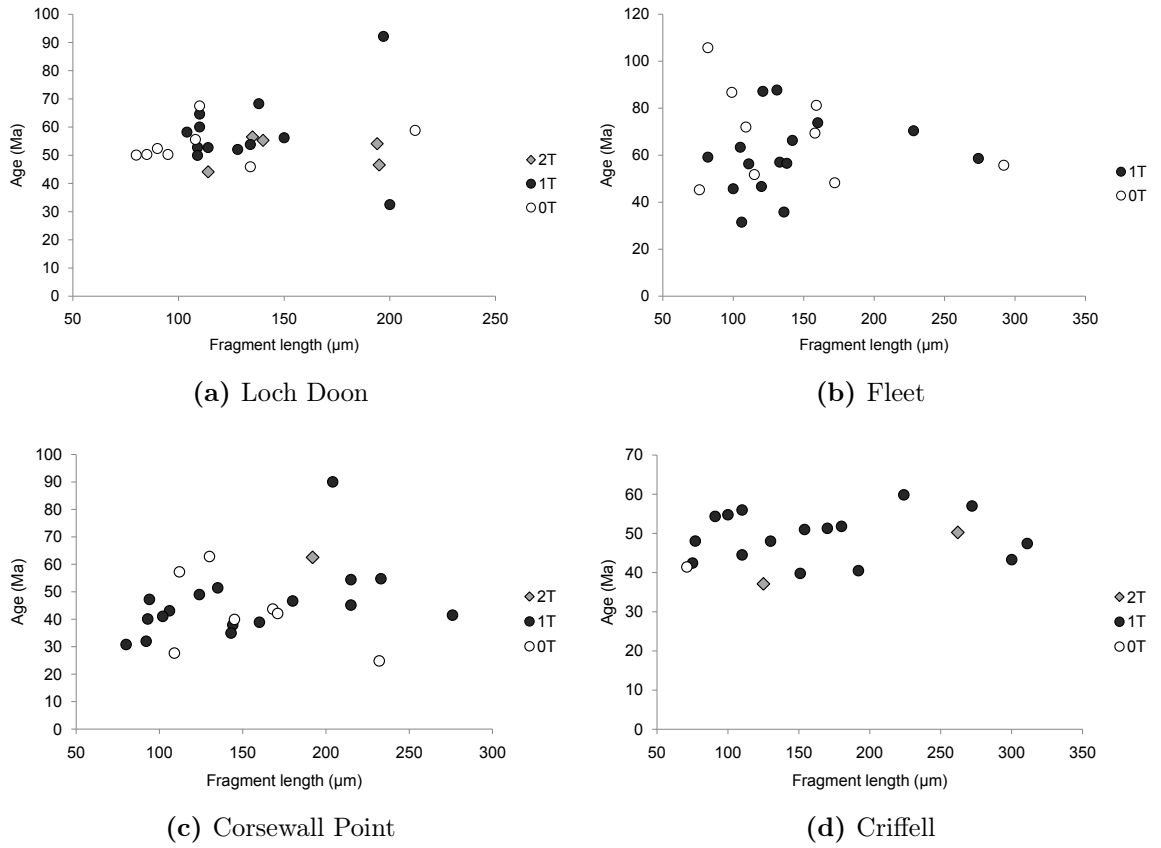

(a) Loch Doon **(b)** Fleet

(c) Corsewall Point **(d)** Criffell

Figure 4.11: Age dispersion fragment distribution (ADFD) plots of AHe ages from Criffell, Fleet, Corsewall Point and Loch Doon samples.

tion between the age and fragment length. For grains with similar diffusion domain size and [eU] the long 1T grains have similar or slightly older ages than 2T grains, with ages decreasing as the length shortens. Finally, the 0T grains should generally be older than the 2T crystals and only rarely slightly younger. The ADFD plots of Criffell, Fleet, Corsewall Point and Loch Doon apatites are given in Fig. 4.11. The AHe ages presented here are the first to be used to test the fragmentation model on natural samples; when synthetic data are used, other factors influencing the AHe age dispersion are kept constant. In this case, the effect of grain size and [eU] combine with the fragmentation to produce a much more difficult to interpret correlation. Despite these difficulties the curved trend that has been predicted for synthetic 1T crystals is seen for the Criffell and Corsewall Point samples. The interpretation of the Fleet data is not straightforward and the low number of aliquots may be the reason for the uncertainties; certainly, when the grains are short, they show the most dispersion, as predicted by the model. The ADFD derived dispersion pattern for Loch Doon apatites is atypical, as the highest dispersion is observed for the longest grains.

In order to further investigate the effect of different factors on age dispersion, ADFD plots including grain size and/or [eU] have been created (Fig. 4.12). The size of the symbols representing the single ages presents either the grain size or [eU]. The ADFD-

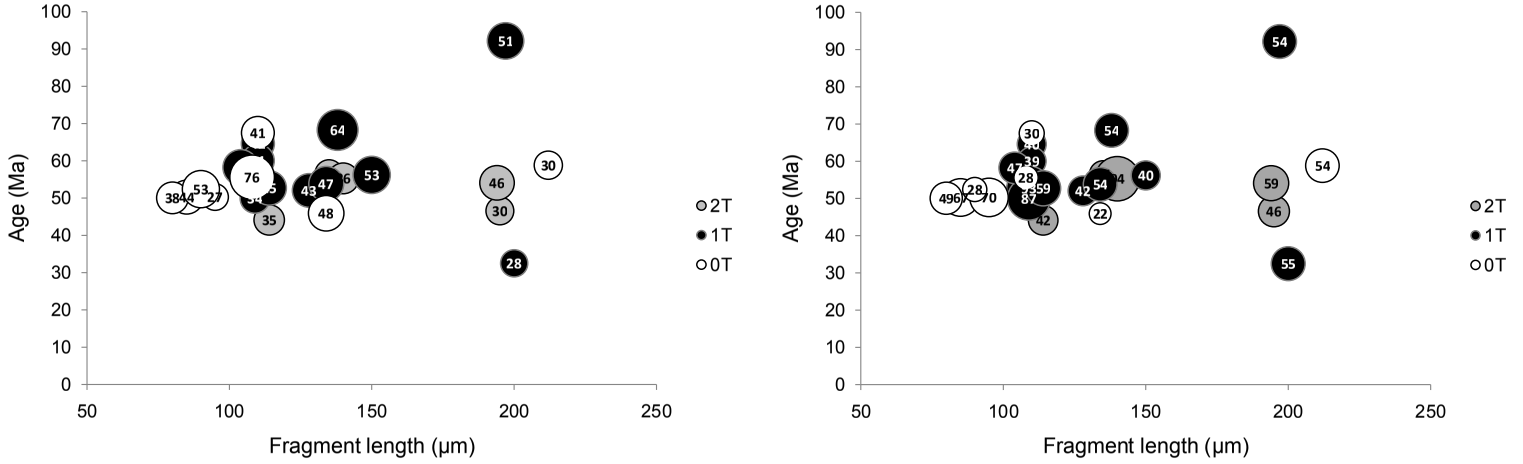

(a) Loch Doon

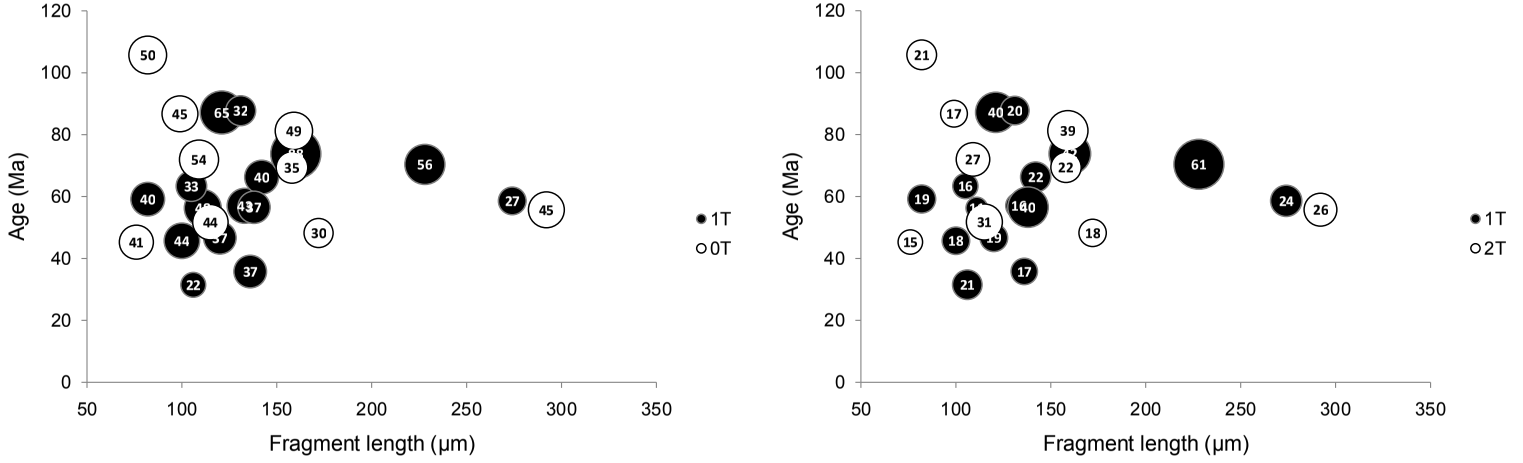

(b) Fleet

Figure 4.12: Grains radii (left-side plots) and eU concentration (right-side plots) in Criffell, Fleet, Corsewall Point and Loch Doon samples, plotted as a circle size on age dispersion fragments distribution (ADFD) plots. Additionally the grain radii in μm and the values of [eU] in ppm are given as a number in the corresponding circle.

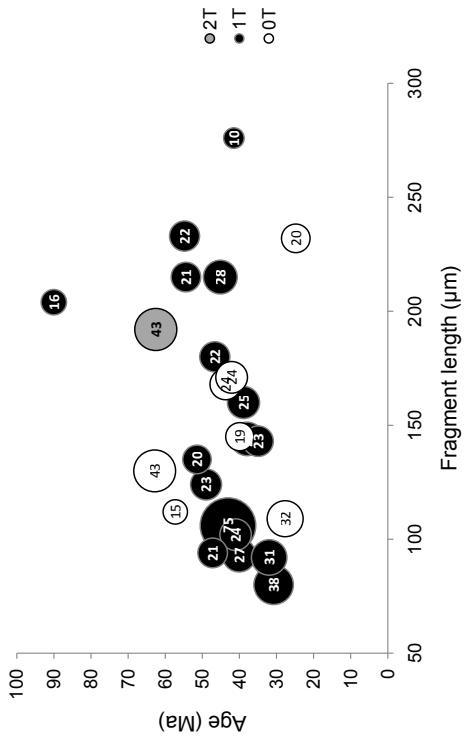

(c) Corsewall Point

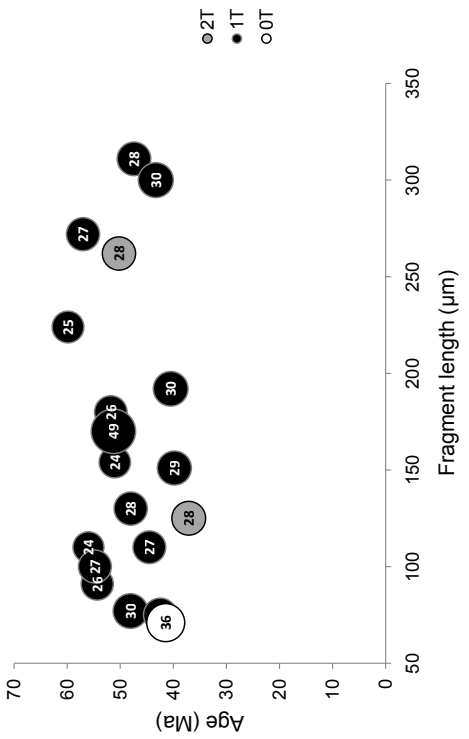

(d) Criffell

Figure 4.12: (continued)

radius plot of Criffell (Fig. 4.12d) indicates that grain size is the dominant factor for age dispersion; the larger the grains the older the age and vice-versa, independent of fragment length. The curved trend that was previously interpreted as an effect of fragmentation is actually due to crystal size, although, the importance of broken crystals cannot be excluded. The few aliquots that show no correlation between AHe age and fragment length and crystal size can be explained by changes in [eU]. The ability to isolate the main factors contributing to age dispersion shows the usefulness of these graphs.

The age of Corsewall Point also show a clear dominance of crystal size controlling the age dispersion (Fig. 4.12c). Most of the old grains are large and some old, smaller grains can be probably explained by the effect of radiation damage; for instance the only 2T grain analysed is old and small, but has one of the highest [eU] in the data set, which would suggest high density of radiation damage. However, the oldest grain has an age that is significantly different to that of the others, has 1T, a relatively small size and low [eU]. None of these factors can explain the age of this grain. This may be due to implantation or zonation. A general trend of increasing age with both size and [eU] is also seen in the 1T grains from the Fleet granite (Fig. 4.12b). The trend is, however, less clear and probably, this dispersion pattern is an effect of a complex interference of all three dispersion causes and/or some additional factor. In case of the Loch Doon apatites, adding the radius size and [eU] information does not help in deciphering the dispersion pattern. Dispersed ages from the long grains do not correlate with radius or with [eU]. On the other hand, the ages of shorter grains, more variable in radius sizes and [eU], do not seem to be influenced by any of these factors and have low dispersion. This pattern is unexpected for a slowly cooled sample and suggests that it is either an effect of a complex interference of all three dispersion causes, which end up almost cancelling each other, or that the rock has been cooled more rapidly than suggested by AFT data.

4.3.5 Modelling fragments

Dispersed ages may be inverted to extract thermal histories. Incorporating the broken grain effect requires the grains to be modelled as fragments and the He diffusion to be solved in in both the axial and radial direction. This can be performed using the Helfrag code (Beucher et al. 2013) (see section 2.4 for description of the software).

For the thermal modelling, the box for prior has been set to 150°C x 200 Ma and six t-T points have been searched with the sixth point set to 20°C at 0 Ma. The constant value of L_0 has been used and set to 600 μm in all four samples. To shorten the computing time, standard Durango kinetics have been used during the modelling. Because 0T fragments cannot be modelled in the current version of the code, the total number of aliquots per sample has been reduced and is as follows: Criffell—18 grains,

Fleet—15 grains, Corsewall Point—18 grains and Loch Doon—17 grains. The results of initial 100 iteration runs (10,000 single models generated) are shown with the age predictions in Fig. 4.13.

After 100 iterations, convergence is still poor and the models cannot be properly assessed. However, some preliminary conclusions can be drawn about the input data. All ages from the Criffell granite are well predicted. The predictions of Loch Doon and Corsewall Point models are also good, but there are single outliers, one at Loch Doon and two at Corsewall Point. The old, unpredicted ages may be an effect of inclusions or He implantation and were removed from the next step of the modelling. The old AHe ages from Fleet cannot be predicted, as it happened when the AFT data and the AHe were modelled using the default mode of the QTQt software. If after 100 iterations, the software could not find any thermal history supporting most of the data, it was decided that age dispersion cannot be explained simply by fragmentation and crystal size. The QTQt software also struggled to find solution that fitted the data when the radiation damage algorithm is included; it is unlikely that including all factors in the same run will help to resolve the observed dispersion. An explanation of those old ages may lie in the distinctive chemical composition of the Fleet apatites, as shown by the D-par values, which are the lowest in the whole dataset, in strong zonation or in some other, still unknown factor. Given the time consuming nature of Helfrag modelling the Fleet sample was not used in the next step.

The Helfrag code was run for 300 iterations on the well-behaved samples from Criffell, Corsewall Point and Loch Doon. The same data have been used to produce models based on the spherical approximation (modelled in QTQt) in order to allow the fragmentation effect to be identified and to assess its influence on AHe ages. For both types of models the Root Mean Square Deviation (RMSD) factor was calculated, based on the measured and the predicted ages. The Helfrag results are presented in Fig. 4.14 and the corresponding QTQt models in Fig. 4.15. The higher number of iterations enhances the modelling precision. Within the temperature range of the AHe thermochronometer sensitivity (30–80°C, yellow shading on the graphs), the thermal histories obtained after running 300 iterations are generally similar to the one obtained after 100 iterations and to the QTQt models, but some important differences may be spotted.

In the case of Criffell model (Fig. 4.14a), the cooling rate proposed by the Helfrag model is slower than the cooling rate derived from the multi-thermochronometer modelling that included the AFT data (Fig. 4.2 GAL14). Although the multi-thermochronometer model was based on the spherical approximation, the AHe ages were well resolved. Whereas in some cases the differences in the low temperatures span between the AHe and AFT based models can be well explained by the fact that short, annealed fission tracks may represent several thermal histories, the dominance of long tracks and narrow

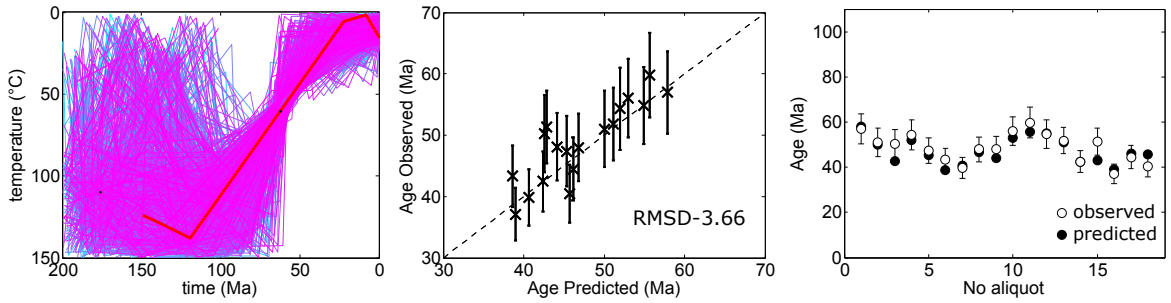

(a) Criffell

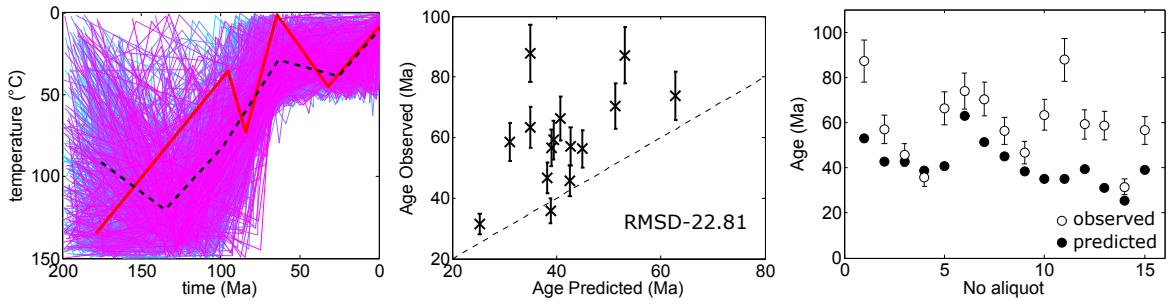

(b) Fleet

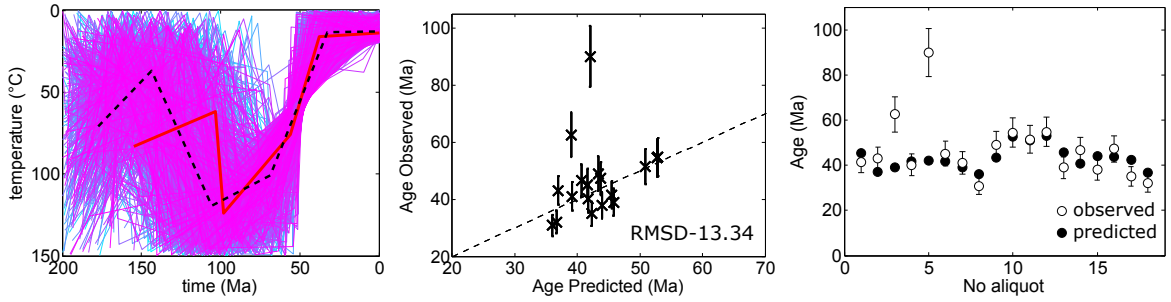

(c) Corsewall Point

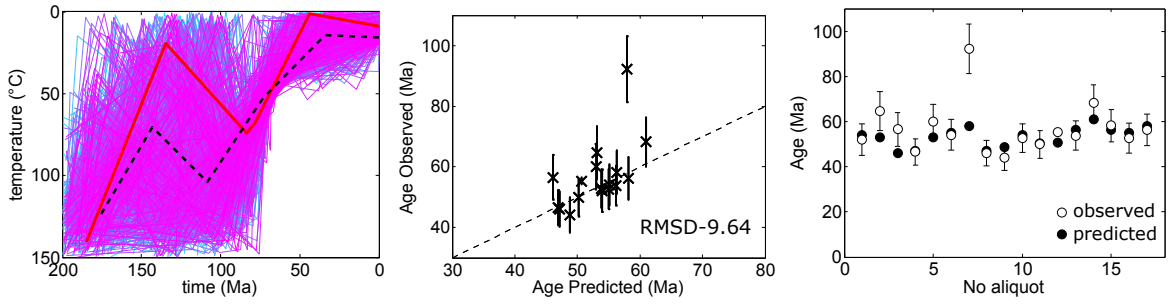

(d) Loch Doon

Figure 4.13: Initial Helfrag model and model predictions after running 100 iterations (10,000 model generated) for Criffell, Fleet, Corsewall Point and Loch Doon samples. Plotted are 10% of the models with lowest misfit. Line colours refer to the misfit value: magenta—high misfit, blue—low misfit. Thick red line is the lowest misfit model and the dashed black line is the average model, that is the average of all plotted models. The middle columns show predicted and observed ages with the error bars and 1:1 line. The right column presents observed and predicted ages plotted as an aliquot number.

FTLD, as in the case of Criffell, almost certainly indicate a rapid cooling event. The relatively slow cooling rate of the Criffell samples as proposed by the Helfrag model is, therefore, equivocal and points to a necessity of adding other constraints, such as AFT data. The slow cooling rate is, however, not an effect of adding fragmentation. Modelling the AHe ages alone using spherical approximation in QTQt produces similar thermal history and the spread of the ages is resolved, although slightly less precisely (Fig. 4.15a). This 'experiment' demonstrates the value of a multi-thermochronometric approach, especially in cases where the rock have been cooled from temperatures higher than the sensitivity of AHe system.

The Helfrag-derived thermal histories of Loch Doon (Fig. 4.14c) are different from the multi-thermochronometer model that included the AFT data. In the Helfrag model

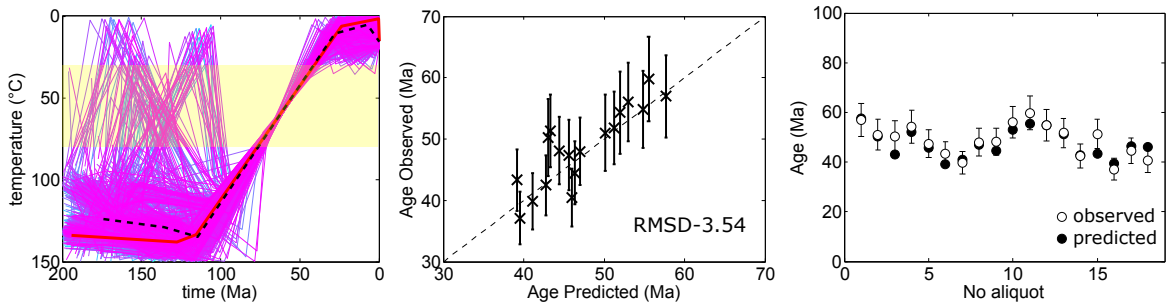

(a) Criffell

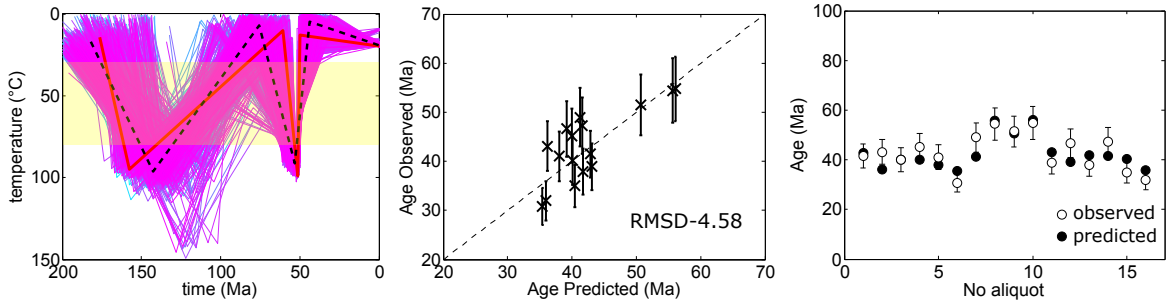

(b) Corsewall Point

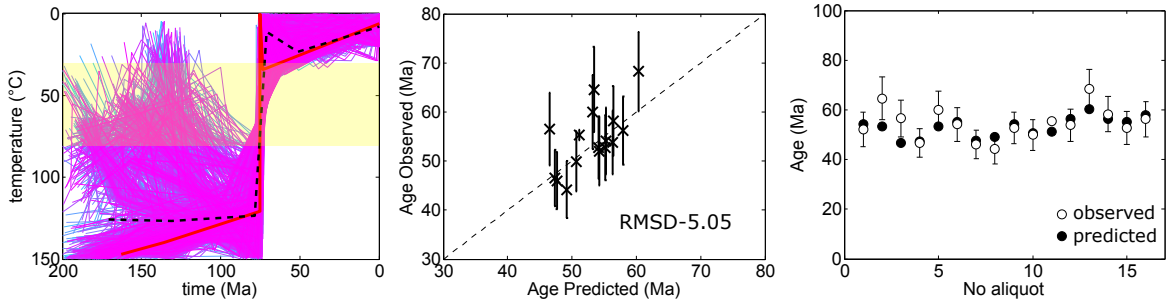

(c) Loch Doon

Figure 4.14: Helfrag model and model predictions after running 300 iterations (30,000 model generated) for Criffell, Corsewall Point and Loch Doon samples. Plotted are 10% of the models with lowest misfit. Line colours refer to the misfit value: magenta—high misfit, blue—low misfit. Thick red line is the lowest misfit model and the dashed black line is the average model, that is the average of all plotted models. The middle columns show predicted and observed ages with the error bars and 1:1 line. The right column presents observed and predicted ages plotted as an aliquot number.

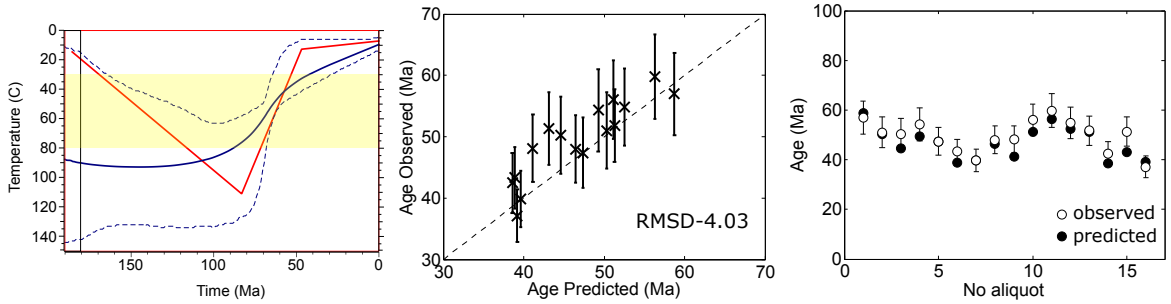

(a) Criffell

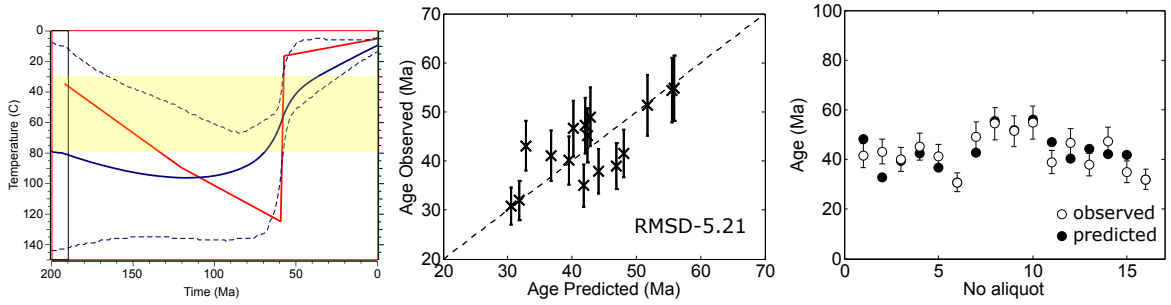

(b) Corsewall Point

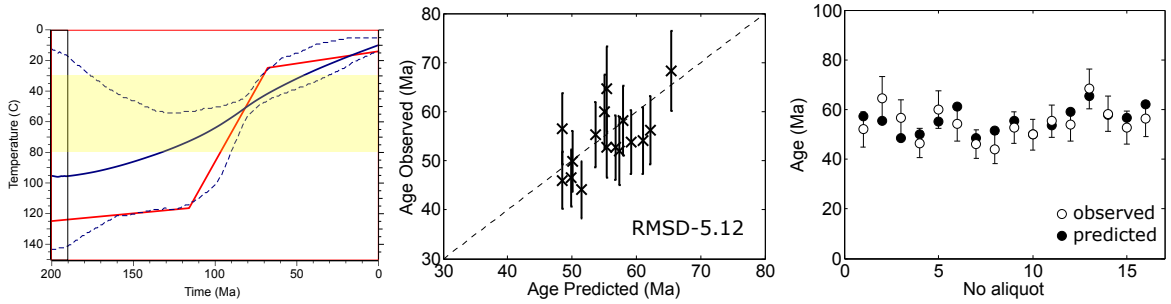

(c) Loch Doon

Figure 4.15: QTQt model and model predictions corresponding to analysed Helfrag models for Criffell, Corsewall Point and Loch Doon samples. Thick red line is the maximum likelihood model; thick blue line is the expected model and dashed blue lines are the 95% credible intervals; thin red line defining a box shows the general range of prior; the light yellow shadow marks the temperature sensitivity range of AHe thermochronometer, 30–80°C. The middle columns show predicted and observed ages with the error bars and 1:1 line. The right column presents observed and predicted ages plotted as an aliquot number.

the cooling rate due to the low dispersion is rapid, almost instantaneous. Although the large magnitude of cooling, bringing rocks from >100°C to <30°C may be treated as an artefact of the large modelling space without any high temperature constraints, there are no clear reasons to discard the rapid cooling signature within the range of the temperatures that the AHe thermochronometer is sensitive to, especially because the timing of cooling, ∼70 Ma, correlates with the onset of regional cooling. The rapid cooling signature could have been, therefore, small and difficult to resolve by modelling AFT data. Moreover, a similar signature is present on the QTQt maximum likelihood model of multi-thermochronometer data when the radiation damage algorithm of Flowers et al. (2009) has been applied (Fig. 4.2 GAL01). The thermal histories derived from modelling AHe ages only, both with Helfrag and using the standard mode in QTQt, show different cooling rate. In contrast to the near-instantaneous cooling resolved by

Helfrag, the QTQt models propose that the cooling was slow and likely monotonous (Fig. 4.15c). Although the age predictions are similar, the RMSD factor of 5.05 and 5.12, the individual single-grain ages are resolved with varying degrees. This suggests that the use of the fragmentation in the case of Loch Doon may have a significant influence on the t-T path derived from thermal modelling and be a proxy for the track lengths distribution especially in case of the samples that have experienced complex geological history.

The largest difference between thermal histories derived from QTQt and Helfrag is seen in the case of Corsewall Point, where the latter model is able to resolve two distinctive cooling events, separated by a reheating episode, which are completely missed by the QTQt models (Fig. 4.14b and 4.15b). The first cooling started at ∼150 Ma and finished by ∼100 Ma. The reheating event occurs in the Late Cretaceous, between ∼100 and ∼50 Ma and it is followed by a rapid cooling event at ∼50 Ma. Such thermal history has not been resolved for the Corsewall Point after 100 iterations or by QTQt models. The timing of the cooling and reheating episodes correlates well with the timing of regional Early Cretaceous and early Palaeogene exhumation events and with the Late Cretaceous reburial (e.g. compare with Ziegler 1988). Thus, although the maximum temperature prior the final cooling at ∼50 Ma is 90–100°C, and therefore higher than than the typical closure temperature of the AHe thermochronometer, the resolved pattern may be a real feature. The duration of the rock at temperatures of ∼70–100°C was probably less than 10 Ma and might not have been long enough to cause total resetting of the AHe thermochronometer. Additionally, the ∼50 Ma cooling episode was almost instantaneous and the corresponding closure temperature would be higher than for moderately and slowly cooled samples, although unlikely it reached 90°C. That might have caused the earlier part of the thermal history to be well resolved, when the large number of apatite grains have been modelled as crystal fragments in Helfrag. Adding fragmentation enhances the age predictions, the RMSD for Helfrag and QTQt models are 4.58 and 5.21, respectively, and it suggests that significant amount of the age dispersion has been generated by fragmentation. The example from Corsewall point seems to indicate that modelling AHe ages using Helfrag is particularly important when rocks have a complex thermal histories, with multiple episode of cooling and heating that may not be resolved when fragmentation is not taken into account.

4.3.6 Discussion

The thermal histories derived from Helfrag are similar to the standard models and the age predictions for the Helfrag models are only slightly better than for the QTQt models based on the assumption of spherical diffusion geometry. This implies that the grain size has probably been the predominant role in generating the AHe age dispersion of single grains. Many grains have a diameter of 60–100 μm. For diameters less than 100 μm the He profile within the crystal may not be differentiated enough

to produce a dispersion measurable outside the uncertainty associated with the age. It is also easier for long-thin and short-thick grains to be preserved and then picked compared to long-thick and short-thin grains. This minimises the age dispersion that can be generated from fragmentation. A difference in the grain size generates a large amount of dispersion that, in most cases, is independent of the fragment geometry. For instance, in the case of slowly cooled rocks, analysing grains that have diameters of 100 μm and 200 μm and random fragment geometry will generate the age spread that is 1.5–2.0 times as much as the maximum age spread generated by the youngest and oldest age from the same width fragments, which are much more difficult to be preserved, picked and analysed (based on Fig. 6 of Brown et al. 2013). In order to generate a sufficiently large age spread from both fragmentation and grain size, the grain picking should be focused on the >100 μm diameter grains, of a variable length and a large proportion of short 1T fragments, and only a few small grains need to be picked.

The way of modelling grains as fragments has an effect on the thermal histories and enhances the age predictions. In most cases, modelling only AHe ages is not sufficient and adding other thermal constraints, e.g. AFT data, is desirable. Combining Helfrag modelling with AFT ages and FTLD, as well as implementing the radiation damage models, could certainly boost the modelling results, however, the already long computing time would increase significantly. Because of this, performing the Helfrag multi-thermochronometer modelling is difficult to apply routinely. The modelling results are not that much different for rapidly and moderately cooled rocks and running the Helfrag code on such samples is not recommended. In the case of slowly cooled samples and samples that experienced complex thermal history, adding the fragmentation may, however, improve our understanding of the observed age spread and better resolve the thermal history of the rock. In such cases, analysing large number of grains, >20, from few samples and aiming at maximising the age dispersion seems to produce better results than analysing many samples, but only few single-grain ages per sample.

4.3.7 Conclusions

The results of the crystal fragment modelling add some important observations to the cooling history of southern Scotland. The Helfrag model resolved more thermal events at Corsewall Point that correspond with Mesozoic-Cenozoic geological evolution, but were not found by the standard models based on the spherical diffusion geometry. In the Loch Doon granite the ∼70 Ma rapid cooling event resolved by Helfrag was not identified in earlier modelling, but is in agreement with the timing of the main cooling episode in the region. In these two cases, the Helfrag modelling seems to add new, important constraints on the low temperature part of the thermal histories. The cooling rate at Criffell derived from fragmentation modelling is slower than the one proposed by the models that include AFT data and points to the importance of including higher thermal constraints, e.g. AFT data.

In general, the difference between the thermal histories derived from fragmentation modelling and models based on the spherical diffusion geometry approximation are not large and the age predictions for the Helfrag models are only slightly better, suggesting that the grain size effect prevails. Rather than suggesting that grain size is the predominant factor in controlling age dispersion in all data sets, the results from analysed datasets may be linked to the actual size of the picked grains. It can be concluded that in order to obtain valuable information from both fragmentation and grain size more than 20 large (width >100 μm) grain fragments of variable length have to be analysed, together with a few smaller grains. The results point to a strategy that favours multiple single-grain AHe ages determinations on carefully selected samples, with good quality apatite crystals of variable dimensions rather than fewer determinations on many samples.

4.4 Thermal histories modelling: some concluding remarks

QTQt is based on Bayesian statistics (section 2.4) and therefore the thermal histories may be biased towards the simplest scenarios. This means that the cooling/heating events which are close to each other in time and/or for which there is no strong geological or thermochronometric constraints may not be resolved. This is particularly true for the 'expected model', which follows the "Occam's razor" hypothesis. The 'max-like' model is the model that best fit the data; it usually provides complex thermal history, that may be, on the other hand, over-complex and not supported by geological evidence, as the data always contain some analytical inaccuracies and noise. When QTQt is used, the expected and max-like models should be compared and assessed using the available geological constraints and taking the data quality into consideration. The importance of comparing the two models is best exhibited by the examples from Loch Doon, where the rapid cooling event at 70–80 Ma is resolved only by the max like model (section 4.2).

Helfrag in its current version searches only for the best fitting scenario, which is equivalent to the QTQt max-like model. The Bayesian statistics can be calculated, but a separate code has to be run on the assembly of all generated models. Helfrag is codified to incorporate fission track data, however, more effort has to be invested to include variable annealing kinetics and track length projections. The software is also not user-friendly. The main advantage of using Helfrag when modelling AHe age dispersion is that the software can be run on multiple cores, which is essential, as the use of finite cylinder geometry increases computing time. Lack of this possibility makes using the fragmentation mode in QTQt difficult. For all these reasons, the most efficient development of these software would be a QTQt version that includes Helfrag, but can be run on computer clusters.

Chapter 5

Heat transfer modelling

5.1 Introduction

The main application of low temperature thermochronology lies in deciphering the denudational history of the crust. Cooling paths derived from inverse modelling of thermochronometeric data can be translated into denudation if the value of the geothermal gradient is known. The geothermal gradient in the upper crust typically varies from 20 to 30°C/km (Turcotte & Schubert 2002). However, our knowledge of palaeogeothermal gradients and how they change through time is limited, as the thermal field in the crust is sensitive to the local heat flow values and thermal conductivity of rocks, as well as short-lived perturbations caused by faulting, magmatism and rapid exhumation (Blackwell & Steele 1989, Turcotte & Schubert 2002, Braun et al. 2006).

Surface heat flow is a combination of basal heating of the lithosphere by mantle convection and heat produced by decay of radioactive elements within the crust (Turcotte & Schubert 2002). Heat flow in oceanic crust is mostly attributed to the high basal temperature. It reaches a maximum at active rifts and decrease rapidly with increasing distance from the rift axis (Pálmason 1973, Makris et al. 1991, Gallagher et al. 1994). Generally, high heat flow values on the continents are restricted to regions that are subjected to active volcanism (Turcotte & Schubert 2002). High continental heat flow can also be associated with a high concentration of the radioactive elements (U, Th and K) which are typically found in continental crust. Typically, heat production from radioactive decay contributes approximately 50% to the surface heat flow in the continents (Turcotte & Schubert 2002), but, in the case of heat productive basement, it may contribute more than 80% (e.g. Neumann et al. 2000).

The thermal conductivity of rocks in the uppermost crust varies from 0.5–7.0 W/m/K (Clauser & Huenges 1995). Local variations of the geothermal gradient between different lithologies may be significant. In a simple model where the crust is considered as a set of layers characterized by different thermal conductivity, each layer will have a specific geothermal gradient. Low conductivity rocks such as mudstone, siltstone, coal

or basalt have an insulating effect on the underlying rocks, the so called blanketing effect (Zhang 1993). This is recognized in many sedimentary basins, where its influence is pronounced due to the potentially large thickness of a sediment infill and may enhance the maturity of organic material. Thus knowing the geothermal gradient in sedimentary basins with accuracy is of interest for the hydrocarbon industry (Lucazeau & Le Douaran 1985, Zhang 1993, Pollack & Cercone 1994). Thermal conductivity is variable even in the same rock type as it depends on temperature, pressure, porosity, composition and saturation (Clauser & Huenges 1995, Eppelbaum et al. 2014). Decrease of thermal conductivity with increasing porosity is important as very often rocks removed during denudation episodes are relatively young and less compacted when compared to the same types of rocks that are preserved elsewhere; the eroded rocks, therefore, were characterised by a higher geothermal gradient than the same, but more compacted rocks that may have been still preserved (Zhang 1993).

Large perturbations of the thermal field in the crust are caused by magmatic underplating at the base of the crust and the intrusion of magmatic bodies within the crust. Although, melt temperatures (1100°C) are high compared to the crust (0–600°C), their impact is restricted to the vicinity of the magmatic body; for example, the thermal perturbations due to dyke or sill emplacement are usually restricted to a distance smaller than the intrusion thickness (e.g. Raymond & Murchison 1991, Brown et al. 1994).

The impact of heterogeneities in the crustal thermal field caused by changes in thermal conductivity of rocks and enhanced radiogenic heat production may be significant. It has been suggested that the high temperature low pressure metamorphism and granitic melt generation in the Proterozoic terranes of Australia is due to the burial of abnormally high heat productive basement (Sandiford & Hand 1998, Hand et al. 1999, McLaren et al. 1999, 2006). Blanketing the heat producing basement is an effective way of increasing the geothermal gradient and has been studied for geothermal energy exploration (Majorowicz & Grasby 2010, Majorowicz & Minea 2012). However, in LTT studies, the effects are usually disregarded; the amount of denudation is commonly calculated for a constant geothermal gradient, often based on the present day value. This assumption generally holds for areas where rocks have had a 'normal' and constant geothermal gradient, but may bring significant inaccuracies where basement rocks were buried under low conductive sedimentary rocks. If this low thermal conductivity is not taken into account, the calculated amount of denudation may be overestimated. Cases of inaccurate reconstructions of denudation due to this effect have been reported for Brazil (Gallagher et al. 1994) and the Lake District region Chadwick et al. (1994). Rates of cooling may also be misinterpreted if the effect of the rock thermal conductivity is not considered and, changes in the eroded lithology may be interpreted as changes in cooling rates (Braun et al. 2006).

In central west Britain, the high pre-Cenozoic palaeotemperatures and characteristic "U-shape" of the AFT ages are not well understood and the attempts to explain this age pattern remain controversial (Green 1986, 2002, Holliday 1993). In this study, the possibility that this pattern is an effect of the heterogeneity of the crustal thermal properties is investigated. Central west Britain could be considered a particularly suitable case to study this issue as the crust is heterogeneous. In detail, (i) young (early Palaeogene) AFT ages are only found in the Lake District, which is underlain by a high heat producing granite batholith, (ii) the Mesozoic sediments that likely covered the region prior to the Cenozoic exhumation were probably characterized by low thermal conductivity (Holliday 1993), and (iii) the early Palaeogene is a time of magmatic activity in NW Scotland and likely of magmatic underplating beneath central west Britain (White & Lovell 1997, Al-Kindi et al. 2003). Given its relatively small size and the lack of evidence for Cenozoic fault reactivation (Needham & Morgan 1997, Akhurst et al. 1998), it can be assumed that central west Britain experienced the same tectonic history and, therefore, its evolution can be defined by a few end-member scenarios.

This chapter aims to answer whether the pattern of thermochronomeric ages in central west Britain can be explained only by difference in crustal thermal properties without spatially variable rock uplift. The chapter provides a brief introduction to heat transfer within the crust and presents a short literature review of the thermal structure of the crust in central west Britain. In section 5.4 results of 1-D modelling are presented aiming to quantify underplating, heat production and blanketing effects. These processes are first modelled separately to investigate their potential effect on the thermal structure of the crust, and then they are modelled together to estimate their combined influence on the thermal history of central west Britain in the Cenozoic. The results of the 3-D modelling using the Pecube code (Braun 2003) are presented in section 5.5. Because the modelling requires several simplifications to be made, the denudation estimates presented here will not be directly used for further geological interpretation. The calculated estimates of geothermal gradients for different crust compositions will be used in Chapter 6 for a detailed quantification of amounts of rock uplift and denudation for the thermal histories presented in Chapter 4.

5.2 Heat transfer equation

In any medium, heat is transferred from hotter to cooler regions via conduction, convection or radiation. Radiation is a process whereby the heat is transferred within the substance in a form of electromagnetic waves; it is the most common way in which heat is transferred in gases or in vacuum, but it plays a negligible role in solids. Convection occurs when heat is transferred between different parts of the body by moving material. Convection is predominant in liquids, whereas in solids it is totally absent. In solid substances conduction is the most common way of transferring heat; it can be

described as a diffusive process whereby heat is transferred through the body itself, by collisions of the molecules that transmit their kinetic energy (Carslaw & Jaeger 1959). The heat transfer within the Earth is regionally variable. Within the mantle it is dominated by convection, whereas in the cold, rigid lithosphere by conduction (Turcotte & Schubert 2002). However, sedimentation and exhumation of rocks cause displacement of the lithosphere boundaries and result in the advective movement of the medium (Braun et al. 2006). The predominance of advection or conduction in heat transfer is given by the Pécelet number, Pe, defined as:

$$Pe = \frac{\tau_c}{\tau_a} = \frac{EL}{\kappa} \tag{5.1}$$

where
τ_c is the timescale for conduction
τ_a is the timescale for advection
E is the exhumation rate
L is the depth to the bottom of the exhumed layer
κ is the thermal diffusivity of the exhumed layer

If the movement of rocks towards the surface is fast, the timescale for advection is larger than the timescale for conduction, Pe is greater than 1 and advection predominates causing significant perturbations of the thermal field in the uppermost crust. If rocks are exhumed slowly, usually <0.1 mm/yr, Pe is less than 1, and conduction dominates (Braun et al. 2006).

In the simplest case of purely conductive heat transfer in a uniform, solid medium, the heat transfer equation has the general form of a diffusion equation:

$$\rho c \frac{dT}{dt} = k\frac{\partial^2 T}{\partial x^2} + k\frac{\partial^2 T}{\partial y^2} + k\frac{\partial^2 T}{\partial z^2} \tag{5.2}$$

where
T is temperature
t is time
ρ is the rock density
c is the rock heat capacity
k is the rock thermal conductivity
x, y & z are the spatial coordinates of the rock particle

The complex heat transfer equation that takes the crustal heat production and advective movement of the rocks into consideration has a following form:

$$\rho c(\frac{\partial T}{\partial t} + v_x\frac{\partial T}{\partial x} + v_y\frac{\partial T}{\partial y} + v_z\frac{\partial T}{\partial z}) = k\frac{\partial^2 T}{\partial x^2} + k\frac{\partial^2 T}{\partial y^2} + k\frac{\partial^2 T}{\partial z^2} + \rho H \qquad (5.3)$$

where

v_x, v_y, v_z are corresponding components of rock velocity

H is rate of the radiogenic heat production per unit mass

These equations have been used in 1-D and 3-D models to investigate the thermal field of the crust in central west Britain and its impact on the thermochronometric data. The following section provides a brief overview on the thermal structure of the crust in central west Britain at present and at the beginning of the Cenozoic.

5.3 Thermal structure of the crust in central west Britain

The present day thermal properties of the crust in Britain have been investigated by several British Geological Survey studies (e.g. Downing & Gray 1986a,b, Rollin 1987, Lee et al. 1987, Busby et al. 2011). The present-day upper crustal geothermal gradient in southern Scotland, the Lake District and northern Wales is 24–30°C/km. This corresponds to the average geothermal gradient in Britain (Busby et al. 2011), although values above 35°C/km are found in the North Pennines.

Late Cretaceous/early Palaeogene palaeotemperatures derived from thermochronometric data (Green et al. 1997, Thomson et al. 1999, Green 2002, Persano et al. 2007, Green et al. 2012 and this study) shows that the temperatures were the hottest where the surface heat flow is usually the highest (Fig. 5.1). There are two regions of clearly elevated surface heat flow: SW England (Cornwall) and N England (the Lake District and North Pennines), where the heat flow value exceeds 80 mW/m^2 (Fig. 5.1). These anomalies are related to the presence of heat producing granite batholiths (Brown et al. 1979, Lee et al. 1987, Webb et al. 1987). In the Lake District and North Pennines gravity, seismic and magnetotellutic data modelling have constrained the depth of these batholiths to between 8 and 12 km (Bott 1974, Evans et al. 1988, Simpson & Warner 1998). The heat production in the granite plutons exposed in central west Britain are in range from 1.9 to 5.2 $\mu W/m^3$ (Table 5.1). These are 2–5 times higher than the average heat production of the Phanereozoic crust that is in range 0.95–1.10 $\mu W/m^3$ (Rudnick et al. 2005).

The heat production of buried granites is unknown. The radiogenic elements are often not uniformly distributed; it is common that the concentration of U, Th and K vary spatially and decrease, usually exponentially, with depth (Lachenbruch 1970). Such vertical variation is considered to be the reason for the apparent conundrum

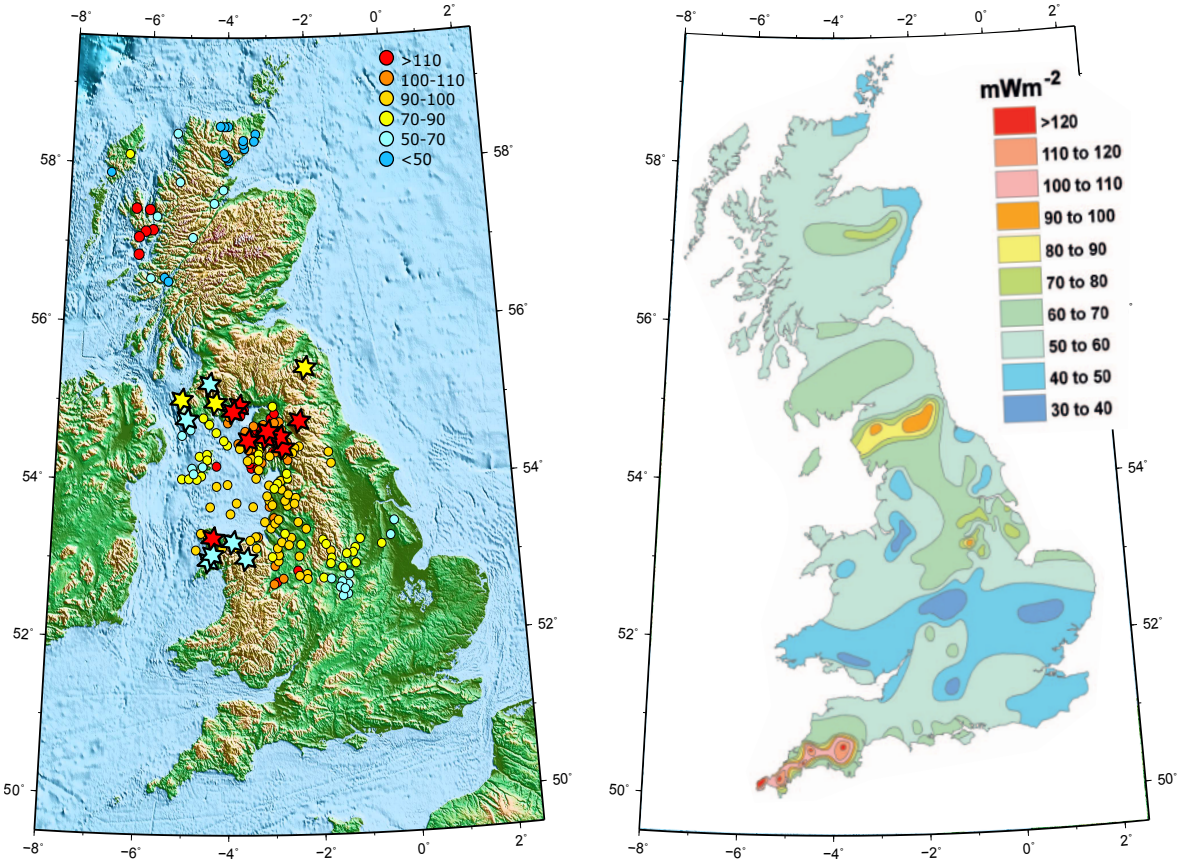

Figure 5.1: Compilation of late Cretaceous/early Palaeogene temperatures (on the left) and surface heat flow in Britain, after Busby et al. (2011) (on the right). Map of palaeotemperatures is based on the published data (Green et al. 1997, Thomson et al. 1999, Green 2002, Persano et al. 2007, Green et al. 2012)—circles and data presented in this study—stars.

between the high values of surface heat production (5–7 μW/m^3) in the Eastern Highlands batholith and its relatively low surface heat flow, 60–75 mW/m^2 (Webb et al. 1987, Lee et al. 1987). Data from the Eastgate and Rookhope boreholes, drilled in the Weardale granite in the North Pennines, show, however, a rather uniform distribution of U, Th and K with depth (Brown et al. 1987, Manning et al. 2007), suggesting that a decreasing radioactive element concentrations may be a common, but not ubiquitous feature of granites. In the case of the Lake District batholith, an exponential decrease of radioactive isotope concentrations also seems unlikely, as it would be at odds with the measured, high value of surface heat flow; for this reason, a constant concentration throughout the batholith has been assumed.

Widespread magmatic activity in NW Britain in the early Palaeogene, most probably associated with the presence of the proto–Iceland mantle plume (e.g. Stuart et al. 2000), may suggest elevated basal heat flow. The study from offshore NW Britain by Clift (1999) showed that the emplacement of magmatic underplating beneath the stretched lithosphere may significantly increase heat flow and, therefore, geothermal gradient. The peak of the heat flow is, however, attained 8–10 Ma after emplacement. The magnitude of the increase depends on the thickness of the underplated layer, the stretching factor of the lithosphere and the asthenospheric temperature (Pedersen 1993,

Table 5.1: Heat production measured in granite intrusions in central west Britain, after Downing & Gray (1986b) and references therein.

Granite intrusion	Heat production (μW/m^3)
Shap	4.3 (5.2)*
Skiddaw	3.5 (4.2)**
Ennerdale	2.8
Eskdale	1.9
Threlkeld	1.9
Weardale	3.7 (4.07)**
Loch Doon	2.5
Fleet	3.0
Criffell	2.2
Cheviot	3.0

*value in brackets refers to heat production estimated from borehole and surface data, (Downing & Gray 1986b, Lee et al. 1987), **value in brackets refers to the average heat production measured in the granite from the Eastgate borehole (Manning et al. 2007)

Clift 1999). Brown et al. (1994) showed that the influence of magmatic underplating on the geothermal gradient in the uppermost crust is rarely large; even a relatively thick magmatic underplating layer (10 km) has to be placed at depths of less than 10–15 km to cause a significant increase of the near-surface geothermal gradient. The crust in central west Britain is ∼30 km thick (Blundell & Parks 1969, Simpson & Warner 1998, Kelly et al. 2007) and the underplating layer is probably 1–3 km (Clift & Turner 1998, Al-Kindi et al. 2003). For such a thicknesses of the crust and magmatic underplating layer the geothermal gradient in the uppermost crust cannot have been changed significantly.

The thickness and the thermal properties of the Mesozoic sediments that, likely, overlay the basement rocks in central west Britain at the beginning of the Palaeogene are unknown. However, most of the sedimentary rocks and, in particular, those Late Mesozoic in age, are expected to have had a much lower thermal conductivity than the Lower Palaeozoic basement. The stratigraphic reconstruction of the overburden in northern England done by Holliday (1993) indicates that the thickness of >3 km, suggested by the first AFT studies (Green 1986, Lewis et al. 1992), would exceed the thickness of Mesozoic strata in the surrounding basins and the total thickness of the sediments on the blocks had to be in range 0.7–1.75 km. The most probable lithostratigraphic sections removed from onshore central west Britain comprise Upper Triassic–Jurassic and Upper Cretaceous rocks, most of which were carbonaceous mudstones (Holliday 1993, Chadwick et al. 1994). Thermal conductivities of the corresponding lithostratigraphic formation preserved in other parts of Britain are given in Table 5.2 and range from ∼1.3 to 2.5 W/m/K. If the eroded layer were less compacted than those still remaining

Table 5.2: Thermal conductivities of the most common Mesozoic lithostratigraphic formations in Britain; Smst:sandy mudstone, Mdst: mudstone, Lmst: limestone, Sdst: sandstone, Slst: siltstone, Slcl: silty clay, Slmd: silty mudstone; compiled after Downing & Gray (1986b).

System	Formation	Lithology	Thermal conductivity, k (W/m/K)	Uncertainty
Cretaceous	Chalk	Chlk	1.79	0.54
	Upper Greensand	Sdst	2.66	0.19
	Gault	Smst	2.32	0.04
		Mdst	1.67	0.11
	Hastings Beds	Slst	2.01	
		Slcl	1.26	
Jurassic	Kimmeridge Clay	Mdst	1.51	0.09
	Ampthill Clay	Mdst	1.51	0.03
	Oxford Clay	Mdst	1.56	0.09
	Kellaways Beds	Mdst	1.52	0.03
	Cornbrash	Lmst	2.29	0.17
	Forest Marble	Mdst+Lmst	1.80	0.07
	Frome Clay	Mdst	1.72	1.10
	Fullers Earth	Mdst	1.95	0.05
	Upper Lias	Sdst	2.87	0.12
		Mdst	1.27	0.03
		Slmd	2.22	1.10
	Middle Lias	Mdst	1.66	0.15
	Lower Lias	Mdst	1.80	1.10
Triassic	Mercia Mudstone	Mdst	1.88	0.03
	Group	Mdst	2.28	0.33
	Sherwood Sandstone	Sdst	3.41	0.09
	Group	Mdst	2.37	0.23

exposed, as would be expected given that they were less buried, those values are likely to be even lower, ∼1.0–1.5 W/m/K (Zhang 1993).

The first thermochronometric studies from central west Britain indicated that rocks now at the surface were at temperatures higher than 110°C in the Late Cretaceous/early Palaeogene (Hurford 1977, Green 1986, Lewis et al. 1992). These were converted to 3–4 km of Cenozoic exhumation, assuming a geothermal gradient similar to the present 30°C/km (Green 1986, Lewis et al. 1992). Chadwick et al. (1994) calculated amounts of denudation in the Lake District and surrounding areas, using the AFT data of Green (1986) and Lewis et al. (1992), the present day value of the heat flow and assuming probable values for the thermal conductivity of the eroded sedimentary rocks. Taking

the thermal heterogeneities into consideration, they concluded that the total Cenozoic denudation in the Lake District was between 1.2 and 2.0 km, of which 0.7–1.5 km was made of Mesozoic sedimentary rocks. Their estimate of overburden is, therefore, similar to that of Holliday (1993). There are, however, some conceptual issues with the work of Chadwick et al. (1994) that need to be addressed. Their 1-D model was based on a simplified equation that allows the amount of overburden to be calculated for given values of heat flow, thermal conductivity and temperature at the base of the eroded layer, neglecting the effect of advection due to erosion and not accounting for the temperature changes through time. The authors explored 3 different compositions of the eroded material. Their calculations result in a controversial spatial distribution of rock uplift, which a minimum in a narrow zone at the centre of the Lake District. Although a higher amount of uplift in the basins and at the flank of the block is plausible, such a sharp spatial variation in the amount of uplift does not seem to be geologically acceptable.

An elevated early Palaeogene geothermal gradient of 61°C/km has been proposed for the centre of the Lake District block by Green (2002) and a slightly lower value of ∼50°C/km for its north-western flank (Green et al. 1997). This increase in the palaeogeothermal gradient was attributed to the elevated basal heat flow in NW Britain during magmatic activity in the British Tertiary Igneous Province and was probably relatively short-lived; based on the data from the Eastgate borehole in the North Pennines, Green et al. (2012) suggested that in the latest Palaeogene/early Neogene, the geothermal gradient in the region was already similar to the present day value.

A two-fold increase of geothermal gradient in the Lake District requires a change in the basal heat flow of about 200%. Assuming a normal basal heat flow of ∼30 mW/m^2 results in the conclusion that 50 to 70% of the surface heat flow, which has been measured to vary between 60 and 100 mW/m^2, is due to radiogenic heat production. If the blanketing effect of the sedimentary cover is disregarded and the crustal heat production is kept constant then an increase in the geothermal gradient to 60°C/km requires a basal heat flow of 90 mW/m^2. This is 200% higher than the present day value. Basal heat flow of 90 mW/m^2 or more, beneath tens of kilometres thick continental crust, is unlikely; heat flow of more than 100 mW/m^2 that result almost entirely from the basal component is observed only in oceanic crust that is less than 10 Ma and thinner than 4 km (Stein & Stein 1992). Assuming a constant elevated geothermal gradient in the crust, would also significantly reduce the thickness of the crust—for a constant geothermal gradient of 60°C/km, the 550°C isotherm, which is the thermal boundary between the crust and the lithospheric mantle, would be at a depth of ∼9 km. Explaining high palaeotemperatures in central west Britain by elevated basal heat flow and constant geothermal gradient that is up to double that of the present-day value is geologically implausible.

The pattern of the AFT ages in central west Britain is still debatable. The presence of thermal anomalies and an increase of geothermal gradient at the end of the Cretaceous are, however, required to combine the AFT-derived palaeotemperatures and the geological estimates of the overburden. An elevated basal heat flow, as suggested by Green (2002) is not powerful enough to produce the necessary increase in geothermal gradient, nor the spatial variation of the AFT ages. A locally elevated heat flow and a low thermal conductivity of the overburden seem to be a more reasonable explanation for the observed age pattern. In the next sections, 1-D and 3-D thermal modelling will be performed on the new thermochronometric data presented in this study. Different uplift scenarios will be tested for the available data on the thermal properties of the rocks in central west Britain and the impact of the crustal thermal heterogeneities on the uppermost crust and thermochronometric data will be quantified and compared with the observed pattern of ages.

5.4 1D numerical model of heat transfer

5.4.1 Introduction

A simple 1-D numerical model has been used to create a thermal field within the lithosphere and quantify the effects of blanketing, underplating and denudation on the thermal field in the uppermost crust. The code, called Exhume, has been written and provided by Prof. Kerry Gallagher, University of Rennes. The code solves the heat transfer equation in 1-D within the lithosphere, which is modelled as a set of layers. The user is allowed to set the number, thickness, thermal conductivity and heat production of each layer as well to set the number and rate of exhumation episodes.

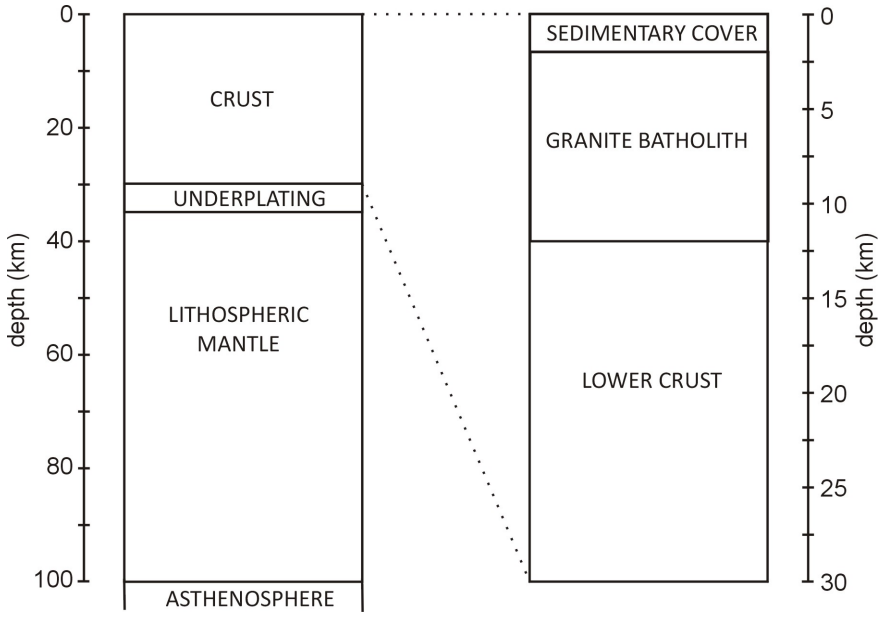

Figure 5.2: Schematic illustration of the modelled lithosphere used in the 1-D model.

In its basic form, the model was inspired by the 1-D thermal model of Brown et al. (1994) that was used for testing the influence of the magmatism on the uppermost crust in the Karoo province. The more complex model geometry used in this study assumes a 100 km thick lithosphere comprising 30 km thick crust with vertically variable thermal properties and 70 km thick lithospheric mantle. A layer of magmatic underplating is emplaced beneath the crust by setting the temperatures of the nodes at the given depth to 1100°C, which is the solidus temperature of basaltic magma at shallow levels. A schematic representation of the modelled lithosphere is shown in Fig. 5.2. Modelled scenarios are set up to constant boundary conditions: surface/upper boundary temperature, T_s, of 10°C and basal heat flow, Q_b, of 30 mW/m^2.

The effects of underplating, heat production and blanketing are quantified separately in sub-sections 5.4.2, 5.4.3 and 5.4.4. The effects will be combined for the range of parameters that most likely resemble the thermal properties of the crust in central west Britain. The obtained t-T paths will be compared with the thermal histories derived from the thermochronometric data.

5.4.2 Quantification of heating due to underplating

A layer of magmatic underplating with initial temperature of 1100°C and variable thickness was added instantaneously beneath the crust. An instantaneous emplacement of the melt gives the maximum estimates for the induced heat flow (Clift 1999). In order to separate the underplating effect from other perturbations, a simple lithospheric composition has been applied to all models, with no erosion occurring during the run. The modelled lithosphere consists of two layers: a 30 km thick crust, underlain by 70 km thick lithospheric mantle. Both have thermal conductivity of 2.5 W/m/K. A heat production term of 1 μW/m^3 has been added to the crust in order to obtain realistic values of geothermal gradient of 20–30°C/km, and surface heat flow of ∼60 mW/m^2. The model was run for 65 Ma and the underplating layer has been added instantaneously at 62 Ma. Six different values of the thickness of the underplating layer have been used: 0, 1, 3, 5, 10, 15 and 20 km.

The geotherms were calculated for the whole lithosphere and the uppermost 5 km of the crust at 61, 59, 57 and 55 Ma (Fig. 5.3 left and right panel, respectively). Thin underplating layers cool quickly; a 1 km thick layer is at ∼600°C after 1 Myr, only ∼40°C higher that the initial temperature of the background. Due to the high thermal resistance of the lithosphere, the heat is transferred slowly; after 1 Ma, the thermal field of the uppermost 15 km of the crust remains undisturbed. Small perturbations occur in the uppermost 5 km after ∼3 Ma and the maximum perturbations are attained after 6–8 Ma, depending on the thickness of the underplating layer. The maximum change of temperature at 5 km varies from ∼25°C to ∼5°C for a thickness of the underplating layer of 20 km and 1 km, respectively. At a depth of 2 km, which corresponds to the

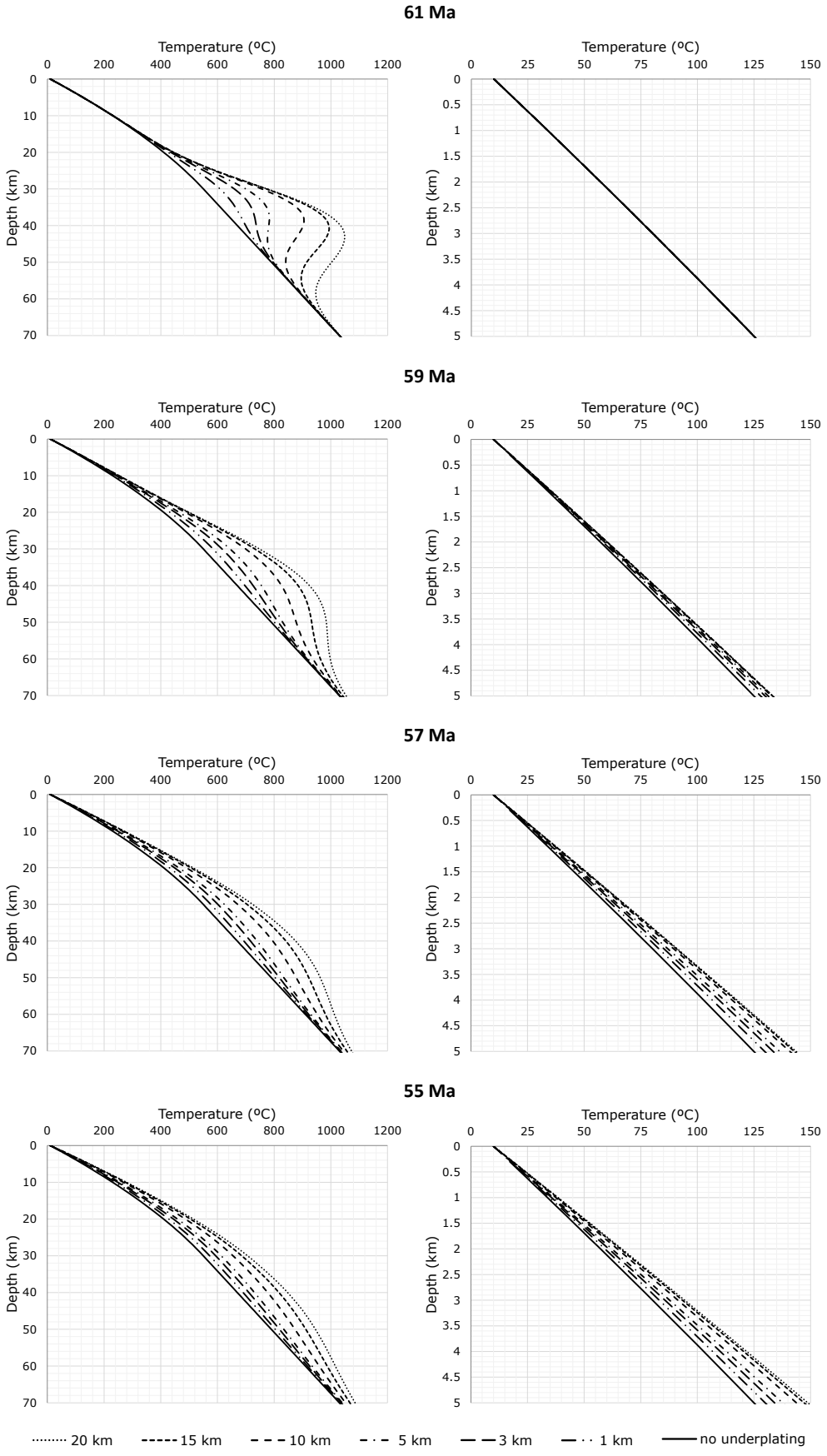

Figure 5.3: The geotherms at 61, 59, 57 and 55 Ma for different thicknesses of magmatic underplating. The undeplating was emplaced instantaneously at 62 Ma at depth of 30 km; the initial temperature of the magma is 1100°C. Left panel—temperature changes within the lithosphere up to a depth of 70 km; right panel—-temperature changes within the uppermost 5 km of the crust.

amount of erosion predicted by geological constraints, temperature rises by ∼10°C for a 20 km thick layer and by only 1–2°C for 1 km thick layer.

In the case where underplating is the only cause of enhanced heat flow, temperature changes in the uppermost 2 km of the crust are, therefore, almost negligible and have no impact on the low temperature thermochronometers. Underplating would have a major effect on the temperature field of the crust if the magma was emplaced at shallower depths. Even in these cases, heating from a less than 5 km thick layer would only perturb the temperatures of rocks in its vicinity. Rapid exhumation can advect the heat produced by at depth, however, it simultaneously enhances cooling of rocks close to the surface. As shown by Brown et al. (1994), in case of exhumation and underplating occurring simultaneously, heating dominates the lower part of the crust, whereas in the upper crust cooling has a predominant effect. This implies that advection of heat from the underplating layer is unlikely to affect the shallowest crustal levels. In summary, apart from the specific conditions, where the crust is thin and/or the magmatic underplating layer thick, underplating does not seem to have an impact on the thermal field of the uppermost crust that could be measured by thermochronometry.

5.4.3 Quantification of heating due to crustal heat production

Radiogenic decay of U, Th and K contributes to the crustal thermal regime and may change the surface heat flow by more than 50%. The effect of heat production has been quantified by adding a heat productive body to the upper crust. The body is assumed to be 12 km thick, to simulate the most probable size of the Lake District and Weardale batholiths (Bott 1974, Simpson & Warner 1998). The modelled lithosphere consists of three layers: (1) 70 km thick lithospheric mantle characterized by thermal conductivity of 2.5 W/m/K and no heat production, (2) 18 km thick lower crust characterized by thermal conductivity of 2.5 W/m/K and constant heat production of 1 μW/m^3, and (3) 12 km thick upper crust characterized by the thermal conductivity of 3 W/m/K and constant and uniform heat production that varies from 0 to 5 μW/m^3 between the runs.

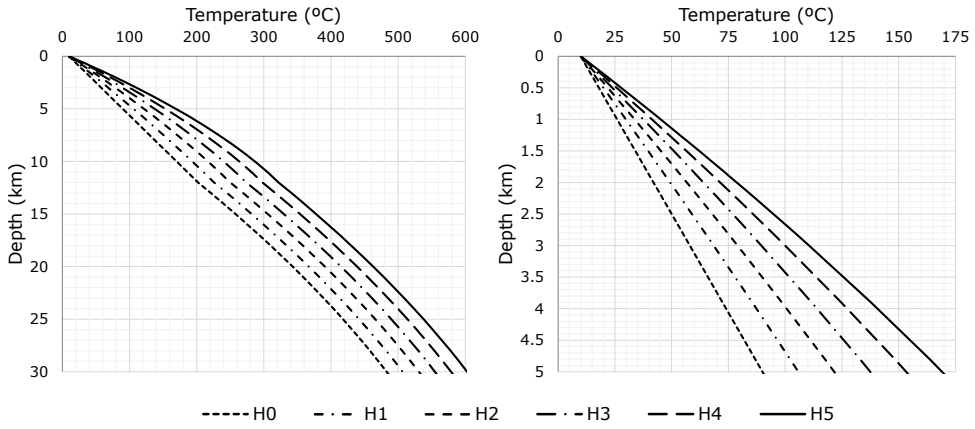

Figure 5.4: The geotherms for the whole crust (left graph) and the uppermost 5 km of the crust (right graph) comprising a 12 km thick body with different value of heat production.

Use of the constant thermal conductivity value aims to isolate an impact of the heat production.

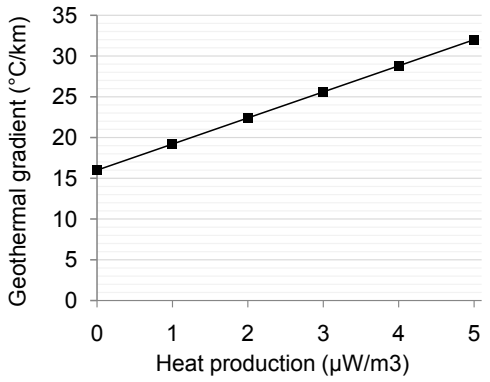

Figure 5.5: Dependence of the radiogenic crustal heat production on the geothermal gradient. The geothermal gradients have been calculated for the uppermost 5 km of the crust that comprises a 12 km thick heat producing body. See text for more details on the model parameters.

The geotherms for the whole crust and for the uppermost 5 km are shown in Fig. 5.4. Increasing the heat production value by 1 μW/m^3 increases the temperature at 5 km depth by ∼15°C and by ∼10°C at 2.5 km. Therefore, the change between the 'normal' upper crustal heat production of 1 μW/m^3 and the maximum modelled value of 5 μW/m^3 gives ∼60°C of total temperature change at depth of 5 km, and ∼40°C at depth of 2.5 km. In such scenario, the surface heat flow is increased by ∼80%.

Changes of the upper crustal geothermal gradient for different values of heat production are shown on Fig. 5.5. For the modelled parameters, the value of geothermal gradient increases by 3.2°C when the heat production is increased by 1 μW/m^3, which implies a ∼67% change of the geothermal gradient if the heat production varied between 1 and 5 μW/m^3. However, some sedimentary rocks characterized by low heat production (e.g. mudstone, siltstone) have a thermal conductivity lower than the value used in the model (k = 3.0 W/m/K—mean crustal thermal conductivity; Turcotte & Schubert 2002). In such cases the geothermal gradient would be higher than the one calculated in the model, due to the effect of the low thermal conductivity of the rocks and the change of the geothermal gradient between the rocks of different heat production would be smaller. In general, the model indicates that crustal heat production may have an effect on the geothermal gradient high enough to perturb the thermochronometric data. An important implication of this finding is that lateral variation in heat production, common when the lithologies change, produces a local variation in the thermochronometric ages that could be erroneously interpreted as different exhumation.

5.4.4 Quantification of heating due to blanketing

The presence of a layer of overlying low conductivity rocks may result in a blanketing effect, which has been investigated by applying several values of thermal conductivity to the top layer of the uppermost crust. The lithosphere consists of 70 km thick lithospheric mantle characterized by thermal conductivity of 2.5 W/m/K and no heat production and a 30 km thick crust characterized by thermal conductivity of 2.5 W/m/K and constant heat production of 1 μW/m^3. The uppermost part of the crust, 0.5–2.0

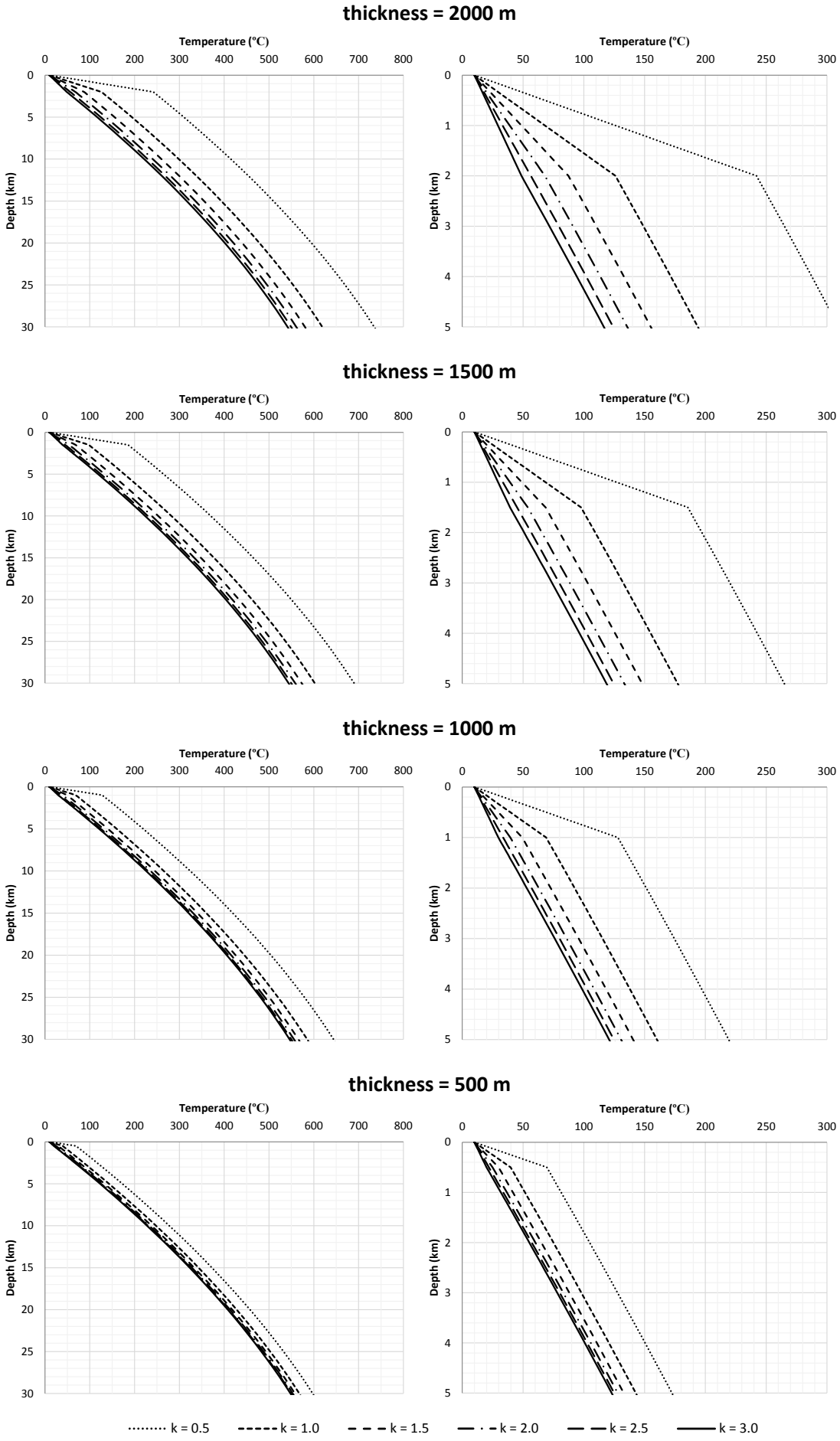

Figure 5.6: The geotherms for the whole crust (left panel) and for the uppermost 5 km of the crust (right panel) covered by the layer having different thermal conductivity (k). The geotherms are shown for four different thicknesses of the low thermal conductivity layer: 500, 1000, 1500 and 2000 m.

km thick was characterized by no heat production and values of thermal conductivity that vary between 0.5–3.0 W/m/K. This combination of parameters should reflect a wide range of possible thicknesses and insulating properties of a sedimentary layer.

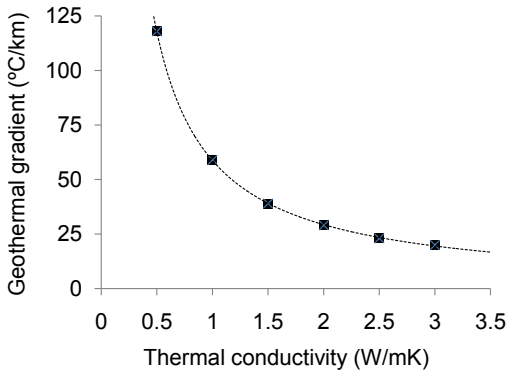

Figure 5.7: Dependence of geothermal gradient on the thermal conductivity of rocks. The geothermal gradient has been calculated for a 1 km thick layer of sediments characterized by different thermal conductivity values. See text for more details on the model parameters.

The calculated geotherms for the whole crust and for the uppermost 5 km are shown in Fig. 5.6. The characteristic kink on the geotherms reflects the boundary between the 'normal' crust and the sedimentary layer. The relation between the geothermal gradient and the thermal conductivity is a power function and, therefore, temperatures increase rapidly for thermal conductivities below 1.0 W/m/K (Fig. 5.7) and the geothermal gradient may reach abnormally high values ∼60–120°C/km. Even for higher values of thermal conductivity, the changes in the upper crust temperatures are still important. The geothermal gradient within the crust below the sedimentary rocks is, however, almost not affected by the presence of the blanket; for the modelled parameters, the geothermal gradient within this layer remains low, 23.3 ± 0.3 °C/km, in all runs.

Thermal conductivity within a sedimentary layer of the same lithology may be variable, as it strongly depends on porosity and saturation (Clauser & Huenges 1995, Eppelbaum et al. 2014); it is, therefore, expected to be lower within less compacted sediments at the top of the section where it is likely to be in the range of ∼1.0–1.5 W/m/K. When such low values are taken into account, the temperature within the underlying crust would be higher by ∼23–53°C or ∼16–35°C for a sediment blanket 1.5 or 1.0 km thick, respectively. The influence of blanketing on the uppermost crustal thermal field is, therefore, significant and the resulting temperature increase can easily affect the thermochronometric data. If the blanketing effect is not taken into consideration when the palaeotemperatures are transferred into exhumation, the denudation amount may be significantly overestimated.

5.4.5 Results from the 1-D modelling

If high heat production and low thermal conductivity are combined, then they would both contribute to increase the thermal field. This is due to the fact that the heat produced by a granite batholith cannot be easily released and the geothermal gradient in the overlying sedimentary layer may become high even if any other thermal per-

turbation, e.g. magmatism and hot fluid flow, are not present. Underplating at the base of the crust and elevated basal heat flow may additionally contribute to increase temperature within the crust, but their effect in the shallowest crustal levels is minor (Brown et al. 1994).

The processes of underplating, heat production and blanketing have been combined in one model that uses a layered lithosphere resembling that of central west Britain. Given that the number of possible evolutionary scenarios is practically infinite, the aim of the 1-D model is not to find the accurate value for each parameter of the lithosphere, but to explore a range of parameter values compatible with the thermal histories derived from the thermochronometric analyses. The modelling has two stages. Firstly, the Lake District, which is the region of highest heat flow in the study area, was modelled, investigating the range of overburden and denudation parameters that reproduce the t-T paths derived from the thermochronometric data. The best fitting values were then used for a 'normal' crust characterized by heat production of 1 μW/m^3. The same denudation scenario was also applied to crust with no sedimentary cover, with or without a heat producing body. The results were then compared to the Late Cretaceous/early Palaeogene temperatures retrieved from the thermochronometric data at different sites in central west Britain to test the hypothesis that the palaeotemperature pattern is the result of the local thermal properties of the crust, rather than spatially-variable denudation.

All models have been run for 65 Ma. The variables were: i) thickness of the sediment layer, ii) thermal conductivity of the sediment layer, iii) thickness of underplating layer, and iv) amount of denudation. Four values for the sediment layer thickness have

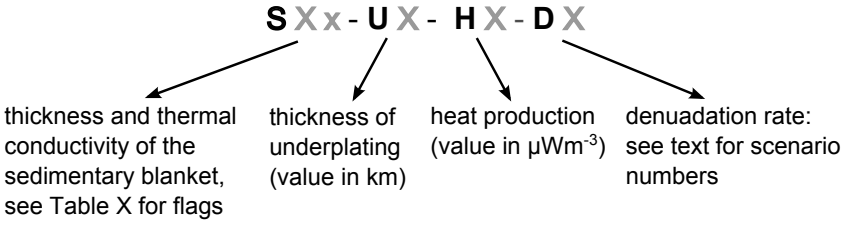

thickness of the sediment layer		thermal conductivity			denudation rate		
value (km)	flag	value (W/m/K)	flag	%	65 - 63 Ma	62 - 50 Ma	50 Ma - rec.
					scenario 1		
0.0	0	0.5	a		0	75	10
0.5	1	1	b		scenario 2		
1	2	1.5	c		0	125	10
1.5	3	2.0	d		scenario 3		
2	4	2.5	e		0	175	10

Figure 5.8: Top: The scheme used for all the models. Bottom: The flags for parameters of the sediment layer and denudation scenarios used in the models. Example: S1b–U3–H4–D1 refers to a model that includes a crust with a 0.5 km thick sediment blanket of thermal conductivity 1.0 W/m/K, a granite batholith with heat production of 4 μW/m^3, a 3 km thick underplating, and is subjected to a slow denudation of 75 m/Myr during 62–50 Ma and then 10 m/Myr.

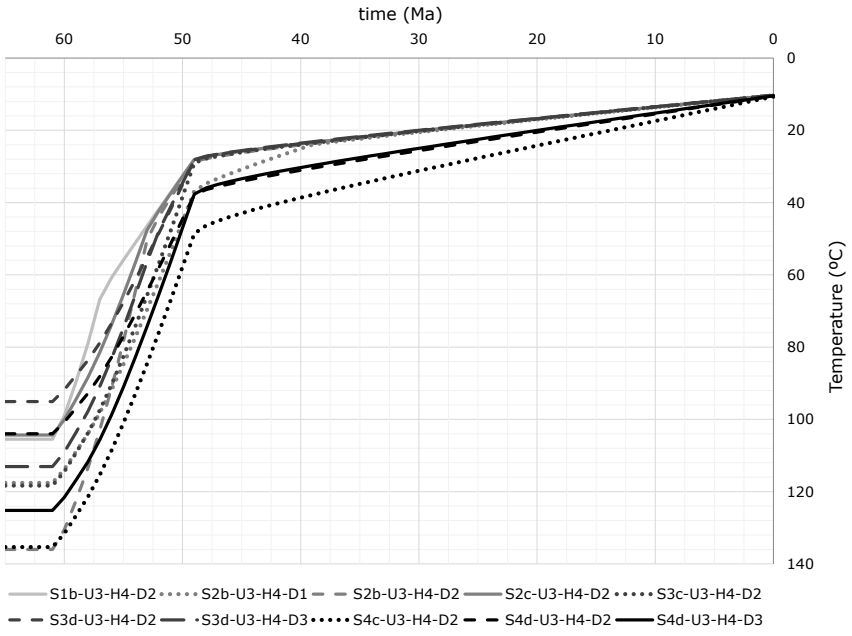

Figure 5.9: The time-temperature paths of rocks that would end up at the surface for 10 models best resembling cooling paths of rocks in the Lake District. See Fig. 5.8 for scenarios names and used parameters.

been used: 0.5, 1.0, 1.5 and 2.0 km. Such a range should embrace all possible geological scenarios. For thermal conductivity of sediments, three values have been used: 1.0, 1.5 and 2.0 W/m/K, which resemble the range of poorly compacted, sedimentary cover (Clauser & Huenges 1995) and are similar to those suggested by Holliday (1993) and Chadwick et al. (1994). Based on the measured values of heat production in the Lake Distict and Weardale plutons, the most representative, average value seem to be $\sim$4.0 μW/m^3 (see Section 5.3). Two values for thickness of the magmatic underplating have been used: 1.0 and 3.0 km. The underplating layer was added instantaneously at 62 Ma. Three scenarios with total denudation of 1.4, 2.0 and 2.6 km have been tested; all scenarios were characterized by fast denudation rates between 62–50 Ma, followed by a slow denudation period in the last 50 Ma. The flags for the denudational scenarios, parameters of the blanket and the name scheme for all models are given in Fig. 5.8.

The t-T paths for 10 models, best resembling the thermal histories derived from the thermochronometric data in the Lake District, show maximum temperatures of $\sim$100–140°C (Fig. 5.9). Maximum temperatures attained by rocks that denudation brought up to the surface depends mostly on the thickness and thermal conductivity of the sediments. The effect of underplating is negligible. The results imply that for the assumed erosional scenarios, the most probable thickness of the sediment layer is 1.5–2.0 km and 1.0-1.5 km, for thermal conductivities of 1.5–2.0 W/m/K and 1.0–1.5 W/m/K, respectively.

For the second stage of modelling a thermal conductivity of 1.5 W/m/K has been assumed and applied to a 1 or 2 km thick blanket. The geotherms for six different crust compositions that experienced 2 km of denudation are shown in Fig. 5.10. Not surprisingly, the maximum temperature of the rocks that would end up on the sur-

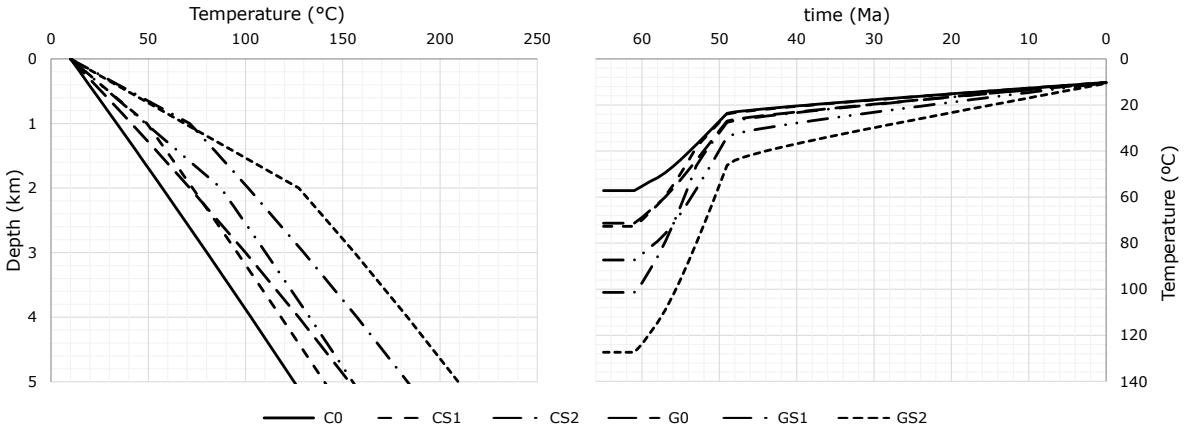

Figure 5.10: The geotherms for the uppermost 5 km of the crust for six different crust compositions: C0–'normal' crust, with low heat production, 1 μW/m^3, uncovered, CS1–'normal' crust covered by a 1 km thick layer of low conductive, 1.5 W/m/K, sediments, CS2–'normal' crust covered by a 2 km thick layer of low conductive, 1.5 W/m/K, sediments, G0–crust comprising a granite batholith, 12 km thick, with a heat production of 4 μW/m^3, uncovered, GS1–crust comprising a granite batholith, covered by 1 km of low conductive, 1.5 W/m/K, sediments, GS2–crust comprising a granite batholith, covered by 2 km of low conductive, 1.5 W/m/K, sediments. Total denudation in all scenarios was 2 km. See text for more details.

face, was the lowest,(∼57°C) in case of the uncovered 'normal' crust and the highest (∼127°C) for the crust comprising a heat productive granite with 2 km thick blanket. Even if a 2 km thick sedimentary cover with a 1.5 W/m/K conductivity may be considered an end-member scenario, the almost 70°C difference between the two model outputs demonstrate the importance of taking the thermal structure of the crust into account when interpreting thermochrometric data. Fig. 5.10 shows also that the temperature in the crust comprising the heat producing granite covered by at least 1 km of low conductive sediments will be high enough to reset the AFT system. In the case of a crust with a 'normal', low heat production, for the same amount of the overburden, the temperature will be high enough to completely reset the AHe, but only partially the AFT system. Although different heat production values (in this case 1 or 4 μW/m^3) solely produce a variation in temperatures, the presence of the blanket additionally enhances this effect. For the rock that would end up on the surface, the temperature difference between the crust with or without the heat productive granite is only 14°C if the sedimentary blanket is absent (lines: C0 and G0 on Fig. 5.10), but if the blanket is 2 km thick, the difference in temperatures reaches 40°C (lines: CS2 and GS2 on Fig. 5.10). In the modelled scenarios, the geothermal gradient in the 'normal' crust is ∼23°C/km, in the granite ∼28–30°C/km, in the sediments overlying the 'normal' crust ∼38–39°C/km and in the sediments overlying the granite ∼59–61°C/km. The high geothermal gradient in the granite case is the combined effect of an increased heat flow due to high heat production in the granite and the blanketing effect of the overlying sedimentary cover.

5.4.6 Summary

The 1-D modelling shows that high radiogenic heat production and low conductive sedimentary blanket are powerful enough to cause significant perturbations within the thermal field of the uppermost crust; these perturbations can affect the thermochronometric ages. For low thermal conductivity, <1.5 W/m/K, the geothermal gradient within the blanket layer may be >40°C/km. The effect of the magmatic underplating has a minor effect on the shallowest crustal levels and, for the thickness and depth of underplating constrained in central west Britain, is negligible.

The results of the 2nd stage of the 1-D modelling imply that the pattern of the late Cretaceous/early Palaeogene temperatures noted in onshore central west Britain may be explained by different heat production and spatially variable thickness of the sedimentary blanket and does not require any significant, lateral changes in the Cenozoic denudation that probably, nowhere in central west Britain exceeded 2 km.

The presented model has, however, some limitations. It is 1 dimensional and so it does not deal with spatial variations of the crustal thermal properties. The Exhume code allows the calculation of the thermal structure of the crust for given, finite parameter values; in order to explore all the possible scenarios using a forward model, an enormous number of runs has to be investigated. Finally, the thermal histories derived for Exhume have to be compared to those reconstructed using the thermochronometric data only visually and the information have to be extracted by hand. For all these reasons, a complex 3-D model has been used in the next step. The last version of the software is implemented by an inversion mode that efficiently searches for the most possible range of denudation scenarios for a given set of thermochronometic data.

5.5 3D numerical modelling of heat transfer

5.5.1 Introduction

The influence of topography on the thermal field of the uppermost crust is well recognized (e.g. Stüwe et al. 1994, Stüwe & Hintermüller 2000, Ehlers & Farley 2003) and it has been shown that the upper crustal isotherms mimic the shape of the Earth surface. Topography may, therefore, significantly affects the pattern of thermochronometric ages, especially for the low temperature systems like the AHe method(e.g. Ehlers & Farley 2003). This effect is pronounced in high relief areas, but, for relatively slow denudation rates, it may also be present in regions where topography is moderate and relatively smooth. The 1-D model has clearly shown that the presence of a high radiogenic heat producing body covered with a low conductivity sedimentary blanket has a marked effect on the thermal field of the shallow crust and cannot be ignored when interpreting thermochronometric ages. Spatially variable thermal properties of the crust

have to be, therefore, accounted for when the thermochronometric data are being used to extract amounts of uplift and denudation. Complex 3-D modelling that accounts for both topographic changes and crustal thermal heterogeneities can be performed using the Pecube software (Braun 2003, Braun et al. 2012).

Pecube solves the heat transfer equation in the following form:

$$\frac{\partial T}{\partial t} + v_x \frac{\partial T}{\partial x} + v_y \frac{\partial T}{\partial y} + v_z \frac{\partial T}{\partial z} = \kappa \frac{\partial^2 T}{\partial x^2} + \kappa \frac{\partial^2 T}{\partial y^2} + \kappa \frac{\partial^2 T}{\partial z^2} + A \tag{5.4}$$

where:
κ is the thermal diffusivity, $\kappa = k/\rho/c$, expressed in km^2/Myr
A is the heat production rate expressed in $^\circ C/Myr$

In this form, the thermal conductivity term is replaced by the thermal diffusivity, the property describing how fast the temperature field of a solid changes with time (Eppelbaum et al. 2014). Such substitution allows efficient accounting for variations in the rocks density, ρ, and heat capacity, c, which in the basic form of the equation (5.3) have to be input directly, and usually are kept constant. It is recommended to use thermal diffusivity, rather than thermal conductivity, especially in the case of non-steady state heat conduction. The combined effect of the sedimentary blanket that keeps the heat within the underlying rock and erosion that produces cooling can be described as the ability of the rock to conduct thermal energy (cooling), versus its ability to store it (heating).

A misfit function (μ) between the observed and predicted data is evaluated using:

$$\mu = \frac{1}{N - p - 1} \sum_{i=1}^{N} \frac{(O_i - P_i)^2}{{\sigma_1}^2} \tag{5.5}$$

where
N is the number of data points
O is the observed age
P is the predicted age
σ is the uncertainty of the observed age
p is the number of model parameters

If μ is lower than 1, the average model fits the data within the given uncertainties.

During this study the misfit function has been evaluated for the central AFT and AHe ages. Although the track length distributions has been determined for almost all samples and several ZHe ages are available, they have not been included in the input data file. This choice was motivated by the fact that Pecube predicts the data

for a standard, constant He diffusion and track annealing kinetics. Without having the opportunity to input variable kinetics, the spread of the ZHe age due to radiation damage makes the data uninformative. The same is true for the fission track length distributions, as the D-Par values indicate that the analysed apatites are variable in composition. In order to take the measured variation in AFT and AHe ages due to chemical composition and radiation damage into consideration, the uncertainties on the data are set to 2σ.

In section 5.5.2 the results of the forward modelling using Pecube will be presented. The aim of the forward modelling is to compare the influence of the different spatial distributions of the crustal thermal properties and derive the best range of parameters for the inversion runs. The inversion stage is presented in section 5.5.3. The last section contains a discussion of aspects of the modelling itself and the influence that simplifications have on the results of the modelling exercise.

5.5.2 Testing scenarios of crustal thermal regimes

5.5.2.1 Introduction

During the first stage of Pecube modelling, a set of forward models have been prepared in order to find preliminary scenarios that reproduce a similar age pattern and have low misfit to the data. The typical Pecube run assumes a 30 km thick crust. The basal and surface temperature are 550°C and 10°C, respectively. The topography is derived from the 1 arc–minute ETOPO1 "Bedrock" digital elevation model (DEM); in order to shorten computing time, skipping factor, the parameter used to lower the DEM resolution, was set to 10. The uplift function was spatially uniform and the rock uplift rate differed between two intervals: a rapid uplift between 62–57 Ma and slow uplift thereafter. At the beginning of the tectonomorphic scenario there is no topography, which is then created between 60–0 Ma. This reconstruction mimics the flooding of the region by the shallow Late Cretaceous sea (Ziegler 1988).

To quantify the bias that would be incorporated in an interpretation of thermochronometric ages when radiogenic heat production in the crust and the blanketing effect are not taken into account, three sets of models of a different geometry are investigated.

5.5.2.2 Uniform crust

The first set of models comprises a uniform crust characterized by thermal diffusivity of 25 km^2/Myr and a heat production of 10, 12 or 15°C/Myr. For spatially uniform uplift, the AFT age distribution does not resemble the observed age pattern and the spread of ages is governed only by changes in topography (Fig. 5.11). For a 10°C/Myr heat production, obtaining ages in the range of 60–70 Ma in the Lake District requires ∼5 km of Cenozoic uplift and underestimated ages in southern Scotland and northern

Table 5.3: Geothermal gradient and predicted AFT ages range for three values of heat production: 10, 12 and 15 °C/Myr (equivalent to 0.8, 0.96 and 1.2 μW/m^3) in a uniform crust characterized by thermal diffusivity of 25 km^2/Myr and total rock uplift of 4 km.

Heat production (°C/Myr)	Geothermal gradient (°C/km)	AFT age range (Ma)
10	23	83–268
12	24	72.6–238
15	25.5	66–181

Wales. The uplift of 4 km results in older ages in Scotland and Wales, to >150 Ma, however, the same old ages are proposed for the Lake District. The assumption of a uniform crust therefore requires the uplift in the Lake District to be >1 km higher than in the surrounding regions.

Higher values of heat production do not change the spatial pattern of the ages. However, because the geothermal gradient increases, the amount of uplift required to obtain the desired age range decreases (Table 5.3). For instance, increasing the heat production term by 5°C/Myr, which is equivalent to 0.4 $\mu W/m^3$, increases the geothermal gradient by 2.5°C/km and, for an uplift of 4 km, reduces the predicted AFT age from 83–268 Ma to 66–181 Ma.

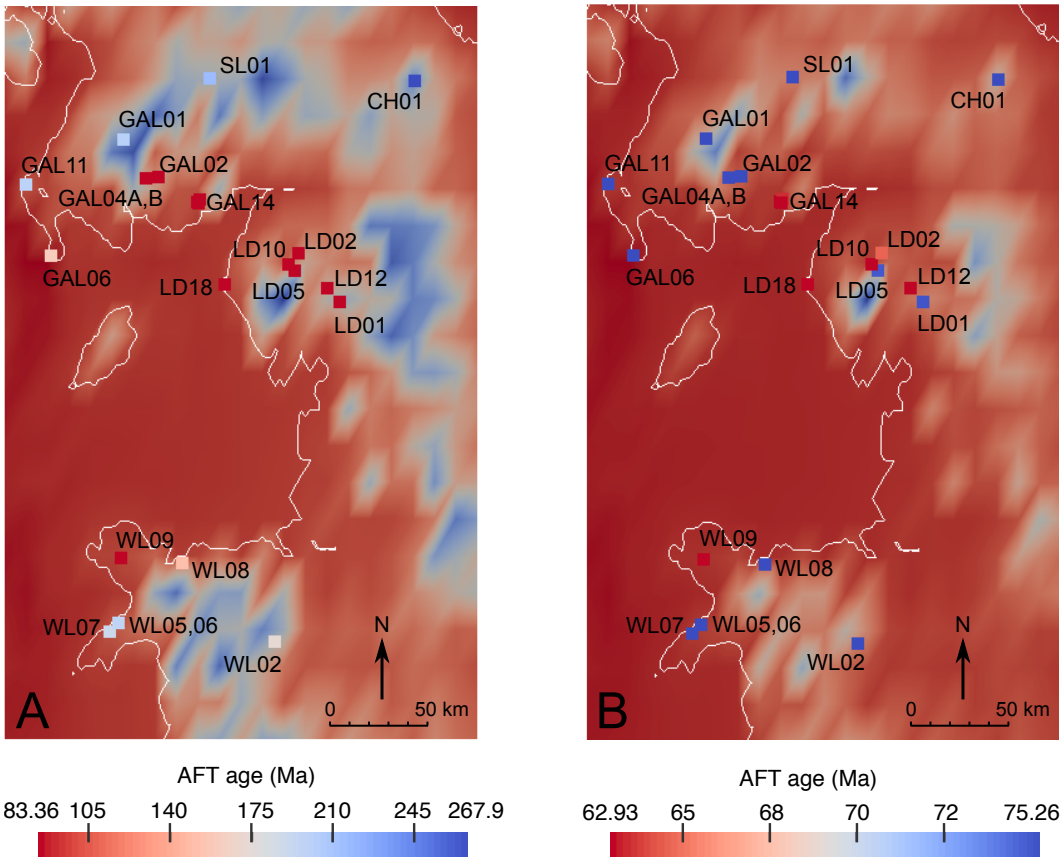

Figure 5.11: Predicted apatite fission track age distributions for a uniform crust and two erosional scenarios: (A) total uplift of 4 km and (B) total uplift of 5 km. Squares are the observed AFT ages (this study). See text for more details on model parameters.

Heat production (°C/Myr)	AFT ages (Ma)	Max temp (°C)
—Uplift = 3.0 km—		
50/30/10	66–350	72–106
40/25/12	73–344	75–104
—Uplift = 3.5 km—		
50/30/10	62–324	84–125
40/25/12	63–312	87–120
—Uplift = 4.0 km—		
50/30/10	62–260	95–143
40/25/12	62–228	99–135

Table 5.4: Predicted ranges of AFT ages and maximum palaeotemperatures for different amounts of uplift and crustal heat production patterns. Heat production values are given in order: LD/Scot/background, where *LD* is the value used for the Lake District batholith and *Scot* is the value used for Criffell, Fleet and Loch Doon plutons. See text for more details on model parameters.

5.5.2.3 Heat production

In the second set of the forward models, heat producing bodies have been added into the upper crust. The Lake District batholith was modelled as a 12 km high cylinder with a radius of 36 km characterized by uniform and constant heat production of 40 or 50°C/Myr, equivalent to 3.2 and 4 μW/m^3, respectively. Three small (10 km radius) bodies characterized by heat production of 25 or 30°C/Myr have been added in southern Scotland at the locations of the Criffell, Fleet and Loch Doon plutons. For values of 40 and 25°C/Myr in the granite bodies, the background heat production has been set to 12°C/Myr; for the heat production in granites of 50 and 30°C/Myr, the background heat generation has been set to 10°C/Myr. This combination allows comparison of age patterns for both spatial moderate and sharp heat production change.

When the high heat production is applied, the predicted AFT ages decrease in the Lake District and their pattern resembles the "U-shape" found in the observed AFT ages (Fig. 5.12). The presence of small heat producing bodies in the three main granite plutons in southern Scotland seems to be helpful in resolving the pattern of ages in the region. The inclusion in the model of these bodies is simply based on the fact that they have a granitic composition and a relatively high heat production of 2.2–3.0 μW/m^3 (Table 5.1). No heat flow anomaly is presented on the heat flow map of southern Scotland, however, the map has low resolution.

To obtain AFT ages similar to the data, 3.5–4.0 km of total uplift is required. Predicted AFT ages in the Late District are insensitive to changes in the amount of uplift, if this is greater than ∼3 km (Table 5.4). The AFT ages in southern Scotland and northern Wales change depending on the amount of uplift. Although the heat produc-

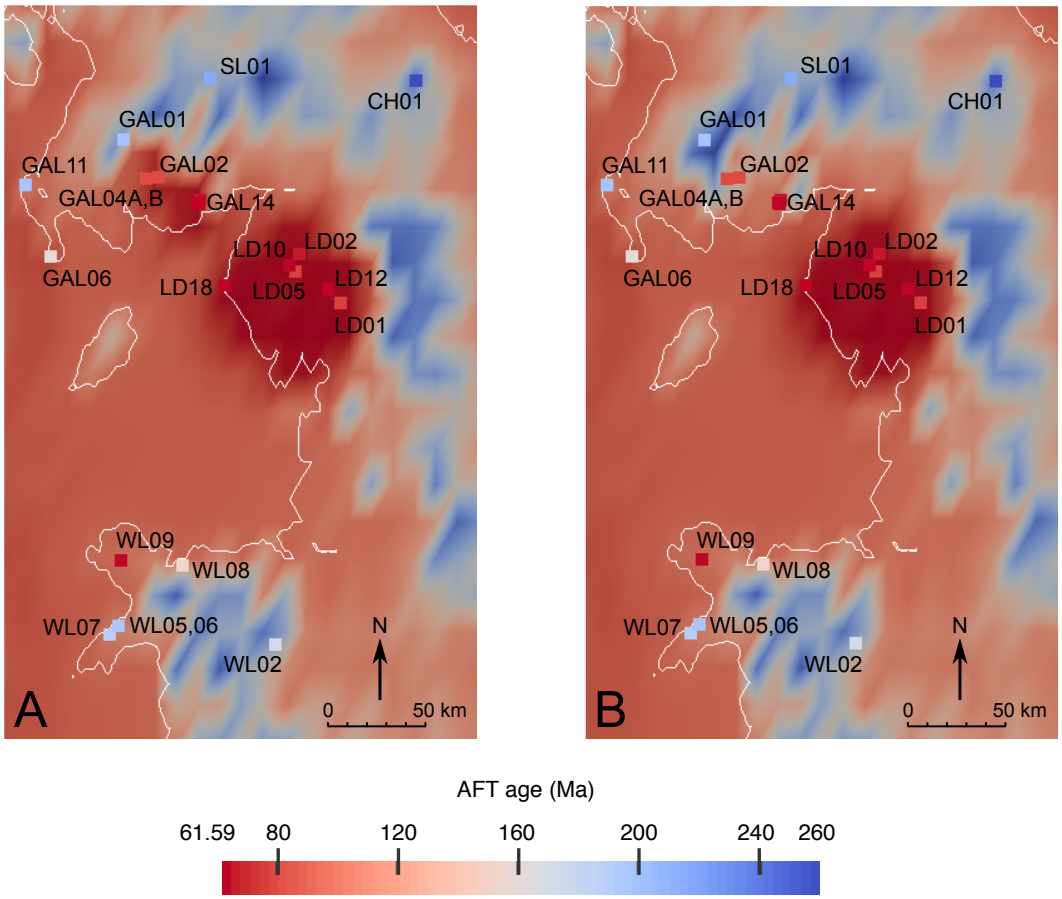

Figure 5.12: Predicted apatite fission track age distributions for a crust comprising heat producing granite batholiths in the Lake District, Criffell, Fleet and Loch Doon (A) or only in the Lake District (B). Heat production of the Lake District granite was set to 50°C/Myr and at Criffell, Fleet and Loch Doon to 30°C/Myr. The same erosional scenario, that gives total uplift of 4 km, has been applied in both models. Squares are the observed AFT ages of samples analysed during this study. See text for more details on model parameters.

tion pattern does not have an important influence on the predicted ages and maximum palaeotemperatures (Table 5.4), if the background heat production is higher, slightly less uplift is required and the ages are reduced.

5.5.2.4 Blanketing and heat production

The third set of the forward models includes a layer of low conductive sediments overlying the whole study area. The sedimentary blanket was present at the beginning of the run as a layer characterized by low thermal diffusivity. The layer thickness is assumed to be spatially uniform. Two values of thermal diffusivity have been used: 15 and 10 km^2/Myr; 15 km^2/Myr is the measured average value for mudstone and chalk after Eppelbaum et al. (2014) and 10 km^2/Myr is a hypothetical value that would characterise uncompacted sediments. Three thicknesses of the sediments layer have been tested: 1.0, 1.5 and 2.0 km. Thermal diffusivity of 10 km^2/Myr has been applied only to a 1 km thick layer; the use of such low value for thicker layers would be unreasonable as thermal conductivity increases with compaction down the profile. The crust below the sediments contain heat productive bodies in the Lake District, Criffell, Fleet and

Heat production (°C/Myr)	AFT ages (Ma)	Max temp (°C)
—Uplift = 2.5 km—		
—Sedim: 1 km, κ = 10 km^2/Myr—		
50/30/10	62–280	92–143
40/25/12	62–252	97–132
—Uplift = 3.0 km—		
—Sedim: 1.5 km, κ = 15 km^2/Myr—		
50/30/10	62–285	92–142
40/25/12	62–260	96–132
—Uplift = 3.0 km—		
—Sedim: 1.0 km, κ = 15 km^2/Myr—		
50/30/10	62–314	86–134
40/25/12	62–297	90–124

Table 5.5: Predicted ranges of AFT ages and maximum palaeotemperatures for different amounts of uplift, sedimentary blanket parameters and crustal heat production patterns. Heat production values are given in order: LD/Scot/background, where *LD* is the value used for the Lake District batholith and *Scot* is the value used for Criffell, Fleet and Loch Doon plutons. See text for more details on model parameters.

Loch Doon, which parameters have been given in the previous subsection.

The results from the models are highly dependant on the thickness and thermal diffusivity of the sedimentary blanket. The acceptable fit to the data for each of the four combinations of the parameters are presented in Fig. 5.13. The ranges of predicted AFT ages and maximum palaeotemperatures for different blanket properties and different heat production patterns are given in Table 5.5. There are no significant changes caused by different heat production pattern. For the same amount of uplift and blanket type, the higher background heat production results in a narrower range of predicted maximum palaeotemperatures; the maximum ages are only slightly younger and the minimum ages do not change for a given amount of uplift.

For thermal conductivity of 15 km^2/Myr, 3 km of uplift results in a good data fit (μ <2.5), if the thickness of the blanket is 1.5 km (Fig 5.13-A). If the blanket is 2.0 km thick, most of the predicted ages in southern Scotland are younger than the data. If the blanket is kept at 2.0 km and the amount of uplift is reduced, the predicted ages in southern Scotland become older and a better fit to the observed data, however, the predicted denudation is too small to remove the sedimentary layer entirely from the hills. The lack of late Mesozoic sedimentary cover in southern Scotland indicates that

Figure 5.13: (On the next page.) Predicted apatite fission track age distributions for a crust comprising heat productive granite batholiths in the Lake District, Criffell, Fleet and Loch Doon covered by four different types of low conductive sedimentary layer: (A) 2.0 km thick layer with thermal diffusivity of 15 km^2/Myr, (B) 1.5 km thick layer with thermal diffusivity of 15 km^2/Myr, (C) 1.0 km thick layer with thermal diffusivity of 15 km^2/Myr and (D) 1.0 km thick layer with thermal diffusivity of 10 km^2/Myr. In these scenarios, rocks were subjected to total uplift of 3 km (A & B), 3.5 km (C) and 2.5 km (D). Squares are the observed AFT ages of samples analysed during this study. See text for more details on model parameters.

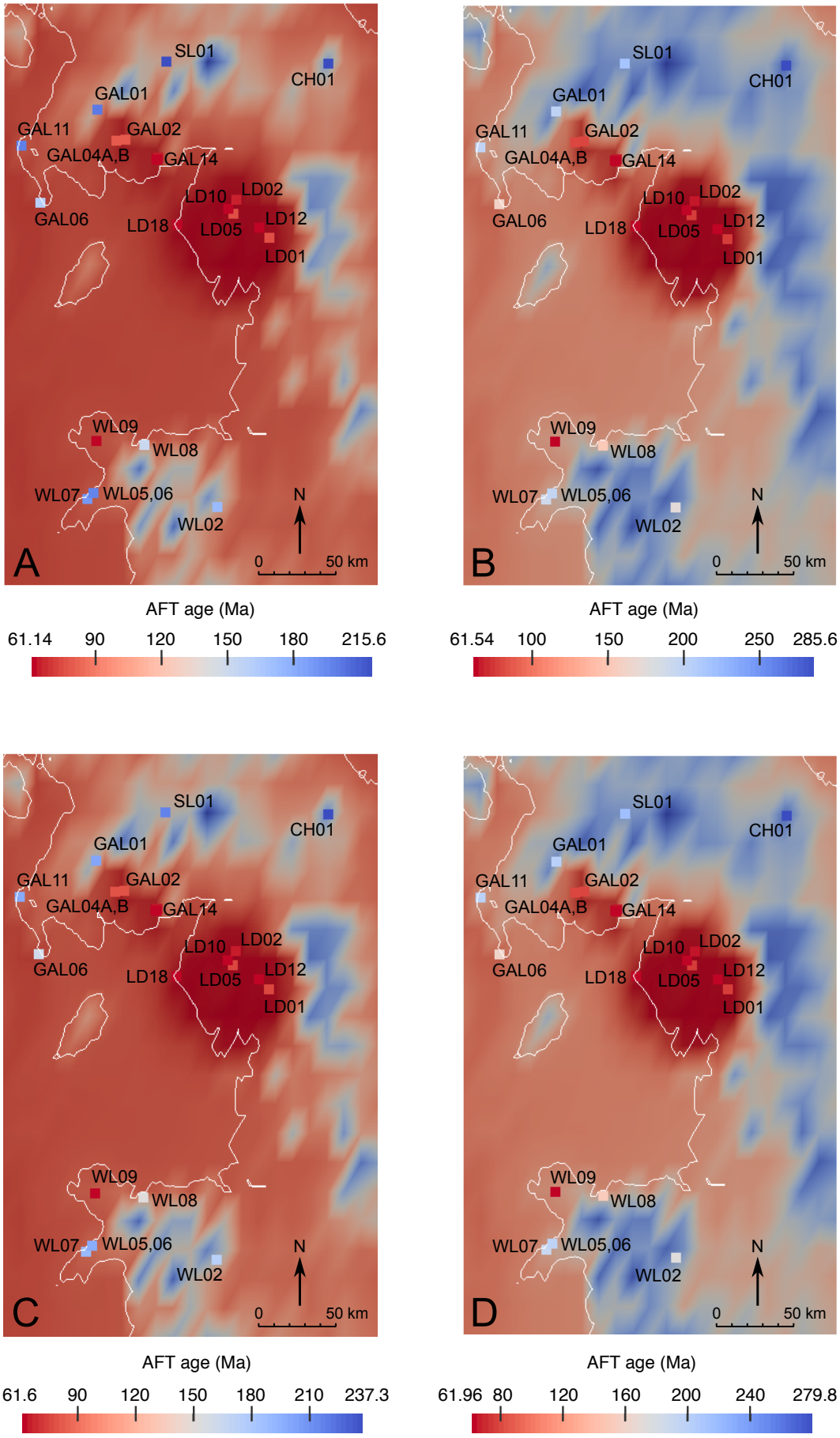

Figure 5.13: (caption on the previous page)

the latter model has to be discarded, unless the thermal diffusivity of the blanket layer is assumed to be higher than 15 km^2/Myr. For a 1 km thick sedimentary layer and 3 km of uplift, the predicted ages of rocks in southern Scotland and northern Wales are older than the observed ones. For 3.5 km of uplift, the ages are, however, too young (Fig. 5.13-C). The best fitting uplift is, therefore, somewhere between 3.0 and 3.5 km. Changing thermal diffusivity from 15 to 10 km^2/Myr reduces the required amount of uplift significantly. A good fit of the data (μ <2.5) can be obtained for uplift values of 2.2–2.5 km (Fig. 5.13-D).

The impact of the low conductivity blanket on the subsurface isotherms is shown in Fig. 5.14. At 80 Ma, the whole sedimentary blanket is present and as it is characterized by low thermal conductivity, the temperature increase within the layer is indicated by the thin spacing between the subsurface isotherms (Fig. 5.14). At 60 Ma, when the crust is being exhumed, the sedimentary layer is being eroded and gradually loses its blanketing ability; the advection, however, brings hot rocks toward the surface and so the geothermal gradient remains high. By present day the sedimentary layer has been entirely removed, the crust has reached steady state and the spacing between the isotherms in the shallow crust is much wider than before, indicating a lower geothermal gradient.

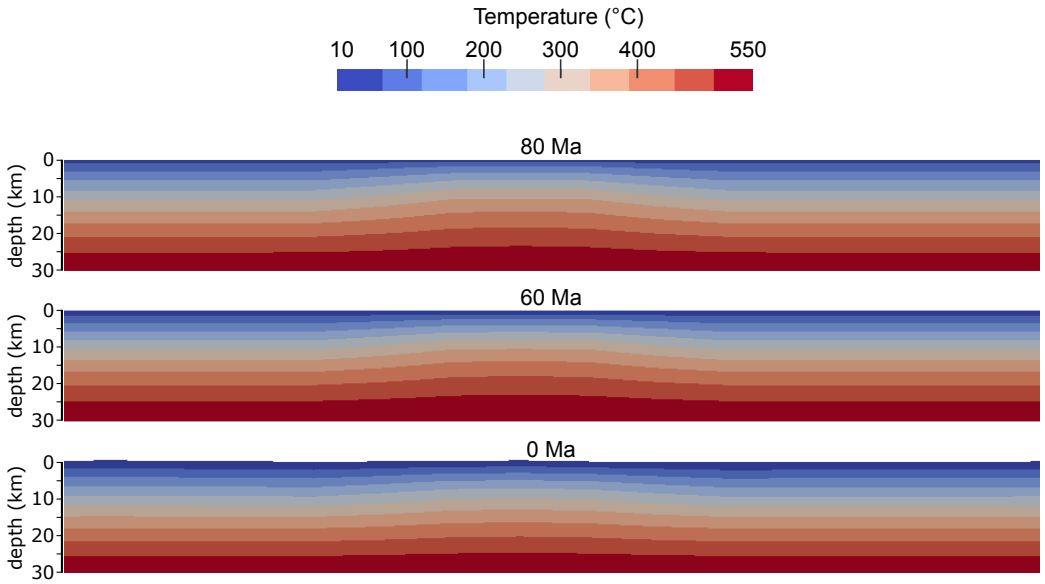

Figure 5.14: Isotherms in a crust at 80 Ma, 60 Ma and 0 Ma for a run comprising 30 km thick crust with 12 km thick heat productive granite batholith (A = 40°C/Myr) and 1 km of low conductive sedimentary blanket (κ = 10 km^2/Myr) that experienced 2.5 km of rock uplift.

5.5.2.5 Summary

The results of the forward modelling presented here show that the impact of heat production and thermal blanketing may be severe, especially if both mechanisms act together. Fig. 5.15 presents the predicted AFT age pattern and perturbations of the

isotherms for an exemplary scenario that includes a heat producing body that, prior to an uplift episode, was covered by a sedimentary blanket. The ages in the region underlain by the heat productive basement are substantially younger, because the crustal isotherms of 110–120°C are at shallower levels than in the surrounding areas.

Assuming that the crust is thermally uniform requires >5 km of rock uplift in the Lake District and ∼4 km of rock uplift in southern Scotland and northern Wales to predict the measured ages. The observed pattern of the ages resembles the observed pattern of ages for spatially uniform uplift if a heat producing body is added in the Lake District and all the study area is covered by a low conductivity sedimentary blanket. The amount of uplift required to predict the thermochronometric ages is sensitive to the thermal diffusivity of the sediments, as well as to the thickness of the blanket. For thermal diffusivity of 10 km^2/Myr and blanket thickness of 1.0 km, the observed age pattern is well resolved (μ <2.5) with 2.2–2.5 km of rock uplift, which implies ∼1.2–1.5 km of total denudation in the central Lake District and ∼2.2–2.5 km of total denudation at the coastal areas. If thermal conductivity for the 1 km thick blanket is 15 km^2/Myr, the required uplift is ∼3.0 km, which implies a total denudation of ∼2–3 km, higher at coastal areas.

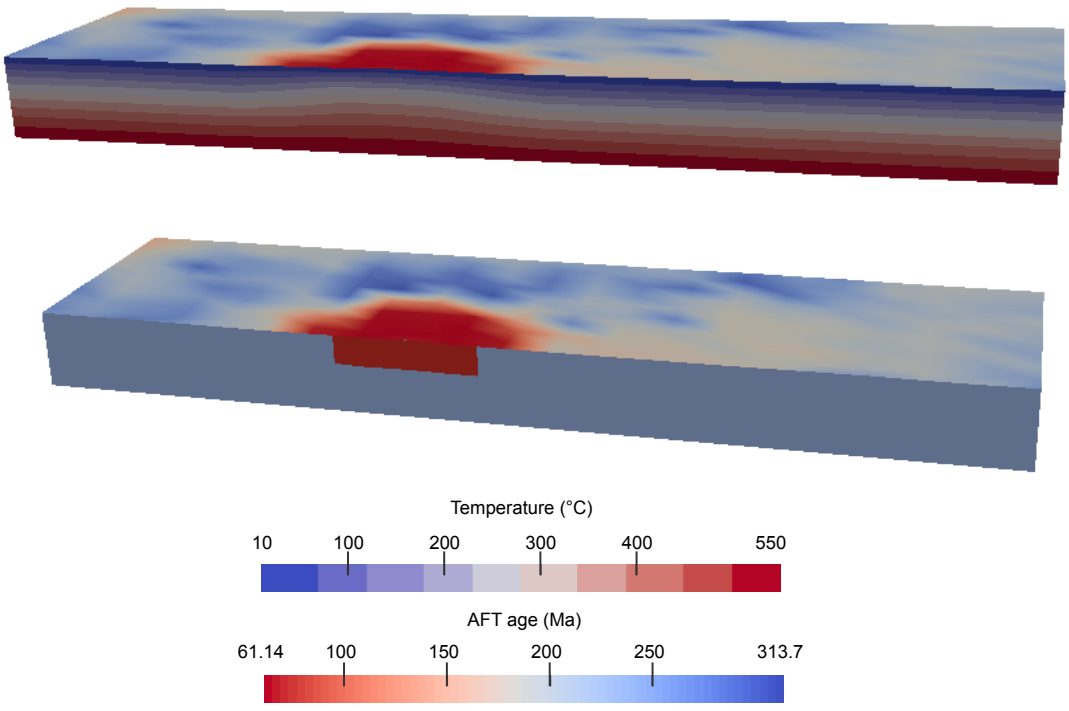

Figure 5.15: Block diagrams showing the relationship between the position of the heat productive body (bottom diagram), the perturbation of the crustal thermal field (upper diagram) and the predicted surface pattern of the apatite fission track ages. The parameters used are: 30 km thick crust comprising 12 km thick heat productive granite batholith, A = 50°C/Myr; background heat production of 10°C/Myr. All the area is covered by 1 km of low conductive sedimentary blanket (κ = 10 km^2/Myr); the ages are generated for a total uplift of 2.5 km (rate of 0.3 km/Myr between 62–57 Ma and 0.0175 km/Myr afterwards). The isotherms on the top diagram are shown for the crust covered by sediments, before the uplift has started.

The number of forward models that have to be run in order to find the best fitting scenario is almost infinite. The most efficient way to search the parameter space is to use the inverse modelling. The inversion results are presented in the following section.

5.5.3 Inverse modelling of thermochronometric data

5.5.3.1 Introduction

The inversion runs were prepared using the range of parameters determined by the results of the forward model. During the first inversion runs, four parameters have been searched: start and end of the first (rapid) uplift interval ($time1$ and $time2$, respectively) and rates of two uplift intervals ($rate1$ and $rate2$, respectively). The ranges for the two 'time' parameters cannot overlap; in the initial runs, $time2$ was found to converge toward the values of t$ime1$, suggesting that the cooling episode was short-lived. To solve this issue, in successive runs, instead of $time2$, a factor x has been implemented that allowed sampling the same time range for both $time1$ and $time2$. The factor x varies from 0 to 1 and the value of $time2$ is calculated using the following equation: $time2 = a + x * (time1 - a)$, where a is the lower boundary of the given range.

In one inversion run, five parameters have been searched, the start and end of the first uplift interval, the rates of the uplift intervals and the thickness of the crust. The addition of the fifth parameter is to account for the fact that the thickness of the crust in central west Britain is not well known at present, nor at 60 Ma ago when plume-induced basal heat flow may had moved the 550°C isotherm, the boundary between the crust and the lithospheric mantle, upward, decreasing, de facto, the thickness of the crust. The run shows that, for values between 25 and 32 km, crustal thickness does not have an effect on the results; low misfit ($\mu < 2$) is resolved for the whole input range and produces the same amount of total rock uplift. In all the other successive runs, the crustal thickness has been set to 30 km.

In the final inversion runs, four parameters have been searched: $time1$, x, $rate1$ and $rate2$. The range for $time1$ have been set to 80–40 Ma, $rate2$ to 0–0.2 km/Myr and $rate1$ to either 0–2 km/Myr or to 0–3 km/Myr depending on the properties of the sedimentary blanket. The misfit was evaluated based on the AFT and central AHe ages with 2σ error. All samples analysed during this study have been used excluding the ages from Anglesey (sample WL09), which is distinctively younger than the surrounding ages and therefore it is either inaccurate, due to low quality of the crystals or related to local-scale fault reactivation in the early Palaeogene. Incorporating these ages in the model could affect the misfit calculation and the re-sampling process, biasing the results.

In the final runs, the properties of the sedimentary blanket and heat production are set

at different values. Two combinations of the blanket properties have been used: a 1.5 km thick layer characterized by thermal diffusivity of 15 km^2/Myr and 1.0 km thick layer characterized by thermal diffusivity of 10 km^2/Myr. For heat production values, three combinations have been tested in order to investigate the influence of different background heat production and changes in heat generation of the granite batholiths. A summary of the inversion runs with run parameters is given in Table 5.6. All inversion runs are based on 2100 single forward models (20 iterations, 100 models each, with a re-sampling ratio of 50%).

Table 5.6: Properties of the sedimentary blanket and heat production used in the final inversion runs with the lowest misfit and values of searched parameters for the best fitting model. κ—thermal diffusivity, THK—thickness of the sedimentary layer, A_{LD}—heat production of the Lake District batholith, A_{Scot}—heat production of granite bodies at Criffeell, Fleet and Loch Doon, A_0—background heat production of the crust, μ—misfit, $time1$—start of rapid uplift, $time2$—end of rapid uplift, $rate1$—rate of rapid uplift, $rate2$—rate of slow uplift, U_T—tectonic uplift.

No	κ	THK	A_{LD}	A_{Scot}	A_0	μ	$time1$	$time2$	$rate1$	$rate2$	U_T
	(km^2/Myr)	(km)		(°C/Myr)				(Ma)		(m/Myr)	(km)
INV-1	15	1.5	50	30	10	1.82	56.0	54.6	1950	6	3.04
INV-2	10	1.0	50	30	10	1.79	57.8	54.6	710	4	2.50
INV-3	10	1.0	50	30	15	2.26	57.7	55.6	640	14	2.12
INV-4	10	1.0	40	25	12	2.43	59.0	57.5	850	22	2.48

5.5.3.2 Results

In all four runs, the predicted AFT age pattern correlates with the observed data (Fig. 5.17). In the runs that were characterized by the background heat production of 10°C/Myr (INV-1 and INV-2), the difference in ages between the Lake District and surrounding area is bigger and the change slightly sharper than in the case of runs with

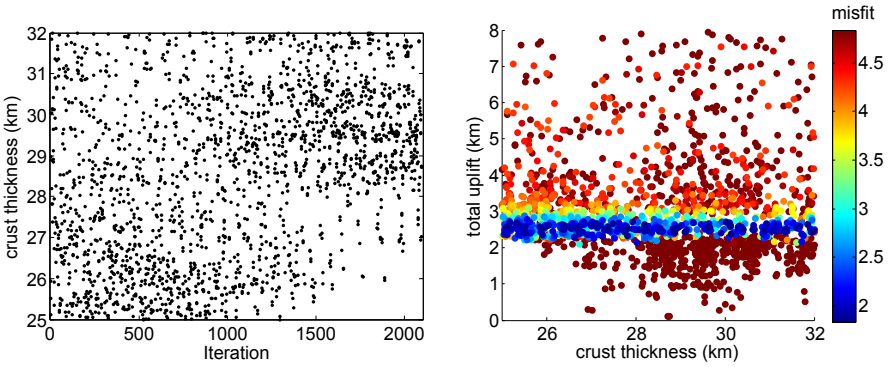

Figure 5.16: Model sensitivity to 'realistic' values of crustal thickness. Parameter sampling for 2100 model iterations (on the left) and misfit weighted scatter diagram presenting crust thickness versus total uplift (on the right). Each dot on the scatter diagram is one model generated during the run and the colour of the dot corresponds to its misfit value, calculated from the difference between the predicted and observed (measured) age. Brown/dark red colours define high misfit; dark blue colour low misfit. The axes of the plot defines a parameters space.

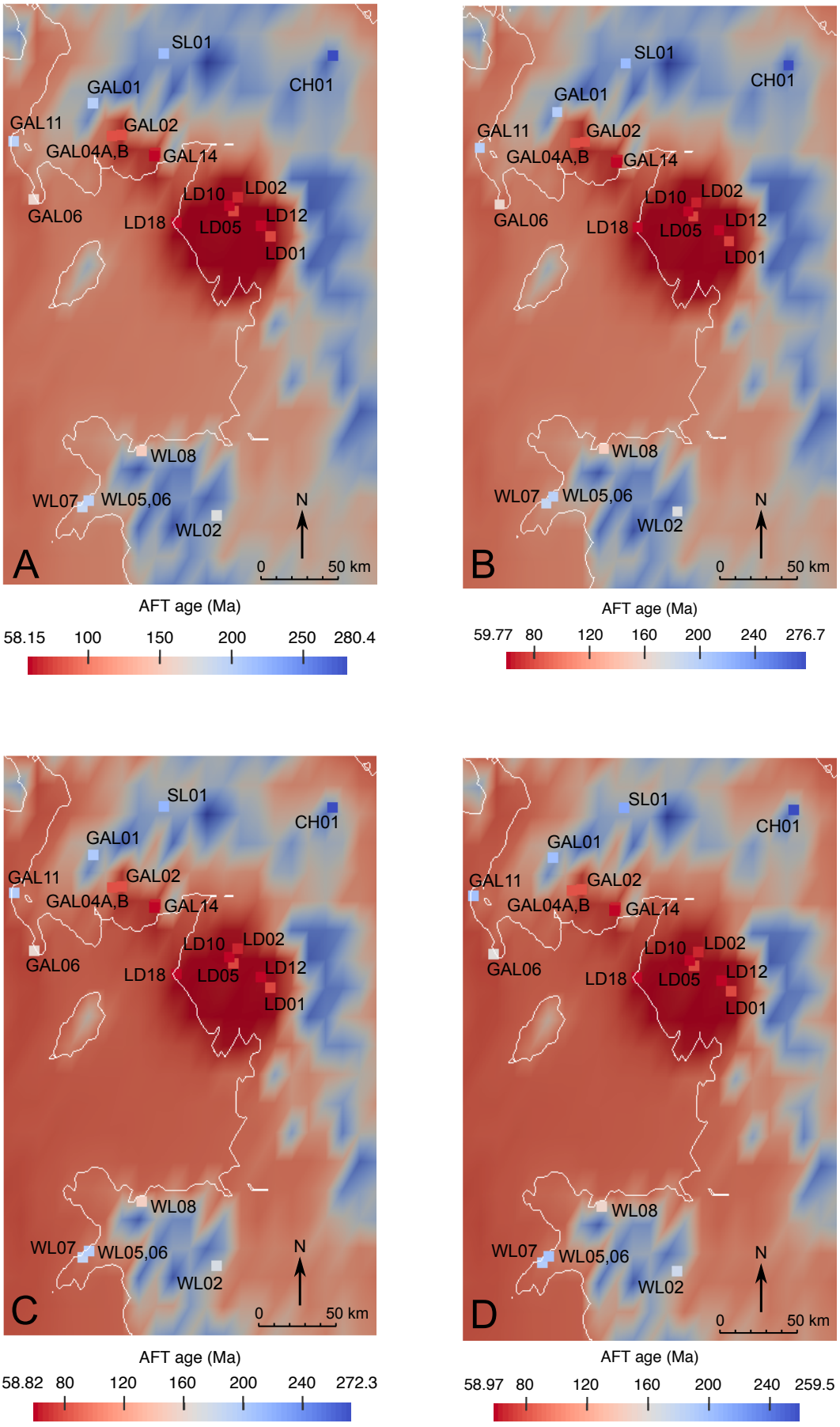

Figure 5.17: Predicted apatite fission track age distributions for the lowest misfit models derived from the four final inversion runs. A—INV-1, B—INV-2, C—INV-3, D—INV-4. Squares are the observed AFT ages of samples analysed during this study. See Table 5.6 for parameters used in the runs.

higher background heat production (INV-3 and INV-4). The latter are characterized also by generally younger ages. The predicted AHe ages are similar in all runs (∼56 ± 1.5 Ma); the difference is well within the 2σ uncertainty on the observed data. The ages do not show a spatial variation and are similar to each other as a rapid pulse of uplift from temperature of at least 80°C is predicted everywhere in the region (Fig. 5.18).

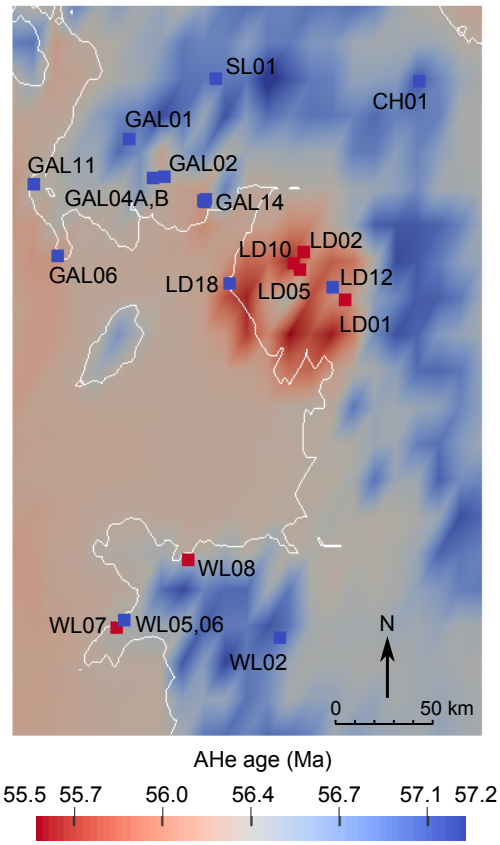

Figure 5.18: Predicted AHe age distribution for the lowest misfit model derived from the inversion run INV-2. See Table 5.6 for parameters used.

In all runs the misfit values are higher than 1, which indicates that some of the predicted AFT ages are outside 2σ error. This difference in misfit is governed mostly by a group of five low elevation, moderately old (150–200 Ma) ages from Llŷn (WL05, WL06 and WL07) and Rhins of Galloway (GAL06 and GAL11), which are otherwise characterised by young ages. For high background heat production (15°C/Myr), the surrounding ages are well predicted, but the predicted ages for Llŷn and Rhins of Galloway are too young (Fig. 5.19). Outside 2σ is also the predicted age of the Cheviot granite (CH01). The misfit is, however, generally low; in runs INV-1 and INV-2, which have the highest background heat production, the lowest misfit is ∼1.8 and exceeds 2.0 only in INV-3 and INV-4. The local-scale discrepancies are to be expected, as the model is a simplified, regional scenario; for this reason and because of the still relatively low misfit value, the results are considered acceptable, especially for INV-2.

Fig. 5.20 presents estimated probability density functions via the Kernel Density Estimator (KDE) plots for each of the four searched parameters. There is a general agreement in timing of the rapid uplift episode that is represented by a clear peak on the KDE plots; the lowest misfit models suggest that the event was short-lived, between ∼58–54 Ma. For the best fitting model of INV-1, the early Palaeogene cooling event is even shorter, ∼56.0–54.6 Ma, but *time*2 is not well resolved. The rate of the rapid uplift episode is generally around 600–900 m/Myr; in the case of shorter uplift in INV-1, the corresponding rate reaches almost 2 km/Myr. These values are not very rapid in absolute terms, but because the rocks removed have a low conductivity, the corresponding cooling rates are fast, ∼20–40°C/Myr. According to the better resolved, first

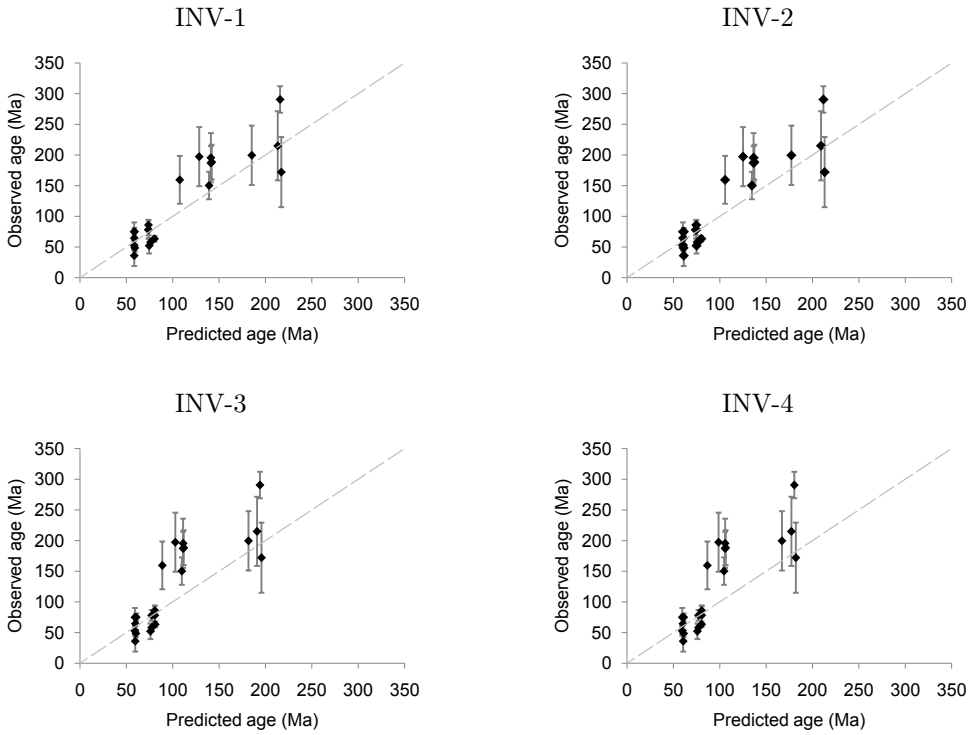

Figure 5.19: Observed versus predicted apatite fission track ages in four final inversion runs. See Table 5.6 for parameters used in the particular runs.

two models, the uplift continued in the last ∼55 Ma, but at low rates of 4–6 m/Myr. These results imply that ∼90% of the Cenozoic uplift occurred in the early Palaeogene. These rates are very low, similar to slow erosion in hot, arid environment (Matmon et al. 2009). Slightly faster rates, 14–22 mm/Myr, for this uplift episode are resolved in the two latter runs, where they implies up to 60–50% of total uplift to occur in the last 55 Ma. Rates of at least 20 mm/Myr are more probable for the Cenozoic climate in region that was warm and humid during the Palaeocene/Eocene climate optimum and cooled towards the time of Pleistocene glaciations (e.g. Zachos et al. 2001). Difficulty in resolving faster erosion rates by the Pecube models may be related to the lack of fission track lengths data. Nonetheless, the Palaeogene denudation likely comprised more than 50% of total Cenozoic denudation. The total amount of Cenozoic uplift varies from about 2.0 to 3.0 km and depends on both the thermal conductivity of the sedimentary blanket as well as the background heat production; the lowest value is consistent with a model including a blanket with a thermal diffusivity of 10 km^2/Myr and background heat production of 15°C/Myr (INV-3); the highest value requires a blanket of thermal diffusivity of 15 km^2/Myr and background heat production of 10°C/Myr (INV-1).

The scatter plots in Fig. 5.21 explore the relationship between *time*1 and *time*2 and between *rate*1 and *rate*2 scaled according to the misfit value. In case of timing, the low misfit field is narrow and well constrained and the lowest misfit value is usually in the middle at ∼57 Ma; other, low misfit scenarios predict the uplift event to have occurred either earlier or later, but the duration of the rapid uplift is the same for all acceptable

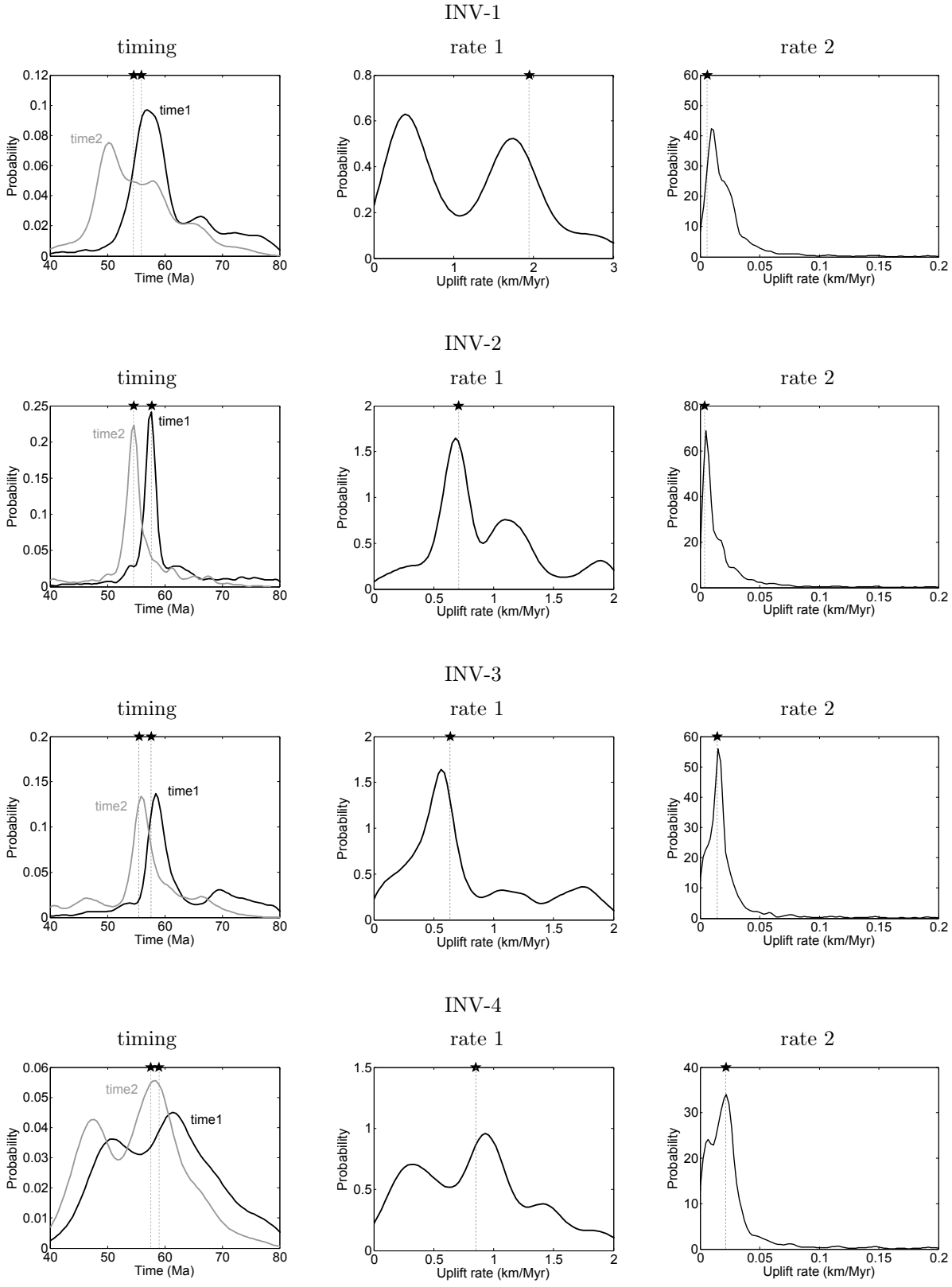

Figure 5.20: Kernel density estimator plots of the parameters sampled during the four final inversion runs. The use of the kernel density estimator instead of probability density function was motivated by the fact that the distribution of the data is unknown. See Table 5.6 for parameters used in the particular runs. The stars are the values for the lowest misfit model.

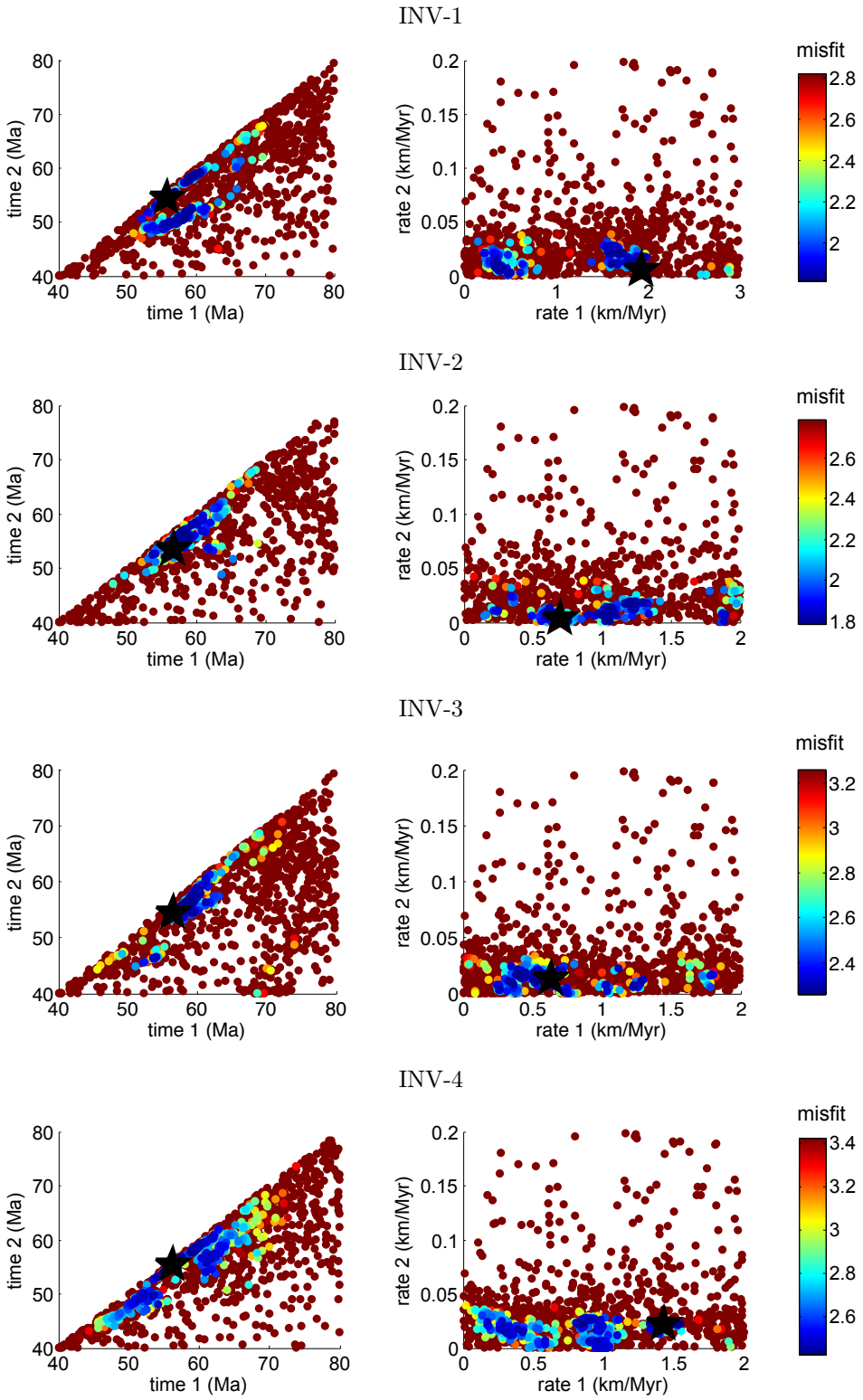

Figure 5.21: Misfit weighted scatter diagrams presenting results of the inversion runs. See Table 5.6 for parameters used in the particular runs. Each dot is one model generated during the run and the color of the dot corresponds to its misfit value. Brown/dark red colours define high misfit and dark blue colour defines low misfit, ; the lower the misfit, the better the agreement between predicted and observed (measured) ages. Stars represent values for the lowest misfit model. Two combinations of the parameters have been used: $time1$ versus $time2$ and $rate1$ versus $rate2$, where $time1$ and $time2$ are the start and end of the rapid uplift and $rate1$ and $rate2$ are rates of the rapid and slow uplift episodes, respectively. The axes of the plots define the parameters space. Note that the diagonal shape of the $time1$ versus $time2$ plot is the result of the fact that the two variables are not independent from each other, as time 2 is defined as $time2 = a + x * (time1 - a)$, where a is the lower boundary of the given range and x is the sampled parameter from a range of 0–1.

models. The Cenozoic uplift rates are not well determined, the acceptable values are variable and converge to two or three low misfit fields (Fig. 5.21). However, the combination of the derived values for the timing and uplift rate parameters always produces the same, well constrained amount of total Cenozoic uplift (Fig. 5.22).

The results have to be carefully analysed as several simplifications used in the models are important. The possible impact of these simplifications is critically assessed in the next section.

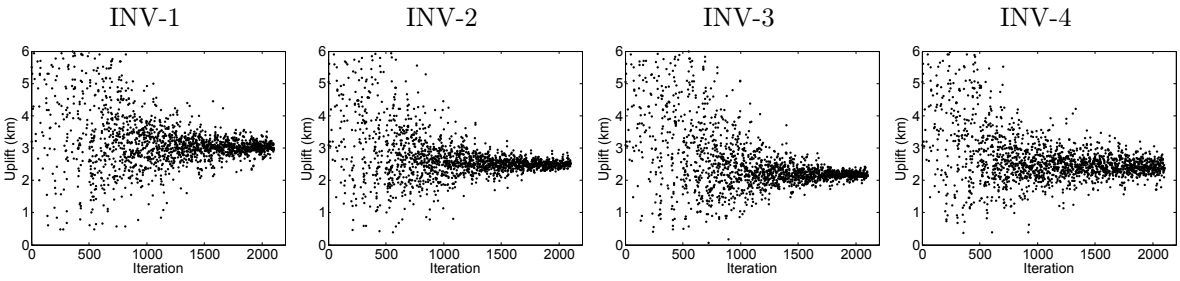

Figure 5.22: Convergence of the amount of total uplift predicted by different inversion scenarios. See Table 5.6 for parameters used in the particular runs.

5.5.4 Discussion

The 1-D and 3-D numerical models have amply demonstrated that accounting for crustal thermal heterogeneities is crucial to extracting the uplift and denudation history of central west Britain from thermochronometric data. The age pattern correlates well with the heat flow anomalies especially in the Lake District, but high heat production seems to be important also in southern Scotland at Criffell, Fleet and, to a lesser extent, at Loch Doon. The results of the Pecube modelling, in particular, indicates that for simple tectonomorphic scenarios, the observed age pattern may be resolved with a spatially variable heat production. By including the blanketing effect of the sedimentary cover, the thermochronometric data produce the amounts of denudation that are in agreement with those estimated from stratigraphical constraints (Holliday 1993).

Several simplifications used in the modelling undoubtedly have an influence on the predicted ages. Those include: spatially uniform amount of uplift, no uplift/subsidence events prior to the uplift episode at ∼60 Ma, uniform distribution of the radiogenic elements within the heat productive bodies, simple cylindrical geometry of the granite batholiths, spatially uniform thickness of the sedimentary blanket, presence of the sediment layer since the beginning of the run and uniform value of thermal conductivity within the layers. Each of these simplifications and its possible effect/s on the distribution of the thermochronometric data is discussed below.

The model assumes that the uplift was spatially uniform. There is no direct indi-

cation that this assumption is wrong, as some of the most probable uplift mechanisms, such as the mantle plume-derived thermal anomaly and magmatic underplating which is expected to be, in broad terms, uniformly distributed underneath the onshore region (Clift & Turner 1998), cause a spatially uniform uplift. However, some studies suggest otherwise. Chadwick et al. (1994), for instance, conclude that the basins offshore experienced higher amounts of uplift due to inversion *sensu-stricto*; it is possible that the basement blocks onshore may have experienced differential uplift. The thickness of the underplating material may have not been uniform. Al-Kindi et al. (2003) suggest that it was thicker in western Britain, implying a differential uplift, decreasing eastward. Local-scale differences in the amount of uplift may explain ages that cannot be predicted by the models. The old AFT ages (∼300 Ma) at Cheviot, for instance, could be the result of a smaller amount of uplift in the eastern part of Britain. The use of a simple uplift scenario, with no tectonic events prior to the Cenozoic may have a non-negligible influence on the derived ages. The geological constraints clearly indicate that this simple scenario is not accurate and that the pre-60 Ma history of central west Britain was complex. However, the main aim of the 3-D modelling is to explore the influence of the crustal thermal heterogeneities on the thermochronometric age. Investigating the pre-Cenozoic geological history of the area is beyond the scope of this modelling experiment. The AFT and AHe ages of the Lake District indicate that rocks now at the surface were at temperatures higher than the PAZ in the pre-Cenozoic and, therefore, their previous history has no effect on the available thermochronometric data. Admittedly, the pre-60 Ma history has an influence on the ages in southern Scotland and northern Wales; in these cases, the amount of Cenozoic uplift estimated by the models should be considered as a maximum. The effect of the presence of heat producing rocks and of a blanketing sedimentary cover is still valid. By assuming, for instance, that southern Scotland and northern Wales were not covered by Cretaceous sediments in the early Cenozoic, the blanketing effect of the Triassic-Jurassic rocks should be close to values of thermal diffusivity of 15 km^2/Myr or higher.

Heat producing granite batholiths were modelled as cylinders with homogeneous distribution of radiogenic elements. For the given amounts of uplift, the AFT ages in the heat productive areas are not sensitive to heat production changes. Heat production is significantly reduced if the concentration of the radiogenic elements decrease exponentially with depth. As discussed in Section 5.3, the assumption of vertically uniform heat production with depth seems to be a good approximation for the Lake District batholith. The shape of the heat productive bodies definitely has an influence on the predicted pattern of the ages. However, for the given data set, small misalignment of the batholiths edges would not make significant changes to the misfit, as the sampling locations are far away from the batholith edges. Although the ZHe data have not been included in the Pecube modelling, the high heat flow in the Skiddaw area (up to 101 mW/m^2, Lee et al. 1987) could explain the ∼126 Ma ZHe ages of the Skiddaw granite).

The model assumes constant thickness of the sedimentary layer that covers the whole region uniformly. Inputting spatially variable thickness of the blanket would be complicated to account for in the 3-D model. To calculate the amounts of denudation in particular locations accurately, the possible thickness of the sedimentary layer at any given site will to be assessed and modelled in 1-D in Chapter 6. Certainly, the coastal areas have experienced higher sedimentation and the highs had thinner cover, if any. The AFT ages in the Lake District are, however, insensitive to the amount of sediments, if the uplift was higher than 3 km. Even if the top of the hills remained uncovered, the model misfit would not be affected by this issue, because the samples come from relatively low elevations (<500 m). A variable sedimentary cover could be the explanation for the Lake District data reported by Green (2002). The AFT ages along a 844 metres long, quasi vertical profile range from 300 Ma at elevations over 580 metres to ∼60 Ma, below 250 metres of altitude. The early Palaeogene palaeotemperatures calculated by Green (2002) suggest a ∼50°C difference between the top and bottom of the profile, which have been taken to indicate an unusually high palaeogeothermal gradient of 61°C/km. A similar pattern in palaeotemperatures could be obtained by assuming that the top of the profiles was not covered by sediments, or that the thickness of the sediments was very small at the top, increasing downhill.

Additionally, the use of a variable thickness of the sedimentary layer would require the thermal conductivity value to vary with depth. For 1 km thick blanket a constant value can be used, as the magnitude of compaction will be relatively low; in the case of 2 or 3 km thick layer, compaction could substantially increase the thermal conductivity of rocks at greater depths. In the models, this issue has been resolved by assuming a 'thin' (1.0 or 1.5 km) blanket and a constant value of thermal conductivity (10 or 15 km^2/Myr, respectively). Underneath the blanket, a higher thermal conductivity value (25 km^2/Myr) was assumed to account for higher conductivity of either basement rocks or more compacted sediments.

Although the 'time' parameters were resolved quite well (Fig. 5.21 and 5.20), the models were not able to fit a unique solution for the uplift rates. The data are, in general, satisfied by a wide range of rapid uplift rates (from 0.2 to 1.7 km/Myr) that strongly depend on the length of the rapid uplift period (from 0 to 10 Myr; Fig. 5.23). Probably, a better result would have been obtained by adding the track length distribution to the models (e.g. Valla et al. 2010). However, as discussed earlier in this section, Pecube predicts ages and track lengths distributions for standard diffusion and annealing kinetics. The influence of chemical composition of apatites on the annealing rate was strong in some cases presented in this study and the current version of Pecube is not capable of dealing with these data complexities. The track length distributions for samples from southern Scotland and northern Wales are the results of the pre- and Cenozoic history of the areas. If those data had been input in Pecube, they would have created incon-

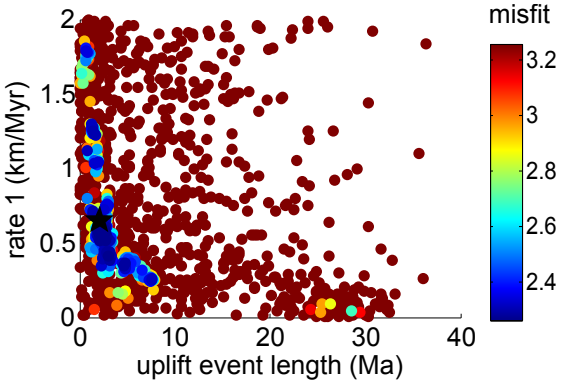

Figure 5.23: Misfit weighted scatter diagram presenting dependence of rapid uplift rate and duration of the uplift episode in run INV-3. See Table 5.6 for parameters used in the run. Each dot is one model generated during the run and the color of the dot corresponds to its misfit value. Brown/dark red colours define high misfit and dark blue colour defines low misfit between the predicted and observed ages.

sistencies due to the fact that the modelled scenario assumes a quiescent pre-Cenozoic thermal history. The use of Durango-like annealing and diffusion kinetics as well as not accounting for the pre-Cenozoic history of southern Scotland and northern Wales certainly influenced the AFT and AHe ages, which was dealt with by setting the age uncertainties to 2σ.

Another possible way to account for different annealing and diffusion kinetics in Pecube would be inputting thermal histories derived from separate QTQt or HeFTy models and calculating the misfit between the input and predicted t-T paths. Such an experiment has been carried out during this study, however, it was not successful. The misfit calculated for the same uplift scenario was slightly lower for the uniform crust than for the crust comprising a granite batholith covered by sediments. The presence of a rapid uplift event was also not always required to obtain a low misfit value. The lowest misfit value was obtained by either rejecting the presence of the rapid uplift episode (the uplift period was shorter than 0.5 Myr and the total amount of uplift during this episode was only few hundreds of meters) or proposed quite large (>1 km) but anomalously rapid uplift. The failure of this attempt probably arises from the fact that QTQt models are complex, quite variable, and in some samples from southern Scotland the ∼60 Ma cooling event was not resolved, likely because temperatures were already below the sensitivity of the thermochronometers used. The high complexity of the single t-T paths and the large uncertainties on each of the t-T points force Pecube to favour simple thermal histories over the complex models when 'averaging' the regional thermal history. More work is therefore required on use of thermal histories as an input data set.

5.6 Conclusions

The modelling results presented in this chapter demonstrate that the impact of variable heat production and thermal conductivities on the thermal field of the uppermost crust is significant. As shown with the example from central west Britain, such crustal heterogeneities may strongly influence the thermochronometric data. The results from the 3-D model indicate that the observed age pattern may be well explained by locally

enhanced heat production and does not require spatially variable uplift. Taking into account the low conductivity of eroded overburden allows the total amount of Cenozoic denudation to be reduced to 1–3 km, highest at the coastal areas, less in the central Lake District.

Fig. 5.24 shows a simple summary sketch demonstrating the proposed Cenozoic thermal history of central west Britain for the two common cases observed in the region: a 'normal' low heat productive crust and the crust comprising a heat productive granite batholith, both covered by a low conductive sedimentary blanket, eroded in the early Palaeogene. Cooling during the Cenozoic is a complex process that results from both denudation itself and enhanced pre-cooling temperatures, due to the low thermal conductivity of the eroded sedimentary layer.

Although the models were based on several simplifications and the pre-Cenozoic history was an important part of thermal evolution, especially in southern Scotland and northern Wales, heat production and thermal blanketing seem to have a dominant role in determining the observed age pattern. The values of geothermal gradients predicted

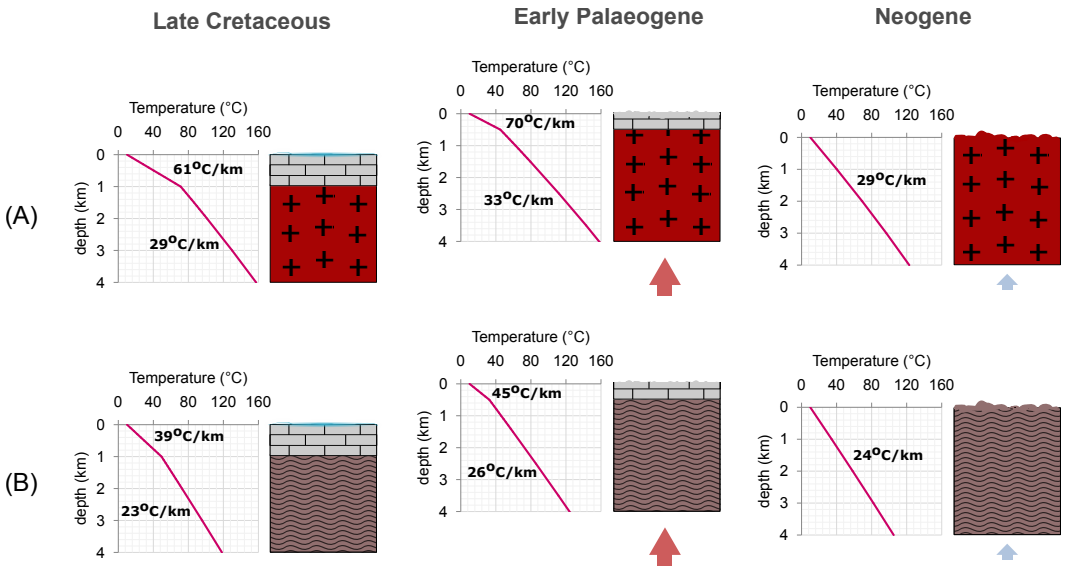

Figure 5.24: Sketch illustrating the temperature change with depth throughout the Cenozoic in (A) a crust comprising heat producing granite batholith (heat production of 4 μW/m^3) and (B) a 'normal' crust (heat production of 1 μW/m^3). In both scenarios the crust is covered by 1 km of low conductivity sediments (thermal conductivity of 1.5 mW/m^2). In the Late Cretaceous, the crust is covered by a sedimentary blanket, characterized by a high geothermal gradient. The sedimentary cover acts as a 'blanket' and increases the temperature of the rock below. If the crust comprises radiogenic granite, the gradient in the sedimentary layer reaches a very high value of 61°C/km (notice, for comparison that when the granite is not present, the geothermal gradient in the crust is only 39°C/km, panel B). Also notice that the geothermal gradient in the underlying crust is not affected by the sedimentary cover and it is similar to present values. During regional uplift in the early Palaeogene, the blanket is eroded and the isotherms are advected towards the surface, slightly increasing the geothermal gradient in the shallow crust. When the sediments are eroded, the basement rocks reach the surface and they are dramatically cooled down; their geothermal gradient returns to 24–29°C/km.

in this chapter will be used in Chapter 6 to calculate denudation amount for every sampling site. This will allow to unravel the post-Caledonian evolution of central west Britain and to suggest the processes responsible for uplift and denudation of the British section of the North Atlantic margin.

Chapter 6

Post-Caledonian exhumation history of central west Britain

6.1 Introduction

The absence of post-Silurian sedimentary rocks makes it difficult to decipher the post-Caledonian history of central west Britain. The basins surrounding the Lake District, Southern Uplands and northern Wales, comprise thick sequences of Carboniferous and Permo-Triassic sediments; however Late Mesozoic and Cenozoic sediments are almost entirely missing (Ziegler 1988). The absence of a sedimentary cover was, for a long time, interpreted as an indication that onshore central Britain was an emerged block since at least the Late Palaeozoic. This was challenged by the first AFT ages which required 3–4 km of Cenozoic denudation to explain the observed palaeotemperatures of >110°C (Hurford 1977, Green 1986, Lewis et al. 1992). However, the amount of post-Caledonian burial, as well as the magnitude and spatial distribution of the early Cenozoic denudation remains unclear, as do the underlying causes. These include the impact of a mantle plume at the base of the lithosphere at ∼62–58 Ma (White & McKenzie 1989), uplift along the rifting margin related to the opening of the North Atlantic at ∼53–55 Ma (Lundin & Doré 2005) and tectonic stress transmitted from the Alpine foreland and/or rift push from the North Atlantic (Ziegler 1990).

Although these processes are almost coeval, the spatial pattern of denudation caused by them is expected to be different. The thermochronometric study and thermal modelling carried out during this research project have quantified the spatial distribution of post-Caledonian evolution of central west Britain. A summary of how the modelled thermal events identified during this study correlate with regional geological events is presented in Fig. 6.1. The combination of low temperature thermochronometry with 1-D and 3-D numerical modelling of the crustal thermal field underneath a changing topography has been essential for constraining the spatial distribution of early Palaeogene denudation. This is, in turn, crucial for unravelling the processes responsible for the uplift event. In general terms, this study emphasises the importance of accurately

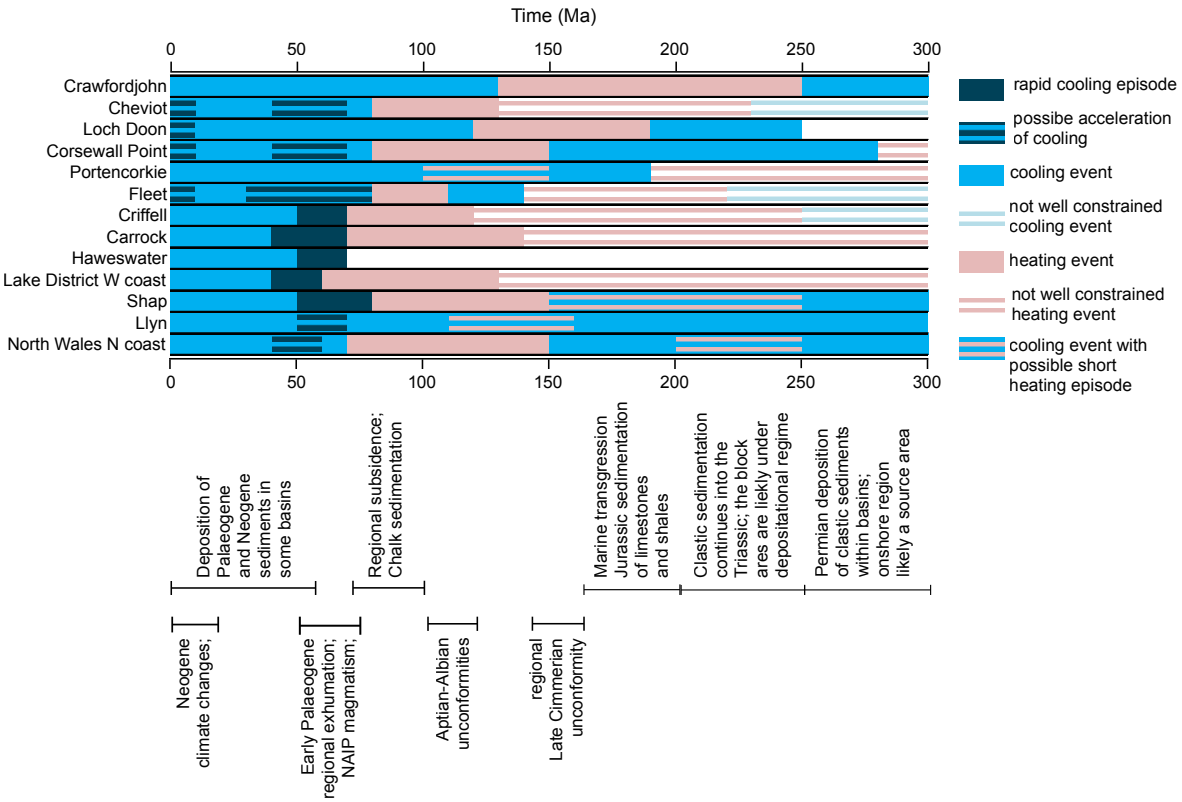

Figure 6.1: Compilation of cooling and re-heating events in the localities that have thermal histories extracted from QTQt and Helfrag inverse modelling. The localities are ordered along the quasi-north-south profile (for sample location see Fig. 3.1). If more than one sample was analysed for any site, the most representative history has been chosen (see Chapter 4 for further details). Under the diagram, the most important depositional and erosional events are marked along the time line.

translating cooling into denudation, especially in the cases when the thermal properties of the crust are locally variable.

The aim of this chapter is to establish the geological history of central west Britain, using the thermal histories obtained during this project and the regional geological information on the North Atlantic region. The focus of the geological reconstructions is on the Cenozoic and, to a lesser extend, on the Mesozoic history of the study area. The chapter deals with three main time periods: pre-Cenozoic (Section 6.2), Palaeogene (Section 6.3) and Neogene (Section 6.4). The pre-Cenozoic events are grouped in one section, as they are discussed only briefly because, in most of the cases, this part of the history is not well constrained. The Palaeogene is the focus of this study and therefore it is discussed more extensively.

6.2 Pre-Cenozoic thermal history (66–460 Ma)

Thermal histories produced during this study do not provide strong constraints on the pre-Cenozoic history. In all cases, the AFT ages are younger than the emplacement age of the sampled intrusions. Only in the Cheviot granite, which yields the oldest AFT

age in the data set (∼300 Ma), the presence of a rapid post-emplacement cooling and a separate Variscan cooling signature can be relatively well resolved. In the Lake District and Criffell, the Late Cretaceous-early Palaeogene temperatures were higher than 110°C, which precludes the possibility of resolving the earlier thermal history. However, a negative correlation of ZHe ages with [eU], when modelled using the radiation model of Guenthner et al. (2013), indicates that within ∼100 Myrs of emplacement, the rocks had been cooled to ∼40–120°C and were reheated prior to reaching the high Late Cretaceous-early Palaeogene temperatures (Fig. 4.1: LD01, LD02; Fig. 4.2: GAL14). The rocks from southern Scotland and northern Wales have AFT ages ranging from 150 to 300 Ma, which allow the Mesozoic history to be partially resolved. Most of these cooling and reheating events are poorly resolved, however, when interpreted as exhumation or burial, they are in general agreement with the regional geological history and are briefly discussed below.

Permo-Triassic—Thermal histories derived from the thermochronometric data show, in general, a cooling regime during the Permian, changing into reheating in the Triassic. This confirms that at least during the Permian extension, much of the central Britain was a source area for clastic sediments deposited in the surrounding basins (Moseley 1978, Woodcock & Strachan 2000). For example, the basal Permian sequence in the EISB, the Brockram breccia, is composed of clasts of the Borrowdale Volcanics and some minor granites that likely were derived from the Lake District block (Akhurst 1997). A strong, rapid Permian cooling signature is not always the result of denudation; for instance, in the Crawfordjohn dyke in the northernmost flank of the Southern Uplands, it is more related to the post-emplacement cooling of late-Variscan intrusion, rather than denudation. A Triassic reheating signature, suggesting burial initiated at that time, is resolved in northern Wales (Fig. 4.3: WL08), in the Fleet pluton (Fig. 4.5), Cheviot hills and Crawfordjohn dyke (Fig. 4.2: CH01 and SL01) in southern Scotland, and on the western coast of the Lake District block (Fig. 4.1: LD18). In contrast, the Llŷn peninsula (Fig. 4.4), Loch Doon pluton and the Rhins of Galloway (Fig. 4.2: GAL01, GAL06, GAL11) appear to have cooled. The Rhins of Galloway comprises the uplifted footwall of the North Channel Bounding Fault; the hangingwall is the North Channel basin that was subjected to dynamic sedimentation throughout the Mesozoic (Needham & Morgan 1997). The cooling signature may, therefore, exhibit a localised exhumation of the footwall during the extension.

Jurassic—Most of the thermal models produced during this study support a reheating event in the Jurassic; the reheating signature is relatively well resolved in northern and central Southern Uplands (Fig. 4.2: GAL01, SL01, CH01; Fig.4.5: Fleet) and on the western flank of the Lake District (Fig. 4.1: LD18). Further work may allow the extent of onshore Jurassic sedimentary cover to be determined. The thermal models from the Rhins of Galloway (Fig. 4.2: GAL06, GAL11) and from northern Wales (Fig. 4.3:

WL08) show instead a Jurassic cooling episode. The Rhins of Galloway appeared to have cooled since the Triassic and may be related to the extension-driven footwall uplift along the North Channel Bounding Fault. Similar, local scale tectonic events may explain the Jurassic cooling signature proposed for northern Wales that was also resolved by the AFT study of Holford et al. (2005a).

Early Cretaceous—In some of the thermal models from southern Scotland (Fig. 4.2: Loch Doon (GAL01), Crawfordjohn (SL01); Fig. 4.5: Fleet; Fig. 4.14: Corsewall Point), the Early Cretaceous is coincident with either a change in cooling rate or a transition from heating to cooling that may be referred to the Late Cimmerian uplift and denudation. The amount of Early Cretaceous cooling varies from 50 to 90°C and can be translated into 1.6–3.0 km of denudation, assuming a palaeogeothermal gradient of 30°C/km. As the thermal conductivity of the Jurassic rocks is low (∼1.5–2.0 W/m/K) the Early Cretaceous geothermal gradient was probably much higher, 40–60°C/km, which reduces the amount of denudation to 1.0–1.8 km. The Late Cimmerian denudational event is observed elsewhere, for instance in the North Sea, and the Porcupine and Bristol Channel Basins, however, its origin and magnitude are under debate (Van Hoorn 1987, Ziegler 1988, Shannon 1991, Jones et al. 2001, Kyrkjebø et al. 2004, Holford et al. 2005a, Yang 2012). In the part of the Irish Sea Basin closest to the study area Green et al. (2001) and Holford et al. (2005a) suggested, based on AFT an vitrinite reflectance (VR) analyses, that the early Cretaceous exhumation reached ∼3 km, which is the maximum estimate of exhumation calculated for southern Scotland in this study.

Late Cretaceous—The QTQt-derived thermal histories from the Fleet pluton (Fig. 4.5) and the EISB coast in northern Wales (Fig. 4.3: WL08), and the Helfrag-derived model from Corsewall Point (Fig. 4.14: Corsewall Point) show Early Cretaceous cooling, followed by a well resolved reheating in the Late Cretaceous that may be explained as the result of burial by chalk. Although very poorly resolved, the central Lake District and Criffell also appear to be reheated (Fig. 4.1: LD01, LD02; Fig. 4.2: GAL14). The t-T paths from the central and northern areas of the Southern Uplands (Loch Doon pluton and Crawfordjohn dyke) suggest a protracted cooling that started at the Jurassic/Cretaceous boundary, which suggest that the last major cooling event that affect this area was related to the Late Cimmerian movements and that the area was not flooded at the time of the Late Cretaceous transgression. This conclusion is consistent with a palaeogeographical reconstruction of the extent of the Late Cretaceous sea (Fig. 6.2) (Hancock 1975), according to which most of the Southern Uplands, North Wales and Scottish Highlands could have remained emerged during the maximum transgression in the Late Campanian. Other reconstructions, however, propose that the Late Cretaceous sea covered the whole of central Britain (e.g. Ziegler 1988), but there are no thermochronometric data that support this hypothesis. It is possible that the region was completely submerged, but that the thickness of the sediments

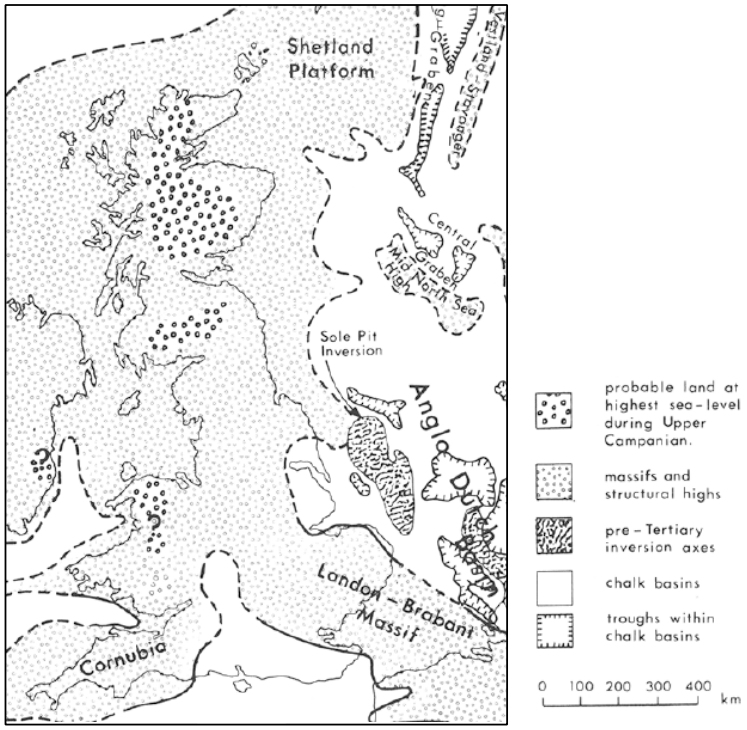

Figure 6.2: Geological reconstruction of onshore and offshore Britain during the Late Cretaceous; shown extent of land is a probable maximum; modified from Hancock (1975).

were not enough to affect the thermochronometers; in these terms, the estimates of Hancock (1975) and Ziegler (1988) should be treated as the minimum and maximum extent of the Late Cretaceous sea, respectively.

6.3 Palaeogene thermal history (∼23–66 Ma)

6.3.1 Introduction

The beginning of the Palaeogene in the North Atlantinc region is marked by a voluminous magmatic activity in the North Atlantic Igneous Province (NAIP) including volcanism in Baffin Island, N and E Greenland, N Ireland, and NW Scotland (Fig. 6.3) that occurred in two distinctive phases: phase I at 62–59 Ma, caused probably by the impingement of the proto-Iceland mantle plume and phase II at 56.5–54 Ma, coincident with the initiation of sea-floor spreading between Greenland and Scandinavia (White & McKenzie 1989, Saunders et al. 2007). An early Palaeogene rock uplift and denudation event, which probably reached its maximum around the Palaeocene/Eocene boudary (∼55 Ma), has been recognized in many parts of the North Atlantic passive margin: in Scandinavia (Huuse 2002, Hendriks & Andriessen 2002, Nielsen et al. 2002), in the North Sea and Faroe-Shetland Basins (Nadin et al. 1997, Shaw Champion et al. 2008, Hartley et al. 2011), in Greenland (Dam et al. 1998, Swift et al. 2008, Petersen et al. 2015), and on the British Isles (Green 1986, Lewis et al. 1992, Hall & Bishop 2002, Jones et al. 2002, Holford et al. 2005a, Persano et al. 2007). Evidence for early Palaeogene denudation is provided by the large volumes of clastic sediments in the Faroe-Shetland

and North Sea Basins (Jordt et al. 2000, Andersen et al. 2000, Gołędowski et al. 2012, Mudge 2015). Several processes have been proposed to initiate the regional uplift in the early Palaeogene. These include transient uplift caused by a mantle plume (e.g. Clift et al. 1998, Jones et al. 2002, Hartley et al. 2011), by magmatic underplating (e.g. White & Lovell 1997, Tiley et al. 2004, Persano et al. 2007), and by the intra-plate stress due to tectonic plate reorganization or the Alpine orogeny (e.g. Nielsen et al. 2007, Cooper et al. 2012, Lundin et al. 2013).

In Britian, several AFT studies indicate that the highest Late Cretaceous-early Palaeogene temperatures (>100°C) were present in the EISB and in the Lake District (Hurford 1977, Green 1986, 1989, Lewis et al. 1992, Green et al. 1997, Thomson et al. 1999, Persano et al. 2007, Green et al. 2012). These estimates were translated to 3–4 km of Cenozoic denudation (Green 1986, Lewis et al. 1992), which in the case of the Lake District is considered to be geologically implausible (Holliday 1993). The high, ~60°C/km early Palaeogene geothermal gradient assumed by Green (2002), reduces the denudation to 1–2 km, which is more consistent with the stratigraphic reconstructions, but the proposed explanation of the elevated gradient is controversial (see section 5.3). The spatial distribution of cooling and changes of the geothermal gradient in the region remain poorly understood, and so the amount and spatial distribution of denudation cannot be accurately resolved. Also the timing of cooling could not be precisely constrained as the pre-Cenozoic temperatures were higher than the sensitivity of AFT thermochronometer. All these uncertainties result in a poor understanding of the processes behind the early Palaeogene uplift and denudation.

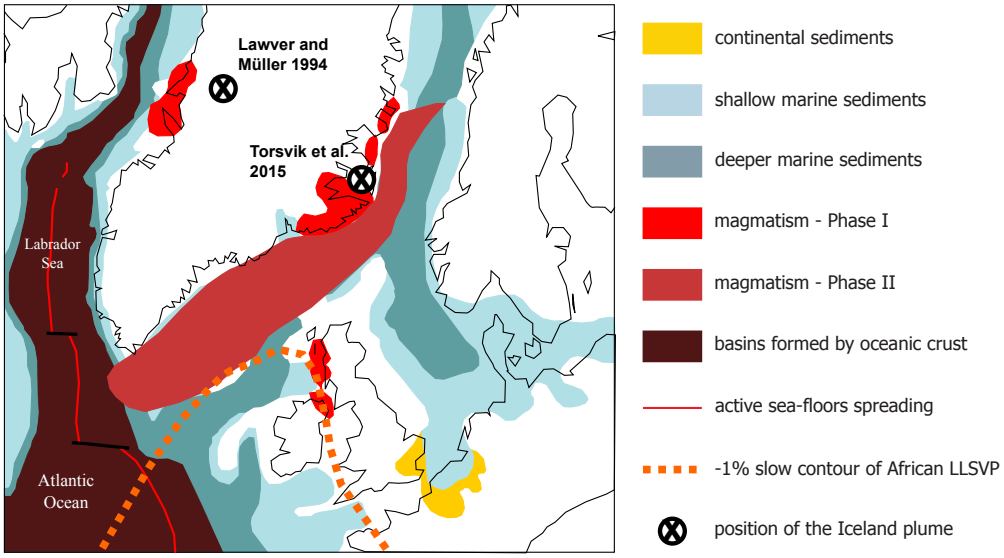

Figure 6.3: Palaeogeographical reconstruction of the North Atlantic passive margin in the early Palaeogene, prior to the onset of spreading, modified after Torsvik et al. (2002). The positions of the proto-Iceland plume at 60 Ma are after Lawver & Müller (1994) and Torsvik et al. (2015). The 1% slow shear wave velocity contour of the African Large Low Shear Velocity Province (LLSVP) after Torsvik et al. (2006) and its relative position to the North Atlantic region after Ganerød et al. (2010).

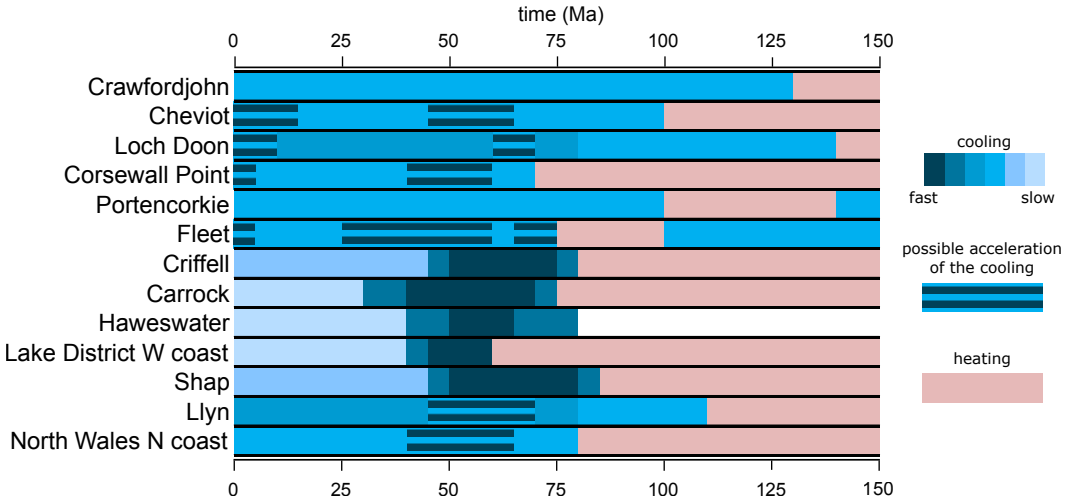

Figure 6.4: Compilation of thermal histories derived from inverse modelling, for the last 150 Ma. The localities are ordered along the quasi-north-south profile (see Fig. 3.1 for locations). If more than one sample was analysed for a given site, the most representative history is presented (see Chapter 4 for further details).

In this section the new thermal histories (Chapter 4) and the results of heat transfer modelling (Chapter 5) are used to determine the amount and spatial distribution of the early Palaeogene denudation and so constrain the processes responsible for the uplift.

6.3.2 Timing and duration of early Palaeogene cooling

The change from reheating to cooling or acceleration of the cooling rate in the latest Cretaceous/earliest Palaeogene is resolved in most of the models (Fig. 6.4). The precision with which the onset of cooling event is resolved is variable; it is the highest in the Lake District, where the amount of cooling is highest, and lowest in southern Scotland and northern Wales. Despite the inherent uncertainties, the onset of cooling appears to be diachronous across the region.

A clear transition from heating to cooling is observed in the Lake District. The cooling episode started at ~60 Ma at the western coast (LD18) and 70–75 Ma inland (LD01, LD02) (Fig. 4.1). A rapid cooling event is well resolved at Criffell (Fig. 4.2: GAL08, GAL09, GAL14) on the south coast of the Southern Uplands with onset at 70–75 Ma. In the Cheviot hills (Fig. 4.2: CH01), Corsewall Point (Fig. 4.2: GAL11; Fig. 4.14), Fleet (Fig. 4.5) and on the northern coast in northern Wales (Fig. 4.3: WL08), there is either a rapid cooling event resolved by the max-like models or a clear transition from heating to cooling at ~60–70 Ma. An acceleration in cooling rate at ~80 Ma is proposed by some models for samples from Loch Doon (Fig. 4.2: GAL01) and Llŷn (Fig. 4.3: WL07). Where the rapid Palaeogene cooling event is resolved, the rate of cooling decreases significantly at or before 40–45 Ma.

The spatial variation in the onset of rapid cooling may be directly related to the seabed topography during the late Campanian (~72 Ma) regression (Fig. 6.5; Hancock 1975).

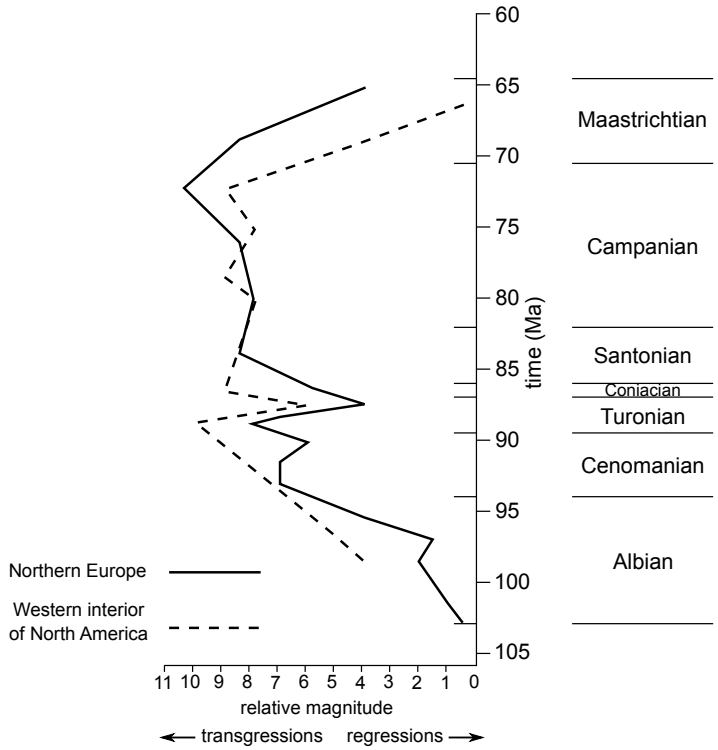

Figure 6.5: Timing and magnitude of regressions and transgressions of the Late Cretaceous sea in Northern Europe and western North America, modified from Hancock (1975).

If the Lake District block, for instance, was already a structural high on the seabed, it would have emerged first and cooling would have started here earlier than in other locations where the sea-bed was flatter and/or deeper and still submerged. This possibility fits well with the t-T paths derived from the Lake District region, where cooling at the coast started later than in the elevated, central part of the block. However the 10 Ma of difference appears to be too large to be simply explained by differences in the seabed altitude. Because there is only one sample from the coast (LD18) and its quality was low, this assumption is equivocal. The relationship between rock elevation and time of onset of cooling is also not clear in Scotland. For instance, on the coast at Criffell in southern Scotland, the onset of cooling was at 70–75 Ma. Therefore, the bulk of models indicate that the cooling started at 70 ± 5 Ma.

The onset of cooling at 70 ± 5 Ma (the Maastrichtian, the latest Cretaceous) has not been explicitly proposed for Britain. In the AFT studies, an 'early Palaeogene' onset of denudation is suggested by Green (1986) and Green (2002), with dates of ∼60 Ma and 65–50 Ma, respectively. However, the beginning of the rapid Cenozoic denudation is referred to a period between 80 and 50 Ma by Green (1989) and to 65 ± 5 Ma by Lewis et al. (1992); both intervals overlap with those found in this study. Cope (1994), based on an analysis of the unconformities and published AFT data, suggested that the uplift started in the late Maastrichtian and continued though the Palaeogene, however, this work did not gain much attention in further studies. In general, uplift in the North Atlantic region related to phase I of the volcanism was proposed to be

minor and occur only in the vicinity to the magmatic centres. The significant regional uplift is mostly related to the phase II volcanism at ∼55 Ma (Saunders et al. 2007). However, there are some indications of Maastrichtian rapid uplift and denudation in E Greenland (Petersen et al. 2015) and inversion in the Vøring Basin (Lundin et al. 2013).

The latest Cretaceous onset of cooling predates the onset of volcanism in SW Scotland and N Ireland (Antrim, 62.6 ± 0.3 Ma; Ganerød et al. 2010) by ∼2–12 Ma. The uplift and erosion prior to the volcanism is, however, apparent in many places. Both in NW Scotland and N Ireland, the Palaeocene lavas lie unconformably on Jurassic or Cretaceous rocks and display evidences of subaerial conditions during extrusion of the lavas (Simms 2000, Bell & Williamson 2002, Hopson 2005, Brown et al. 2009, Williamson & Bell 2012). The unconformity is clearly erosional with breccias and conglomerates at the base (Williamson & Bell 2012). In N Ireland, the lavas (62.6–59.6 Ma; Ganerød et al. 2010) are in the direct contact with chalk, of which the youngest succession, exhibiting significant karstic erosion, is early Maastrichtian (∼70–72 Ma) (Simms 2000). That implies the uplift occurred after ∼70 Ma and before <62.6 Ma. Although, it has been suggested that the thermal uplift directly preceded the eruption of lavas and was restricted to the vicinity of the magmatic centres, the Cenomanian-Maastrichtian boundary is coincident with the onset of regression of the Late Cretaceous sea (Hancock 1975) (Fig. 6.5).

Saunders et al. (2007) pointed out that enhanced sedimentation in the earliest Palaeogene was localized and limited to the vicinity of the magmatic centres, suggesting that erosion was also localized. Latest Cretaceous–early Palaeocene sedimentation in the Faroe-Shetland, Porcupine and North Sea Basins is small when compared with the more recent Cenozoic phases and the maximum influx of thick clastic sediments is attained in the late Palaeocene–Eocene (Liu & Galloway 1997, Stoker et al. 2010, Mudge 2015). A lack of latest Cretaceous clastic sediments in the distal basins and the relatively slow sedimentation rate in the early Palaeocene can be at least partly explained by the nature of the eroded material. During the first phases of denudation, the rocks subjected to erosion were probably the Cretaceous chalk and some Jurassic limestones; this implies the eroded material was largely removed by chemical dissolution and a clastic sequence is therefore not expected (Cope 1994, Simms 2004). There is also the possibility that the sediments produced by the Late Cretaceous/early Palaoegene erosional event were accumulated in proximal basins and that, as it often happens in areas that experience a sudden uplift, they were slumped into the distal basins where they are now found with an apparent Late Palaeocene-Eocene stratigraphic age (Sinclair & Tomasso 2002). Therefore, the Late Palaeocene and Eocene sediments can actually be Early Palaeocene in age.

6.3.3 Spatial distribution of early Palaeogene cooling

The maximum temperatures reached before the early Palaeogene cooling show a characteristic pattern (Chapter 4, Fig. 4.11). Rocks now at the surface were at up to ∼140°C at Criffell in the early Cenozoic and at 110–120°C in the Lake District and Anglesey. Palaeotemperatures decrease to less than 60°C to the north (in southern Scotland) and south (in northern Wales). In the areas were the palaeotemperatures were higher than 100°C, the early Palaeogene cooling rate was generally in the range of 2–10°C/Myr with some max-like models giving rates up to ∼25°C/Myr (e.g. Fig. 4.2: CH01, Fig. 4.14; Corsewall Point). The cooling rates decreased at 40–45 Ma when palaeotemperatures of 20–30°C were attained.

There is a general agreement between the maximum Late Cretaceous palaeotemperatures obtained in this study and the published estimates of Green (1986) and Green et al. (1997) based on the AFT analyses in the Lake District and surrounding basins. One major difference is the lower palaeotemperatures (<90°C) reported for the central Lake District shown on the map of Green et al. (1997). These palaoetemperatures may be related to the fact that the samples were collected at high elevation, but as no information are given about sample location, this possibility cannot be either confirmed or discarded. The AFT data from the elevation profile from around Scafell Pike indicate a quite significant temperature increase downhill (Green 2002). The early Palaeogene temperatures were 55–80°C and 40–75°C at elevations of 966 and 808 metres, respectively, and they were >100°C for the rocks at the bottom of the profile. Rocks analysed during this study are from elevations lower than 500 m and the sampled vertical differences are not enough to observe a temperature decrease. Published AFT data from southern Scotland and northern Wales are scarce. The high palaeotemperatures at Criffell and general westward decrease of palaeotemperatures in southern Scotland are, however, in agreement with the conclusions of Green et al. (1997).

6.3.4 Spatial distribution of early Palaeogene denudation

The difficulty of translating cooling into denudation was extensively discussed in Chapter 5. Although the spatial variation of the present-day geothermal gradient does not correlate with the observed pattern of ages and palaeotemperatures, a strong correlation exists between the cooling ages and the present-day surface heat flow. As shown in Chapter 5, the high heat flow in the Lake District is due to the presence of a heat producing granite batholith that may have significantly affected the age pattern. The models presented in Chapter 5 have been computed to estimate the coupled effect of blanketing and heat production on the amount of denudation. This required assumptions to be made regarding the uniformity of uplift, spatially uniform thickness of the sedimentary blanket, number of uplift phases and geometry of heat producing bodies. More realistic scenarios of landscape evolution increases the number of parameters

used in Pecube, which, in turn, increases the modelling time. Here, for each main data point, the amounts of cooling derived from the QTQt thermal models are translated into denudation, taking into account the radiogenic heat production and a possible range of thicknesses and composition of the sedimentary blanket, at any given site.

It is unlikely that the Mesozoic sediments were uniformly distributed in the study region. The basins were depocentres since the Permian/Early Triassic, whereas the

Table 6.1: Minimum and maximum thicknesses of the Mesozoic sedimentary layer, divided into chalk and 'other' sediments, used for the calculation of the thickness of the eroded basement and of the total early Palaeogene denudation. It is important to point out that the thickness of the sediment column is an input parameter in the calculation, whereas the amount of eroded basement is the output, estimated as the difference between the total amount of denudation required to obtain the observed amount of cooling and the assumed sedimentary cover.

		Thickness of eroded strata (m)			
Locality		Chalk	Other sediments*	Basement	Total
Cheviot	max	200	400	900	1500
	min	400	600	100	1100
Crawfordjohn	max	0	0	1200	1200
	min	0	400	600	1000
Loch Doon	max	0	0	1200	1200
	min	0	400	600	1000
Corsewall Point	max	400	400	400	1200
	min	600	400	0	1000
Portencorkie	max	0	0	1200	1200
	min	100	400	500	1000
Fleet	max	100	400	1000	1500
	min	300	400	500	1200
Criffell	max	500	1000	1000	2500
	min	600	1400	200	2200
LD	max†	300	400	1400	2100
	min†	600	1150	0	-
	min2	400	900	200	1500
Anglesey‡	-	600	1000	600	2200
N Wales coast	max	100	400	900	1400
	min	400	400	200	1000
Llŷn	max	0	0	1200	1200
	min	100	400	500	1000

* 'Other sediments' are the Mesozoic sediments older than Late Cretaceous and include mostly Lower Jurassic and Triassic limestones, mudstones and sandstones
† minimum and maximum estimates after Holliday (1993)
‡ given the low quality of the data and lack of a thermal model for Anglesey, the estimates are produced assuming an early Palaeogene temperature of 120°C

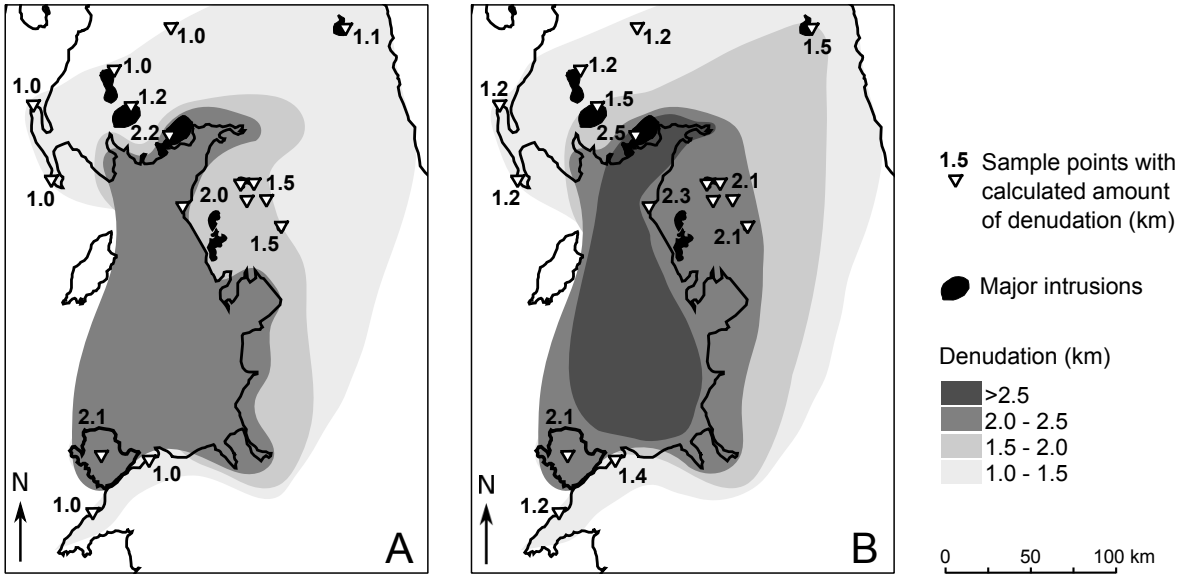

Figure 6.6: Amount of early Palaeogene denudation in central west Britain derived from the AHe and AFT data and the thermal models presented in Chapter 4; A—minimum estimate, B—maximum estimate; see Table 6.1 for the exact values of the sedimentary cover.

Lake District, southern Scotland and northern Wales formed structural highs, which, even if they were buried, they had not accumulated as much sediment as the basins. Holliday (1993) estimated the Mesozoic overburden in northern England to have ranged between 700 and 1750 m, of which 300–600 m was composed of chalk.

Following the calculations of Holliday (1993), the minimum and maximum thicknesses of the Mesozoic overburden have been estimated for each of the main localities analysed during this study. The sedimentary cover has been divided into chalk and 'other sediments', in order to better deal with a vertical variation of the geothermal gradient; thermal conductivity has been set to 1 W/m/K and 2 W/m/K, respectively. It is important to bear in mind that at least part of the eroded succession could have comprised basement rocks. Based on the amount of early Palaeogene cooling derived from the QTQt thermal histories (Chapter 4) and the predicted values of the geothermal gradient (Chapter 5), the amount of eroded basement and the total early Palaeogene denudation have been calculated for given thicknesses of sedimentary cover. The results are presented in Table 6.1. For comparison, the same procedure has been used to calculate the amount of denudation in the EISB, using the values of palaeotemperatures of 90–100°C derived from the study of Lewis et al. (1992); the estimates of 2.0–2.5 km are in good agreement with those reported by other studies (Table 6.2).

The calculated total rock removal has been used to build simplified maps of the distribution of denudation, for the minimum and maximum estimates of sedimentary cover (Fig. 6.6). The highest amounts of denudation, 2.0–2.5 km, are observed in the EISB and on the southern coast of the Southern Uplands at Criffell. Slightly less denudation,

Table 6.2: Compilation of published estimates of early Palaeogene denudation in central Britain.

Author	Method	Region	Denudation (m)
Green 1986	AFT (raw data, no thermal modelling)	Lake District	3000–4000
Lewis et al. 1992	AFT (raw data, no themal modelling)	NW England & EISB	∼3300 km
Green 2002	AFT	The LD block	700–2000
Chadwick et al. 1994	Modelling of AFT	Lake District	1750
		EISB ad SFB	2000-3000
Holliday, 1993	Modelling of AFT	NW England	1400–1700
Cope, 1994	estimate (?)	EISB, N Wales	<2000
		SW Scotland, NW England	1000–2000
Rowley & White, 1998	Stratigraphy modelling	N Wales	500–1000
		others	2000–3000
Jones et al. 2002	Subsidence and AFT lengths modelling	EISB and West Midlands (England)	1000–1500
		NW England, SW Scotland, N Wales	500–1000
Green et al 1997	AFT & VR	EISB	1500-2000
Green et al. 2012	AFT	NE England	850–1150
Hardman et al. 1993	Geochemical modelling	EISB	300–3000
Holford et al. 2005	AFT & VR	EISB	∼2000
Pearson & Russel, 2000	Maturity modelling	NE England	1600–2800
Mackay & White, 2006	Stacking velocity data modelling	EISB	<1000
Colter, 1978	Shale velocity modelling	EISB	2000–3000
Roberts, 1989	VR	EISB	2000
Stuart & Cowan 1991	Maturity modelling	EISB	450
Jackson & Mulholland, 1993	compilation	EISB	2000–2500
Knipe et al. 1993	Structural shortening estimation	EISB	1500–2000

1.5–2.0 km, is predicted for the Lake District. In northern England and southern Scotland the denudation decreases to ∼1 km in the northernmost part of the Southern Uplands. A sharp decrease of the amount of denudation is observed along the coast of the Welsh mainland; the predicted amounts of denudation are in the range of 1.0–1.4 km on the mainland, whereas on Anglesey and in the EISB it exceeds 2 km. This pattern is, however, based solely on the low quality datum from Anglesey and has to be treated with caution.

The published estimates of the amount of early Palaeogene denudation in Britain are variable (Table 6.2). The denudation maps presented in this study and the published offshore estimates are in general agreement. The amounts of onshore denudation proposed in this study are in good agreement with the denudation predictions of Holliday (1993), Cope (1994), Chadwick et al. (1994), Green (2002) and Green et al. (2012). There is no agreement with the high values of >3 km presented by Green (1986) and Lewis et al. (1992).

6.3.5 Causes of early Palaeogene denudation

The timing of cooling, the location of uplift region and the spatial distribution of denudation can be used to provide insights on the causes of uplift.

Timing

The onset of cooling at 70 ± 5 Ma pre-dates the onset of the plume-related magmatic activity in NW Scotland and Northern Ireland by ∼5–10 Ma. The Antrim basalts appear to be the first manifestation, and were erupted at 62.6 ± 0.3 Ma (Ganerød et al. 2010). Offshore northern Britain, a suite of basalt lavas forming seamounts in the Rockall Trough have been dated as Late Cretaceous, suggesting that the plume related magmatic activity could have started as early as ∼70 Ma (O'Connor et al. 2000). However, the Late Cretaceous ages of O'Connor et al. (2000) were later questioned by Chambers et al. (2005) and so far there is no evidence for the volcanism before 62 Ma.

In the 'starting plume' model, rapid rock uplift is generated largely when the mantle plume impinges at the base of the lithosphere, and the surface volcanism is predicted to occur almost simultaneously (Campbell & Griffiths 1990). The plume incubation model predicts that in the case of >125 km think lithosphere, the plume head incubates for 70–150 Myr before initiation of the surface volcanism (White & McKenzie 1989, Kent et al. 1992). However, in the case of thin lithosphere, the incubation period may be less than 10 Myr and rock uplift will occur slightly prior the volcanism (e.g. the Deccan platform; Kent et al. 1992, Sheth & Chandrasekharam 1997). There is an ongoing debate on whether the starting or incubating plume model is applicable for the NAIP. The plume incubation model is generally discarded on the basis that the regional uplift is mostly coincident with the magmatism (Clift et al. 1998). The

chemical composition of the Palaeocene lavas in NW Scotland exhibit high degree of lithospheric contamination (e.g. Ellam 1992). Such contamination and the presence of significant lithospheric thinning can be explained by short plume incubation for ∼10 Myr and 'eroding' the lithospheric mantle (Kerr 1994). This together with the early onset of uplift may suggest that the short, ∼10 Myr-long incubation of the plume in the North Atlantic is likely, although, more work has to be done to confirm this hypothesis.

The onset of denudation precedes the break-up in the North Atlantic (53–55 Ma; Lundin & Doré 2005) by ∼15 Ma that suggest that these events are not directly connected. The first compressional movements in the Alpine zone took place in Late Turonian–Early Sanonian ("the sub-Hercynian phase") and in the Mid-Palaeocene ("the Laramide phase") (Ziegler 1990). The former was responsible for the initial inversion of the Sole Pit High in the Southern North Sea Basin between between the Turonian and the Campanian (∼84–90 Ma), about 15 Ma before the onset of cooling (Van Hoorn 1987, Ziegler 1990). The major inversion in the British basins occurred in the Oligocene, well after the early Palaeogene event (Ziegler 1988, 1990). The timing of uplift and denudation is coincident with the plume activity, rather than rifting and Alpine inversion. However, bearing in mind that the inversion episodes in the surrounding basins started as early as in the Late Cretaceous, these causes of uplift cannot be disregarded simply on the basis of time.

Location

In the early Palaeogene, the Lake District was ∼1000 km away from the Alpine front in the south and ∼1000 km from the spreading axis of the North Atlantic in the north. These distances make the fact that the observed denudation was driven by rift flank uplift or tectonic uplift due to the Alpine compression doubtful. The compressional stress can, however, be transmitted far from the plate boundaries and cause localized inversion or lithospheric buckling (Cloetingh et al. 1999, Holford et al. 2009). The location of the proto-Iceland plume at ∼60 Ma is debatable. According to Lawver & Müller (1994) the proto-Iceland mantle plume was, at that time, located beneath western Greenland (Fig. 6.3), about 2000 km from Britain. This distance suggests that if the plume material spread radially from the plume head, as in the classic models (e.g. White & McKenzie 1989), central west Britain was located outside the plume impact zone. However, recently Torsvik et al. (2015) relocated the plume to eastern Greenland (Fig. 6.3); this new location would reduce the distance to about 1000 km, placing the study area within the plume impact zone. Additionally, seismic data suggest that, rather than having a symmetrical, radial geometry, the early proto-Iceland plume anomaly might have been formed by two intersecting perpendicular sheets, one of which extended from Greenland to NW Britain (Barton & White 1997, Al-Kindi et al. 2003). Some studies proposed also that the NW Scotland and N Ireland magmatism could have been caused by other mantle plumes (e.g. Cope 1994, Ganerød et al. 2010). For

instance, Ganerød et al. (2010) suggested that the palaeolatitude of the British Isles was much more to the South than present day and they suggest that the Canary Island hot spot is a much better candidate for the volcanism than the Icelandic plume, if the positions of these have been fixed in the last 60 Ma. In summary, given the distance from the opening ocean, rift flank uplift can be discarded as a mechanism for uplift and denudation in central west Britain, but plume activity or intra-plate stress are, at this point, an equal possibility.

Spatial distribution

The spatial distribution of denudation, however, does not support the compressional nature of the uplift. In this case, the reactivation of older structures would be expected, creating a sharp change in denudation either side of faults (e.g. Wildman 2015). In central west Britain the amounts of denudation change gradually. The only exception is found in northern Wales, where a sharp change in denudation has been estimated between the EISB and Anglesey on one side of the Menai Strait Fault, and the Welsh mainland on the other. The constraints on the amount of denudation on Anglesey are weak, due to the poor quality of the data; however, a Cenozoic reactivation of the Menai Strait Fault System has been demonstrated via seismic imagining of the strike-slip displacements of the early Palaeogene dykes (Bevins et al. 1996). Cenozoic fault reactivation is also recognized in the regions surrounding the study area, e.g. in N Ireland (Cooper et al. 2012) and along the Great Glen Fault in N Scotland (Le Breton et al. 2013). The timing of these movements has not been further constrained and it may be just a local-scale feature. For all these reasons, and, more importantly, for the overall uniform pattern of early Palaeogene denudation in central west Britain, the cause of uplift is considered to be better explained by dynamic uplift due to a mantle plume and/or permanent uplift due to underplating.

6.3.6 Dynamic and permanent uplift

The timing, location and spatial distribution of the early Palaeogene uplift event seem to be consistent with a mantle plume origin. In the presence of a mantle plume, transient uplift is created by both dynamic support of the upwelling material and thermal expansion; when it ceases its activity, the area underneath which the plume was impinging starts to subside (White & McKenzie 1989, Saunders et al. 2007). According to the model of White & McKenzie (1989), such transient, dynamic uplift may reach up to 1–2 km, within a region of 1–2 km diameter. The present-day high topography in the Lake District, and to a lesser degree, in southern Scotland and northern Wales, requires a component of permanent uplift that counteracts the subsidence when the mantle thermal anomaly has ceased. Permanent uplift is generated via the emplacement of low density magmas beneath (underplating) or within the crust (intrusions) (White & McKenzie 1989, Saunders et al. 2007).

In this section, the calculated amounts of denudation are compared to the uplift that could be driven by underplating and/or a thermal anomaly to further assess the possibility that the early Palaeogene denudation is directly related to the presence of a mantle plume and does not require any other mechanism.

6.3.6.1 Underplating-driven permanent uplift

That underplating material is present underneath the North Atlantic region is well established, but its thickness is still poorly constrained and there are discrepancies between different estimates (Brodie & White 1994, Clift & Turner 1998, Al-Kindi et al. 2003, Tomlinson et al. 2006). None of the proposed models provide a thickness of underplating that is fully consistent with the amounts of denudation predicted in this study and other published estimates summarized in Tables 6.1 and 6.2. The best fit

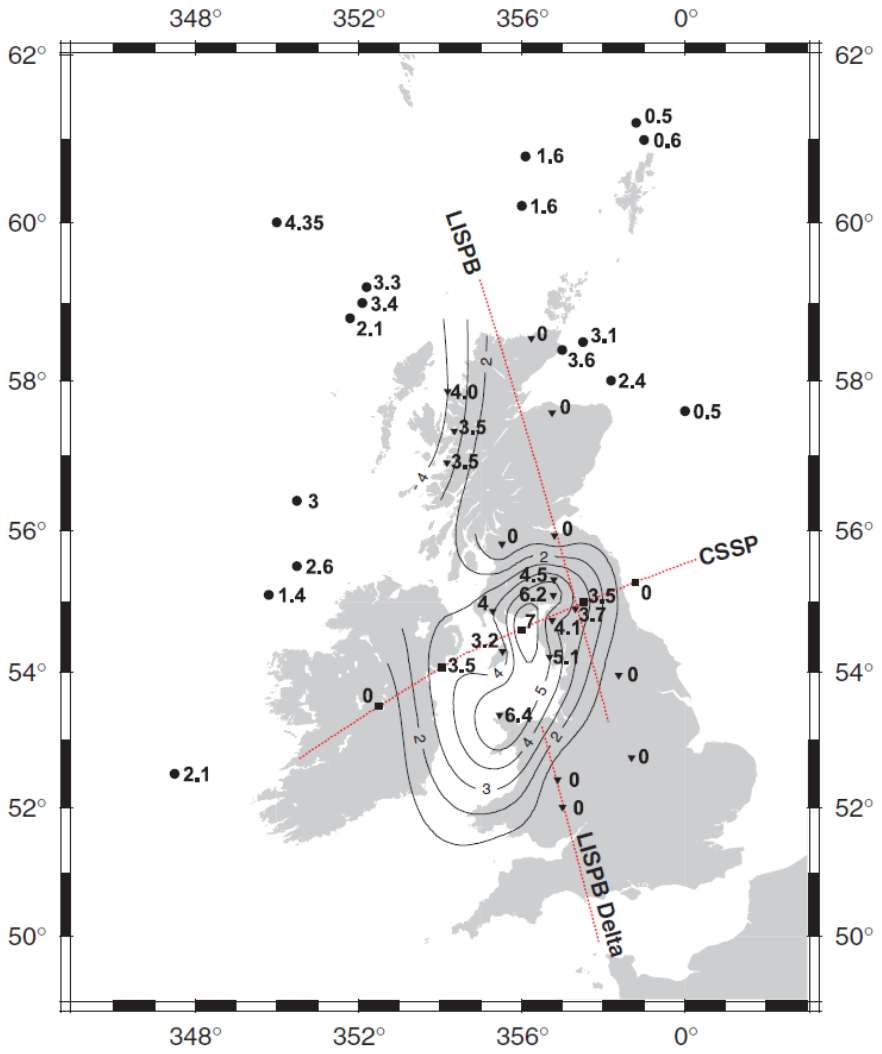

Figure 6.7: Map of thickness of magmatic underplating beneath the British Isles based on the receiver function modelling by Tomlinson et al. (2006) (triangles) and the wide-angle seismic model of Al-Kindi et al. (2003) (squares); offshore estimates (dots) derived from the underplating map of Clift & Turner (1998); after Tomlinson et al. (2006). The dotted red lines show the location of the Lithospheric Seismic Profile in Britain (LISPB; Bamford et al. 1978) and the Caledonian Suture Seismic Experiment (CSSP; Al-Kindi et al. 2003).

is, however, obtained for the values estimated by Al-Kindi et al. (2003) and Tomlinson et al. (2006) (Fig. 6.7). The importance of underplating as a mechanism to explain the early Palaeogene uplift and denudation in Britain has been extensively studied by Tiley et al. (2004), who calculated the amount of denudation that would be produced by the thickness of the underplated material derived from the seismic data of Al-Kindi et al. (2003). The results show that >2 km of denudation could have been produced in the EISB, however, almost no denudation is predicted onshore, where the given thickness of underplating may, at most, isostatically balance the existing topography. If the underplating thicknesses and parameters used in the model of Tiley et al. (2004) are correct, the hypothesis that the early Palaeogene uplift in central Britain was driven by a mantle plume needs to be revisited, as the spatial pattern of denudation and the present-day topography cannot be explained by a combination of transient and permanent uplift.

There may be several reasons why the model used by Tiley et al. (2004) seems to underestimate the amount of uplift onshore. The most important issue may be the isostatic model and neglecting the spatial variation of the model parameters, during the calculations of denudation. The equation to calculate denudation from a given thickness of magmatic underplating, present-day topography (called 'residual uplift' in the paper) and initial water depth assumes Airy isostasy and is taken after White & Lovell (1997), as follows:

$$X = (\frac{\rho_m - \rho_s}{\rho_m - \rho_x})D + (\frac{\rho_m}{\rho_m - \rho_x})T + (\frac{\rho_m - \rho_w}{\rho_m - \rho_x})W \tag{6.1}$$

where
X is thickness of magmatic underplating
D is amount of denudation
T is present-day topography
W is water depth prior the emplacement of the underplating layer
ρ_m is density of mantle/asthenosphere
ρ_s is density of upper crustal rocks, usually sediments
ρ_w is density of water (1.0 g/cm^3)
ρ_x is density of magmatic underplating

A number of observations should be made regarding Equation 6.1. Firstly, in order to keep denudation constant, if the present-day topography changes the thickness of underplating magma needs to change significantly. For instance, an increase in the average topography of 200 m requires the layer of underplating material to be ∼2 km thicker (Fig. 6.8). For an extreme value of lithospheric elastic thickness of 0 km, and spatially constant denudation, the highest peaks (900–1000 metres) would be in iso-

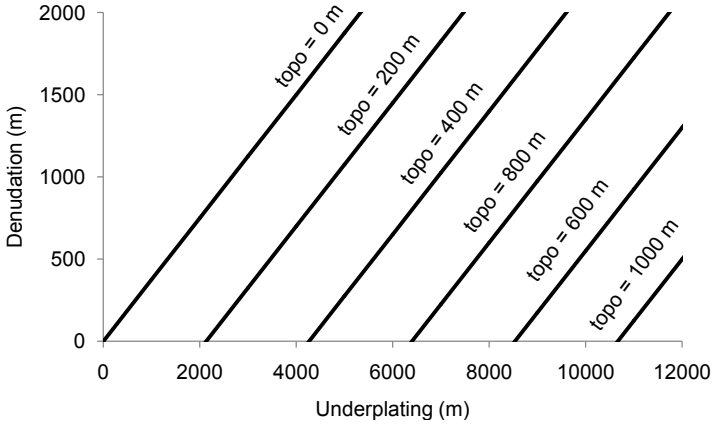

Figure 6.8: Dependence of denudation on thickness of underplating magma and the present-day topography (called 'topo' in the diagram), calculated assuming Airy isostasy using Equation 6.1, after White & Lovell (1997). Parameters used: ρ_m—3.2 g/cm^3, ρ_s—2.4 g/cm^3, ρ_x—2.9 g/cm^3. For simplification, the water depth, W, was assumed to be 0. Note that by adding a positive value for W, the thickness of underplating required to obtain the same amount of denudation and residual topography would be larger.

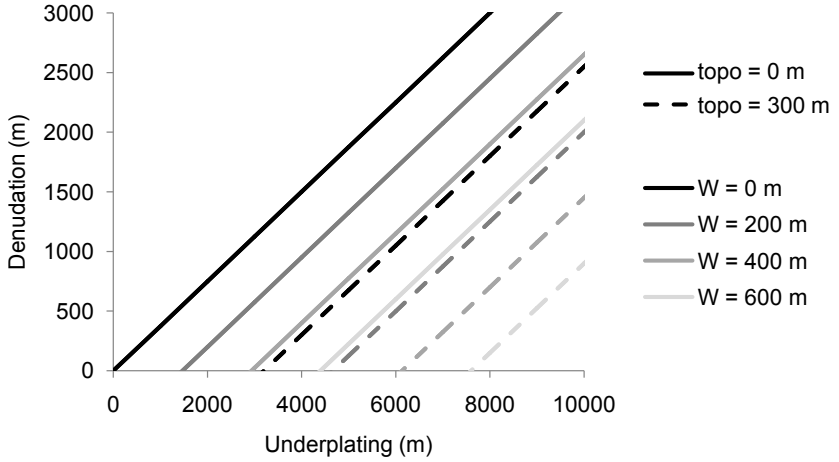

Figure 6.9: Dependence of denudation on thickness of underplating magma, the present-day topography (called 'topo' in the diagram) and initial water depth, W, calculated assuming Airy isostasy using Equation 6.1, after White & Lovell (1997). Used parameters: ρ_m—3.2 g/cm^3, ρ_s—2.4 g/cm^3, ρ_x—2.9 g/cm^3.

static equilibrium only if the underplating layer is ∼10 km thicker than beneath the coastal areas. Using the value of lithospheric elastic thickness proposed by Tiley et al. (2003) of 5 ± 2 km, the average elevation of the region, which, for the Lake District, is 200–250 m and an amount of denudation of 1.5–2.0 km, ∼0.5 km less than in the EISB, the underplating layer would need to be about 1 km thicker beneath the Lake District than the basin offshore. This is not consistent with the seismic data (Al-Kindi et al. 2003, Tomlinson et al. 2006; Fig. 6.7).

Another reason why the model of Tiley et al. (2004) failed to predict the amount of onshore denudation may lie in the use of constant water depth and density of the eroded material. In the Late Cretaceous, these two parameters may have had different values in the Lake District and the EISB. For instance, ∼1.5 km of denudation can be obtained for a water depth of zero and a 4 km thickness of magmatic underplating

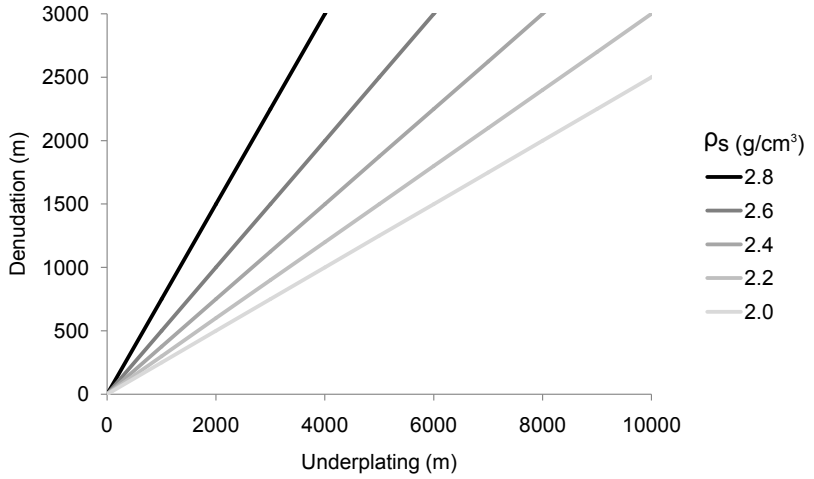

Figure 6.10: Dependence of denudation on thickness of magmatic underplating and density of eroded layer (ρ_s), calculated assuming Airy isostasy using Equation 6.1, after White & Lovell (1997). Used parameters: ρ_m—3.2 g/cm^3, ρ_x—2.9 g/cm^3. To isolate the effect of density on denudation, the water depth, W, and present-day topography, T, were set to 0 m.

(Fig. 6.9). If the water depth increases to 200 m, the same amount of denudation is obtained only if the underplating increases to 4.5 km. The density of the eroded layer is also important. The denser the layer, the less thick the underplating layer is required to maintain denudation (Fig. 6.10). The average depth of the Late Cretaceous sea varied from 100 to 600 m (Hancock 1975). It is likely that the Lake District formed a structural high and thus 100 m seems to be a decent approximation, whereas sea-level can be set to 400–500 m in the EISB. Probably the central and northern parts of the Southern Uplands and some areas in northern Wales were emergent and, therefore, the parameter may be reduced to 0 m. A difference in water depth of 300–400 m can reproduce the estimated amounts of denudation, for the thickness of underplating used in the Tiley et al.'s model. The model would produce the measured amounts of denudation also if, in the Lake District, a large part of the eroded layer was composed of basement rocks that are much denser than the EISB sediments. The basement rocks in the Lake District comprise mainly Ordovician–Silurian volcanics and Early Devonian granites that have densities of ∼2.7–2.8 g/cm^3 and ∼2.6–2.7 g/cm^3, respectively (Bott 1974). The rocks being eroded in the EISB, on the other hand, were mostly Lower Mesozoic sandstones and mudstones that have much lower densities, ∼2.0–2.4 g/cm^3 (Bott 1974, Hobbs et al. 2002). The density difference might have been ∼0.4–0.6 g/cm^3, which implies that the amount of denudation induced by isostatic rebound could have been higher in the the Lake District, even if the underplating layer was a similar thickness.

Once the variable water depth and rock density is taken into account, equation 6.1 can be used to calculate amount of denudation for given thickness of underplating, across central west Britain. The range of parameters and calculated denudation for the main localities are given in Table 6.3. In northern Wales, the amount of denudation

due to underplating driven uplift exceeds the amount of denudation predicted by the thermal models, regardless of the combination of parameters used. This misfit may be due to the fact that estimates of magmatic underplating in this area are not accurate or that the amount of underplating is the result of more than one event and therefore not all the seismically 'imaged' magmatic material is early Palaeogene. In all other localities, the amounts of denudation calculated using equation 6.1 are significantly lower than the total early Palaeogene denudation predicted by the thermal models; this implies that the emplacement of the underplating layer is not sufficient to account for the total denudation that occurred in the region in the early Palaeogene. The 'missing' portion of denudation is relatively constant across the study area and it varies from a minimum of ∼700 m to a maximum of ∼1200 m. This requires a different source of uplift, which will be discussed in the following section.

6.3.6.2 Transient, thermal uplift

The spatial uniformity of the 'missing' portion of denudation requires that the uplift that initiated the erosion was also spatially constant. Assuming local isostasy, the amount of tectonic uplift (U_T) necessary to explain the non-underplating driven denudation can be calculated using the following equation (Braun et al. 2006):

$$U_T = U_r - I = h_i - h_0 + D(1 - \frac{\rho_s}{\rho_m}) \tag{6.2}$$

where
U_T is tectonic uplift
U_r is rock uplift
I is isostatic rebound
h_i is present-day surface elevation
h_0 is initial surface elevation
D is denudation
ρ_s is density of eroded material
ρ_m is density of asthenosphere/mantle

The LTT-derived thermal histories indicate that the onset of cooling slightly predated the magmatic activity in the NAIP, suggesting that the first phase of uplift could not have been created by underplating, but originated by a mechanism that occurred a few million years earlier. For these reasons, it is likely that U_T was related to the dynamic, thermal support from the mantle plume. The term describing the change in surface elevation ($h_i - h_0$) in equation 6.2 can be discarded, as the effect of topography on denudation has been accounted for in equation 6.1. The density of the eroded material during the U_T phase is assumed to be 2.0–2.2 g/cm^3, given that both the basin and the presently onshore areas were covered by sedimentary rocks. Using equation 6.2, the amount of tectonic uplift (U_T) in all localities has been calculated, for density values of

Table 6.3: Ranges of parameters used in the calculation of the underplating driven denudation and non-underplating driven uplift; ρ_s is the density of the eroded material; W is the assumed Late Cretaceous water depth, X is the assumed underplating thickness, based on the maps of Al-Kindi et al. (2003), Tomlinson et al. (2006); T is the average present-day topography, D_T is total early Palaeogene denudation estimated using the LTT data; D_X is the amount of denudation caused by underplating; D_{T-X} is the amount of denudation remaining unexplained by underplating; U_T is the amount of non-underplating driven uplift required to explain D_{T-X}. D_{T-X} was calculated using equation 6.2 for two values of eroded rock density: 2.0 and 2.2 g/cm^3, and assuming no change in elevation. Used constants: $\rho_m = 3.3$ g/cm^3, $\rho_x = 2.9$ g/cm^3, $\rho_w = 1.0$ g/cm^3.

Locality	ρ_s (g/cm^3)	W (m)	X (km)	T (m)	D_T (km)	D_X (km)	D_{T-X} (km)	U_T (m)
Lake District	2.5–2.7	100	4	250	1.5–2.0	0.8	0.7–1.2	237–477
EISB	2.2–2.3	400	6	0	2.0–2.5	1.3	0.1–1.2	233–472
N Southern Uplands	2.4	0–100	2–3	100–250	1.0–1.5	0.3	0.7–1.2	219–456
Criffell	2.3–2.4	300	5	0	2.2–2.5	1.4	0.8–1.2	272–440
northern Wales	2.4	100	5	50	1.0–1.4	*1.8*	-	-
						AVERAGE		240–470

2.0 and 2.2 g/cm^3 and for the minimum and maximum estimates of denudation derived from the thermal histories; the results are reported in Table 6.3. The regional average ranges from 240 to 470 m (355 ± 115 m). By assuming a lower density for the eroded material, as it may be expected as the sediments might had not been compacted, the U_T value could have been up to several hundreds of metres higher. Similarly, if the density of the underplating material was higher than assumed, the U_T has to be higher to account for the total denudation. The average U_T reported in Table 6.3 is consistent with theoretical values calculated considering the effect of density changes due to the presence of an anomalously hot mantle. Numerical models have shown that a temperature increase in the mantle of 100°C can produce ∼500 m of uplift (White & McKenzie 1989).

Several hypotheses have been put forward to explain the effect of a mantle plume in Britain; these include a single, radial proto-Iceland plume centred beneath Greenland (White & McKenzie 1989), hot mantle sheets extending from Greenland to northern Britain (Barton & White 1997, Al-Kindi et al. 2003) or the possibility that Britain was affected by other, small mantle plumes (Cope 1994, Ganerød et al. 2010). Regardless of the character of the mantle anomaly that caused the uplift and its geographical position in relationship to the study area, the calculated 240–470 m of transient uplift is comparable with estimates from other areas in or around Britain. Transient plume related uplift in the Palaeocene has been found in the North Sea and Faroe-Shetland basins, where it reached 300–500 m and 500–900 m, respectively, likely had a pulsed character, and was followed by subsidence in the Eocene (Nadin et al. 1997, Rudge et al. 2008, Shaw Champion et al. 2008, Hartley et al. 2011).

6.3.6.3 Evidence for present-day mantle anomalies

Recent work indicates that hot low density mantle underlies the British Isles (Bott & Bott 2004, Arrowsmith et al. 2005, Davis et al. 2012). Bott & Bott (2004) used the mantle temperature estimates from Goes et al. (2000) in a finite-element model and showed that the present mantle anomaly could have caused isostatic uplift of western Britain and the Irish Sea in the Cenozoic. The model of Bott & Bott (2004) includes four different scenarios, including a crust with or without faults. The results indicate that a large part of Cenozoic uplift in Britain was due to a thermal anomaly in the upper mantle that caused isostatic uplift and reactivation of some pre-existing faults, under a compressional regime. They concluded that the uplift due to a present-day thermal anomaly, together with isostatic uplift induced by denudation, can explain the characteristic asymmetry of the uplift magnitude in the region (the highest uplift in the Irish Sea decreasing slowly eastward and sharply westward), as well as up to 3 km of denudation. The model of Bott & Bott (2004) is also consistent with the mechanisms of the present earthquakes in Britain, which could be explained by tensional, loading stresses to be expected in the presence of a thermal anomaly at depth. The model fails, however, to explain the topography of northern England and Wales and so, it needs further work.

More recently, higher resolution teleseismic studies by Arrowsmith et al. (2005) and Wawerzinek et al. (2008) in Britain and Ireland respectively, confirm the presence of a low velocity region that is interpreted as hot, low density mantle beneath the region. The anomaly is observed beneath the Irish Sea and the western parts of Scotland and England and correlates well with gravity anomalies and high topography, with the exception of the Irish Sea (Fig. 6.11). The authors suggested that this anomaly represents an extended arm of the proto-Iceland plume and its preservation for ∼60 Ma until the present day indicates that either the lithosphere and the upper 100–200 km of the asthenosphere remained coupled and followed the plate motions or that the plume material was trapped within a 'thin spot' (Sleep 1997) in the lithosphere. The idea that the anomaly did not dissipate is somewhat controversial and has been widely criticized (e.g. Westaway 2006, Foulger et al. 2013). Westaway (2006) suggested that the pattern observed by Arrowsmith et al. (2005) is not related to the proto-Iceland plume, but to differences in the thermal properties of the crust, and thus rigidity, that can explain all the upper mantle temperatures, the present day topography and the observed gravity anomaly. Further works suggested that the apparent low wave speeds underneath the British Isles are not low, when compared with the global mean; this conclusion is at odds with the hypothesis of an underlying hot, low density mantle anomaly (Foulger et al. 2013 and reference therein). However, the upper mantle temperature does not need to be high in absolute terms to have an impact on the crust above as the most important variable is the spatial difference in temperature. Higher temperature beneath western Britain than beneath surrounding area is, therefore, likely to trigger some re-

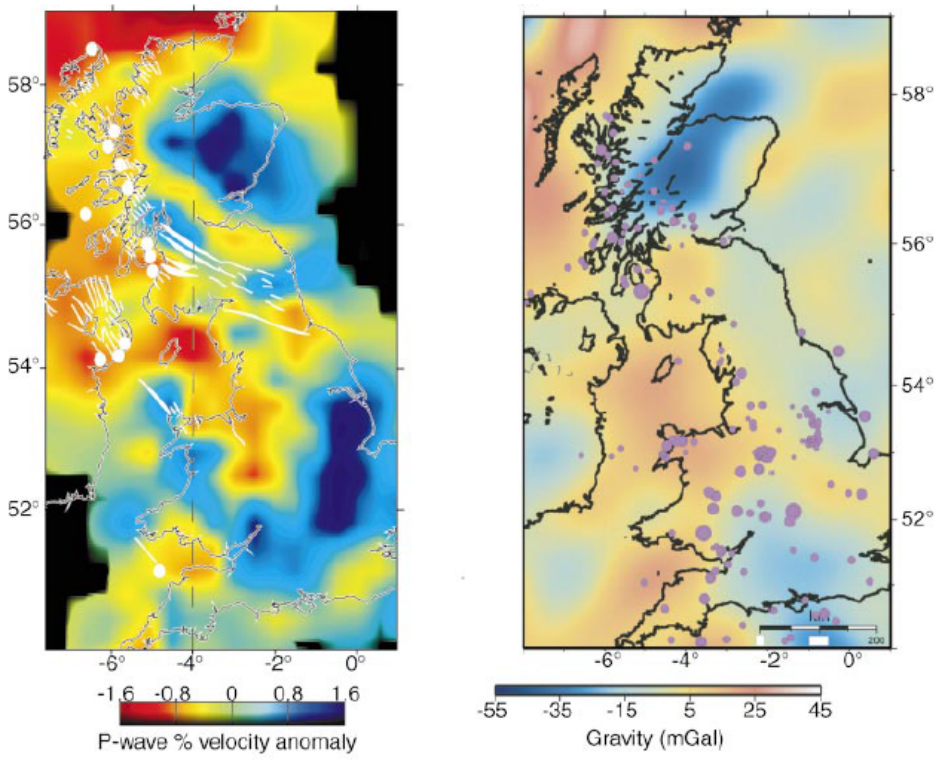

Figure 6.11: Left: P-wave velocity model at depth of 100 km, based on the teleseismic study of Arrowsmith et al. (2005); the white features on the map represent the location of magmatic centres and of the more important dike swarms, connected with the NAIP. Rigth: Map of long-wavelength, free-air gravity anomalies. The purple dots are the locations of earthquakes that took place between 1991 to 2001, after Arrowsmith et al. (2005).

cent surface uplift and it may play a role in sustaining the high elevation inherited from the early Palaeogene plume-related uplift episode. However, its magnitude is probably minor and is not able to explain the present-day topography.

6.3.6.4 Heating from underplating and lower crustal flow

Green et al. (2012) proposed that the early Palaeogene uplift was initiated by the thermal effects of magmatic underplating, which was also responsible for the elevated palaeogeothermal gradient. Further permanent uplift, according to this scenario was due to lower crustal flow that caused lithospheric thickening in northern England. The authors suggested that the early Palaeogene denudation was small and the main phase of uplift and denudation occurred in the Neogene. Some aspects of this model are, however, controversial. The amount of heating due to magmatic underplating seems to be significantly overestimated. As shown in Brown et al. (1994) and in this study (Chapter 5), a magmatic underplating layer has to be either thick or be emplaced at shallow crustal levels to cause significant perturbation of the crustal thermal field in the uppermost crust. If the underplating layer was not added instantaneously, but in form of a few smaller 'pulses' (White & Lovell 1997), as Green et al. (2012) had to assume in order to account for a continuously increasing underplating between 58 and 61 Ma, the thermal impact of the body would be even smaller, as thinner layers cool more rapidly. To calculate thermal perturbations caused by underplating, Green et al. (2012) used

equation (5) of Westaway (2005). However, there is a substantial difference between heating due to underplating and the case study of Westaway (2005). Westaway (2005) studied thermal perturbations due to the removal of the lithospheric mantle. In such a situation, the base of the crust is exposed for a long time to abnormally high temperatures as it is in direct contact with the hot asthenosphere. In the case of underplating, the heat anomaly decays fast because the magmatic layer is within the lithosphere and therefore it is surrounded by cooler material (see Chapter 5, Fig. 5.3). Moreover, according to data and thermal models obtained in this study, most of the Cenozoic denudation took place in the early Palaeogene, not in the Neogene, as supposed by Green et al. (2012). Finally, changes in the gradient can be best explained by variable thermal properties of the uppermost crust, not by deep seated thermal anomalies. The influence of the lower crustal flow cannot be excluded, but it is not needed to explain the early Palaeogene evolution of the region.

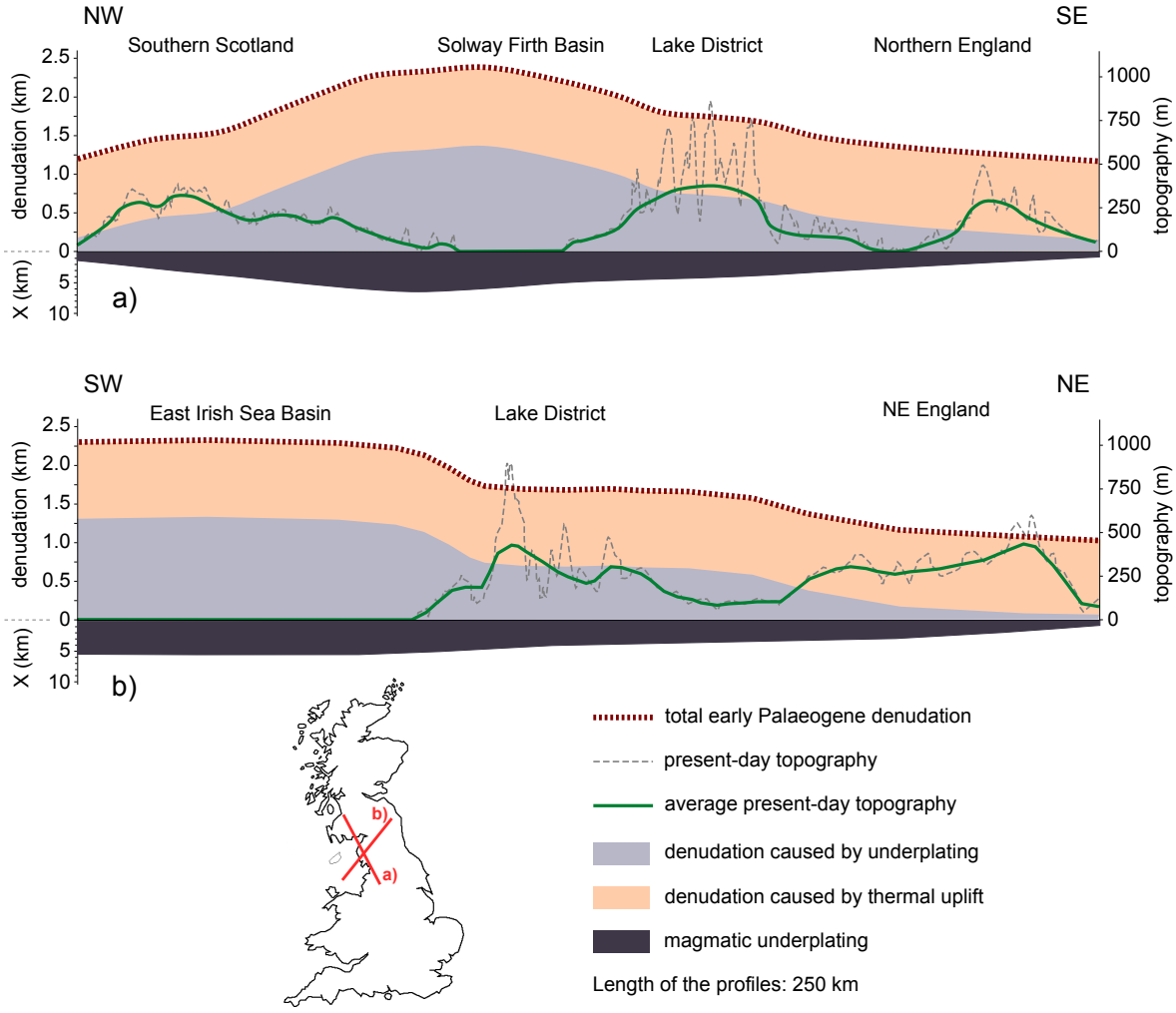

Figure 6.12: Two cross sections, NW-SE and SW-NE, showing the amount of early Palaeogene denudation juxtaposed to the present-day topography (after GoogleEarth data) and thickness of magmatic underplating (after the underplating map of Tomlinson et al. 2006). Total early Palaeogene denudation is marked by the thick, dotted, dark red line and shaded areas represents shares of denudation caused by magmatic underplating and plume-related thermal uplift. The map below shows the locations of the cross section lines.

6.3.6.5 Summary

In summary, a mantle plume origin of the early Palaeogene uplift is in the agreement with the timing, location and spatial distribution of denudation. Combining transient dynamic and thermal plume related uplift and the uplift due to magmatic underplating can explain the observed pattern of denudation, if the water depth and rock density changes are taken into account. Fig. 6.12 presents two summary cross sections that demonstrate the relationship between causes of denudation, topography and magmatic underplating. Invoking other processes, like continuous thermal support from the hot mantle and lower crustal flow is not necessary to explain the first order topography and the early Palaeogene denudation in the region, however they cannot be ruled out and they may have a minor influence. The rapid denudation ceased by the end of the Eocene and only little erosion is expected to occur in the late Palaeogene.

6.4 Neogene–Quaternary thermal history (∼0–23 Ma)

The Neogene–Quaternary uplift is observed in many places all around the world (Hay et al. 2002). However, its character remains controversial and some authors suggest that the observed surface uplift and enhanced erosion is entirely caused by climate change and glacial- and erosion-driven isostatic rebound (Molnar & England 1990). Some authors have pointed out areas of Neogene uplift and abnormally high subsidence along the North Atlantic margin (Fig. 6.13; see Japsen & Chalmers 2000, Anell et al. 2009 for a summary). They challenge the long lasting stability of the region after the early Palaeogene uplift and suggest a Cenozoic evolution that is characterized by multiple episodes of uplift and denudation (Japsen et al. 2006, Stoker et al. 2010, Green et al. 2012). Of these events, the Neogene uplift is often considered the most prominent, as suggested by the high volumes of sediments of this age in the basins offshore northern Britain (Stoker et al. 2010). However, the seismically-derived sedimentary sequences in the North Sea demonstrated that their main source was in Norway and NW Europe, rather than Britain (Jordt et al. 1995, 2000), reinforcing the hypothesis suggested by Hall & Bishop (2002) that the Neogene uplift event in the Scottish Highlands, if present, was of minor magnitude. Onshore, the investigation of a 'Neogene' event using LTT is hindered by the fact that by that time the rocks now at the surface were already at temperatures lower than the range of sensitivities of the methods used.

Thermal histories derived during this study from the combined AHe and AFT data, in most of the cases, do not show a clear Neogene cooling signature. Rocks from the Lake District, northern Wales, Criffell, Portencorkie and Crawfordjohn were already at temperatures of ∼15–25°C at the beginning of the Neogene and do not exhibit any further reheating or acceleration of the cooling rate (Fig. 4.1, 4.3, and 4.2—GAL06 and SL01). Assuming a geothermal gradient of 20–30°C/km, the amount of total Neogene denudation in these areas was less than 500 m. Some thermal models from Loch Doon, Fleet,

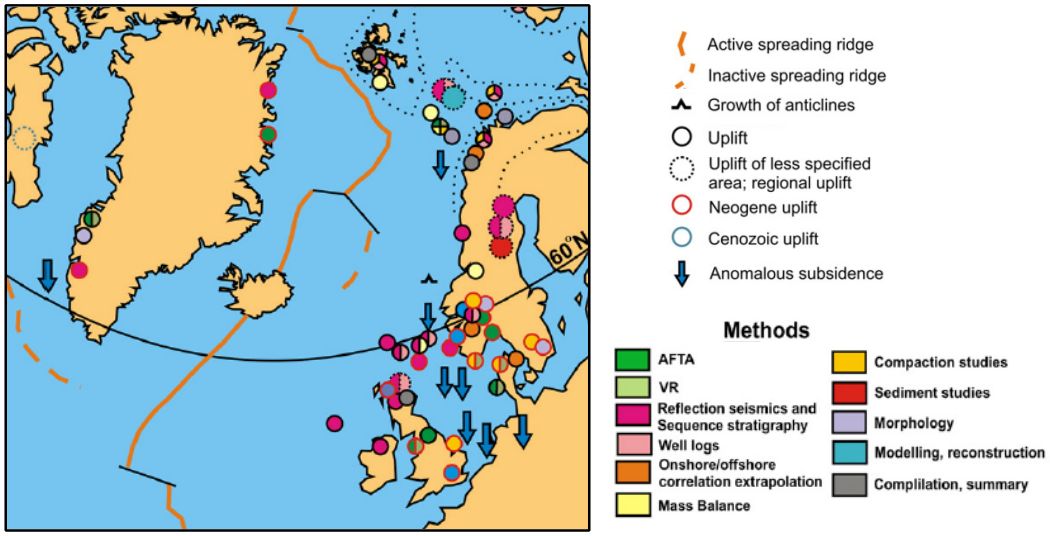

Figure 6.13: Schematic map of the North Atlantic region in the Late Neogene showing principal uplift and subsidence events, modified from Anell et al. (2009).

Cheviot and Corsewall Point show early Neogene palaeotemperatures of ~40–60°C and a small reheating, prior to reaching the maximum Neogene–Quaternary palaeotemperatures at ~15 Ma (Loch Doon; Fig. 4.2—GAL01), or 0–5 Ma (Cheviot, Corsewall Point and Fleet; Fig. 4.2—CH01 and GAL11, and Fig. 4.5—Fleet). In these models, the maximum Neogene–Quaternary palaeotemperatures are usually about 50°C, but they are up to even ~75°C (Corsewall Point, F-rad-dam model). Assuming a geothermal gradient of 20—30°C/km, such palaeotemperatures imply 1.0–1.5 km of Late Neogene–Quaternary denudation that, in an extreme scenario, could reach up to 2.0–3.0 km at Corsewall Point.

The presence of the accelerated Late Neogene–Quaternary cooling cannot be treated with high confidence, as the part of thermal histories between 0–60°C is not well resolved, due to the limited sensitivity of the thermochronometric techniques to this temperature range. Although the application of the AHe analyses increases the sensitivity to the lower temperatures span, the conclusions derived from the upper portions of the thermal histories should still be taken with cautions. Their accuracy may be questionable as the rocks show different t-T paths for different diffusion models and when the 'expected' and 'max-like' models are compared. The 'expected' models usually do not show the rapid Late Neogene–Quaternary cooling signature that is suggested by the max-like models; however, the 95% credible intervals are wide and the cooling lies within the model uncertainties.

No thermal anomalies are expected to affect the uppermost crust in central west Britain in the Neogene. The present-day thermal support of the hot mantle, proposed to be a remnant of the mantle plume (Arrowsmith et al. 2005), does not spatially correspond with the pattern of Neogene denudation as defined by LTT based thermal models. The processes responsible for the accelerated Late Neogene–Quaternary denudation may in-

clude: glacial erosion and post-glacial isostatic rebound, climate changes, lower crustal flow, and intra-plate compression.

Neogene denudation of ∼1.0 km is proposed to affect the Irish Sea basins, reaching ∼1.5 km in the Cardigan Bay basin, where it can be easily recognized due to a preserved Oligocene–Early Miocene succession (Holford et al. 2005a, 2008). About 1 km of Neogene exhumation has also been suggested in the western North Sea (Japsen 1997). Onshore southern England, the denudation pattern exhibits a large, kilometer-scale variation with maxima corresponding to the axes of the Cenozoic compressional structures, like the Weald anticline in the English Channel (Hillis et al. 2008). This compressional Late Neogene uplift has been attributed to intra-plate stress transmitted from the plate boundaries (Hillis et al. 2008, Holford et al. 2008). In central west Britain, reactivation of older structures is not observed and this, together with the small magnitude of the Neogene denudation (<500 m), supports the hypothesis that the Neogene compression was of minor importance in central Britain. Therefore, it seems that the impact of the Oligocene–Neogene compression was probably restricted to the basins and was more pronounced in southern Britain, which was closer to the Alpine front.

Based on a study of upland flats, Westaway (2009) estimated the post-Mid-Pliocene denudation of the Lake District and Pennines to be up to 1 km and suggested that the present-day topography is entirely an effect of post-Mid-Pliocene uplift. He suggested that uplift was governed by lower crustal flow, initiated by surface processes enhanced by climate changes. The same interpretation has been used in an AFT study from the North Pennines (Green et al. 2012). Although the lower crustal flow concept does not seem to explain the early Palaeogene uplift and denudation, it may have contributed to the Neogene uplift and it may explain the increasing westward stability of the crust (Green et al. 2012). The lower crustal flow concept, however, would predict the Neogene denudation to decrease westwards, from the Pennines in eastern Britain to the Lake District, whereas the thermal models derived from this study show that, if a Neogene event existed, it was strongest in the western Southern Uplands.

Considering the global extent of the Neogene–Quaternary uplift, Molnar & England (1990) proposed that the observed uplift is almost entirely caused by isostatic rebound due to enhanced erosion caused by Late Neogene climate changes and Pleistocene glaciations. The strong Pleistocene glaciations in the Lake District and Scotland (Evans et al. 2009) might have had significant impact on the Late Neogene–Quaternary denudation; the Lake District topography is clearly a glacial landscape (Moseley 1978). The coupled effect of isostatic uplift and erosion can be applied, however, only in the areas of high relief, and can emphasise the existing topography, but cannot create it (Doré et al. 2002). The highest peaks in the Lake District, including

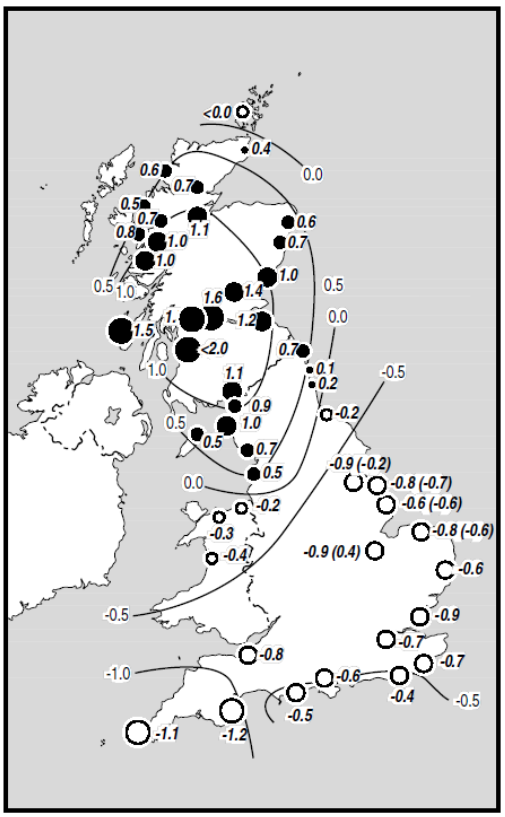

Figure 6.14: The map of uplift and subsidence rates (mm/yr) in the Late Holocene; after Shennan & Horton (2002).

Scafell Pike, lack the signs of glacial erosion and are considered to have formed nunataks or have been covered by cold-based ice during the Pleistocene glaciations (Lamb & Ballantyne 1998, Ballantyne et al. 2009). If there were nunataks, it means that the first order topography in the Lake District had to be established before the onset of glaciation. Considering glacial erosion, which will increase relief as it would be more efficient in the valleys, and post-glacial isostatic rebound after melting the Lake District ice-cap (Evans et al. 2009), the predicted post-Palaeocene ∼500 m of denudation requires 50–100 m of rock uplift for a rock density range observed now in the Lake District and can be attributed to glacial rebound. The post-glacial rebound is probably continuing to the present-day; a neotectonic uplift of ∼0.5–1.0 mm/yr, is observed in the Lake District and values of 1.0–2.0 mm/yr are noted in southern Scotland (Fig. 6.14; Shennan 1989, Shennan & Horton 2002). This may suggest that if the rapid cooling signature in the Late Neogene–Quaternary observed in southern Scotland is accurate, its origin could be a higher post-glacial rebound than elsewhere. However, the small number of samples and low confidence of the resolved signatures preclude this discussion to go further.

The influence of the eroded rocks' density contrast, analysed in detail in the previous section may be used to explain the present-day surface topography in the Lake District. Recently, Braun et al. (2014) showed that denser, not harder, rocks induce higher isostatic rebound and tend to form high topographic relief. Because the elastic thickness in the region is relatively low, 5 ± 2 km (Tiley et al. 2003), the density of the rocks may play an important role in determining the topography of the Lake District and surrounding areas. Assuming that the Mesozoic sediments were entirely removed from the Lake District block in the early Palaeogene, the layer that was being eroded in the Late Neogene–Quaternary would be entirely composed of basement rocks (of a density 2.6–2.8 g/cm^3; Bott 1974). In that case, the density contrast between the rocks in the Lake District and in the basins could have reached as much as 0.6–0.8 g/cm^3. Such difference, for the elastic thickness of 5 ± 2 km (Tiley et al. 2003) and the crust isostatically rebounding after glaciation, may have a topography forming effect of a

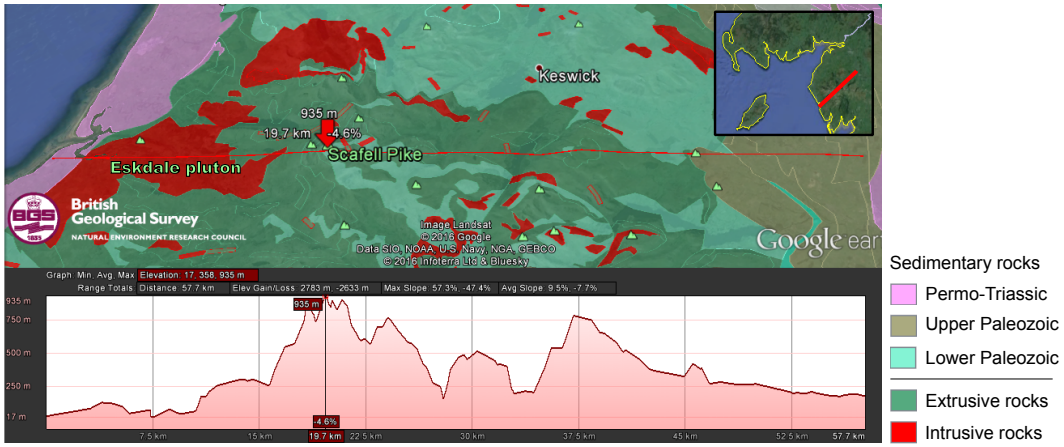

Figure 6.15: Top: Simplified geological map of the Lake District and a cross section line (the location of the line shown on the map in the top-right corner) and profile line (red line) across the the Scafell Pike (red arrow) and Eskdale pluton. Bottom: Topographical profile along the line shown on the map; the vertical line shows the location of the Scafell Pike. Based upon "DiGMapGB-625", with the permission of the British Geological Survey; the map and the profile compiled using Google Earth.

magnitude up to several hundreds of metres. Fig. 6.15 shows a SW–NE oriented topographical profile of the Lake District, crossing the highest peak in the region and the largest intrusion, Scafell Pike and Eskdale granite, respectively. It becomes clear that Scafell Pike and other higher peaks are built of dense Lower Palaeozoic volcanic and sedimentary rocks, not of less dense granites. Additional support to the elevation of the Lake District may come from buoyancy of the block itself that, at depth, is largely composed of the relatively low density granite (Bott 1974).

6.5 Summary

The new thermochronometric data and thermal models obtained in this study allows a better understanding of the post-Caledonian history of central west Britain. Although the research was focused on the early Palaeogene thermal evolution of the region, some important points have been placed also on its Mesozoic and Late Cenozoic history. When combined with the available constraints, the new findings suggest the following history that is also summarised in Fig. 6.16.

1. During the Mesozoic, the Lake District, southern Scotland and northern Wales formed structural highs, which were at least partially submerged and being buried with sediments.

2. The Late-Cimmerian event likely removed the Middle Jurassic–Lower Cretaceous sedimentary cover.

3. The Late Cretaceous transgression covered most of the region, but the northern–central part of the Southern Uplands and some parts of northern Wales likely remained emerged.

4. Widespread chalk deposition during the Late Cretaceous reinforced the blanketing effect of the sedimentary layer and increased palaeotemperatures of rocks that are now at the surface.

5. Marine regression started at the beginning of the Maastrichtian and the structural highs emerged first (cooling started at ∼70 Ma). The chalk was eroded by dissolution, which is consistent with a lack of increased offshore sedimentation. The uplift of ∼300–500 m, was likely transient, caused by thermal support from the mantle plume.

6. During magmatic activity in the NAIP (62–58 Ma), a magmatic layer was underplated beneath the crust and caused further uplift; the main phase of uplift at 65–50 Ma caused regional denudation and influx of clastic sediments into the surrounding basins (onshore older clastic sedimentary rocks and/or basement being eroded).

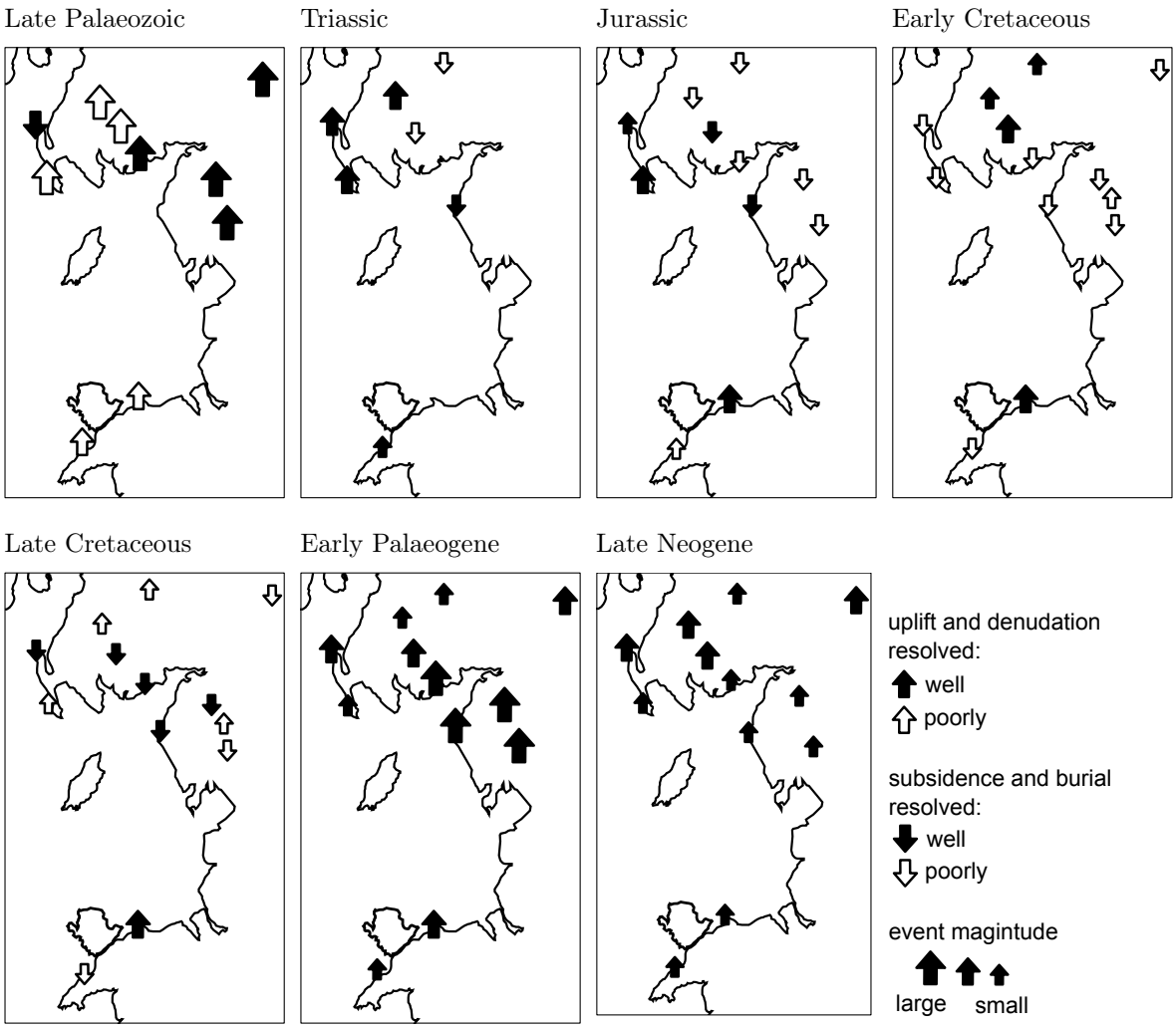

Figure 6.16: Compilation of schematic maps of exhumation and reburial episodes in central west Britain in the Late Palaeozoic, Mesozoic and Cenozoic. The Late Palaeozoic evolution, which was resolved only vaguely, is represented by the map of Devonian events.

7. The EISB and surrounding areas experienced the highest early Palaeogene denudation (2.0–2.5 km) due to a thicker layer of underplated material.

8. Early Palaeogene denudation in the Lake District was high (1.5–2.0 km), but smaller than in the EISB. High palaeotemperatures resulted from a combined effect of blanketing and high heat production within granite batholiths.

9. The cooling rate decreased at ∼40 Ma when the rocks reached temperatures of ∼20–30°C and in most localities, no subsequent reheating and cooling events are resolved.

10. Neogene denudation in most of the localities was, at its maximum, several hundreds of metres and, therefore, the majority of the Cenozoic denudation in central west Britian occurred in the Palaeogne.

11. The accelerated cooling in the Neogene of 40–50°C is resolved only in some models from southern Scotland, but the signature is equivocal, as the rocks were already at temperatures lower than the sensitivity of the analytical techniques used.

12. If it existed, the 'Neogene' uplift and denudation is probably not Neogene in age, but Quaternary caused by glacial erosion and post-glacial rebound.

13. The first order topography of the Lake District seems to be of early Palaeogene age and the present-day high relief is due to glacial erosion and post-glacial rebound; high elevations in the Lake District are likely a result of the removal of high density rocks.

Chapter 7

Conclusions and future work

7.1 Wider implications of this study

The results presented in this study have several wider implications for understanding the large-scale regional geology and the processes governing landscape evolution of continents in non-orogenic areas. This study provides new, methodological insights to increase the precision and accuracy of constraints derived from the thermochronometric data. The main contributions of this study to these fields of research are briefly described below.

Early Cenozoic evolution of the North Atlantic margin

The timing and causes of uplift and denudation in Britain presented in this study differ from those proposed in other parts of the North Atlantic region (e.g. Rohrman et al. 1995, Lundin & Doré 1997), suggesting that the geological history of the margins was complex and the causes of uplift and denudation were spatially variable. The recognition of the mantle plume related uplift in central west Britain improves understanding of mantle dynamics prior to and after the opening of the North Atlantic. Although this study cannot explicitly indicate the source of the thermal anomaly beneath western Britain, it is likely that it was related to the proto-Iceland mantle plume and/or its lobes. The onset of the uplift reconstructed from the thermochronometric-derived t-T paths suggests that the thermal anomaly appeared at the same time as the oldest basaltic lavas were extruded on the Rockall Plateau, ∼10 Ma earlier than the main phase of the surface magmatism. The evidence suggests that the mantle plume arrived at ∼70–75 Ma and incubated below the crust before the main phase of magmatism began at 62 Ma. This study shows, for the first time, that the first order topography in central Britain is Paleogene in age and that it can be explained as the result of a combination of permanent and transient uplift, both related to the mantle plume (section 6.3.3). The timing and distribution of denudation allow, for the first time, to rule out other processes, such as rifting and intra-plate stresses (Chapter 6, section 6.3.5).

Neogene cooling

The study presents new constraints on Neogene cooling and adds some new observations to the ongoing debate about the global Neogene uplift paradox (Molnar & England 1990, Hay et al. 2002). Neogene denudation was relatively small, below the detection limit of the LTT in northern England and Wales; the discrete cooling signature in southern Scotland suggest that denudation was rather Quaternary than Neogene in age and that it was governed by the glacial erosion and post-glacial isostatic rebound. The hypothesis that the Neogene was a time of global accelerated erosion is not consistent with the findings in central Britain, where, if rapid denudation occurred, it was an effect of the Pleistocene glaciations (section 6.4).

Eroding dynamic topography

The amount of denudation due to transient uplift reconstructed in this study has important implications in terms of understanding the processes that drive dynamic topography (Hager et al. 1985, Braun et al. 2013). The results reported in Chapter 6 conclude that even at the plume margins, far away from the upwelling centre, the plume-driven thermal and/or dynamic uplift may have a magnitude large enough to be measured by thermochronometers and, because of its long-wavelength character, it can be successfully separated from the other causes of uplift, for instance from underplating. The same methodology can be applied to other areas where plumes may have had an effect on the evolution of the landscape. This study has clearly demonstrated that a combination of thermochronometric data and numerical modelling of crustal behaviour allows the amount of denudation due to dynamic topography to be calculated (section 6.3.6).

Influence of local crustal thermal properties

One of the novelties of this study is the interpretation of the thermochronometric data, by taking the local thermal heterogeneities of the shallow crust into consideration. Using this approach, the inconsistencies that often characterised the reconstruction of denudation in other works using LTT have either disappeared or been explained. It has been demonstrated that the nature of the material removed via erosion is very important, as low conductivity sediments, especially when covering heat productive basement, may produce abnormally high geothermal gradients, causing drastic changes in predicted cooling amounts and rates (Chapter 5). The individual and combined effects of blanketing and high heat production may not be restricted to Britain, as similar types of rocks and geological scenarios are observed elsewhere. On the continents, for instance, high heat flow values are mostly related to high crustal radiogenic heat production of some igneous and metamorphic rocks, which, concomitantly, are the most common lithologies sampled for thermochronometric analyses. The thermal conductivity of rocks may vary significantly even over relatively short distances and the eroded overburden

is often composed of less compacted and low thermal conductivity sediments. If these characteristics are ignored, as often happens, the amounts of denudation are overestimated. In these terms, it may be a case that the LTT-derived amounts of denudation reported in the literature often exceed those constrained by other methods. The density of the rocks is also an important parameter when calculating the amounts of rock uplift from denudation. Density is a controlling factor of isostasy and, as such, it cannot be ignored when thermochronometric data are used to provide insights on the age of first order topography (section 6.3.6).

Single grain age dispersion

The results from this study confirm the concept that dispersion of single grain AHe and ZHe ages, rather than hindering the precision and accuracy of the conclusions derived from the data, may be a powerful tool to extract high resolution thermal histories of the rocks for a given range of temperatures (Brown et al. 2013). In particular this study demonstrates the importance of considering the effects of radiation damage and grain fragmentation on He diffusion. For instance, the spread in ZHe ages has been successfully explained as an effect of radiation damage (section 3.3.5.2 and 4.2) and, once the proper diffusion kinetics were used, the data were shown to add important constraints on the Mesozoic history of the study area (section 6.2). The use of a diffusion model that includes radiation damage also improves the predictions of AHe ages (section 4.2). An even better explanation of the AHe age dispersion is obtained when the data are modelled using Helfrag (section 4.3). The Helfrag results indicate that the spread of AHe ages may help to unravel discrete cooling episodes that would be, otherwise, undetected, as in the case of the sample from Corsewall Point (section 4.3.5). A thorough investigation of the causes of AHe age variation has revealed that grain size is likely to be the major cause of dispersion, outweighing fragmentation, especially if the grains are small or medium in size (section 4.3.6). The AHe ages presented in this study define a new protocol to be used when selecting grains for the analyses, as the picking procedure should aim at maximising dispersion. The dataset collected in this study also demonstrates that thermal histories are more precisely reconstructed when 20–25 single-grain AHe ages are available for each sample (section 4.3). The new strategy for AHe determinations should, therefore, include the analyses of many single-grain aliquots from carefully selected samples with high quality crystals of variable dimensions and fragmentation, rather than fewer determinations on non-broken crystals of equal size from many samples.

7.2 Future work

Despite the success of this study, there are still many questions left open that would require further work. Below, the most important are briefly described.

Regional geology aspects

The Cenozoic geological history of Britain and of the North Atlantic in general could be better constrained, to pinpoint the time of the major phases of uplift and denudation, and their causes. The low temperature thermochronometers have proven an invaluable tool, especially when combined with other data and numerical modelling of the thermal structure of the crust and of uplift mechanisms (Chapter 6). The same approach should be used to study the evolution of Scotland, Wales and northern England; new datasets should be collected as the existing LTT data from these regions are sparse and based almost entirely on AFT analyses. This extended study would have the aim of constraining the thermal history of central and northern Britain to fully test the hypothesis that the main phase of Cenozoic uplift happened in the early Palaeogene and was driven by the proto-Iceland mantle plume. More extensive, precise quantification of the onset of cooling in the British Isles and other part of the North Atlantic is required to discriminate between the 'starting plume' and 'incubating plume' models as the origin of NAIP. Extending the LTT determinations to southern England, could help to resolve possible compressional pulses of exhumation related to the Alpine-driven intra-plate stress and indicate the southern extent of the mantle plume influence. High quality data needs to be produced for Anglesey, together with a larger dataset for the Welsh mainland, in order to investigate the possibility of Cenozoic fault reactivation. The spatial distribution of denudation in the Lake District can be better constrained by collecting rocks at different elevations. The AFT data set from a quasi-vertical profile is available, however, the maximum palaeotemperatures may not be well constrained, as the rocks are from the high elevations and yield relatively old AFT ages (Green 2002). AHe analyses need to be added to improve the constraints on the thermal histories to better define the time of onset of the early Palaoegene rapid cooling event at different elevations and test the hypothesis that the Lake District was a structural high which experienced a diachronous denudation, as sea level was decreasing (section 6.3.2). The amount of Neogene exhumation could not be resolved precisely; the AHe data are not sensitive enough to measure the small amount of cooling in most of the studied regions. Attempts can be made on either exploiting the AHe dispersion by analysing many grains (probably >25) with different size and fragmentation characteristics, or via $^{4}He/^{3}He$ analyses.

Methodological aspects

Another direction that future work could take is the study of aspects directly concerning the LTT techniques and development of the numerical modelling software used to retrieve the thermal histories. Understanding and constraining the influence of radiation damage on He diffusion has been demonstrated to be crucial for an accurate interpretation of the AHe and ZHe ages. In the case of the ZHe ages presented in this study, thermal histories that fitted all the data were impossible to obtain without using a diffusion algorithm that included the effect of radiation damage. The single grain age dispersion of the AHe ages was small enough to produce thermal histories that roughly predicted the data without adding the radiation damage models. The AHe ages reported in this study, however, are relatively young, and so radiation damage has a minor impact on the diffusion kinetics. Based on the available AFT ages, the AHe data from northern Scotland and England are expected to be much older and, therefore, the effect of radiation damage on He diffusion could be important. More theoretical work has to be dedicated to the influence of crystal fragmentation on age dispersion. The Helfrag code should be improved in order to include no-termination (0T) grains, as well as allow fast and efficient inclusion of the AFT data.

Other aspects

A large effort should be put into improving the ways in which t-T paths are converted into amounts and rates of denudation. The importance of the thermal heterogeneities in the shallow crust needs to be further investigated in areas of high heat flow that may have been covered in the past by low conductivity sedimentary rocks. Two possible locations for such a study are Cornwall (SW England) or the North Pennines (NE England), which are both characterized by high heat values and were likely covered by Late Cretaceous chalk. Assessing how common this situation is around the world would be interesting; if it is recognized in other areas, then existing denudation rates need, potentially, to be revisited.

As our understanding of the parameters important for interpreting thermochronometric data improves, so the software used for retrieving thermal and denudational histories need to be upgraded. In the case of Pecube, for instance, a major improvement would be the possibility of including variable kinetics of track annealing and He diffusion. This would, however, dramatically increase computing time. A much more efficient solution would be finding a successful, efficient way to input thermal histories rather than ages in Pecube (J. Braun, pers. comm.).

7.3 Final remarks

The work presented here, which is the first multi-thermochronometeric study of central west Britain, improves our understanding of the timing and spatial distribution of the Cenozoic exhumation in the region. The combination of AFT, AHe and ZHe data produces strong constraints on the early Palaeogene cooling signature and confirms its ubiquitous, regional character. It also adds stronger constraints on the Late Cretaceous temperatures and the onset of cooling in the areas where the rocks were outside the sensitivity of the AFT thermochronometer. The cooling was probably diachronous, starting ∼70–75 Ma in the central Lake District and ∼60–65 Ma in the coastal areas.

The study demonstrates that carefully constrained timing and spatial distribution of denudation may be successfully used to indicate the causes of uplift in central west Britain where more than one process may have been responsible for denudation and formation of the first order topography. Deciphering the denudation pattern in the region required the spatial thermal heterogeneities of the crust to be recognized and quantified; this was particular important in the case of the Lake District due to the presence of the heat producing granite batholith and low thermal conductivity of the eroded overburden. The pattern of denudation is a relatively flat (∼1 km to 2 km) half dome and correlated with the spatial variation of the thickness of magmatic underplating. The latter, however, cannot produce the total early Palaeogne denudation alone; the 'remaining' part is attributed to the effect of the transient thermal uplift above the hot mantle plume.

The first order topography in the region seems to be early Palaeogene in age. The Neogene uplift, which has been suggested in other studies, is not resolved in the Lake District and northern Wales. A small cooling signature is found in some localities in southern Scotland, where the denudation could have locally reached up to ∼1.5 km. The spatial pattern of denudation and the timing of the event (last 2–3 Ma), Quaternary rather then Neogene, suggest that the main cause of the enhanced denudation was Pleistocene glaciation and subsequent post-glacial isostatic rebound.

Appendix A

Thermochronometric analyses procedure

A.1 Mineral separation

The apatite and zircon crystals for the thermochronometric analyses were extracted from the host rock based on the density and magnetic susceptibility of the minerals. The separation process required the rocks to be first disaggregated to sand-size material. In each case, about 2 kg of rocks were crushed into hand-size blocks using either a hammer or a hydraulic splitter. The blocks were then processed using a jaw-crusher and sieved to extract three groups of material: >2 cm, 2 cm–500 μm, and <500 μm. The material >2 cm was re-run on the jaw-crusher and the material of 2 cm–500 μm was passed through a disc mill for final disaggregation. Only the grains <500 μm were used for the next steps. Apatites and zircons (with densities of 3.2 g/cm^3 and 4.7 g/cm^3, respectively) are heavier than most of the crust-forming minerals (the average 2.7 g/cm^3). A preliminary density separation was carried out on a Gemini shaking table, that allowed the sample to be simultaneously washed in order to remove dust and finest grain fraction. The material was then dried and the heaviest fraction was taken for the magnetic separation as apatites and zircons are characterized by relatively low magnetic susceptibility. The mineral grains were first passed through a vertical Frantz magnetic separator in order to extract the highly magnetic minerals. In the next step a horizontal Frantz magnetic separator was used for a precise separation. The magnet slope was set up to 20° and the material was passed through the magnet with a current of 0.5 A an then, non-magnetic fraction was run again with a current of 1.5 A. The non-magnetic grains were subsequently processed for the heavy liquid separation using the LST (lithium heteropolytungstates) solution of a density 2.8 g/cm^3; such density of the liquid allows the apatite and zircon crystals to sink and other lighter minerals, e.g. quartz and feldspar, to float. The samples, which contained both apatites and zircons, were then taken for further separation in DIM (diiodomethane) heavy liquid of a density 3.3 g/cm^3. This step allowed for a final separation of apatite (float) and zircon (sink) crystals.

A.2 Apatite fission track analysis procedure

A.2.1 Mounting, etching and sample irradiation.

All of the apatite samples were prepared for fission track analyses. The analyses were carried out using the external detector method, which requires fission tracks to be counted on the apatite grain and on its print on a low-U mica, produced during a neutron irradiation (Hurford & Green 1982). The apatite grains were mounted on small 1.6 x 1.6 cm glass slides using an epoxy resin. The grains were poured onto the resin directly from the separate, without earlier picking and evenly distributed. After solidification, the mounts were polished using successively finer abrasive papers until most of the grains were exposed. The exposed surface was burnished using 1.0 and 0.3 μm Alumina powders in order to remove all grazes and scuffs from the surface of the apatite crystals. The polished mounts were then etched for 20 seconds in 5.5 Molar HNO_3 at constant temperature of 20±1°C that allowed fission tracks in the apatite crystals to be enlarged. Each of the etched mounts was covered with a low-U mica sheet and tightly wrapped in plastic film. The samples were packed in the irradiation tubes between the IRMM-540 standard glasses and then irradiated with a low energy neutron flux at the Oregon State University Radiation Centre, USA. The irradiated mica sheets were etched for 20 minutes in concentrated HF to enlarge the induced fission tracks. The glass with the apatite grains and the mica sheet were subsequently mounted together on a larger glass slide, in a way that makes the crystal prints on the mica to be a mirror image of the corresponding apatite grains.

A.2.2 Fission track analyses

The fission tracks were counted in the Glasgow University fission track lab using Zeiss Axioplan microscope with a Trevor Dumitru stage system and the FT Stage 4.04 software. Counting the samples were preceded by the ζ-calibration and fission track lengths measurements training on Durango, Fish Canyon Tuff and Mt. Dromedary apatites. The obtained average ζ value is 313.7 ± 8.3.

Fission track counting—At the beginning, the apatite mount was searched for isolated apatite grains, which are parallel to the surface, free of cleavage and large fractures, and have the minimum countable area of 2200 μm^2 (preferably >6000 μm^2). Simultaneously, the apatite prints on the mica were monitored for U-zonation or U-bearing inclusions. Crystals containing any U-bearing inclusions were discarded and if possible, zoned crystals were avoided. The spontaneous fission tracks were then counted on at least 20 grains. In the cases of samples with low yield of apatites, all countable grains were analysed. The lengths of the fission track etch pits (D-Par) were reported for all counted grains; at least five D-Pars were measured per grain. The prints of the counted grains were automatically located on the mica and the induced tracks were

counted within the exact same location as the corresponding grains. The apatite fission track single grain ages, mean, central and pooled ages and χ^2 test were then calculated using the TrackKey software (Dunkl 2002).

Fission track lengths measurements—Before starting measurements the tablet has been calibrated using a 1 mm graticule with accuracy to 1 μm. Only horizontal, confined tracks on grains parallel to the c-axis were measured and at least five D-Pars were determined for these grains. To account for the anisotropy of the fission track annealing kinetics, the orientation of each measured track was reported, by measuring its angle with the c-axis. If applicable, at least 100 tracks were measured per sample; in the cases when the apatites were characterized by low track density, lengths of all measurable fission track were determined. Wherever possible, only TINT tracks (track-in-track) were measured. The track length measurements were subsequently normalized using the c-axis projection model of Ketcham et al. (2007a). The histograms of fission track lengths distribution were computed for both raw and c-axis projected data sets.

A.3 (U-Th-Sm)/He analyses

A.3.1 Sample preparation

Apatite and zircon crystals for (U-Th-Sm)/He analyses were picked under an optical microscope and apatite grains were also checked under a petrographic microscope to eliminate aliquots which contain inclusions. Subsequently each chosen crystal was photographed, measured (length, width and thickness) and the number of crystals terminations was noted. Each grain was packed tightly in a small, 1 x 1.5 mm Pt tube. In the case of zircon crystals, a small hole has been left within the closed edge of the tube in order to ensure that the packet can be open after the He extraction.

A.3.2 Helium extraction

Pt tubes containing crystals were loaded into 2 mm deep holes within a 6 cm diameter high-purity Cu planchet. The planchet was placed and tightly closed in a stainless steel chamber connected by a flexible steel tube to the gas clean-up system. In order to reduce background H, CH_4 and H_2O the system was pumped for at least 2 hours on a turbo-molecular pump and subsequently on two triode ion pumps for at least 24 h, overseeing that any leakage is not present in the system. Simultaneously the system was heated using a lamp and a heating tape to remove the water vapour from the system. The analyses were performed under a vacuum of pressure $<10^{-9}$ torr. The steel chamber was placed and locked in an Aluminium box connected with the diode laser ($\lambda = 808$ nm). At first a couple of cold and hot (heating of an empty Pt capsule) blanks were run together with ^{4}He calibrations to ensure that the system is clean and to monitor sensitivity of the mass spectrometer. The blanks and calibrations were then

frequently run during the analysis of the samples. Each apatite crystal was heated for 1 minute at temperature of 500–600°C and zircon crystals were heated for 10–20 minutes, depending on the crystal size, at temperatures of 1100–1300°C. The temperature was established by visual observation of color of the heated Pt-foil and a comparison with the temperature-color scale. The extracted gas was left in the system for 5 minutes to accumulate and was purified with two liquid nitrogen cooled charcoal traps. Amounts of H, ^{3}He, ^{4}He and CH_4 were then measured using a Hiden HAL3F quadrupole mass spectrometer. Every crystal was subsequently reheated to check that all ^{4}He has been released from the crystal. The acceptable reheating to heating ratio was 0–2 %. Higher ratios may indicate presence of inclusion or very high ^{4}He concentration within the grain. The former is more typical for apatite, and such aliquots were usually discarded, whereas the latter is common to zircon. All zircon aliquots giving the reheating to heating ratio of more than 2 % were reheated again to ensure that the ^{4}He extraction was complete.

A.3.3 U-Th-Sm contents measurements

Apatite

When all the crystal had been degassed, they were removed from the laser chamber and directly transferred into labelled teflon beakers. The aliquots were spiked with 30 μl of mixed ^{149}Sm, ^{230}Th and ^{235}U spike. 2 ml of 5% HNO_3 was added to each beaker and they were placed on a hot plate at 80°C for minimum 24 hours for total dissolution of apatite crystals. The same procedure was applied for a couple of empty Pt tubes to ensure that the capsule itself is not a significant source of U, Th or Sm, and if needed to correct the measurements. The samples were analysed using inductively coupled plasma mass spectrometry (ICP-MS) in two separate runs, one for U and Th, and the second one for Sm. Additionally regular measurement of U500 of Sm10 standard solutions (for U-Th and Sm runs, respectively) were carried out to account for mass fractionation. The abundances of ^{147}Sm, ^{232}Th and ^{238}U where then determined based on the measured ratios of ^{149}Sm/^{147}Sm, ^{230}Th/^{232}Th and ^{235}U/^{238}U and known spike concentration.

Zircon

In the case of zircons aliquots, it is necessary to prevent formation of $PtAr^{+}$ as it interference with measurements of ^{230}Th and ^{235}U (masses 230 and 235). After degassing, the Pt packets were opened and zircon crystals were removed and placed in microcapsules. Each microcapsule was spiked with 30 μl of mixed ^{230}Th and ^{235}U spike. ^{147}Sm was not measured; Sm contribution to the total He production is negligible due to high concentration of ^{232}Th, ^{235}U and ^{238}U in zircons. At first, 15 μl of concentrated HNO_3 and 130 μl of concentrated HF were added to each microcapsule. The closed microcapsules were transferred into pre-cleaned Parr bomb Teflon liners and 210 μl of concentrated HNO_3 and 5 ml of concentrated HF were added into each liner. The

liners were closed and transferred into the bombs. Tightly closed bombs were placed into the oven and heated for 48 hours at 235°C to allow for total dissolution of zircon crystals. Cooled solution was transferred from the microcapsules to pre-cleaned and labelled teflon beakers and placed on a hotplate to evaporate to dryness. Subsequently, 2 ml of 5% HNO_3 with trace HF was added to every beaker, and the beakers were closed and left on a hotplate for 48 hours at 130°C to reflux. Measurement of ^{232}Th and ^{238}U abundances was carried out in the same way as for apatite aliquots.

A.3.4 The He age calculations

The abundances of ^{4}He, ^{147}Sm, ^{232}Th and ^{238}U were determined, corrected for measured blanks and converted into numbers of atoms. The (U-Th-Sm)/He ages were calculated using the non-iterative procedure of Meesters & Dunai (2005). Together with samples, 4–6 Durango apatites or Fish Canyon Tuff zircons were analysed in order to ensure the accuracy of the analyses. The average age of the Durango aliquots analysed during this study is 32.1 ± 1.4 Ma (compare with 31.4 ± 0.2 Ma; McDowell et al. 2005) and the average of the Fish Canyon Tuff zircons is 30.5 ± 3.0 Ma (compare with 28.3 ± 3.1 Ma; Dobson et al. 2008).

Appendix B

Data logs

The purpose of this appendix is to provide details and full AFT, AHe and ZHe datasets for every analysed sample. The samples are presented in alphabetical order. Each log is divided into three sections, which includes:

I—Sample details: grid references and elevation of a sampling point, basic lithostratigraphic information of the rock and a quality assessment of apatite crystals (the quality assessed based on the shape, transparency, size and abundance of apatite crystals using a scale from 1 to 5, where 1 means very low and 5 very high quality);

II—Apatite fission track data: central age, basic statistics, a table with single grain data, radial plots of single grain ages and histograms of fission track length distribution;

III—(U-Th-Sm)/He data: table with single grain data for all analysed aliquots and plots of the age versus grain size and [eU] concentration; grains that were discarded from the modelling and interpretation are marked in italics. The grains were discarded due to one or more of the following reasons:

- Degassed during He analysis where Durango standards were anomalously young.
- Unreliable measurement of U and/or Th, possible contamination or system instability.
- Extreme outlier (young), possible incomplete degassing of a crystal.
- Extreme outlier (old), possible presence of inclusion, based on picking notes.

Sample details

Grid reference:	NT 94308 21496	Unit:	Cheviot
Elevation:	261 m	Lithology:	Granodiorite
Region:	Cheviot Hills	Apatite quality:	4

Apatite fission track data

Central age:	290.5 ± 13.2 Ma	χ^2:	53.6
Number of grains:	20	P(%):	0.0
Zeta (for IRMM glass):	313.7 ± 8.3		
ρ_D (interpolated):	1.20E+6	MTL measured:	11.08 ± 2.04 μm
N_D:	8874	MTL measured:	13.14 ± 1.21 μm
N_s/N_i:	1.64 ± 0.33	No of track lengths :	202

Table B0: Single grain apatite fission track data; N_s—number of spontaneous tracks, N_i—number of induced tracks, ρ_D—tracks density on the dosimeter, ρ_s—spontaneous track density, ρ_i—induced track density.

No.	N_s	N_i	Area (cm^2)	DPar (μm)	ρ_s (tracks/cm^2)	ρ_i (tracks/cm^2)	ρ_s/ρ_i	Age (Ma)	1σ (Ma)
1	123	77	4.84E+07	2.27	2.54E-06	1.59E-06	1.60	293.9	43.5
2	120	60	3.39E+07	2.03	3.54E-06	1.77E-06	2.00	365.9	58.8
3	188	140	4.36E+07	1.96	4.32E-06	3.21E-06	1.34	247.9	28.6
4	342	223	5.81E+07	2.10	5.89E-06	3.84E-06	1.53	282.4	25.6
5	292	196	6.05E+07	1.99	4.83E-06	3.24E-06	1.49	274.5	26.5
6	245	175	7.74E+07	2.09	3.16E-06	2.26E-06	1.40	258.3	26.6
7	264	159	5.45E+07	1.90	4.85E-06	2.92E-06	1.66	305.2	31.8
8	302	190	6.05E+07	2.25	4.99E-06	3.14E-06	1.59	292.4	28.3
9	215	149	4.84E+07	2.11	4.44E-06	3.08E-06	1.44	266.0	29.4
10	114	46	6.05E+07	1.95	1.88E-06	7.60E-07	2.48	450.4	79.7
11	235	150	5.08E+07	1.94	4.62E-06	2.95E-06	1.57	288.3	31.2
12	321	247	4.84E+07	1.83	6.63E-06	5.10E-06	1.30	240.1	21.4
13	292	213	4.24E+07	1.96	6.89E-06	5.03E-06	1.37	253.0	23.9
14	117	53	8.47E+07	1.82	1.38E-06	6.26E-07	2.21	402.7	67.7
15	346	211	8.47E+07	2.08	4.09E-06	2.49E-06	1.64	301.5	27.7
16	191	101	7.26E+07	1.84	2.63E-06	1.39E-06	1.89	346.5	43.8
17	787	382	1.21E+08	2.41	6.50E-06	3.16E-06	2.06	376.6	25.8
18	241	178	6.05E+07	2.19	3.98E-06	2.94E-06	1.35	249.9	25.7
19	284	181	6.05E+07	1.91	4.69E-06	2.99E-06	1.57	288.8	28.7
20	270	208	6.05E+07	2.23	4.46E-06	3.44E-06	1.30	239.8	23.2

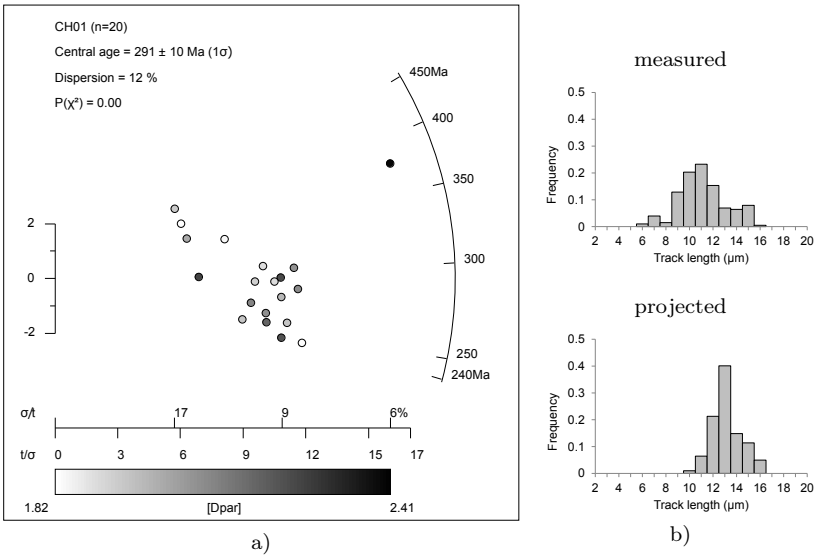

Figure B1: (a) Radial plot of single grain fission track data, prepared using RadialPlotter (Vermeesch, 2009). (b) Histograms of track length distribution. Track length projection after Ketcham et al. (2007).

(U-Th)/He data

Table B1: Single grain apatite (U-Th-Sm)/He data; L, $W1$ and $W2$ crystal dimensions; age_c corrected age.

No.	L (μm)	W1 (μm)	W2 (μm)	T	He (μcc/g)	U (ppm)	Th (ppm)	Sm (ppm)	Th/U	eU (ppm)	age (Ma)	error†	error‡	F_T	age$_c$ (Ma)	error‡
1	117	94	58	2	315.6	15.7	89.4	341.8	5.7	36.7	69.8	1.4	8.4	0.65	107.3	12.1
2	164	80	68	2	244.1	38.5	47.5	392.8	1.2	49.7	40.1	1.0	5.0	0.68	59.0	6.9
3	100	92	70	1	344.2	50.0	69.2	382.8	1.4	66.3	42.5	1.1	5.3	0.71	59.6	7.0
4	85	78	79	1	240.3	29.6	66.7	428.7	2.3	45.3	43.2	1.0	5.3	0.68	63.2	7.3

† analytical error; ‡ analytical error + 10% error (1 standard deviation on Durango aliquots)

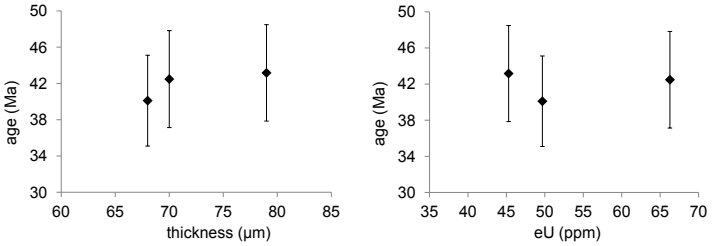

Figure B2: Apatite (U-Th-Sm)/He age versus (a) crystal thickness in μm, (b) [eU] in ppm.

Sample details

Grid reference:	NX 47635 94078	Unit:	Loch Doon pluton
Elevation:	224 m	Lithology:	Granodiorite
Region:	Southern Uplands	Apatite quality:	5

Apatite fission track data

Central age:	199.5 ± 8.9 Ma	χ^2:	30.5
Number of grains:	20	P(%):	4.6
Zeta (for IRMM standard glass):	313.7 ± 36.4	MTL measured:	12.67 ± 1.75 μm
ρ_D (interpolated):	9.44E+5	MTL projected:	13.73 ± 1.32 μm
N_D:	6478	No track lengths measured:	120
N_s/N_i:	1.38 ± 0.22		

Table B2: Single grain apatite fission track data; N_s—number of spontaneous tracks, N_i—number of induced tracks, ρ_D—tracks density on the dosimeter, ρ_s—spontaneous track density, ρ_i—induced track density.

No.	N_s	N_i	Area (cm^2)	DPar (μm)	ρ_s (tracks/cm^2)	ρ_i (tracks/cm^2)	ρ_s/ρ_i	Age (Ma)	1σ (Ma)
1	316	256	9.68E+07	3.07	3.26E-06	2.64E-06	1.23	180.2	16.0
2	151	101	6.05E+07	2.78	2.50E-06	1.67E-06	1.50	217.7	28.7
3	241	157	7.26E+07	3.13	3.32E-06	2.16E-06	1.54	223.4	23.8
4	199	136	8.47E+07	3.11	2.35E-06	1.61E-06	1.46	213.1	24.5
5	239	195	7.26E+07	3.04	3.29E-06	2.69E-06	1.23	179.0	18.0
6	146	107	6.05E+07	3.21	2.41E-06	1.77E-06	1.36	198.9	26.0
7	185	120	8.47E+07	2.96	2.18E-06	1.42E-06	1.54	224.3	27.1
8	150	89	6.05E+07	2.94	2.48E-06	1.47E-06	1.69	244.8	33.5
9	204	123	6.05E+07	2.77	3.37E-06	2.03E-06	1.66	241.0	28.4
10	142	87	7.26E+07	2.81	1.96E-06	1.20E-06	1.63	237.3	33.0
11	121	80	4.84E+07	2.94	2.50E-06	1.65E-06	1.51	220.1	32.4
12	88	74	4.84E+07	2.92	1.82E-06	1.53E-06	1.19	173.7	27.9
13	181	121	6.05E+07	2.84	2.99E-06	2.00E-06	1.50	217.8	26.4
14	158	131	6.05E+07	3.05	2.61E-06	2.17E-06	1.21	176.2	21.4
15	180	158	7.26E+07	2.81	2.48E-06	2.18E-06	1.14	166.5	18.8
16	125	72	8.47E+07	3.06	1.48E-06	8.50E-07	1.74	252.1	38.0
17	74	71	6.05E+07	2.85	1.22E-06	1.17E-06	1.04	152.5	25.7
18	76	68	4.36E+07	3.09	1.74E-06	1.56E-06	1.12	163.4	27.7
19	134	101	4.84E+07	2.75	2.77E-06	2.09E-06	1.33	193.5	26.1
20	107	106	3.87E+07	2.76	2.76E-06	2.74E-06	1.01	147.8	20.7

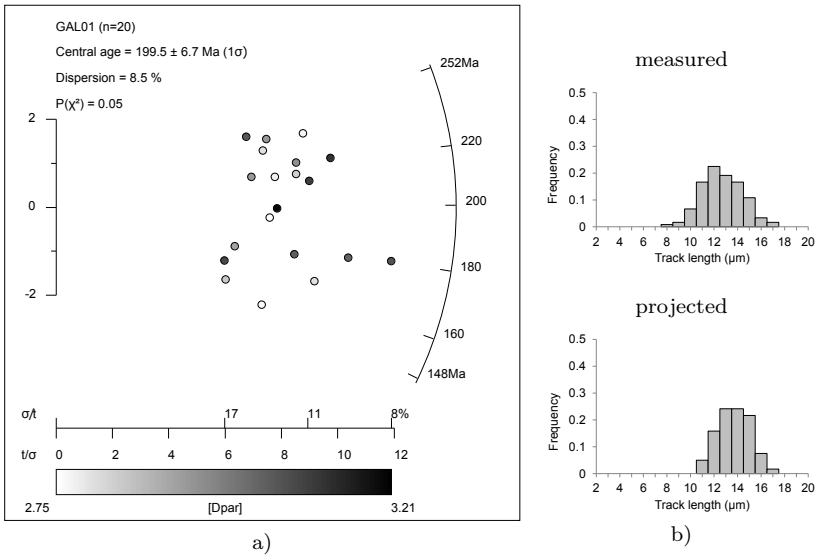

a) b)

Figure B3: (a) Radial plot of single grain fission track data, prepared using RadialPlotter (Vermeesch, 2009). (b) Histograms of track length distribution. Track length projection after Ketcham et al. (2007).

(U-Th)/He data

Table B3: Single grain apatite (U-Th-Sm)/He data; L, $W1$ and $W2$ crystal dimensions; age_c corrected age.

No.	L (μm)	W1 (μm)	W2 (μm)	T	He (μcc/g)	U (ppm)	Th (ppm)	Sm (ppm)	Th/U	eU (ppm)	age (Ma)	error†	error‡	F_T	age_c (Ma)	error‡
1	128	89	83	1	269.3	22.1	85.6	240.0	3.9	42.2	52.0	1.8	7.0	0.72	72.5	9.0
2	110	89	78	1	315.2	17.3	95.8	193.0	5.5	39.8	64.6	2.2	8.7	0.65	98.8	12.1
3	135	60	60	2	241.6	15.3	83.6	162.9	5.5	34.9	56.5	1.7	7.3	0.58	98.3	11.5
4	195	63	55	2	261.4	20.6	107.6	227.4	5.2	45.9	46.5	1.1	5.8	0.61	76.8	8.8
5	110	88	77	1	285.5	21.3	74.6	225.7	3.5	38.8	60.0	1.5	7.5	0.66	91.3	10.7
6	194	98	84	2	387.6	44.7	59.8	177.2	1.3	58.7	54.1	1.4	6.8	0.73	73.7	8.7
7	110	93	71	0	246.9	17.3	52.8	244.9	3.0	29.7	67.5	2.2	9.0	0.75	90.6	11.3
8	197	109	94	1	612.4	41.7	53.5	242.3	1.3	54.2	92.2	1.7	10.9	0.78	118.8	13.6
9	200	61	52	1	217.1	38.6	68.7	221.7	1.8	54.8	32.5	0.8	4.1	0.63	52.0	6.0
10	85	95	81	0	413.5	49.8	75.1	202.8	1.5	67.5	50.3	1.1	6.2	0.77	65.6	7.7
11	114	76	65	2	225.5	26.7	64.2	204.9	2.4	41.8	44.1	1.4	5.8	0.64	69.1	8.3
12	134	105	88	0	127.0	13.9	36.3	225.0	2.6	22.5	45.9	1.3	5.9	0.78	58.7	7.2
13	109	86	82	1	599.7	71.6	92.0	295.2	1.3	93.2	52.8	1.0	6.3	0.72	73.6	8.4
14	109	70	65	1	529.4	70.1	72.3	206.2	1.0	87.1	49.9	1.2	6.2	0.67	75.0	8.7
15	140	78	67	2	633.4	72.2	92.7	269.2	1.3	93.9	55.3	1.1	6.6	0.67	83.0	9.4
16	212	65	56	0	387.2	39.1	62.6	255.3	1.6	53.8	58.8	1.4	7.2	0.67	88.4	10.2
17	95	58	50	0	431.5	48.4	93.7	172.1	1.9	70.4	50.3	1.8	6.9	0.63	80.4	9.9
18	134	100	86	1	352.1	44.5	38.8	193.7	0.9	53.7	53.8	1.1	6.5	0.75	71.6	8.3
19	138	135	120	1	453.6	42.8	48.9	221.8	1.1	54.3	68.3	1.3	8.1	0.81	84.4	9.7
20	104	104	90	1	336.6	37.2	43.1	164.7	1.2	47.4	58.2	1.3	7.1	0.75	77.6	9.1
21	114	105	75	1	377.0	43.7	63.2	224.1	1.4	58.6	52.7	1.3	6.6	0.74	71.4	8.5
22	80	85	68	0	301.4	34.7	62.1	201.4	1.8	49.3	50.1	1.2	6.2	0.73	68.4	8.1
23	90	114	97	0	178.0	16.9	45.8	197.9	2.7	27.7	52.4	1.2	6.4	0.80	65.6	7.7
24	108	159	143	0	191.4	20.1	34.1	184.1	1.7	28.1	55.6	1.3	6.9	0.86	64.6	7.8
25	150	125	87	1	276.7	29.4	46.1	227.0	1.6	40.2	56.2	1.4	7.0	0.78	72.0	8.6

† analytical error; ‡ analytical error + 10% error (1 standard deviation on Durango aliquots)

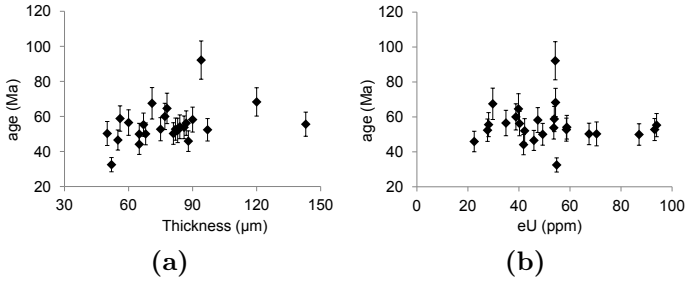

Figure B4: Apatite (U-Th-Sm)/He age versus (a) crystal thickness in μm, (b) [eU] in ppm.

Sample details

Grid reference:	NX 64563 74160	Unit:	Fleet pluton
Elevation:	50 m	Lithology:	Granite
Region:	Southern Uplands	Apatite quality:	4

Apatite fission track data

Central age:	78.1 ± 4.4 Ma	χ^2:	19.0
Number of grains:	19	P(%):	39.1
Zeta (for IRMM glass):	313.7 ± 8.3		
ρ_D (interpolated):	1.24E+6	MTL measured:	12.69 ± 2.31 μm
N_D:	8874	MTL measured:	14.14 ± 1.28 μm
N_s/N_i:	0.42 pm 0.10	No of track lengths:	102

Table B4: Single grain apatite fission track data; N_s—number of spontaneous tracks, N_i—number of induced tracks, ρ_D—tracks density on the dosimeter, ρ_s—spontaneous track density, ρ_i—induced track density.

No.	N_s	N_i	Area (cm^2)	DPar (μm)	ρ_s (tracks/cm^2)	ρ_i (tracks/cm^2)	ρ_s/ρ_i	Age (Ma)	1σ (Ma)
1	30	89	7.26E+07	1.66	4.13E-07	1.23E-06	0.34	65.2	13.9
2	32	52	4.84E+07	1.89	6.61E-07	1.07E-06	0.62	118.6	26.9
3	38	75	3.63E+07	1.43	1.05E-06	2.07E-06	0.51	97.8	19.7
4	28	54	5.81E+07	1.55	4.82E-07	9.30E-07	0.52	100.1	23.5
5	19	46	5.08E+07	1.50	3.74E-07	9.05E-07	0.41	79.8	21.9
6	19	43	3.63E+07	1.64	5.23E-07	1.18E-06	0.44	85.4	23.6
7	29	69	6.05E+07	1.51	4.79E-07	1.14E-06	0.42	81.2	18.1
8	11	42	8.47E+07	1.56	1.30E-07	4.96E-07	0.26	50.7	17.2
9	41	91	3.63E+07	1.62	1.13E-06	2.51E-06	0.45	87.0	16.6
10	17	36	3.87E+07	1.54	4.39E-07	9.30E-07	0.47	91.2	27.0
11	38	73	5.08E+07	1.41	7.48E-07	1.44E-06	0.52	100.5	20.3
12	15	52	6.78E+07	1.64	2.21E-07	7.67E-07	0.29	55.9	16.4
13	33	86	6.78E+07	1.75	4.87E-07	1.27E-06	0.38	74.2	15.3
14	110	282	8.47E+07	1.51	1.30E-06	3.33E-06	0.39	75.4	8.7
15	57	181	8.47E+07	1.49	6.73E-07	2.14E-06	0.31	61.0	9.4
16	12	52	5.81E+07	1.49	2.07E-07	8.95E-07	0.23	44.7	14.4
17	20	39	4.84E+07	1.48	4.13E-07	8.06E-07	0.51	99.0	27.4
18	35	82	4.36E+07	1.63	8.03E-07	1.88E-06	0.43	82.5	16.8
19	36	93	7.62E+07	1.61	4.72E-07	1.22E-06	0.39	74.9	14.8

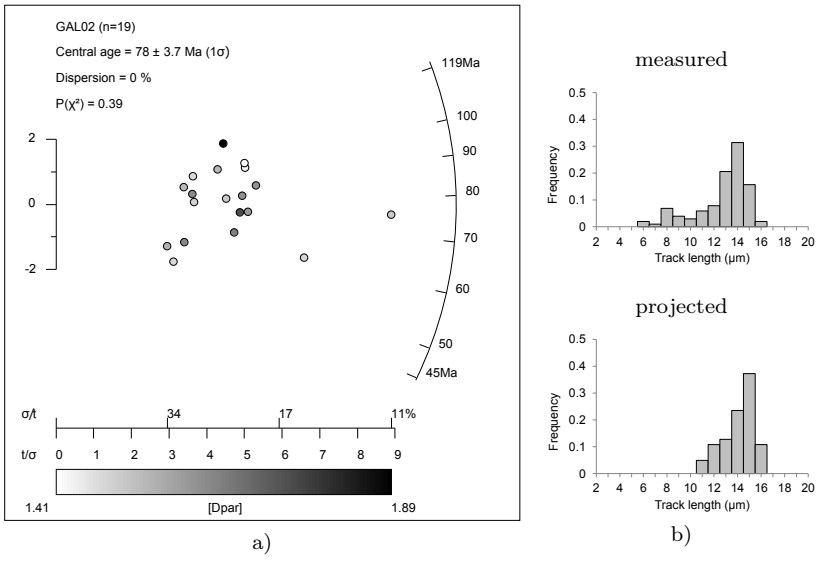

Figure B5: (a) Radial plot of single grain fission track data, prepared using RadialPlotter (Vermeesch, 2009). (b) Histograms of track length distribution. Track length projection after Ketcham et al. (2007).

(U-Th)/He data

Table B5: Single grain apatite (U-Th-Sm)/He data; L, $W1$ and $W2$ crystal dimensions; age_c corrected age.

No.	L (μm)	W1 (μm)	W2 (μm)	T	He (μcc/g)	U (ppm)	Th (ppm)	Sm (ppm)	Th/U	eU (ppm)	age (Ma)	error†	error‡	F_T	age$_c$ (Ma)	error‡
1	121	138	122	1	425.1	19.2	87.1	254.6	4.5	39.7	87.2	1.9	10.6	0.80	109.5	12.9
2	158	77	63	0	194.2	13.0	40.1	412.2	3.1	22.5	69.4	1.8	8.8	0.70	98.7	11.7
3	133	101	71	1	112.9	10.5	23.1	269.6	2.2	15.9	57.0	1.7	7.4	0.73	77.8	9.5
4	100	104	73	1	104.2	13.4	21.2	278.2	1.6	18.4	45.7	1.5	6.1	0.73	62.7	7.8
5	136	87	62	1	75.3	12.4	19.8	222.5	1.6	17.1	35.8	1.3	4.9	0.70	51.2	6.5
6	142	90	71	1	181.5	13.0	38.3	362.6	2.9	22.0	66.3	2.3	8.9	0.71	92.8	11.6
7	160	181	170	1	383.7	17.0	107.7	221.3	6.3	42.4	73.8	1.3	8.7	0.84	87.6	10.1
8	292	97	84	0	182.1	18.3	33.7	522.5	1.8	26.2	55.7	1.1	6.7	0.77	72.4	8.3
9	109	121	93	0	244.0	21.0	27.0	373.7	1.3	27.4	72.0	1.8	9.0	0.81	89.1	10.7
10	228	121	104	1	528.2	43.7	72.9	638.8	1.7	60.9	70.4	1.2	8.3	0.80	88.3	10.1
11	111	107	86	1	78.0	7.2	17.0	146.5	2.4	11.2	56.3	3.1	8.8	0.75	75.4	10.7
12	82	118	81	0	281.3	14.3	30.6	305.8	2.1	21.4	105.7	4.2	14.8	0.79	133.7	17.6
13	172	64	55	0	108.8	10.5	33.1	223.4	3.2	18.3	48.3	2.8	7.6	0.65	74.1	10.2
14	99	107	74	0	186.3	9.3	33.8	287.4	3.6	17.3	86.7	4.1	12.8	0.77	113.2	15.5
15	120	82	67	1	107.8	10.1	36.5	270.9	3.6	18.7	46.7	2.5	7.1	0.69	68.0	9.3
16	159	108	87	0	396.0	31.4	33.7	581.3	1.1	39.3	81.2	1.7	9.8	0.79	102.7	11.9
17	105	76	55	1	122.0	8.3	30.7	211.1	3.7	15.5	63.4	5.7	12.1	0.65	98.0	15.5
18	131	68	58	1	215.9	14.1	24.9	176.8	1.8	20.0	87.7	5.4	14.2	0.65	135.0	18.9
19	82	88	71	1	139.2	13.9	22.4	171.9	1.6	19.1	59.2	3.8	9.8	0.70	85.0	12.3
20	274	58	50	1	174.5	11.0	54.6	502.0	5.0	23.8	58.6	0.9	6.7	0.60	97.7	10.7
21	106	48	39	1	81.9	8.5	53.7	150.7	6.3	21.2	31.5	0.8	3.9	0.50	63.1	7.1
22	76	89	73	0	81.8	8.8	24.2	286.0	2.7	14.5	45.3	0.9	5.4	0.74	61.0	7.0
23	138	89	57	1	278.8	31.2	36.9	585.9	1.2	39.8	56.6	0.9	6.5	0.70	81.4	9.0
24	115	96	80	0	202.0	25.4	25.9	527.3	1.0	31.5	51.7	0.8	6.0	0.77	67.3	7.6

† analytical error; ‡ analytical error + 10% error (1 standard deviation on Durango aliquots)

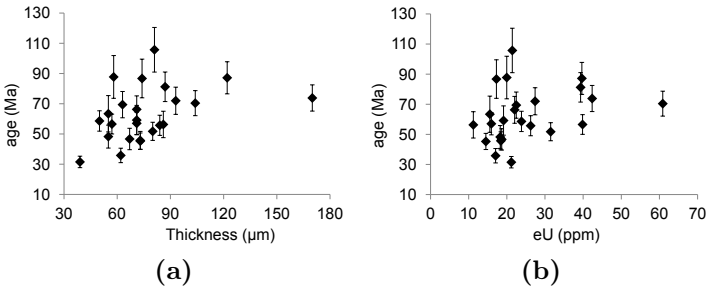

Figure B6: Apatite (U-Th-Sm)/He age versus (a) crystal thickness in μm, (b) [eU] in ppm.

Sample details

Grid reference:	NX 5857473491	Unit:	Fleet pluton
Elevation:	110 m	Lithology:	Granite (pink)
Region:	Southern Uplands	Apatite quality:	3

Apatite fission track data

Central age:	83.7 ± 3.8 Ma	Slide 1 (overetched)	
Number of grains:	18	MTL measured:	13.76 ± 1.83 μm
Zeta (for IRMM glass):	313.7 ± 8.3	MTL projected:	14.61 ± 1.48 μm
ρ_D (interpolated):	9.36E+5	No of track lengths measured: 76	
N_D:	6478	Slide 2	
N_s/N_i:	0.59 ± 0.06	MTL measured:	11.21 ± 2.30 μm
χ^2:	9.3	MTL projected:	13.17 ± 1.35 μm
P(%):	93.2	No of track lengths measured: 110	

Table B6: Single grain apatite fission track data; N_s—number of spontaneous tracks, N_i—number of induced tracks, ρ_D—tracks density on the dosimeter, ρ_s—spontaneous track density, ρ_i—induced track density.

No.	N_s	N_i	Area (cm^2)	DPar (μm)	ρ_s (tracks/cm^2)	ρ_i (tracks/cm^2)	ρ_s/ρ_i	Age (Ma)	1σ (Ma)
1	22	38	4.84E+07	1.57	4.55E-07	7.85E-07	0.58	84.4	22.8
2	130	257	9.80E+07	1.11	1.33E-06	2.62E-06	0.51	73.8	8.2
3	103	162	6.05E+07	1.37	1.70E-06	2.68E-06	0.64	92.7	12
4	53	82	4.84E+07	1.72	1.10E-06	1.69E-06	0.65	94.2	16.8
5	87	165	6.05E+07	1.43	1.44E-06	2.73E-06	0.53	76.9	10.4
6	111	218	9.68E+07	1.48	1.15E-06	2.25E-06	0.51	74.3	8.9
7	92	143	4.84E+07	1.53	1.90E-06	2.95E-06	0.64	93.8	12.8
8	107	196	5.93E+07	1.41	1.80E-06	3.31E-06	0.55	79.7	9.9
9	130	239	5.45E+07	1.45	2.39E-06	4.39E-06	0.54	79.4	9
10	65	127	8.47E+07	1.34	7.67E-07	1.50E-06	0.51	74.7	11.6
11	59	93	4.84E+07	1.72	1.22E-06	1.92E-06	0.63	92.5	15.6
12	56	81	2.90E+07	1.75	1.93E-06	2.79E-06	0.69	100.7	17.7
13	36	55	2.42E+07	1.67	1.49E-06	2.27E-06	0.65	95.4	20.6
14	68	106	4.84E+07	1.41	1.40E-06	2.19E-06	0.64	93.5	14.8
15	84	129	4.36E+07	1.57	1.93E-06	2.96E-06	0.65	94.9	13.6
16	65	112	4.36E+07	1.43	1.49E-06	2.57E-06	0.58	84.6	13.4
17	37	63	3.63E+07	1.20	1.02E-06	1.74E-06	0.59	85.7	17.9
18	41	80	2.90E+07	1.26	1.41E-06	2.75E-06	0.51	74.8	14.5

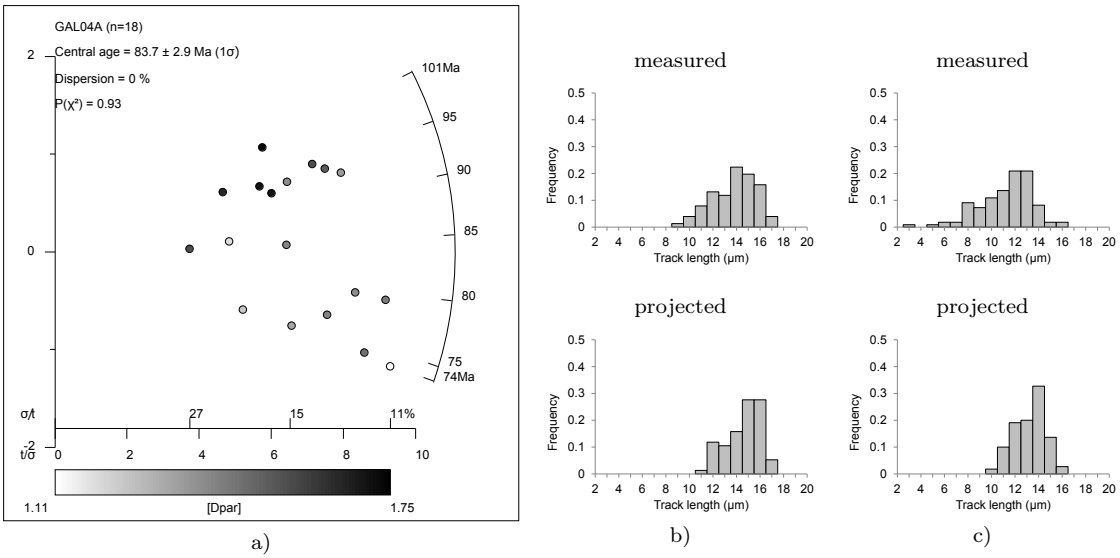

a) b) c)

Figure B7: (a) Radial plot of single grain fission track data, prepared using RadialPlotter (Vermeesch, 2009). (b & c) Histograms of track length distribution. Track length projection after Ketcham et al. (2007).

(U-Th)/He data

Table B7: Single grain apatite (U-Th-Sm)/He data; L, $W1$ and $W2$ crystal dimensions; age_c corrected age.

No.	L (μm)	W1 (μm)	W2 (μm)	T	He (μcc/g)	U (ppm)	Th (ppm)	Sm (ppm)	Th/U	eU (ppm)	age (Ma)	error†	error‡	F_T	age_c (Ma)	error‡
1	118	100	95	1	167.9	17.1	4.4	159.5	0.3	18.1	75.4	2.9	10.4	0.76	99.5	12.8
2	110	64	55	1	157.5	20.7	17.8	243.0	0.9	24.9	51.5	2.0	7.1	0.63	81.2	10.1
3	180	72	55	2	447.5	26.1	30.2	356.0	1.2	33.2	109.0	2.5	13.4	0.65	168.8	19.4
4	118	73	53	1	202.4	19.5	19.2	280.5	1.0	24.0	68.4	2.2	9.1	0.66	104.4	12.7
5	141	110	78	1	392.8	33.3	4.7	214.7	0.1	34.4	93.1	3.8	13.1	0.76	122.1	16.0

† analytical error; ‡ analytical error + 10% error (1 standard deviation on Durango aliquots)

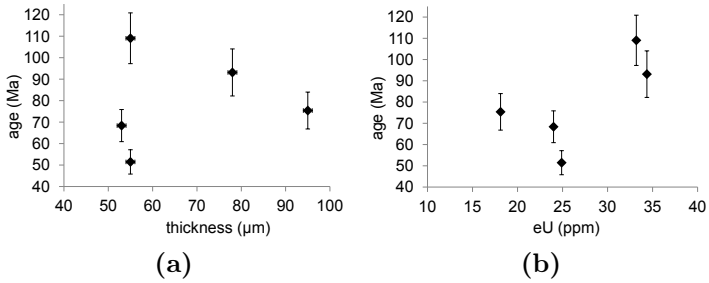

Figure B8: Apatite (U-Th-Sm)/He age versus (a) crystal thickness in μm, (b) [eU] in ppm.

Sample details

Grid reference:	NX 5857473491	Unit:	Fleet pluton
Elevation:	110 m	Lithology:	Granite (light grey)
Region:	Southern Uplands	Apatite quality:	3

Apatite fission track data

Central age:	79.3 ± 4.5 Ma	χ^2:	36.5
Number of grains:	20	P(%):	0.9
Zeta (for IRMM glass):	313.7 ± 8.3		
ρ_D (interpolated):	9.31E+5	MTL measured:	12.37 ± 1.87 μm
N_D:	6478	MTL projected:	13.40 ± 1.32 μm
N_s/N_i:	0.54 ± 0.11	No of track lengths:	105

Table B8: Single grain apatite fission track data; N_s—number of spontaneous tracks, N_i—number of induced tracks, ρ_D—tracks density on the dosimeter, ρ_s—spontaneous track density, ρ_i—induced track density.

No.	N_s	N_i	Area (cm^2)	DPar (μm)	ρ_s (tracks/cm^2)	ρ_i (tracks/cm^2)	ρ_s/ρ_i	Age (Ma)	1σ (Ma)
1	21	61	2.42E+07	2.35	8.68E-07	2.52E-06	0.34	50.1	12.8
2	28	59	4.84E+07	2.30	5.79E-07	1.22E-06	0.47	68.9	15.9
3	44	97	4.36E+07	2.24	1.01E-06	2.23E-06	0.45	65.9	12.1
4	56	106	3.63E+07	2.21	1.54E-06	2.92E-06	0.53	76.7	12.9
5	55	109	5.45E+07	2.22	1.01E-06	2.00E-06	0.50	73.3	12.3
6	36	75	4.84E+07	2.19	7.44E-07	1.55E-06	0.48	69.7	14.3
7	53	101	5.08E+07	2.21	1.04E-06	1.99E-06	0.52	76.2	13.1
8	83	173	4.36E+07	2.42	7.35E-07	2.57E-06	0.29	69.7	9.5
9	25	50	7.26E+07	2.18	1.14E-06	2.38E-06	0.48	72.6	17.9
10	41	80	3.39E+07	2.15	7.38E-07	1.48E-06	0.50	74.4	14.5
11	63	98	2.90E+07	2.05	1.41E-06	2.75E-06	0.51	93.2	15.3
12	107	149	7.26E+07	2.21	8.68E-07	1.35E-06	0.64	104.0	13.5
13	53	80	6.53E+07	2.26	1.64E-06	2.28E-06	0.72	96.0	17.2
14	81	160	4.84E+07	2.46	1.10E-06	1.65E-06	0.66	73.5	10.3
15	77	129	4.84E+07	2.20	1.67E-06	3.31E-06	0.51	86.6	12.7
16	88	154	6.05E+07	2.07	1.27E-06	2.13E-06	0.60	82.9	11.3
17	38	65	6.53E+07	2.14	1.35E-06	2.36E-06	0.57	84.8	17.5
18	184	268	5.45E+07	2.16	6.98E-07	1.19E-06	0.58	99.5	10.0
19	137	189	1.09E+08	2.55	1.69E-06	2.46E-06	0.69	105.0	12.2
20	32	112	9.68E+07	2.25	1.42E-06	1.95E-06	0.72	41.6	8.4

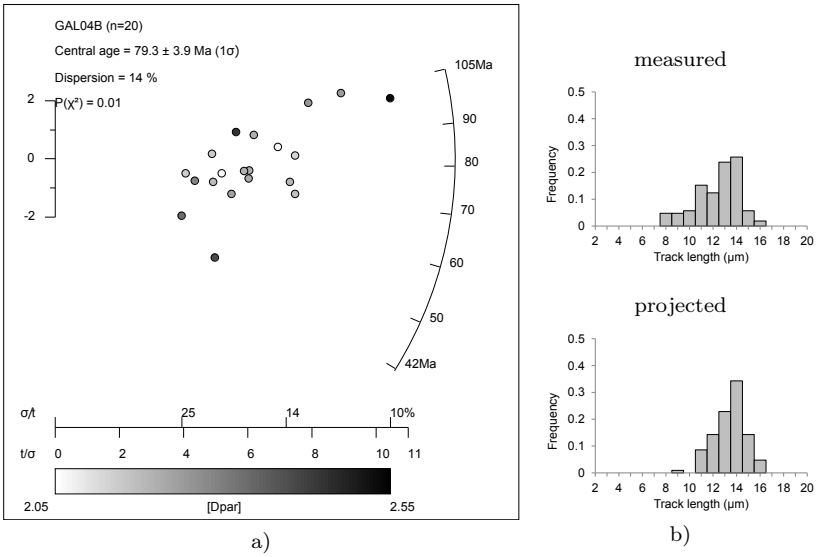

a) b)

Figure B9: (a) Radial plot of single grain fission track data, prepared using RadialPlotter (Vermeesch, 2009). (b) Histograms of track length distribution. Track length projection after Ketcham et al. (2007).

(U-Th)/He data

Table B9: Single grain apatite (U-Th-Sm)/He data; L, $W1$ and $W2$ crystal dimensions; age_c corrected age.

No.	L (μm)	W1 (μm)	W2 (μm)	T	He (μcc/g)	U (ppm)	Th (ppm)	Sm (ppm)	Th/U	eU (ppm)	age (Ma)	error†	error‡	F_T	age$_c$ (Ma)	error‡
1	92	92	82	1	2067.2	260.7	70.3	217.3	0.3	277.2	61.3	2.1	8.2	0.73	84.0	10.5
2	95	129	98	1	133.3	16.1	3.7	187.7	0.2	17.0	63.8	3.1	9.5	0.78	81.6	11.2
3	96	110	81	0	172.1	21.1	6.3	107.7	0.3	22.5	62.5	2.7	8.9	0.79	78.9	10.6
4	139	65	52	0	472.7	28.6	52.7	235.1	1.8	41.0	93.9	2.3	11.7	0.66	143.4	16.7
5	166	143	121	1	126.7	10.3	12.6	241.9	1.2	13.2	77.0	2.0	9.7	0.82	94.1	11.4
6	***113***	***67***	***58***	***1***	***849.8***	***6.4***	***46.9***	***238.1***	***7.3***	***17.5***	***386.2***	***15.2***	***53.8***	***0.63***	***617.9***	***77.0***
7	***169***	***85***	***69***	***1***	***542.0***	***2.5***	***99.5***	***331.1***	***39.1***	***25.9***	***168.0***	***8.7***	***25.5***	***0.69***	***245.3***	***33.2***
8	***128***	***65***	***60***	***0***	***116.5***	***3.6***	***38.3***	***185.4***	***10.5***	***12.7***	***74.1***	***4.1***	***11.5***	***0.65***	***114.2***	***15.5***
9	***85***	***98***	***84***	***1***	***319.7***	***5.5***	***98.0***	***264.4***	***17.8***	***28.5***	***90.7***	***3.7***	***12.8***	***0.70***	***128.8***	***16.6***

† analytical error; ‡ analytical error + 10% error (1 standard deviation on Durango aliquots)

Grains 6, 7, 8 and 9 are discarded because of to abnormally high Th/U ratios due to a problem with U and/or Th measurements (ICP-MS instability).

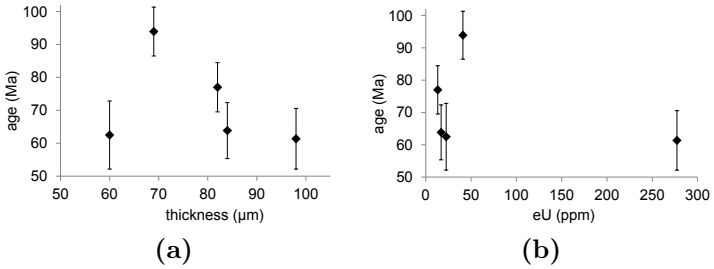

Figure B10: Apatite (U-Th-Sm)/He age versus (a) crystal thickness in μm, (b) [eU] in ppm.

Sample details

Grid reference:	NX 08932 35394	Unit:	Portencorkie
Elevation:	50 m	Lithology:	Granodiorite
Region:	Southern Uplands	Apatite quality:	4

Apatite fission track data

Central age:	159.5 ± 7.3 Ma	Slide 1	
Number of grains:	20	MTL measured:	13.32 ± 1.79 μm
Zeta (for IRMM glass): 313.7	8.3 ±	MTL projected:	14.51 ± 1.18 μm
ρ_D (interpolated):	9.27E+5	No of track lengths measured:	99
N_D:	6478	Slide 2	
N_s/N_i:	1.11 ± 0.18	MTL measured:	12.46 ± 1.87 μm
χ^2:	23.9	MTL projected:	14.00 ± 1.21 μm
P(%):	19.9	No of track lengths measured:	151

Table B10: Single grain apatite fission track data; N_s—number of spontaneous tracks, N_i—number of induced tracks, ρ_D—tracks density on the dosimeter, ρ_s—spontaneous track density, ρ_i—induced track density.

No.	N_s	N_i	Area (cm^2)	DPar (μm)	ρ_s (tracks/cm^2)	ρ_i (tracks/cm^2)	ρ_s/ρ_i	Age (Ma)	1σ (Ma)
1	129	103	1.21E+08	4.62	1.07E-06	8.51E-07	1.25	179.6	24.3
2	80	75	6.05E+07	5.32	1.32E-06	1.24E-06	1.07	153.3	25
3	95	89	7.62E+07	5.93	1.25E-06	1.17E-06	1.07	153.4	23.1
4	113	80	8.47E+07	5.86	1.33E-06	9.45E-07	1.41	202.2	30.1
5	67	83	6.78E+07	4.84	9.89E-07	1.22E-06	0.81	116.30	19.4
6	103	95	1.21E+08	5.39	8.51E-07	7.85E-07	1.08	155.7	22.6
7	59	51	1.09E+08	5.44	5.42E-07	4.68E-07	1.16	166.1	32.1
8	116	114	9.68E+07	5.03	1.20E-06	1.18E-06	1.02	146.3	19.8
9	103	99	1.09E+08	5.13	9.46E-07	9.09E-07	1.04	149.5	21.5
10	127	110	9.68E+07	4.36	1.31E-06	1.14E-06	1.15	165.7	22.1
11	117	95	6.05E+07	4.09	1.93E-06	1.57E-06	1.23	176.6	24.9
12	105	74	7.26E+07	3.02	1.45E-06	1.02E-06	1.42	203.1	31.4
13	135	107	9.68E+07	4.57	1.39E-06	1.11E-06	1.26	180.9	24
14	117	87	1.09E+08	4.23	1.07E-06	7.99E-07	1.34	192.6	27.8
15	116	100	6.05E+07	4.30	1.92E-06	1.65E-06	1.16	166.5	23.2
16	89	76	8.47E+07	4.05	1.05E-06	8.97E-07	1.17	168.1	26.7
17	73	95	7.26E+07	4.07	1.01E-06	1.31E-06	0.77	110.80	17.5
18	68	71	4.84E+07	4.27	1.40E-06	1.47E-06	0.96	137.8	23.7
19	71	84	5.45E+07	4.22	1.30E-06	1.54E-06	0.85	121.7	19.9

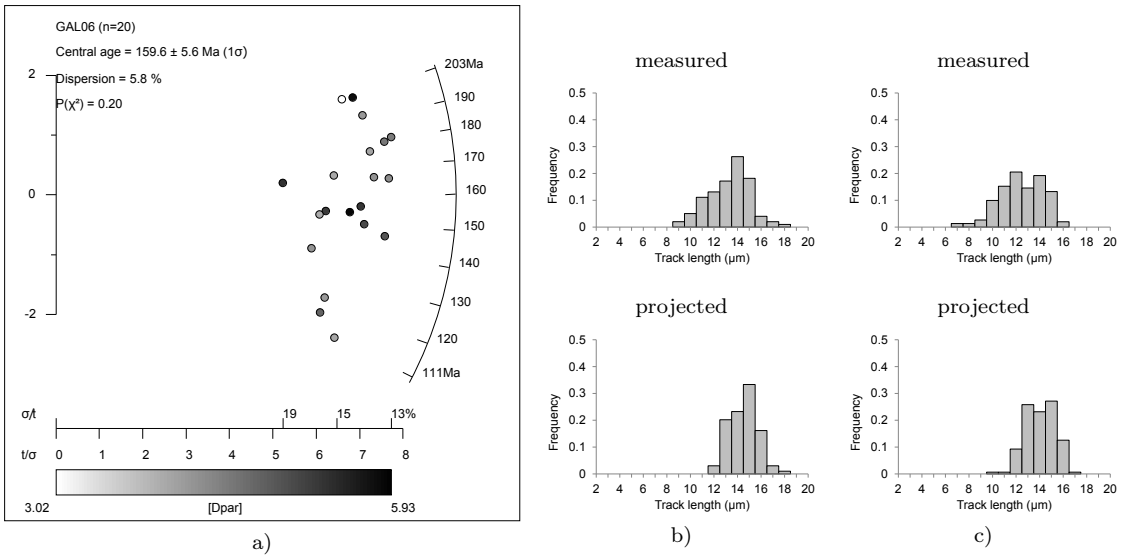

a) b) c)

Figure B11: (a) Radial plot of single grain fission track data, prepared using RadialPlotter (Vermeesch, 2009). (b & c) Histograms of track length distributions. Track length projection after Ketcham et al. (2007).

(U-Th)/He data

Table B11: Single grain apatite (U-Th-Sm)/He data; L, $W1$ and $W2$ crystal dimensions; age_c corrected age.

No.	L (μm)	W1 (μm)	W2 (μm)	T	He (μcc/g)	U (ppm)	Th (ppm)	Sm (ppm)	Th/U	eU (ppm)	age (Ma)	error†	error‡	F_T	age$_c$ (Ma)	error‡
1	194	120	104	2	262.1	16.5	47.9	198.5	2.9	27.8	76.8	1.4	9.1	0.77	100.0	11.4
2	169	103	101	1	258.8	22.4	71.6	239.0	3.2	39.2	53.8	1.0	6.4	0.77	70.4	8.1
3	148	92	86	1	194.7	16.0	60.6	153.1	3.8	30.2	52.6	1.2	6.5	0.73	71.9	8.4
4	106	96	91	2	415.1	25.4	106.7	195.8	4.2	50.5	67.1	1.5	8.2	0.69	97.2	11.2
5	185	158	123	1	226.0	22.1	41.8	216.9	1.9	31.9	57.7	1.4	7.2	0.83	69.5	8.4
6	84	62	48	2	701.2	118.0	168.7	529.1	1.4	157.6	36.5	1.1	4.7	0.56	65.8	7.6
7	131	75	64	2	369.9	45.8	78.0	150.8	1.7	64.1	47.3	1.4	6.1	0.65	72.4	8.6
8	104	71	61	2	400.9	45.2	79.7	191.7	1.8	63.9	51.4	1.7	6.8	0.62	82.8	10.0

† analytical error; ‡ analytical error + 10% error (1 standard deviation on Durango aliquots)

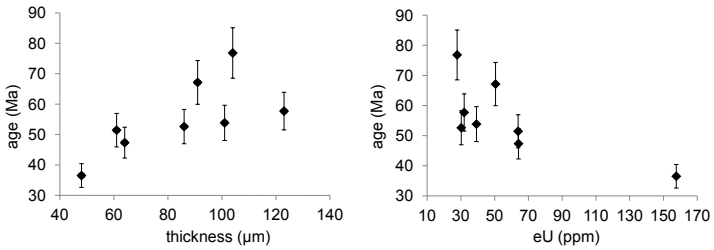

Figure B12: Apatite (U-Th-Sm)/He age versus (a) crystal thickness in μm, (b) [eU] in ppm.

Sample details

Grid reference: NX 83910 60950
Elevation: 56 m
Region: Southern Uplands
Unit: Criffell
Lithology: Granodiorite
Apatite quality: 5

Apatite fission track data

Slide 1 (underetched)		Slide 2	
Central age:	44.8 ± 2.1 Ma	Central age:	52.1 ± 2.5 Ma
Number of grains:	20	Number of grains:	20
Zeta (for IRMM glass):	313.7 ± 8.3	Zeta (for IRMM glass):	313.7 ± 8.3
ρ_D (interpolated):	1.63E+6	ρ_D (interpolated):	1.2E+6
N_D:	11903	N_D:	8874
N_s/N_i:	0.18 ± 0.03	N_s/N_i:	0.28 ± 0.05
χ^2:	14.0	χ^2:	22.8
P(%):	78.6	P(%):	24.8
MTL measured:	12.76 ± 1.82 μm	MTL measured:	13.59 ± 1.59 μm
MTL measured:	14.14 ± 1.20 μm	MTL measured:	14.70 ± 1.07 μm
No of track lengths:	104	No of track lengths:	115

Table B12: Single grain apatite fission track data; N_s—number of spontaneous tracks, N_i—number of induced tracks, ρ_D—tracks density on the dosimeter, ρ_s—spontaneous track density, ρ_i—induced track density.

No.	N_s	N_i	Area (cm^2)	DPar (μm)	ρ_s (tracks/cm^2)	ρ_i (tracks/cm^2)	ρ_s/ρ_i	Age (Ma)	1σ (Ma)
slide 1									
1	53	248	1.21E+08	1.48	4.38E-07	2.05E-06	0.21	54.4	8.4
2	56	267	1.21E+08	1.49	4.63E-07	2.21E-06	0.21	53.4	8.0
3	36	217	1.09E+08	1.61	3.31E-07	1.99E-06	0.17	42.3	7.7
4	39	257	1.21E+08	1.45	3.22E-07	2.12E-06	0.15	38.7	6.7
5	27	172	7.26E+07	1.53	3.72E-07	2.37E-06	0.16	40.0	8.4
6	33	141	5.93E+07	1.68	5.57E-07	2.38E-06	0.23	59.6	11.6
7	42	237	1.09E+08	1.49	3.86E-07	2.18E-06	0.18	45.1	7.7
8	30	215	9.68E+07	1.54	3.10E-07	2.22E-06	0.14	35.6	7.0
9	34	201	8.47E+07	1.45	4.01E-07	2.37E-06	0.17	43.1	8.1
10	32	198	9.68E+07	1.52	3.31E-07	2.05E-06	0.16	41.2	7.9
11	29	157	7.26E+07	1.49	3.99E-07	2.16E-06	0.18	47.1	9.6
12	52	356	1.21E+08	1.58	4.30E-07	2.94E-06	0.15	37.2	5.6
13	57	284	1.21E+08	1.51	4.71E-07	2.35E-06	0.20	51.1	7.6
14	47	265	1.21E+08	1.54	3.88E-07	2.19E-06	0.18	45.2	7.3
15	41	253	1.21E+08	1.50	3.39E-07	2.09E-06	0.16	41.3	7.0
16	45	252	1.21E+08	1.61	3.72E-07	2.08E-06	0.18	45.5	7.5
17	45	268	1.21E+08	1.67	3.72E-07	2.21E-06	0.17	42.8	7.0
18	49	324	1.21E+08	1.51	4.05E-07	2.68E-06	0.15	38.5	6.0
19	45	238	1.21E+08	1.50	3.72E-07	1.97E-06	0.19	48.2	7.9
20	34	149	7.74E+07	1.48	4.39E-07	1.92E-06	0.23	58.1	11.2
slide 2									
1	58	221	1.21E+08	1.97	4.79E-07	1.83E-06	0.26	50.0	7.5
2	37	142	7.26E+07	1.85	5.10E-07	1.96E-06	0.26	49.7	9.3
3	49	195	1.21E+08	1.90	4.05E-07	1.61E-06	0.25	47.9	7.8
4	43	193	1.21E+08	1.93	3.55E-07	1.60E-06	0.22	42.5	7.3
5	57	198	1.21E+08	1.88	4.71E-07	1.64E-06	0.29	54.9	8.4
6	66	225	1.21E+08	1.94	5.45E-07	1.86E-06	0.29	55.9	8.0
7	44	138	8.71E+07	1.85	5.05E-07	1.58E-06	0.32	60.7	10.7
8	42	159	9.80E+07	1.95	4.29E-07	1.62E-06	0.26	50.3	8.9
9	56	157	8.47E+07	1.92	6.61E-07	1.85E-06	0.36	67.9	10.7
10	51	137	8.47E+07	1.79	6.02E-07	1.62E-06	0.37	70.8	11.8
11	45	196	1.21E+08	2.04	3.72E-07	1.62E-06	0.23	43.8	7.3
12	57	163	1.21E+08	1.80	4.71E-07	1.35E-06	0.35	66.6	10.4
13	31	151	8.47E+07	1.97	3.66E-07	1.78E-06	0.21	39.2	7.8
14	41	178	1.21E+08	1.99	3.39E-07	1.47E-06	0.23	43.9	7.7
15	43	151	9.80E+07	1.98	4.39E-07	1.54E-06	0.28	54.3	9.5
16	49	248	1.21E+08	1.99	4.05E-07	2.05E-06	0.20	37.7	6.0
17	56	169	1.21E+08	1.82	4.63E-07	1.40E-06	0.33	63.1	9.9
18	50	191	1.21E+08	2.10	4.13E-07	1.58E-06	0.26	49.9	8.1
19	55	207	1.21E+08	1.89	4.55E-07	1.71E-06	0.27	50.6	7.8
20	58	196	1.21E+08	1.87	4.79E-07	1.62E-06	0.30	56.4	8.6

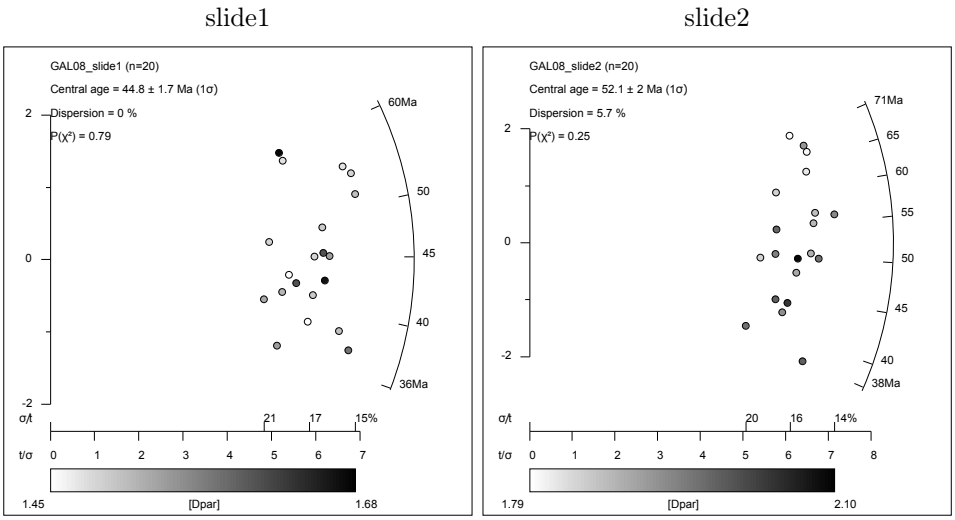

Figure B13: Radial plot of single grain fission track data, prepared using RadialPlotter (Vermeesch, 2009).

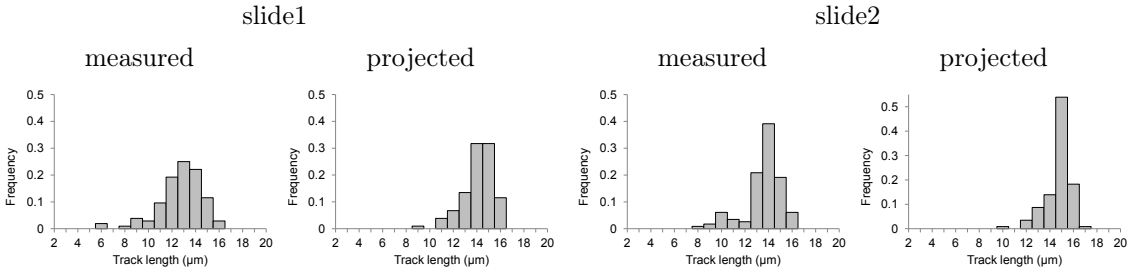

Figure B14: Histograms of track length distribution. Track length projection after Ketcham et al. (2007).

(U-Th)/He data

Table B14: Single grain apatite (U-Th-Sm)/He data; L, $W1$ and $W2$ crystal dimensions; age_c corrected age.

No.	L (μm)	W1 (μm)	W2 (μm)	T	He (μcc/g)	U (ppm)	Th (ppm)	Sm (ppm)	Th/U	eU (ppm)	age (Ma)	error†	error‡	F_T	age_c (Ma)	error‡
1	183	93	66	0	156.9	16.1	39.8	342.4	2.5	25.5	49.8	1.0	6.0	0.74	67.4	7.7
2	220	141	114	0	224.4	14.7	32.3	304.1	2.2	22.3	81.4	1.5	9.6	0.84	97.5	11.2
3	95	100	83	0	138.4	15.1	24.0	241.1	1.6	20.7	54.2	1.3	6.7	0.77	70.0	8.3
4	175	126	115	0	146.3	17.2	27.9	342.0	1.6	23.7	49.9	0.9	5.9	0.83	60.5	7.0
6	***239***	***72***	***62***	***2***	***258.5***	***17.4***	***35.5***	***330.2***	***2.0***	***25.7***	***81.3***	***0.9***	***9.0***	***0.66***	***122.6***	***13.2***
7	***128***	***102***	***88***	***0***	***102.7***	***60.0***	***281.7***	***626.2***	***4.7***	***126.2***	***6.7***	***0.1***	***0.7***	***0.77***	***8.6***	***0.9***
8	***165***	***108***	***93***	***1***	***43.7***	***21.5***	***38.3***	***385.6***	***1.8***	***30.5***	***11.6***	***0.1***	***1.3***	***0.77***	***15.2***	***1.6***
9	***152***	***104***	***90***	***1***	***150.1***	***25.8***	***83.0***	***368.1***	***3.2***	***45.3***	***27.0***	***0.2***	***2.9***	***0.75***	***35.8***	***3.8***
10	***187***	***92***	***79***	***2***	***179.0***	***21.6***	***49.8***	***307.0***	***2.3***	***33.3***	***43.7***	***0.4***	***4.8***	***0.71***	***61.2***	***6.5***
11	***142***	***117***	***101***	***0***	***123.5***	***13.9***	***21.0***	***261.6***	***1.5***	***18.9***	***53.0***	***0.6***	***5.9***	***0.81***	***65.5***	***7.2***

† analytical error; ‡ analytical error + 10% error (1 standard deviation on Durango aliquots)

Grains 6, 7, 8, 9, 10 and 11 are discarded because during the He analysis the ages of Durango aliquots were anomalously young.

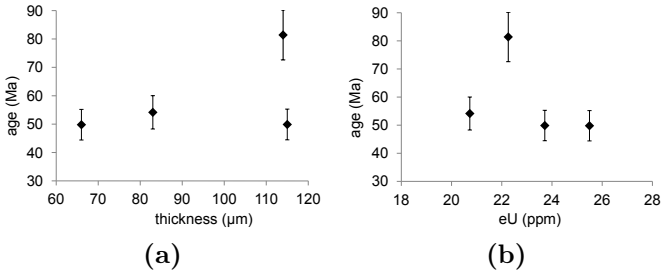

Figure B15: Apatite (U-Th-Sm)/He age versus (a) crystal thickness in μm, (b) [eU] in ppm.

Sample details

Grid reference:	NX 84373 60303	Unit:	Criffell
Elevation:	60 m	Lithology:	Granite
Region:	Southern Uplands	Apatite quality:	5

Apatite fission track data

Slide 1 (underetched)		Slide 2	
Central age:	55.0 ± 2.4 Ma	Central age:	58.0 ± 2.9 Ma
Number of grains:	18	Number of grains:	21
Zeta (for IRMM glass):	313.7 ± 8.3	Zeta (for IRMM glass):	313.7 ± 8.3
ρ_D (interpolated):	1.73E+6	ρ_D (interpolated):	1.21E+6
N_D:	11903	N_D:	8874
N_s/N_i:	0.20 ± 0.02	N_s/N_i:	0.31 ± 0.06
χ^2:	6.9	χ^2:	25.8
P(%):	98.5	P(%):	17.2
MTL measured:	13.76 ± 1.17 μm	MTL measured:	13.74 ± 1.50 μm
MTL projected:	14.72 ± 0.87 μm	MTL projected:	14.78 ± 1.01 μm
No of track lengths:	102	No of track lengths:	97

Table B15: Single grain apatite fission track data; N_s—number of spontaneous tracks, N_i—number of induced tracks, ρ_D—tracks density on the dosimeter, ρ_s—spontaneous track density, ρ_i—induced track density.

No.	N_s	N_i	Area (cm^2)	DPar (μm)	ρ_s (tracks/cm^2)	ρ_i (tracks/cm^2)	ρ_s/ρ_i	Age (Ma)	1σ (Ma)
slide 1									
1	45	208	1.09E+08	1.54	4.13E-07	1.91E-06	0.22	58.4	9.7
2	52	239	7.62E+07	1.56	6.82E-07	3.14E-06	0.22	58.8	9.1
3	60	265	1.21E+08	1.56	4.96E-07	2.19E-06	0.23	61.1	8.9
4	62	342	8.47E+07	1.45	7.32E-07	4.04E-06	0.18	49.0	6.9
5	68	278	9.68E+07	1.51	7.02E-07	2.87E-06	0.24	66.0	9.1
6	65	326	1.21E+08	1.47	5.37E-07	2.69E-06	0.20	53.9	7.5
7	59	352	1.21E+08	1.51	4.88E-07	2.91E-06	0.17	45.3	6.5
8	81	406	1.21E+08	1.60	6.69E-07	3.36E-06	0.20	53.9	6.7
9	79	363	1.21E+08	1.68	6.53E-07	3.00E-06	0.22	58.8	7.5
10	72	371	1.21E+08	1.62	5.95E-07	3.07E-06	0.19	52.4	6.9
11	33	162	7.26E+07	1.46	4.55E-07	2.23E-06	0.20	55.0	10.6
12	56	254	1.21E+08	1.58	4.63E-07	2.10E-06	0.22	59.5	8.9
13	33	176	8.47E+07	1.61	3.90E-07	2.08E-06	0.19	50.7	9.7
14	69	323	1.21E+08	1.58	5.70E-07	2.67E-06	0.21	57.7	7.8
15	29	148	6.53E+07	1.64	4.44E-07	2.27E-06	0.20	53.0	10.9
16	57	275	9.68E+07	1.40	5.89E-07	2.84E-06	0.21	56.0	8.3
17	53	267	8.47E+07	1.45	6.26E-07	3.15E-06	0.20	53.6	8.2
18	62	331	1.21E+08	1.54	5.12E-07	2.74E-06	0.19	50.6	7.1
slide 2									
1	57	171	8.47E+07	2.06	6.73E-07	2.02E-06	0.33	63.0	9.8
2	38	142	8.47E+07	2.20	4.49E-07	1.68E-06	0.27	50.6	9.4
3	34	171	5.93E+07	2.09	5.73E-07	2.88E-06	0.20	37.6	7.1
4	43	125	7.26E+07	2.41	5.92E-07	1.72E-06	0.34	65.0	11.6
5	72	220	7.26E+07	2.26	9.92E-07	3.03E-06	0.33	61.8	8.6
6	51	141	8.47E+07	2.50	6.02E-07	1.66E-06	0.36	68.3	11.3
7	37	97	6.53E+07	2.47	5.66E-07	1.48E-06	0.38	72.0	14.1
8	43	150	6.05E+07	2.23	7.11E-07	2.48E-06	0.29	54.2	9.5
9	59	187	8.47E+07	2.11	6.97E-07	2.21E-06	0.32	59.6	9.1
10	69	196	7.26E+07	2.13	9.50E-07	2.70E-06	0.35	66.5	9.5
11	36	152	4.84E+07	2.08	7.44E-07	3.14E-06	0.24	44.8	8.4
12	58	169	7.62E+07	2.32	7.61E-07	2.22E-06	0.34	64.8	10.0
13	53	153	8.47E+07	2.85	6.26E-07	1.81E-06	0.35	65.4	10.6
14	50	147	7.26E+07	2.32	6.89E-07	2.02E-06	0.34	64.2	10.7
15	49	133	8.47E+07	1.95	5.79E-07	1.57E-06	0.37	69.5	11.8
16	31	95	6.53E+07	2.09	4.74E-07	1.45E-06	0.33	61.6	12.9
17	33	106	6.05E+07	2.22	5.45E-07	1.75E-06	0.31	58.8	11.8
18	86	241	8.71E+07	2.52	9.87E-07	2.77E-06	0.36	67.4	8.7
19	30	142	7.26E+07	2.13	4.13E-07	1.96E-06	0.21	40.0	8.1
20	33	137	7.26E+07	2.40	4.55E-07	1.89E-06	0.24	45.6	8.9
21	31	151	7.26E+07	2.09	4.27E-07	2.08E-06	0.21	38.8	7.7

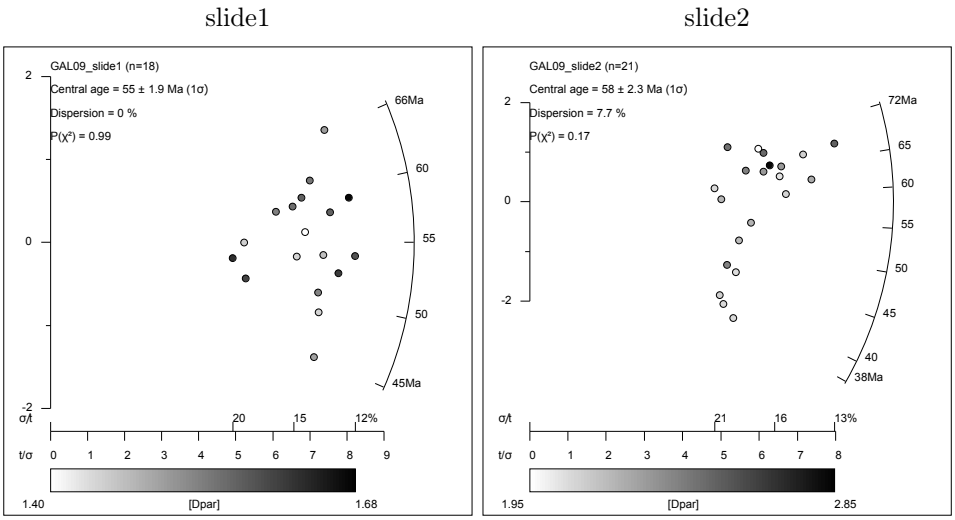

Figure B16: Radial plot of single grain fission track data, prepared using RadialPlotter (Vermeesch, 2009).

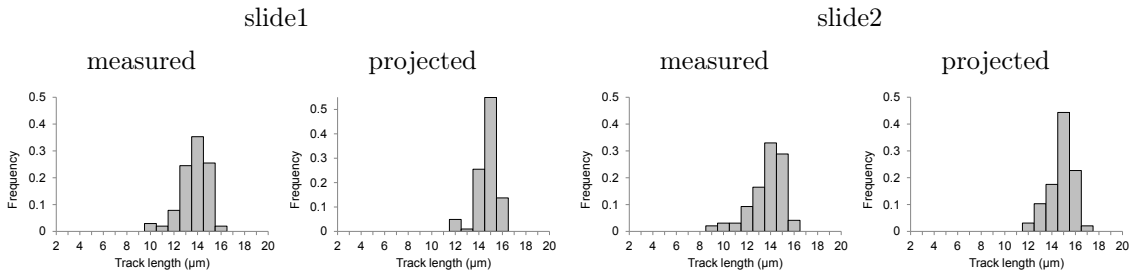

Figure B17: Histograms of track length distribution. Track length projection after Ketcham et al. (2007).

(U-Th)/He data

Table B17: Single grain apatite (U-Th-Sm)/He data; L, $W1$ and $W2$ crystal dimensions; age_c corrected age.

No.	L (μm)	W1 (μm)	W2 (μm)	T	He (μcc/g)	U (ppm)	Th (ppm)	Sm (ppm)	Th/U	eU (ppm)	age (Ma)	error†	error‡	F_T	age$_c$ (Ma)	error‡
1	95	116	85	1	160.3	17.5	17.3	211.6	1.0	21.6	60.4	1.4	7.4	0.76	79.9	9.4
2	135	145	125	1	116.1	14.1	24.1	218.6	1.7	19.8	47.7	0.9	5.7	0.81	58.6	6.8
3	100	77	72	1	162.4	24.3	32.8	280.0	1.4	32.0	41.4	1.0	5.1	0.69	60.4	7.0
4	130	107	93	1	204.0	18.0	33.0	288.2	1.8	25.8	64.1	1.3	7.7	0.76	84.4	9.7
5	210	122	113	0	183.3	18.5	24.6	298.7	1.3	24.3	61.2	1.1	7.3	0.82	74.6	8.6
6	***269***	***101***	***87***	***1***	***214.8***	***20.4***	***53.6***	***449.4***	***2.6***	***33.0***	***52.7***	***0.5***	***5.7***	***0.76***	***69.2***	***7.4***
7	***168***	***143***	***123***	***1***	***154.2***	***21.5***	***45.8***	***803.3***	***2.1***	***32.2***	***38.2***	***0.4***	***4.2***	***0.82***	***46.9***	***5.1***
8	***185***	***135***	***116***	***0***	***215.4***	***12.5***	***32.3***	***271.1***	***2.6***	***20.1***	***86.5***	***0.9***	***9.5***	***0.83***	***104.1***	***11.3***
9	***180***	***93***	***80***	***1***	***216.1***	***16.5***	***43.5***	***358.6***	***2.6***	***26.7***	***65.5***	***0.6***	***7.1***	***0.74***	***89.1***	***9.5***
10	***134***	***134***	***116***	***0***	***143.4***	***14.0***	***25.6***	***306.0***	***1.8***	***20.0***	***57.9***	***0.6***	***6.4***	***0.83***	***69.6***	***7.5***
11	***132***	***97***	***84***	***1***	***95.3***	***18.1***	***42.4***	***350.0***	***2.3***	***28.1***	***27.6***	***0.3***	***3.0***	***0.74***	***37.3***	***4.0***

† analytical error; ‡ analytical error + 10% error (1 standard deviation on Durango aliquots)

Grains 6, 7, 8, 9, 10 and 11 are discarded because during the He analysis the ages of Durango aliquots were anomalously young.

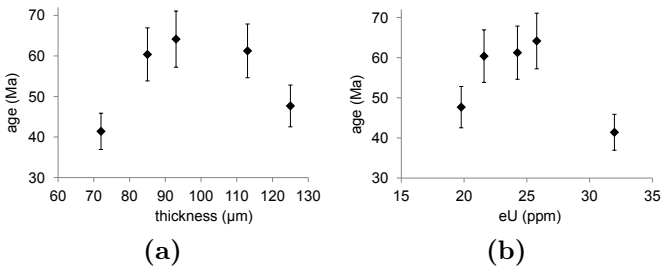

Figure B18: Apatite (U-Th-Sm)/He age versus (a) crystal thickness in μm, (b) [eU] in ppm.

Sample details

Grid reference:	NW 98074 72683	Unit:	Tappins Group
Elevation:	1 m	Lithology:	Conglomerate (granite boulder)
Region:	Southern Uplands	Deposition age:	Early Caradoc (Ordovician)
		Apatite quality:	5

Apatite fission track data

Central age:	197.9 ± 10.1 Ma	Slide 1	
Number of grains:	20	MTL measured:	12.43 ± 1.54 μm
Zeta (for IRMM glass):	313.7 ± 8.3	MTL projected:	13.89 ± 1.00 μm
ρ_D (interpolated):	9.23E+5	No of track lengths:	108
N_D:	6478	Slide 2	
N_s/N_i:	1.41 pm 0.26	MTL measured:	11.34 ± 1.53 μm
χ^2:	46.0	MTL projected:	12.83 ± 1.01 μm
P(%):	0.1	No of track lengths:	125

Table B18: Single grain apatite fission track data; N_s—number of spontaneous tracks, N_i—number of induced tracks, ρ_D—tracks density on the dosimeter, ρ_s—spontaneous track density, ρ_i—induced track density.

No.	N_s	N_i	Area (cm^2)	DPar (μm)	ρ_s (tracks/cm^2)	ρ_i (tracks/cm^2)	ρ_s/ρ_i	Age (Ma)	1σ (Ma)
1	135	110	1.09E+08	4.89	1.24E-06	1.01E-06	1.23	175.3	23.1
2	113	112	8.47E+07	3.91	1.33E-06	1.32E-06	1.01	144.4	19.7
3	192	111	1.21E+08	4.70	1.59E-06	9.17E-07	1.73	245.7	30.2
4	179	111	1.21E+08	4.62	1.48E-06	9.17E-07	1.61	229.3	28.5
5	120	112	9.68E+07	4.91	1.24E-06	1.16E-06	1.07	153.3	20.6
6	176	125	1.21E+08	2.58	1.45E-06	1.03E-06	1.41	200.7	24.2
7	114	78	8.47E+07	4.30	1.35E-06	9.21E-07	1.46	208.2	31.2
8	135	81	1.21E+08	2.81	1.12E-06	6.69E-07	1.67	236.9	34.0
9	152	109	1.09E+08	2.73	1.40E-06	1.00E-06	1.39	198.8	25.6
10	171	96	1.09E+08	3.04	1.57E-06	8.82E-07	1.78	252.9	33.1
11	148	126	1.09E+08	3.85	1.36E-06	1.16E-06	1.17	167.8	20.9
12	138	109	9.68E+07	3.20	1.43E-06	1.13E-06	1.27	180.7	23.8
13	204	149	1.21E+08	2.56	1.69E-06	1.23E-06	1.37	195.2	21.8
14	149	141	8.47E+07	2.65	1.76E-06	1.66E-06	1.06	151.2	18.3
15	138	135	1.21E+08	4.32	1.14E-06	1.12E-06	1.02	146.3	18.2
16	155	116	1.21E+08	3.20	1.28E-06	9.59E-07	1.34	190.6	24.1
17	213	123	1.21E+08	3.26	1.76E-06	1.02E-06	1.73	246.0	28.8
18	196	111	1.21E+08	2.29	1.62E-06	9.17E-07	1.77	250.7	30.7
19	183	124	1.21E+08	2.26	1.51E-06	1.02E-06	1.48	210.2	25.2
20	156	93	1.21E+08	3.09	1.29E-06	7.69E-07	1.68	238.4	32

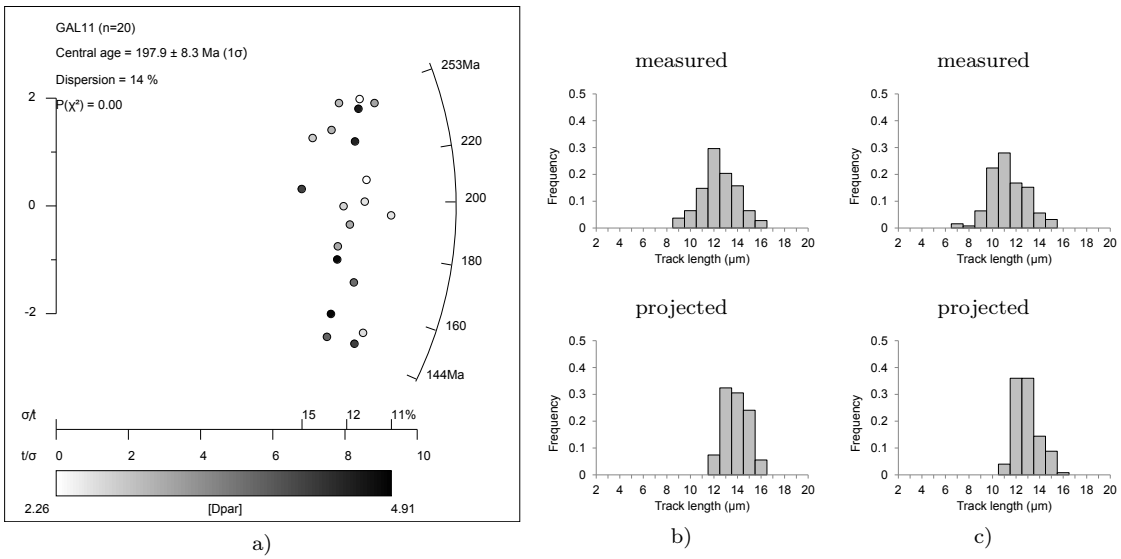

Figure B19: (a) Radial plot of single grain fission track data, prepared using RadialPlotter (Vermeesch, 2009). (b & c) Histograms of track length distributions. Track length projection after Ketcham et al. (2007).

(U-Th)/He data

Table B19: Single grain apatite (U-Th-Sm)/He data; L, $W1$ and $W2$ crystal dimensions; age_c corrected age.

No.	L (μm)	W1 (μm)	W2 (μm)	T	He (μcc/g)	U (ppm)	Th (ppm)	Sm (ppm)	Th/U	eU (ppm)	age (Ma)	error†	error‡	F_T	age$_c$ (Ma)	error‡
1	232	108	106	0	59.9	11.9	33.8	46.4	2.8	19.8	24.8	0.5	3.0	0.80	31.1	3.6
2	276	136	114	1	52.1	6.1	17.8	42.8	2.9	10.3	41.5	0.6	4.8	0.81	51.0	5.7
3	130	135	97	0	326.3	25.3	73.3	140.4	2.9	42.5	62.8	0.9	7.2	0.82	76.8	8.6
4	106	75	56	1	392.9	50.1	105.3	208.2	2.1	74.8	43.1	0.7	5.0	0.66	65.8	7.3
5	145	117	90	0	93.7	11.1	34.7	51.9	3.1	19.3	39.9	0.7	4.6	0.80	50.2	5.7
6	168	194	152	0	125.7	13.8	41.4	97.1	3.0	23.5	43.7	0.9	5.3	0.88	49.9	5.9
7	192	83	72	2	328.0	31.9	47.6	37.9	1.5	43.1	62.5	1.6	7.8	0.70	89.9	10.6
8	171	110	85	0	125.4	14.4	42.5	88.8	2.9	24.4	42.1	0.9	5.1	0.78	53.7	6.3
9	93	112	90	1	134.5	14.8	54.1	79.9	3.7	27.5	40.1	0.9	4.9	0.75	53.8	6.2
10	204	106	91	1	172.8	5.7	42.2	97.1	7.4	15.6	90.0	1.6	10.6	0.76	118.9	13.5
11	215	101	82	1	153.4	16.7	47.5	77.2	2.8	27.8	45.2	1.0	5.5	0.75	60.1	7.0
12	102	86	75	1	120.3	14.3	41.5	34.5	2.9	24.1	41.1	1.0	5.1	0.70	58.6	6.8
13	80	73	55	1	142.0	22.6	65.0	66.1	2.9	37.9	30.8	0.8	3.8	0.63	48.7	5.6
14	124	124	99	1	139.4	13.3	42.7	63.3	3.2	23.3	49.0	1.1	6.0	0.78	63.1	7.4
15	215	292	246	1	142.1	12.3	38.7	93.9	3.2	21.4	54.4	1.1	6.6	0.90	60.7	7.2
16	135	270	217	1	124.2	11.4	35.4	67.8	3.1	19.8	51.4	1.1	6.2	0.88	58.7	6.9
17	233	302	239	1	147.8	12.4	40.9	100.8	3.3	22.1	54.8	1.1	6.6	0.90	60.9	7.2
18	160	140	130	1	119.6	15.1	43.0	82.4	2.8	25.2	38.9	0.8	4.7	0.81	47.9	5.6
19	180	105	68	1	126.0	12.3	41.8	40.3	3.4	22.2	46.6	1.0	5.7	0.73	63.6	7.4
20	144	132	100	1	126.1	16.1	47.4	63.3	2.9	27.3	37.9	0.9	4.6	0.79	48.1	5.7
21	94	140	105	1	122.8	11.8	40.4	42.6	3.4	21.3	47.2	1.0	5.7	0.78	60.5	7.0
22	109	108	66	0	106.4	17.2	61.1	53.9	3.5	31.6	27.7	0.6	3.4	0.75	36.7	4.3
23	112	125	98	0	101.3	9.2	22.4	23.2	2.4	14.5	57.3	1.3	7.1	0.81	70.6	8.4
24	143	112	86	1	96.4	13.6	38.2	75.5	2.8	22.6	35.0	0.8	4.3	0.76	46.1	5.4
25	92	80	53	1	119.0	18.6	51.2	0.0	2.8	30.6	32.0	0.8	4.0	0.65	49.3	5.7

† analytical error; ‡ analytical error + 10% error (1 standard deviation on Durango aliquots)

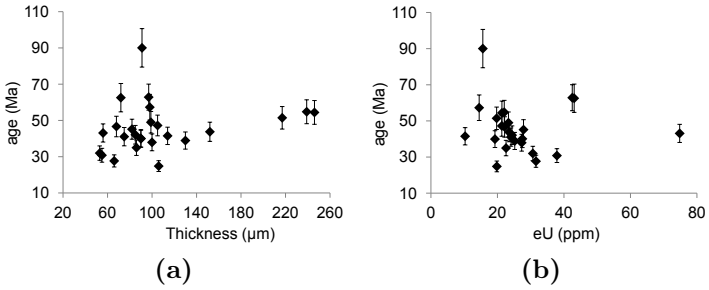

Figure B20: Apatite (U-Th-Sm)/He age versus (a) crystal thickness in μm, (b) [eU] in ppm.

Sample details

Grid reference:	NX 83910 60950	Unit:	Criffell
Elevation:	∼65 m (quarry)	Lithology:	Granite
Region:	Southern Uplands	Apatite quality:	5

Apatite fission track data

Central age:	63.4 ± 2.8 Ma	χ^2:	16.5
Number of grains:	24	P(%):	83.2
Zeta (for IRMM glass):	313.7 ± 8.3		
ρ_D (interpolated):	1.22E+6	MTL measured:	13.89 ± 1.33 μm
N_D:	8874	MTL measured:	14.94 ± 0.87 μm
N_s/N_i:	0.33 ± 0.05	No of track lengths:	105

Table B20: Single grain apatite fission track data; N_s—number of spontaneous tracks, N_i—number of induced tracks, ρ_D—tracks density on the dosimeter, ρ_s—spontaneous track density, ρ_i—induced track density.

No.	N_s	N_i	Area (cm^2)	DPar (μm)	ρ_s (tracks/cm^2)	ρ_i (tracks/cm^2)	ρ_s/ρ_i	Age (Ma)	1σ (Ma)
1	25	96	4.84E+07	1.94	5.17E-07	1.98E-06	0.26	49.6	11.2
2	46	136	6.05E+07	1.97	7.6E-07	2.25E-06	0.34	64.4	11.1
3	48	160	6.05E+07	2.01	7.93E-07	2.64E-06	0.30	57.2	9.5
4	34	147	6.05E+07	1.82	5.62E-07	2.43E-06	0.23	44.1	8.5
5	44	127	8.47E+07	1.98	5.19E-07	1.5E-06	0.35	66.0	11.7
6	46	105	8.47E+07	2.34	5.43E-07	1.24E-06	0.44	83.3	14.9
7	53	145	8.47E+07	2.24	6.26E-07	1.71E-06	0.37	69.6	11.3
8	48	137	6.05E+07	2.17	7.93E-07	2.26E-06	0.35	66.7	11.3
9	66	208	8.47E+07	2.11	7.79E-07	2.46E-06	0.32	60.4	8.7
10	41	119	9.68E+07	2.22	4.24E-07	1.23E-06	0.34	65.6	12.0
11	28	107	7.26E+07	2.19	3.86E-07	1.47E-06	0.26	49.9	10.7
12	59	141	8.47E+07	2.14	6.97E-07	1.66E-06	0.42	79.6	12.5
13	38	99	6.78E+07	2.02	5.61E-07	1.46E-06	0.38	73.0	14.1
14	40	113	7.26E+07	2.07	5.51E-07	1.56E-06	0.35	67.4	12.5
15	39	106	7.26E+07	1.87	5.37E-07	1.46E-06	0.37	70.0	13.3
16	24	83	7.26E+07	2.05	3.31E-07	1.14E-06	0.29	55.1	12.9
17	51	157	8.47E+07	2.12	6.02E-07	1.85E-06	0.32	61.9	10.1
18	37	122	7.26E+07	2.13	5.1E-07	1.68E-06	0.30	57.8	11.0
19	136	391	1.09E+08	2.04	1.25E-06	3.59E-06	0.35	66.2	6.9
20	58	160	9.68E+07	2.05	5.99E-07	1.65E-06	0.36	69.0	10.8
21	45	150	8.47E+07	1.91	5.31E-07	1.77E-06	0.30	57.2	9.8
22	42	107	6.05E+07	2.08	6.94E-07	1.77E-06	0.39	74.7	13.8
23	64	227	1.09E+08	2.20	5.88E-07	2.08E-06	0.28	53.7	7.8
24	36	107	8.47E+07	2.12	4.25E-07	1.26E-06	0.34	64.1	12.5

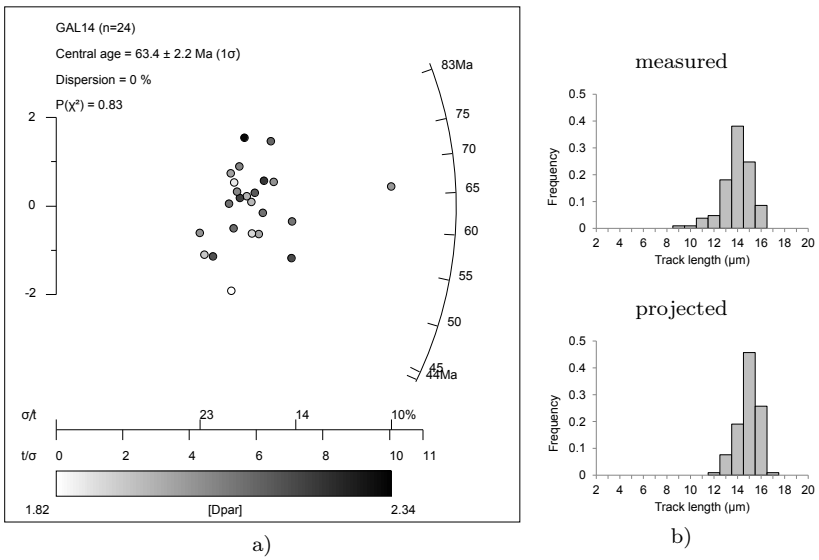

a) b)

Figure B21: (a) Radial plot of single grain fission track data, prepared using RadialPlotter (Vermeesch, 2009). (b) Histograms of track length distribution. Track length projection after Ketcham et al. (2007).

(U-Th)/He data

Table B21: Single grain apatite (U-Th-Sm)/He data; L, $W1$ and $W2$ crystal dimensions; age_c corrected age.

No.	L (μm)	W1 (μm)	W2 (μm)	T	He (μcc/g)	U (ppm)	Th (ppm)	Sm (ppm)	Th/U	eU (ppm)	age (Ma)	error†	error‡	F_T	age$_c$ (Ma)	error‡
1	272	184	158	1	191.6	16.4	47.0	140.4	2.9	27.4	57.0	1.0	6.7	0.86	66.5	7.6
2	154	117	98	1	152.6	14.4	43.1	77.2	3.0	24.5	51.0	1.1	6.2	0.78	65.8	7.7
3	262	75	64	2	168.7	16.1	48.8	58.0	3.0	27.5	50.2	1.2	6.3	0.67	74.8	8.7
4	91	152	112	1	171.1	17.8	34.2	52.9	1.9	25.8	54.3	1.3	6.7	0.80	68.3	8.1
5	311	84	72	1	163.5	17.1	47.5	92.2	2.8	28.2	47.4	1.0	5.7	0.72	65.9	7.6
6	300	63	46	1	162.3	15.9	62.2	258.2	3.9	30.5	43.3	0.6	5.0	0.61	70.9	7.7
7	151	68	54	1	147.1	16.4	53.1	1214.0	3.2	28.9	39.8	0.6	4.6	0.64	62.4	6.8
8	130	96	82	1	162.5	15.8	50.5	128.5	3.2	27.7	48.0	0.7	5.5	0.73	65.6	7.3
9	77	93	72	1	178.4	16.7	57.0	370.7	3.4	30.1	48.1	0.7	5.5	0.70	69.2	7.7
10	110	164	111	1	163.1	13.8	42.4	115.5	3.1	23.8	56.0	0.8	6.4	0.81	69.6	7.8
11	224	171	128	1	184.2	14.8	44.6	0.9	3.0	25.3	59.8	0.9	6.9	0.84	71.4	8.0
12	100	177	146	1	179.9	18.1	37.6	65.5	2.1	26.9	54.8	0.8	6.3	0.83	66.4	7.5
13	180	138	89	1	167.2	15.7	46.0	55.9	2.9	26.5	51.8	0.8	5.9	0.79	65.6	7.3
14	75	90	59	1	146.1	15.5	53.4	182.8	3.4	28.1	42.5	0.7	4.9	0.67	63.6	7.1
15	170	74	65	1	308.0	28.7	87.0	187.2	3.0	49.1	51.3	0.8	5.9	0.68	75.8	8.3
16	125	70	55	2	129.5	14.5	59.5	168.6	4.1	28.5	37.1	0.6	4.3	0.61	60.9	6.7
17	71	104	87	0	181.8	22.2	58.8	58.0	2.6	36.0	41.4	0.6	4.8	0.78	53.1	5.9
18	110	102	73	1	145.4	15.3	48.8	111.8	3.2	26.7	44.5	0.7	5.1	0.72	61.5	6.8
19	192	95	68	1	148.6	17.0	56.0	29.5	3.3	30.2	40.5	0.6	4.7	0.72	56.1	6.2
20	***83***	***163***	***115***	***0***	***127.4***	***46.2***	***92.5***	***0.0***	***2.0***	***67.9***	***15.5***	***0.2***	***1.8***	***0.85***	***18.2***	***2.1***

† analytical error; ‡ analytical error + 10% error (1 standard deviation on Durango aliquots)

Grain 20 was discarded because its age is anomalously young (possible incomplete degassing of a crystal).

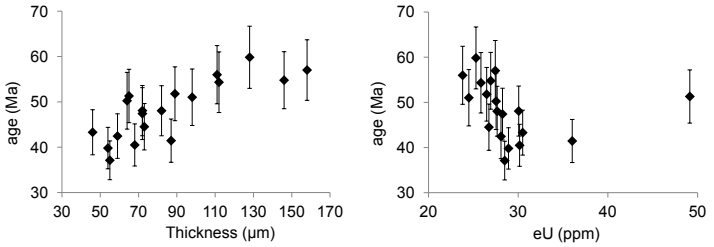

Figure B22: Apatite (U-Th-Sm)/He age versus (a) crystal thickness in μm, (b) [eU] in ppm.

Table B22: Single grain zircon (U-Th)/He data.

Aliquot No	L (um)	W (um)	T	He (ncc/g)	U (ppm)	Th (ppm)	eU (ppm)	age (Ma)	error † (Ma)	F_T	age corr (Ma)	error ‡ (Ma)
1	238	88	2	29214	1271	1479	1618	147.5	1.3	0.79	186.5	28.0
2	216	100	2	28833	960	454	1067	219.5	1.9	0.81	271.7	40.7
3	168	62	2	25387	809	562	941	219.1	1.9	0.71	306.9	46.0
4	180	73	2	23684	614	442	718	266.7	2.3	0.75	356.1	53.4
5	202	102	2	29626	703	441	807	296.3	2.5	0.81	367.7	55.2

† analytical error, ‡ 10% error

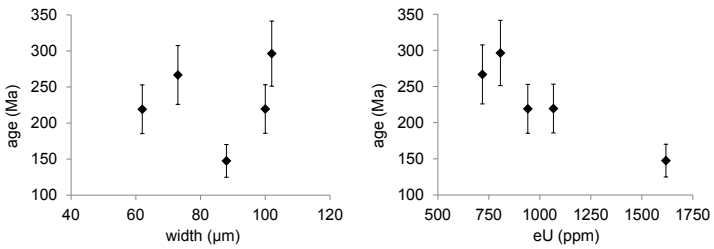

Figure B23: Zircon (U-Th)/He age versus (a) crystal thickness in μm, (b) [eU] in ppm.

Sample details

Grid reference:	NY 555 084	Unit:	Shap
Elevation:	∼380 m (quarry)	Lithology:	Granite
Region:	Lake District	Apatite quality:	5

Apatite fission track data

Slide 1 (underetched)		Slide 2	
Central age:	50.2 ± 2.3 Ma	Central age:	75.0 ± 3.1 Ma
Number of grains:	20	Number of grains:	22
ρ_D (interpolated):	1.72E+6	ρ_D (interpolated):	1.27E+6
N_D:	11903	N_D:	8874
N_s/N_i:	0.19 ± 0.02	N_s/N_i:	0.38 ± 0.05
χ^2:	10.6	χ^2:	16.5
P(%):	93.8	P(%):	73.9
MTL measured:	13.35 ± 1.55 μm	MTL measured:	13.14 ± 1.78 μm
MTL projected:	14.48 ± 1.16 μm	MTL projected:	14.35 ± 1.29 μm
No of track lengths measured:	120	No of track lengths measured:	110

Table B23: Single grain apatite fission track data; N_s—number of spontaneous tracks, N_i—number of induced tracks, ρ_D—tracks density on the dosimeter, ρ_s—spontaneous track density, ρ_i—induced track density.

No.	N_s	N_i	Area (cm^2)	DPar (μm)	ρ_s (tracks/cm^2)	ρ_i (tracks/cm^2)	ρ_s/ρ_i	Age (Ma)	1σ (Ma)
slide 1									
1	32	182	9.68E+07	1.625	3.31E-07	1.88E-06	0.18	47.2	9.1
2	63	264	1.21E+08	1.782	5.21E-07	2.18E-06	0.24	64.0	9.1
3	47	235	1.09E+08	1.811	4.32E-07	2.16E-06	0.20	53.7	8.7
4	49	273	1.21E+08	1.758	4.05E-07	2.26E-06	0.18	48.2	7.6
5	47	216	1.21E+08	1.591	3.88E-07	1.79E-06	0.22	58.4	9.5
6	49	290	1.21E+08	1.635	4.05E-07	2.04E-06	0.17	45.4	7.1
7	30	185	8.47E+07	1.654	3.54E-07	2.18E-06	0.16	43.6	8.7
8	45	224	9.68E+07	1.678	4.65E-07	2.31E-06	0.20	53.9	8.9
9	47	276	9.68E+07	1.523	4.86E-07	2.85E-06	0.17	45.7	7.3
10	49	246	1.21E+08	1.682	4.05E-07	2.03E-06	0.20	53.5	8.5
11	43	268	1.21E+08	1.609	3.55E-07	2.21E-06	0.16	43.1	7.2
12	32	173	8.47E+07	1.543	3.78E-07	2.04E-06	0.18	49.7	9.7
13	50	247	1.21E+08	1.577	4.13E-07	2.04E-06	0.20	54.3	8.6
14	38	240	1.21E+08	1.477	3.14E-07	1.98E-06	0.16	42.5	7.5
15	43	195	9.68E+07	1.612	4.44E-07	2.01E-06	0.22	59.1	10.1
16	42	233	1.21E+08	1.546	3.47E-07	1.93E-06	0.18	48.4	8.2
17	29	150	8.47E+07	1.532	3.42E-07	1.77E-06	0.19	51.9	10.6
18	50	313	7.26E+07	1.439	6.89E-07	4.31E-06	0.16	42.9	6.6
19	41	198	1.09E+08	1.485	3.76E-07	1.82E-06	0.21	55.6	9.7
20	42	237	1.21E+08	1.471	3.47E-07	1.96E-06	0.18	47.6	8.1
slide 2									
1	75	193	1.21E+08	1.83	6.20E-07	1.60E-06	0.39	76.9	10.7
2	98	232	1.21E+08	1.84	8.10E-07	1.92E-06	0.42	83.6	10.3
3	56	167	1.09E+08	1.89	5.14E-07	1.53E-06	0.34	66.5	10.4
4	64	209	1.21E+08	1.76	5.29E-07	1.73E-06	0.31	60.7	8.8
5	59	142	1.21E+08	1.77	4.88E-07	1.17E-06	0.42	82.2	13.0
6	65	205	1.21E+08	1.89	5.37E-07	1.69E-06	0.32	62.9	9.1
7	75	186	1.21E+08	1.83	6.20E-07	1.54E-06	0.40	79.8	11.2
8	60	178	1.09E+08	1.61	5.51E-07	1.63E-06	0.34	66.8	10.2
9	70	168	1.09E+08	1.74	6.43E-07	1.54E-06	0.42	82.5	12.0
10	84	226	1.09E+08	1.76	7.71E-07	2.08E-06	0.37	73.6	9.6
11	48	170	1.09E+08	1.81	4.41E-07	1.56E-06	0.28	56.0	9.3
12	74	194	1.21E+08	1.90	6.12E-07	1.60E-06	0.38	75.5	10.5
13	72	216	1.21E+08	1.84	5.95E-07	1.79E-06	0.33	66.1	9.2
14	81	207	1.21E+08	1.68	6.69E-07	1.71E-06	0.39	77.5	10.4
15	78	169	1.09E+08	1.85	7.16E-07	1.55E-06	0.46	91.3	12.8
16	83	196	1.21E+08	1.79	6.86E-07	1.62E-06	0.42	83.8	11.2
17	67	189	1.09E+08	1.77	6.15E-07	1.74E-06	0.35	70.2	10.2
18	77	207	1.09E+08	1.85	7.07E-07	1.90E-06	0.37	73.7	10.1
19	75	199	1.09E+08	1.85	6.89E-07	1.83E-06	0.38	74.6	10.3
20	68	177	1.09E+08	2.01	6.24E-07	1.63E-06	0.38	76.1	11.1
21	86	189	1.21E+08	1.89	7.11E-07	1.56E-06	0.46	90.0	12.0
22	93	228	1.21E+08	1.84	7.69E-07	1.88E-06	0.41	80.7	10.2

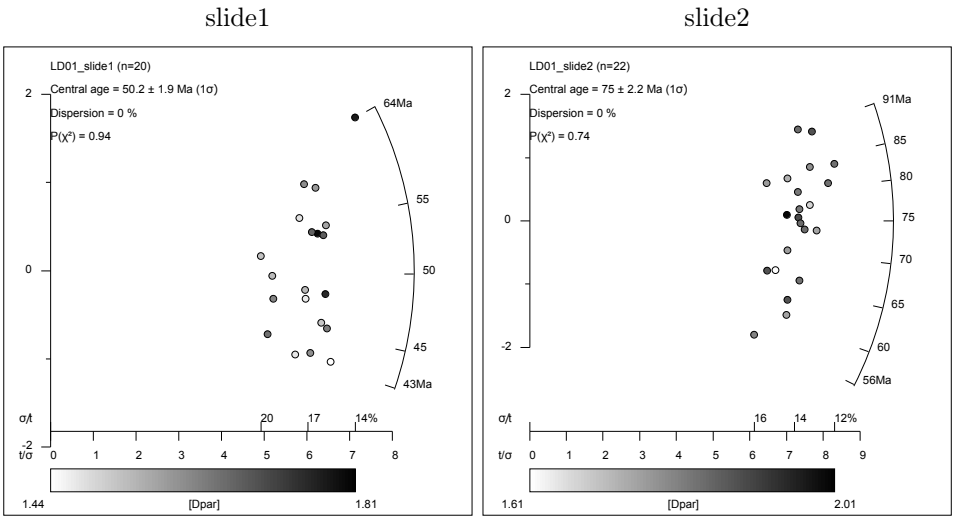

Figure B24: Radial plot of single grain fission track data, prepared using RadialPlotter (Vermeesch, 2009).

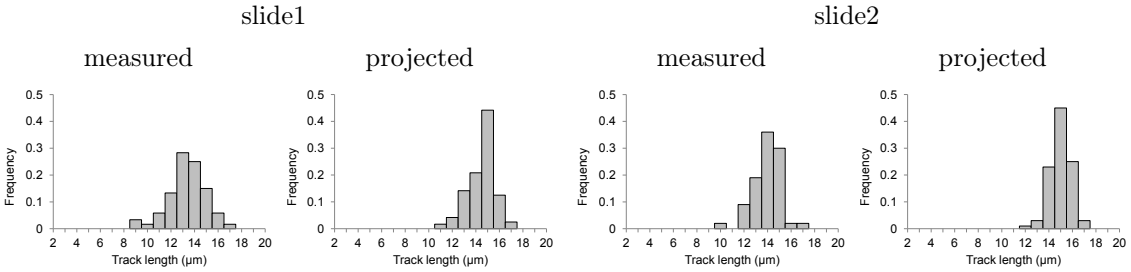

Figure B25: Histograms of track length distribution. Track length projection after Ketcham et al. (2007).

(U-Th)/He data

Table B25: Single grain apatite (U-Th-Sm)/He data; L, $W1$ and $W2$ crystal dimensions; age_c corrected age.

No.	L (μm)	W1 (μm)	W2 (μm)	T	He (μcc/g)	U (ppm)	Th (ppm)	Sm (ppm)	Th/U	eU (ppm)	age (Ma)	error†	error‡	F_T	age$_c$ (Ma)	error‡
1	173	122	99	0	217.8	29.1	39.4	198.4	1.4	38.3	46.5	1.1	5.8	0.81	57.1	6.9
2	130	128	99	1	68.3	20.9	32.4	127.4	1.6	28.5	19.7	0.5	2.5	0.79	25.0	3.0
3	167	121	86	1	116.0	21.8	37.9	148.2	1.7	30.7	30.9	0.7	3.8	0.78	39.9	4.7
4	100	120	87	0	118.6	25.9	33.1	96.5	1.3	33.7	28.9	0.7	3.6	0.80	36.1	4.3
5	191	118	110	1	159.0	25.7	32.7	102.5	1.3	33.4	39.1	0.9	4.9	0.80	49.2	5.9
6	83	178	126	1	154.3	17.5	73.6	89.8	4.2	34.8	36.4	1.0	4.6	0.80	45.3	5.5
7	230	75	64	2	190.9	16.2	69.7	195.6	4.3	32.5	47.9	1.4	6.2	0.66	72.1	8.6
8	115	184	132	1	180.1	15.1	70.1	120.9	4.6	31.6	46.6	1.2	5.9	0.82	56.6	6.8
9	158	122	70	1	271.5	21.5	97.8	179.1	4.6	44.5	49.9	1.3	6.3	0.75	66.9	8.0
10	235	94	81	2	214.0	18.8	154.9	202.4	8.3	55.2	31.7	0.8	4.0	0.72	44.4	5.2
11	***174***	***153***	***132***	***1***	***389.3***	***15.9***	***143.1***	***160.7***	***9.0***	***49.5***	***64.2***	***0.5***	***6.9***	***0.82***	***78.6***	***8.4***
12	***227***	***171***	***148***	***1***	***211.2***	***13.7***	***63.2***	***145.9***	***4.6***	***28.6***	***60.3***	***0.5***	***6.6***	***0.84***	***71.6***	***7.7***
13	***236***	***199***	***172***	***1***	***127.3***	***13.8***	***33.2***	***162.8***	***2.4***	***21.6***	***48.2***	***0.6***	***5.4***	***0.87***	***55.7***	***6.1***
14	***164***	***151***	***130***	***1***	***172.9***	***15.8***	***73.0***	***137.8***	***4.6***	***33.0***	***42.9***	***0.4***	***4.7***	***0.82***	***52.4***	***5.7***
15	***180***	***143***	***123***	***1***	***157.9***	***56.2***	***56.0***	***151.5***	***1.0***	***69.4***	***18.7***	***0.4***	***2.2***	***0.82***	***22.8***	***2.6***
16	***131***	***117***	***101***	***1***	***166.8***	***13.8***	***63.9***	***72.1***	***4.6***	***28.8***	***47.5***	***0.4***	***5.1***	***0.77***	***61.7***	***6.5***
17	***133***	***142***	***122***	***0***	***93.1***	***15.0***	***60.4***	***132.2***	***4.0***	***29.2***	***26.1***	***0.2***	***2.8***	***0.84***	***31.2***	***3.3***
18	***177***	***187***	***161***	***1***	***124.3***	***13.3***	***65.9***	***137.2***	***4.9***	***28.8***	***35.3***	***0.3***	***3.8***	***0.85***	***41.6***	***4.4***
19	***310***	***135***	***116***	***2***	***91.8***	***16.7***	***102.2***	***192.7***	***6.1***	***40.7***	***18.5***	***0.1***	***2.0***	***0.80***	***23.2***	***2.4***
20	***230***	***112***	***96***	***1***	***249.4***	***16.8***	***88.4***	***157.4***	***5.3***	***37.6***	***54.2***	***0.4***	***5.8***	***0.77***	***70.1***	***7.4***
21	***223***	***193***	***167***	***1***	***167.0***	***13.6***	***63.5***	***125.7***	***4.7***	***28.6***	***47.8***	***0.4***	***5.1***	***0.86***	***55.8***	***5.9***

† analytical error; ‡ analytical error + 10% error (1 standard deviation on Durango aliquots)

Grains 11–21 are discarded because during the He analysis the ages of Durango aliquots were anomalously young.

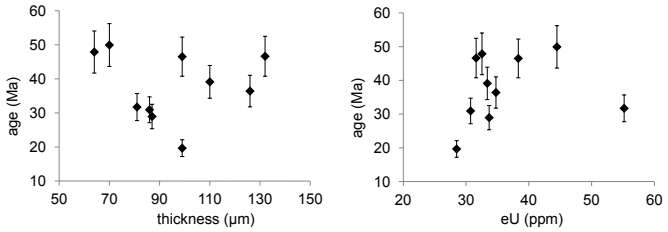

Figure B26: Apatite (U-Th-Sm)/He age versus (a) crystal thickness in μm, (b) [eU] in ppm.

Table B26: Single grain zircon (U-Th)/He data.

Aliquot No	L (um)	W (um)	T	He (ncc/g)	U (ppm)	Th (ppm)	eU (ppm)	age (Ma)	error † (Ma)	F_T	age corr (Ma)	error ‡ (Ma)
1	605	150	2	37568	586	765	766	393.2	3.6	0.88	445.8	66.9
2	527	130	2	36671	630	666	786	374.2	3.3	0.87	432.6	64.9
3	295	121	2	38054	909	697	1072	286.6	2.4	0.84	339.6	50.9
4	406	91	2	30858	1047	818	1239	202.6	1.7	0.81	248.9	37.3

† analytical error, ‡ 15% error

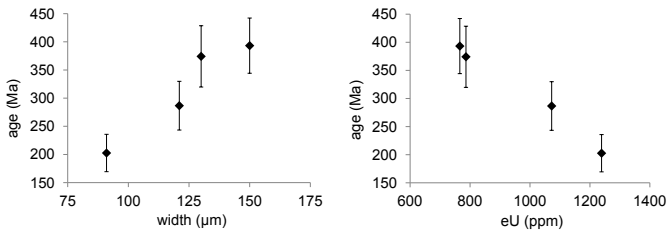

Figure B27: Zircon (U-Th)/He age versus (a) crystal thickness in μm, (b) [eU] in ppm.

Sample details

Grid reference:	NY 35005 33359	Unit:	Carrock
Elevation:	445 m	Lithology:	Gabbro
Region:	Lake District	Apatite quality:	5

Apatite fission track data

Slide 1 (underetched)		Slide 3	
Central age:	55.2 ± 5.1 Ma	Central age:	64.5 ± 6.2 Ma
Number of grains:	26	Number of grains:	20
Zeta (for IRMM glass):	313.7 ± 8.3	Zeta (for IRMM glass):	313.7 ± 8.3
ρ_D (interpolated):	1.73E+6	ρ_D (interpolated):	1.23E+6
N_D:	11903	N_D:	8873
N_s/N_i:	0.21 *pm* 0.08	N_s/N_i:	0.35 *pm* 0.11
χ^2:	15.6	χ^2:	9.2
P(%):	92.7	P(%):	96.9
MTL measured:	13.59 ± 0.68 μm	MTL measured:	13.79 ± 1.36 μm
MTL projected:	14.66 ± 0.28 μm	MTL projected:	14.90 ± 0.97 μm
No of track lengths:	4	No of track lengths:	16
Slide 2		MTL measured:	14.55 ± 1.49 μm
No of track lengths:	76	MTL projected:	15.39 ± 0.99 μm

Table B27: Single grain apatite fission track data; N_s—number of spontaneous tracks, N_i—number of induced tracks, ρ_D—tracks density on the dosimeter, ρ_s—spontaneous track density, ρ_i—induced track density.

No.	N_s	N_i	Area (cm^2)	DPar (μm)	ρ_s (tracks/cm^2)	ρ_i (tracks/cm^2)	ρ_s/ρ_i	Age (Ma)	1σ (Ma)
slide 1									
1	10	42	1.21E+08	1.53	8.26E-08	3.47E-07	0.24	64.3	22.7
2	9	28	1.21E+08	1.48	7.44E-08	2.31E-07	0.32	86.6	33.3
3	7	22	1.21E+08	1.63	5.79E-08	1.82E-07	0.32	85.8	37.3
4	8	28	1.21E+08	1.77	6.61E-08	2.31E-07	0.29	77.1	31.0
5	10	59	1.21E+08	1.74	8.26E-08	4.88E-07	0.17	45.8	15.7
6	5	24	1.21E+08	1.69	4.13E-08	1.98E-07	0.21	56.3	27.7
7	4	25	1.21E+08	1.76	3.31E-08	2.07E-07	0.16	43.3	23.3
8	7	30	9.68E+07	1.73	7.23E-08	3.10E-07	0.23	63.0	26.5
9	8	27	1.21E+08	1.59	6.61E-08	2.23E-07	0.30	79.9	32.2
10	6	24	1.21E+08	1.78	4.96E-08	1.98E-07	0.25	67.5	30.9
11	3	21	1.21E+08	1.58	2.48E-08	1.74E-07	0.14	38.6	23.9
12	7	17	1.21E+08	1.65	5.79E-08	1.40E-07	0.41	110.8	49.8
13	5	30	1.21E+08	1.73	4.13E-08	2.48E-07	0.17	45.1	21.8
14	4	25	8.71E+07	1.73	4.59E-08	2.87E-07	0.16	43.3	23.3
15	2	28	1.21E+08	1.65	1.65E-08	2.31E-07	0.07	19.4	14.2
16	2	16	1.09E+08	1.53	1.84E-08	1.47E-07	0.13	33.8	25.4
17	6	23	8.47E+07	1.61	7.08E-08	2.72E-07	0.26	70.4	32.3
18	4	33	1.21E+08	1.62	3.31E-08	2.73E-07	0.12	32.8	17.4
19	5	30	1.21E+08	1.55	4.13E-08	2.48E-07	0.17	45.1	21.8
20	11	50	1.21E+08	1.36	9.09E-08	4.13E-07	0.22	59.4	19.9
21	9	36	1.21E+08	1.48	7.44E-08	2.98E-07	0.25	67.5	25.2
22	7	42	9.68E+07	1.70	7.23E-08	4.34E-07	0.17	45.1	18.4
23	4	30	1.21E+08	1.53	3.31E-08	2.48E-07	0.13	36.1	19.2
24	2	22	9.68E+07	1.53	2.07E-08	2.27E-07	0.09	24.6	18.2
25	6	22	1.21E+08	1.67	4.96E-08	1.82E-07	0.27	73.6	34.0
26	5	30	1.09E+08	1.64	4.59E-08	2.75E-07	0.17	45.1	21.8
slide 3									
1	7	11	7.62E+07	2.36	9.18E-08	1.44E-07	0.64	121.6	58.9
2	6	18	1.21E+08	2.43	4.96E-08	1.49E-07	0.33	64.0	30.2
3	8	19	1.09E+08	2.30	7.35E-08	1.74E-07	0.42	80.7	34.1
4	3	13	9.68E+07	2.25	3.10E-08	1.34E-07	0.23	44.4	28.4
5	6	24	1.09E+08	2.26	5.51E-08	2.20E-07	0.25	48.1	22.0
6	10	28	1.21E+08	2.29	8.26E-08	2.31E-07	0.36	68.5	25.3
7	6	22	1.21E+08	2.35	4.96E-08	1.82E-07	0.27	52.4	24.2
8	6	17	1.21E+08	2.55	4.96E-08	1.40E-07	0.35	67.7	32.2
9	5	22	8.47E+07	2.33	5.90E-08	2.60E-07	0.23	43.7	21.7
10	6	26	1.21E+08	2.42	4.96E-08	2.15E-07	0.23	44.4	20.1
11	11	20	1.21E+08	2.41	9.09E-08	1.65E-07	0.55	105.2	39.6
12	6	14	1.21E+08	2.68	4.96E-08	1.16E-07	0.43	82.2	40.2
13	12	25	1.21E+08	2.45	9.92E-08	2.07E-07	0.48	91.9	32.4
14	11	33	1.09E+08	2.30	1.01E-07	3.03E-07	0.33	64.0	22.4
15	11	42	1.21E+08	2.44	9.09E-08	3.47E-07	0.26	50.3	17.1
16	7	21	1.21E+08	2.32	5.79E-08	1.74E-07	0.33	64.0	28.0
17	12	42	1.21E+08	2.52	9.92E-08	3.47E-07	0.29	54.9	18.0
18	5	20	9.68E+07	2.35	5.17E-08	2.07E-07	0.25	48.1	24.1
19	5	17	7.74E+07	2.40	6.46E-08	2.20E-07	0.29	56.5	28.8
20	14	33	1.21E+08	2.49	1.16E-07	2.73E-07	0.42	81.3	26.0

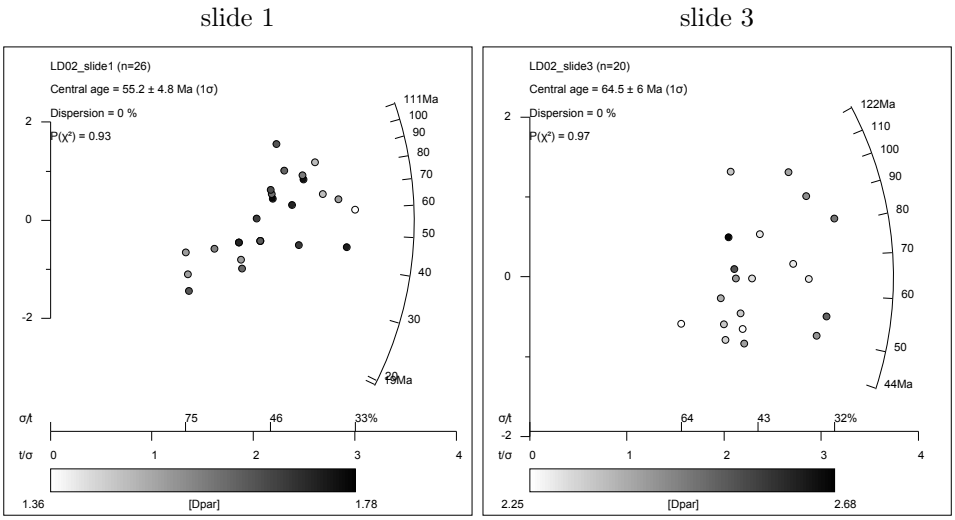

Figure B28: Radial plot of single grain fission track data, prepared using RadialPlotter (Vermeesch, 2009).

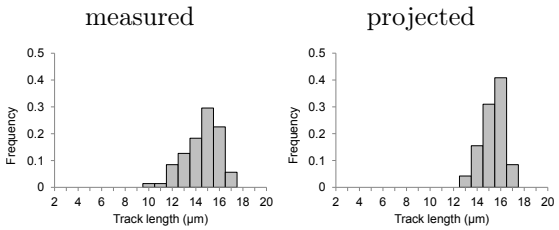

Figure B29: Histograms of track length distribution (slide2). Track length projection after Ketcham et al. (2007).

(U-Th)/He data

Table B29: Single grain apatite (U-Th-Sm)/He data; L, $W1$ and $W2$ crystal dimensions; age_c corrected age.

No.	L (μm)	W1 (μm)	W2 (μm)	T	He (μcc/g)	U (ppm)	Th (ppm)	Sm (ppm)	Th/U	eU (ppm)	age (Ma)	error†	error‡	F_T	age$_c$ (Ma)	error‡
1	225	91	72	0	12.7	3.0	4.4	198.0	1.5	4.1	24.3	1.6	4.1	0.75	32.4	4.9
2	297	135	116	0	15.2	2.3	3.8	168.4	1.6	3.2	36.3	1.1	4.8	0.83	43.5	5.5
3	199	149	153	0	19.4	3.0	5.0	142.9	1.7	4.2	36.7	1.1	4.7	0.86	42.9	5.3
4	139	148	136	1	27.7	4.4	8.3	167.2	1.9	6.4	34.8	1.1	4.5	0.82	42.4	5.3
5	185	122	100	0	14.1	1.3	5.9	117.9	4.4	2.7	40.6	1.7	5.8	0.81	50.4	6.8
6	350	260	156	1	32.3	3.0	8.8	175.1	2.9	5.1	49.7	0.9	5.9	0.88	56.4	6.6
7	155	70	61	1	26.5	3.1	12.0	96.8	3.9	5.9	36.2	7.4	11.0	0.66	55.2	12.9
8	160	184	131	0	19.7	1.7	6.8	122.1	4.1	3.3	47.3	1.3	6.0	0.86	54.8	6.8
9	208	143	111	1	29.1	2.4	10.6	134.6	4.4	4.9	47.6	2.1	6.9	0.81	58.6	8.0
10	274	112	130	0	22.9	1.9	7.2	231.2	3.7	3.6	48.1	2.2	7.1	0.81	59.6	8.2
11	140	124	97	0	37.0	4.6	17.8	190.2	3.8	8.8	33.6	1.6	5.0	0.81	41.7	5.8
12	82	131	112	0	18.0	1.9	9.3	189.9	4.8	4.1	34.0	0.8	4.2	0.82	41.4	4.9
13	135	83	66	1	19.3	0.6	8.6	127.2	13.9	2.6	56.5	1.7	7.4	0.68	83.6	10.1
14	271	236	112	0	22.3	2.0	7.8	230.2	3.9	3.8	44.7	0.7	5.2	0.87	51.6	5.9
15	***117***	***63***	***64***	***0***	***23.9***	***2.3***	***5.4***	***32.0***	***2.4***	***3.5***	***55.0***	***31.7***	***37.2***	***0.67***	***82.6***	***40.0***

† analytical error; ‡ analytical error + 10% error (1 standard deviation on Durango aliquots)

Grain 15 was discarded because of the very high analytical error

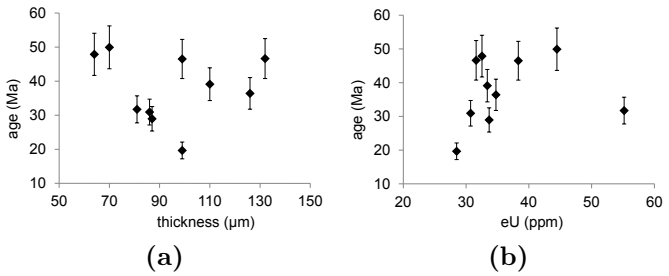

Figure B30: Apatite (U-Th-Sm)/He age versus (a) crystal thickness in μm, (b) [eU] in ppm.

Sample details

Grid reference:	NY 35125 33476	Unit:	Carrock
Elevation:	345 m	Lithology:	Granite
Region:	Lake District	Apatite quality:	0 (zircons only)

(U-Th)/He data

Table B30: Single grain apatite (U-Th)/He data; L, W and D crystal dimensions; age_c corrected age.

Aliquot No	L (um)	W (um)	T	He (ncc/g)	U (ppm)	Th (ppm)	eU (ppm)	age (Ma)	error † (Ma)	F_T	age corr (Ma)	error ‡ (Ma)
1	226	90	2	9030	175	225	228	319.3	2.9	0.79	403.1	60.5
2	180	71	2	12619	183	256	243	416.0	3.8	0.74	562.9	84.4
3	205	90	2	10498	185	229	239	352.9	3.2	0.79	448.4	67.3
4	160	67	2	9373	211	212	260	290.6	2.5	0.72	401.4	60.2

† analytical error, ‡ 15% error

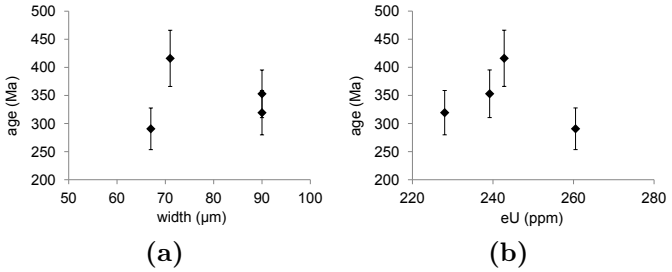

Figure B31: Zircon (U-Th)/He age versus (a) crystal thickness in μm, (b) [eU] in ppm.

Sample details

Grid reference:	NY 32874 24395	Unit:	Threlkeld
Elevation:	192 m	Lithology:	Microgranite
Region:	Lake District	Apatite quality:	1

Apatite fission track data

Central age:	74.9 ± 7.6 Ma	χ^2:	3.1
Number of grains:	11	P(%):	98.0
Zeta (for IRMM glass):	313.7 ± 8.3		
ρ_D (interpolated):	8.87E+5	No of track lengths:	0
N_D:	6478		
N_s/N_i:	0.57 ± 0.10		

Table B31: Single grain apatite fission track data; N_s—number of spontaneous tracks, N_i—number of induced tracks, ρ_D—tracks density on the dosimeter, ρ_s—spontaneous track density, ρ_i—induced track density.

No.	N_s	N_i	Area (cm^2)	DPar (μm)	ρ_s (tracks/cm^2)	ρ_i (tracks/cm^2)	ρ_s/ρ_i	Age (Ma)	1σ (Ma)
1	7	12	1.45E+07	-	4.82E-07	8.26E-07	0.58	80.7	38.4
2	49	96	7.26E+07	-	6.75E-07	1.32E-06	0.51	70.6	12.6
3	18	44	3.87E+07	-	4.65E-07	1.14E-06	0.41	56.7	15.9
4	15	27	3.39E+07	-	4.43E-07	7.97E-07	0.56	76.8	24.8
5	7	11	2.90E+07	-	2.41E-07	3.79E-07	0.64	87.9	42.6
6	11	15	3.03E+07	-	3.64E-07	4.96E-07	0.73	101.2	40.3
7	12	23	2.42E+07	-	4.96E-07	9.50E-07	0.52	72.2	25.8
8	6	14	2.18E+07	-	2.75E-07	6.43E-07	0.43	59.4	29.0
9	6	11	1.69E+07	-	3.54E-07	6.49E-07	0.55	75.4	38.4
10	20	28	3.03E+07	-	6.61E-07	9.26E-07	0.71	98.6	29.0
11	13	22	2.54E+07	-	5.12E-07	8.66E-07	0.59	81.7	28.7

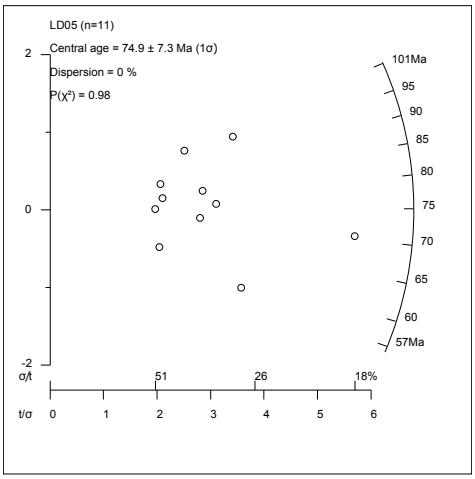

Figure B32: Radial plot of single grain fission track data, prepared using RadialPlotter (Vermeesch, 2009).

Sample details

Grid reference:	NY 29679 27869	Unit:	Skiddaw
Elevation:	347 m	Lithology:	Granite
Region:	Lake District	Apatite quality:	2

Apatite fission track data

Central age:	52.9 ± 4.0 Ma	χ^2:	26.3
Number of grains:	17	P(%):	5.0
Zeta (for IRMM glass):	313.7 ± 8.3		
ρ_D (interpolated):	8.83E+5	MTL measured:	14.16 ± 1.14 μm
N_D:	6478	MTL projected:	14.87 ± 0.83 μm
N_s/N_i:	0.41 ± 0.12	No of track lengths:	10

Table B32: Single grain apatite fission track data; N_s—number of spontaneous tracks, N_i—number of induced tracks, ρ_D—tracks density on the dosimeter, ρ_s—spontaneous track density, ρ_i—induced track density.

No.	N_s	N_i	Area (cm^2)	DPar (μm)	ρ_s (tracks/cm^2)	ρ_i (tracks/cm^2)	ρ_s/ρ_i	Age (Ma)	1σ (Ma)
1	9	30	2.90E+07	-	3.10E-07	1.03E-06	0.30	41.4	15.8
2	31	106	4.36E+07	-	7.12E-07	2.43E-06	0.29	40.4	8.3
3	57	142	9.68E+07	-	5.89E-07	1.47E-06	0.40	55.4	8.8
4	45	101	1.21E+08	-	3.72E-07	8.35E-07	0.45	61.4	11.2
5	7	32	3.03E+07	-	2.31E-07	1.06E-06	0.22	30.2	12.6
6	16	28	2.42E+07	-	6.61E-07	1.16E-06	0.57	78.7	24.8
7	24	48	3.63E+07	-	6.61E-07	1.32E-06	0.50	68.9	17.3
8	23	54	3.87E+07	-	5.94E-07	1.39E-06	0.43	58.7	14.7
9	9	18	9.68E+07	-	9.30E-08	1.86E-07	0.50	68.9	28.2
10	25	62	4.84E+07	-	5.17E-07	1.28E-06	0.40	55.6	13.3
11	26	82	4.24E+07	-	6.14E-07	1.94E-06	0.32	43.8	9.9
12	12	19	5.08E+07	-	2.36E-07	3.74E-07	0.63	86.9	32.1
13	32	65	6.53E+07	-	4.90E-07	9.95E-07	0.49	67.8	14.8
14	40	91	5.08E+07	-	7.87E-07	1.79E-06	0.44	60.6	11.6
15	45	94	7.74E+07	-	5.81E-07	1.21E-06	0.48	66.0	12.1
16	45	200	1.21E+08	-	3.72E-07	1.65E-06	0.23	31.1	5.2
17	34	111	1.21E+08	-	2.81E-07	9.17E-07	0.31	42.3	8.4

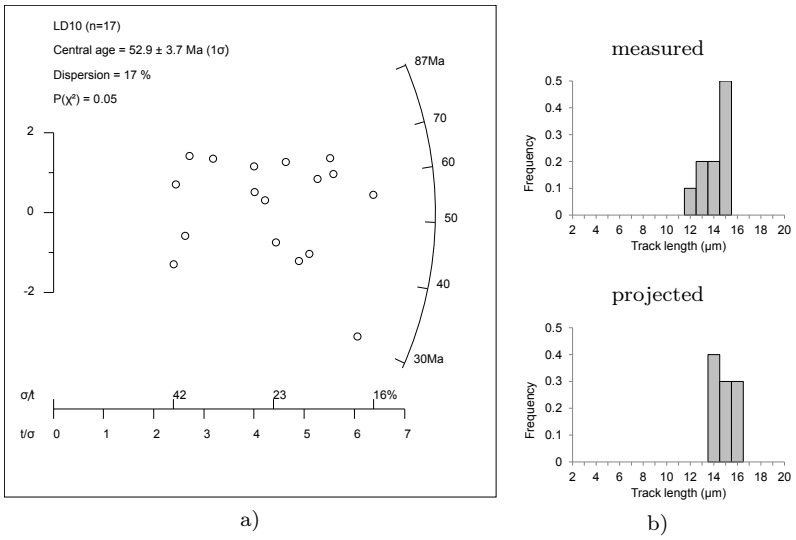

a) b)

Figure B33: (a) Radial plot of single grain fission track data, prepared using RadialPlotter (Vermeesch, 2009). (b) Histograms of track length distribution. Track length projection after Ketcham et al. (2007).

(U-Th)/He data

Table B33: Single grain zircon (U-Th)/He data.

Aliquot No	L (um)	W (um)	T	He (ncc/g)	U (ppm)	Th (ppm)	eU (ppm)	age (Ma)	error † (Ma)	F_T	age corr (Ma)	error ‡ (Ma)
1	420	104	2	19525	1120	532	1245	128.3	1.1	0.84	153.7	23.1
2	187	76	2	17708	1801	253	1861	78.3	0.7	0.76	102.6	15.4
3	265	78	2	27685	2001	953	2225	102.1	0.9	0.78	131.2	19.7

† analytical error, ‡ 15% error

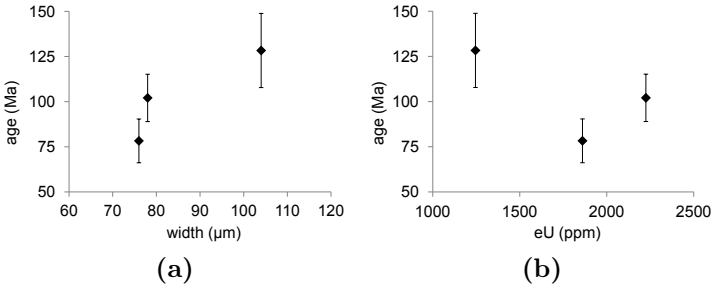

Figure B34: Zircon (U-Th)/He age versus (a) crystal thickness in μm, (b) [eU] in ppm.

Sample details

Grid reference:	NY 49456 15212	Unit:	Haweswater
Elevation:	258 m	Lithology:	Gabbro
Region:	Lake District	Apatite quality:	1

Apatite fission track data

Central age:	35.9 ± 8.5 Ma	χ^2:	4.2
Number of grains:	7	P(%):	65.2
Zeta (for IRMM glass):	313.7 ± 8.3		
ρ_D (interpolated):	8.87E+5	No of track lengths:	0
N_D:	6478		
N_s/N_i:	0.30 ± 0.15		

Table B34: Single grain apatite fission track data; N_s—number of spontaneous tracks, N_i—number of induced tracks, ρ_D—tracks density on the dosimeter, ρ_s—spontaneous track density, ρ_i—induced track density.

No.	N_s	N_i	Area (cm^2)	DPar (μm)	ρ_s (tracks/cm^2)	ρ_i (tracks/cm^2)	ρ_s/ρ_i	Age (Ma)	1σ (Ma)
1	5	9	2.54E+07	-	1.97E-07	3.54E-07	0.56	76.8	42.9
2	4	10	2.18E+07	-	1.84E-07	4.59E-07	0.40	55.4	32.8
3	4	18	5.08E+07	-	7.87E-08	3.54E-07	0.22	30.8	17.1
4	2	14	3.63E+07	-	5.51E-08	3.86E-07	0.14	19.8	15.0
5	3	15	3.27E+07	-	9.18E-08	4.59E-07	0.20	27.8	17.6
6	3	18	3.87E+07	-	7.75E-08	4.65E-07	0.17	23.1	14.4

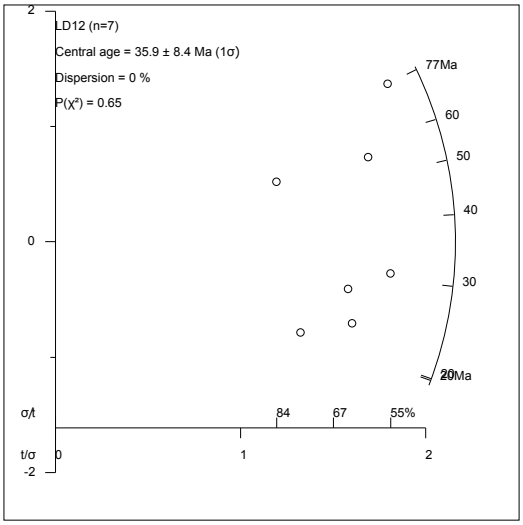

Figure B35: Radial plot of single grain fission track data, prepared using RadialPlotter (Vermeesch, 2009).

(U-Th)/He data

Table B35: Single grain apatite (U-Th-Sm)/He data; L, $W1$ and $W2$ crystal dimensions; age_c corrected age.

No.	L (μm)	W1 (μm)	W2 (μm)	T	He (μcc/g)	U (ppm)	Th (ppm)	Sm (ppm)	Th/U	eU (ppm)	age (Ma)	error†	error‡	F_T	age$_c$ (Ma)	error‡
1	126	84	65	2	47.7	4.9	12.7	145.1	2.6	7.9	48.8	2.4	7.3	0.64	76.1	10.0
2	113	88	69	0	37.9	4.3	11.7	140.6	2.7	7.1	42.9	2.3	6.6	0.74	58.4	8.1
3	147	82	49	1	45.4	6.0	12.4	202.3	2.1	8.9	41.0	2.1	6.2	0.66	62.3	8.3
4	113	94	65	2	44.8	5.4	12.8	158.5	2.4	8.4	43.0	5.9	10.2	0.63	67.8	12.7
M1	100	67	58	-	52.9	5.8	15.8	272.0	2.7	9.5	44.1	2.0	6.4	0.63	70.5	9.1

† analytical error; ‡ analytical error + 10% error (1 standard deviation on Durango aliquots)

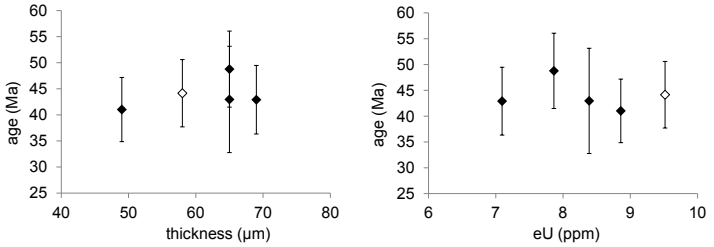

(a) **(b)**

Figure B36: Apatite (U-Th-Sm)/He age versus (a) crystal thickness in μm, (b) [eU] in ppm.

Sample details

Grid reference:	NX 96725 17881	Unit:	Whitehaven Sandstone Formation
Elevation:	10 m	Lithology:	Sandstone
Region:	Lake District	Deposition age:	Bolsovian (Upper Carboniferous)
		Apatite quality:	3

Apatite fission track data

Central age:	48.5 ± 3.1 Ma	χ^2:	18.5
Number of grains:	16	P(%):	23.9
Zeta (for IRMM glass):	313.7 ± 8.3		
ρ_D (interpolated):	8.71E+5	No of track lengths:	0
N_D:	6478		
N_s/N_i:	0.37 ± 0.11		

Table B36: Single grain apatite fission track data; N_s—number of spontaneous tracks, N_i—number of induced tracks, ρ_D—tracks density on the dosimeter, ρ_s—spontaneous track density, ρ_i—induced track density.

No.	N_s	N_i	Area (cm^2)	DPar (μm)	ρ_s (tracks/cm^2)	ρ_i (tracks/cm^2)	ρ_s/ρ_i	Age (Ma)	1σ (Ma)
1	87	227	5.93E+07	4.74	1.47E-06	3.83E-06	0.38	52.1	6.7
2	26	48	4.84E+07	3.82	5.37E-07	9.92E-07	0.54	73.6	18.0
3	18	63	3.87E+07	3.90	4.65E-07	1.63E-06	0.29	38.9	10.5
4	94	247	5.81E+07	4.06	1.62E-06	4.25E-06	0.38	51.8	6.5
5	36	70	6.78E+07	3.68	5.31E-07	1.03E-06	0.51	69.9	14.5
6	12	23	2.42E+07	4.32	4.96E-07	9.50E-07	0.52	70.9	25.3
7	24	74	4.84E+07	3.76	4.96E-07	1.53E-06	0.32	44.2	10.5
8	10	42	4.36E+07	3.21	2.30E-07	9.64E-07	0.24	32.4	11.5
9	23	91	5.93E+07	3.65	3.88E-07	1.53E-06	0.25	34.4	8.1
10	30	87	8.47E+07	3.48	3.54E-07	1.03E-06	0.34	46.9	10.0
11	18	74	4.24E+07	3.03	4.25E-07	1.75E-06	0.24	33.1	8.8
12	12	24	2.54E+07	3.65	4.72E-07	9.45E-07	0.50	67.9	24.1
13	12	45	4.84E+07	3.52	2.48E-07	9.30E-07	0.27	36.3	11.9
14	28	102	4.36E+07	3.46	6.43E-07	2.34E-06	0.27	37.4	8.1
15	16	39	2.90E+07	4.15	5.51E-07	1.34E-06	0.41	55.8	16.6
16	13	29	4.24E+07	3.99	3.07E-07	6.85E-07	0.45	61.0	20.4

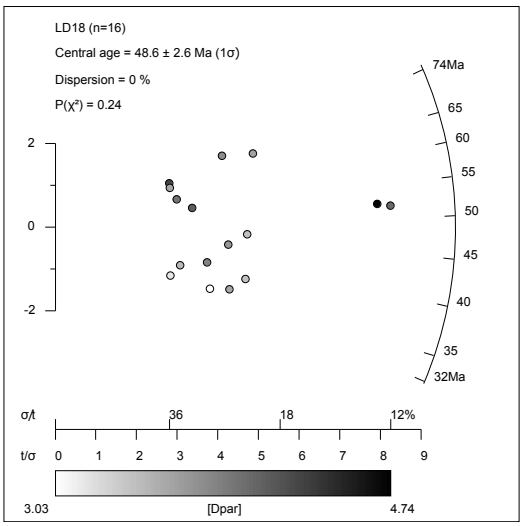

Figure B37: Radial plot of single grain fission track data, prepared using RadialPlotter (Vermeesch, 2009).

(U-Th)/He data

Table B37: Single grain apatite (U-Th-Sm)/He data; L, $W1$ and $W2$ crystal dimensions; age_c corrected age.

No.	L (μm)	W1 (μm)	W2 (μm)	T	He (μcc/g)	U (ppm)	Th (ppm)	Sm (ppm)	Th/U	eU (ppm)	age (Ma)	error†	error‡	F_T	age_c (Ma)	error‡
1	230	72	68	0	53.5	7.4	7.2	238.0	1.0	9.1	46.8	1.8	6.5	0.71	66.1	8.4
2	220	44	40	2	267.1	27.4	110.0	241.5	4.0	53.3	41.0	1.2	5.3	0.49	84.0	9.6
3	89	85	83	0	368.3	18.1	115.3	203.0	6.4	45.2	66.5	1.7	8.4	0.74	90.4	10.8
4	170	107	95	1	255.5	16.2	18.9	480.6	1.2	20.6	41.4	1.1	5.3	0.77	53.7	6.5
5	124	105	100	1	252.9	40.2	54.0	159.9	1.3	52.9	39.2	0.9	4.9	0.76	51.4	6.1
6	175	83	69	1	454.3	39.9	243.7	36.8	6.1	97.2	38.4	0.7	4.5	0.70	55.2	6.2

† analytical error; ‡ analytical error + 10% error (1 standard deviation on Durango aliquots)

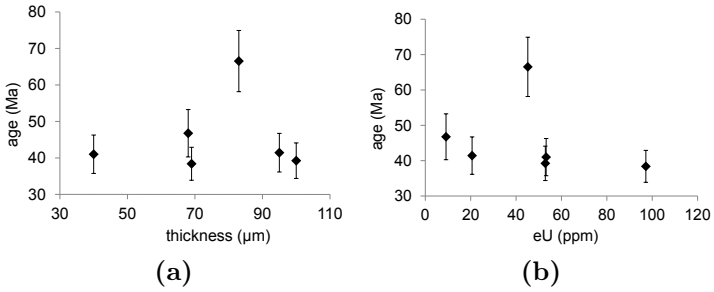

Figure B38: Apatite (U-Th-Sm)/He age versus (a) crystal thickness in μm, (b) [eU] in ppm.

Sample details

Region:	Southern Uplands	Unit:	Crawfordjohn
Grid reference:	NS 91901 23753	Lithology:	Essexite
Elevation:	310 m	Apatite quality:	5

Apatite fission track data

Central age:	215.0 ± 14.3 Ma	χ^2:	8.4
Number of grains:	24	P(%):	99.8
Zeta (for IRMM glass):	313.7 ± 8.3		
ρ_D (interpolated):	1.25+6	MTL measured:	11.20 ± 1.72 μm
N_D:	8874	MTL projected:	13.14 ± 1.09 μm
N_s/N_i:	1.15 ± 0.21	No of track lengths:	101

Table B38: Single grain apatite fission track data; N_s—number of spontaneous tracks, N_i—number of induced tracks, ρ_D—tracks density on the dosimeter, ρ_s—spontaneous track density, ρ_i—induced track density.

No.	N_s	N_i	Area (cm^2)	DPar (μm)	ρ_s ($tracks/cm^2$)	ρ_i ($tracks/cm^2$)	ρ_s/ρ_i	Age (Ma)	1σ (Ma)
1	10	10	3.03E+07	1.74	3.31E-07	3.31E-07	1.00	193.1	86.6
2	28	20	5.08E+07	1.84	5.51E-07	3.94E-07	1.40	268.8	79.1
3	19	18	4.84E+07	2.00	3.93E-07	3.72E-07	1.06	203.7	67.3
4	28	25	6.05E+07	1.89	4.63E-07	4.13E-07	1.12	215.9	59.7
5	18	11	3.87E+07	1.82	4.65E-07	2.84E-07	1.64	313.1	120.2
6	24	17	4.84E+07	1.80	4.96E-07	3.51E-07	1.41	271.0	86.3
7	19	14	3.63E+07	1.88	5.23E-07	3.86E-07	1.36	260.7	92.1
8	28	27	8.47E+07	1.88	3.31E-07	3.19E-07	1.04	200.2	54.3
9	31	28	5.93E+07	1.64	5.23E-07	4.72E-07	1.11	213.5	56.0
10	34	39	7.26E+07	1.91	4.68E-07	5.37E-07	0.87	168.7	39.9
11	25	18	4.84E+07	1.68	5.17E-07	3.72E-07	1.39	266.7	82.8
12	19	18	5.08E+07	1.82	3.74E-07	3.54E-07	1.06	203.7	67.3
13	26	33	6.78E+07	1.75	3.84E-07	4.87E-07	0.79	152.7	40.3
14	23	28	5.08E+07	1.92	4.53E-07	5.51E-07	0.82	159.1	45.0
15	29	23	4.24E+07	1.85	6.85E-07	5.43E-07	1.26	242.6	68.1
16	29	26	5.08E+07	1.82	5.71E-07	5.12E-07	1.12	215.1	58.4
17	21	15	6.05E+07	1.72	3.47E-07	2.48E-07	1.40	268.8	91.2
18	32	28	7.26E+07	1.82	4.41E-07	3.86E-07	1.14	220.3	57.3
19	22	20	5.45E+07	1.87	4.04E-07	3.67E-07	1.10	212.1	65.8
20	28	23	4.84E+07	1.83	5.79E-07	4.75E-07	1.22	234.4	66.3
21	22	22	6.05E+07	1.86	3.64E-07	3.64E-07	1.00	193.1	58.5
22	16	15	4.84E+07	1.81	3.31E-07	3.10E-07	1.07	205.8	74.2
23	30	24	4.36E+07	1.77	6.89E-07	5.51E-07	1.25	240.5	66.2
24	21	20	4.36E+07	1.79	4.82E-07	4.59E-07	1.05	202.6	63.6

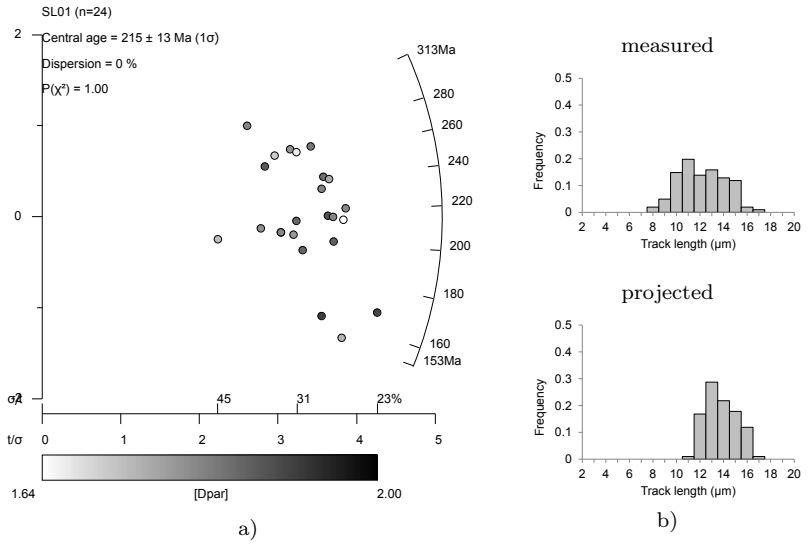

Figure B39: (a) Radial plot of single grain fission track data, prepared using RadialPlotter (Vermeesch, 2009). (b) Histograms of track length distribution. Track length projection after Ketcham et al. (2007).

(U-Th)/He data

Table B39: Single grain apatite (U-Th-Sm)/He data; L, $W1$ and $W2$ crystal dimensions; age_c corrected age.

No.	L (μm)	W1 (μm)	W2 (μm)	T	He (μcc/g)	U (ppm)	Th (ppm)	Sm (ppm)	Th/U	eU (ppm)	age (Ma)	error†	error‡	F_T	age$_c$ (Ma)	error‡
1	155	80	63	0	237.5	10.4	83.1	145.0	8.0	29.9	64.7	9.4	15.8	0.70	92.5	18.6
2	167	113	81	0	194.4	5.7	57.9	112.6	10.2	19.3	82.1	2.2	10.4	0.77	106.2	12.9
3	218	60	51	1	123.8	6.7	82.5	84.8	12.3	26.1	38.8	1.6	5.4	0.61	63.5	7.9
4	162	100	81	0	109.4	5.3	37.2	93.8	7.0	14.1	63.3	11.8	18.1	0.76	83.3	20.1
5	156	70	60	0	52.0	4.6	30.5	53.2	6.6	11.8	36.0	27.9	31.5	0.67	53.6	33.3

† analytical error; ‡ analytical error + 10% error (1 standard deviation on Durango aliquots)

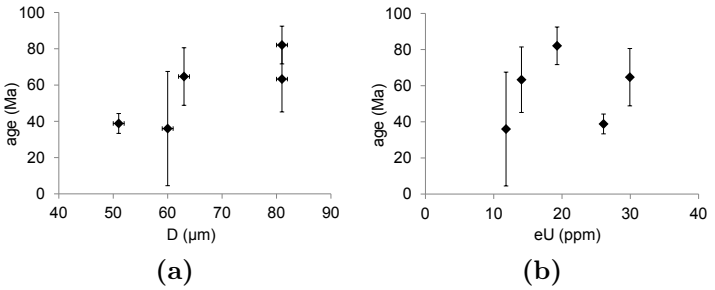

Figure B40: Apatite (U-Th-Sm)/He age versus (a) crystal thickness in μm, (b) [eU] in ppm.

Sample details

Region:	northern Wales	Unit:	-
Grid reference:	SJ 19114 34708	Lithology:	Diorite
Elevation:	168 m	Apatite quality:	2

Apatite fission track data

Central age:	172.1 ± 28.6 Ma	χ^2:	4.4
Number of grains:	19	P(%):	99.9
Zeta (for IRMM glass):	313.7 ± 8.3		
ρ_D (interpolated):	8.11E+5	No of track lengths:	0
N_D:	6478		
N_s/N_i:	1.36 ± 0.46		

Table B40: Single grain apatite fission track data; N_s—number of spontaneous tracks, N_i—number of induced tracks, ρ_D—tracks density on the dosimeter, ρ_s—spontaneous track density, ρ_i—induced track density.

No.	N_s	N_i	Area (cm^2)	DPar (μm)	ρ_s (tracks/cm^2)	ρ_i (tracks/cm^2)	ρ_s/ρ_i	Age (Ma)	1σ (Ma)
1	5	4	7.26E+07	-	6.89E-08	5.51E-08	1.25	176.2	118.3
2	6	5	2.90E+07	-	2.07E-07	1.72E-07	1.20	169.2	102.6
3	10	8	4.36E+07	-	2.30E-07	1.84E-07	1.25	176.2	83.7
4	4	6	3.63E+07	-	1.10E-07	1.65E-07	0.67	94.6	61.1
5	1	1	3.39E+07	-	2.95E-08	2.95E-08	1.00	141.3	199.9
6	2	3	2.90E+07	-	6.89E-08	1.03E-07	0.67	94.6	86.4
7	2	2	2.42E+07	-	8.26E-08	8.26E-08	1.00	141.3	141.4
8	4	2	3.87E+07	-	1.03E-07	5.17E-08	2.00	279.6	242.3
9	6	3	6.05E+07	-	9.92E-08	4.96E-08	2.00	279.6	197.9
10	6	3	3.27E+07	-	1.84E-07	9.18E-08	2.00	279.6	197.9
11	4	2	2.90E+07	-	1.38E-07	6.89E-08	2.00	279.6	242.3
12	5	3	3.39E+07	-	1.48E-07	8.85E-08	1.67	233.9	170.9
13	5	6	4.84E+07	-	1.03E-07	1.24E-07	0.83	118.0	71.5
14	3	3	5.45E+07	-	5.51E-08	5.51E-08	1.00	141.3	115.5
15	7	5	3.63E+07	-	1.93E-07	1.38E-07	1.40	197.0	115.5
16	4	4	4.84E+07	-	8.26E-08	8.26E-08	1.00	141.3	100.0
17	3	2	2.90E+07	-	1.03E-07	6.89E-08	1.50	210.8	192.6
18	3	2	2.54E+07	-	1.18E-07	7.87E-08	1.50	210.8	192.6
19	3	4	3.87E+07	-	7.75E-08	1.03E-07	0.75	106.3	81.2

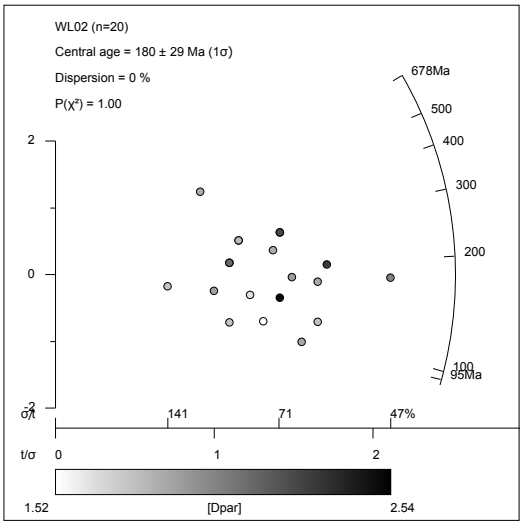

Figure B41: Radial plot of single grain fission track data, prepared using RadialPlotter (Vermeesch, 2009).

(U-Th)/He data

Table B41: Single grain apatite (U-Th-Sm)/He data; L, $W1$ and $W2$ crystal dimensions; age_c corrected age.

No.	L (μm)	W1 (μm)	W2 (μm)	T	He (μcc/g)	U (ppm)	Th (ppm)	Sm (ppm)	Th/U	eU (ppm)	age (Ma)	error†	error‡	F_T	age$_c$ (Ma)	error‡
1	135	53	45	0	99.1	2.9	25.6	1325.3	8.9	8.9	77.2	5.8	13.5	0.57	135.9	19.4
2	130	64	55	0	53.2	1.1	19.7	366.3	17.2	5.8	70.1	6.0	13.0	0.63	111.1	17.1
3	***115***	***60***	***54***	***0***	***207.7***	***3.6***	***21.8***	***1652.1***	***6.1***	***8.7***	***158.1***	***9.8***	***25.6***	***0.63***	***252.6***	***35.1***
4	***108***	***70***	***60***	***0***	***66.3***	***0.4***	***3.8***	***336.1***	***10.3***	***1.3***	***321.4***	***109.8***	***142.0***	***0.67***	***482.6***	***158.1***
M1	118	64	55	-	23.0	1.0	8.5	497.1	8.1	3.0	51.5	0.6	5.8	0.65	79.6	8.6

† analytical error; ‡ analytical error + 10% error (1 standard deviation on Durango aliquots)

Grains 4 and 5 were excluded because they are extreme outliers (old).

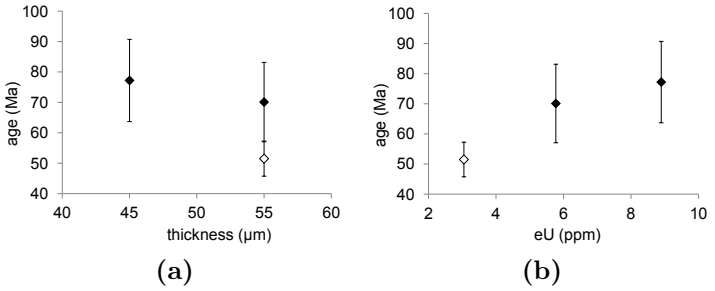

Figure B42: Apatite (U-Th-Sm)/He age versus (a) crystal thickness in μm, (b) [eU] in ppm.

Sample details

Region:	Llŷn	Unit:	Granfor Inner
Grid reference:	SH 36559 45979	Lithology:	Tonalite (pink)
Elevation:	219 m	Apatite quality:	3

Apatite fission track data

Central age:	187.0 ± 13.7 Ma	χ^2:	11.1
Number of grains:	21	P(%):	94.4
Zeta (for IRMM glass):	313.7 ± 8.3		
ρ_D (interpolated):	1.26E+6	No of track lengths:	0
N_D:	8874		
N_s/N_i:	1.03 ± 0.30		

Table B42: Single grain apatite fission track data; N_s—number of spontaneous tracks, N_i—number of induced tracks, ρ_D—tracks density on the dosimeter, ρ_s—spontaneous track density, ρ_i—induced track density.

No.	N_s	N_i	Area (cm^2)	DPar (μm)	ρ_s (tracks/cm^2)	ρ_i (tracks/cm^2)	ρ_s/ρ_i	Age (Ma)	1σ (Ma)
1	22	31	3.39E+07	1.61	6.49E-07	9.15E-07	0.71	138.8	38.9
2	20	26	3.63E+07	1.47	5.51E-07	7.16E-07	0.77	150.3	44.9
3	21	14	2.54E+07	1.57	8.26E-07	5.51E-07	1.50	289.8	100.3
4	13	16	2.42E+07	1.42	5.37E-07	6.61E-07	0.81	158.6	59.4
5	23	26	4.36E+07	1.89	5.28E-07	5.97E-07	0.88	172.5	49.6
6	29	20	2.54E+07	1.56	1.14E-06	7.87E-07	1.45	280.4	81.9
7	9	10	2.42E+07	1.71	3.72E-07	4.13E-07	0.90	175.5	80.8
8	21	24	3.63E+07	1.68	5.79E-07	6.61E-07	0.88	170.6	51.2
9	15	10	4.84E+07	1.56	3.10E-07	2.07E-07	1.50	289.8	118.6
10	24	20	3.63E+07	1.66	6.61E-07	5.51E-07	1.20	232.9	70.8
11	7	7	3.63E+07	1.66	1.93E-07	1.93E-07	1.00	194.7	104.2
12	18	21	4.36E+07	1.47	4.13E-07	4.82E-07	0.86	167.2	53.9
13	34	36	6.05E+07	1.77	5.62E-07	5.95E-07	0.94	184.0	44.3
14	26	34	2.90E+07	1.64	8.95E-07	1.17E-06	0.76	149.4	39.2
15	47	49	4.84E+07	1.62	9.71E-07	1.01E-06	0.96	186.8	38.5
16	25	23	4.24E+07	1.65	5.90E-07	5.43E-07	1.09	211.3	61.4
17	18	24	3.39E+07	1.65	5.31E-07	7.08E-07	0.75	146.5	45.9
18	24	26	4.84E+07	1.53	4.96E-07	5.37E-07	0.92	179.9	51.2
19	16	17	4.36E+07	1.60	3.67E-07	3.90E-07	0.94	183.4	64.1
20	8	9	2.42E+07	1.59	3.31E-07	3.72E-07	0.89	173.3	84.4
21	11	6	3.63E+07	1.47	3.03E-07	1.65E-07	1.83	352.5	179.2

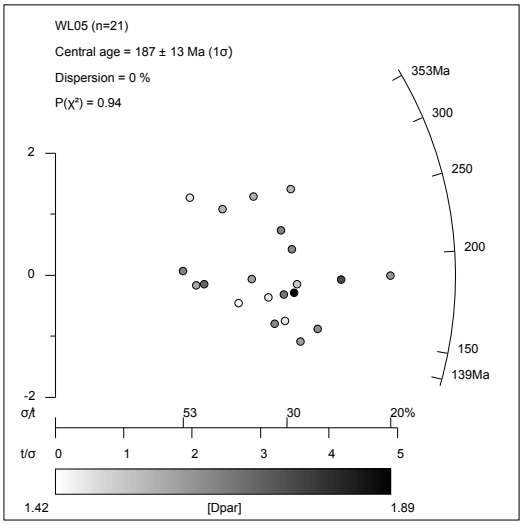

Figure B43: Radial plot of single grain fission track data, prepared using RadialPlotter (Vermeesch, 2009).

(U-Th)/He data

Table B43: Single grain apatite (U-Th-Sm)/He data; L, $W1$ and $W2$ crystal dimensions; age_c corrected age.

No.	L (μm)	W1 (μm)	W2 (μm)	T	He (μcc/g)	U (ppm)	Th (ppm)	Sm (ppm)	Th/U	eU (ppm)	age (Ma)	error†	error‡	F_T	age$_c$ (Ma)	error‡
1	120	115	115	1	100.0	6.1	22.8	389.9	3.7	11.5	68.6	1.6	8.5	0.78	88.5	10.5
2	169	89	89	1	84.6	4.1	19.4	425.0	4.7	8.7	75.6	1.8	9.4	0.73	103.6	12.2
3	138	93	80	1	61.3	3.7	16.7	378.9	4.5	7.7	61.9	2.2	8.4	0.72	85.5	10.8
4	125	77	77	1	111.0	5.7	29.2	483.8	5.1	12.6	69.2	2.2	9.1	0.69	100.9	12.3
M1	103	81	70	-	95.9	6.1	23.9	484.8	3.9	11.7	64.1	1.6	8.0	0.71	90.6	10.6
M2	106	55	47	-	72.4	5.2	22.1	429.0	4.2	10.4	54.3	2.4	7.8	0.58	94.0	11.8
M3	153	69	59	-	71.9	5.1	15.4	355.6	3.0	8.7	64.7	2.0	8.5	0.67	96.4	11.6

† analytical error; ‡ analytical error + 10% error (1 standard deviation on Durango aliquots)

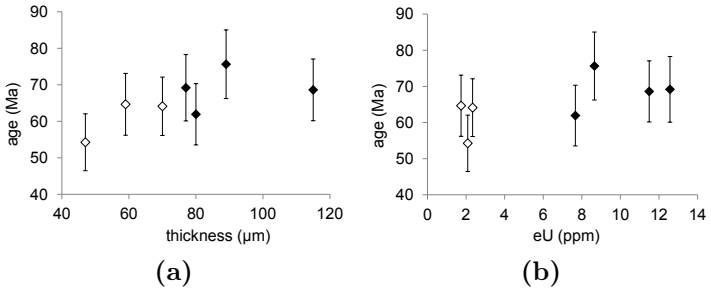

Figure B44: Apatite (U-Th-Sm)/He age versus (a) crystal thickness in μm, (b) [eU] in ppm.

Sample details

Region:	Llŷn	Unit:	Granfor Inner
Grid reference:	SH 36559 45980	Lithology:	Tonalite (grey)
Elevation:	220 m	Apatite quality:	3

Apatite fission track data

Central age:	195.5 ± 20.1 Ma	χ^2:	32.3
Number of grains:	20	P(%):	2.9
Zeta (for IRMM glass):	313.7 ± 8.3		
ρ_D (interpolated):	9.03E+5	No of track lengths:	0
N_D:	6478		
N_s/N_i:	1.50 ± 0.67		

Table B44: Single grain apatite fission track data; N_s—number of spontaneous tracks, N_i—number of induced tracks, ρ_D—tracks density on the dosimeter, ρ_s—spontaneous track density, ρ_i—induced track density.

No.	N_s	N_i	Area (cm^2)	DPar (μm)	ρ_s (tracks/cm^2)	ρ_i (tracks/cm^2)	ρ_s/ρ_i	Age (Ma)	1σ (Ma)
1	28	32	4.84E+07	1.95	5.79E-07	6.61E-07	0.88	122.8	32.0
2	33	25	7.26E+07	1.86	4.55E-07	3.44E-07	1.32	184.3	49.2
3	12	7	3.63E+07	1.77	3.31E-07	1.93E-07	1.71	238.3	113.6
4	9	16	2.90E+07	1.94	3.10E-07	5.51E-07	0.56	79.2	33.1
5	18	20	4.84E+07	1.81	3.72E-07	4.13E-07	0.90	126.2	41.2
6	35	15	4.84E+07	1.84	7.23E-07	3.10E-07	2.33	322.3	99.9
7	24	8	3.39E+07	1.99	7.08E-07	2.36E-07	3.00	411.5	168.4
8	36	17	6.05E+07	1.90	5.95E-07	2.81E-07	2.12	293.2	86.7
9	24	16	3.63E+07	1.96	6.61E-07	4.41E-07	1.50	209.0	67.7
10	14	9	2.42E+07	1.85	5.79E-07	3.72E-07	1.56	216.6	92.8
11	20	16	3.63E+07	1.79	5.51E-07	4.41E-07	1.25	174.7	58.8
12	28	12	4.36E+07	1.86	6.43E-07	2.75E-07	2.33	322.3	111.6
13	6	9	3.27E+07	1.87	1.84E-07	2.75E-07	0.67	93.7	49.5
14	4	4	2.18E+07	1.85	1.84E-07	1.84E-07	1.00	140.1	99.2
15	18	12	2.90E+07	1.84	6.20E-07	4.13E-07	1.50	209.0	78.1
16	39	17	5.08E+07	1.87	7.67E-07	3.35E-07	2.29	317.0	92.6
17	31	15	3.63E+07	2.06	8.54E-07	4.13E-07	2.07	286.3	90.4
18	14	18	3.63E+07	1.79	3.86E-07	4.96E-07	0.78	109.2	39.1
19	13	13	4.24E+07	1.68	3.07E-07	3.07E-07	1.00	140.1	55.1
20	16	14	2.54E+07	1.78	6.30E-07	5.51E-07	1.14	159.9	58.7

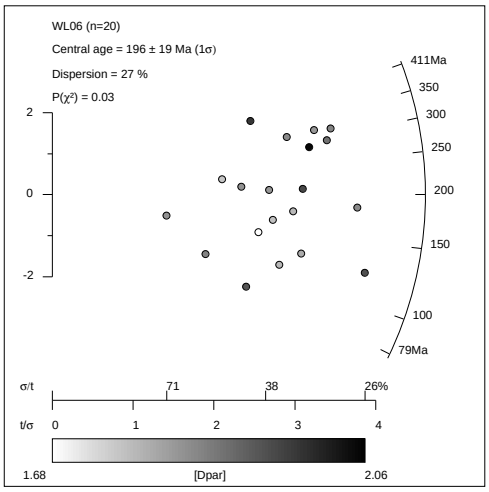

Figure B45: Radial plot of single grain fission track data, prepared using RadialPlotter (Vermeesch, 2009).

(U-Th)/He data

Table B45: Single grain apatite (U-Th-Sm)/He data; L, $W1$ and $W2$ crystal dimensions; age_c corrected age.

No.	L (μm)	W1 (μm)	W2 (μm)	T	He (μcc/g)	U (ppm)	Th (ppm)	Sm (ppm)	Th/U	eU (ppm)	age (Ma)	error†	error‡	F_T	age$_c$ (Ma)	error‡
1	154	75	64	1	69.7	8.6	8.8	450.6	1.0	10.7	51.0	2.2	7.3	0.69	74.2	9.6
2	92	96	60	1	66.0	7.4	5.4	428.6	0.7	8.7	59.1	4.1	10.0	0.69	85.2	12.6
3	112	107	86	1	60.4	5.8	6.3	365.9	1.1	7.3	64.1	3.0	9.4	0.75	85.1	11.5
4	161	85	84	1	48.5	7.6	8.0	394.4	1.1	9.4	40.3	1.5	5.6	0.73	55.3	7.1
5	127	90	84	1	58.5	6.4	6.9	355.0	1.1	8.0	56.8	2.8	8.5	0.73	77.9	10.6
M1	*113*	*81*	*70*	-	*77.8*	*4.1*	*16.2*	*417.9*	*3.9*	*8.0*	*75.4*	*2.6*	*10.2*	*0.72*	*104.6*	*13.1*
M2	*108*	*102*	*88*	-	*84.3*	*4.2*	*10.4*	*345.5*	*2.5*	*6.6*	*97.8*	*3.4*	*13.1*	*0.77*	*127.3*	*16.1*
M3	*117*	*71*	*61*	-	*98.7*	*4.8*	*6.7*	*350.4*	*1.4*	*6.3*	*119.5*	*6.0*	*17.9*	*0.67*	*177.3*	*23.7*

† analytical error; ‡ analytical error + 10% error (1 standard deviation on Durango aliquots)

Aliquots M1, M2 and M3 were discarded due to the ICP-MS instability.

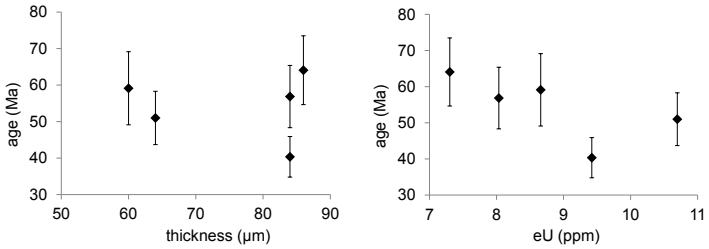

(a) **(b)**

Figure B46: Apatite (U-Th-Sm)/He age versus (a) crystal thickness in μm, (b) [eU] in ppm.

Sample details

Region:	Llŷn	Unit:	Penrhyn Bodeilas
Grid reference:	SH 31833 42093	Lithology:	Tonalite
Elevation:	26 m	Apatite quality:	5

Apatite fission track data

Central age:	188.4 ± 14.2 Ma	χ^2:	4.4
Number of grains:	19	P(%):	100.0
Zeta (for IRMM glass):	313.7 ± 8.3		
ρ_D (interpolated):		MTL measured:	12.89 ± 1.74 μm
8.99E+5		MTL projected:	13.82 ± 1.41 μm
N_D:	6478	No of track lengths:	100
N_s/N_i:	1.41 ± 0.24		

Table B46: Single grain apatite fission track data; N_s—number of spontaneous tracks, N_i—number of induced tracks, ρ_D—tracks density on the dosimeter, ρ_s—spontaneous track density, ρ_i—induced track density.

No.	N_s	N_i	Area (cm^2)	DPar (μm)	ρ_s ($tracks/cm^2$)	ρ_i ($tracks/cm^2$)	ρ_s/ρ_i	Age (Ma)	1σ (Ma)
1	29	14	6.05E+07	1.92	4.79E-07	2.31E-07	2.07	285.7	93.3
2	29	21	7.26E+07	2.12	3.99E-07	2.89E-07	1.38	191.8	55.3
3	23	17	7.74E+07	1.78	2.97E-07	2.20E-07	1.35	188.0	60.4
4	35	27	1.09E+08	1.86	3.21E-07	2.48E-07	1.30	180.2	46.5
5	23	16	7.74E+07	1.54	2.97E-07	2.07E-07	1.44	199.6	65.2
6	31	27	7.62E+07	2.01	4.07E-07	3.54E-07	1.15	159.9	42.4
7	22	18	8.71E+07	2.05	2.53E-07	2.07E-07	1.22	170.1	54.3
8	20	12	4.36E+07	2.07	4.59E-07	2.75E-07	1.67	230.8	84.6
9	18	13	5.81E+07	2.01	3.10E-07	2.24E-07	1.38	192.3	70.2
10	25	16	6.53E+07	1.95	3.83E-07	2.45E-07	1.56	216.6	69.6
11	30	25	1.21E+08	1.87	2.48E-07	2.07E-07	1.20	167.0	45.5
12	28	22	8.47E+07	2.20	3.31E-07	2.60E-07	1.27	177.0	50.7
13	28	27	8.71E+07	1.94	3.21E-07	3.10E-07	1.04	144.6	39.2
14	23	16	6.53E+07	2.04	3.52E-07	2.45E-07	1.44	199.6	65.2
15	23	16	7.26E+07	1.87	3.17E-07	2.20E-07	1.44	199.6	65.2
16	12	7	5.45E+07	2.05	2.20E-07	1.29E-07	1.71	237.3	113.1
17	23	17	6.53E+07	1.75	3.52E-07	2.60E-07	1.35	188.0	60.4
18	25	18	8.47E+07	1.92	2.95E-07	2.13E-07	1.39	192.9	59.9
19	41	31	1.09E+08	1.95	3.76E-07	2.85E-07	1.32	183.8	44.1

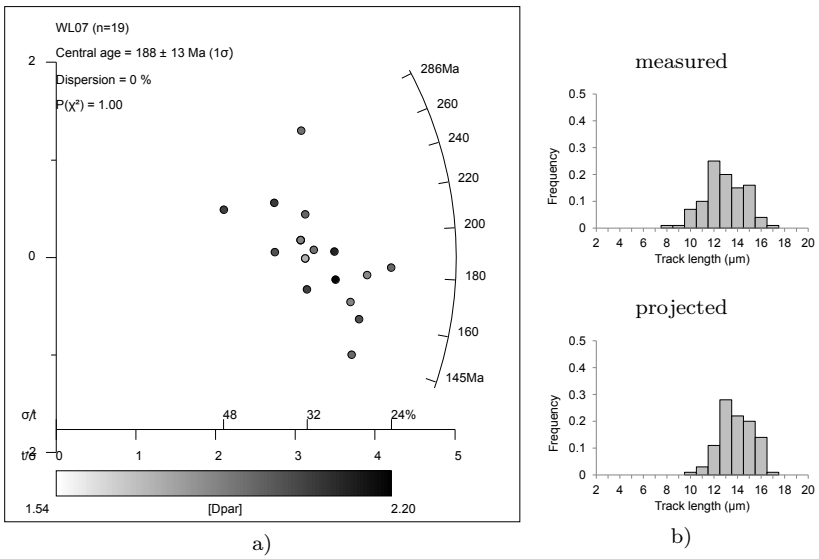

a) b)

Figure B47: (a) Radial plot of single grain fission track data, prepared using RadialPlotter (Vermeesch, 2009). (b) Histograms of track length distribution. Track length projection after Ketcham et al. (2007).

(U-Th)/He data

Table B47: Single grain apatite (U-Th-Sm)/He data; L, $W1$ and $W2$ crystal dimensions; age_c corrected age.

No.	L (μm)	W1 (μm)	W2 (μm)	T	He (μcc/g)	U (ppm)	Th (ppm)	Sm (ppm)	Th/U	eU (ppm)	age (Ma)	error†	error‡	F_T	age$_c$ (Ma)	error‡
1	110	106	60	0	39.4	5.1	6.7	525.7	1.3	6.7	44.1	3.0	7.4	0.75	59.0	8.9
2	170	96	89	0	37.9	6.0	8.4	529.3	1.4	8.0	36.0	1.5	5.1	0.77	46.6	6.2
3	125	69	59	1	23.9	4.1	3.8	278.0	0.9	5.0	36.8	5.3	9.0	0.66	55.8	10.9
4	123	90	79	0	27.8	3.9	4.3	462.0	1.1	4.9	42.1	3.3	7.5	0.76	55.5	8.8
5	145	81	66	1	30.5	5.6	6.5	544.7	1.2	7.1	32.3	2.3	5.5	0.70	46.2	6.9
M1	***178***	***150***	***129***	-	***76.0***	***3.1***	***5.7***	***395.8***	***1.8***	***4.5***	***125.4***	***2.5***	***15.0***	***0.85***	***148.3***	***17.3***
M2	***131***	***130***	***112***	-	***69.6***	***2.8***	***9.0***	***346.0***	***3.2***	***4.9***	***106.3***	***2.5***	***13.1***	***0.81***	***131.8***	***15.7***
M3	***163***	***101***	***87***	-	***41.7***	***2.9***	***11.2***	***369.4***	***3.8***	***5.6***	***57.0***	***1.5***	***7.2***	***0.75***	***76.4***	***9.1***

† analytical error; ‡ analytical error + 10% error (1 standard deviation on Durango aliquots)

Aliquots M1, M2 and M3 were discarded due to the ICP-MS instability.

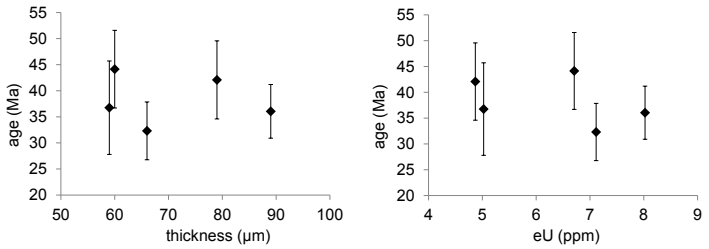

Figure B48: Apatite (U-Th-Sm)/He age versus (a) crystal thickness in μm, (b) [eU] in ppm.

Sample details

Region:	northern Wales	Unit:	-
Grid reference:	SH 71565 75663	Lithology:	Granophyre
Elevation:	∼200 m (quarry)	Apatite quality:	4

Apatite fission track data

Central age:	150.2 ± 11.2 Ma	χ^2:	13.4
Number of grains:	20	P(%):	81.9
Zeta (for IRMM glass):	313.7 ± 8.3		
ρ_D (interpolated):	8.95E+5	MTL measured:	12.82 ± 1.81 μm
N_D:	6478	MTL measured:	13.81 ± 1.36 μm
N_s/N_i:	1.15 ± 0.31	No of track lengths:	100

Table B48: Single grain apatite fission track data; N_s—number of spontaneous tracks, N_i—number of induced tracks, ρ_D—tracks density on the dosimeter, ρ_s—spontaneous track density, ρ_i—induced track density.

No.	N_s	N_i	Area (cm^2)	DPar (μm)	ρ_s ($tracks/cm^2$)	ρ_i ($tracks/cm^2$)	ρ_s/ρ_i	Age (Ma)	1σ (Ma)
1	16	10	3.63E+07	2.20	4.41E-07	2.75E-07	1.60	220.8	89.2
2	22	19	6.05E+07	2.25	3.64E-07	3.14E-07	1.16	160.5	50.5
3	15	13	4.84E+07	2.32	3.10E-07	2.69E-07	1.15	160.0	60.8
4	21	30	6.05E+07	2.19	3.47E-07	4.96E-07	0.70	97.50	27.9
5	20	15	4.24E+07	2.18	4.72E-07	3.54E-07	1.33	184.5	63.3
6	32	22	6.05E+07	2.42	5.29E-07	3.64E-07	1.45	201.0	56
7	25	24	4.84E+07	2.35	5.17E-07	4.96E-07	1.04	144.6	41.5
8	20	13	4.36E+07	2.27	4.59E-07	2.98E-07	1.54	212.4	75.9
9	26	17	5.81E+07	2.19	4.48E-07	2.93E-07	1.53	211.2	66.2
10	14	15	4.84E+07	2.31	2.89E-07	3.10E-07	0.93	129.7	48.4
11	23	30	4.84E+07	2.27	4.75E-07	6.20E-07	0.77	106.70	29.7
12	24	23	7.26E+07	2.15	3.31E-07	3.17E-07	1.04	144.8	42.5
13	18	21	4.84E+07	2.25	3.72E-07	4.34E-07	0.86	119.2	38.5
14	24	25	5.45E+07	2.33	4.41E-07	4.59E-07	0.96	133.4	38.3
15	18	23	6.05E+07	2.21	2.98E-07	3.80E-07	0.78	108.9	34.4
16	26	20	5.08E+07	2.27	5.12E-07	3.94E-07	1.30	180 .0	53.8
17	23	13	5.81E+07	2.36	3.96E-07	2.24E-07	1.77	243.7	84.9
18	29	29	6.05E+07	2.22	4.79E-07	4.79E-07	1.00	138.9	36.7
19	19	19	3.63E+07	2.28	5.23E-07	5.23E-07	1.00	138.9	45.2
20	32	32	7.26E+07	2.27	4.41E-07	4.41E-07	1.00	138.9	35.0

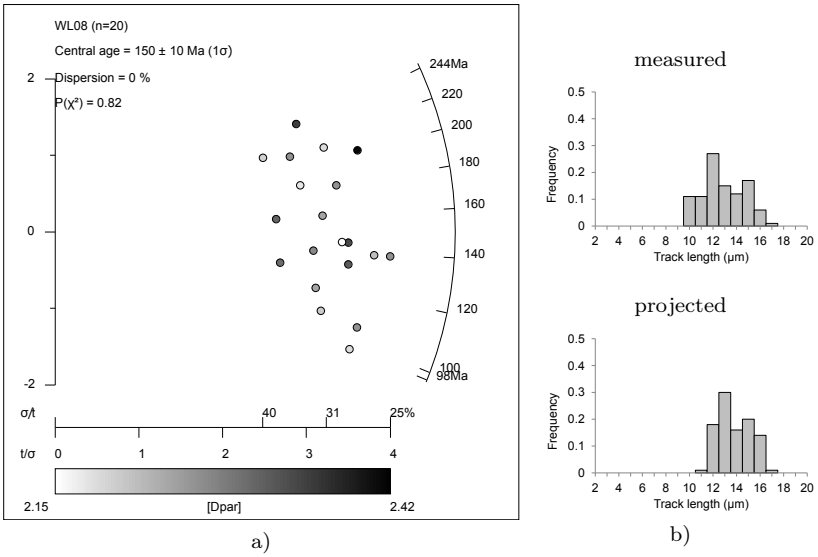

a) b)

Figure B49: (a) Radial plot of single grain fission track data, prepared using RadialPlotter (Vermeesch, 2009). (b) Histograms of track length distribution. Track length projection after Ketcham et al. (2007).

(U-Th)/He data

Table B49: Single grain apatite (U-Th-Sm)/He data; L, $W1$ and $W2$ crystal dimensions; age_c corrected age.

No.	L (μm)	W1 (μm)	W2 (μm)	T	He (μcc/g)	U (ppm)	Th (ppm)	Sm (ppm)	Th/U	eU (ppm)	age (Ma)	error†	error‡	F_T	age$_c$ (Ma)	error‡
1	214	95	64	0	73.3	13.3	14.6	597.5	1.1	16.7	34.6	1.3	4.8	0.75	46.4	5.9
2	120	104	74	0	42.8	5.9	7.4	376.0	1.3	7.6	43.7	2.4	6.8	0.77	56.6	8.1
3	148	73	54	1	71.8	15.4	17.2	516.8	1.1	19.4	29.5	1.4	4.4	0.66	44.6	5.9
4	149	82	70	0	54.1	7.1	9.6	374.6	1.4	9.4	45.4	2.1	6.6	0.73	62.0	8.3
5	191	83	57	0	89.1	11.9	21.9	571.6	1.8	17.1	41.2	1.2	5.3	0.71	58.2	7.0
M1	*123*	*97*	*84*	-	*74.7*	*7.4*	*21.0*	*353.4*	*2.8*	*12.3*	*48.1*	*1.1*	*5.9*	*0.77*	*62.9*	*7.3*
M2	*149*	*81*	*70*	-	*118.3*	*4.8*	*25.4*	*526.8*	*5.3*	*10.8*	*84.9*	*2.1*	*10.6*	*0.72*	*118.2*	*13.9*
M3	*147*	*72*	*62*	-	*117.8*	*7.6*	*36.9*	*387.9*	*4.9*	*16.3*	*57.7*	*1.3*	*7.0*	*0.68*	*84.7*	*9.7*

† analytical error; ‡ analytical error + 10% error (1 standard deviation on Durango aliquots)

Aliquots M1, M2 and M3 were discarded due to the ICP-MS instability.

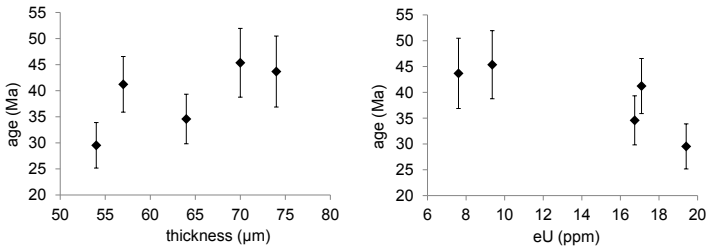

Figure B50: Apatite (U-Th-Sm)/He age versus (a) crystal thickness in μm, (b) [eU] in ppm.

Sample details

Grid reference:	SH 39503 79488	Unit:	Coedana
Elevation:	∼60 m (quarry)	Lithology:	Granite
Region:	Anglesey	Apatite quality:	1

Apatite fission track data

Central age:	50.6 ± 4.8 Ma	χ^2:	17.0
Number of grains:	15	P(%):	25.7
Zeta (for IRMM glass):	313.7 ± 8.3		
ρ_D (interpolated):	8.91E+5	No of track lengths: 0	
N_D:	6478		
N_s/N_i:	0.41 ± 0.21		

Table B50: Single grain apatite fission track data; N_s—number of spontaneous tracks, N_i—number of induced tracks, ρ_D—tracks density on the dosimeter, ρ_s—spontaneous track density, ρ_i—induced track density.

No.	N_s	N_i	Area (cm^2)	DPar (μm)	ρ_s (tracks/cm^2)	ρ_i (tracks/cm^2)	ρ_s/ρ_i	Age (Ma)	1σ (Ma)
1	7	27	3.39E+07	-	2.07E-07	7.97E-07	0.26	36.1	15.4
2	7	22	2.18E+07	-	3.21E-07	1.01E-06	0.32	44.3	19.3
3	5	26	2.42E+07	-	2.07E-07	1.07E-06	0.19	26.8	13.1
4	8	27	2.42E+07	-	3.31E-07	1.12E-06	0.30	41.3	16.7
5	12	32	4.84E+07	-	2.48E-07	6.61E-07	0.38	52.2	17.7
6	10	27	4.84E+07	-	2.07E-07	5.58E-07	0.37	51.6	19.1
7	3	9	4.36E+07	-	6.89E-08	2.07E-07	0.33	46.4	31.0
8	7	23	5.45E+07	-	1.29E-07	4.22E-07	0.30	42.4	18.3
9	17	45	7.62E+07	-	2.23E-07	5.90E-07	0.38	52.6	15.0
10	35	99	6.53E+07	-	5.36E-07	1.52E-06	0.35	49.2	9.8
11	4	7	7.26E+07	-	5.51E-08	9.64E-08	0.57	79.4	49.8
12	14	41	6.05E+07	-	2.31E-07	6.78E-07	0.34	47.5	14.8
13	17	62	5.08E+07	-	3.35E-07	1.22E-06	0.27	38.2	10.5
14	14	15	2.42E+07	-	5.79E-07	6.20E-07	0.93	129.1	48.1
15	14	17	2.90E+07	-	4.82E-07	5.85E-07	0.82	114.1	41.3

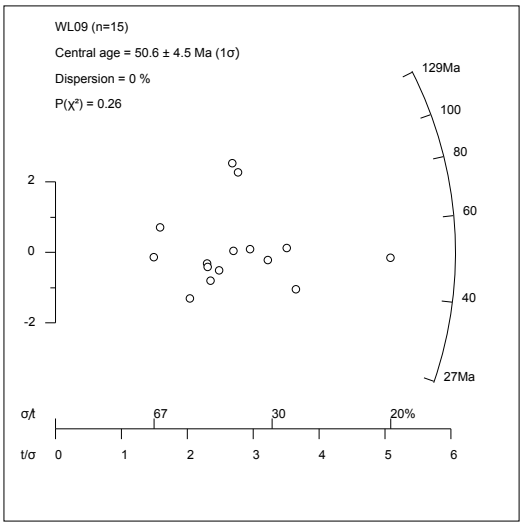

Figure B51: Radial plot of single grain fission track data, prepared using RadialPlotter (Vermeesch, 2009).

(U-Th)/He data

Table B51: Single grain apatite (U-Th-Sm)/He data; L, $W1$ and $W2$ crystal dimensions; age_c corrected age.

No.	L (μm)	W1 (μm)	W2 (μm)	T	He (μcc/g)	U (ppm)	Th (ppm)	Sm (ppm)	Th/U	eU (ppm)	age (Ma)	error†	error‡	F_T	age_c (Ma)	error‡
M1	137	99	85	-	78.4	26.3	17.5	70.0	0.7	30.4	21.2	0.4	2.5	0.76	27.8	3.2
M2	110	78	67	-	106.9	12.2	19.9	78.7	1.6	16.9	51.8	1.2	6.4	0.70	73.8	8.6

† analytical error; ‡ analytical error + 10% error (1 standard deviation on Durango aliquots)

Bibliography

Akhurst, M. C., Barnes, R. P., Chadwick, R. A., Millward, D., Norton, M. G., Maddock, R. H., Kimbell, G. S. & Milodowski, A. E. (1998), 'Structural evolution of the Lake District Boundary Fault Zone in west Cumbria, UK', *Proceedings of the Yorkshire Geological Society* **52**, 139–158.

Akhurst, M. C., ed. (1997), *Geology of the west Cumbria district*, Vol. 28, British Geological Survey.

Al-Kindi, S., White, N., Sinha, M., England, R. & Tiley, R. (2003), 'Crustal trace of a hot convective sheet', *Geology* **31**, 207–210.

Andersen, M. S., Nielsen, T., Sørensen, A. B., Boldreel, L. O. & Kuijpers, A. (2000), 'Cenozoic sediment distribution and tectonic movements in the Faroe region', *Global and Planetary Change* **24**, 239–259.

Anderton, R. (1993), Sedimentation and basin evolution in the Paleogene of the Northern North Sea and Faeroe–Shetland basins, *in* 'Geological Society, London, Petroleum Geology Conference series', Vol. 4, Geological Society of London, pp. 31–31.

Anell, I., Thybo, H. & Artemieva, I. A. (2009), 'Cainozoic uplift and sub-sidence in the North Atlantic region: geological evidence revisited', *Tectonophysics* **486**, 169–184.

Arrowsmith, S. J., Kendall, M., White, N., VanDecar, J. C. & Booth, D. C. (2005), 'Seismic imaging of a hot upwelling beneath the British Isles', *Geology* **33**, 345–348.

Ault, A. K. & Flowers, R. M. (2012), 'Is apatite U-Th zonation information necessary for accurate interpretation of apatite (U-Th)/He thermochronometry data?', *Geochimica et Cosmochimica Acta* **79**, 60–78.

Balestrieri, M. L., Stuart, F. M., Persano, C., Abbate, E. & Bigazzi, G. (2005), 'Geomorphic development of the escarpment of the Eritrean margin, southern Red Sea from combined apatite fission-track and (U-Th)/He thermochronometry', *Earth and Planetary Science Letters* **231**, 97–110.

Ballantyne, C. K., Stone, J. O. & Fifield, L. K. (2009), 'Glaciation and deglaciation of the SW Lake District, England: implications of cosmogenic 36 Cl exposure dating', *Proceedings of the Geologists' Association* **120**, 139–144.

Bamford, D., Nunn, K., Prodehl, C. & Jacob, B. (1978), 'LISPB—IV. Crustal structure of northern Britain', *Geophysical Journal International* **54**, 43–60.

Barbarand, J., Carter, A., Wood, I. & Hurford, A. (2003), 'Compositional and structural control of fission-track annealing in apatite', *Chemical Geology* **198**, 107–137.

Barton, A. J. & White, R. S. (1997), 'Crustal structure of Edoras Bank continental margin and mantle thermal anomalies beneath the North Atlantic', *Journal of Geophysical Research: Solid Earth (1978–2012)* **102**, 3109–3129.

Beaumont, C., Keen, C. E. & Boutilier, R. (1982), 'A comparison of foreland and rift margin sedimentary basins', *Philosophical Transactions of the Royal Society of London A: Mathematical, Physical and Engineering Sciences* **305**, 295–317.

Bell, B. R. & Williamson, I. T. (2002), *The Geology of Scotland (ed. N. H. Trewin)*, Geological Society of London, chapter Tertiary igneous activity.

Beucher, R., Brown, R. W., Roper, S., Stuart, F. & Persano, C. (2013), 'Natural age dispersion arising from the analysis of broken crystals: Part II. Practical application to apatite (U-Th)/He thermochronometry', *Geochimica et Cosmochimica Acta* **120**, 395–416.

Bevins, R. E., Horák, J. M., Evans, A. D. & Morgan, R. (1996), 'Palaeogene dyke swarm, NW Wales: evidence for Cenozoic sinistral fault movement', *Journal of the Geological Society* **153**, 177–180.

Blackwell, D. D. & Steele, J. L. (1989), *Thermal conductivity of sedimentary rocks: measurement and significance*, Springer.

Bluck, B. J., Dempster, T. J., Aftalion, M., Haughton, P. D. W. & Rogers, G. (2006), 'Geochronology of a granitoid boulder from the Corsewall Formation (Southern Uplands): implications for the evolution of southern Scotland', *Scottish Journal of Geology* **42**, 29–35.

Blundell, D. J. & Parks, R. (1969), 'A study of the crustal structure beneath the Irish Sea', *Geophysical Journal International* **17**, 45–62.

Bott, M. H. P. (1974), 'The geological interpretation of a gravity survey of the English Lake District and the Vale of Eden', *Journal of the Geological Society of London* **130**, 309–331.

Bott, M. H. P. & Bott, J. D. J. (2004), 'The Cenozoic uplift and earthquake belt of mainland Britain as a response to an underlying hot, low-density upper mantle', *Journal of the Geological Society* **161**, 19–29.

Boyce, J. W., Hodges, K. V., Olszewski, W. J., Jercinovic, M. J., Carpenter, B. D. & Reiners, P. W. (2006), 'Laser microprobe (U-Th)/He geochronology', *Geochimica et Cosmochimica Acta* **70**, 3031–3039.

Brandon, M. T., Roden-Tice, M. & Garver, J. I. (1998), 'Late Cenozoic exhumation of the Cascadia accretionary wedge in the Olympic Mountains, northwest Washington State', *Geological Society of America Bulletin* **110**, 985–1009.

Braun, J. (2003), 'Pecube: A new finite-element code to solve the 3D heat transport equation including the effects of a time-varying, finite amplitude surface topography', *Computers & Geosciences* **29**(6), 787–794.

Braun, J. (2010), 'The many surface expressions of mantle dynamics', *Nature Geoscience* **3**(12), 825–833.

Braun, J. & Beaumont, C. (1989), 'A physical explanation of the relation between flank uplifts and the breakup unconformity at rifted continental margins', *Geology* **17**, 760–764.

Braun, J., Robert, X. & Simon-Labric, T. (2013), 'Eroding dynamic topography', *Geophysical Research Letters* **40**, 1494–1499.

Braun, J., Simon-Labric, T., Murray, K. E. & Reiners, P. W. (2014), 'Topographic relief driven by variations in surface rock density', *Nature Geoscience* **7**, 534–540.

Braun, J., van der Beek, P. & Batt, G. (2006), *Quantitative Thermochronology*, Cambridge University Press. pp. 270.

Braun, J., Van Der Beek, P., Valla, P., Robert, X., Herman, F., Glotzbach, C., Pedersen, V., Perry, C., Simon-Labric, T. & Prigent, C. (2012), 'Quantifying rates of landscape evolution and tectonic processes by thermochronology and numerical modeling of crustal heat transport using PECUBE', *Tectonophysics* **524**, 1–28.

Bray, R. J., Green, P. F. & Duddy, I. R. (1992), Thermal history reconstruction using apatite fission track analysis and vitrinite reflectance: a case study from the UK East Midlands and Southern North Sea, *in* R. F. P. Hardman, ed., 'Exploration Britain: Geological insights for the next decade', Geological Society, London, pp. 3–25. Special Publications, 67.

Brodie, J. & White, N. (1994), 'Sedimentary basin inversion caused by igneous underplating: Northwest European continental shelf', *Geology* **22**, 147–150.

Brookfield, M. E. (1980), 'Permian intermontane basin sedimentation in southern Scotland', *Sedimentary Geology* **27**(3), 167–194.

Brown, D. J., Holohan, E. P. & Bell, B. R. (2009), 'Sedimentary and volcano-tectonic processes in the British Paleocene Igneous Province: a review', *Geological Magazine* **146**, 326–352.

Brown, G. C., Cassidy, J., Locke, C. A., Plant, J. A. & Simpson, P. R. (1981), 'Caledonian plutonism in Britain: A summary', *Journal of Geophysical Research: Solid Earth* **86**, 10502–10514.

Brown, G. C., Plant, J. & Lee, M. K. (1979), 'Geochemical and geophysical evidence on the geothermal potential of Caledonian granites in Britain', *Nature* **280**, 129–131.

Brown, G. C., Webb, P. C., Ixer, R. A. & Plant, J. A. (1987), 'Geochemistry of granites beneath the north Pennines and their role in orefield mineralization'.

Brown, P. E., Miller, J. A. & Grasty, R. L. (1968), Isotopic ages of late Caledonian granitic intrusions in the British Isles, *in* 'Proceedings of the Yorkshire Geological and Polytechnic Society', Vol. 36, pp. 251–276.

Brown, P. E., Soper, N. J. & Miller, J. A. (1964), Age of the principal intrusions of the Lake District, *in* 'Proceedings of the Yorkshire Geological and Polytechnic Society', Vol. 34, pp. 331–342.

Brown, R., Gallagher, K. & Duane, M. (1994), 'A quantitative assessment of the effects of magmatism on the thermal history of the Karoo sedimentary sequence', *Journal of African Earth Sciences* **18**, 227–243.

Brown, R. W., Beucher, R., Roper, S., Persano, C., Stuart, F. & Fitzgerald, P. (2013), 'Natural age dispersion arising from the analysis of broken crystals. Part I: Theoretical basis and implications for the apatite (U–Th)/He thermochronometer', *Geochimica et Cosmochimica Acta* **122**, 478–497.

Busby, J., Kingdon, A. & Williams, J. (2011), 'The measured shallow temperature field in Britain', *Quarterly Journal of Engineering Geology and Hydrogeology* **44**, 373–387.

Campbell, I. H. & Griffiths, R. W. (1990), 'Implications of mantle plume structure for the evolution of flood basalts', *Earth and Planetary Science Letters* **99**, 79–93.

Carlson, W. D., Donelick, R. A. & Ketcham, R. A. (1999), 'Variability of apatite fission-track annealing kinetics: I. Experimental results', *American Mineralogist* **84**, 1213–1223.

Carslaw, H. S. & Jaeger, J. C. (1959), *Conduction of heat in solids*, Clarendon Press Oxford.

Ceramicola, S., Stoker, M., Praeg, D., Shannon, P., De Santis, L., Hoult, R., Hjelstuen, B., Laberg, S. & Mathiesen, A. (2005), 'Anomalous Cenozoic subsidence along the 'passive' continental margin from Ireland to mid-Norway', *Marine and Petroleum Geology* **22**, 1045–1067.

Chadwick, R. A., Holliday, D. W., Holloway, S. & Hulbert, A. G. (1993), The evolution and hydrocarbon potential of the Northumberland–Solway Basin, *in* 'Geological Society, London, Petroleum Geology Conference series', Vol. 4, Geological Society of London, pp. 717–726.

Chadwick, R. A., Kirby, G. A. & Baily, H. E. (1994), 'The post-Triassic structural evolution of northwest England and adjacent parts of the East Irish Sea', *Proceedings of the Yorkshire Geological and Polytechnic Society* **50**, 91–102.

Chamberlain, K. R. & Bowring, S. A. (2000), 'Apatite-feldspar U-Pb thermochronometer: A reliable, mid-range (450°C), diffusion-controlled system', *Chemical Geology* **172**, 73–200.

Chambers, L. M., Pringle, M. S. & Parrish, R. R. (2005), 'Rapid formation of the Small Isles Tertiary centre constrained by precise 40Ar/39Ar and U-Pb ages', *Lithos* **79**, 367–384.

Cherniak, D. J. (1993), 'Lead diffusion in titanite and preliminary results on the effects of radiation damage on Pb transport', *Chemical Geology* **110**, 177–194.

Clark, M. K., Farley, K. A., Zheng, D., Wang, Z. & Duvall, A. R. (2010), 'Early Cenozoic faulting of the northern Tibetan Plateau margin from apatite (U-Th)/He ages', *Earth and Planetary Science Letters* **296**, 78–88.

Clauser, C. & Huenges, E. (1995), Thermal Conductivity of Rocks and Minerals, *in* 'Rock Physics And Phase Relations: A Handbook of Physical Constants (ed. T.J. Ahrens)', American Geophysical Union, pp. 105–126.

Clift, P. D. (1999), 'The thermal impact of Paleocene magmatic underplating in the Faeroe–Shetland–Rockall region', *Petroleum Geology* **5**, 585–593.

Clift, P. D., Carter, A. & Hurford, A. J. (1998), 'The erosional and uplift history of NE Atlantic passive margins: constraints on a passing plume', *Journal of the Geological Society* **155**, 787–800.

Clift, P. D. & Turner, J. (1998), 'Paleogene igneous underplating and subsidence anomalies in the Rockall-Faeroe-Shetland area', *Marine and Petroleum Geology* **15**, 223–243.

Cloetingh, S. A. P. L., Cornu, T., Ziegler, P. A., Beekman, F. & Group, E. T. E. W. (2006a), 'Neotectonics and intraplate continental topography of the northern Alpine Foreland', *Earth-Science Reviews* **74**, 127–196.

Cloetingh, S. A. P. L., Gradstein, F. M., Kooi, H., Grant, A. C. & Kaminski, M. M. (1990), 'Plate reorganization: a cause of rapid late Neogene subsidence and sedimentation around the North Atlantic?', *Journal of the Geological Society* **147**, 495–506.

Cloetingh, S., Burov, E. & Francois, T. (2013), 'Thermo-mechanical controls on intra-plate deformation and the role of plume-folding interactions in continental topography', *Gondwana Research* **24**, 815–837.

Cloetingh, S., Burov, E. & Poliakov, A. (1999), 'Lithosphere folding: Primary response to compression?(from central Asia to Paris basin)', *Tectonics* **18**, 1064–1083.

Cloetingh, S., Ziegler, P. A., Beekman, F., Andriessen, P. A. M., Hardebol, N., Van Wijk, J. & Dèzes, P. (2006b), 'Thermo-mechanical controls on Alpine deformation of NW Europe', *Geological Society, London, Memoirs* **32**(1), 113–127.

Cooper, M. R., Anderson, H., Walsh, J. J., Van Dam, C. L., Young, M. E., Earls, G. & Walker, A. (2012), 'Palaeogene Alpine tectonics and Icelandic plume-related magmatism and deformation in Northern Ireland', *Journal of the Geological Society* **169**, 29–36.

Cope, J. C. W. (1994), 'A latest Cretaceous hotspot and the southeasterly tilt of Britain', *Journal of the Geological Society* **151**, 905–908.

Corrigan, J. D. & Crowley, K. D. (1992), 'Unroofing of the Himalayas; a view from apatite fission track analysis of Bengal Fan sediments', *Geophysical Research Letters* **19**, 2345–2348.

Coward, M. P. (1995), 'Structural and tectonic setting of the Permo-Triassic basins of northwest Europe', *Geological Society, London, Special Publications* **91**, 7–39.

Cox, K. G. (1993), 'Continental magmatic underplating', *Philosophical Transactions of the Royal Society of London A: Mathematical, Physical and Engineering Sciences* **342**(1663), 155–166.

Coyle, D. A. & Wagner, G. A. (1998), 'Positioning the titanite fission-track partial annealing zone', *Chemical Geology* **149**, 117–125.

Croudace, I. W. (1982), 'The geochemistry and petrogenesis of the Lower Paleozoic granitoids of the Lleyn Peninsula, North Wales', *Geochimica et Cosmochimica Acta* **46**, 609–621.

Dam, G., Larsen, M. & Sønderholm, M. (1998), 'Sedimentary response to mantle plumes: implications from Paleocene onshore successions, West and East Greenland', *Geology* **26**, 207–210.

Davies, R., Cloke, I., Cartwright, J., Robinson, A. & Ferrero, C. (2004), 'Post-breakup compression of a passive margin and its impact on hydrocarbon prospectivity: An example from the Tertiary of the FaeroeShetland Basin, United Kingdom', *AAPG bulletin* **88**, 1–20.

Davis, M. W., White, N. J., Priestley, K. F., Baptie, B. J. & Tilmann, F. J. (2012), 'Crustal structure of the British Isles and its epeirogenic consequences', *Geophysical Journal International* **190**, 705–725.

Dickin, A. P. (2005), *Radiogenic Isotope Geology*, second edition edn, Cambridge University Press. pp. 492.

Dobson, K. J., Stuart, F. M. & Dempster, T. J. (2010), 'Constraining the post-emplacement evolution of the Hebridean Igneous Province (HIP) using low-temperature thermochronology: how long has the HIP been cool?', *Journal of the Geological Society* **167**(5), 973–984.

Dobson, K. J., Stuart, F. M., Dempster, T. J. & EIMF (2008), 'U and Th zonation in Fish Canyon Tuff zircons: Implications for a zircon (U-Th)/He standard', *Geochimica et Cosmochimica Acta* **72**, 4745–4755.

Dodson, M. H. (1973), 'Closure temperature in cooling geochronological and petrological systems', *Contributions to Mineralogy and Petrology* **40**, 259–274.

Donelick, R. A. (1991), 'Crystallographic orientation dependence of mean etchable fission track length in apatite: an empirical model and experimental observations', *American Mineralogist* **76**, 83–91.

Donelick, R. A., Ketcham, R. A. & Carlson, W. (1999), 'Variability of apatite fission-track annealing kinetics: II. Crystallographic orientation effects', *American Mineralogist* **84**, 1224–134.

Donelick, R. A., Roden, M. K., Mooers, J. D., Carpenter, B. S. & Miller, D. S. (1990), 'Etchable length reduction of induced fission tracks in apatite at room temperature (∼23°C): crystallographic orientation effects and "initial" mean lengths', *Nuclear Tracks and Radiation Measurements* **17**, 261–65.

Doré, A. G., Cartwright, J. A., Stoker, M. S., Turner, J. P. & White, N. J. (2002), 'Exhumation of the North Atlantic margin: introduction and background', *Geological Society, London, Special Publications* **196**, 1–12.

Doré, A. G. & Jensen, L. N. (1996), 'The impact of late Cenozoic uplift and erosion on hydrocarbon exploration: offshore Norway and some other uplifted basins', *Global and Planetary Change* **12**, 415–436.

Doré, A. G. & Lundin, E. R. (1996), 'Cenozoic compressional structures on the NE Atlantic margin; nature, origin and potential significance for hydrocarbon exploration', *Petroleum Geoscience* **2**, 299–311.

Doré, A. G., Lundin, E. R., Jensen, L. N., Birkeland, Ø., Eliassen, P. E. & Fichler, C. (1999), Principal tectonic events in the evolution of the northwest European Atlantic margin, *in* A. J. Fleet & S. A. R. Boldy, eds, 'Petroleum Geology of Northwest Europe: Proceedings of the 5th Conference', Geological Society, London, pp. 41–61.

Downing, R. A. & Gray, D. A. (1986a), 'Geothermal resources of the United Kingdom', *Journal of the Geological Society* **143**, 499–507.

Downing, R. A. & Gray, D., eds (1986b), *Geothermal energy–the potential in the United Kingdom*, HMSO, British Geological Survey, Keyworth (United Kingdom).

Ehlers, T. A. (2005), 'Crustal thermal processes and the interpretation of thermochronometer data', *Reviews in Mineralogy and Geochemistry* **58**, 315–350.

Ehlers, T. A., Armstrong, P. A. & Chapman, D. S. (2001), 'Normal fault thermal regimes and the interpretation of low-temperature thermochronometers', *Physics of the Earth and Planetary Interiors* **126**, 179–194.

Ehlers, T. A. & Farley, K. A. (2003), 'Apatite (U–Th)/He thermochronometry: methods and applications to problems in tectonic and surface processes', *Earth and Planetary Science Letters* **206**(1), 1–14.

Ellam, R. (1992), 'Lithospheric thickness as a control on basalt geochemistry', *Geology* **20**, 153–156.

Eppelbaum, L., Kutasov, I. & Pilchin, A. (2014), Thermal Properties of Rocks and Density of Fluids, *in* 'Applied Geothermics', Springer, pp. 99–149.

Evans, C. J., Kimbell, G. S. & Rollin, K. E. (1988), Hot Dry Rock Potential in Urban Areas, Investigation of the Geothermal Potential of the UK, Technical report, British Geological Survey Report.

Evans, D. J. A., Livingstone, S. J., Vieli, A. & Cofaigh, C. Ó. (2009), 'The palaeoglaciology of the central sector of the British and Irish Ice Sheet: reconciling glacial geomorphology and preliminary ice sheet modelling', *Quaternary Science Reviews* **28**, 739–757.

Farley, K. A. (2000), 'Helium diffusion from apatite: general behavior as illustrated by Durango fluorapatite', *Journal of Geophysical Research* **105**, 2903–2914.

Farley, K. A. (2002), (U-Th)/He dating: techniques, calibrations, and applications, *in* D. P. Porcelli, C. J. Ballentine & R. Wieler, eds, 'Noble Gases in Geochemistry and Cosmochemistry', Mineralogical Society of America/Geochemical Society, Washington, pp. 819–843.

Farley, K. A., Shuster, D. L. & Ketcham, R. A. (2011), 'U and Th zonation in apatite observed by laser ablation ICPMS, and implications for the (U-Th)/He system', *Geochimica et Cosmochimica Acta* **75**, 4515–4530.

Farley, K. A., Wolf, R. & Silver, L. (1996), 'The effect of long alpha-stopping distances on (U-Th)/He dates', *Geochimica et Cosmochimica Acta* **60**, 4223–4229.

Fitzgerald, P. G., Baldwin, S. L., Webb, L. E. & O'Sullivan, P. B. (2006), 'Interpretation of (U-Th)/He single grain ages from slowly cooled crustal terranes: a case study from the Transantarctic Mountains of southern Victoria Land', *Chemical Geology* **225**(1), 91–120.

Fitzgerald, P. G., Sorkhabi, R. B., Redfield, T. F. & Stump, E. (1995), 'Uplift and denudation of the central Alaska Range; a case study in the use of apatite fission track thermochronology to determine absolute uplift parameters', *Journal of Geophysical Research* **100**, 20175–20191.

Fleischer, R. L., Price, P. B. & Walker, R. M. (1975), *Nuclear Tracks in Solids*, University of California Press, Berkeley. 605 p.

Fletcher, R., Kusznir, N., Roberts, A. & Hunsdale, R. (2013), 'The formation of a failed continental breakup basin: The Cenozoic development of the Faroe-Shetland Basin', *Basin Research* **25**, 532–553.

Flowers, R. M. & Kelley, S. A. (2011), 'Interpreting data dispersion and inverted dates in apatite (U-Th)/He and fission-track datasets: an example from the US midcontinent', *Geochimica et Cosmochimica Acta* **75**, 5169–5186.

Flowers, R. M., Ketcham, R. A., Shuster, D. L. & Farley, K. A. (2009), 'Apatite (U-Th)/He thermochronometry using a radiation damage accumulation and annealing model', *Geochimica et Cosmochimica Acta* **73**, 2347–2365.

Foster, D. A., Gleadow, A. J. W. & Mortimer, G. (1994), 'Rapid Pliocene exhumation in the Karakoram (Pakistan), revealed by fission-track thermochronology of the K2 gneiss', *Geology* **22**, 19–22.

Foulger, G. R., Panza, G. F., Artemieva, I. M., Bastow, I. D., Cammarano, F., Evans, J. R., Hamilton, W. B., Julian, B. R., Lustrino, M., Thybo, H. et al. (2013), 'Caveats on tomographic images', *Terra Nova* **25**, 259–281.

Fraser, A. J. & Gawthorpe, R. L. (1990), 'Tectono-stratigraphic development and hydrocarbon habitat of the Carboniferous in northern England', *Geological Society, London, Special Publications* **55**, 49–86.

Galbraith, R. F. (2005), *Statistics for Fission Track Analysis*, Chapman and Hall, Boca Raton, Florida. 219 p.

Galbraith, R. F. & Laslett, G. M. (1993), 'Statistical models for mixed fission track ages', *Nuclear Tracks and Radiation Measurements* **21**, 459–470.

Gallagher, K. (1995), 'Evolving temperature histories from apatite fission track data', *Earth and Planetary Science Letters* **136**, 421–435.

Gallagher, K. (2012), 'Transdimensional inverse thermal history modeling for quantitative thermochronology', *Journal of Geophysical Research* **117**. B02408.

Gallagher, K. & Brown, R. (1999), 'Denudation and uplift at passive margins: the record on the Atlantic Margin of southern Africa', *Philosophical Transactions of the Royal Society of London A: Mathematical, Physical and Engineering Sciences* **357**, 835–859.

Gallagher, K., Brown, R. & Johnson, C. (1998), 'Fission track analysis and its applications to geological problems', *Annual Review of Earth and Planetary Sciences* **26**, 519–572.

Gallagher, K., Hawkesworth, C. J. & Mantovani, M. S. M. (1994), 'The denudation history of the onshore continental margin of SE Brazil inferred from apatite fission track data', *Journal of Geophysical Research: Solid Earth (1978–2012)* **99**, 18117–18145.

Ganerød, M., Smethurst, M. A., Torsvik, T. H., Prestvik, T., Rousse, S., McKenna, C., Van Hinsbergen, D. J. J. & Hendriks, B. W. H. (2010), 'The North Atlantic Igneous Province reconstructed and its relation to the plume generation zone: the Antrim lava group revisited', *Geophysical Journal International* **182**, 183–202.

Gautheron, C., Barbarand, J., Ketcham, R. A., Tassan-Got, L., van der Beek, P., Pagel, M., Pinna-Jamme, R., Couffignal, F. & Fialin, M. (2013), 'Chemical influence on α-recoil damage annealing in apatite: Implications for (U-Th)/He dating', *Chemical Geology* **351**, 257–267.

Gautheron, C. & Tassan-Got, L. (2010), 'A Monte Carlo approach to diffusion applied to noble gas/helium thermochronology', *Chemical Geology* **273**, 212–224.

Gautheron, C., Tassan-Got, L., Barbarand, J. & Pagel, M. (2009), 'Effect of alpha-damage annealing on apatite (U-Th)/He thermochronology', *Chemical Geology* **266**, 157–170.

Gautheron, C., Tassan-Got, L., Ketcham, R. A. & Dobson, K. J. (2012), 'Accounting for long alpha-particle stopping distances in (U-Th-Sm)/He geochronology: 3D modeling of diffusion, zoning, implantation, and abrasion', *Geochimica et Cosmochimica Acta* **96**, 44–96.

Gleadow, A. J. W. & Duddy, I. R. (1981), 'A natural long-term track annealing experiment for apatite', *Nuclear Tracks and Radiation Measurements* **5**, 169–174.

Glotzbach, C., Bernet, M. & van der Beek, P. (2011), 'Detrital thermochronology records changing source areas and steady exhumation in the Western European Alps', *Geology* **39**, 239–242.

Goes, S., Govers, R. & Vacher, P. (2000), 'Shallow mantle temperatures under Europe from P and S wave tomography', *Journal of Geophysical Research* **105**, 153–11.

Gołędowski, B., Nielsen, S. B. & Clausen, O. R. (2012), 'Patterns of Cenozoic sediment flux from western Scandinavia', *Basin Research* **24**, 377–400.

Green, P. F. (1986), 'On the thermo-tectonic evolution of northern England: evidence from fission track analysis', *Geological Magazine* **123**, 493–506.

Green, P. F. (1988), 'The relationship between track shortening and fission track age reduction in apatite: combined influences of inherent instability, annealing anisotropy, length bias and system calibration', *Earth and Planetary Science Letters* **89**, 335–352.

Green, P. F. (1989), 'Thermal and tectonic history of the East Midlands shelf (onshore UK) and surrounding regions assessed by apatite fission track analysis', *Journal of the Geological Society* **146**, 755–773.

Green, P. F. (2002), 'Early Tertiary paleo-thermal effects in northern England: reconciling results from apatite fission track analysis with geological evidence', *Tectonophysics* **349**, 131–144.

Green, P. F., Crowhurst, P. V., Duddy, I. R., Japsen, P. & Holford, S. P. (2006), 'Conflicting (U-Th)/He and fission track ages in apatite: enhanced He retention, not anomalous annealing behaviour', *Earth and Planetary Science Letters* **250**, 407–427.

Green, P. F., Duddy, I. R. & Bray, R. J. (1995), Applications of thermal history reconstruction in inverted basins, *in* J. G. Buchanan & P. G. Buchanan, eds, 'Basin Inversion', Geological Society, London, pp. 148–165. Special Publications, 88.

Green, P. F., Duddy, I. R. & Bray, R. J. (1997), Variation in thermal history styles around the Irish Sea and adjacent areas: implications for hydrocarbon occurrence and tectonic evolution, *in* N. S. Meadows, S. P. Trueblood, M. Hardman & G. Cowan, eds, 'Petroleum Geology of the Irish Sea and Adjacent Areas', Geological Society, London, pp. 73–93. Special Publication 124.

Green, P. F., Duddy, I. R., Gleadow, A. J. W. & Lovering, J. F. (1989), Apatite fission-track analysis as a paleotemperature indicator for hydrocarbon exploration, *in* N. D. Naeser & T. H. McCulloh, eds, 'Thermal History of Sedimentary Basins', Springer-Verlag, New York, pp. 181–195.

Green, P. F., Duddy, I. R., Gleadow, A. J. W., Tingate, P. R. & Laslett, G. M. (1986), 'Thermal annealing of fission tracks in apatite 1. A qualitative description', *Chemical Geology* **59**, 237–253.

Green, P. F., Thomson, K. & Hudson, J. D. (2001), 'Recognition of tectonic events in undeformed regions: contrasting results from the Midland Platform and East Midlands Shelf, Central England', *Journal of the Geological Society* **158**, 59–73.

Green, P. F., Westaway, R., Manning, D. A. C. & Younger, P. L. (2012), 'Cenozoic cooling and denudation in the North Pennines (northern England, UK) constrained by apatite fission-track analysis of cuttings from the Eastgate Borehole', *Proceedings of the Geologists' Association* **123**, 450–463.

Guenthner, W. R., Reiners, P. W., Ketcham, R. A., Nasdala, L. & Giester, G. (2013), 'Helium diffusion in natural zircon: Radiation damage, anisotropy, and the interpretation of zircon (U-Th)/He thermochronology', *American Journal of Science* **313**(3), 145–198.

Hager, B. H., Clayton, R. W., Richards, M. A., Comer, R. P. & Dziewonski, A. M. (1985), 'Lower mantle heterogeneity, dynamic topography and the geoid', **313**, 541–545.

Hall, A. & Bishop, P. (2002), 'Scotland's denudational history: an integrated view of erosion and sedimentation at an uplifted passive margin', *Geological Society, London, Special Publications* **196**, 271–290.

Halliday, A. N., Aftalion, M., van Breemen, O. & Jocelyn, J. (1979), 'Petrogenetic significance of Rb-Sr and U-Pb isotopic systems in the 400 Ma old British Isles granitoids and their hosts', *Geological Society, London, Special Publications* **8**, 653–661.

Hames, W. E. & Bowring, S. A. (1994), 'An empirical evaluation of the argon diffusion geometry in muscovite', *Earth and Planetary Science Letters* **124**, 161–169.

Hancock, J. M. (1975), 'The petrology of the Chalk', *Proceedings of the Geologists' Association* **86**, 499–535.

Hand, M., Sandiford, M. & Wyborn, L. (1999), 'Some thermal consequences of high heat production in the Australian Proterozoic', *Geophysical Journal International* **127**, 1.

Hardman, M., Buchanan, J., Herrington, P. & Carr, A. (1993), Geochemical modelling of the East Irish Sea Basin: its influence on predicting hydrocarbon type and quality, *in* 'Geological Society, London, Petroleum Geology Conference series', Vol. 4, Geological Society of London, pp. 809–821.

Harrison, T. M. (1981), 'Diffusion of ^{40}Ar in hornblende', *Contributions to Mineralogy and Petrology* **78**, 324–331.

Harrison, T. M., Duncan, I. & McDougall, I. (1985), 'Diffusion of ^{40}Ar in biotite: temperature, pressure and compositional effects', *Geochimica et Cosmochimica Acta* **49**, 2461–2468.

Hartley, R. A., Roberts, G. G., White, N. & Richardson, C. (2011), 'Transient convective uplift of an ancient buried landscape', *Nature Geoscience* **4**, 562–565.

Hasebe, N., Barbarand, J., Jarvis, K., Carter, A. & Hurford, A. J. (2004), 'Apatite fission-track chronometry using laser ablation ICP-MS', *Chemical Geology* **207**, 135–145.

Hay, W. W., Soeding, E., DeConto, R. M. & Wold, C. N. (2002), 'The Late Cenozoic uplift–climate change paradox', *International Journal of Earth Sciences* **91**, 746–774.

Hendriks, B. W. H. & Andriessen, P. A. M. (2002), 'Pattern and timing of the post-Caledonian denudation of northern scandinavia constrained by apatite fission-track thermochronology', *Geological Society, London, Special Publications* **196**, 117–137.

Hendriks, B. W. H. & Redfield, T. F. (2005), 'Apatite fission track and (U-Th)/He data from Fennoscandia: An example of underestimation of fission track annealing in apatite', *Earth and Planetary Science Letters* **236**, 443–458.

Hillis, R. R., Holford, S. P., Green, P. F., Dore, A. G., Gatliff, R. W., Stoker, M. S., Thomson, K., Turner, J. P., Underhill, J. R. & Williams, G. A. (2008), 'Cenozoic exhumation of the southern British Isles', *Geology* **36**, 371–374.

Hobbs, P., Hallam, J. R., Forster, A., Entwisle, D., Jones, L. D., Cripps, A. C., Northmore, K. J., Self, S. & Meakin, J. L. (2002), 'Engineering geology of British rocks and soils: Mudstones of the Mercia Mudstone Group'.

Holden, N. E. & Hoffman, D. C. (2000), 'Spontaneous fission half-lives for ground-state nuclides (Technical Report)', *Pure and Applied Chemistry* **72**, 1525–1562.

Holford, S. E., Turner, J. P. & Green, P. F. (2005a), Reconstructing the Mesozoic-Cenozoic exhumation history of the Irish Sea basin system using apatite fission track analysis and vitrinite reflectance, *in* A. G. Doré & B. A. Vining, eds, 'Petroleum Geology of Northwest Europe: Proceedings of the 6th Conference', Geological Society, London, pp. 1007–1030.

Holford, S. P., Green, P. F., Duddy, I. R., Turner, J. P., Hillis, R. R. & Stoker, M. S. (2009), 'Regional intraplate exhumation episodes related to plate-boundary deformation', *Geological Society of America Bulletin* **121**, 1611–1628.

Holford, S. P., Green, P. F. & Turner, J. P. (2005b), 'Palaeothermal and compaction studies in the Mochras borehole (NW Wales) reveal early Cretaceous and Neogene exhumation and argue against regional Palaeogene uplift in the southern Irish Sea', **162**, 829–840.

Holford, S. P., Green, P. F., Turner, J. P., Williams, G. A., Hillis, R. R., Tappin, D. R. & Duddy, I. R. (2008), 'Evidence for kilometre-scale Neogene exhumation driven by compressional deformation in the Irish Sea basin system', *Geological Society, London, Special Publications* **306**, 91–119.

Holliday, D. W. (1993), 'Mesozoic cover over northern England: interpretation of apatite fission track data', *Journal of the Geological Society* **150**, 657–660.

Hopson, P. (2005), *A stratigraphical framework for the Upper Cretaceous Chalk of England and Scotland with statements on the Chalk of Northern Ireland and the UK Offshore Sector*, British Geological Survey.

Hourigan, J. K., Reiners, P. W. & Brandon, M. T. (2005), 'U-Th zonation-dependent alpha-ejection in (U-Th)/He chronometry', *Geochimica et Cosmochimica Acta* **69**, 3349–3365.

House, M. A., Farley, K. A. & Kohn, B. P. (1999), 'An empirical test of helium diffusion in apatite: borehole data from the Otway Basin, Australia', *Earth and Planetary Science Letters* **170**, 463–474.

House, M. A., Wernicke, B. P. & Farley, K. A. (2001), 'Paleo-geomorphology of the Sierra Nevada, California, from (U-Th)/He ages in apatite', *American Journal of Science* **301**, 77–102.

Huismans, R. S. & Beaumont, C. (2008), 'Complex rifted continental margins explained by dynamical models of depth-dependent lithospheric extension', *Geology* **36**, 163–166.

Hurford, A. J. (1977), 'Fission track dates from two Galloway granites, Scotland', *Geological Magazine* **114**, 299–304.

Hurford, A. J. & Green, P. F. (1982), 'A users' guide to fission track dating calibration', *Earth and Planetary Science Letters* **59**, 343–354.

Hurford, A. J. & Green, P. F. (1983), 'The zeta age calibration of fission-track dating', *Chemical Geology* **1**, 285–317.

Huuse, M. (2002), 'Cenozoic uplift and denudation of southern Norway: insights from the North Sea Basin', *Geological Society, London, Special Publications* **196**, 209–233.

Japsen, P. (1997), 'Regional Neogene exhumation of Britain and the western North Sea', *Journal of the Geological Society* **154**, 239–247.

Japsen, P., Bonow, J. M., Green, P. F., Chalmers, J. A. & Lidmar-Bergström, K. (2006), 'Elevated, passive continental margins: Long-term highs or Neogene uplifts? New evidence from West Greenland', *Earth and Planetary Science Letters* **248**, 330–339.

Japsen, P. & Chalmers, J. A. (2000), 'Neogene uplift and tectonics around the North Atlantic: overview', *Global and Planetary Change* **24**, 165–173.

Japsen, P., Chalmers, J. A., Green, P. F. & Bonow, J. M. (2012), 'Elevated, passive continental margins: Not rift shoulders, but expressions of episodic, post-rift burial and exhumation', *Global and Planetary Change* **90**, 73–86.

Japsen, P., Green, P. F., Bonow, J. M., Rasmussen, E. S., Chalmers, J. A. & Kjennerud, T. (2010), Episodic uplift and exhumation along North Atlantic passive margins: implications for hydrocarbon prospectivity, *in* 'Geological Society, London, Petroleum Geology Conference series', Vol. 7, pp. 979–1004.

Jelinek, A. R., Chemale, F., van der Beek, P. A., Guadagnin, F., Cupertino, J. A. & Viana, A. (2014), 'Denudation history and landscape evolution of the northern East-Brazilian continental margin from apatite fission-track thermochronology', *Journal of South American Earth Sciences* **54**, 158–181.

Jonckheere, R. & Wagner, G. A. (2000), 'On the occurrence of anomalous fissiontracks in apatite and titanite', *American Mineralogist* **85**, 1744ÂŰ–1753.

Jones, S. M., White, N., Clarke, B. J., Rowley, E. & Gallagher, K. (2002), Present and past influence of the Iceland Plume on sedimentation, *in* A. G. Dore, J. A. Cartwright, M. S. Stoker, J. P. Turner & N. White, eds, 'Exhumation of the North Atlantic Margin: Timing, Mechanisms and Implications for Petroleum Exploration', Geological Society, London, pp. 13–25. Special Publication 196.

Jones, S. M., White, N. & Lovell, B. (2001), 'Cenozoic and Cretaceous transient uplift in the Porcupine Basin and its relationship to a mantle plume', *Geological Society, London, Special Publications* **188**, 345–360.

Jordt, H., Faleide, J. I., Bjørlykke, K. & Ibrahim, M. T. (1995), 'Cenozoic sequence stratigraphy of the central and northern North Sea Basin: tectonic development, sediment distribution and provenance areas', *Marine and Petroleum Geology* **12**, 845–879.

Jordt, H., Thyberg, B. I. & Nøttvedt, A. (2000), 'Cenozoic evolution of the central and northern North Sea with focus on differential vertical movements of the basin floor and surrounding clastic source areas', *Geological Society, London, Special Publications* **167**, 219–243.

Kelly, A., England, R. W. & Maguire, P. K. H. (2007), 'A crustal seismic velocity model for the UK, Ireland and surrounding seas', *Geophysical Journal International* **171**, 1172–1184.

Kent, R. W. & Fitton, J. G. (2000), 'Mantle sources and melting dynamics in the British Palaeogene Igneous Province', *Journal of Petrology* **41**, 1023–1040.

Kent, R. W., Storey, M. & Saunders, A. D. (1992), 'Large igneous provinces: Sites of plume impact or plume incubation?', *Geology* **20**, 891–894.

Kerr, A. C. (1994), 'Lithospheric thinning during the evolution of continental large igneous provinces: A case study from the North Atlantic Tertiary province', *Geology* **22**, 1027–1030.

Ketcham, R. A. (2005), 'Forward and inverse modeling of low-temperature thermochronometry data', *Reviews in Mineralogy and Geochemistry* **58**, 275–314.

Ketcham, R. A., Carter, A. C., Donelick, R. A., Barbarand, J. & Hurford, A. J. (2007a), 'Improved measurement of fission-track annealing in apatite using c-axis projection', *American Mineralogist* **92**, 789–798.

Ketcham, R. A., Carter, A. C., Donelick, R. A., Barbarand, J. & Hurford, A. J. (2007b), 'Improved modeling of fission-track annealing in apatite', *American Mineralogist* **92**, 799–810.

Ketcham, R. A., Donelick, R. A., Balestrieri, M. L. & Zattin, M. (2009), 'Reproducibility of apatite fission-track length data and thermal history reconstruction', *Earth and Planetary Science Letters* **284**, 504–515.

Ketcham, R. A., Donelick, R. A. & Carlson, W. D. (1999), 'Variability of apatite fission-track annealing kinetics: III. Extrapolation to geological time scales', *American Mineralogist* **84**, 1235–1255.

Ketcham, R. A., Donelick, R. A. & Donelick, M. B. (2000), 'AFTSolve: A program for multi-kinetic modeling of apatite fission-track data', *Geological Materials Research* .

Ketcham, R. A., Gautheron, C. & Tassan-got, L. (2011), 'Accounting for long alpha-particle stopping distances in (U-Th-Sm)/He geochronology: refinement of the baseline case', *Geochimica et Cosmochimica Acta* **75**, 7779–7791.

Kirby, E., Reiners, P. W., Krol, M. A., Whipple, K. X., Hodges, K. V., Farley, K. A., Tang, W. & Chen, Z. (2002), 'Late Cenozoic evolution of the eastern margin of the Tibetan Plateau: Inferences from 40Ar/39Ar and (U-Th)/He thermochronology', *Tectonics* **21**.

Kyrkjebø, R., Gabrielsen, R. H. & Faleide, J. I. (2004), 'Unconformities related to the Jurassic–Cretaceous synrift–post-rift transition of the northern North Sea', *Journal of the Geological Society* **161**, 1–17.

Lachenbruch, A. H. (1970), 'Crustal temperature and heat production: Implications of the linear heat-flow relation', *Journal of Geophysical Research* **75**, 3291–3300.

Lamb, A. L. & Ballantyne, C. K. (1998), 'Palaeonunataks and the altitude of the last ice sheet in the SW Lake District, England', *Proceedings of the Geologists' Association* **109**, 305–316.

Laslett, G. M., Green, P. F., Duddy, I. R. & Gleadow, A. J. W. (1987), 'Thermal annealing of fission tracks in apatite 2. A quantitative analysis', *Chemical Geology* **65**, 1–13.

Lawver, L. A. & Müller, R. D. (1994), 'Iceland hotspot track', *Geology* **22**, 311–314.

Le Breton, E., Cobbold, P. R. & Zanella, A. (2013), 'Cenozoic reactivation of the Great Glen Fault, Scotland: additional evidence and possible causes', *Journal of the Geological Society* **170**, 403–415.

Lee, M. K., Brown, G. C., Webb, P. C., Wheildon, J. & Rollin, K. E. (1987), 'Heat flow, heat production and thermo-tectonic setting in mainland UK', *Journal of the Geological Society* **144**, 35–42.

Lewis, C. L. E., Green, P. F., Carter, A. & Hurford, A. J. (1992), 'Elevated K/T palaeotemperatures throughout northwest England: three kilometres of Tertiary erosion?', *Earth and Planetary Science Letters* **112**, 131–145.

Lippolt, H. J., Leitz, M., Wernicke, R. S. & Hagedorn, B. (1994), '(U+Th)/He dating of apatite: Experience with samples from different geochemical environments', *Chemical Geology* **112**, 179–191.

Lister, G. S., Etheridge, M. A. & Symonds, P. A. (1991), 'Detachment models for the formation of passive continental margins', *Tectonics* **10**, 1038–1064.

Lithgow-Bertelloni, C. & Silver, P. G. (1998), 'Dynamic topography, plate driving forces and the African superswell', *Nature* **395**, 269–272.

Liu, X. & Galloway, W. E. (1997), 'Quantitative determination of Tertiary sediment supply to the North Sea Basin', *AAPG bulletin* **81**, 1482–1509.

Lovera, O. M., Richter, F. M. & Harrison, T. M. (1989), '^{40}Ar/^{39}Ar thermochronology for slowly cooled samples having a distribution of diffusion domain sizes', *Journal of Geophysical Research* **94**, 17 917–17 936.

Lucazeau, F. & Le Douaran, S. (1985), 'The blanketing effect of sediments in basins formed by extension: a numerical model. Application to the Gulf of Lion and Viking graben', *Earth and Planetary Science Letters* **74**, 92–102.

Lundin, E. R. & Doré, A. G. (1997), 'A tectonic model for the Norwegian passive margin with implications for the NE Atlantic: Early Cretaceous to break-up', *Journal of the Geological Society* **154**, 545–550.

Lundin, E. R. & Doré, A. G. (2005), NE Atlantic break-up: a re-examination of the Iceland mantle plume model and the Atlantic–Arctic linkage, *in* 'Geological Society, London, Petroleum Geology Conference series', Vol. 6, Geological Society of London, pp. 739–754.

Lundin, E. R., Doré, A. G., Rønning, K. & Kyrkjebø, R. (2013), 'Repeated inversion and collapse in the Late Cretaceous–Cenozoic northern Vøring Basin, offshore Norway', *Petroleum Geoscience* **19**, 329–341.

Maclennan, J. & Lovell, B. (2002), 'Control of regional sea level by surface uplift and subsidence caused by magmatic underplating of Earth's crust', *Geology* **30**, 675–678.

Majorowicz, J. & Grasby, S. E. (2010), 'Heat flow, depth–temperature variations and stored thermal energy for enhanced geothermal systems in Canada', *Journal of Geophysics and Engineering* **7**, 232.

Majorowicz, J. & Minea, V. (2012), 'Geothermal energy potential in the St–Lawrence River area, Québec', *Geothermics* **43**, 25–36.

Makris, J., Tsironidis, J. & Richter, H. (1991), 'Heatflow density distribution in the Red Sea', *Tectonophysics* **198**, 383–393.

Manning, D. A. C., Younger, P. L., Smith, F. W., Jones, J. M., Dufton, D. J. & Diskin, S. (2007), 'A deep geothermal exploration well at Eastgate, Weardale, UK: a novel exploration concept for low-enthalpy resources', *Journal of the Geological Society* **164**, 371–382.

Matmon, A., Simhai, O., Amit, R., Haviv, I., Porat, N., McDonald, E., Benedetti, L. & Finkel, R. (2009), 'Desert pavement—coated surfaces in extreme deserts present the longest-lived landforms on Earth', *Geological Society of America Bulletin* **121**, 688–697.

McDowell, F. W., McIntosh, W. C. & Farley, K. A. (2005), 'A precise 40Ar–39Ar reference age for the Durango apatite (U-Th)/He and fission-track dating standard', *Chemical Geology* **214**, 249–263.

McKenzie, D. (1978), 'Some remarks on the development of sedimentary basins', *Earth and Planetary science letters* **40**, 25–32.

McKenzie, D. (1984), 'A possible mechanism for epeirogenic uplift', *Nature* **307**, 616–618.

McLaren, S., Sandiford, M. & Hand, M. (1999), 'High radiogenic heat–producing granites and metamorphism—An example from the western Mount Isa inlier, Australia', *Geology* **27**, 679–682.

McLaren, S., Sandiford, M., Powell, R., Neumann, N. & Woodhead, J. (2006), 'Palaeozoic intraplate crustal anatexis in the Mount Painter Province, South Australia: timing, thermal budgets and the role of crustal heat production', *Journal of Petrology* **47**, 2281–2302.

Meesters, A. G. C. A. & Dunai, T. J. (2002a), 'Solving the production-diffusion equation for finite diffusion domains of various shapes. Part I. Implications for low-temperature (U-Th)/He thermochronology', *Chemical Geology* **186**, 333–344.

Meesters, A. G. C. A. & Dunai, T. J. (2002b), 'Solving the production-diffusion equation for finite diffusion domains of various shapes. Part II. Applications to cases with α-ejection and non-homogeneous distribution of the source', *Chemical Geology* **186**, 347–363.

Meesters, A. G. C. A. & Dunai, T. J. (2005), 'A noniterative solution of the (U-Th)/He age equation', *Geochemistry, Geophysics, Geosystems* **6**.

Mitchell, J. G. (1972), 'Potassium–argon ages from the Cheviot Hills, northern England', *Geological Magazine* **109**, 421–426.

Molnar, P. & England, P. (1990), 'Late Cenozoic uplift of mountain ranges and global climate change: chicken and egg?', *Nature* **346**, 29–34.

Moseley, F., ed. (1978), *The Geology of the Lake District*, Occasional publication no. 3, Yorkshire Geological Society. pp.284.

Mudge, D. C. (2015), 'Regional controls on Lower Tertiary sandstone distribution in the North Sea and NE Atlantic margin basins', *Geological Society, London, Special Publications* **403**, 17–42.

Nadin, E. S. & Martin, A. J. (2012), 'Apatite thermochronometry within a knickzone near the Higher Himalaya front, central Nepal: No resolvable fault motion in the past one million years', *Tectonics* **31**.

Nadin, P. A., Kusznir, N. J. & Cheadle, M. J. (1997), 'Early Tertiary plume uplift of the North Sea and Faeroe-Shetland basins', *Earth and Planetary Science Letters* **148**, 109–127.

Naeser, C. W. (1981), 'The fading of fission tracks in the geologic environment: data from deep drill holes', *Nuclear Tracks and Radiation Measurements* **5**, 248–250.

Nasdala, L., Reiners, P. W., Garver, J. I., Kennedy, A. K., Stern, R. A., Balan, E. & Wirth, R. (2004), 'Incomplete retention of radiation damage in zircon from Sri Lanka', *American Mineralogist* **89**, 219–231.

Nasdala, L., Wenzel, M., Vavra, G., Irmer, G., Wenzel, T. & Kober, B. (2001), 'Metamictisation of natural zircon: accumulation versus thermal annealing of radioactivity-induced damage', *Contributions to Mineralogy and Petrology* **141**, 125–144.

Needham, T. & Morgan, R. (1997), 'The East Irish Sea and adjacent basins: new faults or old?', *Journal of the Geological Society* **154**, 145–150.

Neumann, N., Sandiford, M. & Foden, J. (2000), 'Regional geochemistry and continental heat flow: implications for the origin of the South Australian heat flow anomaly', *Earth and Planetary Science Letters* **183**, 107–120.

Nielsen, S. B., Paulsen, G. E., Hansen, D. L., Gemmer, L., Clausen, O. R., Jacobsen, B. H., Balling, N., Huuse, M. & Gallagher, K. (2002), 'Paleocene initiation of Cenozoic uplift in Norway', *Geological Society, London, Special Publications* **196**, 45–65.

Nielsen, S. B., Stephenson, R. & Thomsen, E. (2007), 'Dynamics of Mid-Palaeocene North Atlantic rifting linked with European intra-plate deformations', *Nature* **450**, 1071–1074.

O'Connor, J. M., Stoffers, P., Wijbrans, J. R., Shannon, P. M. & Morrissey, T. (2000), 'Evidence from episodic seamount volcanism for pulsing of the Iceland plume in the past 70 Myr', *Nature* **408**, 954–958.

Osadetz, K. G., Kohn, B. P., Feinstein, S. & O'Sullivan, P. B. (2002), 'Thermal history of Canadian Williston basin from apatite fission-track thermochronology—implications for petroleum systems and geodynamic history', *Tectonophysics* **349**, 221–249.

O'Sullivan, P. B. & Parrish, R. R. (1995), 'The importance of apatite composition and single-grain ages when interpreting fission track data from plutonic rocks: a case study from the Coast Ranges, British Columbia', *Earth and Planetary Science Letters* **132**, 213–224.

Pálmason, G. (1973), 'Kinematics and heat flow in a volcanic rift zone, with application to Iceland', *Geophysical Journal International* **33**, 451–481.

Pedersen, T. (1993), 'Heat flow in rift basins above a hot asthenosphere', *Terra Nova* **5**, 144–149.

Persano, C. (2003), A combination of apatite fission track and (U-Th)/He thermochronometers to constrain the escarpment evolution in south eastern Australia: a case study of high elevation passive margins, PhD thesis, University of Glasgow.

Persano, C., Barfod, D. N., Stuart, F. M. & Bishop, P. (2007), 'Constraints on early Cenozoic underplating-driven uplift and denudation of western Scotland from low temperature thermochronometry', *Earth and Planetary Science Letters* **263**, 404–419.

Persano, C., Stuart, F. M., Bishop, P. & Barford, D. N. (2002), 'Apatite (U-Th)/He age constraints on the development of the Great Escarpment on the southeastern Australian passive margin', *Earth and Planetary Science Letters* **200**, 79–90.

Petersen, T. G., Hamann, N. E. & Stemmerik, L. (2015), 'Tectono-sedimentary evolution of the Paleogene succession offshore Northeast Greenland', *Marine and Petroleum Geology* **67**, 481–497.

Pidgeon, R. T. & Aftalion, M. (1978), Cogenetic and inherited zircon U-Pb systems in granites: Palaeozoic granites of Scotland and England, *in* 'Crustal evolution in northwestern Britain and adjacent regions', Vol. 10, Scottish Academic Press Glasgow, pp. 183–220.

Pollack, H. N. & Cercone, K. R. (1994), 'Anomalous thermal maturities caused by carbonaceous sediments', *Basin research* **6**, 47–51.

Praeg, D., Stoker, M. S., Shannon, P. M., Ceramicola, S., Hjelstuen, B., Laberg, J. S. & Mathiesen, A. (2005), 'Episodic Cenozoic tectonism and the development of the NW European 'passive' continental margin', *Marine and Petroleum Geology* **22**, 1007–1030.

Rahl, J. M., Reiners, P. W., Campbell, I. H., Nicolescu, S. & Allen, C. M. (2003), 'Combined single-grain (U-Th)/He and U/Pb dating of detrital zircons from the Navajo Sandstone, Utah', *Geology* **31**, 761–764.

Raymond, A. C. & Murchison, D. G. (1991), 'The relationship between organic maturation, the widths of thermal aureoles and the thicknesses of sills in the Midland Valley of Scotland and Northern England', *Journal of the Geological Society* **148**, 215–218.

Read, H. H. (1961), 'Aspects of Caledonian magmatism in Britain', *Geological Journal* **2**, 653–683.

Reiners, P. W. (2005), 'Zircon (U-Th)/He thermochronometry', *Reviews in Mineralogy and Geochemistry* **58**, 151–179.

Reiners, P. W. & Farley, K. A. (1999), 'Helium diffusion and (U-Th)/He thermochronometry of titanite', *Geochimica et Cosmochimica Acta* **63**, 3845–3859.

Reiners, P. W. & Farley, K. A. (2001), 'Influence of crystal size on apatite (U-Th)/He thermochronology: an example from the Bighorn Mountains, Wyoming', *Earth and Planetary Science Letters* **188**, 413–420.

Reiners, P. W., Farley, K. A. & Hickes, H. J. (2002), 'He diffusion and (U-Th)/He thermochronometry of zircon: initial results from Fish Canyon Tuff and GoldButte, Nevada', *Tectonophysics* **349**, 297–308.

Reiners, P. W. & Nicolescu, S. (2006), Measurement of parent nuclides for (U-Th)/He chronometry by solution sector ICP-MS, Technical Report Report 1, ARHDL.

Reiners, P. W., Spell, T. L., Nicolescu, S. & Zanetti, K. A. (2004), 'Zircon (U-Th)/He thermochronometry: He diffusion and comparisons with 40Ar/39Ar dating', *Geochimica et Cosmochimica Acta* **68**, 1857–1887.

Reiners, P. W., Zhou, Z., Ehlers, T. A., Xu, C., Brandon, M. T., Donelick, R. A. & Nicolescu, S. (2003), 'Post-orogenic evolution of the Dabie Shan, eastern China, from (U-Th)/He and fission-track thermochronology', *American Journal of Science* **303**, 489–518.

Robson, D. A. (1977), 'The structural history of the Cheviot and adjacent regions', *Scottish Journal of Geology* **13**, 255–262.

Rohrman, M., van der Beek, P., Andriessen, P. & Cloetingh, S. (1995), 'Meso-Cenozoic morphotectonic evolution of southern Norway: Neogene domal uplift inferred from apatite fission track thermochronology', *Tectonics* **14**, 704–718.

Rollin, K. E. (1987), Catalogue of geothermal data for the land area of the United Kingdom. Third revision: April 1987. Investigation of the Geothermal Potential of the UK, Technical report, British Geological Survey, Keyworth.

Rudge, J. F., Shaw Champion, M. E., White, N., McKenzie, D. & Lovell, B. (2008), 'A plume model of transient diachronous uplift at the Earth's surface', *Earth and Planetary Science Letters* **267**, 146–160.

Rudnick, R. L., Holland, H. D. & Turekian, K. K., eds (2005), *The Crust*, Elsevier, Amsterdam.

Rundle, C. C. (1979), 'Ordovician intrusions in the English Lake District', *Journal of the Geological Society* **136**, 29–38.

Rundle, C. C. (1981), 'The significance of isotopic dates from the English Lake District for the Ordovician–Saurian time-scale', *Journal of the Geological Society* **138**, 569–572.

Rutherford, E. (1905), 'Present problems in radioactivity', *Popular Science* **67**, l–34.

Sambridge, M. (1999a), 'Geophysical inversion with a neighbourhood algorithm—I. Searching a parameter space', *Geophysical Journal International* **138**, 479–494.

Sambridge, M. (1999b), 'Geophysical inversion with a neighbourhood algorithm—II. Appraising the ensemble', *Geophysical Journal International* **138**, 727–746.

Sandiford, M. & Hand, M. (1998), 'Australian Proterozoic high–temperature, low–pressure metamorphism in the conductive limit', *Geological Society, London, Special Publications* **138**, 109–120.

Saunders, A. D., Jones, S. M., Morgan, L. A., Pierce, K. L., Widdowson, M. & Xu, Y. G. (2007), 'Regional uplift associated with continental large igneous provinces: the roles of mantle plumes and the lithosphere', *Chemical Geology* **241**, 282–318.

Scotchman, I. C., Carr, A. D. & Parnell, J. (2006), 'Hydrocarbon generation modelling in a multiple rifted and volcanic basin: a case study in the Foinaven Sub-basin, Faroe-Shetland Basin, UK Atlantic margin', *Scottish Journal of Geology* **42**, 1–19.

Shannon, P. M. (1991), 'The development of Irish offshore sedimentary basins', *Journal of the Geological Society* **148**, 181–189.

Shaw Champion, M. E., White, N. J., Jones, S. M. & Lovell, J. P. B. (2008), 'Quantifying transient mantle convective uplift: An example from the Faroe-Shetland basin', *Tectonics* **27**(1).

Shennan, I. (1989), 'Holocene crustal movements and sea-level changes in Great Britain', *Journal of Quaternary Science* **4**, 77–89.

Shennan, I. & Horton, B. (2002), 'Holocene land-and sea-level changes in Great Britain', *Journal of Quaternary science* **17**, 511–526.

Shepherd, T., Beckinsale, R., Rundle, C. & Durham, J. (1976), 'Genesis of carrock fell tungsten deposit, cumbria: fluid inclusion and isotopic study', *Bulletin of the Institution of Mining and Metallurgy* **85**, 63–74.

Sheth, H. C. & Chandrasekharam, D. (1997), 'Early alkaline magmatism in the Deccan Traps: implications for plume incubation and lithospheric rifting', *Physics of the earth and planetary interiors* **104**, 371–376.

Shuster, D. L. & Farley, K. A. (2004), '4He/3He thermochronometry', *Earth and Planetary Science Letters* **217**, 1–17.

Shuster, D. L. & Farley, K. A. (2009), 'The influence of artificial radiation damage and thermal annealing on helium diffusion kinetics in apatite', *Geochimica et Cosmochimica Acta* **73**, 183–196.

Shuster, D. L., Flowers, R. M. & Farley, K. A. (2006), 'The influence of natural radiation damage on helium diffusion kinetics in apatite', *Earth and Planetary Science Letters* **249**, 148–161.

Silk, E. C. H. & Barnes, R. S. (1959), 'Examination of fission fragment tracks with an electron microscope', *Philosophical Magazine* **4**, 970–972.

Simms, M. J. (2000), 'The sub-basaltic surface in northeast Ireland and its significance for interpreting the Tertiary history of the region', *Proceedings of the Geologists' Association* **111**, 321–336.

Simms, M. J. (2004), 'Tortoises and hares: Dissolution, erosion and isostasy in landscape evolution', *Earth Surface Processes and Landforms* **29**, 477–494.

Simpson, F. & Warner, M. (1998), 'Coincident magnetotelluric, P-wave and S-wave images of the deep continental crust beneath the Weardale granite, NE England: seismic layering, low conductance and implications against the fluids paradigm', *Geophysical Journal International* **133**, 419–434.

Sinclair, H. D. & Tomasso, M. (2002), 'Depositional evolution of confined turbidite basins', *Journal of Sedimentary Research* **72**, 451–456.

Sleep, N. H. (1997), 'Lateral flow and ponding of starting plume material', *Journal of Geophysical Research: Solid Earth (1978–2012)* **102**, 10001–10012.

Soper, N. J., England, R. W., Snyder, D. B. & Ryan, P. D. (1992), 'The Iapetus suture zone in England, Scotland and eastern Ireland: a reconciliation of geological and deep seismic data', *Journal of the Geological Society* **149**, 697–700.

Spiegel, C., Kohn, B., Belton, D., Berner, Z. & Gleadow, A. (2009), 'Apatite (U-Th-Sm)/He thermochronology of rapidly cooled samples: the effect of He implantation', *Earth and Planetary Science Letters* **285**, 105–114.

Spiegel, C., Kohn, B. L., Raza, A., Rainer, T. & Gleadow, A. J. W. (2007), 'The effect of long-term low-temperature exposure on apatite fission track stability: a natural annealing experiment in the deep ocean', *Geochimica et Cosmochimica Acta* **71**, 4512–4537.

Stanley, C. J. & Vaughan, D. J. (1982), 'Copper, lead, zinc and cobalt mineralization in the English Lake District: classification, conditions of formation and genesis', *Journal of the Geological Society* **139**(5), 569–579.

Stein, C. A. & Stein, S. (1992), 'A model for the global variation in oceanic depth and heat flow with lithospheric age', *Nature* **359**, 123–129.

Stephenson, D. (2003), *Carboniferous and Permian igneous rocks of Great Britain, north of the Variscan Front*, Vol. 27, Joint Nature Conservation Committee.

Stockli, D. F., Farley, K. A. & Dumitru, T. A. (2000), 'Calibration of the apatite (U-Th)/He thermochronometer on an exhumed fault block, White Mountains, California', *Geology* **28**, 983–986.

Stoker, M. S., Holford, S. P., Hillis, R. R., Green, P. F. & Duddy, I. R. (2010), 'Cenozoic post-rift sedimentation off northwest Britain: Recording the detritus of episodic uplift on a passive continental margin', *Geology* **38**, 595–598.

Stone, P. & Merriman, R. J. (2004), 'Basin thermal history favours an accretionary origin for the Southern Uplands terrane, Scottish Caledonides', *Journal of the Geological Society* **161**, 829–836.

Stuart, F. M., Ellam, R. M., Harrop, P. J., Fitton, J. G. & Bell, B. R. (2000), 'Constraints on mantle plumes from the helium isotopic composition of basalts from the British Tertiary Igneous Province', *Earth and Planetary Science Letters* **177**, 273–285.

Stüwe, K. & Hintermüller, M. (2000), 'Topography and isotherms revisited: the influence of laterally migrating drainage divides', *Earth and Planetary Science Letters* **184**, 287–303.

Stüwe, K., White, L. & Brown, R. (1994), 'The influence of eroding topography on steady–state isotherms. Application to fission track analysis', *Earth and Planetary Science Letters* **124**, 63–74.

Swift, D. A., Persano, C., Stuart, F. M., Gallagher, K. & Whitham, A. (2008), 'A reassessment of the role of ice sheet glaciation in the long-term evolution of the East Greenland fjord region', *Geomorphology* **97**, 109–125.

Tagami, T. & O'Sullivan, P. B. (2005), 'Fundamentals of fission-track thermochronology', *Reviews in Mineralogy and Geochemistry* **58**, 19–47.

Tassone, D. R., Holford, S. P., Stoker, M. S., Green, P., Johnson, H., Underhill, J. R. & Hillis, R. R. (2014), 'Constraining Cenozoic exhumation in the Faroe-Shetland region using sonic transit time data', *Basin Research* **26**, 38–72.

Thomson, K., Underhill, J. R., Green, P. F., Bray, R. J. & Gibson, H. J. (1999), 'Evidence from apatite fission track analysis for the post-Devonian burial and exhumation history of the northern Highlands, Scotland', *Marine and Petroleum Geology* **16**, 27–39.

Tiley, R., McKenzie, D. & White, N. (2003), 'The elastic thickness of the British Isles', *Journal of the Geological Society* **160**, 499–502.

Tiley, R., White, N. & Al-Kindi, S. (2004), 'Linking Paleogene denudation and magmatic underplating beneath the British Isles', *Geological Magazine* **141**, 345–351.

Tomlinson, J. P., Denton, P., Maguire, P. K. H. & Booth, D. C. (2006), 'Analysis of the crustal velocity structure of the British Isles using teleseismic receiver functions', *Geophysical Journal International* **167**, 223–237.

Torsvik, T. H., Amundsen, H. E., Trønnes, R. G., Doubrovine, P. V., Gaina, C., Kusznir, N. J., Steinberger, B., Corfu, F., Ashwal, L. D., Griffin, W. L. et al. (2015), 'Continental crust beneath southeast Iceland', *Proceedings of the National Academy of Sciences* **112**, E1818–E1827.

Torsvik, T. H., Carlos, D., Mosar, J., Cocks, L. R. M. & Malme, T. N. (2002), 'Global reconstructions and North Atlantic paleogeography 440 Ma to recent', *BATLAS—Mid Norway plate reconstruction atlas with global and Atlantic perspectives* pp. 18–39.

Torsvik, T. H., Smethurst, M. A., Burke, K. & Steinberger, B. (2006), 'Large igneous provinces generated from the margins of the large low-velocity provinces in the deep mantle', *Geophysical Journal International* **167**, 1447–1460.

Tripathy-Lang, A., Hodges, K. V., Monteleone, B. D. & Soest, M. C. (2013), 'Laser (U-Th)/He thermochronology of detrital zircons as a tool for studying surface processes in modern catchments', *Journal of Geophysical Research: Earth Surface* **118**, 1333–1341.

Turcotte, D. L. & Schubert, G. (2002), *Geodynamics*, Cambridge University Press.

Valla, P. G., Herman, F., Van Der Beek, P. A. & Braun, J. (2010), 'Inversion of thermochronological age-elevation profiles to extract independent estimates of denudation and relief history-I: Theory and conceptual model', *Earth and Planetary Science Letters* **295**, 511–522.

van der Beek, P. A., Robert, X., Mugnier, J. L., Bernet, M., Huyghe, P. & Labrin, E. (2006), 'Late Miocene - Recent denudation of the central Himalaya and recycling in the foreland basin assessed by detrital apatite fission-track thermochronology of Siwalik sediments, Nepal', *Basin Research* **18**, 413–434.

Van Der Beek, P., Van Melle, J., Guillot, S., Pêcher, A., Reiners, P. W., Nicolescu, S. & Latif, M. (2009), 'Eocene Tibetan plateau remnants preserved in the northwest Himalaya', *Nature Geoscience* **2**, 364–368.

Van Hoorn, B. (1987), 'The south Celtic Sea/Bristol Channel Basin: origin, deformation and inversion history', *Tectonophysics* **137**, 309–334.

Vermeesch, P. (2008), 'Three new ways to calculate average (U-Th)/He ages', *Chemical Geology* **249**, 339–347.

Vermeesch, P. (2009), 'RadialPlotter: a Java application for fission track, luminescence and other radial plots', *Radiation Measurements* **44**, 409–410.

Vermeesch, P. (2012), 'On the visualisation of detrital age distributions', *Chemical Geology* **312**, 190–194.

Vermeesch, P., Seward, D., Latkoczy, C., Wipf, M., Günther, D. & Baur, H. (2007), 'α-Emitting mineral inclusions in apatite, their effect on (U–Th)/He ages, and how to reduce it', *Geochimica et Cosmochimica Acta* **71**, 1737–1746.

Vermeesch, P. & Tian, Y. (2014), 'Thermal history modelling: HeFTy vs. {QTQt}', *Earth-Science Reviews* **139**, 279–290.

Vernon, A. J., Van Der Beek, P. A., Sinclair, H. D., Persano, C., Foeken, J. & Stuart, F. M. (2009), 'Variable late Neogene exhumation of the central European Alps: Low-temperature thermochronology from the Aar Massif, Switzerland, and the Lepontine Dome, Italy', *Tectonics* **28**.

Wagner, G. A. & den Haute, P. V. (1992), *Fission Track Dating*, Elsevier, Amsterdam.

Warnock, A. C., Zeitler, P. K., Wolf, R. A. & Bergman, S. C. (1997), 'An evaluation of low-temperature apatite U-Th/He thermochronometry', *Geochimica et Cosmochimica Acta* **61**, 5371–5377.

Warrington, G. (1997), 'The Penarth Group-Lias Group succession (Late Triassic-Early Jurassic) in the East Irish Sea Basin and neighbouring areas: a stratigraphical review', *Geological Society, London, Special Publications* **124**, 33–46.

Wawerzinek, B., Ritter, J. R. R., Jordan, M. & Landes, M. (2008), 'An upper-mantle upwelling underneath Ireland revealed from non-linear tomography', *Geophysical Journal International* **175**, 253–268.

Webb, P. C., Lee, M. K. & Brown, G. C. (1987), 'Heat flow–heat production relationships in the UK and the vertical distribution of heat production in granite batholiths', *Geophysical Research Letters* **14**, 279–282.

Wegmann, K. W., Zurek, B. D., Regalla, C. A., Bilardello, D., Wollenberg, J. L., Kopczynski, S. E., Ziemann, J. M., Haight, S. L., Apgar, J. D., Zhao, C. et al. (2007), 'Position of the Snake River watershed divide as an indicator of geodynamic processes in the greater Yellowstone region, western North America', *Geosphere* **3**, 272–281.

Westaway, R. (2005), 'Active low-angle normal faulting in the Woodlark extensional province, Papua New Guinea: A physical model', *Tectonics* **24**.

Westaway, R. (2006), 'Investigation of coupling between surface processes and induced flow in the lower continental crust as a cause of intraplate seismicity', *Earth Surface Processes and Landforms* **31**, 1480–1509.

Westaway, R. (2009), 'Quaternary uplift of northern England', *Global and Planetary Change* **68**, 357–382.

White, N. & Lovell, B. (1997), 'Measuring the pulse of a plume with the sedimentary record', *Nature* **387**, 888–891.

White, R. & McKenzie, D. (1989), 'Magmatism at rift zones: the generation of volcanic continental margins and flood basalts', *Journal of Geophysical Research: Solid Earth (1978–2012)* **94**, 7685–7729.

Wildman, M. (2015), Reassessing the structural and geomorphic evolution of a 'classic' Atlantic type passive margin: an integrated study of the Namaqualand sector of the South African continental margin., PhD thesis, University of Glasgow.

Williamson, I. T. & Bell, B. R. (2012), 'The Staffa Lava Formation: graben-related volcanism, associated sedimentation and landscape character during the early development of the Palaeogene Mull Lava Field, NW Scotland', *Scottish Journal of Geology* **48**, 1–46.

Wolf, R. W., Farley, K. A. & Silver, L. T. (1996), 'Helium diffusion and low temperature thermochronometry of apatite', *Geochimica et Cosmochimica Acta* **60**, 4231–4240.

Woodcock, N. H. & Strachan, R. A., eds (2000), *Geological history of Britain and Ireland*, Oxford: Blackwell Science. pp.423.

Yang, Y. (2012), 'Tectonostratigraphic evolution of the northern Porcupine Basin, Irish Atlantic margin, during the Late Jurassic–Early Cretaceous, implication for a regional compressional event', *Marine and Petroleum Geology* **36**, 140–153.

Zachos, J., Pagani, M., Sloan, L., Thomas, E. & Billups, K. (2001), 'Trends, Rhythms, and Aberrations in Global Climate 65 Ma to Present', *Science* **292**, 686–693.

Zeitler, P. K., Herczig, A. L., McDougall, I. & Honda, M. (1987), 'U-Th-He dating of apatite: A potential thermochronometer', *Geochimica et Cosmochimica Acta* **51**, 2865–2868.

Zhang, Y. K. (1993), 'The thermal blanketing effect of sediments on the rate and amount of subsidence in sedimentary basins formed by extension', *Tectonophysics* **218**(4), 297–308.

Ziegler, P. A. (1988), 'Evolution of the Arctic–North Atlantic and the Western Tethys—a visual presentation of a series of paleogeographic-paleotectonic maps', *AAPG memoir* **43**, 164–196.

Ziegler, P. A. (1990), 'Collision related intra-plate compression deformations in Western and Central Europe', *Journal of Geodynamics* **11**, 357–388.

Ziegler, P. A. (1992), 'North Sea rift system', *Tectonophysics* **208**, 55–75.